frontiers | Research Topics

Exploring the key targets and compounds that manipulate brain neurocircuits against mental disorders and psychiatric, volume II

Edited by
Weijie Xie, Zezhi Li, Yuan Li, Song Zhang, Dereje Kebebe Borga and Yuwei Wang

Published in
Frontiers in Pharmacology
Frontiers in Neuroscience

ISSN 1664-8714
ISBN 978-2-8325-6640-4
DOI 10.3389/978-2-8325-6640-4

Generative AI statement
Any alternative text (Alt text) provided alongside figures in the articles in this ebook has been generated by Frontiers with the support of artificial intelligence and reasonable efforts have been made to ensure accuracy, including review by the authors wherever possible. If you identify any issues, please contact us.

About Frontiers

Frontiers is more than just an open access publisher of scholarly articles: it is a pioneering approach to the world of academia, radically improving the way scholarly research is managed. The grand vision of Frontiers is a world where all people have an equal opportunity to seek, share and generate knowledge. Frontiers provides immediate and permanent online open access to all its publications, but this alone is not enough to realize our grand goals.

Frontiers journal series

The Frontiers journal series is a multi-tier and interdisciplinary set of open-access, online journals, promising a paradigm shift from the current review, selection and dissemination processes in academic publishing. All Frontiers journals are driven by researchers for researchers; therefore, they constitute a service to the scholarly community. At the same time, the *Frontiers journal series* operates on a revolutionary invention, the tiered publishing system, initially addressing specific communities of scholars, and gradually climbing up to broader public understanding, thus serving the interests of the lay society, too.

Dedication to quality

Each Frontiers article is a landmark of the highest quality, thanks to genuinely collaborative interactions between authors and review editors, who include some of the world's best academicians. Research must be certified by peers before entering a stream of knowledge that may eventually reach the public - and shape society; therefore, Frontiers only applies the most rigorous and unbiased reviews. Frontiers revolutionizes research publishing by freely delivering the most outstanding research, evaluated with no bias from both the academic and social point of view. By applying the most advanced information technologies, Frontiers is catapulting scholarly publishing into a new generation.

What are Frontiers Research Topics?

Frontiers Research Topics are very popular trademarks of the *Frontiers journals series*: they are collections of at least ten articles, all centered on a particular subject. With their unique mix of varied contributions from Original Research to Review Articles, Frontiers Research Topics unify the most influential researchers, the latest key findings and historical advances in a hot research area.

Find out more on how to host your own Frontiers Research Topic or contribute to one as an author by contacting the Frontiers editorial office: frontiersin.org/about/contact

Exploring the key targets and compounds that manipulate brain neurocircuits against mental disorders and psychiatric, volume II

Topic editors

Weijie Xie — Tongji University, China
Zezhi Li — Guangzhou Medical University, China
Yuan Li — Shanghai Jiao Tong University, China
Song Zhang — Shanghai Jiao Tong University, China
Dereje Kebebe Borga — Jimma University, Ethiopia
Yuwei Wang — SingHealth, Singapore

Citation

Xie, W., Li, Z., Li, Y., Zhang, S., Borga, D. K., Wang, Y., eds. (2025). *Exploring the key targets and compounds that manipulate brain neurocircuits against mental disorders and psychiatric, volume II*. Lausanne: Frontiers Media SA.
doi: 10.3389/978-2-8325-6640-4

Table of contents

frontiers | Frontiers in Pharmacology

TYPE Editorial
PUBLISHED 14 April 2025
DOI 10.3389/fphar.2025.1601881

OPEN ACCESS

EDITED AND REVIEWED BY
Nicholas M. Barnes,
University of Birmingham, United Kingdom

*CORRESPONDENCE
Song Zhang,
zhangsong1031@163.com

†These authors have contributed equally to this work

RECEIVED 28 March 2025
ACCEPTED 01 April 2025
PUBLISHED 14 April 2025

CITATION
Xie W, Li Y and Zhang S (2025) Editorial: Exploring the key targets and compounds that manipulate brain neurocircuits against mental disorders and psychiatric volume II. *Front. Pharmacol.* 16:1601881. doi: 10.3389/fphar.2025.1601881

Editorial: Exploring the key targets and compounds that manipulate brain neurocircuits against mental disorders and psychiatric volume II

Weijie Xie[1,2†], Yuan Li[2†] and Song Zhang[3*]

[1]Shanghai Pudong New Area Mental Health Center, Tongji University School of Medicine, Shanghai, China, [2]Shanghai Key Laboratory of Psychotic Disorders, Brain Health Institute, National Center for Mental Disorders, Shanghai Mental Health Center, Shanghai Jiaotong University School of Medicine, Shanghai, China, [3]Department of Anesthesiology, Renji Hospital, School of Medicine, Shanghai Jiao Tong University, Shanghai, China

KEYWORDS

neurophamacology, neurocircuit, brain network, molecular target, compoud

Editorial on the Research Topic
Exploring the key targets and compounds that manipulate brain neurocircuits against mental disorders and psychiatric volume II

Introduction

More than 970 million people worldwide suffer from mental disorders, which remain a major cause of disability despite advancements in pharmacological treatments (Chen et al., 2025; Syed et al., 2025). Understanding and treating mental disorders involves comprehending the complex interactions between molecular mechanisms, neural circuits, and behavioral outcomes. This Research Topic "*Exploring the Key Targets and Compounds that Manipulate Brain Neurocircuits Against Mental Disorders and Psychiatric Diseases Volume II*", compiles 12 innovative studies that collectively advance our knowledge of neurocircuit modulation through diverse pharmacological, genetic, and systems-level approaches. These contributions highlight emerging therapeutic strategies, mechanistic insights, and technological advancements, offering a roadmap for future breakthroughs in psychiatry and neuropharmacology.

Targeting neuroinflammation and oxidative stress

Neuroinflammation and oxidative stress are pivotal contributors to neurodegenerative and psychiatric disorders. Two studies exemplify how novel compounds can mitigate these processes. Hou et al. synthesized 2H-1,4-benzoxazin-3(4H)-one derivatives fused with 1,2,3-triazole, demonstrating potent anti-inflammatory effects in LPS-stimulated microglia. These compounds suppressed pro-inflammatory cytokines (IL-1β, IL-6, TNF-α) and

activated the Nrf2-HO-1 pathway, underscoring their dual antioxidant and anti-inflammatory potential. Similarly, Lai et al. revealed that (+)-catechin alleviates corticosterone-induced oxidative stress and pyroptosis in PC12 cells by activating PI3K/AKT and Nrf2/HO-1/NF-κB pathways. Both studies emphasize the therapeutic promise of targeting oxidative-inflammatory cascades, particularly through Nrf2 activation, to preserve neuronal integrity.

Advancing neuroimaging and neurogenesis research

Cutting-edge neuroimaging techniques continue to unravel how neuromodulators and disease states reshape brain networks. Hagan et al. demonstrated that intranasal oxytocin enhances small-world topology in resting-state networks, particularly in regions governing social cognition. This suggests oxytocin's therapeutic potential lies in optimizing information flow within critical circuits. Complementing this, Liu et al. employed bibliometric analysis to identify adult hippocampal neurogenesis (AHN) as a hotspot, linking its dysfunction to Alzheimer's disease and anxiety. Meanwhile, Che et al. used ^{1}H-MRS to correlate hippocampal metabolite ratios with cognitive decline in general paresis patients, highlighting neuroimaging's role in tracking neurodegeneration. Together, these studies illustrate how multimodal imaging and meta-analyses can bridge molecular changes to brain neurocircuit-level dysfunctions.

Pharmacological interventions: efficacy and metabolic challenges

The efficacy and side effects of psychotropic drugs remain central to clinical psychiatry. Zhao et al. compared five antidepressants in cancer patients, revealing escitalopram, duloxetine, and vortioxetine as superior to sertraline, with trazodone augmentation enhancing outcomes. However, metabolic side effects of antipsychotics, such as olanzapine-induced weight gain, pose significant challenges. Huang et al. identified lipid metabolism dysregulation in the lateral septum as a key driver of olanzapine's adverse effects, implicating APOA1/APOC3/APOH genes. Conversely, Zhang et al. demonstrated that the α_2-adrenoceptor agonist dexmedetomidine alleviates pain by restoring neuronal metabolism and spinal perfusion, suggesting metabolic modulation as a dual therapeutic strategy. These findings underscore the need for precision medicine to balance efficacy and safety.

Unraveling genetic and molecular mechanisms

Genetic variants and molecular pathways underlying neurodevelopmental and neurodegenerative disorders are increasingly elucidated. Xue et al. linked a novel FLNA frameshift variant to periventricular nodular heterotopia, showing disrupted F-actin organization in patient-derived iPSCs. Similarly, Guo et al. implicated EphrinB2/EphB2 signaling in maternal separation-induced visceral hyperalgesia, where spinal glia-neuron crosstalk drives pain sensitization. Multi-omics approaches further illuminated peripheral biomarkers in multiple sclerosis, with B-cell expansion and reduced sphingolipids distinguishing subtypes (Zhou et al.). These studies demonstrate how genetic, cellular, and omics tools can unravel the mechanisms of disease and pinpoint potential therapeutic targets.

Neuroprotection and mitochondrial dynamics

Mitochondrial dysfunction is a common thread in brain injury and neurodegeneration. Zhu et al. demonstrated that Dl-3-n-butylphthalide (NBP) mitigates cerebral ischemia/reperfusion injury by enhancing mitochondrial fusion via AMPK/Mfn1 activation. This aligns with broader efforts to harness mitochondrial dynamics as a neuroprotective strategy, providing hope for stroke and related disorders.

Conclusion and future prospects

This Research Topic underscores the complexity of mental disorders and the need for interdisciplinary approaches, including multi-target therapies (e.g., Nrf2 activators, PI3K/AKT enhancers), precision neuroimaging, genetic and omics-driven insights, and mitigating drug side effects. Future research should prioritize translational studies bridging preclinical findings to clinical trials, leveraging emerging technologies like single-cell omics and AI-driven drug discovery. By integrating these avenues, we advance our understanding and ability to manipulate the neural circuits related to mental health, ultimately aiming to apply these advancements in clinical settings.

Author contributions

WX: Conceptualization, Writing – original draft, Writing – review and editing, Funding acquisition. YL: Conceptualization, Writing – review and editing, Writing – original draft. SZ: Funding acquisition, Conceptualization, Writing – review and editing, Writing – original draft.

Funding

The author(s) declare that financial support was received for the research and/or publication of this article. This work was funded by the National Natural Science Foundation of China (82101622, W-J X., 82371536, SZ), the New Quality Clinical Specialty Program of High-end Medical Disciplinary Construction in Shanghai Pudong New Area (2025-PWXZ-08) and The Outstanding Leaders Training Program of Shanghai Pudong New Area Health Commission (PWRl 2024-06) and Tongji University Medicine-X Interdisciplinary Research Initiative (2025-0708-ZD-03).

Acknowledgments

This Editorial summarizes the main findings from the 12 articles in this Research Topic, highlighting the collaborative efforts aimed at advancing neuropsychiatric research. We extend our gratitude to all contributors and reviewers for their invaluable insights.

Conflict of interest

The authors declare that the research was conducted in the absence of any commercial or financial relationships that could be construed as a potential conflict of interest.

Generative AI statement

The author(s) declare that no Generative AI was used in the creation of this manuscript.

Publisher's note

References

Chen, D., Momen, N. C., Ejlskov, L., Bødkergaard, K., Werenberg Dreier, J., Sørensen, H. T., et al. (2025). Socioeconomic inequalities in mortality associated with mental disorders: a population-based cohort study. *World Psychiatry* 24 (1), 92–102. doi:10.1002/wps.21278

Syed, S., Howe, L. D., Lacey, R. E., Deighton, J., Qummer Ul Arfeen, M., Feder, G., et al. (2025). Adverse childhood experiences in firstborns and mental health risk and health-care use in siblings: a population-based birth cohort study of half a million children in England. *Lancet Public Health* 10 (2), e111–e123. doi:10.1016/S2468-2667(24)00301-3

frontiers | Frontiers in Pharmacology

TYPE Original Research
PUBLISHED 22 February 2024
DOI 10.3389/fphar.2024.1357953

OPEN ACCESS

EDITED BY
Yuan Li,
Shanghai Jiao Tong University, China

REVIEWED BY
Wen Wang,
Capital Medical University, China
Cong Liu,
Oujiang Laboratory (Zhejiang Lab for Regenerative Medicine, Vision and Brain Health), China

*CORRESPONDENCE
Qi Wan,
qiwan1@hotmail.com

†These authors have contributed equally to this work

RECEIVED 19 December 2023
ACCEPTED 09 February 2024
PUBLISHED 22 February 2024

CITATION
Zhu T, Dong S, Qin N, Liu R, Shi L and Wan Q (2024), Dl-3-n-butylphthalide attenuates cerebral ischemia/reperfusion injury in mice through AMPK-mediated mitochondrial fusion. *Front. Pharmacol.* 15:1357953.
doi: 10.3389/fphar.2024.1357953

Dl-3-n-butylphthalide attenuates cerebral ischemia/reperfusion injury in mice through AMPK-mediated mitochondrial fusion

Ting Zhu[1†], Shanshan Dong[1,2†], Na Qin[1], Rujuan Liu[1,2], Liuliu Shi[1,3] and Qi Wan[1*]

[1]Department of Pathophysiology, Institute of Neuroregeneration & Neurorehabilitation, School of Basic Medicine, Qingdao University, Qingdao, China, [2]Department of Rehabilitation Medicine, The Affiliated Hospital of Qingdao University, Qingdao, China, [3]Department of Neurosurgery, The Affiliated Hospital of Qingdao University, Qingdao, China

Introduction: NBP is a compound isolated from celery seeds, which was approved by the National Medical Products Administration in 2002 for clinical treatment of ischemic stroke. However, in brain ischemia/reperfusion (I/R) injury, the related research on mitochondrial dynamics and its mechanism of action of NBP still need to be further studied. The aim of this study was to assess NBP on cerebral pathology in ischemic stroke *in vivo*, with a specific focus on the molecular mechanisms of how NBP promotes mitochondrial fusion.

Methods: Male C57BL/6 mice were utilized in this study and were subjected to middle cerebral artery occlusion/reperfusion (MCAO/R). Pre-ischemia, NBP was administered through intraperitoneal (i.p.) injection for 7 days.

Results: Our findings demonstrated that NBP effectively reduced infarct volume, improved neurological dysfunction, enhanced cerebral blood flow, and promoted mitochondrial fusion in mice subjected to MCAO/R. More importantly, the pro-fusion effects of NBP were found to be linked to the activation of AMPK/Mfn1 pathway, and with the activation of neurological function, which was partially eliminated by inhibitors of AMPK.

Discussion: Our results revealed that NBP is a novel mitochondrial fusion promoter in protecting against ischemic stroke through the AMPK-mediated Mfn1. These findings contribute to the understanding of novel mechanisms involved in the protection of neurological function following NBP treatment for ischemic stroke.

KEYWORDS

ischemic stroke, Dl-3-n-butylphthalide, mitochondrial fusion, AMPK, Mfn1

Introduction

Stroke, a disease characterized by a substantial disability rate and elevated mortality rate, has emerged as a prominent contributor to global mortality rates in recent times, with ischemic stroke (IS) being the prevailing subtype (Wang et al., 2021; Xie et al., 2024). According to the latest epidemiological survey results, there are about

2.4 million new stroke patients in China every year, most of whom will be left with varying degrees of neurological dysfunction, which brings a serious burden to patients, families and society (Zhu et al., 2024). In recent years, extensive research has been conducted on the pathological mechanisms underlying brain ischemia/reperfusion (I/R) injury, including the excessive production of reactive oxygen species (ROS), disturbances in calcium ion (Ca^{2+}) homeostasis, excitotoxic effects, apoptosis, and mitophagy. Notably, Ca^{2+} overload and ROS burst manifest in the initial phase of neuronal injury, leading to various modes of cell death, such as apoptosis and autophagy. The management of cerebral I/R injury continues to pose significant clinical difficulties, necessitating the identification of precise therapeutic targets for improved treatment outcomes and prognoses.

The dynamics of mitochondrial fusion and fission have a significant correlation with the onset and progression of cerebral I/R injury. While inhibiting excessive mitochondrial fission has proven advantageous for various diseases, it can have detrimental effects on the integrity of mitochondrial DNA (mtDNA) and respiratory complexes during cerebral I/R injury (Yang et al., 2021). Concurrently, mitochondrial fusion plays a crucial role in maintaining mitochondrial health. This process involves several proteins, including three membrane GTPases: mitofusin 1 (Mfn1), mitofusin 2 (Mfn2), and optic atrophy protein 1 (Opa1) (Wu et al., 2021). The process of mitochondrial fusion serves to enhance oxidative phosphorylation and facilitate the redistribution of mitochondrial DNA within both impaired and intact mitochondria (Huang et al., 2023). By increasing the expression of fusion-related proteins, the promotion of mitochondrial fusion effectively mitigates cerebral ischemic injury without compromising overall mitochondrial quantity in the basal brain. Consequently, this approach proves to be a safer alternative to inhibiting mitochondrial fission. Therefore, the identification and development of efficacious therapeutic medications that target the promotion of mitochondrial fusion hold substantial importance in the realm of ischemic stroke treatment.

NBP, a compound derived from celery seeds, was officially sanctioned by the National Medical Products Administration in 2002 for the therapeutic management of ischemic stroke (Wang S. et al., 2018). Extensive research has demonstrated the potential of NBP to enhance neurological recuperation in individuals suffering from acute stroke-induced disability (Wang S. et al., 2018), vascular dementia (Huang et al., 2017) and Alzheimer's disease (Wang et al., 2019). The protective effects of NBP in ischemic stroke are believed to be attributed to its ability to ameliorate local microcirculation, suppress neuronal apoptosis, and mitigate neuroinflammation (Zhang et al., 2018; Wei et al., 2021). Recent studies have shown that NBP significantly alleviates demyelinating in white matter lesion models by promoting mitochondrial dynamics and improves spatial learning and memory in mice (Feng et al., 2021). However, in cerebral I/R injury, the related research on mitochondrial dynamics and its mechanism of action of NBP still need to be further studied. We investigated the effects of NBP on cerebral pathology in ischemic stroke *in vivo*, focusing on the molecular mechanisms by which NBP promotes mitochondrial fusion. Our results have revealed that NBP is a novel mitochondrial fusion promoter in protecting against ischemic stroke through the AMPK-mediated Mfn1.

Methods

Animals

All animal care and experimental procedures were approved by the Institutional Animal Care guidelines and the Animal Care and Ethics Committee of Qingdao University. C57BL/6 male mice (approval codes: QDU-AEC-2021101) weighing 20–25 g were purchased from Jinan Pengyue Experimental Animals Breeding Co., Ltd., were housed with a 12-hour light/dark cycle, with free access to food and water, at a temperature of 20°C–25°C and humidity of 50%–60%. The mice were given at least 3 days to get used to the new environment before being used in experiments. Every effort was made to minimize the number of mice used and minimize suffering.

MCAO surgery

Following a 7-day injection period with either 20 mg kg^{-1} NBP or 0.9% normal saline, C57BL/6 mice were subjected to anesthesia using 3.5% isoflurane, with maintenance at 1.5% isoflurane throughout the MCAO surgery. To ensure a stable body temperature of 37°C, a heating pad was utilized. Under sterile conditions, a midline incision was made to expose the right neck vessels, allowing for discrete isolation of the right common carotid artery (CCA), external carotid artery (ECA), and internal carotid artery (ICA). The monofilament suture should be carefully inserted from the lumen of the CCA into the ICA, extending approximately 9–10 mm beyond the bifurcation of the CCA to effectively occlude the origin of the MCA. Following this, the incision on the neck should be sutured, and the mouse should be placed in a nursing box maintained at a temperature of 37°C ± 0.5°C. After a period of 1.5 h of arterial occlusion, the filament should be withdrawn to allow for blood reperfusion. In the case of Sham-operated control mice, the same procedure should be followed, with the exception of filament insertion.

In vivo drug treatment

NBP (obtained from CSPC NBP Pharmaceutical Co., Ltd) was dissolved in 0.9% normal saline prior to administration. All mice were randomly divided into three groups, as followed: Sham group, MCAO/R group, and NBP group. For drug administration, NBP (20 mg kg^{-1}) or 0.9% saline was given every day to continuous intraperitoneal injection for 7 days prior to MCAO surgery. To further estimate the neuroprotective effect of NBP, 24 h after MCAO/R, mice were measured for cerebral blood flow, neurological deficits score, and grasp strength test, after which mice were sacrificed for TTC, Western blotting, Cresyl violet staining, and immunofluorescence.

Cerebral blood flow

The laser speckle blood monitor manufactured by PERIMED in Sweden was employed for the purpose of conducting laser scatter imaging on the brains of mice. Following a 24-hour period of blood reperfusion, the mice were subjected to anesthesia. Subsequently, an incision was made in the center of the mice's scalp to expose the skull,

and the laser speckle imaging procedure was carried out using the imager positioned directly above the skull.

Grip-strength test

A grip force meter (HUAYON, China) was used to assess grip strength of mice. At 24 h after reperfusion, the mice were tested for grip strength. Mice were held by their tails and placed on the device, the mice were then gently pulled backward until loss of grip. Every mouse was tested for three times and calculate the mean of three measurements for each animal.

TTC staining

At 24 h post-reperfusion, the infarct volume following MCAO was quantified using a solution of 2,3,5-triphenyltetrazolium chloride (TTC). The brain tissue was uniformly sectioned into six coronal slices, which were then incubated with a 2% TTC solution at 37°C for 15 min in the absence of light. Subsequently, the slices were fixed in 4% paraformaldehyde (PFA) at 4°C overnight. The normal tissue exhibited a deep red stain, while the infarcted region appeared white. To determine the infarct volume, TTC-stained sections were captured using photography, and the resulting images were subjected to analysis using ImageJ software.

Nissl staining

Frozen sections of brain tissue were fixed with 4% paraformaldehyde for 15 min and washed three times with PBS. Cresyl Violet Staining (Solarbio, China) was added to brain slices and incubated at 55°C for 1 h. Wash off the excess staining and differentiate by Nissl differentiation solution for a few seconds until the background is nearly colorless. Seal with glycerin jelly mounting medium and photographed with upright microscope (Nikon, Japan) and analyzed with ImageJ.

TUNEL staining

One Step TUNEL Apoptosis Assay Kit purchased from Beyotime was used to detect apoptotic cells. First, frozen sections of brain tissue were fixed with 4% paraformaldehyde for 30 min. Then, PBS wash three times, 5 min each time. Block with 10% goat serum and 0.3% Triton X-100 for 1 h. The block buffer was discarded, and appropriate amount of TUNEL detection solution (TdT enzyme: fluorescent labeling solution = 1: 9) was added, and incubated at 37°C for 1 h without light. Discard the detection solution, wash three times with PBS, and seal the tablet with a sealing solution containing DAPI. The results were taken by fluorescence microscope and analyzed by ImageJ.

Transmission electron microscope (TEM)

After 24 h of the reperfusion, 1-cubic mm of fresh brain tissue was taken and rapidly immersed into the Glutaraldehyde at 4°C for 2–4 h. The tissue was rinsed with 0.1 M phosphate buffer 3 times, 15 min each time. The tissue was fixed with 1% osmic acid at room temperature for 2 h, and washed with 0.1 M phosphate buffer 3 times, 15 min each time. After gradient dehydration, infiltration and embedding, the tissue was cut into ultrathin slices of 60–80 nm. The sections were stained with 2% uranium acetate and lead citrate for 15 min, and then the sections were dried overnight. Then the samples were observed under a TEM, and images were collected and analyzed.

Western blotting

The cerebral ischemic cortex was homogenized in RIPA buffer. The homogenized protein was centrifuged at high speed, then the supernatant was extracted and the precipitation was discarded. Then the total protein concentration was determined with the BCA kit. 20 μg total protein samples from cortex were separated using SDS-PAGE and transferred to a PVDF membrane. The membranes were blocked using blocking solution (5% non-fat milk in TBST, pH 7.4) at room temperature for 60 min. Discard blocking solution and incubation with the primary antibody overnight at 4°C. Primary antibodies included: Opa1 (1:2000, Proteintech), Mfn1 (1: 2000, Proteintech), Mfn2 (1: 2000, Proteintech) and β-actin (1: 5000, Proteintech), AMPK (1:4000, Abclonal), pAMPK (1:5000, Abclonal), NDUFB8 (1:500, Abclonal), SDHB (1:500, Abclonal), UQCRC2 (1:500, Abclonal), MTCO2 (1:500, Abclonal), ATP5A1 (1: 500, Abclonal). The following day, membranes were washed with TBST (10 min × 3) each time and subsequently incubated with secondary antibodies (1: 8000) for 2 h at room temperature. Membranes were then washed three times with TBST (10 min × 3). Protein expression was examined by using Chemiluminescent HRP Substrate (Millipore) and Cytiva. Densitometric values was quantified with ImageJ and were normalized with respect to β-actin immunoreactivity to correct for any loading and transfer differences among samples.

Prediction of NBP targets and molecular docking

The SDF file of NBP was acquired from PubChem (https://pubchem.ncbi.nlm.nih.gov/compound/11092), and the PharmMapper Server (http://www.lilab-ecust.cn/pharmmapper/) was employed using the "All Targets" model to forecast the potential targets. The procedure was documented with a submission ID. Autodock Vina 1.1.2 was utilized to assess the binding affinity and binding sites between NBP and AMPK. The structures of NBP were obtained from the PubChem database, while the AMPK structure was obtained through the QuickPrep procedure.

Drug affinity responsive target stability (DARTS)

The tissue lysates were diluted to achieve a uniform final volume. Subsequently, they were incubated with NBP at concentrations of 1, 2, 4, and 8 mg/mL for a duration of 1.5 h, while being gently agitated

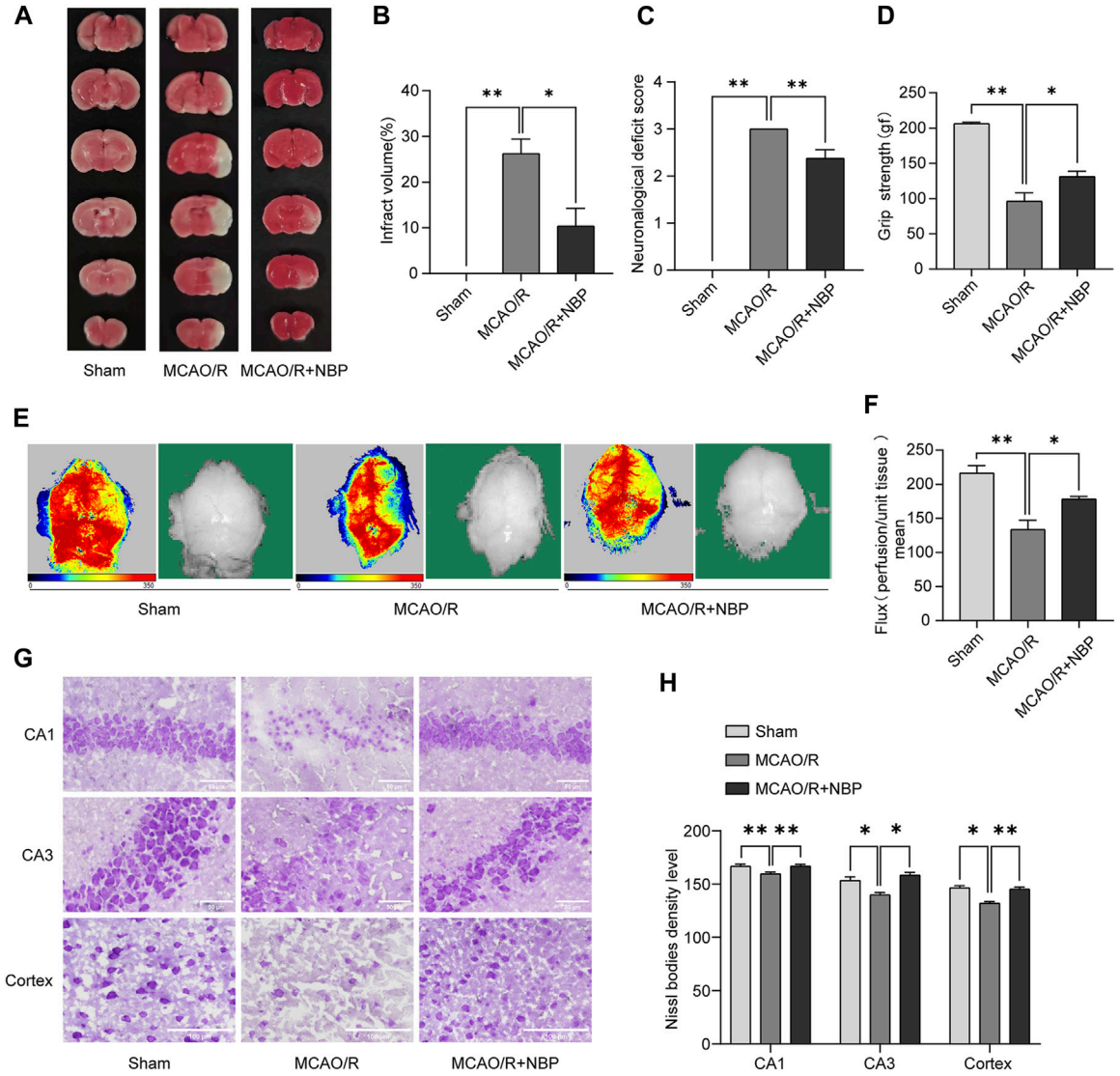

FIGURE 1
NBP alleviated infarction volume, neuronal loss, and facilitated restoration of cerebral blood flow in mice subjected to MCAO. NBP was intraperitoneally injected for 7 days before MCAO surgery. **(A)** Effects of NBP on infarction volumes. **(B)** Quantitative analysis of infarct volumes (n = 5). **(C)** Longa score in mice with MCAO/R at 24 h after reperfusion (n = 8). **(D)** Grasping ability test in mice with MCAO/R at 24 h after reperfusion (n = 6–9). **(E)** The images of cerebral blood flow of cortex. The magnitude of cerebral blood flow is represented by different colors, with blue to red indicating low to high. **(F)** Quantitative analysis of cerebral blood flow in different groups (n = 6). **(G)** Nissl staining of the hippocampal and cortex regions of each group (n = 3–4). **(H)** Nissl bodies density level in hippocampal CA1, CA3 and cortex regions in all the groups. Scale bar = 50 μm in hippocampal region, scale bar = 100 μm in cortex region. Data are expressed as the mean ± SEM and were analyzed by ANOVA, $^{*}p < 0.05$ and $^{**}p < 0.01$.

on a shaker. Following this, the samples were subjected to a reaction with protease at a concentration of 2 μg/mL in a reaction buffer for a period of 10 min. Subsequently, the loading buffer was introduced, and the p-AMPK protein was analyzed through Western blotting.

Statistical analysis

Experimental data were collected from three independent experiments and are expressed as the means ± standard errors (SEMs). All analyses were statistically evaluated using SPSS17 software (IBM Corporation, New York, NY, USA). Group differences after significant ANOVAs were measured by *post hoc* Bonferroni test. A p-value of less than 0.05 was considered statistically significant.

Results

NBP reduced cerebral infarction volume, improved neurological dysfunction, and increased cerebral blood flow in MCAO/R-induced mice

TTC staining and neurologic deficit test were conducted to evaluate the extent of infarct volume and neurological function

10.3389/fphar.2024.1357953

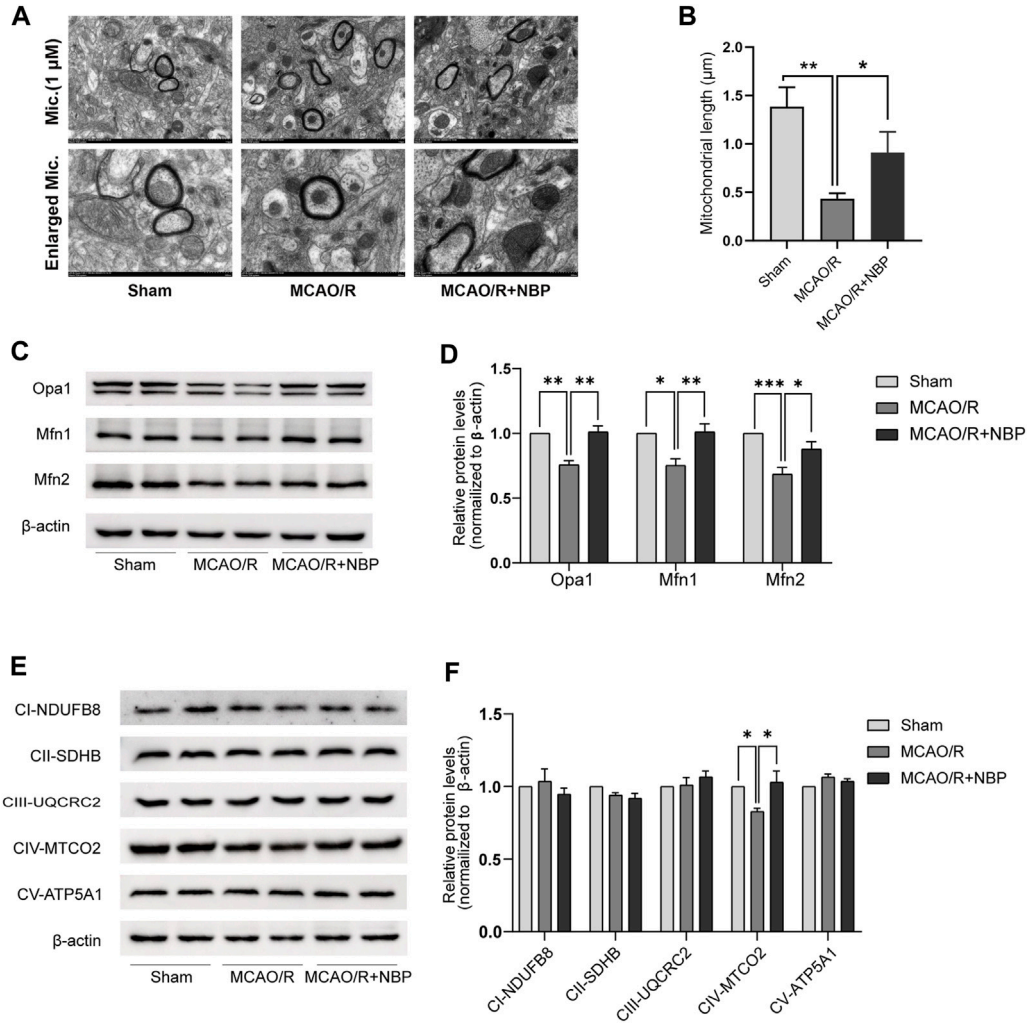

FIGURE 2
NBP promoted mitochondrial fusion and restored mitochondrial function in mice subjected to MCAO. **(A)** Mitochondrial morphology was observed by TEM. Scale bars = 500 nm. **(B)** Quantification of mean mitochondrial length. **(C, D)** Representative blots and quantitative analysis of mitochondrial fusion-related proteins including Opa1, Mfn1, and Mfn2 (n = 6). **(E, F)** Representative blots and quantitative analysis of mitochondrial respiratory chain complex I–V (CI–V) (n = 6). Data are expressed as the mean ± SEM and were analyzed by ANOVA, $^{*}p < 0.05$, $^{**}p < 0.01$ and $^{***}p < 0.001$.

24 h post-reperfusion. As illustrated in Figures 1A, B, the mice subjected to MCAO/R treatment exhibited a distinct demarcation of infarction within the cerebral infarction core and penumbra. Notably, the administration of NBP significantly reduced the infarct volume in comparison to the MCAO/R group. Figures 1C, D also showed that treatment with NBP could improve the neurological deficits after I/R injury in mice.

Cerebral blood flow in mice was evaluated by Laser Doppler blood flow. As shown in Figures 1E, F, the groups pretreated with 20 mg kg^{-1} NBP for 7 days showed significantly increased cerebral blood flow compared to the MCAO/R group.

NBP inhibited neuronal loss in MCAO/R-induced mice

As shown in Figures 1G, H, the Nissl staining analysis revealed that most neurons in the hippocampal CA1, CA3 and cortex regions in the MCAO/R group exhibited a shrunken phenotype, weak staining and were distributed irregularly. This observation indicated that neurons were predominantly deteriorated and that many Nissl bodies were lost in these neurons. Conversely, the administration of NBP for a duration of 7 days before MCAO surgery resulted in strong staining and a well-organized arrangement of neurons in the hippocampal CA1, CA3 and cortex regions, in comparison to the MCAO/R group.

NBP promoted mitochondrial fusion in MCAO/R-induced mice

The evaluation of mitochondrial fusion involved the determination of mitochondrial size. In comparison to the Sham group, the MCAO/R-induced brains exhibited a shorter mean mitochondrial length (Figure 2A). Notably, NBP

10.3389/fphar.2024.1357953

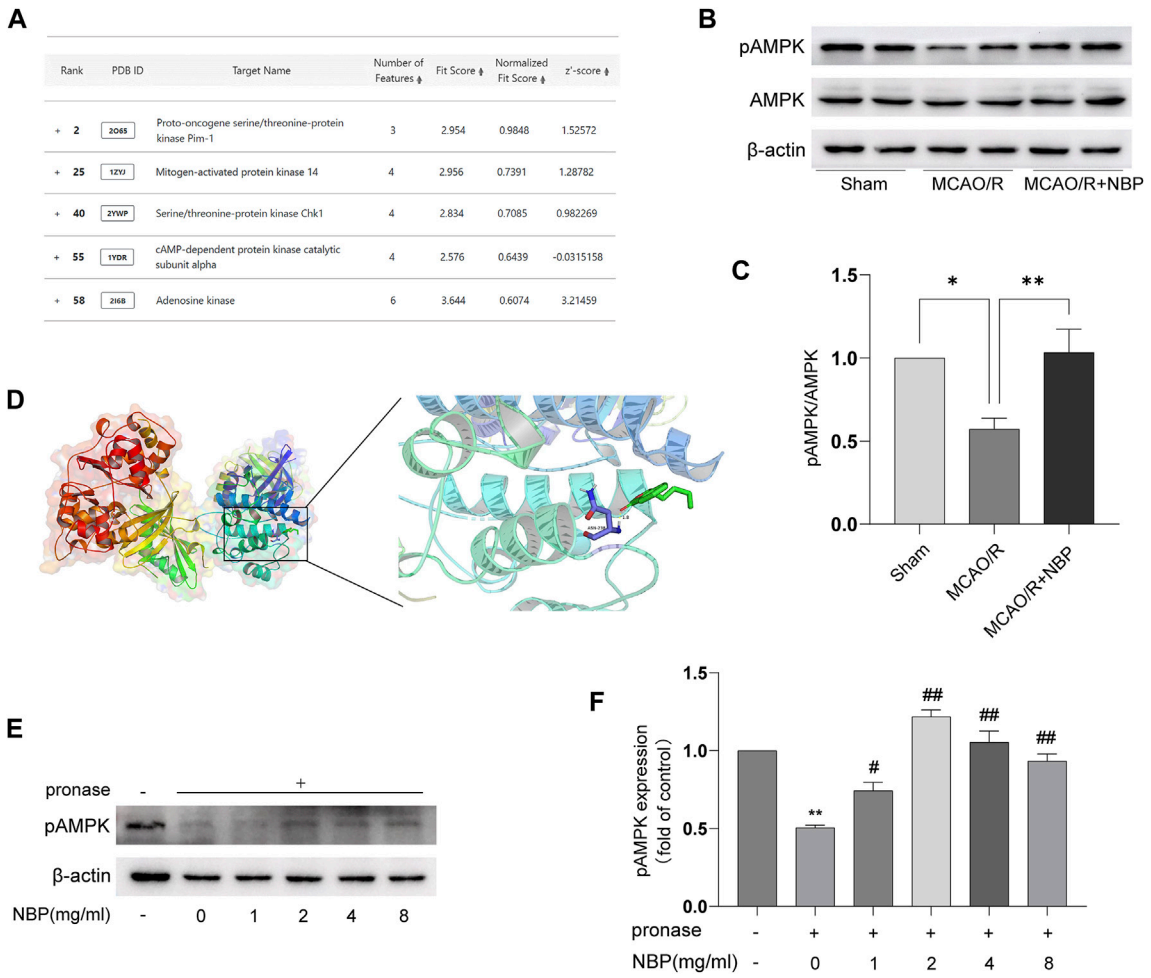

FIGURE 3
NBP directly binds to AMPK proteins. **(A)** Listing of potential candidates involved in kinase activity. Representative blots **(B)** and quantitative analysis **(C)** of pAMPK/AMPK (n = 6). **(D)** Docking analysis of NBP covalent binding mode to pAMPK. **(E, F)** NBP promoted pAMPK resistance to proteases by analyzing DARTS.

pretreatment promoted mitochondrial fusion in MCAO/R-induced brains, as reflected by the increased mean mitochondrial length (Figure 2B).

Subsequently, an examination was conducted on the expression patterns of mitochondrial fission proteins (Opa1, Mfn1, and Mfn2) as well as mitochondrial respiratory chain complex I–V. It was observed that the levels of Opa1, Mfn1, and Mfn2, which are fusion proteins associated with mitochondria, were notably diminished in the tissues of mice induced with MCAO/R. However, the administration of NBP effectively reversed the decline in protein expression of Opa1, Mfn1, and Mfn2 in the brain tissues affected by MCAO/R, as depicted in Figures 2C, D. The expression of mitochondrial complexes IV was significantly diminished in the brain tissues induced by MCAO/R, among the mitochondrial respiratory chain complex I-V. However, this reduction was partially reversed by pretreatment with NBP, as evidenced by Figures 2E, F. Collectively, these findings suggest that NBP pretreatment enhances mitochondrial fusion and improves mitochondrial function in the context of cerebral I/R in mice.

NBP activated AMPK following cerebral I/R injury

NBP has a small molecular weight, is highly fat-soluble, and easily passes through the blood-brain barrier. It is postulated that NBP has the capability to penetrate the cell membrane and directly interact with specific adaptor molecules. In order to identify the precise target of NBP, the structural data of SDF form of NBP was subjected to PharmMapper analysis using the "All Targets" model. The resulting list comprised the top 300 potential targets (job ID: 230131073910) (Supplementary Table S1), ranked in descending order based on the normalized fit score. Since mitochondrial fusion is normally regulated by kinases, functional annotations select the candidates that contain "Participate in kinase activity" and identify the five candidates, as shown in Figure 3A, which are "Proto-oncogene serine/threonine-protein kinase Pim-1" (Rank 2), "Mitogen-activated protein kinase 14" (Rank 25), "Serine/threonine-protein kinase Chk1" (Rank 40), "cAMP-dependent protein kinase catalytic subunit alpha" (Rank 55), and "Adenosine kinase" (Rank 58). According to the information

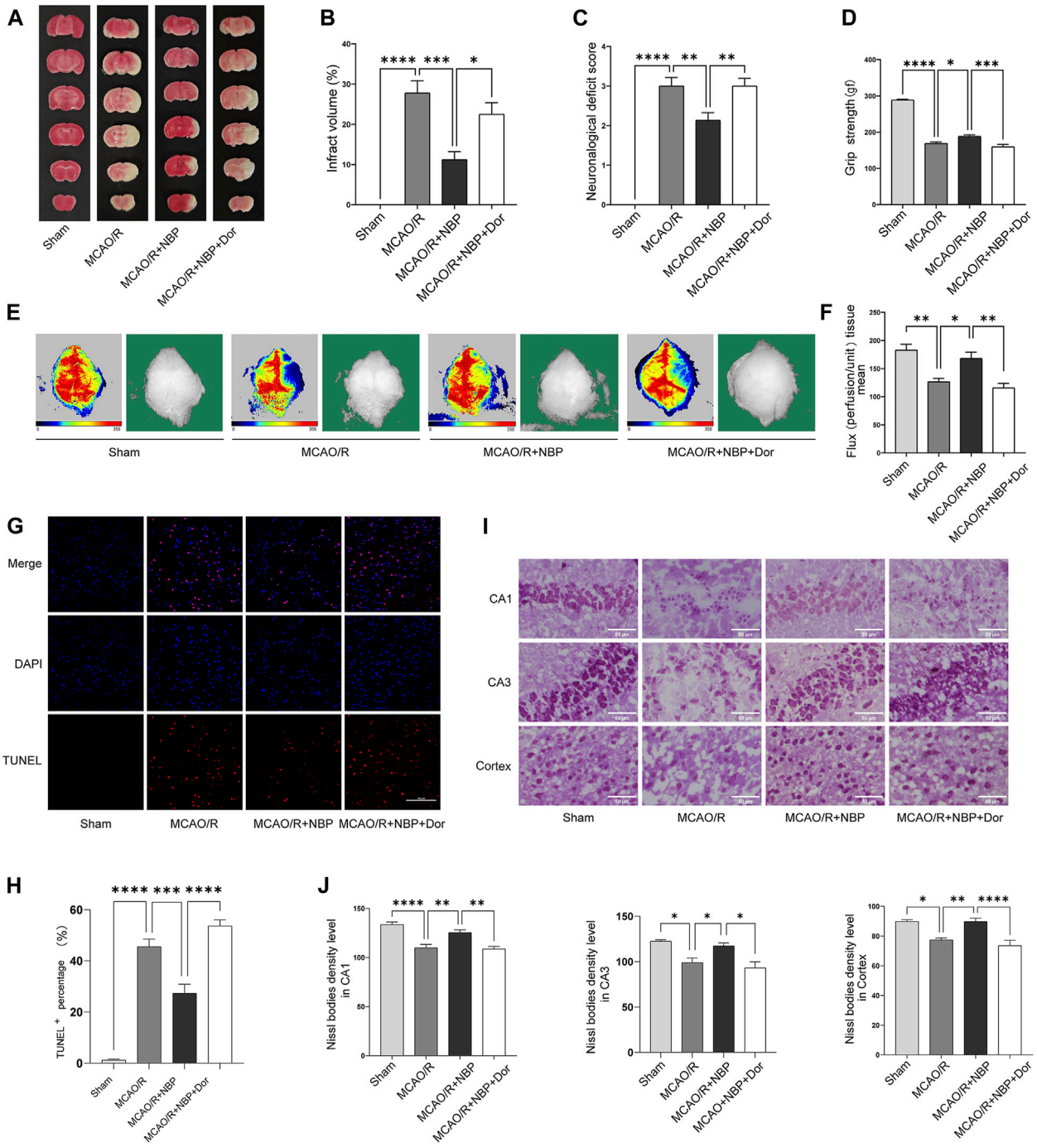

FIGURE 4
NBP alleviated infarction volume, neuronal loss, and facilitated restoration of cerebral blood flow, partly reversed by the inhibitor dorsomorphin. Mice were pretreated with or without NBP in the presence or absence of dorsomorphin for 7 d. **(A)** Effects of dorsomorphin on infarction volumes intervened with NBP. **(B)** Quantitative analysis of infarct volumes (n = 5). **(C)** Longa score (n = 12–16). **(D)** Grasping ability test (n = 11–15). **(E)** The images of cerebral blood flow of cortex. The magnitude of cerebral blood flow is represented by different colors, with blue to red indicating low to high. **(F)** Quantitative analysis of cerebral blood flow in different groups (n = 5–6). **(G)** TUNEL staining in the cortex region of each group (n = 3). **(H)** TUNEL$^+$ percentage in the cortex region. Scale bar = 100 μm. **(I)** Nissl staining in the hippocampal and cortex regions of each group (n = 3–7). **(J)** Density levels of the Nissl staining in hippocampal CA1, CA3 and cortex regions. Scale bar = 50 μm. Data are expressed as the mean ± SEM and were analyzed by ANOVA, $^*p < 0.05$, $^{**}p < 0.01$, $^{***}p < 0.001$, and $^{****}p < 0.0001$.

provided by Universal Protein Resource (UniProt), Proto-oncogene serine/threonine-protein kinase Pim-1 is involved in cell survival and cell proliferation; Mitogen-activated protein kinase 14 is one of the four p38 MAPKs which play an important role in inflammatory response; Serine/threonine-protein kinase Chk1 regulates cell cycle progression; Arginine kinase catalyzes the reversible transfer of the terminal phosphoryl group of ATP to L-arginine. The biological functions of these four kinases are not related to the mitochondrial protective effects

of NBP. Hence, AMPK was considered to be the most likely target candidates.

AMPK is a key direct regulator of mitochondrial dynamics. It can be activated by its upstream kinase or protect cells from pathological stimuli by responding to a decrease in ATP/AMP or ATP/ADP ratio. Hence, AMPK was identified as the primary candidate for targeting. Figures 3B, C also showed that NBP significantly increased pAMPK/AMPK protein expression in the MCAO/R-induced brain tissues. To further investigate the interaction between NBP and AMPK, computational docking was employed. The AutoDock Vina binding test revealed a potential favorable binding of NBP to pAMPK, with a maximum binding affinity of −5.7 kcal/mol (Figure 3D). To further support the direct interaction of NBP, a DARTS experiment was conducted using tissue lysates. The results from Figures 3E, F obtained from DARTS analysis demonstrated that the concentration of NBP exhibited inhibitory effects on p-AMPK degradation induced by pronase. These results suggest a direct interaction between NBP and AMPK.

Inhibition of AMPK with dorsomorphin partly blunted the neuroprotective effects of NBP in MCAO/R-induced mice

To explore whether AMPK is involved in anti-cerebral I/R injury effect of NBP, AMPK inhibitors (dorsomorphin) was used to inhibit AMPK in MCAO/R-induced mice pretreatment with NBP. As shown in Figures 4A, B, the MCAO/R-induced cerebral infarct volume was suppressed by NBP, and this neuroprotective effect was weakened after blockade of the AMPK pathway. Moreover, pretreatment with NBP could relieve neurological dysfunction, increase grip strength and cerebral blood flow, inhibit cell apoptosis, improve Nissl's body morphology after I/R injury in mice, but this effect was also blocked following treatment with dorsomorphin (Figures 4C–J).

Inhibition of AMPK with dorsomorphin partly blunted the expression on Mfn1 of NBP in MCAO/R-induced mice

To determine whether NBP regulates mitochondrial fusion via the AMPK pathway, we continue to use dorsomorphin to inhibit AMPK in MCAO/R-induced mice pretreatment with NBP. We analyzed the expression patterns of mitochondrial fusion proteins. Of the expression of Opa1, Mfn1 and Mfn2, only the expression of Mfn1 was significantly lower in the dorsomorphin and NBP co-treated group than in the NBP-treated group. No significant differences in Opa1 and Mfn2 level were observed in the dorsomorphin and NBP co-treated group, which suggests that Mfn1 expression were modulated by the AMPK signaling pathway (Figures 5A, B).

Discussion

NBP, a compound derived from celery seeds, received approval from the National Medical Products Administration in 2002 for clinical treatment of ischemic stroke (Yao et al., 2018). The protective mechanism of NBP against ischemic stroke may be related to improving local microcirculation, inhibiting neuronal apoptosis and neuroinflammation (Wang Y. et al., 2018; Wei et al., 2021). However, further research is needed on the related studies of NBP on mitochondrial dynamics and its mechanism of action in brain I/R injury. We investigated the effect of NBP on MCAO/R-induced ischemic stroke and its potential mechanism involving mitochondrial fission. Our results showed that NBP reduces cerebral infarction volume, improves neurological dysfunction, and increases cerebral blood flow. NBP also increased the protein expression of mitochondrial fusion proteins Opa1, Mfn1 and Mfn2, and mitochondrial respiratory chain complex IV. In addition, to verify the relationship between AMPK and mitochondrial fusion, we injected the AMPK inhibitor dorsomorphin intraperitoneally and examined the expression of these fusion proteins. The results showed that dorsomorphin could significantly inhibit the expression of mitochondrial fusion protein Mfn1 intervened with NBP. These results suggest that NBP may promote mitochondrial fusion and ultimately alleviate I/R symptoms by regulating the AMPK-mediated Mfn1 pathway.

Mitochondria are present in most cell types and are the main productive structure. Mitochondria contain many enzyme systems, which can be coupled with oxidative phosphorylation through electron transport chains to generate adenosine triphosphate, providing huge energy for life activities (Annesley and Fisher, 2019; Qin et al., 2021; Al Amir Dache and Thierry, 2023). The realization of mitochondrial function is inseparable from structural changes. Mitochondrial fusion and division are fundamental to function. In typical scenarios, the processes of mitochondrial fusion and division operate in harmony, ensuring a dynamic equilibrium that upholds the cellular morphology, structure, and functionality of mitochondria (Youle and van der Bliek, 2012; Adebayo et al., 2021).

Fusion is an intracellular adaptation that enhances communication between mitochondria and the host cell (Bertholet et al., 2016). Developing therapeutic strategies to regulate mitochondrial fusion process is of utmost importance. A mounting body of empirical evidence highlights the significance of various fusion proteins, such as Opa1, and Mfn1/2. Therefore, there is a critical need to develop a novel drug target that regulates this crucial biological process. The data presented in this study indicate that NBP administration leads to an increase in the protein expression of Opa1, Mfn1, and Mfn2 in brain tissues affected by MCAO/R. Furthermore, the mitochondrial respiratory chain complex plays a crucial role in biological oxidation processes, primarily by facilitating the transport of electrons and protons to generate ATP (Rich and Maréchal, 2010). Complex IV, as the terminal complex of the respiratory chain, utilizes the proton gradient to synthesize ATP, thereby enabling energy conversion (Rich and Maréchal, 2010; Kadenbach, 2021). NBP has demonstrated efficacy in restoring the expression of mitochondrial complex IV in brain tissues subjected to MCAO/R. Taken together, these data indicated that NBP promoted mitochondrial fusion and mitochondrial function in I/R brains.

AMP-activated protein kinase (AMPK) is a crucial serine-threonine (Ser/Thr) protein kinase complex involved in the regulation of cellular energy status and monitoring of cellular metabolic state. Its activity is primarily modulated by the AMP/ATP ratio, and its activation can also be facilitated by its upstream kinase. Under conditions of stress, AMPK initiates the process of biosynthesis to generate new mitochondria as a means of replacing damaged ones (Toyama et al., 2016). Upon activation, AMPK is capable of directly phosphorylating serine or threonine residues on target molecules (Li et al., 2016) thereby

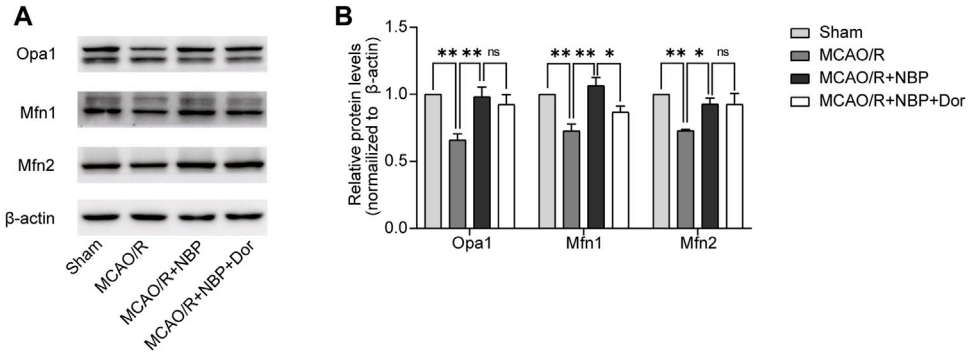

FIGURE 5
NBP promoted mitochondrial fusion and restored mitochondrial function, partly reversed by the inhibitor dorsomorphin. Mice were pretreated with or without NBP in the presence or absence of dorsomorphin for 7 d. **(A, B)** Representative blots and quantitative analysis of mitochondrial fusion-related proteins including Opa1, Mfn1, and Mfn2 (n = 3). Data are expressed as the mean ± SEM and were analyzed by ANOVA, $^{*}p < 0.05$ and $^{**}p < 0.01$.

regulating mitochondrial fission through its control over the mitochondrial fission factor, a key receptor on the outer membrane for Drp1 (Toyama et al., 2016). In this study, we have observed that NBP activates AMPK. Furthermore, the inhibitory effect of NBP on Mfn1 at the mitochondrial membrane is dependent on the presence of AMPK, as demonstrated through AMPK silencing experiments. These findings indicate that the protective impact of NBP on IS is, in part, achieved by activating the AMPK-mediated Mfn1 signaling pathway.

Conclusion

Our research findings indicate that NBP has the ability to modulate mitochondrial homeostasis by activating AMPK, leading to the mitigation of cerebral I/R injury. Importantly, our study presents novel evidence that the administration of NBP can effectively decrease infarct volume and enhance neurological functions by facilitating AMPK-mediated mitochondrial fusion in *in vivo* models of ischemic stroke.

Data availability statement

The original contributions presented in the study are included in the article/Supplementary Material, further inquiries can be directed to the corresponding author.

Ethics statement

The animal study was approved by Institutional Animal Care guidelines and the Animal Care and Ethics Committee of Qingdao University. The study was conducted in accordance with the local legislation and institutional requirements.

Author contributions

TZ: Conceptualization, Formal Analysis, Methodology, Software, Writing–original draft. SD: Conceptualization, Formal Analysis, Methodology, Software, Writing–original draft. NQ: Methodology, Writing–review and editing. RL: Formal Analysis, Investigation, Visualization, Writing–review and editing. LS: Formal Analysis, Investigation, Visualization, Writing–review and editing. QW: Methodology, Resources, Supervision, Writing–review and editing.

Funding

The author(s) declare financial support was received for the research, authorship, and/or publication of this article. This research was supported by the Shandong Medical and Health Science and Technology Development Plan Project (No. 202102041137), the National Natural Science Foundation of China (No. 82204663); the Natural Science Foundation of Shandong Province (No. ZR2022QH058).

Conflict of interest

The authors declare that the research was conducted in the absence of any commercial or financial relationships that could be construed as a potential conflict of interest.

Publisher's note

Supplementary material

The Supplementary Material for this article can be found online at: https://www.frontiersin.org/articles/10.3389/fphar.2024.1357953/full#supplementary-material

References

Adebayo, M., Singh, S., Singh, A. P., and Dasgupta, S. (2021). Mitochondrial fusion and fission: the fine-tune balance for cellular homeostasis. *Faseb J.* 35 (6), e21620. doi:10.1096/fj.202100067R

Al Amir Dache, Z., and Thierry, A. R. (2023). Mitochondria-derived cell-to-cell communication. *Cell Rep.* 42 (7), 112728. doi:10.1016/j.celrep.2023.112728

Annesley, S. J., and Fisher, P. R. (2019). Mitochondria in Health and disease. *Cells* 8 (7), 680. doi:10.3390/cells8070680

Bertholet, A. M., Delerue, T., Millet, A. M., Moulis, M. F., David, C., Daloyau, M., et al. (2016). Mitochondrial fusion/fission dynamics in neurodegeneration and neuronal plasticity. *Neurobiol. Dis.* 90, 3–19. doi:10.1016/j.nbd.2015.10.011

Feng, Y., Guo, M., Zhao, H., Han, S., Hao, Y., Yuan, Y., et al. (2021). Dl-3-n-Butylphthalide alleviates demyelination and improves cognitive function by promoting mitochondrial dynamics in white matter lesions. *Front. Aging Neurosci.* 13, 632374. doi:10.3389/fnagi.2021.632374

Huang, J., Chen, L., Yao, Z. M., Sun, X. R., Tong, X. H., and Dong, S. Y. (2023). The role of mitochondrial dynamics in cerebral ischemia-reperfusion injury. *Biomed. Pharmacother.* 162, 114671. doi:10.1016/j.biopha.2023.114671

Huang, Y., Li, Z., and Nan, G. (2017). Effect of hippocampal L-NBP on BDNF and TrkB expression and neurological function of vascular dementia rats. *Mol. Med. Rep.* 16 (5), 7673–7678. doi:10.3892/mmr.2017.7539

Kadenbach, B. (2021). Complex IV - the regulatory center of mitochondrial oxidative phosphorylation. *Mitochondrion* 58, 296–302. doi:10.1016/j.mito.2020.10.004

Li, A., Zhang, S., Li, J., Liu, K., Huang, F., and Liu, B. (2016). Metformin and resveratrol inhibit Drp1-mediated mitochondrial fission and prevent ER stress-associated NLRP3 inflammasome activation in the adipose tissue of diabetic mice. *Mol. Cell Endocrinol.* 434, 36–47. doi:10.1016/j.mce.2016.06.008

Qin, Y., Jiang, X., Yang, Q., Zhao, J., Zhou, Q., and Zhou, Y. (2021). The functions, methods, and mobility of mitochondrial transfer between cells. *Front. Oncol.* 11, 672781. doi:10.3389/fonc.2021.672781

Rich, P. R., and Maréchal, A. (2010). The mitochondrial respiratory chain. *Essays Biochem.* 47, 1–23. doi:10.1042/bse0470001

Toyama, E. Q., Herzig, S., Courchet, J., Lewis, T. L., Jr., Losón, O. C., Hellberg, K., et al. (2016). Metabolism. AMP-activated protein kinase mediates mitochondrial fission in response to energy stress. *Science* 351 (6270), 275–281. doi:10.1126/science.aab4138

Wang, C. Y., Xu, Y., Wang, X., Guo, C., Wang, T., and Wang, Z. Y. (2019). Dl-3-n-Butylphthalide inhibits NLRP3 inflammasome and mitigates alzheimer's-like pathology via nrf2-TXNIP-TrX Axis. *Antioxid. Redox Signal* 30 (11), 1411–1431. doi:10.1089/ars.2017.7440

Wang, L., Zhu, T., Xu, H. B., Pu, X. P., Zhao, X., Tian, F., et al. (2021). Effects of notoginseng leaf triterpenes on small molecule metabolism after cerebral ischemia/reperfusion injury assessed using MALDI-MS imaging. *Ann. Transl. Med.* 9 (3), 246. doi:10.21037/atm-20-4898

Wang, S., Ma, F., Huang, L., Zhang, Y., Peng, Y., Xing, C., et al. (2018a). Dl-3-n-Butylphthalide (NBP): a promising therapeutic agent for ischemic stroke. *CNS Neurol. Disord. Drug Targets* 17 (5), 338–347. doi:10.2174/1871527317666180612125843

Wang, Y., Huang, Y., Xu, Y., Ruan, W., Wang, H., Zhang, Y., et al. (2018b). A dual AMPK/Nrf2 activator reduces brain inflammation after stroke by enhancing microglia M2 polarization. *Antioxid. Redox Signal* 28 (2), 141–163. doi:10.1089/ars.2017.7003

Wei, Z. Z., Chen, D., Lee, M. J. H., Zhao, Y., Gu, X., Yu, S. P., et al. (2021). DL-3-n-butylphthalide increases collateriogenesis and functional recovery after focal ischemic stroke in mice. *Aging Dis.* 12 (7), 1835–1849. doi:10.14336/ad.2020.1226

Wu, M., Gu, X., and Ma, Z. (2021). Mitochondrial quality control in cerebral ischemia-reperfusion injury. *Mol. Neurobiol.* 58 (10), 5253–5271. doi:10.1007/s12035-021-02494-8

Xie, X., Wang, L., Dong, S., Ge, S., and Zhu, T. (2024). Immune regulation of the gut-brain axis and lung-brain axis involved in ischemic stroke. *Neural Regen. Res.* 19 (3), 519–528. doi:10.4103/1673-5374.380869

Yang, M., He, Y., Deng, S., Xiao, L., Tian, M., Xin, Y., et al. (2021). Mitochondrial quality control: a pathophysiological mechanism and therapeutic target for stroke. *Front. Mol. Neurosci.* 14, 786099. doi:10.3389/fnmol.2021.786099

Yao, C. L., Pan, H. Q., Wang, H., Yao, S., Yang, W. Z., Hou, J. J., et al. (2018). Global profiling combined with predicted metabolites screening for discovery of natural compounds: characterization of ginsenosides in the leaves of Panax notoginseng as a case study. *J. Chromatogr. A* 1538, 34–44. doi:10.1016/j.chroma.2018.01.040

Youle, R. J., and van der Bliek, A. M. (2012). Mitochondrial fission, fusion, and stress. *Science* 337 (6098), 1062–1065. doi:10.1126/science.1219855

Zhang, G., Zhang, T., Li, N., Wu, L., Gu, J., Li, C., et al. (2018). Tetramethylpyrazine nitrone activates the BDNF/Akt/CREB pathway to promote post-ischaemic neuroregeneration and recovery of neurological functions in rats. *Br. J. Pharmacol.* 175 (3), 517–531. doi:10.1111/bph.14102

Zhu, T., Liu, H., Gao, S., Jiang, N., Chen, S., and Xie, W. (2024). Effect of salidroside on neuroprotection and psychiatric sequelae during the COVID-19 pandemic: a review. *Biomed. Pharmacother.* 170, 115999. doi:10.1016/j.biopha.2023.115999

frontiers | Frontiers in Pharmacology

TYPE Original Research
PUBLISHED 21 March 2024
DOI 10.3389/fphar.2024.1359319

OPEN ACCESS

EDITED BY
Weijie Xie,
Tongji University, China

REVIEWED BY
Khalil Ali Ahmad,
University of Texas MD Anderson Cancer Center, United States
Yang Hong Xu,
Chinese Academy of Sciences (CAS), China
Muhammad Usman,
Western University, Canada

*CORRESPONDENCE
Jiao-Qiong Guan,
eyjqguan@scut.edu.can
Le Ma,
male412810253@sjtu.edu.cn

†These authors have contributed equally to this work and share first authorship

RECEIVED 21 December 2023
ACCEPTED 20 February 2024
PUBLISHED 21 March 2024

CITATION
Zhang K, Ren Y-Q, Xue Y, Duan D, Zhou T, Ding Y-Z, Li X, Gong W-K, Guan J-Q and Ma L (2024), Alpha 2-adrenoceptor participates in anti-hyperalgesia by regulating metabolic demand.
Front. Pharmacol. 15:1359319.
doi: 10.3389/fphar.2024.1359319

Alpha 2-adrenoceptor participates in anti-hyperalgesia by regulating metabolic demand

Ke Zhang[1,2†], Yu-Qing Ren[3†], Yan Xue[3†], Dongxia Duan[2], Tong Zhou[2], Ying-Zhuo Ding[4], Xiang Li[5], Wan-Kun Gong[2], Jiao-Qiong Guan[2*] and Le Ma[2*]

[1]Department of Anesthesiology, Affiliated Shanghai Sixth People's Hospital, Shanghai Jiao Tong University School of Medicine, Shanghai, China, [2]Shanghai Key Laboratory of Psychotic Disorders, Brain Health Institute, National Center for Mental Disorders, Shanghai Mental Health Center, Shanghai Jiao Tong University School of Medicine, Shanghai, China, [3]Department of Anesthesiology, Renji Hospital, Shanghai Jiao Tong University School of Medicine, Shanghai, China, [4]Shanghai Eye Disease Prevention and Treatment Center/Shanghai Eye Hospital, Department of Pharmacy, Shanghai, China, [5]Department of Orthopedics, The Fifth People's Hospital of Shanghai, Fudan University, Shanghai, China

The α2-adrenoceptor agonist dexmedetomidine is a commonly used drug for sedatives in clinics and has analgesic effects; however, its mechanism of analgesia in the spine remains unclear. In this study, we systematically used behavioural and transcriptomic sequencing, pharmacological intervention, electrophysiological recording and ultrasound imaging to explore the analgesic effects of the α2-adrenoceptor and its molecular mechanism. Firstly, we found that spinal nerve injury changed the spinal transcriptome expression, and the differential genes were mainly related to calcium signalling and tissue metabolic pathways. In addition, α2-adrenoceptor mRNA expression was significantly upregulated, and α2-adrenoceptor was significantly colocalised with markers, particularly neuronal markers. Intrathecal dexmedetomidine suppressed neuropathic pain and acute inflammatory pain in a dose-dependent manner. The transcriptome results demonstrated that the analgesic effect of dexmedetomidine may be related to the modulation of neuronal metabolism. Weighted gene correlation network analysis indicated that turquoise, brown, yellow and grey modules were the most correlated with dexmedetomidine-induced analgesic effects. Bioinformatics also annotated the involvement of metabolic processes and neural plasticity. A cardiovascular–mitochondrial interaction was found, and ultrasound imaging revealed that injection of dexmedetomidine significantly enhanced spinal cord perfusion in rats with neuropathic pain, which might be regulated by pyruvate dehydrogenase kinase 4 (pdk4), cholesterol 25-hydroxylase (ch25 h) and GTP cyclohydrolase 1 (gch1). Increasing the perfusion doses of dexmedetomidine significantly suppressed the frequency and amplitude of spinal nerve ligation-induced miniature excitatory postsynaptic currents. Overall, dexmedetomidine exerts analgesic effects by restoring neuronal metabolic processes through agonism of the α2-adrenoceptor and subsequently inhibiting changes in synaptic plasticity.

KEYWORDS

α2-adrenoceptor, pain, transcriptome, cardiovascular-mitochondrial interaction, metabolic processes

Introduction

Chronic pain is a complex sensory or emotional experience (Frediani and Bussone, 2019). Nerve injury commonly leads to excessive activation of pain circuits and alterations in spinal-mediated pain transmission and synapse-associated cellular signals (Luo et al., 2014). Inflammatory factors stimulate a variety of calcium ion channels, including calcium store-operated calcium channels and mu-opioid receptors, to promote neuronal firing and pain sensations; specific channel inhibitors or antagonists can significantly inhibit calcium-activated cellular transduction and neurotransmitter release to exert a powerful analgesic role (Ma et al., 2021; Wang et al., 2023). Therefore, finding new intervention targets plays an important role in the development of analgesic drugs.

Synapses consume ATP (Adenosine 5′-triphosphate) to participate in neural plasticity, and the disturbance of energy haemostasis prevents them from performing host functions properly, leading to defective neurotransmission and synaptic connections. Glutamate transmission in the spinal cord is significantly enhanced after nerve injury, and the strength of its synaptic connections is increased by three to five times (Zhang et al., 2019). Chronic pain significantly changes mitochondria-related markers; in particular, it leads to significant damage to mitochondrial DRP1 and persistent overactivation of ROS (reactive oxygen species) (Dai et al., 2020). Macrophages actively control the expansion of an inflammatory damage away from the inflammation site by transferring mitochondria to sensory neurons (van der Vlist et al., 2022). During the regression of inflammatory pain in mice, M2-like macrophages infiltrate the dorsal root ganglion containing the cellular body of sensory neurons and resume the oxidative phosphorylation of these neurons (Niehaus et al., 2021; van der Vlist et al., 2022). Urolithin A improves mitochondrial autophagy and respiration in primary chondrocytes during the pathological state of arthritis, thereby reducing cartilage degeneration, synovial inflammation and pain; such improvements are associated with increased mitochondrial autophagy and mitochondrial content in the joints of mice (D Amico et al., 2022). A mutual response exists between mitochondria and local blood vessels, and it guides the supply of substances to maintain mitochondrial respiration and ATP production (Marcu et al., 2017). Transient pain signal transduction requires enhanced blood flow to satisfy the synapse demand (Claron et al., 2021). Therefore, the imbalance of energy metabolism may be the key cause of pain.

The α2-adrenoceptor agonist dexmedetomidine (DEX) is a commonly used sedative in clinical practice and has analgesic effects; however, its mechanism of analgesia in the spine remains unclear. In this study, we investigated the effects and molecular mechanisms of DEX in pain by transcriptome sequencing, behavioural, electrophysiological and ultrasound imaging. Our results show that spinal nerve injury leads to changes in spinal transcriptome expression, and the differential genes are mainly related to calcium signalling and tissue metabolic pathways. DEX modulates mitochondrial activity. The mRNA expression of α2-adrenoceptor was significantly upregulated, and it was significantly co-localised with markers mainly in neuronal markers. Intrathecal DEX suppressed neuropathic pain and acute inflammatory pain in a dose-dependent manner. The transcriptome results also demonstrated that the analgesic effect of DEX may be related to the modulation of neuronal metabolism. A cardiovascular-mitochondrial interaction exists, and ultrasound imaging showed that injection of DEX significantly enhanced spinal cord perfusion in rats with neuropathic pain. Increasing the perfusion doses of DEX significantly suppressed the frequency and amplitude of spinal nerve ligation-induced miniature excitatory postsynaptic currents (mEPSCs). Dexmedetomidine exerts analgesic effects by restoring neuronal metabolic processes through agonism of the α2-adrenoceptor and subsequently inhibiting changes in synaptic plasticity.

Methods

Rat model of chronic pain induced by spinal nerve ligation

Two-month-old adult male Wistar rats were intraperitoneally injected with 50 mg/kg pentobarbital sodium. After anaesthesia, the rats were opened along the midline of the iliac bone in the back with a length of about 2 cm. The left muscle was bluntly separated. Two parallel spinal nerves L4 and L5 were observed. Relative to the L4 nerve, the spinal L5 was located close to the vertebrae. The L5 nerve was gently stirred and ligated with a hook made of glass electrodes. A medical–surgical blade was used to remove the fascia near the sacrum, detect the relatively vertical L6 nerve, lates it, uses an appropriate amount of penicillin to prevent bacterial infection and closes the wound. The sham operation group was similar to the spinal nerve ligation group, where spinal nerves L5 and L6 were separated but only medical surgical lines were used to surround these nerves without ligation. At 10 days after the operation, the adaptive environment and handle rats were started. The mechanical pain threshold of the left hind foot of the rats was measured by Von Frey's electronic pain meter. Rats that weighed less than 8 g and had no significant difference in movement posture on both sides were regarded as successful modelling and used for subsequent experiments (Deuis et al., 2017).

Catheterisation of subarachnoid space in rats

The experimental rats were anesthetised by intraperitoneal injection of pentobarbital sodium (50 mg/kg). The iliac crest position was marked. A 22 cm polyethylene catheter (PE-10 catheter: inner diameter: 0.30 mm; external diameter: 0.55 mm) was implanted into the arachnoid space of the spine, and a typical tail flashing phenomenon was observed. The tip of the catheter was close to the vertical position of the last rib and spine of the rat, and the catheter was fixed at the neck and iliac bone. The catheter was left from the skin of the neck of the rat to prevent the animal from biting and damaging it. An appropriate amount of penicillin was administered to the skin opening to prevent surgical infection and close the wound. The rats were transferred to a heated blanket to restore consciousness and then placed in a single cage. Two days after recovery, the intubation was checked, and the rats were injected with 10% lidocaine in artificial cerebrospinal fluid

through the neck catheter by using a 15 μL micro-sample injector, followed by a 15 μL artificial cerebrospinal fluid flush tube. The rats had bilateral posterior foot paralysis and weakness, and the bilateral posterior foot movement was the same after the metabolism of anaesthetic drugs. The results indicated the successful placement of intrathecal catheter in rats, and the model was used in subsequent experiments.

Measurement of pain threshold in rats

The rats were acclimatized to the experimental environment 3 days before the start of the behavioural study. According to the experimental plan, the rats were placed in the laboratory for at least 30 min at the same time every day. On the first day, the rats were placed in a feeding box and were gently stroked on the back for 1 min twice. On the second day, the rats were gently placed on an iron rack and gently stroked along the direction of the hair for 1–2 min each time. Similar operations were performed until the day before the experiment. This operation allows the rats to be familiar with the experimental operator through odor and steps conducted, reduce the adverse emotional changes caused by the operation by establishing a familiar relationship between the operator and the tested rats and reduce errors and inaccurate measurements that may be introduced by other factors. After handling, the rats were transferred to a clear Plexiglass box to detect the mechanical pain threshold. The box was placed on a metal mesh 40 cm away from the experimental table. After 30 min of adaptation, the rats were stimulated vertically upward at the intersection of the third and fourth toes of the left hind foot by using 2450 CE electronic Von Frey (2450 CE electronic Von Frey) equipped with 15 fibres until the rats showed typical foot retraction or foot lift response when escaping injury. Paw withdrawal latency (mechanical pain threshold) was recorded when the rat avoided injury. The threshold value of each rat at a certain point in time was the mean value of three consecutive measurements with an interval of 3 min.

Real-time fluorescence quantitative PCR

The rats were injected intraperitoneally with pentobarbital sodium (50 mg/kg). The spine was cut along the iliac bone, and the tissue was separated from the left and right sides with fine surgical scissors to the last rib to quickly separate the spinal cord L3–L5 enlargement. Pre-cooled artificial cerebrospinal fluid was used to clean the residual blood in the enlarged part of the waist. The surgical site was separated by a surgical blade and transferred to liquid nitrogen for rapid cooling and storage at −80°C. Total RNA was extracted by Trizol reagent. All consumables required for the whole experiment were subjected to DEPC (Diethyl pyrocarbonate) water treatment, and the experimental table was treated with RNA enzyme scavenger. Prior to extraction, the preserved tissue was recovered at −80 °C for 5 min at room temperature. About 1 mL of Trizol and three RNA-free homogenising magnetic beads were added to the homogenate at 60 Hz/90 s and split at room temperature for 10 min. The sample was then added with 200 μL of trichloromethane, swirled for 3–5 s and centrifuged at 12,000 rpm/4°C for 10 min. The centrifuged EP tube was then divided into three layers.

The uppermost layer dissolves RNA, and the middle layer dissolves DNA. The middle layer of liquid should not be touched when absorbing the supernatant to prevent mixing into RNA and affecting the reliability of the experiment. The supernatant was added with pre-cooled isopropyl alcohol (1:1), reversed and mixed several times. The sample was placed at −20°C for 2 h and centrifuged at 12,000 rpm/4°C for 10 min. The EP tube was gently reversed to discard the supernatant, and the white precipitate formed was regarded as RNA. The precipitate was added with 1 mL of pre-cooled DEPC water with 75% ethanol, reversed several times, centrifuged at 7,500 rpm/4°C for 10 min and washed repeatedly. After discarding the supernatant, a 10 μL tip head was used to remove excess liquid from the tube wall. The sample was left at room temperature until the RNA dried. The RNA was then dissolved in 50 μL of DEPC water. RNA concentration and purity was measured by Nanodrop, and the qualified RNA A260/A280 was between 1.8 and 2.0, which can be used for further experiments.

Here are the primers for the experiment:

Ch25 h: Forward primer 5′- CCTAAGTCACGTCCTGATCTGC-3′,

Reverse primer 5′- GAGGACGAGTTCTGGTGATGCA-3’;

Itpkc: Forward primer 5′- TACCAGCGATCCTGAGGACAGA-3′,

Reverse primer 5′- AGTGCTTATGGAAGGAGACCACG-3’;

Gch1: Forward primer 5′- AGCAAGTCCTTGGTCTCAGTAAAC-3′,

Reverse primer 5′- ACCGCAATCTGTTTGGTGAGGC-3’;

Chsy1: Forward primer 5′- CGACAGGAACTTTCTCTTCGTGG-3′,

Reverse primer 5′- CCTCGCTAGAGAAGAACTCCAC-3’;

Arl5c: Forward primer 5′- GAGGAGCTGTATAAGATGCTGGC-3′,

Reverse primer 5′- GGTGGTCTTTGATGGCACTGAG-3′

Pdk4: Forward primer 5′- GTCGAGCATCAAGAAAACCGTCC-3′,

Reverse primer 5′- GCGGTCAGTAATCCTCAGAGGA-3′

GAPDH: Forward primer 5′-ACCACAGTCCATGCCATCAC-3′,

Reverse primer 5′- TCCACCACCCTGTTGCTGTA-3′

Immunofluorescence staining

Tissue separation: The rats were anesthetised by intraperitoneal injection of pentobarbital sodium (50 mg/kg). The thorax was cut along the sternal angle, the apex of the heart was exposed and the right auricle was cut quickly. About 100 mL of pre-cooled normal saline was injected to empty the circulating blood. The liver tissue slowly turned white from being red. About 100 mL of 4% paraformaldehyde solution was continuously injected. The tissue was then separated along the iliac bone towards the neck, the enlarged lumbar part of the spinal cord L3-L5 was removed and the outer membrane of the tissue was gently separated in normal saline.

Fixation and dehydration: The removed tissue was immediately transferred to 4% paraformaldehyde solution, stored overnight at 4°C and then transferred to 30% sucrose solution prepared by PBS until the tissue completely sank to the bottom of the solution. The solution was replaced with a new one to completely sink to the bottom to complete tissue dehydration. The dehydrated frozen section tissue was washed twice in phosphate buffer saline (PBS) and placed on clean dust-free paper to completely absorb moisture. The tissue was marked on the opposite side of the blade and transferred to an embedding box with an OTC embedding agent. After forming at −80°C, the sample was transferred from container glass to sample holder for fixation. The sample was sliced with Leica frozen microtome. The ambient temperature of the microtome box was −20°C, and the temperature of the cutter head was −20°C. The spinal cord tissue layer V was sliced in the direction of the cutter head with a thickness of 30 μm. The slices were placed on a 12-well plate, immersed in PBS and stored at 4°C for 1 week.

Blocking: The slices were removed with a glass hook and placed into a 2 mL centrifuge tube with a rounded bottom containing 5% BSA/0.5% Triton sealing solution. The sample was incubated at room temperature for 1 h and rotate at 40 rpm in a shaker.

Incubation of primary antibody: Liquid in the centrifuge tube was slowly poured into a 0.22 μm filter. The sections were transferred to six-well plates, wash with PBS for 5 min and transfer to 1%BSA antibody diluting solution. The corresponding antibody was incubated with the primary antibody.

Secondary antibody incubation: The sections were transferred to a 1% BSA-configured antibody diluter, and all fluorescent secondary antibodies were diluted at 1:1000. The sample was incubated at room temperature for 2 h and rotated at 40 rpm. Imaging and fluorescence intensity analyses were performed with Olympus FV10-ASW 4.2 viewer.

Spinal cord transcriptome sequencing and analysis

The total RNA of spinal cord L3-L5 was extracted using RNeasy Mini Kit (Qiagen), and the A260/A280 values of qualified RNA were between 1.8 and 2.0, which could be used for further experiments. After fragmentation, PCR, purification and other operations were used to build a database for subsequent sequencing. Lian Chuan Biotechnology Co., Ltd. was commissioned to use the second-generation sequencing platform Illumine Novaseq 6000 for sequencing using the PE150 standard. The expression value was normalised to fragments per kilobase of exon model per million mapped fragments (FPKM). Count unit and value were selected for subsequent analysis. In this study, R (Windows 10 64-bit) was used for analysis. A domestic image site was selected and the corresponding configurations were performed after the installation. The required R packages were then set up through the installation. During the transcriptome analysis, differential genes were selected for DESeq2 package analysis, in which genes with log2 (expression change multiple) > log2 (1.5) and corrected p-value < 0.05 were included. Signal pathway enrichment was annotated using the Kyoto Encyclopaedia of Genes and Genomes (KEGG) database. The results were presented in the pattern of pathway enrichment and pathway connection relationships.

Weighted gene co-expression network analysis (WGCNA) can use known gene expression information to correlate with the corresponding indicators for significance association analysis according to previous study (DOI:10.1155/2021/9923537). The gene expression is more in line with the scale-free network when taken to the NTH power. WGCNA mainly focuses on the gene association of some key nodes and introduces the concepts of weight network and soft threshold: lognd = kœ-logk β. In general, correlation $R^2 > 0.8$ can meet the scaling data distribution, where d is the connectivity of nodes, and k is a natural number. Based on the screening principle of the soft threshold, the constructed network should be more in line with the scale-free network characteristics. We set the soft threshold values of 0.95, 0.90, 0.85, 0.80, 0.75 and 0.70. The module with β = 8 was selected according to the above parameters for analysis. After the correlation network was constructed, the cluster tree and corresponding modules were visualised. The correlation between the module and gene expression was established, and the gene expression data corresponding to the module was further extracted. The average of gene significance of all genes in a module was defined as modular significance. The modular significance values were compared among different modules. Modules of interest that are highly associated with a particular clinical feature of a disease were selected for subsequent analysis. Genes that achieved highly similar expression relationships were grouped and divided into different modules. Each module was identified and correlated with behavioural phenotypes, such as ligation, nerve damage, pain, anxiety and paw withdrawal threshold (PWT) and included in WGCNA.

Electrophysiological section of the spinal cord (L3–L5)

The experimental rats were rapidly anesthetised with isoflurane, the back skin was separated from the iliac crest to the last rib and the spine L3–L5 was quickly cut with scissors along the rib perpendicular to the spine and 1.5 cm away from the iliac crest. The spine was transferred to a pre-cooled slicing solution (234 mM sucrose, 3.6 mM KCl, 1.2 mM $MgCl_2$, 1.2 mM NaH_2PO_4, 12 mM glucose, 2.5 mM $CaCl_2$ and 25 mM $NaHCO_3$). After 90 s, the separated spine was slowly and gently pushed out the section fluid from a small position in the back end. A 20 mL syringe was used to flush out the spinal cord L3–L5 part with spinal nerve roots. A 1 cm^3 agar block (1.5%) served as a spinal cord support and was fixed to the sample holder by using 401 glue to prevent it from falling off. Leica VT1200S microtome was used to slice the spinal cord with an amplitude of 1.00 mm, a velocity of 0.06–0.14 mm and a thickness of 300–400 μm. Cerebrospinal fluid (125 mM NaCl, 3 mM KCl, 1.25 mMNaH_2PO_4, 26 mM $NaHCO_3$, 1 mM $MgCl_2$ and 2 mM $CaCl_2$) was transferred to oxygen-saturated artificial cerebrospinal fluid at 32°C. Glucose and 10 mM D-glucose were incubated for 30 min at room temperature and restored for 30 min before recording.

Electrophysiological recording

Lamina II neurons in the dorsal horn of the spinal cord were recorded with a glass electrode made of borosilicate (impedance

4–6 MΩ, diameter 0.5 mm, diameter 1.0 mm). mEPSC was recorded by adding a glass electrode to K^+ internal fluid (140 mM K-gluconate, 10 mM HEPES, 1.1 mM EGTA, 2 mM $MgCl_2$, 2 mm); 3 mM MgATP and 0.3 mM Tris-guanosine triphosphate (adjusted to pH 7.4 by using CsOH), 10 μmol strychnine; 100 μmol picrotoxin (PTX); and 1 μmol tetrodotoxin (TTX) under a clamping voltage of −70 mV. mIPSC was recorded by adding a glass electrode to the CsCI internal solution (140 mM CsCl, 10 mM HEPES, 1.1 mM EGTA, 2 mM $MgCl_2$, 2 mm); 3 mM MgATP and 0.3 mM Tris-guanosine triphosphate (adjusted to pH 7.4 by using CsOH); 20 μmol CNQX; 50 μmol D-AP5; and 1 μmol tetrodotoxin in the external solution at a clamping voltage of −70 mV.

Laminectomy and functional spinal ultrasound imaging (fUS)

Laminectomy was performed between the 12th thoracic and second lumbar vertebrae by intraperitoneal injection of metomidine (0.4 mg/kg) and ketamine (40 mg/kg) under deep anaesthesia. This window allows the entire ultrasonic probe (14 mm) to be positioned in the sagittal plane. Once the laminectomy was complete, the animal was placed on a 'spinal cord' stereotaxic frame, in which the lumbar spine was suspended. Lidocaine (Xylovet, Ceva, France, 2 mg/mL) was applied topically to the exposed muscle and to the insertion point of the spinal brace. Anaesthesia was maintained but reduced with subcutaneous infusion by using an injection pump at rates of 0.1 mg/kg/h for metomidine and 12.5 mg/kg/h for ketamine. A waiting time of about 1 h and 30 min after induction was maintained to obtain repeatable results. Imaging was then conducted to obtain a stable and light level of anaesthesia (breathing rate of about 120 bpm). During surgical procedures and imaging, the body temperature of the animals was maintained at 37°C by using heating blankets and intra-rectal probes (Physitemp, Clifton, NJ). Heart and respiratory rates were monitored (Mouse Ox Plus, Ugo Basile, Italy). Each imaging session lasted for 4–6 h. About 2 mL of saline was gently dripped onto the spinal cord (the dura remains intact), and the cavity formed by the laminectomy was filled with an ultrasound gel. The ultrasonic probe (f5-15MHz, 128 components, Vermon, Tours, France) was fixed above the window by using a three-axis motor system. The probe was connected to an ultrasonic ultrafast scanner (Vera Sonics, Kirk-land, WA:128 channels, 62.5 mHz sampling). Data were processed by Neuroscan real-time acquisition software (Iconeus, Paris, France; Inserm Biomedical Ultrasound Technology Research Accelerator, France).

Materials

The antibodies used in our study. The NeuN Mouse mAb (Millipore, MAB377, 1:1000-1:200); The GFAP Mouse mAb (Millipore, MAB3402, 1:1000-1:200), and the Iba-1 Rabbit mAb (Abcam, ab178846,1:2000-1:500).

Statistical analysis

All data were calculated using GraphPad Prism 8 software and presented as mean ± standard error of the mean (mean ± SEM). Unpaired student's t-test and one-way ANOVA were used for statistical analysis. $p < 0.05$ and $p < 0.01$ indicated statistical significance. Data were analysed by experimenters blinded to the experimental conditions of the study.

Results

Chronic pain causes abnormal metabolic changes at the lesion site

Energy metabolism disorders are related to nerve conduction activities and important in neurological diseases. To explore changes in energy metabolism in chronic pain, we used spinal nerve ligation to construct a paradigm in a chronic pain model of rats (Figure 1A). The spinal cords of mice in the spinal nerve ligation (SNL) and sham groups were separated, and the lymphocele site was collected to extract RNA for transcriptome sequencing. During the testing of almost 23,670 genes, differential expression analysis showed enriched genes involved in major cellular processes including calcium signalling pathway, metabolic pathways, apelin signalling, nitrogen metabolism and biosynthesis following neuropathic pain (Figures 1B,C). The results indicated that the signal pathways of glucose, lipids, nutrients and energy metabolism in the spinal cord of rats were significantly changed after chronic pain. Hence, metabolic abnormalities would occur at the pain site, suggesting that metabolic imbalance may be the key cause of pain.

α-2 Acetylcholine receptor agonist significantly alleviates pain hypersensitivity in rats

α2-Acetylcholine receptors (α2-ADR) are metabolically related and involved in pain, but their specific distribution and location in cells and synapses remain unclear. Firstly, we detected the expression of α2-ADR on the presynaptic and postsynaptic membranes with QPCR. The expression of α2-ADR on the presynaptic and postsynaptic membranes was significantly enhanced after the onset of pain (Figure 2A, B). Double immunofluorescence analysis of α2-ADR with NeuN, GFAP and Iba1 was conducted to assess the cell types of α2-ADR. α2-ADR was mainly distributed in neurons, rather than microglia or astrocytes (Figures 2C–E). In addition, the intrathecal agonist DEX significantly suppressed nerve injury-induced neuropathic pain and formalin-induced acute pain in dose gradient-dependent manner (Figures 2F, G).

Activation of alpha-2 acetylcholine receptors significantly reverses pain-induced changes in metabolic pathways

Pain can cause changes in spinal cord metabolic pathways, and the activation of alpha-2 acetylcholine receptors can significantly improve pain phenotypes. By tissue sequencing of SNL and SNL-

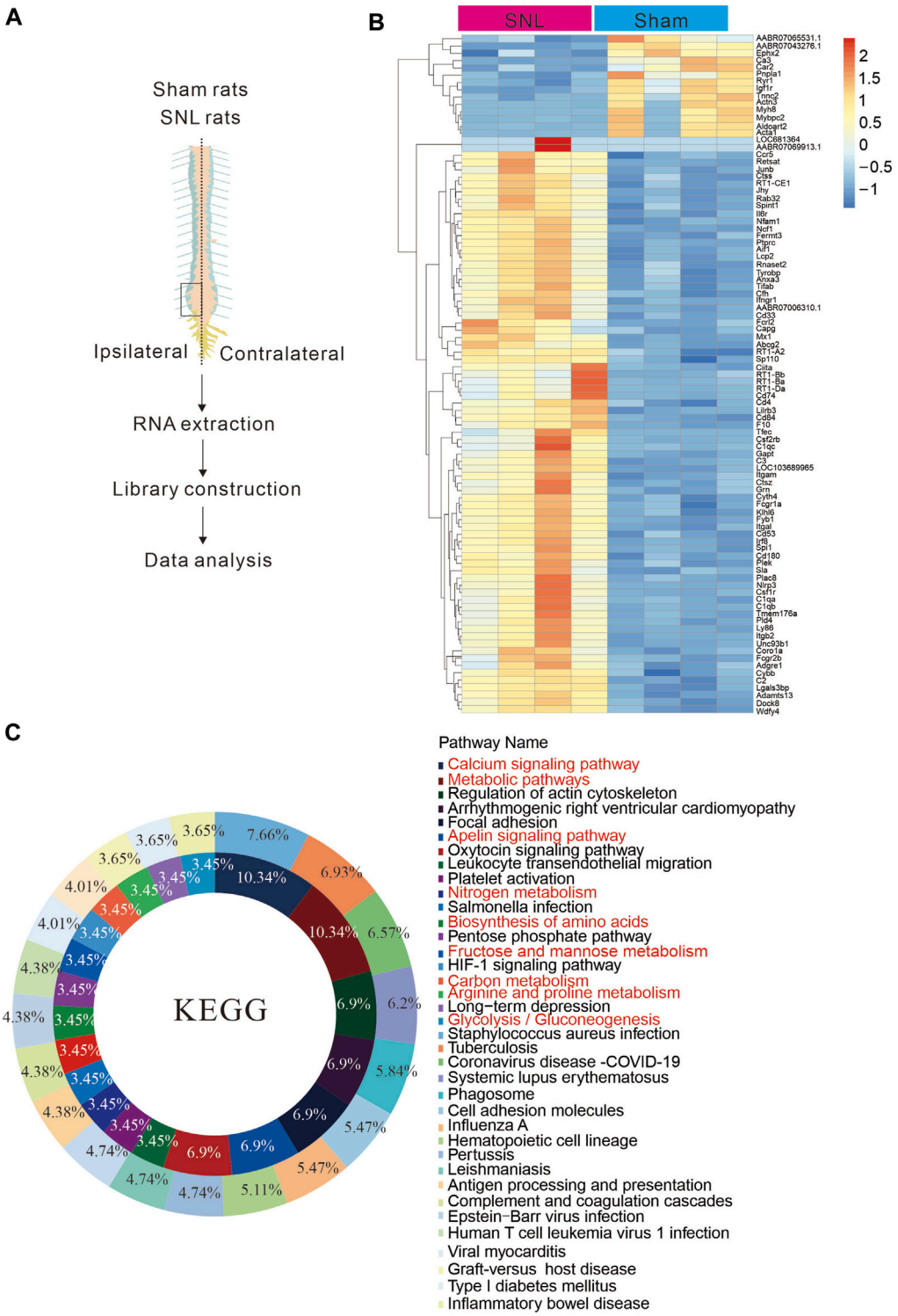

FIGURE 1
Chronic pain is associated with metabolic abnormalities **(A)** Sequence diagram of spinal nerve ligation chronic pain tissue in rats. **(B, C)**. Tissue sequencing heat map and KEEG analysis results. The results suggest that chronic pain may cause abnormal energy metabo.

DEX, we found that administration of the α-2 acetylcholine receptor agonist DEX significantly improved pain-induced metabolic abnormalities, including the following: alanine, aspartate and glutamate metabolism; nitrogen metabolism; arginine biosynthesis; cAMP signalling pathway; carbon metabolism; and biosynthesis of amino acids and metabolic pathways (Figure 3A, B). Therefore, DEX exerted analgesic effects by promoting neuronal metabolism in neuropathic pain.

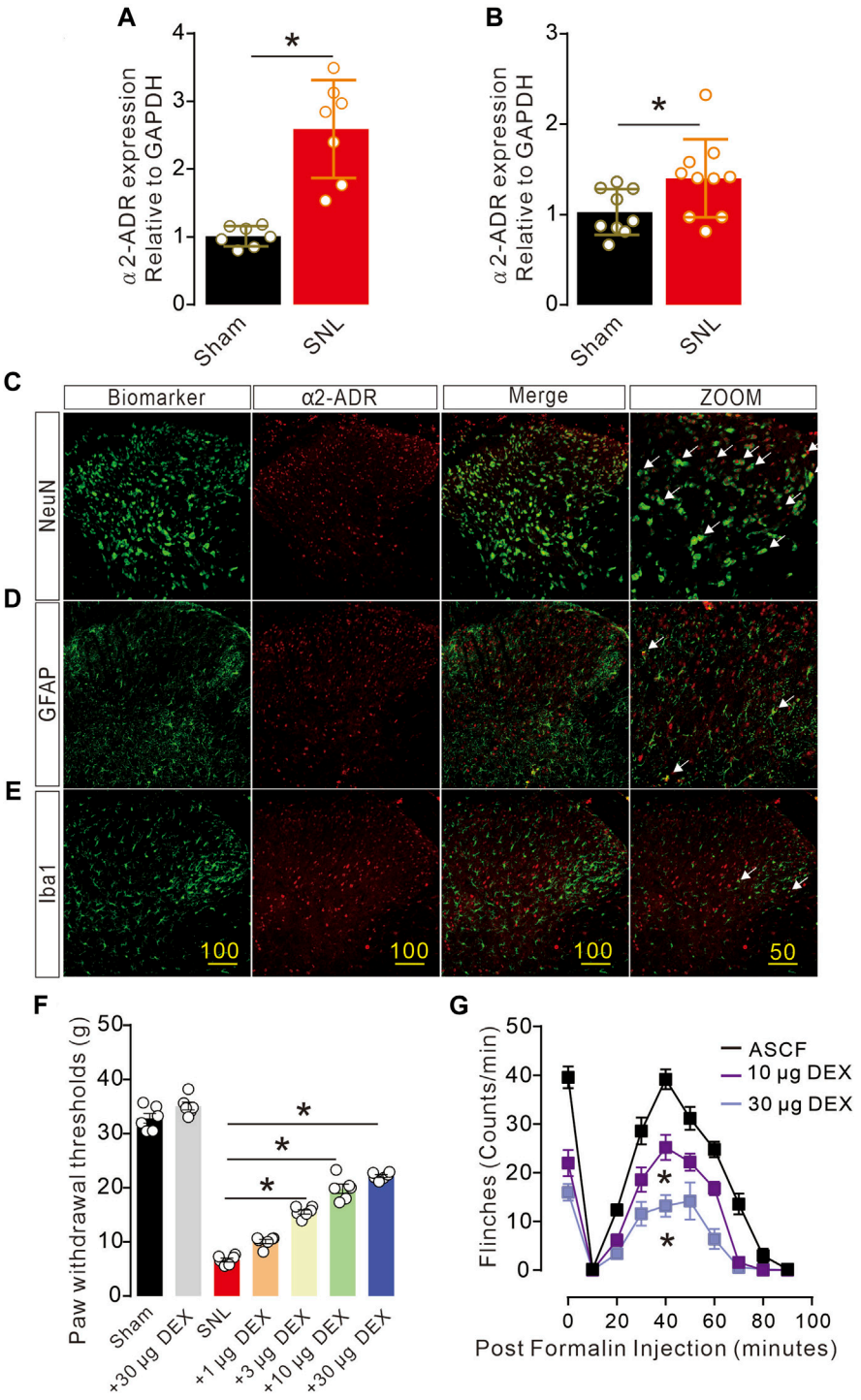

FIGURE 2
Activation of α2-ADR can improve the pain phenotype of rats **(A, B)**. The QPCR of α2-ADR receptors showed that pain caused a significant increase in presynaptic and postsynaptic α2-ADR receptors (presynaptic: t_{12} = 5.663, p = 0.001, two-tailed unpaired t-test; postsynaptic α2-ADR receptors t_{17} = 2.269, p = 0.0366 *$p < 0.05$, **$p < 0.01$). **(C–F)**. Immunofluorescence staining of α2-ADR receptor distribution showed that α2-ADR receptor was mainly distributed on neurons, and only a small part was distributed on astrocytes and microglia. f. The α2-ADR receptors agonist DEX significantly increased the foot contraction threshold in a dose-dependent manner ($F_{(6, 35)}$ = 311.8, $p < 0.0001$, two-way ANOVA followed by Sidak's post-tests, *$p < 0.05$). g. The alpha2-ADR receptor agonist DEX also alleviated formalin-induced inflammatory pain ($F_{(2, 120)}$ = 131.8, $p < 0.0001$, two-way ANOVA followed by Sidak's post-tests, *$p < 0.05$).

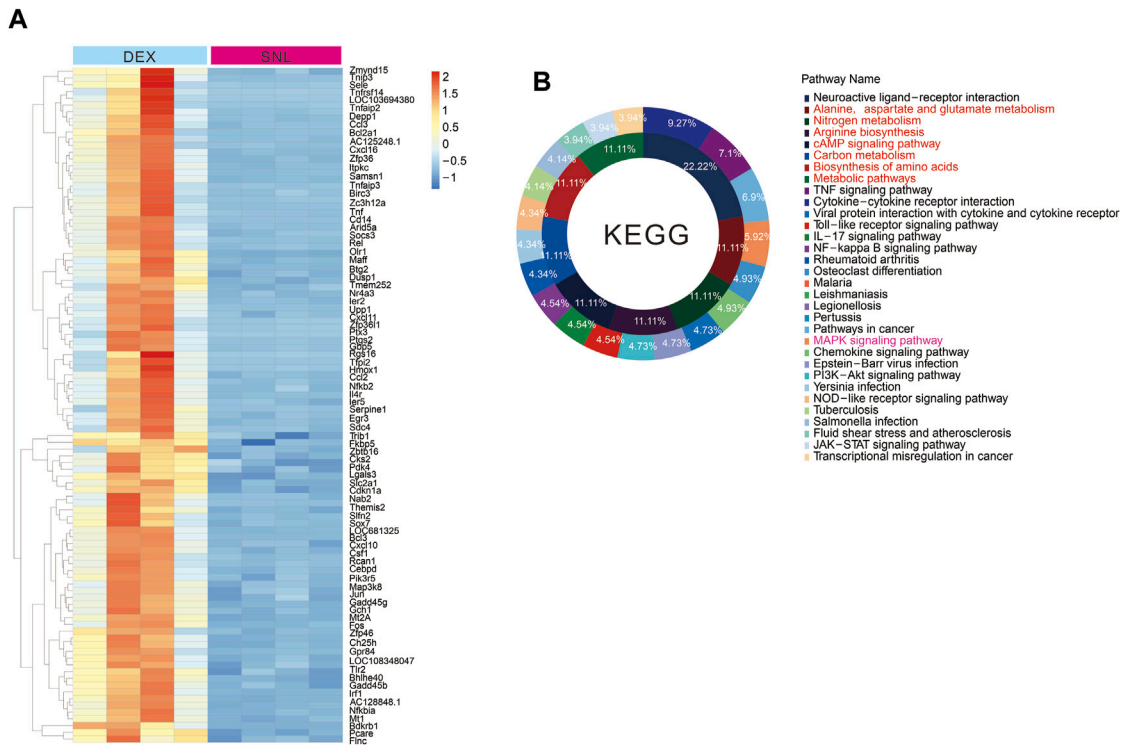

FIGURE 3
Activation of alpha-2 acetylcholine receptors can improve the metabolic abnormalities caused by pain **(A, B)**. Tissue sequencing heat map and KEEG analysis results. The administration of DEX can significantly change the metabolic abnormalities caused by SNL.

WGCNA selects the core module of DEX-induced analgesia

Alpha-2 acetylcholine receptor agonists induced large-scale gene transcriptional alterations. As such, WGCNA was applied to classify and analyse correlated genes and gene expression relationship. The two parts of gene expression cluster analysis and biometric correlation can be linked together. Characteristics associated with neuropathic pain, including spinal nerve ligation, pain, anxiety and PWT (paw withdrawal threshold), can be translated into a data distribution. The detected genes were then categorised according to their similarity principle, and a similar class of genes is grouped into the same module. WGCNAs and gene modules were established based on the expression data of rat spinal cord (L3–L5) samples. Correlation analysis was conducted with the basic characteristics of the samples (L5/L6 spinal nerve ligation, pain, anxiety and foot withdrawal reaction time, etc.) to obtain the key modules of DEX-induced analgesia and related gene pathways.

After the sample information was corrected and standardised, it was associated with the sample biological indicators. A sample cluster tree and a heat map of biological phenotypes were obtained (Figure 4A, B). To make the data close to the distribution characteristics of scale-free networks, this study determined that the minimum integer value when the fitting coefficient R^2 approached or reached 0.85 met the analysis requirements. The soft threshold $\beta = 8$ also met the data analysis requirements.

WGCNA includes gene sets classified according to similar expression and divides the embryonic gene expression modules through Cluster Tree Cut. Repeated checks were carried out until the data set and the internal structure of the data became stable, and the clustering system tree and corresponding module graph were obtained (Figure 4C). Topological overlap matrix (TOM) was used to describe dissimilarity between data modules. In particular, 1-TOM was used to represent the dissimilarity of gene modules (a value equal to 0 indicates a lack of data connection between two modules) to describe the relationship between modules accurately. Top correlated modules including turquoise, brown, yellow and grey were selected for analysis (correlation coefficient is ranging from 0.71 to 0.54) based on the completed system cluster tree and module heat map to fully understand gene signalling pathways associated with alpha-2 acetylcholine receptor agonism (Figure 4C–E).

Enrichment analysis of pain-related gene and signal pathway analysis

A significant correlation was found between gene module and alpha-2 acetylcholine receptor agonism-induced analgesic effects in neuropathic rats (correlation coefficient ranging from 0.71 to 0.54). The functional enrichment analysis of GO and KEGG showed that thousands of signal pathways were obtained, among which metabolism-related pathways had significant changes (Figure 5A–D). Biological process (BP) was mainly associated with metabolism, cellular metabolism, biosynthesis, nitrogen biosynthesis and RNA metabolism (Figure 5B). In molecular function (MF) analysis, signalling receptor binding, transmembrane signalling receptor activity, calcium ion

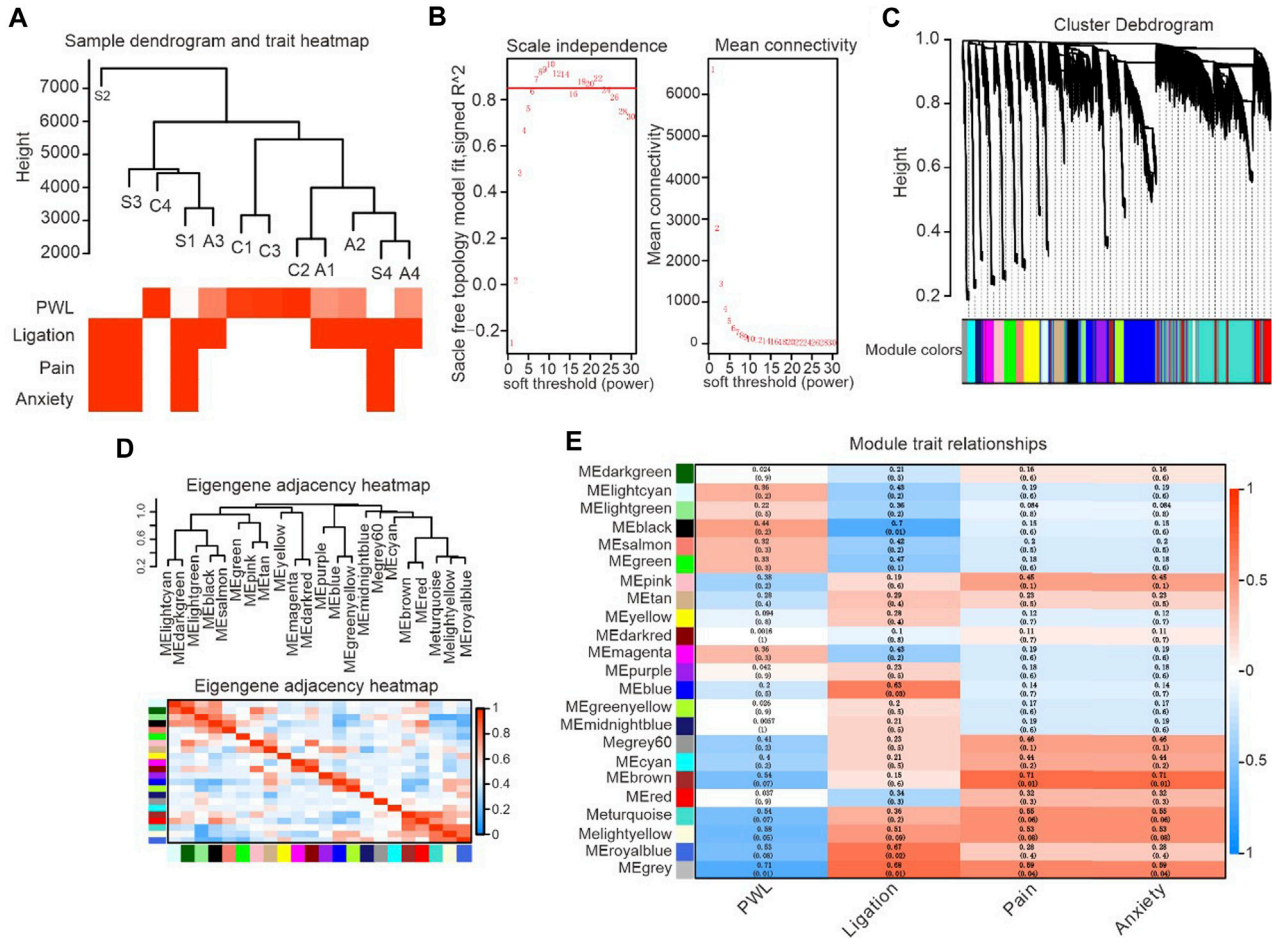

FIGURE 4
Identification of critical modules correlated with the paw withdrawal latency in DEX-induced analgesic effects. **(A)**. Gene expression system tree map and biometric heat map, representing gene expression and biometric clustering display. **(B)**. WGCNA soft threshold filtering and testing, representing the relationship between Y-axis unscaled fitting data and X-axis soft threshold parameters. **(C)**. The tree map of clustering system was obtained from the database, and the hierarchical linkage clustering method was used. The lower color showed the relationship of gene expression heterogeneity. **(D)**. The figure shows the correlation analysis between the enriched modules and PWL, with red indicating positive correlation and blue indicating negative correlation. **(E)**. The color in the figure represents the correlation coefficient between biometrics and modules, with red representing positive correlation and green representing negative correlation.

binding and GPCR activity were remarkably enriched (Figure 5C). In addition, KEGG were related to metabolic pathways, MAPK signalling pathways, neuroactive ligand receptor interaction, cAMP signalling pathway, calcium signalling pathway and Jak stat signalling (Figure 5D). These data proved that analgesic effects induced by alpha-2 acetylcholine receptor agonism targeted metabolic capacity and neural plasticity in neuropathic pain.

Activation of alpha-2 acetylcholine receptors significantly enhances blood supply at the site of spinal cord injury

Chronic pain causes metabolic abnormalities, and the activation of alpha-2 acetylcholine receptors can significantly alleviate pain behaviour. The vascular system should respond to synapse demand. To identify the mechanism of alpha-2 acetylcholine receptors acting on pain sensations, we detected blood flow at the site of spinal cord injury by ultrasonic blood flow imaging (Figure 6A, B). DEX significantly improved blood supply at the site of pain and promoted pain recovery, but it did not affect normal mice. The ΔF value of blood flow in the SNL group was significantly increased after DEX administration (Figure 6C-D). Hence, alpha-2 acetylcholine receptors can enhance blood flow, increase energy supply and promote pain recovery.

Alpha-2 acetylcholine receptor agonist DEX can upregulate key metabolism-related genes

After WGCNAs, enrichment gene analysis and ultrasonic imaging verification, we detected the expression of key genes activated by DEX through QPCR because these genes may guide blood and metabolic supply. DEX significantly increased the expression of key genes, such as pyruvate dehydrogenase kinase 4

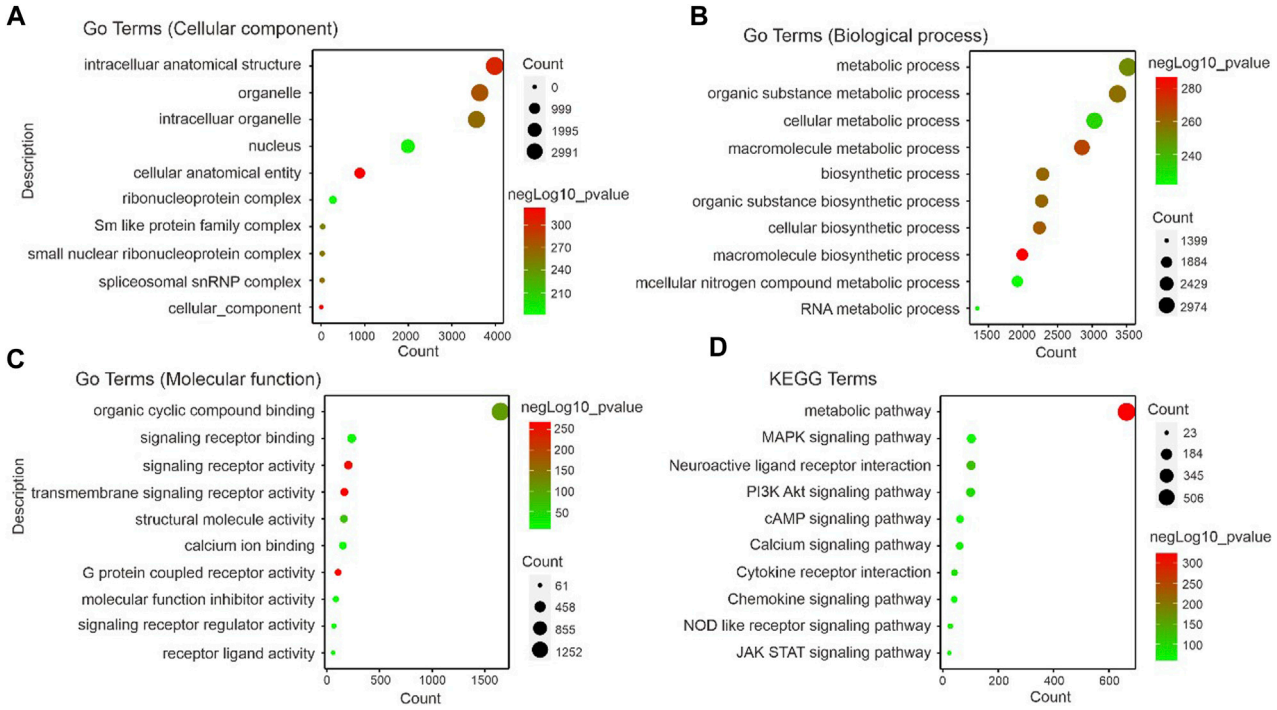

FIGURE 5
Identification of correlated signaling in DEX-induced analgesic effects **(A–C)**. GO displays the cellular component, biological process and molecular function related signal pathways. Importantly, the results in **(B)** show that a large number of metabolism-related signaling pathways are altered. **(D)**. The foot withdrawal time threshold is associated with the brown module. KEGG displays the enrichment results of signal pathways, indicating the pathways enriched by genes contained in the modules most relevant to PWL analyzed by WGCNA. The size of the dots represents the number of genes enriched to the relevant signal pathways, and the color represents the -log10*p*-value.

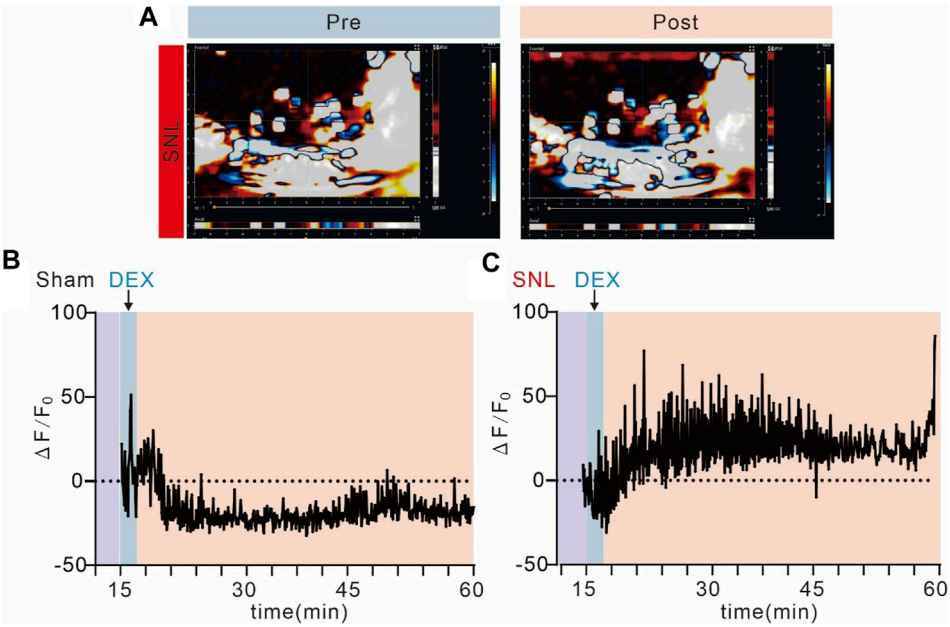

FIGURE 6
Alpha-2 acetylcholine receptors promote blood supply to spinal cord injuries **(A)**. Ultrasound imaging of spinal cord blood flow in SNL chronic pain mice before and after administration of DEX. **(B, C)**. Spinal cord blood flow in SNL chronic pain mice was significantly enhanced after DEX administration, but not in the sham group.

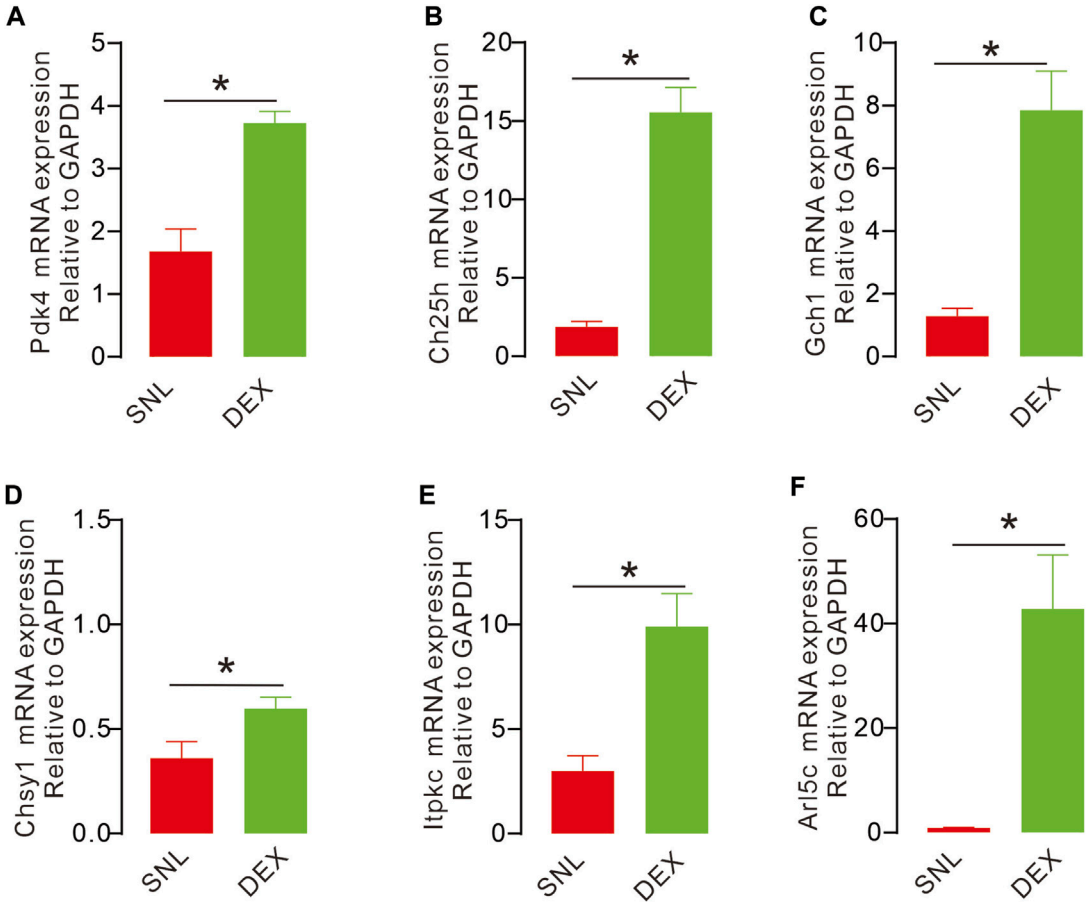

FIGURE 7
DEX causes upregulation of key metabolism-related genes **(A, C–F)**. The expression of key genes in different groups with QPCR. The expression of Arl5c, Ch25h, Itpkc, Pdk4, Gch1 were significantly increased after injection with DEX, compared with the sham operation group and SNL group, the expression was significant. **(D)**. Compared with the sham operation group, the expression of Chsy1 was significantly decreased. (Pdk4, (t_{14} = 5.068, p = 0.0002, *p < 0.05; Ch25h, t_{14} = 8.366, p < 0.0001, *p < 0.051; Gch1, t_{14} = 5.156, p = 0.0001, *p < 0.05; Chsy1, t_{14} = 2.473, p = 0.0268, *p < 0.05; Itpkc, t_{14} = 3.975, p = 0.0014, *p < 0.05; Arl5c, t_{14} = 4.051, p = 0.0012, *p < 0.05).

(Pdk4), cholesterol 25-hydroxylase (Ch25h), GTP cyclohydrolase 1 (Gch1), ADP ribosylation factor-like GTPase 5C (Arl5c), inositol–trisphosphate 3-kinase C (Itpkc) and chondroitin sulphate synthase 1 (Ghsy1) (Figures 7A–F). Our data demonstrated that these genes were remarkably affected in mediating analgesic effects on pain.

Changes in neuronal plasticity occur at the injury site in rats with chronic pain

Chronic pain often causes changes in neuroplasticity. This work aimed to explore changes in electrophysiological indicators of neurons at the injured site of spinal nerve ligation rats and determine if alpha-2 acetylcholine receptors can rescue such changes. By whole-cell patch clamp technique, we recorded the activity of spinal dorsal horn neurons in the sham and SNL groups. By analysing the micro-excitatory postsynaptic current mEPSC and micro-inhibitory postsynaptic current mIPSC, we found that pain caused by spinal nerve ligation significantly increased the frequency and amplitude of mEPSCs of spinal dorsal horn neurons (Figure 8A). These results suggest that pain can induce abnormal enhancement of excitatory synaptic transmission in neurons, and the use of α2-acetylcholine receptor agonist DEX can effectively inhibit the abnormal enhancement (Figures 8B–E). Chronic spinal nerve ligation can also cause abnormal reduction of IPSC, but DEX does not improve it (Figures 8F–J). Collectively, these data demonstrated that DEX produced analgesic effects by alleviating glutamatergic transmission by regulating metabolic demand and vascular response in neuropathic pain.

Discussion

nAChR is a ligand-gated ion channel formed by the pentameric arrangement of alpha and beta subunits (Mineur et al., 2023). The extracellular domain contains many binding sites of ligands that alter receptors through allosteric mechanisms (Rosenberg et al., 2002). Functional studies have shown that nAChRs help to control resting membrane potential, regulate synaptic transmission and mediate rapid excitatory transmission. The dysfunction of nAChR has been linked to several human diseases, such as

10.3389/fphar.2024.1359319

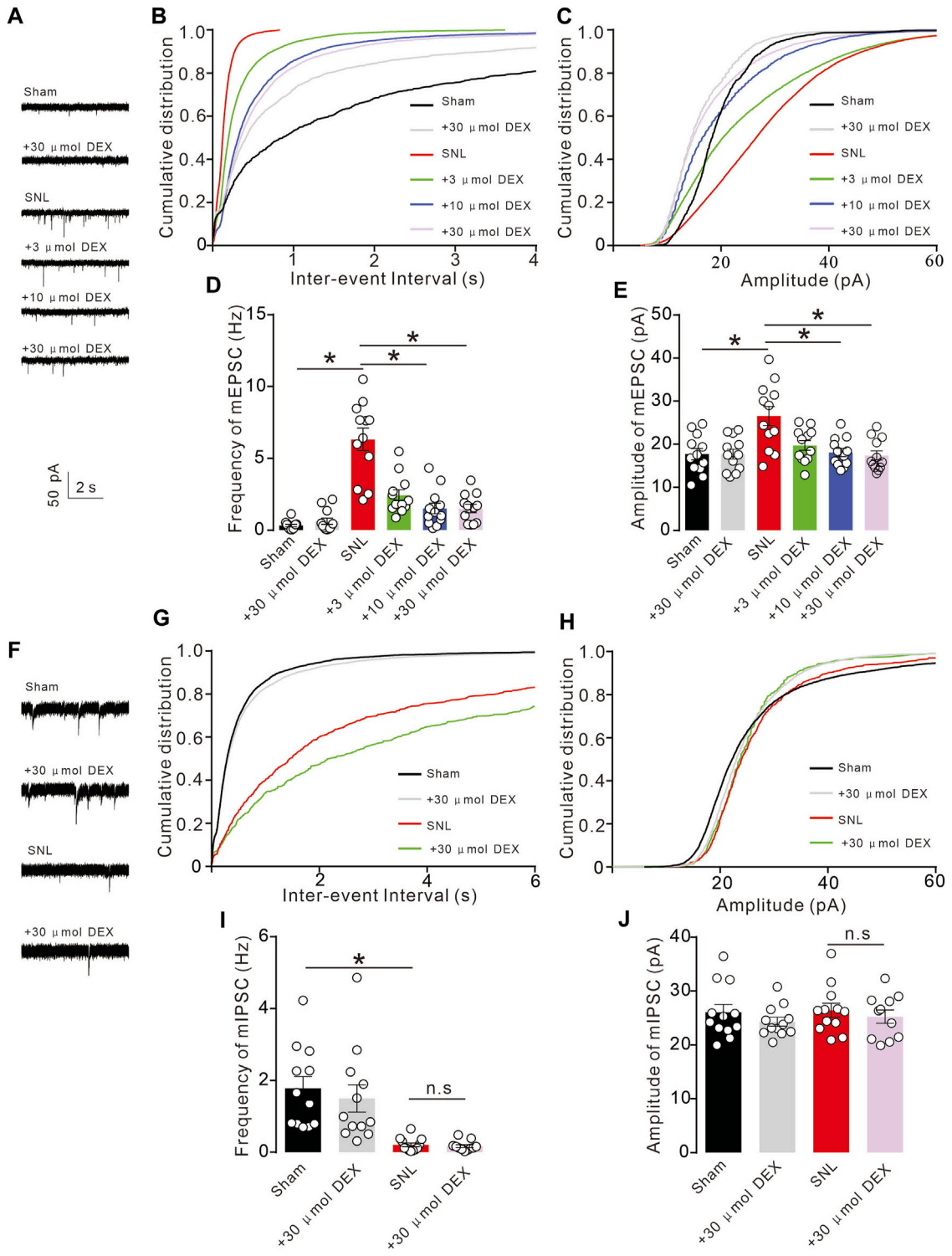

FIGURE 8
Chronic pain causes abnormal synaptic transmission of spinal cord neurons **(A)**. Chronic SNL pain results in abnormal increase of mEPSC in spinal dorsal horn neurons. **(B–E)**. The increase in mEPSC frequency and amplitude induced by SNL was significantly inhibited by DEX administration (Frequency: $F_{(5, 66)} = 27.94$, $p < 0.0001$, Amplitude: $F_{(5, 66)} = 6.698$, $p < 0.0001$, *$p < 0.05$, two-way ANOVA followed by Sidak's post-tests). **(F)**. SNL chronic pain can inhibit mIPSC, but giving DEX does not reverse it. **(G–J)**. SNL chronic pain can inhibit mIPSC frequency, but giving DEX does not improve it (Frequency: $F_{(3, 43)} = 10.63$, $p < 0.0001$, Amplitude: $F_{(3, 43)} = 0.6052$, $p = 0.6152$, *$p < 0.05$, two-way ANOVA followed by Sidak's post-tests).

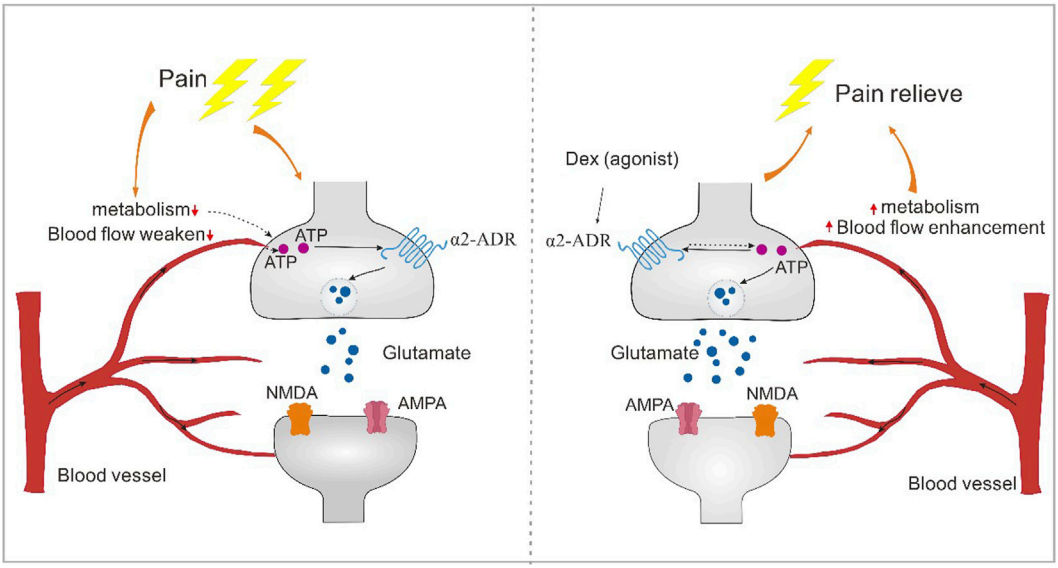

FIGURE 9
The alpha2-acetylcholine receptor regulates pain through energy metabolism. Blood vessels have the effect of responding to tissue metabolism. Blood flow at the pain site is weakened, resulting in abnormal energy supply to neurons, resulting in abnormal synaptic transmission. α2-acetylcholine receptors can enhance blood flow, increase the regulation of neuronal activity, reverse abnormal changes in synaptic plasticity, and thus regulate the occurrence of pain.

schizophrenia, Alzheimer's and Parkinson's disease (Spasova et al., 2022). In the present study, the expression of the α2-acetylcholine receptor at the injury site was significantly enhanced in the model of pain induced by nerve injury. Spinal nerve ligation is the most classic chronic pain model, which can cause nerve damage at the lesion site and lead to severe pain reactions. Therefore, SNL was chosen as the pain model in our study. We also observed a significant increase in presynaptic and postsynaptic mRNA expression. The neuropathic pain is mainly related to the imbalance of mitochondrial metabolism and the change in synaptic plasticity. Evidence suggests that α2-acetylcholine receptor agonists are closely related to mitochondrial homeostasis, and DEX significantly enhances the level of blood perfusion in the spinal cord, thereby confirming its regulatory function on energy metabolites required by mitochondria. In whole-cell perfusion experiments, we observed that DEX inhibited spinal cord glutaminergic neurotransmission in a dose-dependent manner, which may be related to its function in regulating mitochondrial metabolism. In summary, our study observed a correlation between DEX and pain at the global and neuronal levels.

Mitochondria are the only site of ATP synthesis, and it is necessary to guide nearby blood vessels to dilate through AMPK and NO to increase the blood supply at the mitochondrial site of local synaptic sites (Gou et al., 2023). However, the contents of neurons at the site of nerve injury will diffuse out of the cell, in which ATP is an important inflammatory mediator. ATP binds to receptors such as P2Y12, resulting in spinal cord glutaminergic neurotransmission. SNL significantly increased P2Y12 receptor levels, and injection of a P2Y12 antagonist (MRS2395 or clopidogrel) attenuated microglial activation; partial sciatic nerve ligation (PSNL) induced excessive micro-excitatory postsynaptic current (mEPSC), and this effect was significantly attenuated in P2Y12-knocked out mice (Yu et al., 2019). Abnormal levels of ATP in blood vessels are associated with a variety of diseases, such as inflammation, hypoxia and atherosclerosis. The heterogeneous distribution of ATP in the network, the heterogeneity between different concentrations and the same level of blood vessels play an important role in performing different functions (Gou et al., 2023). Astrocyte expression is closely related to ATP in the regulation of neuronal activity. Neurotransmitter receptors, including the P2 receptor, can release ATP in response to various stimuli and cause physiological reactions in response to extracellular ATP (Gu and Wiley, 2006). This process has reciprocal feedback with calcium ions and participates in neural activity. In addition, astrocytes direct the communication between neurons and blood vessels through their connecting blood vessels. In conclusion, ATP-mediated dynamic communication among neurons, astrocytes and blood vessels is a key molecule for information processing or integration in the central nervous system. Thus, theoretically, we observed the dynamic relationship between DEX and blood flow.

Synaptic transmission is a dynamic energy-consuming process and includes biological metabolism, which is based on ATP activity. Mitochondrial damage causes many diseases. In spinal cord injury, mitochondrial imbalance is the main feature that leads to irreversible body disability (Kang et al., 2020). ROS is a product of mitochondrial oxidative metabolism and is involved in maintaining REDOX balance. In physiological states, ROS production and elimination balance each other. However, in pathological states such as nerve injury, the contents of neurons overflow, leading to mitochondrial breakage and ROS accumulation in tissue parts, resulting in mitochondrial damage, further expanding the chaotic mitochondrial oxidative damage and

developing into serious mitochondria-mediated nervous system diseases (Smirnova et al., 2001). Therefore, mitochondrial homeostasis should be regulated and neural activity should be inhibited by regulating the α2-acetylcholine receptor. Neuronal energy metabolism is a complex life process designed for basic pathways of glucose metabolism: glycolysis, gluconeogenesis, glycogenesis, lipid, cholesterol, and glycogenolysis, which may engage in synaptic transmission. Our results revealed that cholesterol hydroxylase promotes cholesterol metabolism in extrahepatic tissues by converting cellular cholesterol to circulating oxysterols, thereby regulating various biological processes, especially in pain states; the upregulation of cholesterol hydroxylase (CH25H) remarkably increased the production of oxysterol metabolites and guide neuronal metabolic homeostasis (Choi et al., 2019). PDK4 is a repressor of the conversion of pyruvate into acetyl-CoA by the PHD complex in regulating ATP homeostasis during pathologic states. We demonstrated that PDK4 was upregulated following α2-acetylcholine agonism and promoted the ATP supply.

Therefore, in our study, we further support transcriptomic studies that demonstrated through FUS and whole-cell records that mitochondrial metabolic homeostasis is the main cause of α2-acetylcholine receptor analgesia. Damage to the binding of DEX, its agonist, leads to upregulated receptors that promote the communication between blood vessels and local synapses, thereby regulating mitochondrial ATP production and playing an analgesic role.

Conclusion

Blood vessels respond to tissue metabolism. Blood flow at the pain site is weakened, resulting in abnormal energy supply to neurons and abnormal synaptic transmission. α2-Acetylcholine receptors can enhance blood flow, increase the regulation of neuronal activity, reverse abnormal changes in synaptic plasticity and regulate the occurrence of pain (Figure 9).

Data availability statement

The original contributions presented in the study are publicly available. This data can be found here: https://www.ncbi.nlm.nih.gov/bioproject/1082875.

Ethics statement

The animal study was approved by the Apply through IACUC Ethics of Shanghai Jiao Tong University, (No. 10902). The study was conducted in accordance with the local legislation and institutional requirements.

Author contributions

KZ: Data curation, Methodology, Writing–original draft, Writing–review and editing. Y-QR: Data curation, Investigation, Writing–review and editing. YX: Formal Analysis, Investigation, Methodology, Writing–original draft. DD: Data curation, Formal Analysis, Methodology, Writing–review and editing. TZ: Conceptualization, Writing–review and editing. Y-ZD: Formal Analysis, Investigation, Methodology, Writing–review and editing. XL: Data curation, Methodology, Writing–review and editing. W-KG: Data curation, Methodology, Writing–original draft. J-QG: Data curation, Methodology, Writing–original draft. LM: Data curation, Methodology, Writing–original draft.

Funding

The author(s) declare financial support was received for the research, authorship, and/or publication of this article. The study is supported by the Postdoctoral Science Foundation of China (2021M692118, W-JX; 2022M712126, W-KG; 2023M742355, GZC20231656, KZ) and Shanghai Mental Health Center (2021-YJ11 and 2023-YJ02).

Conflict of interest

The authors declare that the research was conducted in the absence of any commercial or financial relationships that could be construed as a potential conflict of interest.

Publisher's note

References

Choi, W. S., Lee, G., Song, W. H., Koh, J. T., Yang, J., Kwak, J. S., et al. (2019). The CH25H-CYP7B1-RORα axis of cholesterol metabolism regulates osteoarthritis. *Nature* 566 (7743), 254–258. doi:10.1038/s41586-019-0920-1

Claron, J., Hingot, V., Rivals, I., Rahal, L., Couture, O., Deffieux, T., et al. (2021). Large-scale functional ultrasound imaging of the spinal cord reveals in-depth spatiotemporal responses of spinal nociceptive circuits in both normal and inflammatory states. *Pain* 162 (4), 1047–1059. doi:10.1097/j.pain.0000000000002078

Dai, C. Q., Guo, Y., and Chu, X. Y. (2020). Neuropathic pain: the dysfunction of Drp1, mitochondria, and ROS homeostasis. *Neurotox. Res.* 38 (3), 553–563. doi:10.1007/s12640-020-00257-2

D Amico, D., Olmer, M., Fouassier, A. M., Valdés, P., Andreux, P. A., Rinsch, C., et al. (2022). Urolithin A improves mitochondrial health, reduces cartilage degeneration, and alleviates pain in osteoarthritis. *Aging Cell* 21 (8), e13662. doi:10.1111/acel.13662

Deuis, J. R., Dvorakova, L. S., and Vetter, I. (2017). Methods used to evaluate pain behaviors in rodents. *Front. Mol. Neurosci.* 10, 284. doi:10.3389/fnmol.2017.00284

Frediani, F., and Bussone, G. (2019). When does the brain choose pain? *Neurol. Sci.* 40, S27–S29. doi:10.1007/s10072-019-03849-9

Gou, Z., Zhang, H. D., and Misbah, C. (2023). Heterogeneous ATP patterns in microvascular networks. *J. R. Soc. Interface* 20, 20230186. doi:10.1098/rsif.2023.0186

Gu, B. J., and Wiley, J. S. (2006). Rapid ATP-induced release of matrix metalloproteinase 9 is mediated by the P2X7 receptor. *Blood* 12 (107), 4946–4953. doi:10.1182/blood-2005-07-2994

Kang, L., Liu, S., Li, J., Tian, Y., Xue, Y., and Liu, X. (2020). The mitochondria-targeted anti-oxidant MitoQ protects against intervertebral disc degeneration by ameliorating mitochondrial dysfunction and redox imbalance. *Cell Prolif.* 53 (3), e12779. doi:10.1111/cpr.12779

Luo, C., Kuner, T., and Kuner, R. (2014). Synaptic plasticity in pathological pain. *Trends Neurosci.* 37 (6), 343–355. doi:10.1016/j.tins.2014.04.002

Ma, L., Peng, S., Wei, J., Zhao, M., Ahmad, K. A., Chen, J., et al. (2021). Spinal microglial β-endorphin signaling mediates IL-10 and exenatide-induced inhibition of synaptic plasticity in neuropathic pain. *Cns Neurosci. Ther.* 27 (10), 1157–1172. doi:10.1111/cns.13694

Marcu, R., Zheng, Y., and Hawkins, B. J. (2017). Mitochondria and angiogenesis. *Mitochondrial Dyn. Cardiovasc. Med.* 982, 371–406. doi:10.1007/978-3-319-55330-6_21

Mineur, Y. S., Soares, A. R., Etherington, I. M., Abdulla, Z. I., and Picciotto, M. R. (2023). Pathophysiology of nAChRs: limbic circuits and related disorders. *Pharmacol. Res.* 191. doi:10.1016/j.phrs.2023.106745

Niehaus, J. K., Taylor-Blake, B., Loo, L., Simon, J. M., and Zylka, M. J. (2021). Spinal macrophages resolve nociceptive hypersensitivity after peripheral injury. *Neuron* 109 (8), 1274–1282.e6. doi:10.1016/j.neuron.2021.02.018

Rosenberg, M. M., Blitzblau, R. C., Olsen, D. P., and Jacob, M. H. (2002). Regulatory mechanisms that govern nicotinic synapse formation in neurons. *J. Neurobiol.* 53 (4), 542–555. doi:10.1002/neu.10112

Smirnova, E., Griparic, L., Shurland, D. L., and van der Bliek, A. M. (2001). Dynamin-related protein Drp1 is required for mitochondrial division in mammalian cells. *Mol. Biol. Cell* 12 (8), 2245–2256. doi:10.1091/mbc.12.8.2245

Spasova, V., Mehmood, S., Minhas, A., Azhar, R., Anand, S., Abdelaal, S., et al. (2022). Impact of nicotine on cognition in patients with schizophrenia: a narrative review. *Cureus J. Med. Sci.* 14 (4), e24306. doi:10.7759/cureus.24306

van der Vlist, M., Raoof, R., Willemen, H. L. D. M., Prado, J., Versteeg, S., Martin Gil, C., et al. (2022). Macrophages transfer mitochondria to sensory neurons to resolve inflammatory pain. *Neuron* 110 (4), 613–626.e9. doi:10.1016/j.neuron.2021.11.020

Wang, W., Wang, Q., Huang, J., Li, H., Li, F., Li, X., et al. (2023). Store-operated calcium entry mediates hyperalgesic responses during neuropathy. *Febs Open Bio* 13, 2020–2034. doi:10.1002/2211-5463.13699

Yu, T. T., Zhang, X., Shi, H., Tian, J., Sun, L., Hu, X., et al. (2019). P2Y12 regulates microglia activation and excitatory synaptic transmission in spinal lamina II neurons during neuropathic pain in rodents. *Cell Death Dis.* 10, 165. doi:10.1038/s41419-019-1425-4

Zhang, S. B., Lin, S. Y., Liu, M., Liu, C. C., Ding, H. H., Sun, Y., et al. (2019). CircAnks1a in the spinal cord regulates hypersensitivity in a rodent model of neuropathic pain. *Nat. Commun.* 10, 4119. doi:10.1038/s41467-019-12049-0

frontiers | Frontiers in Pharmacology

TYPE Original Research
PUBLISHED 17 April 2024
DOI 10.3389/fphar.2024.1382381

OPEN ACCESS

EDITED BY
Weijie Xie,
Tongji University, China

REVIEWED BY
Lyuchun Cui,
Shanghai Mental Health Center, China
Fang Wang,
Tongji University, China

*CORRESPONDENCE
Haishan Shi,
julia2k@126.com
Zezhi Li,
biolpsychiatry@126.com
Yuping Ning,
ningjeny@126.com

RECEIVED 05 February 2024
ACCEPTED 26 March 2024
PUBLISHED 17 April 2024

CITATION
Che X, Miao T, Shi H, Li Z and Ning Y (2024), Hippocampal region metabolites and cognitive impairment in patients with general paresis: based on ^{1}H-proton magnetic resonance spectroscopy.
Front. Pharmacol. 15:1382381.
doi: 10.3389/fphar.2024.1382381

Hippocampal region metabolites and cognitive impairment in patients with general paresis: based on ^{1}H-proton magnetic resonance spectroscopy

Xin Che[1,2,3], Tianyang Miao[1,2,3], Haishan Shi[1,2,3]*, Zezhi Li[1,2,3]* and Yuping Ning[1,2,3]*

[1]The Affiliated Brain Hospital, Guangzhou Medical University, Guangzhou, China, [2]Guangdong Engineering Technology Research Center for Translational Medicine of Mental Disorders, Guangzhou, China, [3]Key Laboratory of Neurogenetics and Channelopathies of Guangdong Province and the Ministry of Education of China, Guangzhou Medical University, Guangzhou, China

Background: This study utilizes Hydrogen proton magnetic resonance spectroscopy (^{1}H-MRS) to investigate metabolite concentrations in the bilateral hippocampus of general paresis (GP) patients.

Methods: A total of 80 GP patients and 57 normal controls (NCs) were enrolled. Metabolite ratios in the bilateral hippocampus were measured using ^{1}H-MRS. Cognitive function was assessed using the Mini-Mental State Examination (MMSE). Based on MMSE scores, participants were categorized into normal control, mild cognitive impairment, and moderate-severe dementia groups. Metabolite ratios (N-acetylaspartate (NAA)/creatine (Cr), choline (Cho)/creatine (Cr), N-acetylaspartate (NAA)/choline (Cho), myoinositol (MI)/creatine (Cr), choline (Cho)/N-acetylaspartate (NAA)) were compared between groups, and correlations between metabolite ratios and cognitive performance were examined.

Results: MMSE scores progressively decreased in the normal, mild cognitive impairment, and moderate-severe dementia groups ($p < 0.001$). The moderate-severe dementia group showed significantly lower NAA/Cr ratios in the left hippocampus region (L-NAA/Cr ratios) ($p < 0.001$) and higher Cho/NAA ratios in the left hippocampus region (L-Cho/NAA ratios) ($p < 0.05$) compared to the other groups. However, differences in L-NAA/Cr and L-Cho/NAA ratios between the mild cognitive impairment group and the NC group were not significant in the hippocampus region ($p > 0.05$). NAA/Cho and NAA/Cr ratios in the right hippocampus region (R-NAA/Cho and R-NAA/Cr ratios) in the moderate-severe dementia group were lower than those in the control group ($p < 0.05$). No correlation was found between metabolite ratios and MMSE scores in bilateral hippocampus regions.

Conclusion: There are distinctive metabolic characteristics in the hippocampus of GP patients. GP patients exhibited lower NAA/Cr and NAA/Cho ratios in the bilateral hippocampus, indicating neuron loss in these areas, which may become more pronounced as the disease progresses.

KEYWORDS

general paresis, general paresis of insane, magnetic resonance spectroscopy, *Treponema pallidum*, hippocampus

Introduction

Although syphilis, an infection caused by *Treponema pallidum* (*T. pallidum*) primarily transmitted through sexual behaviors, was nearly eradicated from China 50 years ago, it has experienced a gradual resurgence (Wang et al., 2011). Furthermore, reports indicate that the incidence of syphilis continued to rise between January 2005 and December 2020 in China (Zheng et al., 2023). Researchers have observed the presence of *T. pallidum* and an increased number of spirochetal plaques in the cerebral cortex of certain patients diagnosed with general paresis (GP), suggesting the invasion of the central nervous system by *T. pallidum* in individuals affected by syphilis. When the cerebral cortex shows extensive deterioration or manifests dementia symptoms, this condition is commonly referred to as "general paralysis of the insane" (GPI), "dementia paralytica," or simply "general paralysis" (Miklossy, 2015; Chakravarthi and Joshi, 2021; Ha et al., 2024).

Hydrogen proton magnetic resonance spectroscopy (^{1}H-MRS) is a non-invasive technique employed to explore alterations in neurogenesis-related metabolites within the live human hippocampus concerning particular tasks or disease states. This method allows for the assessment of energy metabolism, neuronal function, and glial response in the human brain, particularly useful in the study of neurodegenerative disorders (Maul et al., 2020), brain tumors (Tomiyasu and Harada, 2022), central nervous system infection (Liu et al., 2023) and psychiatric disorders (Port, 2020). N-acetylaspartate (NAA), choline (Cho), myoinositol (MI), and creatine (Cr) are frequently identified metabolites in ^{1}H-MRS. NAA is indicative of neuron densities, Cho is linked to membrane breakdown and turnover, MI serves as an organic osmolyte and a marker for glial cells, while Cr is recognized as a marker for energy metabolism (Lucassen et al., 2020; Tomiyasu and Harada, 2022).

Although significant abnormal structural changes may not be apparent in the early stages of Alzheimer's Disease (AD), in HIV-positive individuals, and in patients with neurosyphilis, metabolic disorders are detected through ^{1}H-MRS abnormalities. These abnormalities unveil distinct metabolic patterns across various brain regions, which are associated with the progression of the respective diseases (Pw et al., 2014; Zeng et al., 2021).

It has been established that patients with AD exhibit deposition of Aβ and phosphorylated-tau in the brain. Similarly, patients with GP demonstrate pathophysiological features similar to those observed in AD (Danics et al., 2021). Morphologically, the distribution of spirochete colonies in patients with GP mirrors the deposition pattern of senile plaques. Spirochetes are predominantly found in the hippocampus and frontal cortex, and their buildup correlates with consequential alterations. GP patients commonly experience a broad decline in cognitive function, chiefly marked by memory impairment, frequently accompanied by mental symptoms like impulsivity and delusions (Chiara et al., 2023). These symptoms could indicate neuronal damage in regions such as the hippocampus, and ^{1}H-MRS may indirectly indicate the extent of such damage. However, there has been limited exploration of metabolite concentrations in the hippocampus of patients with GP using ^{1}H-MRS, and even fewer studies have investigated the correlations between metabolite levels and cognitive function in these patients.

Therefore, through the utilization of ^{1}H-MRS, we assessed the metabolic alterations in the hippocampus of patients with GP and examined the associations between metabolite levels in the bilateral hippocampus and the cognitive function of GP patients. This investigation aimed to reflect the extent of neuronal damage and the severity of the disease.

Subjects and methods

Subjects

All patients were recruited from the inpatient units of the Affiliated Brain Hospital of Guangzhou Medical University, and written informed consent was obtained from patients or their guardians, particularly in cases of severe cognitive impairment.

Comprehensive assessments were conducted, involving thorough history taking, physical and neurological examinations, neuropsychological assessments, appropriate laboratory tests, and magnetic resonance imaging (MRI) scans. Special attention was given to laboratory tests, specifically checking vitamin B12, folate, and thyroid hormone status to rule out dementia caused by anemia or thyroid hypofunction, thereby enhancing the accuracy of clinical diagnoses.

Cognitive function was evaluated using the Mini-Mental State Examination (MMSE), and diagnoses were reviewed by a senior neurologist with subspecialty training in neurodegenerative disorders.

Patients meeting the criteria for general paresis were carefully selected based on the following criteria: 1) meeting the DSM-IV criteria for dementia with a duration exceeding 1 year; 2) testing positive for the rapid plasma reagin (RPR) or the toluidine red unheated serum test (TRUST), and *T. pallidum* hemagglutination (TPHA) in both serum and cerebrospinal fluid (CSF); 3) having white cell counts in CSF of 10×10^6/L and/or protein levels exceeding 500 mg/L. Exclusion criteria included patients with concurrent human immunodeficiency virus infection or cerebral infection caused by other microorganisms (Wang et al., 2011; Haishan et al., 2015).

The criteria for the normal control group included: 1) absence of neurological or psychiatric disorders; 2) no abnormal findings in conventional brain MR imaging; 3) no complaints of cognitive disorders; 4) an MMSE total score of 27 or higher.

MRI data acquisition

^{1}H-MRS and structural MRI examinations were conducted using a Philips 3T Achieva MR scanner (Philips Medical Systems, Best, Netherlands). We selected the hippocampus as the region of interest. T1-weighted images facilitated tissue segmentation, and manual editing of the hippocampus was performed. A point-resolved spectroscopy (PRESS) sequence was employed to simultaneously acquire water-suppressed ^{1}H-MRS from the bilateral hippocampus regions. The timing parameters were set at TR/TE/NSA 2000ms/35ms/128, with an in-plane resolution of $25 \times 10\ mm^2$ and a 10-mm-thick section, aligned approximately along the long axis of the hippocampus (Figure 1).

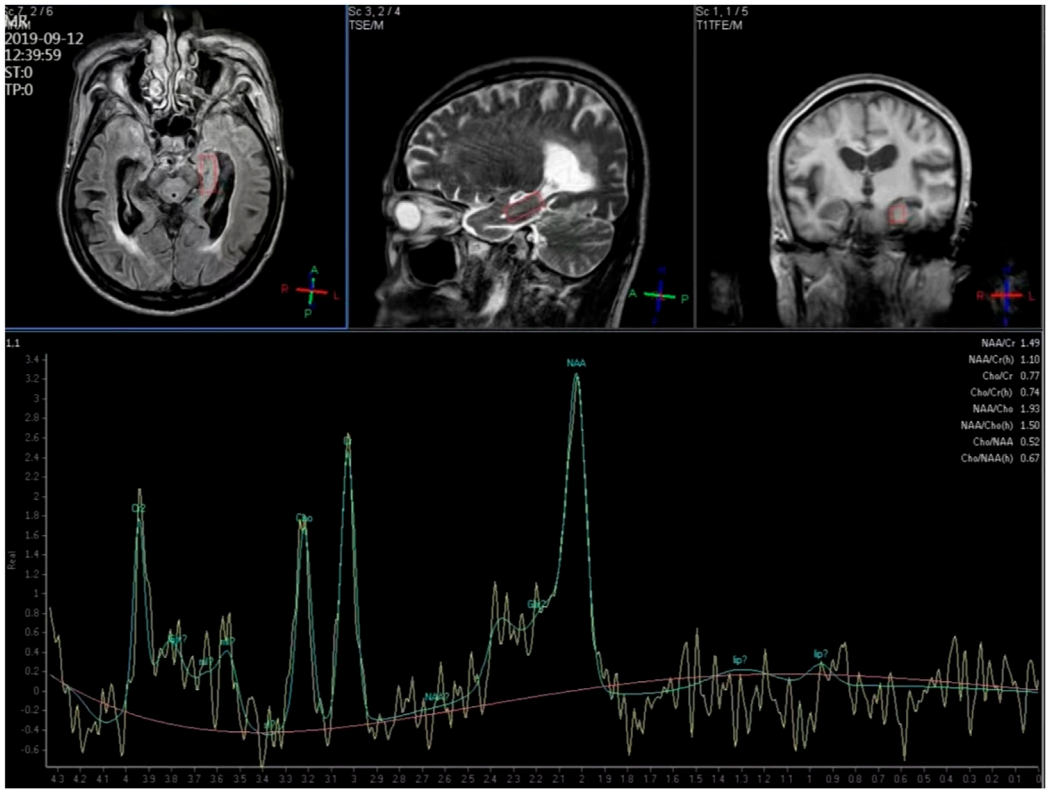

FIGURE 1
Hydrogen proton magnetic resonance spectroscopy for the left hippocampus region.

Structural MRI together with ^{1}H-MRS, including shimming and adjustments, required approximately 40 min of acquisition time. Peak areas of NAA, Cr, Cho and MI were estimated using fully automated spectral-fitting software. The ratios of the area under each peak were expressed relative to Cr in each spectrum. Voxel placements for spectroscopy and all data analysis were carried out by a trained radiologist who was blind to each subject's diagnosis.

Statistical analysis

G*power software was used to calculate the power and effect size. A total of at least 52 subjects were included, with a minimum of 26 subjects in each group. Data analysis was conducted using the Statistical Package for Social Sciences (SPSS, version 29). Descriptive statistics including mean ± standard deviation (M±SD), median, and percentiles were calculated. Demographic and clinical variables between two groups were assessed using chi-square analysis and Independent-Sample *t*-Test. Two-group comparisons were performed with Independent-Sample *t*-Test or Mann-Whitney U Test. For comparisons among three groups, Oneway-ANOVA or Kruskal-Wallis H Test was employed, followed by *post hoc* Bonferroni's test for multiple comparisons. This analysis included demographic and clinical characteristics data, energy metabolism data, and cognitive assessments.

Correlations between ^{1}H-MRS data and cognitive scale scores were examined using Spearmen correlations, and false discovery rate (FDR) correction was applied. A p-value less than 0.05 was considered statistically significant, and all tests were two-tailed.

Results

Demographic and clinical charateristics

We recruited 80 patients with GP and 57 NC subjects. There were no significant differences in age between the GP and the NC groups ($p > 0.05$). GP group had significant lower scores on MMSE test ($p < 0.001$) (Figure 2). There were significant differences between groups. Participants in each group were categorized based on their level of education. No significant differences were observed between the two groups in terms of education level (Table 1).

Metabolite concentrations in the GP and NC groups

Metabolite concentrations in bilateral hippocampus of the GP and the NC groups were compared. GP patients showed significantly lower NAA/Cr and NAA/Cho ratios in bilateral hippocampus region ($p < 0.05$) compared to the NC subjects. It also exhibited a significantly higher Cho/NAA ratios in bilateral hippocampus region ($p < 0.05$) compared to the NC subjects. Differences in Cho/

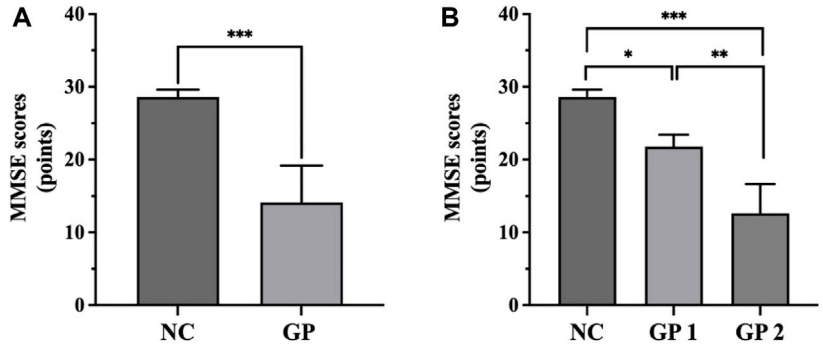

FIGURE 2
Comparisons of MMSE scores among groups. **(A)** GP group had significant lower scores on MMSE test. **(B)** GP 2 group had significant lower scores on MMSE test compared to the NC and GP 1 groups. NC: control group. GP 1: mild cognitive impairment group. GP 2: moderate-severe dementia group. $*p < 0.05$, $**p < 0.01$, $***p < 0.001$.

TABLE 1 Demographic and clinical characteristics of GP and NC subjects.

	NC	GP	t/H/x^2	*p*	*Post Hoc*
n	57	80	—	—	—
Male/Female	24/33	68/12	27.77	<0.001	
Age (years)	58.40 ± 7.41	55.76 ± 9.15	1.80	0.07	
MMSE (points)	29.00 (28.00, 29.00)	14.00 (11.25, 18.00)	−9.99	<0.001	NC >GP
Education level (illiterate/elementary education/ middle school education/bachelor's degree and above)	1/20/30/6	1/24/44/11	0.91[a]	0.88	

[a]Fisher's exact test.

Cr and MI/Cr ratios between the GP and the NC groups were not significant in bilateral hippocampus region ($p > 0.05$) (Table 2; Figure 3).

According to the MMSE scores, participants were recruited and divided into three groups: 57 normal controls with MMSE score 27 to 30 (control group, NC group), 13 patients with MMSE score 20 to 26 (mild cognitive impairment group, GP 1 group) and 67 patients with MMSE score 0 to 19 (moderate-severe dementia group, GP 2 group).

There were no significant differences in age and education level between three groups ($p > 0.05$). Moderate-severe dementia group had significant lower scores on MMSE test compared to the others ($p < 0.05$). There were differences in sex between three groups (Table 3; Figure 2).

Metabolite concentrations in the mild cognitive impairment group, moderate-severe dementia group and NC groups

Metabolite concentrations in bilateral hippocampus of three groups were compared. GP patients showed significantly lower NAA/Cr and NAA/Cho ratios in the left hippocampus region (L-NAA/Cr and L-NAA/Cho ratios) compared to the NC subjects. So we did ANOVA test for multiple comparisons. Moderate-severe dementia groups showed significantly lower L-NAA/Cr and L-NAA/Cho ratios ($p < 0.05$), compared with the other two groups. But differences in L-NAA/Cr and L-NAA/Cho ratios between the mild cognitive impairment group and the NC groups were not significant ($p > 0.05$).

It also exhibited a significantly lower NAA/Cho and NAA/Cr ratios in right side of the hippocampus region (R-NAA/Cho and R-NAA/Cr ratios) in moderate-severe group ($p < 0.05$) compared to the NC subjects. Additionally, there were no difference between the GP 2 and GP 1 groups, nor between the GP 1 and NC groups ($p > 0.05$).

Conversely, Moderate-severe dementia group showed significantly higher L-Cho/NAA ratios ($p < 0.001$), compared with the other two groups. But differences in L-Cho/NAA ratios between the GP 1 and NC group were not significant ($p > 0.05$). It also showed a significantly higher Cho/NAA ratios in right side of the hippocampus region (R-Cho/NAA ratios) in GP 2 group ($p < 0.05$) compared to the NC subjects. We found no significant difference in R-Cho/NAA between the GP 1 and NC groups. Furthermore, there was no significant difference in R-Cho/NAA levels between the GP 1 and GP 2 groups ($p > 0.05$).

When we compared the differences of Cho/Cr and MI/Cr ratio in bilateral hippocampus region observed in all groups by means of Kruskal-Wallis Test analyze we did not find significant differences ($p > 0.05$) (Table 4; Figure 3).

TABLE 2 Comparisons of metabolite concentrations of GP and NC subjects.

	NC	GP	t/H	*p*	*Post Hoc*
L-NAA/Cr	1.72 ± 0.31	1.42 ± 0.30	5.81	<0.001	NC >GP
L-Cho/Cr	0.92 ± 0.18	0.87 ± 0.19	1.56	0.12	—
L-NAA/Cho	1.93 (1.53, 2.17)	1.65 (1.37, 1.88)	−2.99	0.003	NC >GP
L-Cho/NAA	0.52 (0.46, 0.65)	0.61 (0.53, 0.73)	−2.79	0.005	NC <GP
L-MI/Cr	0.71 (0.53, 0.92)	0.77 (0.60, 0.96)	−1.39	0.17	—
R-NAA/Cr	1.64 (1.45, 1.87)	1.49 (1.27, 1.71)	−2.67	0.008	NC >GP
R-Cho/Cr	0.90 (0.77, 1.08)	0.90 (0.77, 1.08)	−0.28	0.78	—
R-NAA/Cho	1.87 (1.49, 2.24)	1.59 (1.36, 1.85)	−3.10	0.002	NC >GP
R-Cho/NAA	0.54 (0.45, 0.67)	0.63 (0.53, 0.73)	−2.97	0.003	NC <GP
R-MI/Cr	0.70 (0.35, 1.00)	0.81 (0.52, 1.07)	−1.11	0.27	—

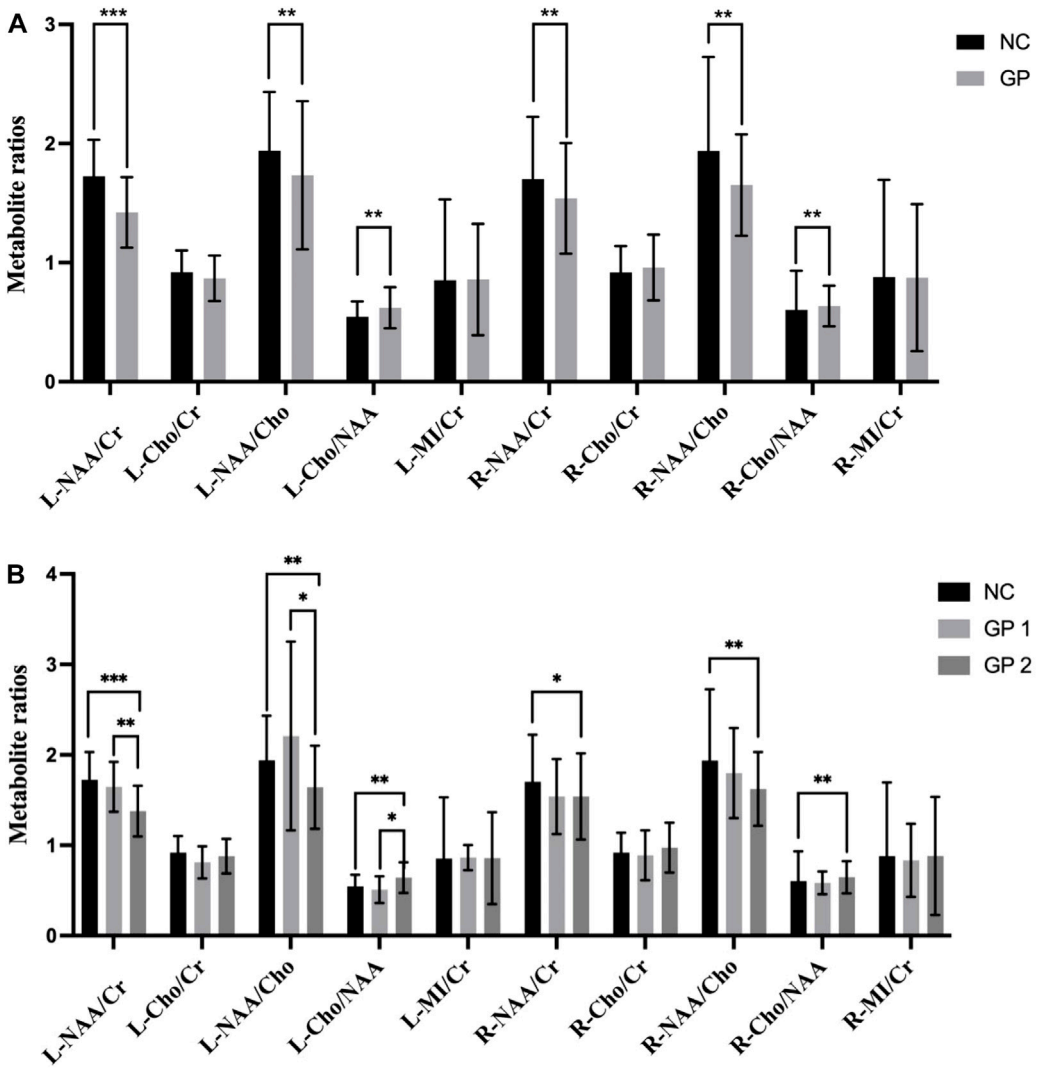

FIGURE 3
Comparisons of the ratios of metabolite concentrations in bilateral hippocampus. **(A)** Metabolite concentrations of NC and GP groups were compared. **(B)** Metabolite concentrations in bilateral hippocampus of NC, GP 1 group and GP 2 group were compared. L: the left hippocampus region. R: the right hippocampus region. NAA: N-acetylaspartate. Cr: creatine. Cho: choline. MI: myoinositol. $*p < 0.05$, $**p < 0.01$, $***p < 0.001$.

TABLE 3 Demographic and clinical characteristics among the group.

	NC	GP 1	GP 2	t/H/x^2	*p*
n	57	13	67	—	—
Male/Female	24/33	12/1	56/11	28.14	<0.001
Age (years)	58.40 ± 7.41	54.54 ± 8.69	56.00 ± 9.28	1.77	0.17
MMSE (points)	29.00 (28.00, 29.00)	22.00 (20.00, 23.00)	13.00 (10.00, 15.00)	110.94	<0.001
Education level (illiterate/elementary education/ middle school education/bachelor's degree and above)	1/20/30/6	0/5/5/3	1/19/39/8	3.75[a]	0.75

[a]Fisher's exact test.

TABLE 4 Comparisons of metabolite concentrations among the groups.

	NC	GP 1	GP 2	*F/H*	*p*	Two-by-two comparison
L-NAA/Cr	1.72 ± 0.31	1.65 ± 0.28	1.38 ± 0.28	22.52	<0.001	NC, GP 1> GP 2
L-Cho/Cr	0.92 ± 0.18	0.81 ± 0.18	0.88 ± 0.19	1.95	0.15	—
L-NAA/Cho	1.93 (1.53, 2.17)	1.95 (1.69, 2.20)	1.60 (1.30, 1.82)	17.31	<0.001	NC, GP 1 >GP 2
L-Cho/NAA	0.52 (0.46, 0.65)	0.51 (0.46, 0.59)	0.62 (0.55, 0.75)	15.23	<0.001	NC, GP 1 <GP 2
L-MI/Cr	0.71 (0.53, 0.92)	0.90 (0.74, 0.97)	0.75 (0.58, 0.96)	4.17	0.12	—
R-NAA/Cr	1.64 (1.45, 1.87)	1.48 (1.22, 2.01)	1.49 (1.28, 1.69)	7.20	0.027	NC >GP 2
R-Cho/Cr	0.90 (0.77, 1.08)	0.85 (0.67, 1.14)	0.91 (0.80, 1.08)	1.20	0.55	—
R-NAA/Cho	1.87 (1.49, 2.24)	1.74 (1.57, 1.87)	1.54 (1.36, 1.85)	10.92	0.004	NC >GP 2
R-Cho/NAA	0.54 (0.45, 0.67)	0.58 (0.54, 0.64)	0.65 (0.53, 0.74)	9.98	0.007	NC <GP 2
R-MI/Cr	0.70 (0.35, 1.00)	0.90 (0.46, 1.16)	0.75 (0.50, 1.07)	1.35	0.51	—

Associations between metabolite concentrations and neuropsychological measures

To explore the relationships between the clinical characteristics and ^{1}H-MRS data in GP group, we analyzed the possible correlation of the metabolite concentrations with MMSE. There was no correlation between metabolite ratios and MMSE scores in hippocampus regions (Table 5).

Discussion

Neurosyphilis traditionally encompasses five main groups: asymptomatic neurosyphilis, syphilitic meningitis, meningovascular syphilis, general paresis, and tabes dorsalis. General paresis, the chronic encephalitic form of neurosyphilis (Ha et al., 2024). GP is a noteworthy cause of dementia, and while diagnosis has historically relied on clinical manifestations and laboratory findings, neuroimaging and neuropsychological tests can offer diagnostic insights and aid in understanding the disease's course and prognosis (Wang et al., 2011; Ha et al., 2024). Cortical atrophy, a common finding in neurosyphilis, was also observed in our study. Most GP patients exhibited varying degrees of diffuse atrophy, as evidenced by ^{1}H-MRS and MRI results. Cerebral atrophy, likely a consequence of neuron loss, contributes to dementia (Chiara et al., 2023).

Our findings revealed men account for a larger proportion of those with GP. Syphilis spirochetes can directly cause neurological damage, and the activation of the aberrant immune system induced by these spirochetes is believed to indirectly harm target tissues and organs (Carlson et al., 2011). Retrospective searches identified sex as a risk factor for neurosyphilis, with men being more prone to developing neurosyphilis among untreated syphilis cases in clinics. The gender gap may stem from immune system disparities, though other factors such as the influence of traditional Chinese culture, where women tend to be more conservative, reducing syphilis infection rates, and differences in the frequency of testing and treating the infection also play a role (Ta and Se, 2019).

Patterns of regional metabolite change in patients with GP

^{1}H-MRS stands out among imaging modalities as it provides both qualitative and quantitative insights into the biochemical composition of brain tissue. This technique is valuable for

TABLE 5 Associations between metabolite concentrations and the neuropsychological measures in GP group.

	MMSE		
	r	*p*	Corrected p
L-NAA/Cr	0.282	0.011	0.08
L-Cho/Cr	−0.117	0.30	0.33
L-NAA/Cho	0.224	0.046	0.09
L-Cho/NAA	−0.224	0.046	0.09
L-MI/Cr	−0.136	0.23	0.31
R-NAA/Cr	0.131	0.25	0.31
R-Cho/Cr	−0.130	0.25	0.31
R-NAA/Cho	0.272	0.015	0.08
R-Cho/NAA	−0.254	0.023	0.08
R-MI/Cr	−0.066	0.56	0.56

assessing neuronal integrity, treatment effects, and exploring new therapies (Graff-Radford et al., 2014).

NAA is regarded as a marker of neuronal integrity (Tomiyasu and Harada, 2022). In our study, significantly lower NAA/Cr ratios were observed in the bilateral hippocampus region of subjects with GP, reflecting neuronal loss or compromised neuronal metabolism, particularly evident in patients with moderate to severe dementia.

Cr is linked to high-energy phosphate metabolism, and its levels tend to rise when energy metabolism declines. While certain research indicates that elevated Cr levels may signify a compensatory response to NAA loss, other studies utilize Cr as a reference due to its relatively stable concentration (Zeng et al., 2021; Tomiyasu and Harada, 2022).

Both hemispheres of the hippocampus in the GP group exhibited lower NAA/Cr ratios compared to the NC group, with a more pronounced trend noted in the left hippocampus region. Particularly noteworthy was the significant difference in NAA/Cr ratios observed among various severity groups within the GP cohort. Numerous studies support the role of NAA/Cr as a marker of neural functional integrity, suggesting that a decreased NAA/Cr ratio in the hippocampus indicates a greater loss of nerve cells. The observed pathophysiological mechanisms are attributed to the proliferation of *T. pallidum*, resulting in the occlusion of small blood vessels, hypoxic conditions, collapse of vessel walls, and reduced cerebral blood flow in the temporal lobe and limbic system (Czarnowska-Cubała et al., 2013; Xiang et al., 2013; Shang et al., 2020).

In our study, the more significant decrease in NAA/Cr ratios observed in patients with moderate to severe dementia suggests pronounced neuronal damage, which may be less apparent in the early stages of dementia. Results for individuals within the normal to mild general paresis range are inconclusive. This variability could be attributed to the differing extents of affected brain regions at various stages of dementia. Dementia associated with neurosyphilis is characterized by cortical hypointensity throughout the entire cortical thickness and brain atrophy, primarily impacting the frontal and temporal lobes. Patients with neurosyphilis-related dementia commonly exhibit clinically significant neuropsychiatric disturbances, including anger, aggression, irritability, and apathy, which are indicative of frontal lobe lesions (Zhong et al., 2017; Ha et al., 2024). As the disease progresses, spirochetal deposition may increase and gradually spread to other brain regions, causing extensive lesions in the temporal lobe or diffuse brain atrophy. And then, it shows significant abnormalities in brain metabolism and cognitive impairment. Thus, GP display a distinct metabolic pattern with a significant decrease in NAA and neuron count as the disease progresses. ^{1}H-MRS emerges as a valuable tool for monitoring clinical progression in patients.

Choline is a rate-limiting precursor in acetylcholine synthesis and a component of cell membrane phosphatidylcholine, often used as a marker for cellular density and membrane turnover (Maul et al., 2020; Tomiyasu and Harada, 2022). Moreover, the higher choline content in astrocytes and oligodendrocytes compared to neurons may suggest alterations in membrane phospholipids in GP, contributing to abnormal membrane repair processes, synaptic loss, and the formation of amyloid beta peptide. Higher choline contents have been detected in microglia-rich brain regions such as the thalamus (Urenjak et al., 1993; Plummer et al., 2023). The observed reduction in NAA/Cho and NAA/Cr in our patients reflects changes in membrane metabolism and neuronal loss.

Myoinositol is considered a glial marker, and elevated MI levels can result from increased glial content or activation (Tomiyasu and Harada, 2022). However, in our study, there was no significant difference in the MI/Cr ratios between the GP and NC groups in the bilateral hippocampus region. This suggests that gliosis in the bilateral hippocampus among GP patients may not be as severe as in AD patients, leading to nonsignificant differences in MI/Cr ratios among groups.

The lack of significant differences in Cho/Cr ratios among groups may be attributed to various factors. Cho/Cr ratios have shown inconsistent results in different studies. Different diseases, Brain regions, disease severity and course were influence factors (Wang et al., 2015; Joyce et al., 2022; Guan et al., 2022). In the future, other regions of the brain could be included to assess the significance of Cho/Cr ratios.

The relationships between neuropsychological measures and the metabolite concentrations in GP

Our study revealed significantly lower neuropsychological assessment scores (MMSE) in the GP group compared to the NC group. However, within the GP group, no correlation was observed between metabolite ratios and MMSE scores in hippocampal regions. This does not imply that ^{1}H-MRS may not reflect the cognitive function of GP patients. One possible explanation is that a subset of patients with general paresis are more prone to experiencing diffuse cerebral atrophy. Moreover, syphilis can lead to cerebral vascular syndrome (Ha et al., 2024). It may have characteristics of vascular cognitive impairment such as white matter lesions, unlike AD, is not primarily characterised by medial temporal lobe or hippocampal atrophy. And some GP patients present with mental symptoms that are manifestations of frontal lobe syndrome. Another reason is that MMSE test is be preliminary screening scale for cognitive impairment, encompassing

domains such as memory, attention, language ability, calculation and spatial ability. This test requires short time relatively, which is beneficial for patients to cooperate. However, MMSE test evaluates cognitive domains are limited which absences of testing for executive function. MMSE is lack of sensitivity for screening the early stage of dementia (Hammant et al., 2023). Thus, there was no correlation between MMSE scores and metabolite ratios.

Researchers have shown distinct patterns of CSF biomarkers (Aβ and tau) in GP and AD patients. The unique CSF Aβ pattern in general paresis suggests abnormal Aβ metabolism (Luo et al., 2015; Chiara et al., 2023). This raises questions about the potential association of GP pathogenesis with neurodegenerative factors. In clinical practice, a subset of GP patients does not experience improved cognitive function after penicillin antisyphilitic treatment. This prompts inquiries into whether these patients may have concurrent AD. Exploring the use of drugs employed for AD treatment, such as cholinesterase inhibitors, in GP patients warrants consideration. Our study identified a higher proportion of male patients in the GP group than females, prompting speculation about potential protective factors in females against syphilis. The exploration of metabolic characteristics in multiple brain regions in GP could enhance our understanding and guide treatment strategies. In conclusion, further studies are crucial to comprehensively understand the extent and persistence of brain injuries in GP.

There were several limitations that warrant consideration. The brain regions associated with cognitive functions include the frontal lobe, temporal lobe, parietal lobe, corpus callosum, among others. However, the clinical manifestations of patients with GP are diverse. In this study, we solely analyzed the levels of metabolites in the hippocampus. It is worth noting that different regions of brain damage may exhibit distinct metabolic characteristics. Future research could investigate the metabolic profiles of multiple brain regions and the concentrations of individual metabolites in patients with GP to obtain a more comprehensive understanding of the metabolic alterations in the GP brain.

Conclusion

Hydrogen proton magnetic resonance spectroscopy is a non-invasive method used to assess neuronal function in GP. GP patients exhibited significantly lower NAA/Cr and NAA/CHO ratios in the hippocampus, particularly in moderate and severe dementia period, indicating neuron loss in these areas, which may become more pronounced as the disease progresses, suggesting distinctive metabolic characteristics in the hippocampus of GP patients. Our findings highlight neuronal injuries in the bilateral hippocampus of GP patients. Research on the metabolic characteristics of multiple brain regions is essential for better-informed treatment approaches. Our ongoing goal is to enhance treatment strategies for GP through continued research.

Data availability statement

The raw data supporting the conclusion of this article will be made available by the authors, without undue reservation.

Ethics statement

The studies involving humans were approved by The Affiliated Brain Hospital, Guangzhou Medical University. The studies were conducted in accordance with the local legislation and institutional requirements. The participants provided their written informed consent to participate in this study. Written informed consent was obtained from the individual(s) for the publication of any potentially identifiable images or data included in this article.

Author contributions

XC: Data curation, Formal Analysis, Investigation, Writing–original draft, Writing–review and editing. TM: Data curation, Project administration, Writing–review and editing. HS: Data curation, Project administration, Resources, Writing–review and editing. ZL: Data curation, Formal Analysis, Methodology, Project administration, Supervision, Writing–review and editing. YN: Data curation, Resources, Supervision, Writing–review and editing.

Funding

The author(s) declare that no financial support was received for the research, authorship, and/or publication of this article. This study was funded by the Natural Science Foundation of Guangdong Province (2023A1515011728), Guangzhou Municiple Health Commission (2023C-TS26), Plan on enhancing scientific research in GMU (02-410-230221XM), Project of Guangzhou Municipal Science and Technology Bureau (2023A03J0835), Guangzhou Municipal Key Discipline in Medicine (2021–2023), Guangzhou High-level Clinical Key Specialty, Guangzhou Research oriented Hospital, and Project of Guangzhou Municipal Science and Technology Bureau (2023A03J0831).

Conflict of interest

The authors declare that the research was conducted in the absence of any commercial or financial relationships that could be construed as a potential conflict of interest.

The author(s) declared that they were an editorial board member of Frontiers, at the time of submission. This had no impact on the peer review process and the final decision.

Publisher's note

References

Carlson, J. A., Dabiri, G., Cribier, B., and Stewart, S. (2011). The immunopathobiology of syphilis: the manifestations and course of syphilis are determined by the level of delayed-type hypersensitivity. *Am. J. Dermatopathol.* 33 (5), 433–460. doi:10.1097/DAD.0b013e3181e8b587

Chakravarthi, S. T., and Joshi, S. G. (2021). An association of pathogens and biofilms with alzheimer's disease. *Microorganisms* 10 (1), 56. doi:10.3390/microorganisms10010056

Chiara, M., Domeniko, H., Marta, D. C., Alessia, P., Davide, P., Luca, T., et al. (2023). Alzheimer's disease and neurosyphilis: meaningful commonalities and differences of clinical phenotype and pathophysiological biomarkers. *J. Alzheimer's Dis.* 94 (2), 611–625. doi:10.3233/JAD-230170

Czarnowska-Cubała, M., Wiglusz, M. S., Jerzy Cubała, W., Jakuszkowiak-Wojten, K., Landowski, J., and Krysta, K. (2013). MR findings in neurosyphilis--a literature review with a focus on a practical approach to neuroimaging. *Psychiatr. Danub.* 25 (Suppl. 2 (September), S153–S157.

Danics, K., Forrest, S. L., Kapas, I., Erber, I., Schmid, S., Törő, K., et al. (2021). Neurodegenerative proteinopathies associated with neuroinfections. *J. Neural Transm.* 128 (10), 1551–1566. doi:10.1007/s00702-021-02371-7

Graff-Radford, J., Boeve, B. F., Murray, M., Ferman, T. J., Tosakulwong, N., Lesnick, T. G., et al. (2014). Regional proton magnetic resonance spectroscopy patterns in dementia with lewy bodies. *Neurobiol. Aging* 35 (6), 1483–1490. doi:10.1016/j.neurobiolaging.2014.01.001

Guan, J.-tian, Zheng, X., Lai, L., Sun, S., Geng, Y., Zhang, X., et al. (2022). Proton magnetic resonance spectroscopy for diagnosis of non-motor symptoms in Parkinson's disease. *Front. Neurology* 13 (February), 594711. doi:10.3389/fneur.2022.594711

Ha, T., Tadi, P., and Dubensky, L. (2024). "Neurosyphilis," in StatPearls. *Treasure island (FL)* (FL, USA: StatPearls Publishing). http://www.ncbi.nlm.nih.gov/books/NBK540979/.

Haishan, S., Zhong, X., Hou, Le, Dong, Z., Luo, X., Chen, X., et al. (2015). Hydrogen proton magnetic resonance spectroscopy of hippocampus of patients with general paresis of insane and Alzheimer's disease. *Chin. J. Neurology* 48 (1), 36–39. doi:10.3760/cma.j.issn.1006-7876.2015.01.009

Hammant, A., Chithiramohan, T., Haunton, V., and Beishon, L. (2023). Cognitive testing following transient ischaemic attack: a systematic review of clinical assessment tools. *Cogent Psychol.* 10 (1), 2196005. doi:10.1080/23311908.2023.2196005

Joyce, J. M., La, P. L., Walker, R., and Harris, A. D. (2022). Magnetic resonance spectroscopy of traumatic brain injury and subconcussive hits: a systematic review and meta–analysis. *J. Neurotrauma* 39 (21–22), 1455–1476. doi:10.1089/neu.2022.0125

Liu, H., Wang, J., Yuan, Y., Gu, J., and Yan, Y. (2023). Hippocampal metabolic alterations and cognitive dysfunction in varicella zoster virus meningitis: a single-center case series study. *Med. Sci. Monit. Int. Med. J. Exp. Clin. Res.* 29, e939670. doi:10.12659/MSM.939670

Lucassen, P. J., Fitzsimons, C. P., Salta, E., and Maletic-Savatic, M. (2020). Adult neurogenesis, human after all (again): classic, optimized, and future approaches. *Behav. Brain Res.* 381, 112458. doi:10.1016/j.bbr.2019.112458

Maul, S., Giegling, I., and Rujescu, D. (2020). Proton magnetic resonance spectroscopy in common dementias—current status and perspectives. *Front. Psychiatry* 11, 769. doi:10.3389/fpsyt.2020.00769

Miklossy, J. (2015). Historic evidence to support a causal relationship between spirochetal infections and alzheimer's disease. *Front. Aging Neurosci.* 7, 46. doi:10.3389/fnagi.2015.00046

Plummer, A. M., Matos, Y. L., Lin, H. C., Ryman, S. G., Birg, A., Quinn, D. K., et al. (2023). Gut-brain pathogenesis of post-acute COVID-19 neurocognitive symptoms. *Front. Neurosci.* 17, 1232480. doi:10.3389/fnins.2023.1232480

Port, J. D. (2020). Magnetic resonance spectroscopy for psychiatry: progress in the last decade. *Neuroimaging Clin. N. Am.* 30 (1), 25–33. doi:10.1016/j.nic.2019.09.002

Pw, C., Mak, Hk, Chan, Y., Chan, T., and Ho, Km (2014). Hippocampal MR spectroscopic abnormalities in a cohort of syphilitic patients with HIV and neurosyphilis infection. *Am. J. Nucl. Med. Mol. Imaging* 5 (1), 83–94. https://pubmed.ncbi.nlm.nih.gov/25625030/.

Shang, X.-J., He, C.-F., Tang, B., Chang, X.-Li, Chao, Ci, and Sang, H. (2020). Neuroimaging features, follow-up analyses, and comparisons between asymptomatic and symptomatic neurosyphilis. *Dermatology Ther.* 10 (2), 273–283. doi:10.1007/s13555-020-00361-3

Ta, P., and Kidd, Se (2019). Trends in deaths due to syphilis, United States, 1968-2015. *Sex. Transm. Dis.* 46 (1), 37–40. doi:10.1097/OLQ.0000000000000899

Tomiyasu, M., and Harada, M. (2022). *In vivo* human MR spectroscopy using a clinical scanner: development, applications, and future prospects. *Magnetic Reson. Med. Sci.* 21 (1), 235–252. doi:10.2463/mrms.rev.2021-0085

Urenjak, J., Williams, S. R., Gadian, D. G., and Noble, M. (1993). Proton nuclear magnetic resonance spectroscopy unambiguously identifies different neural cell types. *J. Neurosci.* 13 (3), 981–989. doi:10.1523/JNEUROSCI.13-03-00981.1993

Wang, H., Tan, L., Wang, H.-Fu, Liu, Y., Yin, R.-H., Wang, W.-Y., et al. (2015). Magnetic resonance spectroscopy in alzheimer's disease: systematic review and meta-analysis. *J. Alzheimer's Dis.* 46 (4), 1049–1070. doi:10.3233/JAD-143225

Wang, J., Guo, Q., Zhou, P., Zhang, J., Zhao, Q., and Hong, Z. (2011). Cognitive impairment in mild general paresis of the insane: AD-like pattern. *Dementia Geriatric Cognitive Disord.* 31 (4), 284–290. doi:10.1159/000326908

Xiang, T., Li, G., Xiao, L., Chen, Si, Zeng, H., Yan, Bo, et al. (2013). Neuroimaging of six neurosyphilis cases mimicking viral encephalitis. *J. Neurological Sci.* 334 (1–2), 164–166. doi:10.1016/j.jns.2013.08.019

Zeng, H.-M., Han, H.-Bo, Zhang, Q.-F., and Bai, H. (2021). Application of modern neuroimaging Technology in the diagnosis and study of alzheimer's disease. *Neural Regen. Res.* 16 (1), 73–79. doi:10.4103/1673-5374.286957

Zheng, J., Zhang, N., Shen, G., Liang, F., Yang, Z., He, X., et al. (2023). Spatiotemporal and seasonal trends of class A and B notifiable infectious diseases in China: retrospective analysis. *JMIR Public Health Surveillance* 9, e42820. doi:10.2196/42820

frontiers | Frontiers in Pharmacology

TYPE Original Research
PUBLISHED 14 June 2024
DOI 10.3389/fphar.2024.1419098

OPEN ACCESS

EDITED BY
Weijie Xie,
Tongji University, China

REVIEWED BY
Ning Jiang,
Chinese Academy of Medical Sciences and Peking Union Medical College, China
Junhua Yang,
Guangdong Pharmaceutical University, China

*CORRESPONDENCE
Peijun Ju,
jupeijunpp@163.com
Jianhua Chen,
jianhua.chen@smhc.org.cn

†These authors have contributed equally to this work and share first authorship

RECEIVED 17 April 2024
ACCEPTED 23 May 2024
PUBLISHED 14 June 2024

CITATION
Huang L, Sun Y, Luo C, Wang W, Shi S, Sun G, Ju P and Chen J (2024), Characterizing defective lipid metabolism in the lateral septum of mice treated with olanzapine: implications for its side effects.
Front. Pharmacol. 15:1419098.
doi: 10.3389/fphar.2024.1419098

Characterizing defective lipid metabolism in the lateral septum of mice treated with olanzapine: implications for its side effects

Lixuan Huang[1†], Ying Sun[1,2†], Chao Luo[1], Wei Wang[1,2], Si Shi[1], Genmin Sun[1], Peijun Ju[1,2,3*] and Jianhua Chen[1,2,3,4,5*]

[1]Shanghai Mental Health Center, Shanghai Jiao Tong University School of Medicine, Shanghai, China, [2]Shanghai Key Laboratory of Psychotic Disorders, Shanghai Mental Health Center, Shanghai, China, [3]Shanghai Institute of Traditional Chinese Medicine for Mental Health, Shanghai, China, [4]Yueyang Hospital of Integrated Traditional Chinese and Western Medicine, Shanghai University of Traditional Chinese Medicine, Shanghai, China, [5]First Affiliated Hospital of Xinjiang Medical University, Urumqi, China

Schizophrenia significantly impacts cognitive and behavioral functions and is primarily treated with second-generation antipsychotics (SGAs) such as olanzapine. Despite their efficacy, these drugs are linked to serious metabolic side effects which can diminish patient compliance, worsen psychiatric symptoms and increase cardiovascular disease risk. This study explores the hypothesis that SGAs affect the molecular determinants of synaptic plasticity and brain activity, particularly focusing on the lateral septum (LS) and its interactions within hypothalamic circuits that regulate feeding and energy expenditure. Utilizing functional ultrasound imaging, RNA sequencing, and weighted gene co-expression network analysis, we identified significant alterations in the functional connection between the hypothalamus and LS, along with changes in gene expression in the LS of mice following prolonged olanzapine exposure. Our analysis revealed a module closely linked to increases in body weight and adiposity, featuring genes primarily involved in lipid metabolism pathways, notably *Apoa1*, *Apoc3*, and *Apoh*. These findings suggest that olanzapine may influence body weight and adiposity through its impact on lipid metabolism-related genes in the LS. Therefore, the neural circuits connecting the LS and LH, along with the accompanying alterations in lipid metabolism, are likely crucial factors contributing to the weight gain and metabolic side effects associated with olanzapine treatment.

KEYWORDS

olanzapine, lateral septum, functional ultrasound imaging, RNA sequencing, WGCNA

1 Introduction

Schizophrenia is a debilitating mental disorder that emerges in early adulthood and significantly impairs cognitive and behavioral functions (Solmi et al., 2023). According to current clinical guidelines, the treatment regimen primarily includes second-generation antipsychotics (SGAs) such as olanzapine, clozapine, and risperidone. Although SGAs represent a cornerstone in schizophrenia management, their usage is marred by significant metabolic side effects. These include weight gain, dyslipidemia, and insulin resistance. These effects further diminish patient compliance, exacerbate psychiatric symptoms, and heighten the risk of cardiovascular diseases and mortality (Correll et al., 2014; Vancampfort

et al., 2015; Hirsch et al., 2017; Vantaggiato et al., 2019). Peripheral metabolic abnormalities have recently been recognized to be regulated by the central nervous system (Myers and Olson, 2012; Ruud et al., 2017; Seicol et al., 2019; Shen et al., 2024). The possibility that these atypical antipsychotic drugs may influence the molecular determinants of synaptic plasticity and brain activity while exerting their therapeutic effects also affects the central response to the side effects of these drugs (Ibi et al., 2017; de Bartolomeis et al., 2022). Current understanding of the adverse effects induced by olanzapine indicates a complex interplay among brain activity, particularly involving the hypothalamic area and its interaction with other brain regions, though these mechanisms necessitate further clarification (Martins et al., 2010; Stanley et al., 2010; Chen et al., 2022; Huang et al., 2022; Fang et al., 2023; Meng et al., 2023). It is highly worthwhile to explore the changes in central network functional connectivity corresponding to the induction of peripheral obesity and metabolic side effects by olanzapine.

Currently, it is known from a sample of patients with schizophrenia that olanzapine can modulate long- and short-range functional connectivity in the resting brain (Guo et al., 2017). The regulation of metabolism is intricate, extending beyond isolated brain regions to encompass complex neural circuits. The hypothalamic neurocircuits have garnered lots of attention. The hypothalamic neurocircuits, extensively researched and crucial for central regulation of feeding and energy expenditure, are intricately linked to the mesolimbic reward system, governing the hedonic aspects of food consumption and weight gain (Timper and Brüning, 2017). Brain areas such as the lateral hypothalamus (LH), lateral septum (LS), ventral tegmental area (VTA), and nucleus accumbens (NAcc) have been implicated in the homeostatic and hedonic control of feeding in experimental models of diet-induced obesity (Marcos et al., 2023). Among them, the LSv functions as a most important node in mediating melanocortin action on body-weight regulation. It is known that such as the LS region, suggests a more comprehensive system of metabolic control (Terrill et al., 2016; Terrill et al., 2018; Calderwood et al., 2022; Gabriella et al., 2022). The LS influences feeding behavior, aggression, food seeking, and stress responses, with emerging evidence pointing to its involvement in weight regulation through hypothalamus-LS circuit and its potential susceptibility to SGA effects (Wong et al., 2016; Carus-Cadavieco et al., 2017; Xu et al., 2023b; Wang et al., 2023). Therefore, exploring the involvement of LS in central side effects of Olanzapine is of significant importance.

Our study aims to elucidate the intricate and long-term metabolic effects of olanzapine, with a specific focus on the LS region in mediating these effects. We propose that olanzapine exerts its influence on metabolic function and weight regulation by modulating the LS area, thereby contributing to the adverse metabolic outcomes observed in schizophrenia treatment. Employing advanced methodologies such as functional ultrasound imaging (fUS) to investigate LS-hypothalamus connectivity, and utilizing RNA sequencing combined with weighted gene co-expression network analysis (WGCNA) (Zhang and Wong, 2022), our investigation explores the genetic landscape altered by olanzapine in the LS region. Our results demonstrate that prolonged exposure to olanzapine disrupts LS-hypothalamus connectivity and alters gene expression associated with lipid metabolism in the LS region, highlighting the involvement of key genes such as *Apoa1*, *Apoc3*, and *Apoh* in these processes. By elucidating the central role of olanzapine in modulating LS-hypothalamus dynamics and gene expression patterns related to lipid metabolism, our findings not only enhance understanding of SGA-induced metabolic disturbances but also lay the groundwork for potential therapeutic interventions aimed at mitigating these side effects.

2 Materials and methods

2.1 Study design

This research aimed to elucidate the role of olanzapine in inducing weight gain and related metabolic dysfunctions, with a particular focus on its impact on the LS region of the brain. Using a mouse model to replicate the side effects of antipsychotic drugs observed in humans, we specifically focused on female mice due to their distinct response to olanzapine, as highlighted in previous research. Retrospective clinical studies have identified the female gender as a predictor for antipsychotic-induced weight gain with atypical antipsychotics (Gebhardt et al., 2009). Animal studies have also shown that female rats experience more significant weight changes after long-term olanzapine use compared to male rats (Choi et al., 2007). Age-matched female mice were randomized into two groups (n = 15 per group) to receive either an olanzapine-supplemented diet or a standard chow diet. Body weight was monitored weekly as a measure of olanzapine's effects, with the aim of minimizing animal stress. The study duration was 12 weeks, with a significant weight gain checkpoint at 8 weeks. At the end of the treatment, we randomly selected nine mice from each group for body composition measurement, serum lipoprotein analysis and scRNA-seq, while the remaining six underwent fUS scanning. LS brain regions in this cohort of mice were used to validate the results of scRNA-seq.

2.2 Animals

All animal experimental protocols were approved by the Institutional Animal Care and Use Committee of Shanghai Mental Health Center. Mice were housed in an SPF-grade experimental animal room under standard laboratory conditions (12-h on/off; lights on at 7:00 a.m.) in a temperature-controlled environment with food and water available *ad libitum*. Female C57BL/6 mice were obtained from Gempharmatech Co., Ltd (Nanjing, China) at about 8 weeks of age.

2.3 Animal treatment

After 1 week of acclimation in the animal room, female mice were placed either on control chow diet (maintenance feed) or olanzapine (PHR 1825, Merck, Germany) diet (50 mg/kg in maintenance feed). Olanzapine dosage referenced from previous literature maintains effective blood level (Morgan et al., 2014). Feed for the mice was customized and purchased from Jiangsu Xietong

Pharmaceutical Bio-engineering Co., Ltd. (Nanjing, China). Body weight was monitored on each Friday morning. Feeding was continued for 12 weeks.

2.4 Preparation for fUS

fUS preparation is implemented with reference to previous literature (Brunner et al., 2021). Mice designated for fUS testing underwent a preparatory procedure that began with anesthesia, using isoflurane for both induction (3%) and maintenance (1%) to ensure minimal discomfort. Following anesthesia, the scalp was carefully removed, and tissues were cleared to fully expose the cranial surface. A custom stainless steel head locator was then securely attached to the skull using dental adhesive to facilitate precise positioning during fUS testing. The skull's surface was meticulously thinned using a specialized cranial drill and grinder. Care was taken to avoid any abrasion to the skull, ensuring the integrity of the cranial structure was maintained. After the cranial preparation, an ultrasound coupling agent was applied to keep the skull moist, followed by a protective covering of dental silicone light body. Mice were given a 3-day recovery period post-surgery, during which they received careful monitoring and pain management as needed. To acclimatize the mice to the fUS assay setup, they were placed in a fixation frame for 1 h daily. This step was critical to reduce stress and ensure accurate and consistent fUS measurements.

2.5 fUS procedures

We utilized a fUS scanning protocol based on established methodologies as detailed in prior studies (Grohs-Metz et al., 2022). The imaging was conducted using specialized small animal fUS equipment provided by Iconeus (Paris, France), which included a linear ultrasonic probe (15 MHz central frequency) with 128 piezoelectric transducers. This probe was integrated with the ultrafast Iconeus One ultrasound scanner (128 channels), facilitating the emission and reception of ultrasonic plane waves, as well as the processing of the resulting Power Doppler signals. The clutter filtering technique applied for the isolation of blood signals was performed via spatiotemporal singular value decomposition, a method thoroughly documented in the literature. The compiled fUS images were derived from 200 compounded ultrafast frames, acquired at a rate of 500 Hz. Each frame aggregated the ultrasonic echoes from a series of 11 tilted plane waves (ranging from −10 to 10°, with 2-degree intervals) emitted at a pulse repetition frequency of 5,500 Hz. The final image sequence was produced at a frame rate of 2.5 Hz, translating to one Power Doppler image every 400 milliseconds, and featured a spatial resolution of 100 × 100 × 400 μm. For the scanning procedure, once the animals were secured and their scalps prepared and treated with isotonic coupling gel, the ultrasonic probe was positioned approximately 1 mm above the scalp to ensure full immersion in the gel. The probe's location was determined using Iconeus Studio software to target an oblique plane, which encompassed the neuroanatomical regions of interest (ROIs) associated with the LS and hypothalamus. 20 min of Power Doppler images were captured for each session. The initial 15 min served as an acclimatization period to calm the mice, followed by a 5-min official recording phase utilized for the analysis.

2.6 Tissue harvesting and body composition measurement

Mice were terminally anesthetized with isoflurane and 1% chloralhydrate. After anesthesia, 200ul blood samples were collected from the mice by orbital blood sampling. LS tissues were micro-dissected under a surgical microscope and then flash-frozen in liquid nitrogen. The rest of body were stored on ice and send to get body composition measurement. Fat and lean mass of mice body were detected using an EchoMRI-100H Body Composition Analyzer (EchoMRI, USA) with EchoMRI 2016 software.

2.7 Serum processing and lipid profiling

The serum was separated by centrifugation at 900 *g* for 5 min at 4°C using a Centrifuge 5430 R (Eppendorf, Germany), 1 hour after blood collection. Total cholesterol (TC), triglycerides (TG), high-density lipoprotein cholesterol (HDL-C), and low-density lipoprotein cholesterol (LDL-C) levels were quantified using enzyme-linked immunosorbent assay (ELISA) kits (Nanjing Jiancheng Bioengineering Institute), following the manufacturer's instructions.

2.8 RNA isolation and library preparation

Due to the small size of the LS region, samples from each three mice were pooled to ensure sufficient RNA volume for sequencing, addressing the challenge of low tissue yield. Total RNA extraction from pooled LS regions used TRIzol reagent (Invitrogen, CA, USA), with purity and concentration verified by NanoDrop 2000 (Thermo Scientific, USA). RNA integrity was assessed with an Agilent 2,100 Bioanalyzer. The VAHTS universal V6 RNA-seq Library Prep Kit was utilized for library construction, with OE Biotech Co., Ltd. (Shanghai, China) performing transcriptome sequencing and analysis.

2.9 RNA-seq and differentially expressed genes analysis

The sequencing of libraries was carried out on an Illumina NovaSeq 6,000 platform, producing 150 bp paired-end reads. Each sample yielded approximately 51.74 million raw reads. These raw reads, in FASTQ format, were initially processed with fastp (Chen et al., 2018) to remove low-quality reads, resulting in clean reads. Subsequently, around 48.78 million clean reads per sample were obtained for further analysis. Mapping of clean reads to the reference genome was conducted using HISAT2(Kim et al., 2015), followed by the calculation of the fragments per kilobase of transcript per million mapped reads (FPKM) (Roberts et al., 2011) for each gene. Gene read counts were determined using HTSeq-count (Anders et al.,

2015). To assess the replicability of biological samples, PCA (Principal Component Analysis) was carried out using R (version 3.2.0). Differential gene expression analysis was executed using DESeq2 (Love et al., 2014), with a Q value of <0.05 and a fold change >2 or <0.5 as criteria for significant differential expression. Hierarchical clustering analysis of differentially expressed genes (DEGs) was conducted in R to illustrate the gene expression patterns across various groups and samples. Enrichment analyses for Gene Ontology (GO) and Kyoto Encyclopedia of Genes and Genomes (KEGG) pathways of the DEGs were performed based on the hypergeometric distribution, using R to identify significantly enriched terms. R was also employed to generate column diagrams, chord diagrams, and bubble diagrams to visually represent the significant enrichment terms.

2.10 WGCNA of RNA-seq data

WGCNA was conducted utilizing the FPKM expression dataset with the WGCNA package in R (Langfelder and Horvath, 2008). Genes exhibiting variance values exceeding 25% were excluded, resulting in a selection of genes with high expression levels for further analysis. Module identification was achieved through the application of a tree-cutting algorithm. Traits such as weight gain, TC, TG, HDL-C, LDL-C, fat mass, and lean mass were incorporated as diagnostic markers for assessing weight and metabolic changes. These traits facilitated the correlation analysis with identified gene modules. Functional annotation of the modules was performed using the org. Hs.e.g.,.db annotation package. Enrichment analyses for GO and KEGG pathways were executed employing the clusterProfiler package in R (Yu et al., 2012), providing insights into the biological functions and pathways associated with the genes within the significant modules.

2.11 Identify the known targets of olanzapine

To identify the known gene targets of olanzapine, we utilized the GeneCards database[1]. GeneCards serves as an exhaustive, searchable repository that amalgamates information from approximately 150 gene-centric databases. It encompasses a wide array of functional data essential for the annotation and prediction of human genes, alongside comprehensive genomics, transcriptomics, and proteomics data. The search for relevant gene targets was conducted by entering "olanzapine" as the keyword, facilitating a targeted exploration of the database's extensive resources.

2.12 Protein-protein interaction (PPI) network construction and analysis

For the purpose of delineating the PPI network encompassing both the modules and the overlapping targets between these modules and the established targets of olanzapine, we engaged the STRING database[2]. This database is renowned for its comprehensive compilation of PPI data, derived from both empirical research and computational predictions. Within this framework, the confidence level of each interaction is quantitatively expressed through a score, which spans from 0 to 1, facilitating a nuanced assessment of interaction reliability. Subsequently, genes common to both the modules of interest and the known targets of olanzapine were imported into the analysis. The raw PPI network data thus obtained was then transferred to Cytoscape 3.10.1 for further examination. Utilizing the topological parameter known as "degree," we conducted an analysis to discern the central targets within the network. These targets, ranked according to their degree values, were then extracted to construct a focused visualization of the PPI network. This visualization highlighted the central targets, thereby offering a refined view of the main PPI network and elucidating potential key players in the biological processes influenced by olanzapine.

2.13 Quantitative reverse transcription polymerase chain reaction (qRT-PCR)

The LS tissues were processed using a rotor–stator homogenizer for disruption and homogenization. Total RNA was extracted from the frozen, dissected LS tissues employing the phenol-chloroform extraction method. We converted 400 ng of total RNA into complementary DNA (cDNA) utilizing the RevertAid First Strand cDNA Synthesis Kit (91255466, Thermo Fisher Scientific, USA). The relative mRNA expression levels of Actin, Apoa1, Apoc3, and Apoh were quantified through qRT-PCR, employing TB Green Premix Ex Taq II (AMG1484A, Takara Bio, Japan). The fluorescence of TB Green was detected and analyzed using the LightCycler480 system (Roche Diagnostics, Switzerland). Gene expression was normalized against the expression of mouse Actin mRNA. The $2^{(-\Delta\Delta Ct)}$ method was utilized for the relative quantification of gene expression, with results presented as log ($2^{(-\Delta\Delta Ct)}$). Primer sequences used in the analysis were as follows: *Actin* forward: GCTCTTTTCCAGCCTTCCTT, *Actin* reverse: TGATCCACATCTGCTGGAAG, *Apoa1* forward: GGC AGAGACTATGTGTCCCAGTT, *Apoa1* reverse: CCCAGTTTT CCAGGAGATTCAG, *Apoc3* forward: CATCTGCCCGAGCTG AAGA, *Apoc3* reverse: GCTTGTTCCATGTAGCCCTGTAC, *Apoh* forward: GCAGAGATGGCACTATCGAGATTCC, *Apoh* reverse: CGACTTCAGCACGGTGTCAGTTC.

2.14 fUS data processing

Temporal Power Doppler signals were extracted from ROIs defined using the Allen Mouse Brain Common Coordinate Framework (Wang et al., 2020), with alignment to individual animals and imaging sessions, as detailed in prior studies (Nouhoum et al., 2021). Signals from all voxels within an ROI

1 GeneCards database (https://www.genecards.org, version 5.0)

2 STRING database (https://string-db.org, version 11.5)

10.3389/fphar.2024.1419098

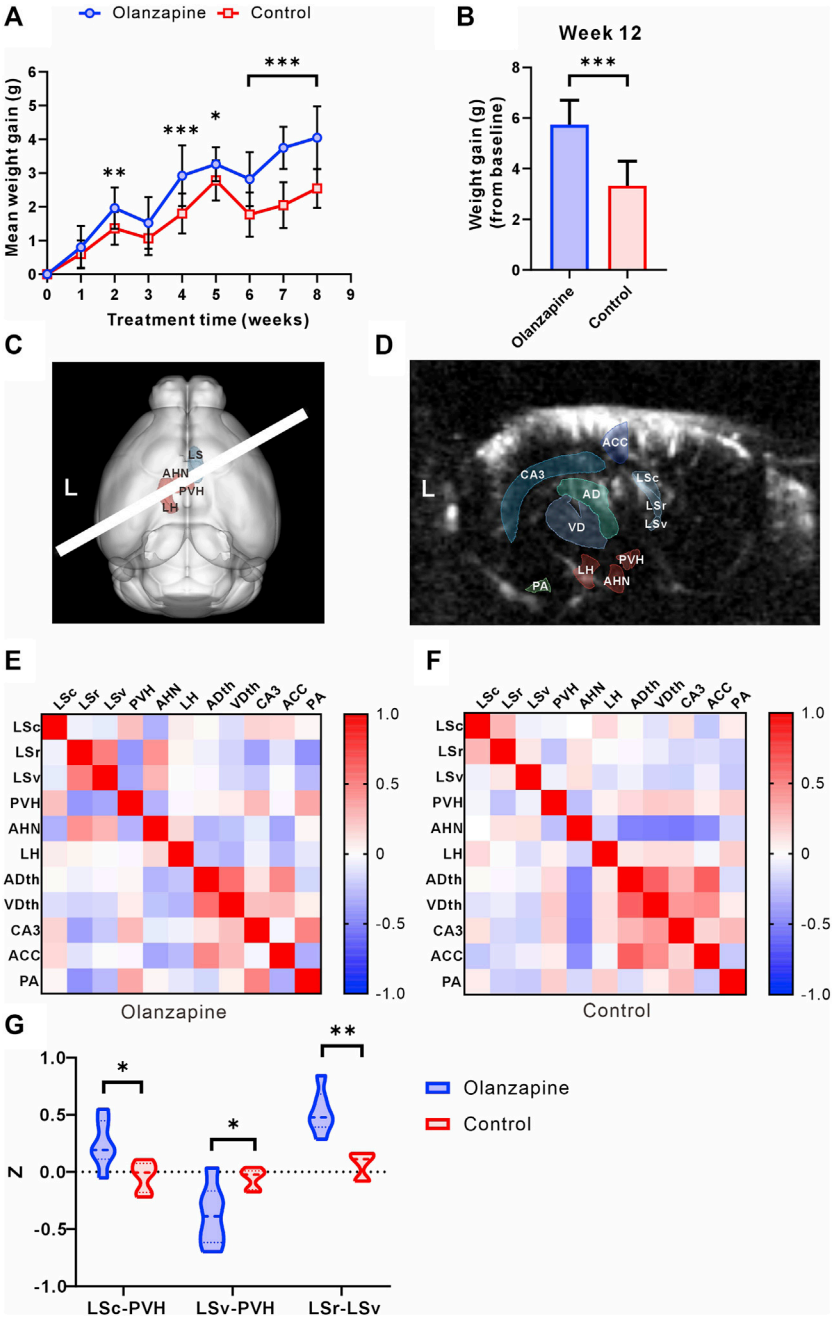

FIGURE 1
Results of statistical analysis for weight gain and functional connectivity changes between two groups. **(A)** Body weight gain of mice from olanzapine group (Olanzapine) and control group (Control) during first 8 weeks of treatment. N = 15 per group. Sidak's multiple comparisons test after Geisser-Greenhouse correction. **(B)** Body weight gain measured at the end of 12 weeks treatment. N = 15 per group. Unpaired t-test. F = 1.004, $p < 0.001$, $R^2 = 0.6266$, t = 6.854, degrees of freedom (df) = 28. **(C)** 3D registration enabled linear probe positioning (white bar) through the LS (red region) and hypothalamus (cyan region). **(D)** Anatomical delineations derived from the Allen Common Coordinate Framework overlaid on a representative fUS Doppler image show coverage of ROIs. **(E)** Heatmap of Pearson correlation coefficient between selected ROIs in olanzapine group. **(F)** Heatmap of Pearson correlation coefficient between selected ROIs in control group. **(G)** Differences in functional connectivity z-values between olanzapine and control groups for LSc-PVH (Unpaired t-test, F = 2.637, $p = 0.0192$, $R^2 = 0.4370$, t = 2.786, df = 10), LSv-PVH (Welch's t-test, F = 9.488, $p = 0.0309$, $R^2 = 0.5468$, t = 2.800, df = 6.042) and LSc-LSv (Mann-Whitney U test, $p = 0.0022$). N = 6 per group. The data are shown as mean ± SD. *$p < 0.05$, **$p < 0.01$, ***$p < 0.001$. LSc lateral septum caudal part, LSr lateral septum rostral part, LSv lateral septum ventral part, LH lateral hypothalamic area, AHN anterior hypothalamic nucleus, PVH paraventricular hypothalamic nucleus, ACC anterior cingulate cortex, CA3 hippocampal CA3 region, ADth anterior group of the dorsal thalamus, VDth ventral group of the dorsal thalamus, PA posterior amygdala nucleus.

were normalized and then detrended using a fourth-order polynomial to mitigate low-frequency drifts. Subsequently, a low pass filter with a cutoff at 0.1 Hz was applied to retain only the frequencies relevant to resting-state functional connectivity. Connectivity matrices were constructed by calculating the Pearson product-moment correlation coefficients between ROI

pairs. For comparative analysis of functional connectivity among different brain regions, Pearson's r-values underwent Fisher's z transformation for normalization, followed by subsequent statistical evaluation.

2.15 Statistical analysis

Data analysis and visualization were performed using GraphPad Prism eight software (GraphPad Software, USA). Results are presented as mean ± standard deviation (SD). Two-way ANOVA followed by Sidak's multiple comparisons test was utilized for repeated measures such as weight gain. The Geisser-Greenhouse correction was applied to ensure variance homogeneity. The Shapiro-Wilk test was employed to verify data distribution normality, and variance homogeneity was assessed via the F-test. Variables that followed a normal distribution and exhibited homogeneity of variances were analyzed using the independent samples t-test, while the Mann-Whitney U test was used for variables that did not conform to normal distribution. When variance homogeneity was not achieved, Welch's correction was applied. Statistical significance was determined by a two-tailed test with a significance threshold set at $p < 0.05$.

3 Results

3.1 Screening for specific brain functional connectivity associated with obesity in mice treated with olanzapine

At the outset, the study groups were comparable in terms of body weight. However, over the course of the 8-week observation period, mice treated with olanzapine experienced a significantly greater increase in body weight, culminating in consistently higher body weights than those of the control group by the study's conclusion (Figures 1A, B). The administration of olanzapine was distinctly linked to an accelerated average body weight gain, markedly exceeding that observed in the control group.

To investigate the central abnormalities induced by olanzapine-induced obesity, we first used fUS to screen for resting-state functional connectivity in various brain regions. We found that awake fUS analyses offered deeper insights, where we delineated the LS into its caudal (LSc), rostral (LSr), and ventral (LSv) parts following the Allen Mouse Brain Common Coordinate Framework. We investigated the functional connectivity with key hypothalamic regions: the lateral hypothalamic area (LH), the anterior hypothalamic nucleus (AHN), and the paraventricular nucleus (PVH) (Figure 1C). In addition, for a broader perspective, we contrasted LS connectivity with other salient brain regions captured within the same fUS scan slice, such as the Anterior cingulate cortex (ACC), the hippocampal CA3 region (CA3), the Anterior group of the dorsal thalamus (ADth), the Ventral group of the dorsal thalamus (VDth), and the Posterior amygdalar nucleus (PA) (Figure 1D). Our analyses revealed group-dependent variations in these connectivities (Figures 1E, F), notably an increase in the functional connectivity z of LSc-PVH in the olanzapine group, while the z of LSv-PVH was significantly reduced. Our study further revealed that olanzapine's influence extends beyond LS-hypothalamic functional connectivity; it also modulates the functional interplay within the LS brain regions themselves. Specifically, we observed a significant enhancement in the functional connectivity between LSc and LSv in the group treated with olanzapine (Figure 1G). These findings indicate that chronic olanzapine administration modulates LS-hypothalamic functional connectivity.

Given the significant impact of olanzapine on both body weight gain and functional connectivity, particularly involving the LS and hypothalamus, our findings pave the way for deeper investigations into the LS's role in mediating these effects. The substantial correlation between functional connectivity changes and weight gain underscores the necessity of further detailed analyses of the LS to uncover the underlying mechanisms of olanzapine's metabolic side effects.

3.2 Body composition and biochemical parameters of mice

Building on our findings regarding body weight and functional connectivity, we delved deeper into the metabolic implications of olanzapine treatment by assessing changes in body composition and lipid metabolism. Utilizing EchoMRI, we observed marked alterations in body composition among olanzapine-treated mice. Specifically, these mice exhibited a significant increase in both the absolute fat mass and its proportion of the total body mass. Interestingly, while absolute lean mass was higher in the olanzapine group, its proportion relative to total body mass was significantly diminished, highlighting the distinct impact of olanzapine on body composition (Figures 2A–C).

Serum lipid profile analysis further elucidated olanzapine's metabolic effects. By the study's conclusion, olanzapine administration had notably elevated TC and LDL-C levels, signaling a shift towards less favorable lipid metabolism (Figures 2D, G). Contrarily, levels of TG and HDL-C did not show significant differences between the olanzapine and control groups (Figures 2E, F).

These combined results not only corroborate the significant influence of olanzapine on body weight and functional brain connectivity but also reveal its profound effects on body composition and lipid profiles. The notable increase in fat accumulation and adverse shifts in lipid metabolism underscore the comprehensive metabolic alterations induced by olanzapine treatment. Such findings underscore the critical need for further detailed exploration of the LS area to uncover the mechanistic pathways through which olanzapine exerts these multifaceted metabolic effects.

3.3 RNA-seq analysis of the LS region

To elucidate the impact of olanzapine on metabolic side effects, including weight gain, within the LS area, we performed RNA-seq analysis on samples from two groups of mice. Our goal was to identify differentially expressed genes (DEGs) associated with the metabolic phenotypes induced by olanzapine treatment.

Employing a rigorous data processing and analysis workflow, we obtained between 50.22 and 54.81 million raw reads per sample. Quality filtering preserved approximately 47.96–50.04 million clean reads for each sample. Successful alignment with the reference

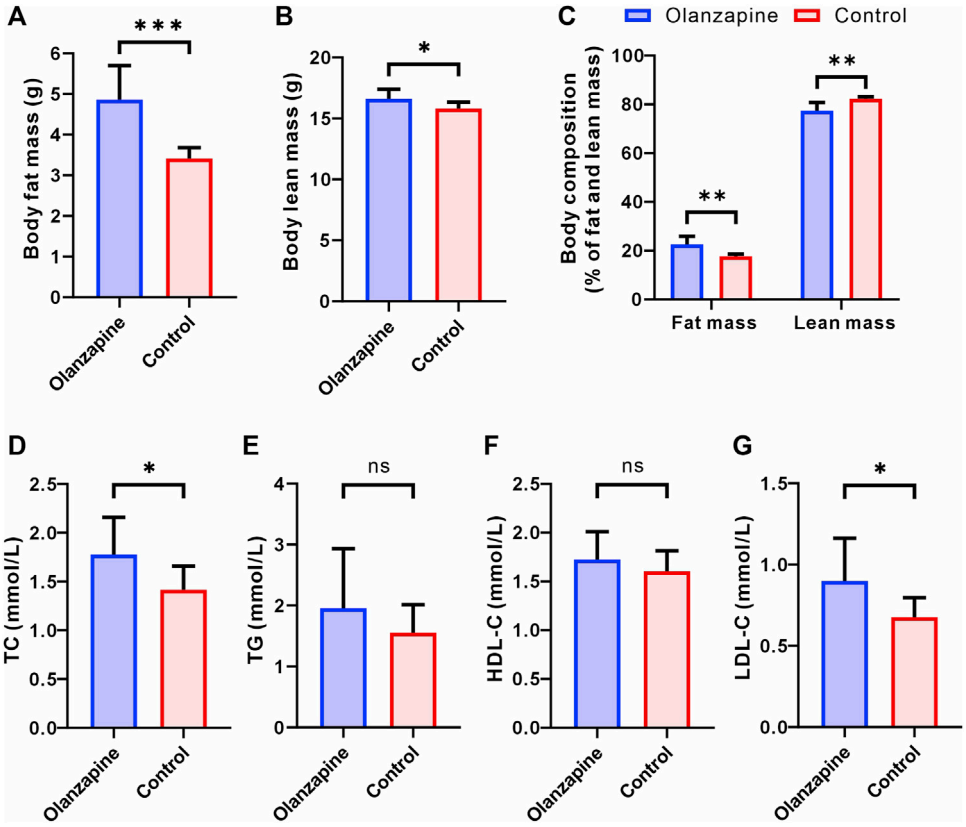

FIGURE 2
Results of statistical analysis for body composition and serum lipoprotein levels between two groups. N = 9 per group. **(A)** Body fat mass of mice after removal of the head. Welch's t-test, F = 9.525, p = 0.0006, R^2 = 0.7170, t = 4.948, df = 9.662. **(B)** Body lean mass of mice after removal of the head. Unpaired t-test. F = 2.128, p = 0.0214, R^2 = 0.2890, t = 2.550, df = 16. **(C)** Body composition of mice after removal of the head. Welch's t-test, F = 14.50, p = 0.0023, R^2 = 0.6577, t = 4.181, df = 9.098. **(D)** Serum TC level measured at the end of 12 weeks treatment. Unpaired t-test. F = 2.503, p = 0.0295, R^2 = 0.2632, t = 2.391, df = 16. **(E)** Serum TG level measured at the end of 12 weeks treatment. Welch's t-test, F = 4.608, p = 0.2912, R^2 = 0.0977, t = 1.107, df = 11.32. **(F)** Serum HDL-C level measured at the end of 12 weeks treatment. Unpaired t-test. F = 1.849, p = 0.3219, R^2 = 0.0613, t = 1.022, df = 16. **(G)** Serum LDL-C level measured at the end of 12 weeks treatment. Welch's t-test, F = 4.841, p = 0.0414, R^2 = 0.3221, t = 2.304, df = 11.17. The data are shown as mean ± SD. *p < 0.05, **p < 0.01, ***p < 0.001.

genome was achieved, demonstrating a mapping rate of 98.16%–98.31%, which enabled the calculation of FPKM values for 35,415 genes. A stringent selection criterion—Q value <0.05 and a fold change >2 or <0.5—facilitated the identification of 735 significantly DEGs.

Among these, 593 genes were found to be upregulated, and 142 genes downregulated in the olanzapine group compared to controls (Figure 3A). Subsequent pathway enrichment analysis of these DEGs revealed notable findings. GO analysis indicated significant enrichment in biological processes such as lipoprotein metabolic processes and cholesterol efflux. Cellular component analysis highlighted enrichment in entities like high-density lipoprotein particle, very-low-density lipoprotein particle, and chylomicron. Furthermore, molecular function analysis pointed to an enrichment in functions including monooxygenase activity, aromatase activity, and arachidonic acid epoxygenase activity (Figure 3B). KEGG pathway analysis revealed enrichment in pathways critical to lipid metabolism, such as linoleic acid metabolism, PPAR signaling, and cholesterol metabolism (Figure 3C).

These findings underscore olanzapine's influence on the expression of lipid metabolism-related genes within the LS brain regions, suggesting a molecular basis for the metabolic side effects observed. To fully understand the implications of these alterations, it is essential to integrate these data with the comparative analysis of the olanzapine and control groups.

3.4 WGCNA applied to RNA-Sequencing data

To bridge the gap between RNA-seq data and the metabolic alterations caused by olanzapine, we employed WGCNA. This sophisticated approach enabled us to construct co-expression networks from the FPKM values, effectively grouping genes into five distinct modules based on their expression patterns: MEturquoise, MEblue, MEbrown, MEyellow, and MEgrey (Figures 4A, B). The MEgrey module consisted of genes not significantly correlated with any specific metabolic trait, serving as a contrast to the other more functionally targeted modules.

We then explored the correlation of module eigengenes (MEs) with various phenotypic traits linked to olanzapine's metabolic effects (Figure 4C). The MEblue module emerged as particularly noteworthy, showing a strong association with both weight gain and body fat mass (R = 0.98, p = 0.0007; R = 0.94, p = 0.005). This finding

10.3389/fphar.2024.1419098

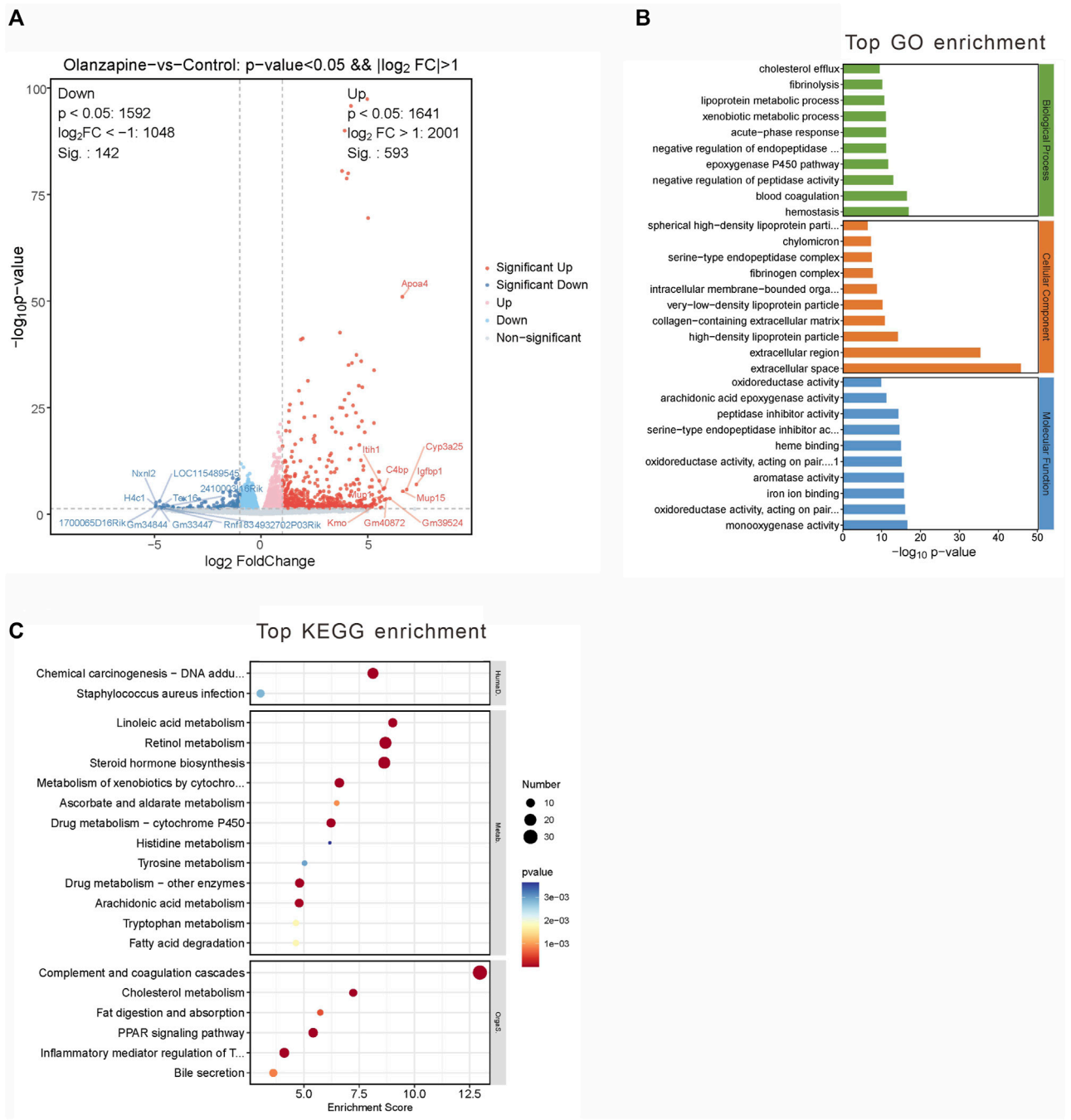

FIGURE 3
DEGs between two groups and gene analysis of DEGs. **(A)** Volcano plot of DEGs. Red represents 593 upregulated genes and blue represents 142 downregulated genes with $|\log_2(FC)|>1$ and $p < 0.05$. **(B)** Top 10 GO terms related to biological processes, cellular component and molecular function. **(C)** KEGG enrichment analysis of MEblue module. Terms are arranged by p-value. The number of gene types is represented by the gene number.

highlights the MEblue module's central role in the observed weight and fat accumulation. On the other hand, the MEbrown module displayed a significant correlation with TC levels and body lean mass (R = 0.9, p = 0.01; R = 0.83, p = 0.04), revealing distinct gene networks that may drive specific facets of the metabolic changes induced by olanzapine.

Our WGCNA findings pinpoint critical gene networks within the MEblue and MEbrown modules as central to olanzapine's metabolic side effects. This sets the stage for an in-depth exploration of these modules to understand the specific mechanisms at play.

3.5 Analysis of the MEblue module

The MEblue module, comprising 97 genes, featured 84 DEGs that were upregulated in the olanzapine-treated group compared to

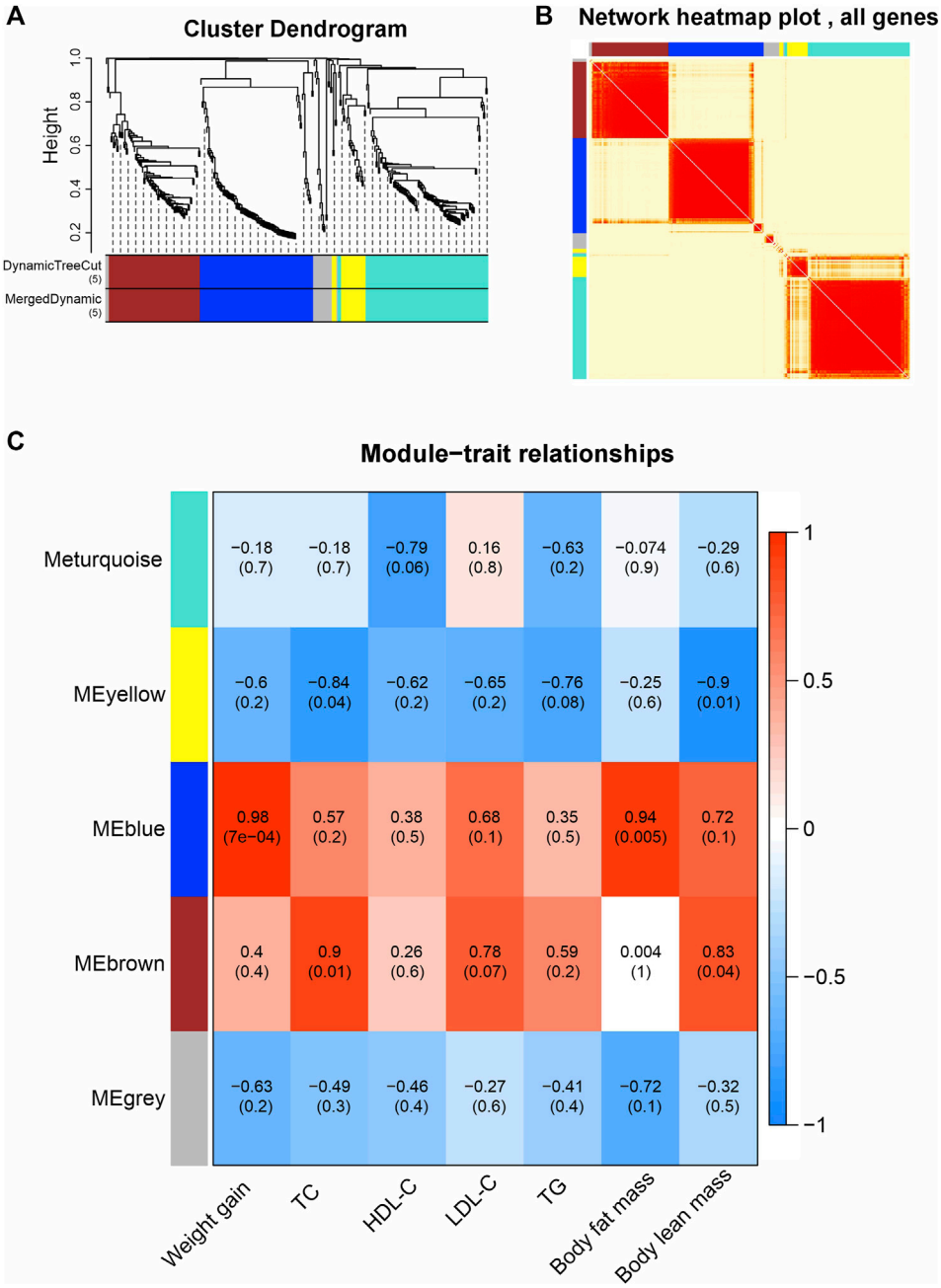

FIGURE 4
Weighted gene co-expression network analysis (WGCNA). **(A)** Average connectivity analysis for different soft threshold powers. **(B)** Heatmap of correlations among WGCNA modules. **(C)** Heatmap of correlations between sample traits and WGCNA module eigengene. Upper values in each table cell indicate correlations. *p* values for association testing are the lower values in brackets.

controls. To unravel the biological significance of these genes, we conducted GO and KEGG enrichment analyses.

The GO analysis segmented these 84 genes into three main categories: biological processes, cellular components, and molecular functions (Figure 5A). The top GO keywords were chosen based on their *p*-values. The module genes provided information about potential biological processes such as negative regulation of peptidase activity, peptide hormone response, and acute-phase response. Identified cellular components pathway included very-low-density and high-density lipoprotein particles, among others. Molecular functions of interest were lipase inhibitor activity and signaling receptor binding. KEGG enrichment analysis revealed involvement in systemic functions like complement and coagulation cascades, cholesterol metabolism, and the PPAR signaling pathway, indicating the module's potential impact on metabolic processes (Figure 5B).

These findings suggest that the MEblue module has a significant impact on metabolic processes altered by olanzapine treatment, offering insights into the molecular mechanisms driving these changes.

10.3389/fphar.2024.1419098

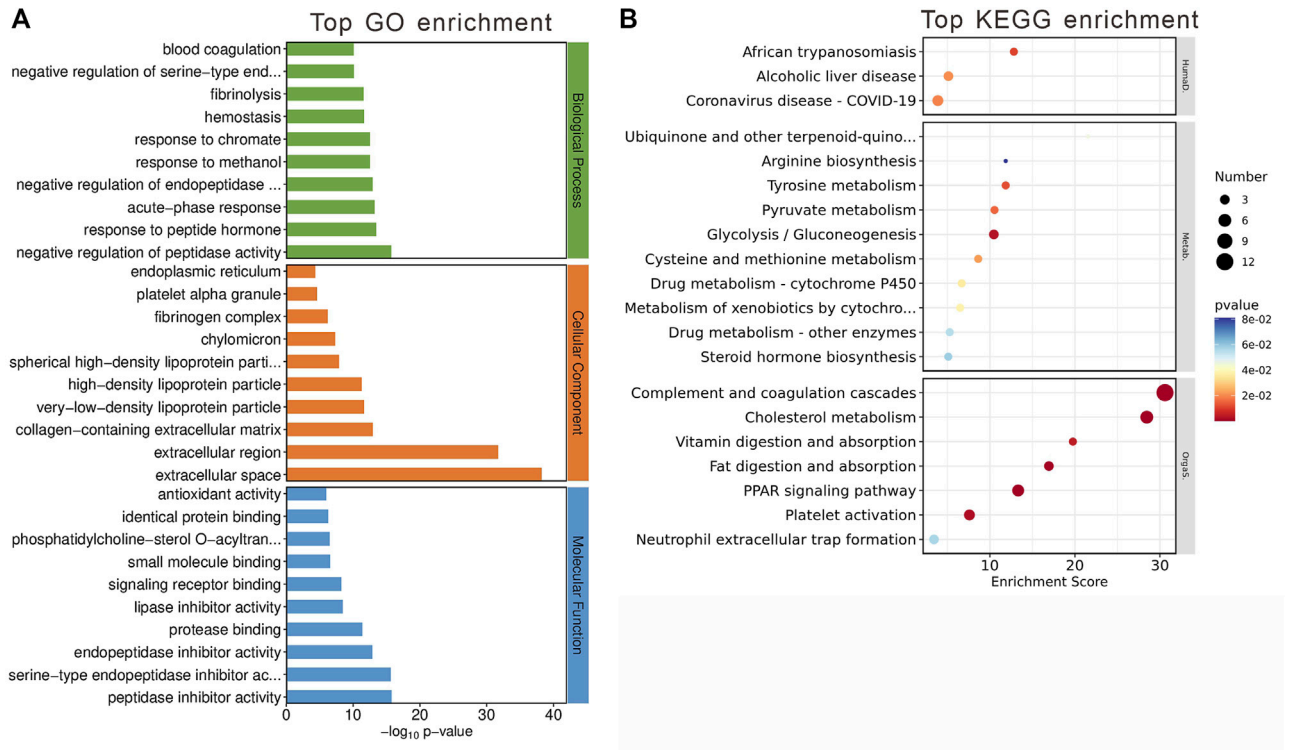

FIGURE 5
Gene Analysis for the MEblue module genes. **(A)** Top 10 GO terms related to biological processes, cellular component and molecular function. **(B)** KEGG enrichment analysis of MEblue module. Terms are arranged by *p*-value. The number of gene types is represented by the gene number.

3.6 Analysis of the MEbrown module

Contained within the MEbrown module are 78 genes, of which 9 have been pinpointed as DEGs between the olanzapine-treated and control groups. Also, all identified DEGs within this module were upregulated following olanzapine treatment. To decipher the biological implications of these alterations, we conducted GO and KEGG enrichment analyses on these genes.

The GO enrichment analysis unveiled these genes' involvement in pivotal biological processes, notably including canonical Wnt signaling and the regulation of SMAD protein signal transduction. When examining cellular components, our analysis highlighted significant associations with the postsynaptic density and various intracellular components. In terms of molecular functions, a noteworthy finding was the genes' interactions with type 3 metabotropic glutamate receptors, underscoring their potential role in neurotransmission and neuronal signaling (Figure 6A).

KEGG enrichment analysis further elucidated the module's significance, revealing involvement in critical signaling pathways such as TGF-beta and estrogen signaling pathways (Figure 6B). These pathways are crucial for a wide range of cellular functions, suggesting that the genes within the MEbrown module play roles in complex signaling networks that could be linked to the metabolic and neurological effects observed with olanzapine treatment.

3.7 Analysis of target genes within MEblue and MEbrown modules

To identify crucial genes within the MEblue and MEbrown modules potentially contributing to olanzapine's metabolic side effects, we cross-referenced the modules' DEGs with 397 olanzapine target genes listed in the GeneCards database. Among these, seven genes were identified as common between the olanzapine targets and the DEGs of the MEblue module, all showing upregulation in response to olanzapine treatment (Figure 7A). These overlapping genes were significantly enriched in key metabolic pathways, including cholesterol metabolism, PPAR signaling, and fat digestion and absorption. Notably, *Apoa1*, *Apoc3*, and *Apoh* emerged as genes of particular interest due to their roles in lipid metabolism (Figures 7B, C).

Leveraging the STRING online tool, we developed a protein-protein interaction (PPI) network for the 84 genes bridging the MEblue module and DEGs. Analyzed using Cytoscape 3.10.1, this network initially featured 65 nodes and 788 edges, illustrating the extensive interconnectivity among these genes. Within this network, *Apoa1*, *Apoc3*, and *Apoh* stood out for their high degree of connectivity, suggesting a central role in the module's biological significance (Figure 7D).

To corroborate the RNA-seq findings, we conducted qRT-PCR analyses to validate the transcriptional profiles of *Apoa1*, *Apoc3*, and *Apoh* in LS tissues from olanzapine-treated mice. The mRNA expression levels of these genes were significantly higher in the olanzapine group compared to controls, consistent with the RNA-

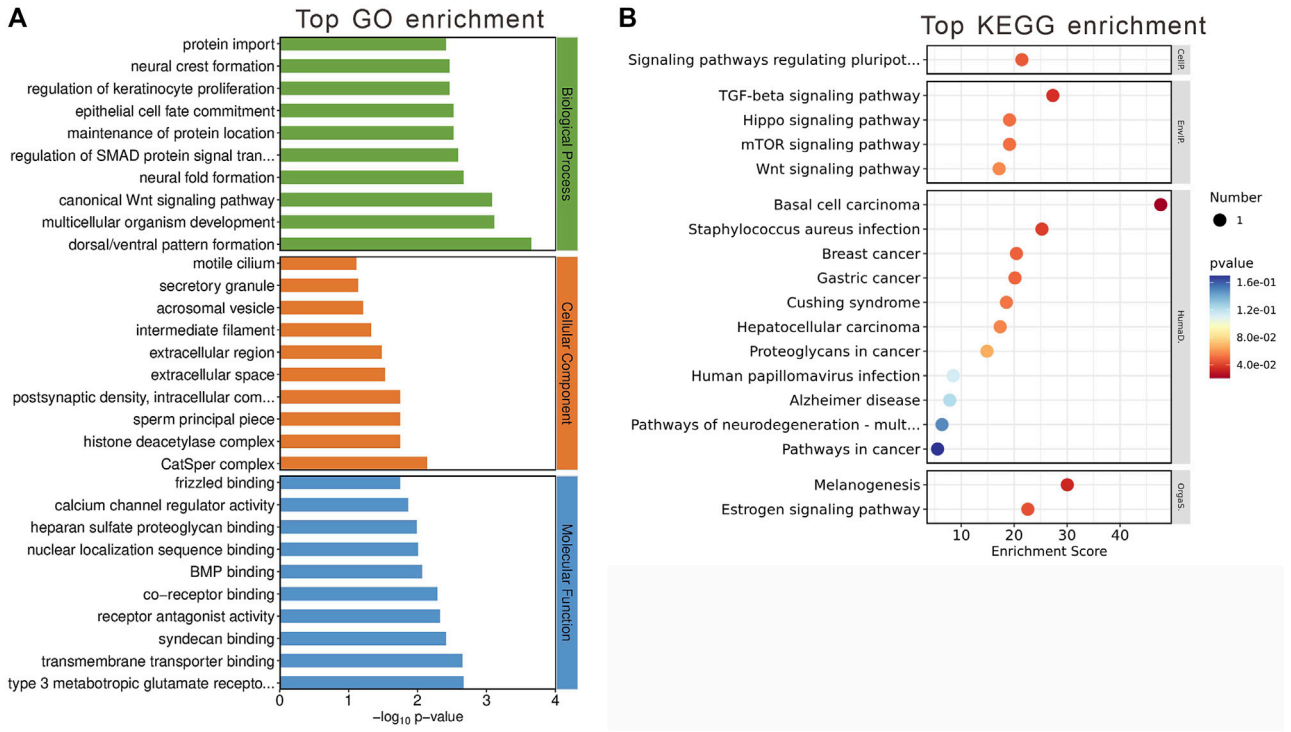

FIGURE 6
Gene Analysis for the MEbrown module genes. **(A)** Top 10 GO terms related to biological processes, cellular component and molecular function. **(B)** KEGG enrichment analysis of MEbrown module. Terms are arranged by *p*-value. The number of gene types is represented by the gene number.

seq data. This validation highlights olanzapine's influence on the expression of genes critical to lipid metabolism and supports their involvement in the drug's metabolic effects.

In contrast, the overlap between olanzapine targets and the MEbrown module yielded five genes. However, none exhibited differential expression between the olanzapine and control groups. This suggests unique regulatory mechanisms or roles in response to olanzapine that may not involve changes in gene expression.

In summary, our analysis has elucidated a subset of olanzapine's target genes within the MEblue module that are significantly associated with metabolic pathways, particularly lipid metabolism. The validation of these genes' expression profiles, notably *Apoa1*, *Apoc3*, and *Apoh*, underscores their potential role in olanzapine-induced metabolic alterations. While the analysis of the MEbrown module revealed a different set of target genes, the lack of differential expression suggests that alternative mechanisms are involved.

4 Discussion

In line with previous findings, long-term olanzapine treatment led to hyperphagia, obesity, and insulin resistance (Luo et al., 2021; Burschinski et al., 2023). Our st udy aimed to investigate whether olanzapine administration not only improves central psychiatric symptoms but also affects central regulatory neural projections linked to obesity onset. Consequently, we examined key neural circuits impacted by chronic olanzapine treatment, revealing modulation of functional connectivity between the LH and LS brain regions.

Additionally, we observed altered gene expression in the LS region of mice. Through RNA-seq and WGCNA, we identified a gene module closely associated with increased body weight and adiposity, prominently featuring genes involved in lipid metabolism pathways, such as *Apoa1*, *Apoc3*, and *Apoh*. These findings suggest that olanzapine influences body weight and adiposity by affecting lipid metabolism-related genes in the LS brain region and altering its functional connectivity with the LH.

In CNS, olanzapine interfere profoundly with glucose and lipid homeostasis acting mostly on hypothalamus (Carli et al., 2021). Distubances of neuronal activity and axon projection were induced by olanzapine treatment (Kim et al., 2022). Furthermore, modulation of hypothalamic AMPK signaling by olanzapine controls energy balance and body weight. Given that homeostatic inputs from the hypothalamus are integrated with hedonic feeding signals from mesolimbic pathways and signals from superordinate regions to generate an orchestrated response in feeding behavior, glucose metabolism, and energy homeostasis regulation, We conducted fUS to identify the LS as a key brain region with functional connectivity to fUS.Two key neural pathways between the LS and the hypothalamus, from the paraventricular nucleus of the hypothalamus to the ventral LS, and from the dorsal LS to the lateral hypothalamic area, are implicated in both physiological and psychological functions. (Carus-Cadavieco et al., 2017; Xu et al., 2019; Mu et al., 2020). Furthermore, recent studies highlight that extended inhibition of projections from melanocortin-4 receptor-expressing neurons in the paraventricular hypothalamus to the LS may precipitate obesity due to reduced energy expenditure (Xu et al., 2023b). We observed a significant alteration in the functional connectivity between the LS and the

10.3389/fphar.2024.1419098

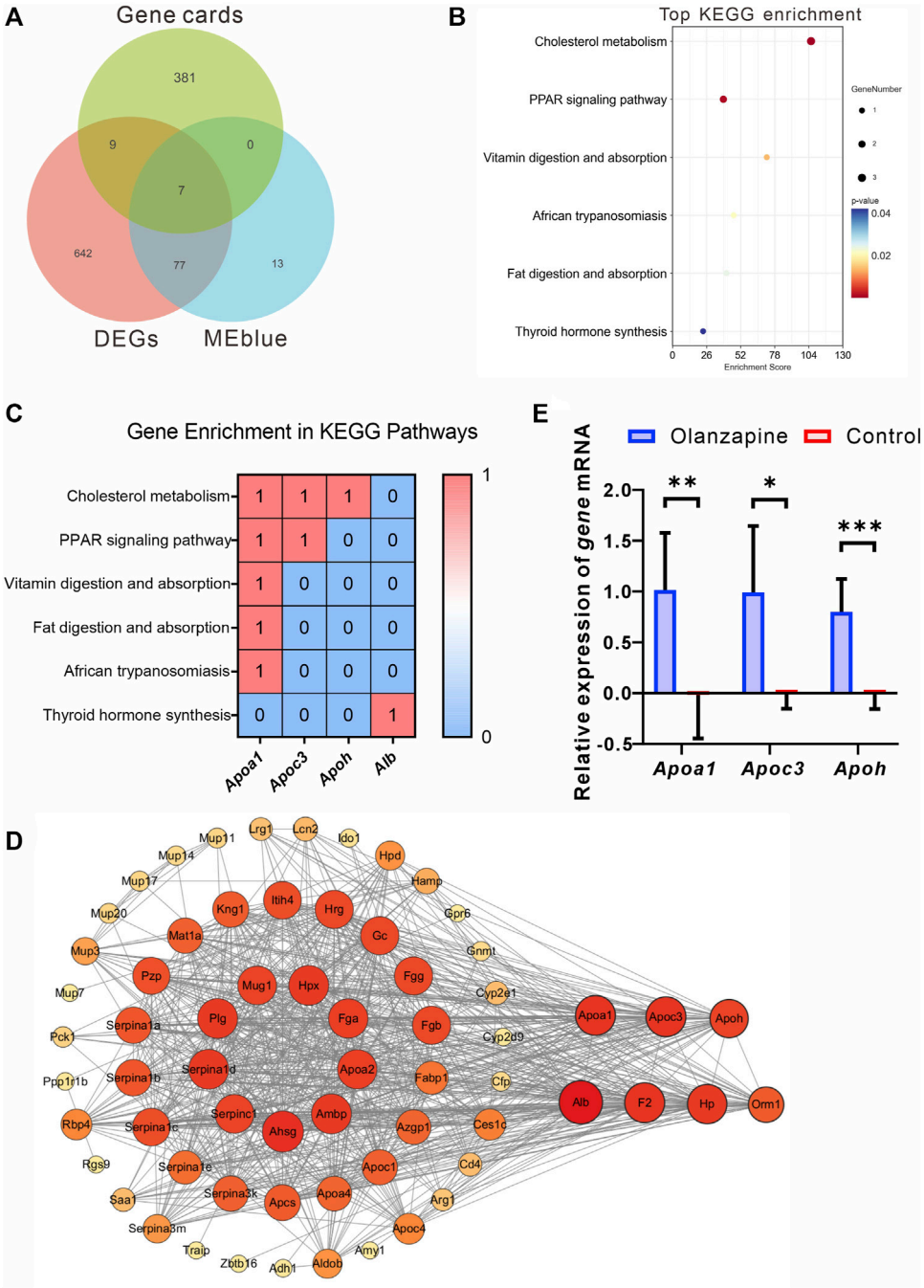

FIGURE 7
Identification, analysis and qRT-PCR validation of key genes. **(A)** Venn diagram showing the genes from Genecards, MEblue and DEGs. **(B)** The top terms of KEGG enrichment analysis sorted by the *p*-value for overlapping genes in Genecards, MEblue and DEGs. The number of gene types is represented by the gene number. **(C)** Heatmap of association between Apoa1, Apoc3, and Apoh with lipid metabolism pathways. Values in each table cell indicate whether gene was enriched in this KEGG pathway (1) or not (0). **(D)** The PPI network of the 65 overlapping genes. The node color and size represent the magnitude of the degree value. **(E)** The level of *Apoa1* (Mann-Whitney U test, $p = 0.0022$), *Apoc3* (Welch's t-test, F = 18.90, $p = 0.0128$, $R^2 = 0.7034$, t = 3.620, df = 5.528), and *Apoh* (Unpaired t-test. F = 4.474, $p = 0.0003$, $R^2 = 0.7535$, t = 5.529, df = 10. mRNA expression in the lateral septum area. N = 6 per group. The data are shown as mean ± SD. $^*p < 0.05$, $^{**}p < 0.01$, $^{***}p < 0.001$.

hypothalamus in mice treated with olanzapine, particularly in the neural projections between the PVH and the LS, indicating substantial neurophysiological changes. Although not every pathway from the LS to the hypothalamus showed significant alteration, the overall trend in connectivity suggests a broad, possibly cumulative, impact of long-term olanzapine administration on these critical neural circuits. At the same time, the altered functional connectivity between the PVH and different regions of the LS was not consistent, also reflecting the more complex effects of olanzapine on this neural circuit.

The initiation of our discussion delves into the pivotal role of the LS area within the central nervous system, focusing on its established significance in regulating metabolic and behavioral processes. The LS

emerges as a central hub orchestrating a range of emotions such as reward, feeding, anxiety, fear, sociability, and memory (Rizzi-Wise and Wang, 2021). Evidence indicates the LS's integral role in various facets of feeding behavior, including the motivation to seek food, actual food consumption, and taste preference. The motivation for food, reflecting the pursuit rather than the act of eating, has been studied in relation to the function of specific receptors in the LS. Beyond its impact on food motivation, the LS also directly influences food consumption through the pharmacological modulation of various receptors. Therefore, in the current study, we explored the underlying mechanisms using a broad approach and performed global transcriptomic analysis of the LS, a valuable tool allowing for the accurate and unbiased identification of genes differentially regulated between treatments. Using this approach, we have identified LS genes altered in response to olanzapine treatment and have suggested both known and novel candidate genes that merit further investigation.

Our comprehensive exploration of olanzapine's metabolic side effects has unveiled its substantial impact on body weight, functional brain connectivity, body composition, and lipid metabolism, systematically revealing the depth of olanzapine's influence on metabolic processes. In our study, C57BL/6 mice subjected to a diet containing olanzapine demonstrated significant body weight gain, particularly noted in an increased fat mass ratio. This finding highlights the drug's potent effect on promoting weight gain, an adverse outcome frequently observed in clinical settings. The pronounced increase in body weight and fat mass underscores the urgent need to understand the mechanisms driving these changes, aiming to mitigate such undesirable effects in patients undergoing olanzapine treatment. The administration of olanzapine also resulted in notable changes in body composition, characterized by an increase in fat mass and alterations in serum lipid profiles, with elevated TC and LDL-C levels. These alterations in lipid metabolism provide a clearer picture of how olanzapine disrupts metabolic homeostasis, further supported by our detailed RNA-seq analysis.

In this study, we found 735 genes significantly altered in the LS following olanzapine treatment, including previously identified genes such as *Apoa1*, *Soat2*, and *Crp*, which are closely related to lipid transport, cholesterol synthesis, and inflammation (Pramfalk et al., 2022; Endres et al., 2024). We observed changes in a variety of genes regulating energy, with a notable increase in apolipoprotein-related genes such as *Apoa1*, *Apoa2*, *Apob*, *Apoc3*, *Apoh* and *Apom*. Through RNA-seq analysis of the LS region, we identified a robust set of DEGs, indicating a shift towards less favorable lipid metabolic pathways. The application of WGCNA allowed us to dissect these effects at a molecular level, pinpointing the MEblue and MEbrown modules as central to the observed metabolic changes. Specifically, the MEblue module's association with weight gain and fat accumulation, enriched in cholesterol metabolism and PPAR signaling pathways, underscores olanzapine's impact on lipid homeostasis (Pinna, 2023). Conversely, the MEbrown module's link to canonical Wnt signaling and SMAD protein signal transduction regulation points towards olanzapine's broader effects on cellular signaling networks (Chambers et al., 2009; Kim et al., 2021).

Crucially, our analysis of target genes within these modules, particularly the enrichment of *Apoa1*, *Apoc3* and *Apoh* in key metabolic pathways, validates the RNA-seq findings and underscores their potential role in mediating olanzapine's adverse metabolic outcomes. The absence of differential expression in the MEbrown module's olanzapine targets suggests distinct regulatory mechanisms or roles in response to olanzapine, inviting further investigation. The significant roles of apolipoprotein A-Ⅰ (APOA-Ⅰ), apolipoprotein-Ⅲ (APOC-Ⅲ) and apolipoprotein H (APOH) in lipid metabolism are well-established, with these apolipoproteins participating in essential processes like cholesterol transport, triglyceride regulation, and innate immunity (Agar et al., 2011; Norata et al., 2015; Zewinger et al., 2020; Giammanco et al., 2023).

Recent advancements have highlighted the significance of apolipoproteins in the central nervous system (CNS), particularly due to the brain's high lipid content and reliance on internal cholesterol synthesis, necessitated by the blood-brain barrier which limits external lipid entry (Björkhem and Meaney, 2004). This has led to the discovery of distinct apolipoprotein compositions and regulatory mechanisms within the CNS, separate from peripheral systems. The critical role of central apolipoproteins in lipid metabolism and immune regulation within the CNS is becoming evident, given neurons' sensitivity to immune disruptions and their dependency on consistent lipid supplies (Endres, 2021). This role is further underscored by their contribution to neurological disease pathogenesis. Central apolipoproteins, some originating peripherally and others synthesized locally (e.g., APOA-I in brain endothelial cells, APOH in astrocytes and neurons), are implicated in neurodegenerative disorders such as Parkinson's disease and Alzheimer's disease (AD) (Elliott et al., 2010; Xu et al., 2023a). At the same time, some researches focus on the role of central lipid metabolism in modulating systemic metabolism and obesity. Hypothalamic astrocytes, influenced by angiopoietin-like four and peroxisome proliferator–activated receptor gamma, regulate fatty acid homeostasis, which impacts neuronal responses to metabolic changes and protects against diet-induced obesity (Varela et al., 2021). This brain region also signals nutritional status to peripheral tissues like the liver, affecting glucose production, lipogenesis, and TG secretion through fatty acid sensing and autonomic nervous system activity (Bruce et al., 2017). These mechanisms underscore the potential of targeting central lipid metabolism to treat metabolic disorders.

Research in schizophrenia has shown a notable decrease in APOA-I across five tissues (cerebrospinal fluid, brain, liver, red blood cells, and serum) in patients, potentially contributing to their heightened risk of metabolic disorders (Huang et al., 2008). Consequently, some researchers propose using metabolic syndrome counteracting drugs to mitigate antipsychotics' weight and metabolic side effects by raising APOA-I levels (Xiang et al., 2019). Contrarily, other studies indicate antipsychotic usage increases APOA-I levels in serum and cerebrospinal fluid, correlating with rises in body mass index, TC, and TG (Martins-De-Souza et al., 2010; Song et al., 2014). Variations in study samples and antipsychotic medications used may explain these divergent findings.

Simultaneously, research has highlighted that lipoprotein metabolism's role extends beyond the metabolic side effects in schizophrenia to include the disorder's psychiatric symptoms. For instance, a study identified a strong link between low HDL serum levels and increased aggression in female schizophrenia patients (Herceg et al., 2022). In contrast, another study observed that rising serum HDL levels during the first year of antipsychotic treatment corresponded with reduced negative symptoms (Gjerde et al., 2018). These insights indicate that lipid metabolism, particularly within the central nervous system, may influence schizophrenia's psychiatric

symptoms and could be a target for antipsychotic medications. Furthermore, it is speculated that antipsychotic-induced alterations in central lipid metabolism might contribute to their metabolic side effects, such as weight gain. This intertwining of lipid metabolism with psychiatric manifestations, especially in schizophrenia, opens an intriguing perspective on the comprehensive effects of antipsychotic treatments. The alterations in apolipoprotein gene expression induced by olanzapine may serve as a double-edged sword, affecting both the metabolic profile and psychiatric symptoms of schizophrenia patients. This dual influence calls for an integrated treatment approach that addresses the multifaceted nature of schizophrenia, balancing psychiatric symptom management with metabolic health.

The upregulation of apolipoprotein genes, including *Apoa1*, *Apoc3*, and *Apoh*, in the olanzapine-treated group unveils a profound modulation of lipid metabolism, reminiscent of their known peripheral roles yet extending this regulatory capacity deep into the neural circuits of the brain. This observation not only underscores the direct effect of olanzapine on CNS lipid metabolism but also hints at a potential mechanism contributing to the drug's metabolic side effects.

5 Conclusion

In this study, the reduced functional connectivity between the LS and the hypothalamus observed via fUS imaging enriches our understanding of olanzapine's neural impact. These findings, combined with the molecular insights into lipid metabolism gene expression, suggest a comprehensive model wherein olanzapine's effects permeate from molecular to systemic levels, affecting both brain functionality and overall metabolic regulation. The insights garnered from this research pave the way for future investigations aimed at dissecting the specific mechanisms by which olanzapine modulates lipid metabolism in the brain. Changes in central lipid metabolism may contribute to the weight gain and metabolic side effects associated with olanzapine treatment. This study offers valuable insights for future research into olanzapine's precise mechanisms in modulating brain lipid metabolism.

Data availability statement

The data presented in the study are deposited in the Gene Expression Omnibus (GEO) repository, accession number GSE268867.

Ethics statement

Ethical approval was not required for the study involving humans in accordance with the local legislation and institutional requirements. Written informed consent to participate in this study was not required from the participants or the participants' legal guardians/next of kin in accordance with the national legislation and the institutional requirements. The animal study was approved by the Institutional Animal Care and Use Committee of Shanghai Mental Health Center. The study was conducted in accordance with the local legislation and institutional requirements.

Author contributions

LH: Writing–review and editing, Writing–original draft. YS: Writing–review and editing, Writing–original draft. CL: Writing–review and editing. WW: Writing–review and editing. SS: Writing–review and editing. GS: Writing–review and editing. PJ: Writing–review and editing, Writing–original draft. JC: Writing–review and editing.

Funding

The author(s) declare that financial support was received for the research, authorship, and/or publication of this article. This research was supported by the National Natural Science Foundation of China (82071500), Shanghai Science and Technology Innovation Program (21Y11921100), the Program of Shanghai Academic/Technology Research Leader (21XD1423300), Shanghai Municipal Administrator of Traditional Chinese Medicine (ZY-(2021-2023)-0207-01), Shanghai Pujiang Program (21PJD063), Open Project Funded by the Shanghai Institute of Traditional Chinese Medicine for Mental Health (grant numbers SZB2023204), the Natural Science Foundation of Shanghai, China (grant number 23ZR1454600), and Feixiang Personnel Training Program of Shanghai Mental Health Center (grant numbers 2018-FX-02).

Acknowledgments

Authors of this manuscript are grateful to OE Biotech, Inc., (Shanghai, China) for assisting in sequencing and bioinformatics analysis.

Conflict of interest

The authors declare that the research was conducted in the absence of any commercial or financial relationships that could be construed as a potential conflict of interest.

Publisher's note

Supplementary material

The Supplementary Material for this article can be found online at: https://www.frontiersin.org/articles/10.3389/fphar.2024.1419098/full#supplementary-material

References

Agar, C., de Groot, P. G., Mörgelin, M., Monk, S. D. D. C., van Os, G., Levels, J. H. M., et al. (2011). β2-glycoprotein I: a novel component of innate immunity. *Blood* 117 (25), 6939–6947. doi:10.1182/blood-2010-12-325951

Anders, S., Pyl, P. T., and Huber, W. (2015). HTSeq--a Python framework to work with high-throughput sequencing data. *Bioinforma. Oxf. Engl.* 31 (2), 166–169. doi:10.1093/bioinformatics/btu638

Björkhem, I., and Meaney, S. (2004). Brain cholesterol: long secret life behind a barrier. *Arteriosclerosis, Thrombosis, Vasc. Biol.* 24 (5), 806–815. doi:10.1161/01.ATV.0000120374.59826.1b

Bruce, K. D., Zsombok, A., and Eckel, R. H. (2017). Lipid processing in the brain: a key regulator of systemic metabolism. *Front. Endocrinol.* 8, 60. doi:10.3389/fendo.2017.00060

Brunner, C., Grillet, M., Urban, A., Roska, B., Montaldo, G., and Macé, E. (2021). Whole-brain functional ultrasound imaging in awake head-fixed mice. *Nat. Protoc.* 16 (7), 3547–3571. doi:10.1038/s41596-021-00548-8

Burschinski, A., Schneider-Thoma, J., Chiocchia, V., Schestag, K., Wang, D., Siafis, S., et al. (2023). Metabolic side effects in persons with schizophrenia during mid-to long-term treatment with antipsychotics: a network meta-analysis of randomized controlled trials. *World Psychiatry Official J. World Psychiatric Assoc. (WPA)* 22 (1), 116–128. doi:10.1002/wps.21036

Calderwood, M. T., Tseng, A., Gabriella, I., and Stanley, B. G. (2022). Feeding behavior elicited by mu opioid and GABA receptor activation in the lateral septum. *Pharmacol. Biochem. Behav.* 217, 173395. doi:10.1016/j.pbb.2022.173395

Carli, M., Kolachalam, S., Longoni, B., Pintaudi, A., Baldini, M., Aringhieri, S., et al. (2021). Atypical antipsychotics and metabolic syndrome: from molecular mechanisms to clinical differences. *Pharm. Basel, Switz.* 14 (3), 238. doi:10.3390/ph14030238

Carus-Cadavieco, M., Gorbati, M., Ye, L., Bender, F., van der Veldt, S., Kosse, C., et al. (2017). Gamma oscillations organize top-down signalling to hypothalamus and enable food seeking. *Nature* 542 (7640), 232–236. doi:10.1038/nature21066

Chambers, S. M., Fasano, C. A., Papapetrou, E. P., Tomishima, M., Sadelain, M., and Studer, L. (2009). Highly efficient neural conversion of human ES and iPS cells by dual inhibition of SMAD signaling. *Nat. Biotechnol.* 27 (3), 275–280. doi:10.1038/nbt.1529

Chen, S., Zhou, Y., Chen, Y., and Gu, J. (2018). fastp: an ultra-fast all-in-one FASTQ preprocessor. *Bioinforma. Oxf. Engl.* 34 (17), i884–i890. doi:10.1093/bioinformatics/bty560

Chen, X., Liu, L., Zeng, Y., Li, D., Liu, X., and Hu, C. (2022). Olanzapine induces weight gain in offspring of prenatally exposed poly I:C rats by reducing brown fat thermogenic activity. *Front. Pharmacol.* 13, 1001919. doi:10.3389/fphar.2022.1001919

Choi, S., DiSilvio, B., Unangst, J., and Fernstrom, J. D. (2007). Effect of chronic infusion of olanzapine and clozapine on food intake and body weight gain in male and female rats. *Life Sci.* 81 (12), 1024–1030. doi:10.1016/j.lfs.2007.08.009

Correll, C. U., Robinson, D. G., Schooler, N. R., Brunette, M. F., Mueser, K. T., Rosenheck, R. A., et al. (2014). Cardiometabolic risk in patients with first-episode schizophrenia spectrum disorders: baseline results from the RAISE-ETP study. *JAMA Psychiatry* 71 (12), 1350–1363. doi:10.1001/jamapsychiatry.2014.1314

de Bartolomeis, A., De Simone, G., Ciccarelli, M., Castiello, A., Mazza, B., Vellucci, L., et al. (2022). Antipsychotics-induced changes in synaptic architecture and functional connectivity: translational implications for treatment response and resistance. *Biomedicines* 10 (12), 3183. doi:10.3390/biomedicines10123183

Elliott, D. A., Weickert, C. S., and Garner, B. (2010). Apolipoproteins in the brain: implications for neurological and psychiatric disorders. *Clin. Lipidol.* 51 (4), 555–573. doi:10.2217/CLP.10.37

Endres, D., von Zedtwitz, K., Nickel, K., Runge, K., Maier, A., Domschke, K., et al. (2024). Association of rheumatological markers with neuronal antibodies, cerebrospinal fluid, electroencephalography, and magnetic resonance imaging findings in 224 patients with psychotic syndromes. *Brain, Behav. Immun.* 119, 482–493. doi:10.1016/j.bbi.2024.04.001

Endres, K. (2021). Apolipoprotein A1, the neglected relative of Apolipoprotein E and its potential role in Alzheimer's disease. *Neural Regen. Res.* 16 (11), 2141–2148. doi:10.4103/1673-5374.310669

Fang, X., Gao, C., Wu, W., Hu, X., Shao, M., Zhou, C., et al. (2023). The role of the gut microbiome in weight-gain in schizophrenia patients treated with atypical antipsychotics: evidence based on altered composition and function in a cross-sectional study. *Psychiatry Res.* 328, 115463. doi:10.1016/j.psychres.2023.115463

Gabriella, I., Tseng, A., Sanchez, K. O., Shah, H., and Stanley, B. G. (2022). Stimulation of GABA receptors in the lateral septum rapidly elicits food intake and mediates natural feeding. *Brain Sci.* 12 (7), 848. doi:10.3390/brainsci12070848

Gebhardt, S., Haberhausen, M., Heinzel-Gutenbrunner, M., Gebhardt, N., Remschmidt, H., Krieg, J.-C., et al. (2009). Antipsychotic-induced body weight gain: predictors and a systematic categorization of the long-term weight course. *J. Psychiatric Res.* 43 (6), 620–626. doi:10.1016/j.jpsychires.2008.11.001

Giammanco, A., Spina, R., Cefalù, A. B., and Averna, M. (2023). APOC-III: a gatekeeper in controlling triglyceride metabolism. *Curr. Atheroscler. Rep.* 25 (3), 67–76. doi:10.1007/s11883-023-01080-8

Gjerde, P. B., Dieset, I., Simonsen, C., Hoseth, E. Z., Iversen, T., Lagerberg, T. V., et al. (2018). Increase in serum HDL level is associated with less negative symptoms after one year of antipsychotic treatment in first-episode psychosis. *Schizophrenia Res.* 197, 253–260. doi:10.1016/j.schres.2017.10.042

Grohs-Metz, G., Smausz, R., Gigg, J., Boeckers, T., and Hengerer, B. (2022). Functional ultrasound imaging of recent and remote memory recall in the associative fear neural network in mice. *Behav. Brain Res.* 428, 113862. doi:10.1016/j.bbr.2022.113862

Guo, W., Liu, F., Chen, J., Wu, R., Li, L., Zhang, Z., et al. (2017). Olanzapine modulation of long- and short-range functional connectivity in the resting brain in a sample of patients with schizophrenia. *Eur. Neuropsychopharmacol. J. Eur. Coll. Neuropsychopharmacol.* 27 (1), 48–58. doi:10.1016/j.euroneuro.2016.11.002

Herceg, D., Mimica, N., Herceg, M., and Puljić, K. (2022). Aggression in women with schizophrenia is associated with lower HDL cholesterol levels. *Int. J. Mol. Sci.* 23 (19), 11858. doi:10.3390/ijms231911858

Hirsch, L., Yang, J., Bresee, L., Jette, N., Patten, S., and Pringsheim, T. (2017). Second-generation antipsychotics and metabolic side effects: a systematic review of population-based studies. *Drug Saf.* 40 (9), 771–781. doi:10.1007/s40264-017-0543-0

Huang, J. T. J., Wang, L., Prabakaran, S., Wengenroth, M., Lockstone, H. E., Koethe, D., et al. (2008). Independent protein-profiling studies show a decrease in apolipoprotein A1 levels in schizophrenia CSF, brain and peripheral tissues. *Mol. Psychiatry* 13 (12), 1118–1128. doi:10.1038/sj.mp.4002108

Huang, P.-P., Zhu, W.-Q., Xiao, J.-M., Zhang, Y.-Q., Li, R., Yang, Y., et al. (2022). Alterations in sorting and secretion of hepatic apoA5 induce hypertriglyceridemia due to short-term use of olanzapine. *Front. Pharmacol.* 13, 935362. doi:10.3389/fphar.2022.935362

Ibi, D., de la Fuente Revenga, M., Kezunovic, N., Muguruza, C., Saunders, J. M., Gaitonde, S. A., et al. (2017). Antipsychotic-induced Hdac2 transcription via NF-κB leads to synaptic and cognitive side effects. *Nat. Neurosci.* 20 (9), 1247–1259. doi:10.1038/nn.4616

Kim, D., Langmead, B., and Salzberg, S. L. (2015). HISAT: a fast spliced aligner with low memory requirements. *Nat. Methods* 12 (4), 357–360. doi:10.1038/nmeth.3317

Kim, J., Lee, N., Suh, S. B., Jang, S., Kim, S., Kim, D.-G., et al. (2022). Metformin ameliorates olanzapine-induced disturbances in POMC neuron number, axonal projection, and hypothalamic leptin resistance. *BMB Rep.* 55 (6), 293–298. doi:10.5483/BMBRep.2022.55.6.026

Kim, T. W., Piao, J., Koo, S. Y., Kriks, S., Chung, S. Y., Betel, D., et al. (2021). Biphasic activation of WNT signaling facilitates the derivation of midbrain dopamine neurons from hESCs for translational use. *Cell. Stem Cell.* 28 (2), 343–355.e5. doi:10.1016/j.stem.2021.01.005

Langfelder, P., and Horvath, S. (2008). WGCNA: an R package for weighted correlation network analysis. *BMC Bioinforma.* 9, 559. doi:10.1186/1471-2105-9-559

Love, M. I., Huber, W., and Anders, S. (2014). Moderated estimation of fold change and dispersion for RNA-seq data with DESeq2. *Genome Biol.* 15 (12), 550. doi:10.1186/s13059-014-0550-8

Luo, C., Wang, X., Huang, H.-X., Mao, X.-Y., Zhou, H.-H., and Liu, Z.-Q. (2021). Coadministration of metformin prevents olanzapine-induced metabolic dysfunction and regulates the gut-liver axis in rats. *Psychopharmacology* 238 (1), 239–248. doi:10.1007/s00213-020-05677-8

Marcos, J. L., Olivares-Barraza, R., Ceballo, K., Wastavino, M., Ortiz, V., Riquelme, J., et al. (2023). Obesogenic diet-induced neuroinflammation: a pathological link between hedonic and homeostatic control of food intake. *Int. J. Mol. Sci.* 24 (2), 1468. doi:10.3390/ijms24021468

Martins, P. J. F., Haas, M., and Obici, S. (2010). Central nervous system delivery of the antipsychotic olanzapine induces hepatic insulin resistance. *Diabetes* 59 (10), 2418–2425. doi:10.2337/db10-0449

Martins-De-Souza, D., Wobrock, T., Zerr, I., Schmitt, A., Gawinecka, J., Schneider-Axmann, T., et al. (2010). Different apolipoprotein E, apolipoprotein A1 and prostaglandin-H2 D-isomerase levels in cerebrospinal fluid of schizophrenia patients and healthy controls. *World J. Biol. Psychiatry Official J. World Fed. Soc. Biol. Psychiatry* 11 (5), 719–728. doi:10.3109/15622971003758748

Meng, J.-J., Shen, J.-W., Li, G., Ouyang, C.-J., Hu, J.-X., Li, Z.-S., et al. (2023). Light modulates glucose metabolism by a retina-hypothalamus-brown adipose tissue axis. *Cell.* 186 (2), 398–412.e17. doi:10.1016/j.cell.2022.12.024

Morgan, A. P., Crowley, J. J., Nonneman, R. J., Quackenbush, C. R., Miller, C. N., Ryan, A. K., et al. (2014). The antipsychotic olanzapine interacts with the gut microbiome to cause weight gain in mouse. *PloS One* 9 (12), e115225. doi:10.1371/journal.pone.0115225

Mu, M.-D., Geng, H.-Y., Rong, K.-L., Peng, R.-C., Wang, S.-T., Geng, L.-T., et al. (2020). A limbic circuitry involved in emotional stress-induced grooming. *Nat. Commun.* 11 (1), 2261. doi:10.1038/s41467-020-16203-x

Myers, M. G., and Olson, D. P. (2012). Central nervous system control of metabolism. *Nature* 491 (7424), 357–363. doi:10.1038/nature11705

Norata, G. D., Tsimikas, S., Pirillo, A., and Catapano, A. L. (2015). Apolipoprotein C-iii: from pathophysiology to pharmacology. *Trends Pharmacol. Sci.* 36 (10), 675–687. doi:10.1016/j.tips.2015.07.001

Nouhoum, M., Ferrier, J., Osmanski, B. F., Ialy-Radio, N., Pezet, S., Tanter, M., et al. (2021). A functional ultrasound brain GPS for automatic vascular-based neuronavigation. *Sci. Rep.* 11 (1), 15197. doi:10.1038/s41598-021-94764-7

Pinna, G. (2023). Role of PPAR-allopregnanolone signaling in behavioral and inflammatory gut-brain Axis communications. *Biol. Psychiatry* 94 (8), 609–618. doi:10.1016/j.biopsych.2023.04.025

Pramfalk, C., Ahmed, O., Pedrelli, M., Minniti, M. E., Luquet, S., Denis, R. G., et al. (2022). Soat2 ties cholesterol metabolism to β-oxidation and glucose tolerance in male mice. *J. Intern. Med.* 292 (2), 296–307. doi:10.1111/joim.13450

Rizzi-Wise, C. A., and Wang, D. V. (2021). Putting together pieces of the lateral septum: multifaceted functions and its neural pathways. *ENeuro* 8 (6), ENEURO.0315. doi:10.1523/ENEURO.0315-21.2021

Roberts, A., Trapnell, C., Donaghey, J., Rinn, J. L., and Pachter, L. (2011). Improving RNA-Seq expression estimates by correcting for fragment bias. *Genome Biol.* 12 (3), R22. doi:10.1186/gb-2011-12-3-r22

Ruud, J., Steculorum, S. M., and Brüning, J. C. (2017). Neuronal control of peripheral insulin sensitivity and glucose metabolism. *Nat. Commun.* 8, 15259. doi:10.1038/ncomms15259

Seicol, B. J., Bejarano, S., Behnke, N., and Guo, L. (2019). Neuromodulation of metabolic functions: from pharmaceuticals to bioelectronics to biocircuits. *J. Biol. Eng.* 13, 67. doi:10.1186/s13036-019-0194-z

Shen, S., Liao, Q., Gu, L., Zhu, Y., Liu, Y., Zhang, X., et al. (2024). G protein-coupled receptor-biased signaling: potential drug discovery to facilitate treatment of metabolic diseases. *Acta Mater. Medica* 3 (1). doi:10.15212/amm-2023-0041

Solmi, M., Seitidis, G., Mavridis, D., Correll, C. U., Dragioti, E., Guimond, S., et al. (2023). Incidence, prevalence, and global burden of schizophrenia - data, with critical appraisal, from the Global Burden of Disease (GBD) 2019. *Mol. Psychiatry* 28, 5319–5327. doi:10.1038/s41380-023-02138-4

Song, X., Li, X., Gao, J., Zhao, J., Li, Y., Fan, X., et al. (2014). APOA-I: a possible novel biomarker for metabolic side effects in first episode schizophrenia. *PloS One* 9 (4), e93902. doi:10.1371/journal.pone.0093902

Stanley, S., Pinto, S., Segal, J., Pérez, C. A., Viale, A., DeFalco, J., et al. (2010). Identification of neuronal subpopulations that project from hypothalamus to both liver and adipose tissue polysynaptically. *Proc. Natl. Acad. Sci. U. S. A.* 107 (15), 7024–7029. doi:10.1073/pnas.1002790107

Terrill, S. J., Jackson, C. M., Greene, H. E., Lilly, N., Maske, C. B., Vallejo, S., et al. (2016). Role of lateral septum glucagon-like peptide 1 receptors in food intake. *Am. J. Physiology. Regul. Integr. Comp. Physiology* 311 (1), R124–R132. doi:10.1152/ajpregu.00460.2015

Terrill, S. J., Wall, K. D., Medina, N. D., Maske, C. B., and Williams, D. L. (2018). Lateral septum growth hormone secretagogue receptor affects food intake and motivation for sucrose reinforcement. *Am. J. Physiology. Regul. Integr. Comp. Physiology* 315 (1), R76-R83–R83. doi:10.1152/ajpregu.00339.2017

Timper, K., and Brüning, J. C. (2017). Hypothalamic circuits regulating appetite and energy homeostasis: pathways to obesity. *Dis. Models Mech.* 10 (6), 679–689. doi:10.1242/dmm.026609

Vancampfort, D., Stubbs, B., Mitchell, A. J., De Hert, M., Wampers, M., Ward, P. B., et al. (2015). Risk of metabolic syndrome and its components in people with schizophrenia and related psychotic disorders, bipolar disorder and major depressive disorder: a systematic review and meta-analysis. *World Psychiatry Official J. World Psychiatric Assoc. (WPA)* 14 (3), 339–347. doi:10.1002/wps.20252

Vantaggiato, C., Panzeri, E., Citterio, A., Orso, G., and Pozzi, M. (2019). Antipsychotics promote metabolic disorders disrupting cellular lipid metabolism and trafficking. *Trends Endocrinol. Metabolism TEM* 30 (3), 189–210. doi:10.1016/j.tem.2019.01.003

Varela, L., Kim, J. G., Fernández-Tussy, P., Aryal, B., Liu, Z. W., Fernández-Hernando, C., et al. (2021). Astrocytic lipid metabolism determines susceptibility to diet-induced obesity. *Sci. Adv.* 7 (50), eabj2814. doi:10.1126/sciadv.abj2814

Wang, M., Li, P., Li, Z., da Silva, B. S., Zheng, W., Xiang, Z., et al. (2023). Lateral septum adenosine A2A receptors control stress-induced depressive-like behaviors via signaling to the hypothalamus and habenula. *Nat. Commun.* 14 (1), 1880. doi:10.1038/s41467-023-37601-x

Wang, Q., Ding, S.-L., Li, Y., Royall, J., Feng, D., Lesnar, P., et al. (2020). The allen mouse brain common coordinate framework: a 3D reference atlas. *Cell.* 181 (4), 936–953. doi:10.1016/j.cell.2020.04.007

Wong, L. C., Wang, L., D'Amour, J. A., Yumita, T., Chen, G., Yamaguchi, T., et al. (2016). Effective modulation of male aggression through lateral septum to medial hypothalamus projection. *Curr. Biol. CB* 26 (5), 593–604. doi:10.1016/j.cub.2015.12.065

Xiang, S.-Y., Zhao, J., Lu, Y., Chen, R.-M., Wang, Y., Chen, Y., et al. (2019). Network pharmacology-based identification for therapeutic mechanism of Ling-Gui-Zhu-Gan decoction in the metabolic syndrome induced by antipsychotic drugs. *Comput. Biol. Med.* 110, 1–7. doi:10.1016/j.compbiomed.2019.05.007

Xu, Q.-Q., Yang, W., Zhong, M., Lin, Z.-X., Gray, N. E., and Xian, Y.-F. (2023a). Animal models of Alzheimer's disease: preclinical insights and challenges. *Acta Mater. Medica* 2 (2). doi:10.15212/amm-2023-0001

Xu, Y., Jiang, Z., Li, H., Cai, J., Jiang, Y., Otiz-Guzman, J., et al. (2023b). Lateral septum as a melanocortin downstream site in obesity development. *Cell. Rep.* 42 (5), 112502. doi:10.1016/j.celrep.2023.112502

Xu, Y., Lu, Y., Cassidy, R. M., Mangieri, L. R., Zhu, C., Huang, X., et al. (2019). Identification of a neurocircuit underlying regulation of feeding by stress-related emotional responses. *Nat. Commun.* 10 (1), 3446. doi:10.1038/s41467-019-11399-z

Yu, G., Wang, L.-G., Han, Y., and He, Q.-Y. (2012). clusterProfiler: an R package for comparing biological themes among gene clusters. *Omics a J. Integr. Biol.* 16 (5), 284–287. doi:10.1089/omi.2011.0118

Zewinger, S., Reiser, J., Jankowski, V., Alansary, D., Hahm, E., Triem, S., et al. (2020). Apolipoprotein C3 induces inflammation and organ damage by alternative inflammasome activation. *Nat. Immunol.* 21 (1), 30–41. doi:10.1038/s41590-019-0548-1

Zhang, T., and Wong, G. (2022). Gene expression data analysis using Hellinger correlation in weighted gene co-expression networks (WGCNA). *Comput. Struct. Biotechnol. J.* 20, 3851–3863. doi:10.1016/j.csbj.2022.07.018

frontiers | Frontiers in Neuroscience

TYPE Original Research
PUBLISHED 18 June 2024
DOI 10.3389/fnins.2024.1416738

OPEN ACCESS

EDITED BY
Song Zhang,
Shanghai Jiao Tong University, China

REVIEWED BY
Jingjing Yuan,
First Affiliated Hospital of Zhengzhou University, China
Mei Han,
National Institutes of Health (NIH), United States
Tingting Li,
University of Maryland, United States

*CORRESPONDENCE
Xiyao Gu
✉ gxykevin@126.com
Shushan Jia
✉ jiashushan@163.com

†These authors have contributed equally to this work

RECEIVED 13 April 2024
ACCEPTED 06 June 2024
PUBLISHED 18 June 2024

CITATION
Liu Y, Zhang J, Gu X and Jia S (2024) Mapping the current trends and hotspots of adult hippocampal neurogenesis from 2004–2023: a bibliometric analysis.
Front. Neurosci. 18:1416738.
doi: 10.3389/fnins.2024.1416738

Mapping the current trends and hotspots of adult hippocampal neurogenesis from 2004–2023: a bibliometric analysis

Ye Liu[1,2,3†], Jian Zhang[4†], Xiyao Gu[1,2,3*] and Shushan Jia[1*]

[1]The Second School of Clinical Medicine of Binzhou Medical University, Yantai, Shandong Province, China, [2]Department of Anesthesiology, Department of Radiology, Renji Hospital, Shanghai Jiao Tong University School of Medicine, Shanghai, China, [3]Key Laboratory of Anesthesiology (Shanghai Jiao Tong University), Ministry of Education, Shanghai, China, [4]Department of Anesthesiology, The International Peace Maternity and Child Health Hospital, Shanghai Jiao Tong University School of Medicine, Shanghai, China

Objective: We utilized bibliometric and data visualization techniques to discern the primary research domains and emerging frontiers in the field of adult hippocampal neurogenesis (AHN).

Methods: We systematically searched the Web of Science database for AHN-related articles published between 2004 and 2023. The retrieved articles were filtered based on publication types (articles and reviews) and language (English). We employed CiteSpace, VOSviewer, and the online bibliometric platform (bibliometric.com) to visualize and analyze the collected data.

Results: In total, 1,590 AHN-related publications were discovered, exhibiting a steady increase in yearly publications over time. The United States emerged as the leading contributor in AHN research in terms of both publication quantity and national influence. Among all research institutions in the field of AHN, the University of California System exhibited the highest impact. Kempermann, Gerd was the most active author. The publications of the top three active authors primarily focused on the functions of AHN, and reversing hippocampal damage and cognitive impairment by improving AHN. An analysis of reference co-citation clustering revealed 8 distinct research clusters, and the notable ones included "adult hippocampal neurogenesis," "neurogenesis," "hippocampus," "dentate gyrus," "neural stem cell," and "depression." Additionally, a burst keyword detection indicated that 'anxiety' is a current research hotspot in the field of AHN.

Conclusion: This in-depth bibliographic assessment of AHN offers a deeper insight into the present research hotspots in the field. The association between AHN and cognitive diseases, such as Alzheimer's disease (AD) and anxiety, has emerged as a prominent research hotspot.

KEYWORDS

adult hippocampal neurogenesis, neurogenesis, web of science, bibliometric analysis, Citespace, VOSviewer, co-citation analysis

1 Introduction

The process of adding new neurons to the hippocampal region throughout life is referred to as adult hippocampal neurogenesis (AHN) (Kempermann et al., 2015). For decades, AHN has been extensively studied in rodents and non-human primates (Zhang et al., 2023), and many studies have also determined the extent of lifelong neurogenesis in humans (Spalding et al., 2013; Boldrini et al., 2018; Sorrells et al., 2018). Hippocampal neural stem cells in the subgranular zone (SGZ) of the dentate gyrus (DG) primarily differentiate into dentate granule neurons, which constitute the majority of excitatory neurons in the DG region (Denoth-Lippuner and Jessberger, 2021). Functionally, the DG receives input from the entorhinal cortex and sends information to CA3 and CA1 through a trisynaptic circuit, playing a key role in learning and memory (Babcock et al., 2021). AHN is the most robust form of plasticity in the adult brain and may contribute to the development of memory (Goncalves et al., 2016). Studies have shown that AHN enhances the plasticity of the hippocampus, which may be related to spatial memory, emotional memory, pattern separation, cognitive flexibility, and emotional regulation. Abnormal AHN can disrupt cognition, leading to memory deficits (Altman, 1963). Considering the importance of AHN for healthy brain function, many studies deciphered the physiological mechanisms of AHN.

Abnormal AHN has been well-documented in various diseases of the central nervous system, including neurodegenerative and neuropsychiatric disorders (Lazarov and Hollands, 2016). The morphology of adult-born dentate granule cells was abnormal in autopsy specimens of patients with various neurodegenerative diseases, such as amyotrophic lateral sclerosis, Huntington's disease, Parkinson's disease, Lewy body dementia, and frontotemporal dementia. In addition, changes were observed in the expression of differentiation markers of these cells. The proportions of hippocampal neural stem cells change in the resting and proliferative phases, altering the dynamic balance of the neurogenic niche. These changes reduce the phagocytic ability of microglia, trigger astrogliosis, and alter the microvascular structure of the DG, leading to hippocampal dysfunction in the physiological and pathological aging process of humans (Terreros-Roncal et al., 2021). Several studies have shown that AHN is reduced in patients suffering from depressive disorders such as Major Depressive Disorder (MDD) (Berger et al., 2020). MDD is a prevalent mental illness, primarily manifested as anxiety, low spirits, and slowed cognition. Studies on human post-mortem brain tissue have shown a decrease in the number of hippocampal neurons in patients with MDD and reduced angiogenesis in the neurogenic niche (Boldrini et al., 2012). These changes may be the main reasons for abnormal regulation of emotion, depression, and anxiety. Whether AHN has other potential functions, in addition to cognitive function and emotional regulation, still requires further scientific research.

Research on the mechanism of AHN primarily focuses on the initiation and maintenance of AHN. The neurogenic niche plays a crucial role in the production and functional maintenance of AHN. The composition of niche cells includes neural stem cells (NSCs), neural progenitor cells, neuroglial cells, endothelial cells, and immune cells, such as microglia and macrophages (Li et al., 2022). Under steady-state conditions, NSCs provide signaling molecules, such as the neurotransmitter GABA and the Notch ligand Delta-like 1 (Dll1) (Kawaguchi et al., 2013), through autocrine and paracrine manners to regulate the dormant state of NSCs. Microglia phagocytose apoptotic IPCs (Sierra et al., 2010), and astrocytes release cytokines, such as IL-1β and IL-6, to promote the neuronal differentiation of NSCs (Barkho et al., 2006). The presence of antibody plaques and tau tangles in the brain of patients with AD, and even the interaction of amyloid peptides with hippocampal niche macromolecules, such as palmitic acid and metals, can lead to chronic inflammation, oxidative stress, microglial activation, and abnormal function of astrocytes (Babcock et al., 2021). This affects NSC survival, neuronal differentiation, and the maturation and integration of newborn neurons (Li et al., 2022). Considering the importance of the neurogenic niche in the generation and maintenance of AHN changes in niches and their effect on AHN in different diseases need further in-depth research.

Bibliometric analysis utilizes statistical techniques to measure numerical data associated with scientific endeavors. It provides structured knowledge systems by handling the characteristics of references like journals, authors, institutions, and so on. Nevertheless, quantitative approaches are rarely employed in the field of AHN. We analyzed AHN studies to assess global research patterns and prospective areas of interest from 2004 to 2023. Additionally, we forecasted the direction of research in this domain for the upcoming years.

2 Methods

2.1 Data source and search strategy

On March 15, 2024, we completed the search on the Web of Science Core Collection database (Science Citation Index Expanded (SCI-EXPANDED) – 1900-present). The search strategy was: 'Adult hippocampal neurogenesis' (Title) or 'Adult hippocampal neurogenesis' (Abstract) or 'Adult hippocampal neurogenesis' (Author keywords). The search spanned from January 1, 2004, to December 31, 2023. Detailed information, such as publication types (articles or reviews), author details (full names, addresses, and affiliations), citation data (times cited in Web of Science core collection and all databases), and publication characteristics (year, date, volume, issue, page range, DOI, PubMed ID, research areas, and open access designations), were collected from the Web of Science database on the same day. All analyses were performed using the acquired data to prevent biases arising from citation information updates.

2.2 Data extraction and statistical analysis

The dataset for this study comprised the full records of the retrieved papers, such as titles, authors, abstracts, and cited references. These data were exported as plain text. We analyzed the number and year of publication, total citations, average citations per publication, countries/regions, institutions, authors, references, and keywords. Data were then uploaded to the Online Analysis Platform of Literature Metrology,[1] VOS viewer (Version 1.6.20, Leiden University,

1 https://bibliometric.com/

Netherlands,), and CiteSpace (Version 6.2.R4, 64-bit, Drexel University, Philadelphia, PA, United States) for bibliometric analysis.

CiteSpace is specialized visual analysis software designed to analyze trends and dynamic changes in scientific literature. It identifies key points within a given field (Chen and Song, 2019). In this study, CiteSpace was used to analyze the collaborative relationships and co-citation of institutions, cited authors, subject categories, and references and detect citation bursts for references. We initiated our analysis by setting suitable parameters, which included the width of the time slice and the threshold. To simplify the network, we opted for the "Pathfinder Network Scaling Algorithm." The "Logarithmization" option was employed to maintain a balanced link distribution within the network. Furthermore, we activated the "Burst Citation Detection" option, a method specifically designed to detect emerging trends in scientific literature.

VOS viewer is a software used to construct bibliometric networks of the scientific literature (Yeung et al., 2020). In this study, we employed this software to analyze and visualize co-occurrence networks of keywords. The relatedness in co-occurrence analysis was determined based on the number of documents, in which keywords occurred together. Different nodes represent different elements in the network maps generated by the VOS viewer, while the size of nodes is proportional to the number of publications or frequency. The color of nodes and lines indicates different appearance years or clusters. The line between the nodes represents the associations such as co-authorship or co-citation. The strength of links was assessed by the indicator of total link strength. When visualizing the results, we chose the "Cluster View," which can group keywords based on their co-occurrence patterns.

The Online Analysis Platform of Literature Metrology (see text footnote 1) is a web-based tool used to examine the yearly publication trends of the top ten most productive countries/regions and explore collaborations among countries. We first uploaded our dataset, then selected "Country/Region" and "Year" as the dimensions for analysis. We used the "Collaboration Network Analysis" feature to explore the collaboration relationships between different countries/regions. We also looked at the results of the "Publication Trend Analysis" to understand the changes in the number of publications and citations in each country/region.

By employing these diverse bibliometric tools, we aimed to thoroughly analyze and illustrate data related to AHN. Our findings offer valuable insight into the trends and movements in the field.

3 Results

3.1 Bibliometric analysis of publications

The number of publications and citations within a specific period directly reflects the development trend of scientific knowledge in a particular field. We identified 1,590 original and review articles for bibliometric analysis. The annual changes in publications related to AHN research are shown in Figure 1A. Although the number of AHN publications occasionally fluctuates, it was generally on an upward trajectory, peaking in 2021 (132 publications). The difference between 2004 and 2021 (13 and 132, respectively) indicated that AHN is increasingly attracting global attention. In total, 64 countries/regions participated. Figure 1B depicts a world map illustrating the contribution of each country. The color gradient on the map corresponds to the number of publications. The publications mainly came from North America, East Asia, and Western Europe. More specifically, the United States contributed nearly one-third of the publications (522, 32.83%), almost three times that of mainland China (230, 14.47%) and Germany (218, 13.71%) (Table 1). Meanwhile, these publications have received 93,004 citations, with an average of 58.49 citations per publication. The increase in the number of publications and citations highlights the prospects and significance of AHN research.

3.2 Basic knowledge structures of AHN research

3.2.1 Collaborating countries/regions and institutions in AHN research

We conducted a country/region collaboration analysis using CiteSpace to reflect the collaborative relationships among countries/regions in the field of AHN. The analysis revealed 64 nodes and 314 edges, representing 64 countries/regions contributing to AHN research. The United States, France, Germany, and Italy were defined as centers for international cooperation and exchange with other countries (purple circles, Figure 2A). Notably, the distance between these circles was long, indicating a lack of cooperation between countries. "Centrality" is an important indicator used to describe network characteristics, reflecting the influence and importance of nodes within the network. Table 2 shows that the influence of the United States (0.70) was far greater than that of other countries/regions, followed by Germany (0.27) and Italy (0.18). Although the number of publications in China ranked second, China's influence was only 0.06. China has shown rapid growth since 2012, and for the first time in 2021, China surpassed Germany in terms of the total number of papers, ranking second (Figure 1A). This trend suggests that the contribution of China may increase in the near future.

Additionally, the institutional graph contained 735 nodes and 3,284 edges, with a relatively low density (density = 0.0122). The results indicated that 735 institutions have contributed to this field, but research groups were relatively distributed among various institutions (Figure 2B). Tables 1, 2 comprehensively list the top 20 institutions with the most output and the greatest influence, along with their number of publications and centrality. The Helmholtz Association contributed the most publications, followed by Technische Universitat Dresden and Institut National de la Sante et de la Recherche Medicale (Inserm). The University of California System possessed the most influence (0.20), followed by the National Institutes of Health (NIH) – USA (0.16) and the University of Texas System (0.15). These three institutions were all from the United States, indicating a close cooperative relationship among various institutions in the United States. These findings also indicate that institutions in other countries/regions need to strengthen scientific cooperation.

3.2.2 Analysis of authors

The author collaboration analysis identified 5,574 nodes and 19,982 edges, indicating that 5,574 authors contributed to 19,982 publications (Figure 3). The relatively low density (0.0013) suggests weak collaboration among authors in AHN research. Kempermann, Gerd (69), Hen, Rene (26), and Thuret, Sandrine (25) were the most active authors in terms of publication frequency (Table 3).

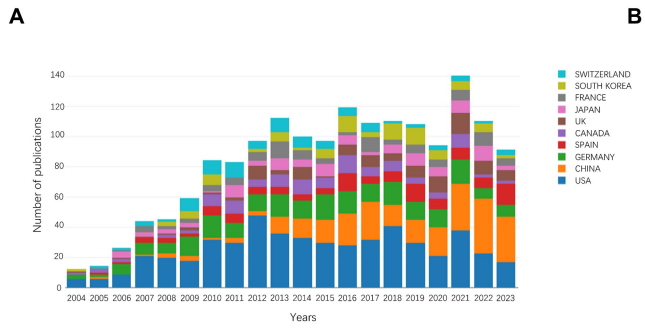

FIGURE 1
(A) The annual number of publications in the top 10 most productive countries from 2004 to 2023. **(B)** A world map depicting the contribution of each country/region based on publication counts.

TABLE 1 Top 10 countries/regions and institution in terms of publications for AHN.

Ranking	Country/region	Publications	Ranking	Institution	Publications
1	USA	522	1	Helmholtz Association	100
2	China	230	2	Technische Universitat Dresden	78
3	Germany	218	3	Institut National de la Sante et de la Recherche Medicale (Inserm)	61
4	Spain	112	4	German Center for Neurodegenerative Diseases (DZNE)	53
5	Canada	102	5	Consejo Superior de Investigaciones Cientificas (CSIC)	53
6	France	97	6	University of Texas System	53
7	Japan	95	7	Humboldt University of Berlin	48
8	South Korea	88	8	Charite Universitatsmedizin Berlin	47
9	Switzerland	84	9	Free University of Berlin	47
10	UK	77	10	Columbia University	44

Kempermann, Gerd initially focused on the functional significance of AHN (Kempermann et al., 2004; Kempermann, 2015) and existing evidence (Kempermann et al., 2018). His research is now focused on improving AHN, reversing hippocampal damage, and learning memory disorders (Leiter et al., 2022). Hen, Rene is dedicated to exploring the relationship between emotional disorders such as anxiety and depression (Santarelli et al., 2003; Samuels and Hen, 2011; Anacker and Hen, 2017; Jimenez et al., 2018), and neurogenesis. He has investigated the pathogenesis and therapeutic significance of adult major depression and loss of hippocampal neuroplasticity (Tartt et al., 2022). Thuret, Sandrine focused on diet (Vauzour et al., 2017), nutritional status (Marx et al., 2021), mental health (Zainuddin and Thuret, 2012), and hippocampal neurogenesis.

3.3 Overview of research trends and hotspots

3.3.1 Analysis of highly-cited studies

Citation analysis is the cornerstone of bibliometric analysis. Generally, a higher number of citations and citation frequency can reflect the strong influence and high academic value of a paper in a specific field. We listed the top 10 papers with the most citations and the highest centrality in the AHN field in Table 4. Notably, the papers written by Moreno-Jiménez EP had the most citations in this field, with 161 citations. Moreno-Jiménez EP and their colleagues obtained human brain samples under strict conditions. The authors found thousands of immature neurons in the DG of neurologically healthy human subjects, continuing to the ninth decade of life. These neurons showed varying degrees of maturity at different stages of AHN differentiation. The number and maturity of these neurons gradually declined with the progression of AD. These results indicate that AHN persists in physiological and pathological aging in humans and support the notion that impaired neurogenesis may be a potential mechanism for memory deficits in AD (Moreno-Jiménez et al., 2019). In 2013, Spalding KL and their colleagues published a paper with the highest citation in the centrality ranking in "Cell." The authors assessed the generation of human hippocampal cells by measuring the concentration of nuclear bomb-test-derived ^{14}C in genomic DNA and proposed an integrated model of cell turnover dynamics. The authors found that in adult humans, 700 new neurons were added

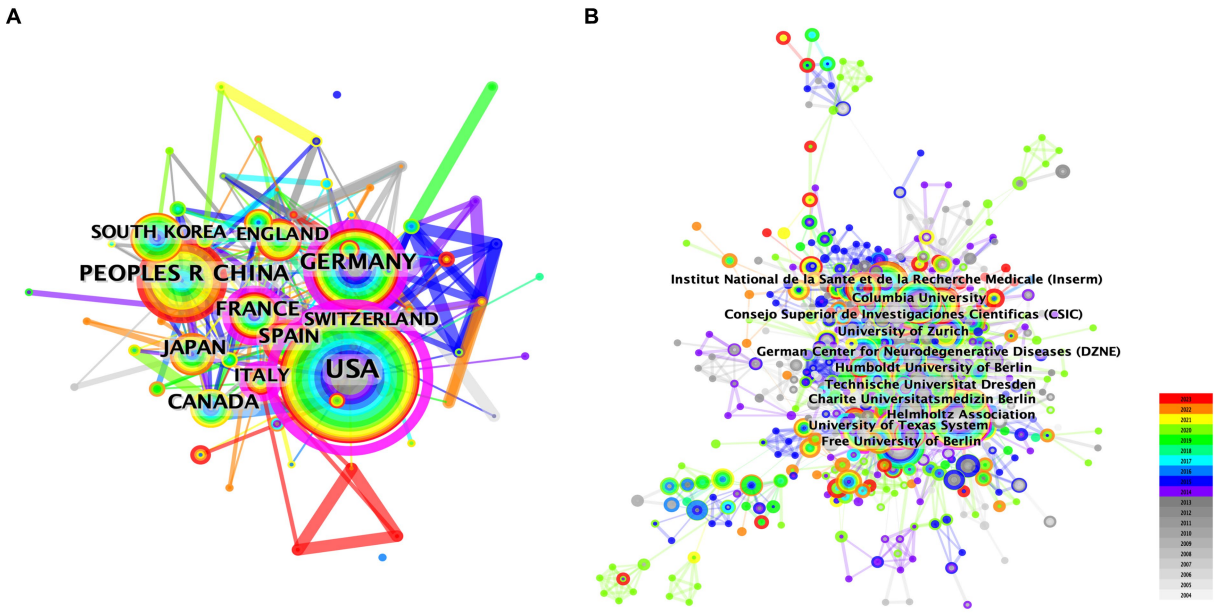

FIGURE 2
The network map of collaborating countries/regions **(A)** and institutions **(B)** in AHN research.

TABLE 2 Top 10 countries/region and institutions in terms of centrality for AHN.

Ranking	Country/region	Centrality	Ranking	Institution	Centrality
1	USA	0.70	1	University of California System	0.20
2	Germany	0.27	2	National Institutes of Health (NIH) – USA	0.16
3	Italy	0.18	3	University of Texas System	0.15
4	France	0.14	4	Harvard University	0.14
5	UK	0.10	5	University of Amsterdam	0.13
6	Spain	0.07	6	Helmholtz Association	0.12
7	Switzerland	0.07	7	Institut National de la Sante et de la Recherche Medicale (Inserm)	0.10
8	South Africa	0.07	8	Johns Hopkins University	0.10
9	Peoples R China	0.06	9	Chinese Academy of Sciences	0.09
10	Sweden	0.06	10	State University System of Florida	0.09

to each hippocampus every day, equivalent to an annual turnover rate of 1.75% in the renewal site. The renewal process was slightly decelerated with aging. This result indicates that neurons continue to regenerate during adulthood, and the generation of adult hippocampal neurons may contribute to the function of the human brain (Spalding et al., 2013).

3.3.2 References co-citation analysis

To identify milestone references and the focus of ongoing research, we conducted a co-citation analysis of references using CiteSpace and found eight major clusters (Figure 4A). We created a timeline view of these cluster evolutions to track the focus over time (Figure 4B). Early research focused on physical activity (#0), hippocampus-dependent learning (#2), and following olfactory bulbectomy (#6). As our understanding of adult neurogenesis deepened, the unique role of AHN or adult hippocampal neurogenesis in the hippocampal brain region was gradually discovered. People began to focus on investigating adult hippocampal neurogenesis (#1) and proneurogenic effect (#7). In addition, targeting adult neurogenesis (#4) also attracted widespread attention. Although the current focus on AHN is not particularly high, the approach of targeting AHN in various cognitive diseases will gradually become a hotspot and trend for future research. Currently, the most prominent trends include Alzheimer's disease (#3) and antidepressant effects (#5). AHN abnormalities have been found in various cognitive diseases, and improvements in AHN can significantly improve the cognitive function of these diseases. Therefore, the current most prominent trend is that people are increasingly paying attention to the relationship between various diseases related to the hippocampal

brain region and AHN. Among them, the most widely researched diseases are neurodegenerative diseases and neuropsychiatric diseases.

3.3.3 Analysis of most frequently appearing keywords

Keyword co-occurrence analysis is another common method in bibliometric analysis used To identify popular research topics. Co-occurrence analysis assesses the relevance between keywords based on the number of documents in which they appear together (Wu et al., 2021). In this study, we extracted author keywords from 1,590 publications and analyzed them using VOSviewer. Table 5 lists the 20 keywords with the highest frequency. In addition to "adult hippocampal neurogenesis," The following keywords appeared more than 210 times: "Dentate gyrus," "neurons," "neural stem cells," "brain," and "synaptic plasticity." As shown In The VOSviewer keyword co-occurrence visualization (Figure 5A), all keywords were divided into four different clusters and were marked. From major to minor, we summarized neurodegenerative diseases, neuropsychiatric diseases, neurogenic niches, and the potential functions of AHN. These common keywords were mainly linked to the role of AHN in various central nervous system diseases, cognitive functions, and the basic composition of neurogenic niches in AHN.

Additionally VOSviewer color-coded the keywords based on their average year of appearance (Figure 5B). Keywords appearing early are represented in blue while those appearing recently are highlighted in red. Notably keywords such as "doublecortin" "proliferation" and "dentate gyrus" stood out in the early stages of research. In contrast keywords like "Alzheimer's disease" "microglia" and "neurodegeneration" showed a more recent average year of appearance. This is consistent with our findings from the co-citation analysis of references indicating that AHN is receiving increasing attention in the field of neurodegenerative diseases related to cognitive dysfunction and has become a hotspot in current research.

TABLE 3 Top 10 authors and cited authors in terms of publications for AHN.

Ranking	Author	Publications
1	Kempermann, Gerd	69
2	Hen, Rene	26
3	Thuret, Sandrine	25
4	Llorens-martin, Maria	21
5	Eisch, Amelia J	19
6	Amrein, Irmgard	18
7	Lucassen, Paul J	17
8	Song, Hongjun	17
9	Gage, Fred H	17
10	Galea, Liisa A M	16

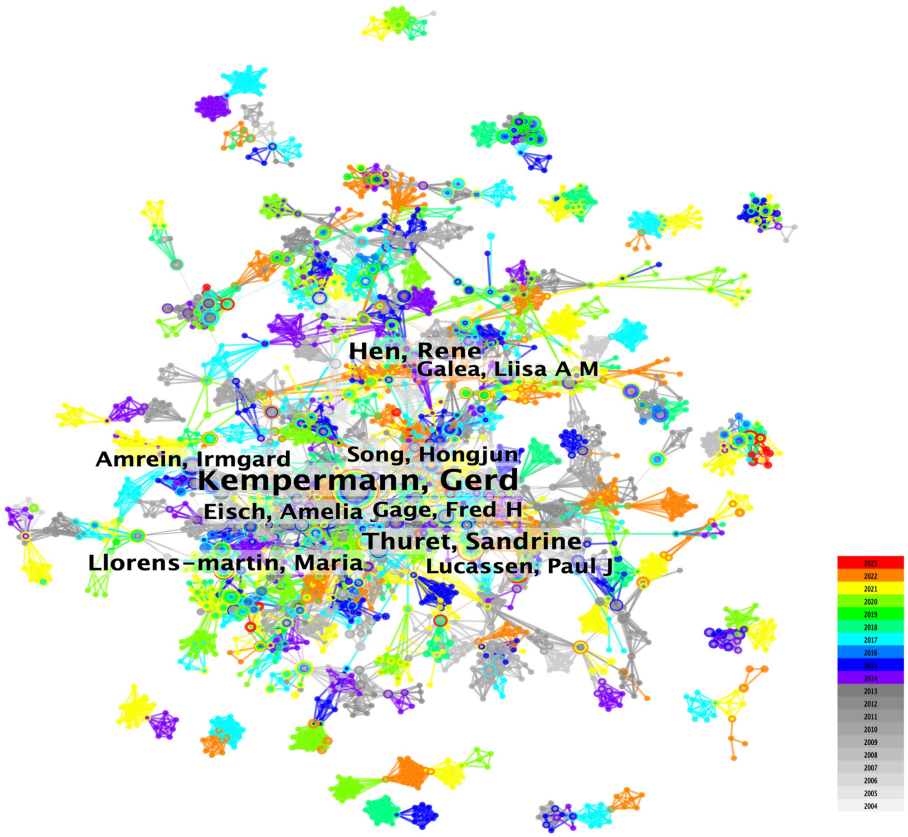

FIGURE 3
Overlay visualization map of author co-authorship analysis generated by VOSviewer software.

TABLE 4 Top 10 co-cited references related to AHN in terms of co-citations counts and centrality.

Ranking	Co-citation counts	Cited reference	Representative author (publication year)	Ranking	Centrality	Cited reference	Representative author (publication year)
1	161	Adult hippocampal neurogenesis is abundant in neurologically healthy subjects and drops sharply in patients with Alzheimer's disease	Moreno-Jiménez et al. (2019)	1	0.2	Dynamics of hippocampal neurogenesis in adult humans	Spalding et al. (2013)
2	115	Human Hippocampal Neurogenesis Persists throughout Aging	Boldrini et al. (2018)	2	0.15	Young dentate granule cells mediate pattern separation, whereas old granule cells facilitate pattern completion	Nakashiba et al. (2012)
3	110	New neurons and new memories: how does adult hippocampal neurogenesis affect learning and memory?	Deng et al. (2010)	3	0.14	A functional role for adult hippocampal neurogenesis in spatial pattern separation	Clelland et al. (2009)
4	105	Human hippocampal neurogenesis drops sharply in children to undetectable levels in adults	Sorrells et al. (2018)	4	0.13	Requirement of hippocampal neurogenesis for the behavioral effects of antidepressants	Santarelli et al. (2003)
5	103	Adult hippocampal neurogenesis and cognitive flexibility—linking memory and mood	Anacker and Hen (2017)	5	0.12	Spatial relational memory requires hippocampal adult neurogenesis	Dupret et al. (2008)
6	99	Mechanisms and functional implications of adult neurogenesis	Zhao et al. (2008)	6	0.11	Increasing adult hippocampal neurogenesis is sufficient to improve pattern separation	Sahay et al. (2011)
7	96	Increasing adult hippocampal neurogenesis is sufficient to improve pattern separation	Sahay et al. (2011)	7	0.09	Enhanced synaptic plasticity in newly generated granule cells of the adult hippocampus	Schmidt-Hieber et al. (2004)
8	94	Dynamics of hippocampal neurogenesis in adult humans	Spalding et al. (2013)	8	0.09	Activation of local inhibitory circuits in the dentate gyrus by adult-born neurons	Drew et al. (2016)
9	93	Human Adult Neurogenesis: Evidence and Remaining Questions	Kempermann et al. (2018)	9	0.08	Human Hippocampal Neurogenesis Persists throughout Aging	Boldrini et al. (2018)
10	89	A functional role for adult hippocampal neurogenesis in spatial pattern separation	Clelland et al. (2009)	10	0.08	Neurogenesis-dependent and -independent effects of fluoxetine in an animal model of anxiety/depression	David et al. (2009)

3.3.4 Keywords and reference citation burst detection

Burst detection, an algorithm developed by Kleinberg, is an effective analytical tool for capturing concepts or topics widely discussed in a specific period. We applied burst detection to extract key references in the AHN research field. Figure 6A shows the top 25 references with the most significant citation bursts. In this graphical representation, the blue line represents the time interval, and the red segment represents the period when the reference burst occurred. Among these references, the one with the strongest burst value was an article written by Moreno-Jiménez et al. (64.64), which is also the most cited article in this field. This article had the strongest burst value and the most citations because the authors used human brain samples to provide direct evidence for the presence of AHN in the human brain, a question that has long been controversial. The authors also compared the brain samples of AD patients with neurologically healthy subjects, providing evidence for neural damage as a potential mechanism for cognitive dysfunction. Following closely, the reference with the second highest burst value was a review published by Deng et al. (2010) (47.38). The authors summarized the different contributions of newborn neurons at different maturity stages in learning and memory (Deng et al., 2010). In addition, although the burst of some references gradually weakened, 8 references showed continuous bursts. This finding indicates that these research topics have been receiving attention in recent years. We summarized these 8 references in a continuous burst state, mainly covering the role of AHN in aging, AD, health, and other disease states, and providing evidence for the existence of AHN (Anacker and Hen, 2017; Anacker et al., 2018; Boldrini et al., 2018; Kempermann et al., 2018; Sorrells et al., 2018; Moreno-Jiménez et al., 2019; Tobin et al., 2019; Toda et al., 2019).

Burst keyword detection is used to identify emerging concepts that are frequently cited over a period of time. In the past twenty years, "anxiety" ranked first with the highest burst intensity (13.27), followed by "mechanisms" (12.37), "adult hippocampal neurogenesis" (11.31), "central nervous system" (10.64), and "rat hippocampus" (10.32) (Figure 6B). Both "anxiety" and "mechanisms" began to burst in 2019 and their burst continued until 2023, accompanied by "memory" (6.45), "mouse model" (6.36), "activation" (10.01), and "Alzheimer's disease" (7.19), indicating that these are current research hotspots.

4 Discussion

4.1 Primary findings

This study used bibliometric methods to analyze 1,590 articles on AHN from 2004 to 2023. The number of publications in the field of AHN has increased over the past 20 years. The United States led other countries in terms of both the number of publications and centrality. However, the number of publications in the field of AHN in mainland China has been steadily increasing since 2012, and in 2021, it surpassed Germany for the first time, ranking second in terms of total publications. Among research institutions, the Helmholtz Association contributed the most publications, while the University of California System had the greatest influence. In terms of authors, Kempermann, Gerd was the most active author in terms of publication number. The main focus of these studies was on the evidence of AHN in the human brain and the relationship between abnormal AHN and cognitive impairment in AD. Analysis of clusters of commonly cited publications showed that the main research topics over the past 20 years have focused on the relationship between abnormal AHN and cognitive diseases, such as AD and depression, and treatments targeting AHN. Keyword analysis also illuminated that research on AHN and neurodegenerative diseases and neuropsychiatric diseases is currently a hot topic in the field of AHN.

4.2 Results of the study in context

4.2.1 The current academic situation of countries/regions and institutions regarding AHN research

Analysis of countries and institutions showed that the United States and Europe were undoubtedly the leaders in the

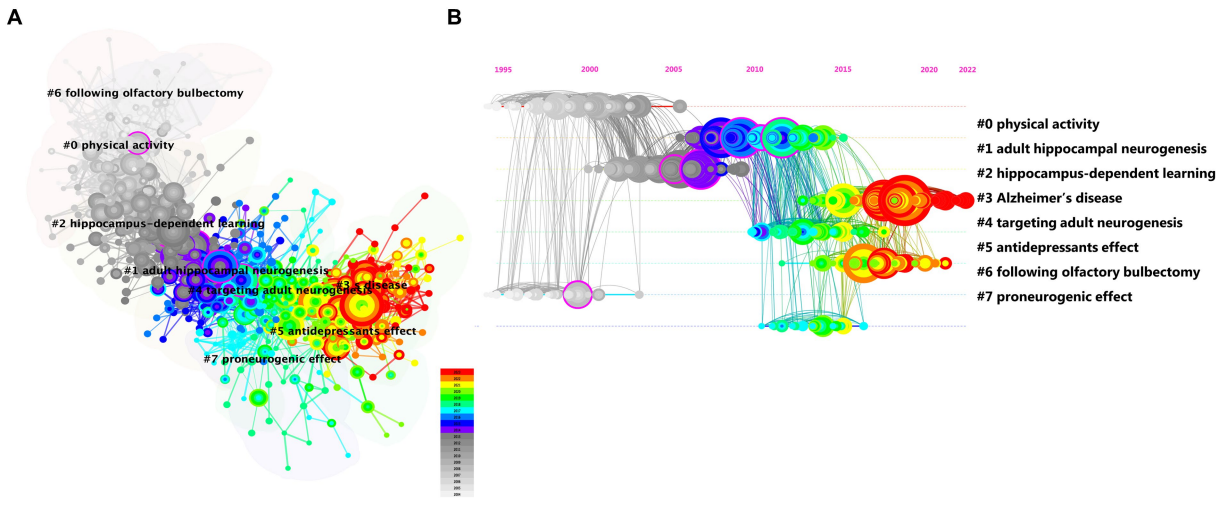

FIGURE 4
The cluster view map **(A)** and timeline view map **(B)** of reference co-citation analysis were generated by CiteSpace.

TABLE 5 Top 10 keywords in terms of frequency and centrality in AHN research.

Ranking	Keyword	Frequency	Ranking	Keyword	Centrality
1	Dentate gyrus	747	1	Cell-proliferation	0.11
2	Adult neurogenesis	419	2	Rat	0.08
3	Adult hippocampal neurogenesis	318	3	Enriched environment	0.08
4	Neurons	290	4	Messenger-rna	0.08
5	Neural stem cells	273	5	Mice	0.07
6	Brain	245	6	Cell proliferation	0.07
7	Hippocampal neurogenesis	240	7	Environmental enrichment	0.07
8	Synaptic plasticity	216	8	Depression	0.07
9	Proliferation	175	9	Antidepressant treatment	0.07
10	Progenitor cells	171	10	Element binding protein	0.07

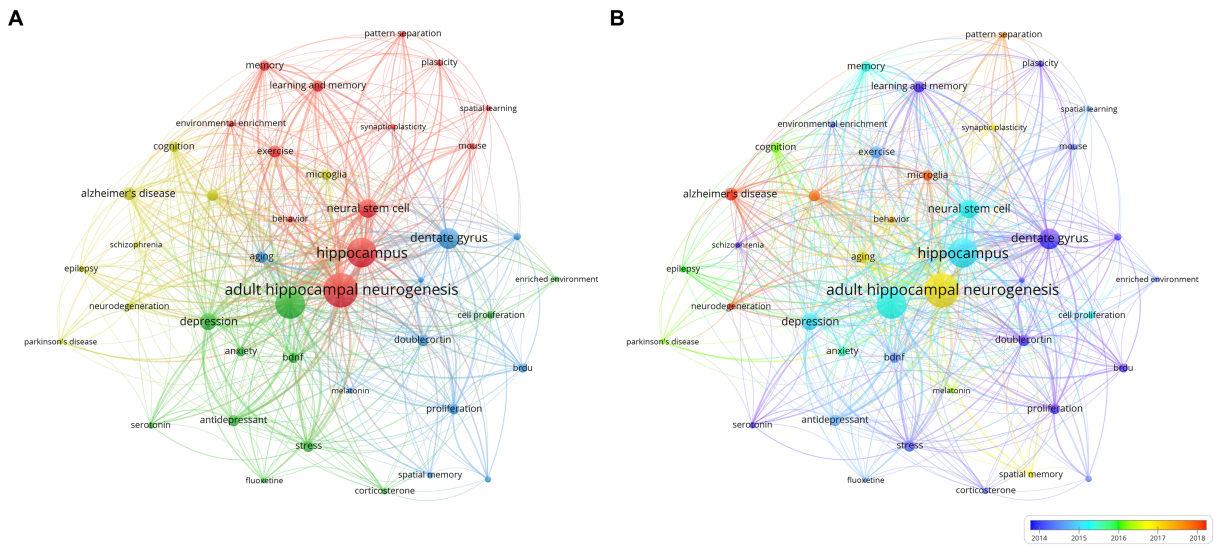

FIGURE 5
Overlay visualization map of keywords co-occurrence analysis in clusters **(A)** or in timeline **(B)**.

field of AHN research, with the United States leading in terms of both the number of publications and centrality. The early initiation of AHN research in the United States and Europe has led to the current trend. This outcome could be attributed to the substantial research investment in the AHN field by the United States and Europe, as well as their prolific contributions to the field of health sciences. The number of publications in China has grown rapidly over the past twenty years, and in 2021 it jumped to second place. However, in terms of the centrality of AHN, the influence of China was weak. Although, the growth trend of publications in the field of AHN in China indicates the attention and exploration of Chinese scientific researchers in the field of AHN, and it is believed that in the near future, the central position of China in the field of AHN will significantly improve. In addition, international cooperation in AHN research is currently limited, and cooperation is mainly concentrated in the United States and some European countries. Based on the low density of cooperation analysis, we suggest that research institutions should eliminate academic barriers, strengthen exchanges, and promote the progress of AHN research.

4.2.2 AHN exists in the human brain and is closely related to cognitive functions

AHN exists in both rodent and human brains and is closely related to cognitive functions. Researchers, such as Kempermann G, have made significant contributions to this field, providing evidence for the existence of AHN and its function in the brain. Using human brain samples, Moreno-Jiménez and Spalding not only confirmed the existence of AHN in the adult human brain but also measured changes in neurons with aging and evaluated the process of cell turnover integration. Their work has greatly advanced the progress of scientific research in the field of AHN, providing a theoretical basis for the

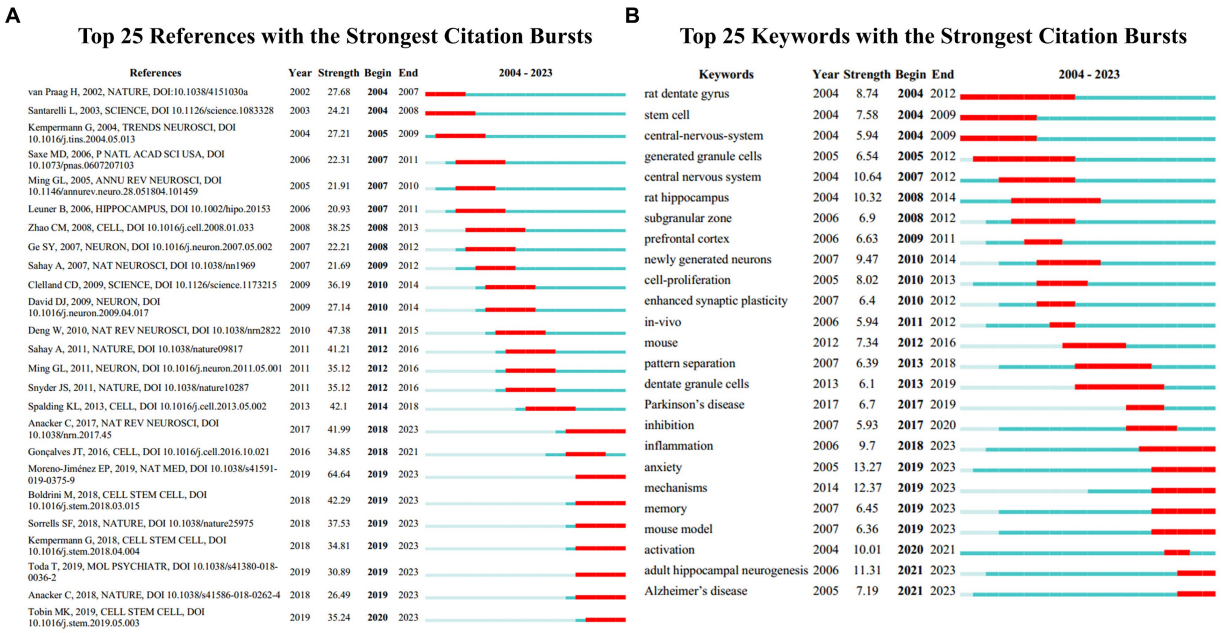

FIGURE 6
(A) References with the strongest citation bursts in publications on AHN research between 2004 and 2023. **(B)** Keywords with the strongest citation bursts in publications on AHN research between 2004 and 2023. The blue lines represent time intervals, while the red segments represent the periods when reference bursts occur.

existence of AHN and confirming the contribution of adult hippocampal neurogenesis to human brain function.

Neurons can inherently generate action potentials. Electrophysiological studies of adult dentate gyrus indicated that this ability appears rapidly (within a week) after mitosis. For a period of time thereafter, new granule cells exhibit an excitatory rather than inhibitory response to the typical inhibitory neurotransmitter GABA (Chancey et al., 2013), suggesting that these cells are more likely to be excited to generate action potentials, while mature granule cells are strongly inhibited by GABA (Amaral et al., 2007; Pelkey et al., 2017). Adult-generated granule neurons also display other unusual electrophysiological characteristics that disappear as they reach full maturity, including enhanced synaptic plasticity and a lower threshold for LTP induction (Ge et al., 2007). The high plasticity of adult-generated neurons allows playing a unique role in functions associated with the hippocampus. Different parts of the hippocampus have different functions, with the dorsal hippocampus supporting spatial navigation learning and memory, and the ventral hippocampus being crucial for anxiety and stress regulation (Fanselow and Dong, 2010). Reports indicated that a reduction number of new neurons impairs cognitive performance in hippocampal-dependent tests, including object recognition memory, contextual fear conditioning, and spatial learning and memory in the Morris water maze, Barnes maze, and radial arm maze (Cameron and Glover, 2015). Rodents lacking new neurons exhibit impairments in social behavior. Adult neurogenesis in the hippocampal region is necessary for stress-induced social avoidance (Lagace et al., 2010) and social recognition memory (Cope and Gould, 2019).

Although researchers have observed abnormalities in AHN in various diseases through animal models of cognitive disorders, these abnormalities can manifest in several ways: a decrease in the number of newborn neurons, abnormal morphology and growth patterns, and an inability to integrate into the existing hippocampal spatial network structure (Richetin et al., 2017; Torres-López et al., 2023). Researchers have found that correcting these AHN abnormalities can improve cognitive function, but the weight of these abnormal AHN phenotypes in cognitive dysfunction remains unknown. Therefore, some scholars believe that AHN is not a key factor in these cognitive disorders, but there is a certain correlation. We believe that the reason for this controversy is due to the current lack of understanding of AHN. Although research on adult hippocampal neurogenesis was mentioned as early as the 1960s, the detailed mechanism of AHN has not been fully elucidated to this day due to the lack of tools and the difficulty in defining cell phenotypes. However, it is gratifying that with the application of transgenic technology and multiphoton microscopy, researchers can not only label AHN-related cell populations with fluorescent proteins, but also use real-time imaging systems to continuously monitor the neural activity of neurons in the DG region (Corenblum et al., 2016; Danielson et al., n.d.). In addition, the progress of technologies such as single-cell RNA sequencing, spatial metabolomics, proteomics, and interactomics (Alexandrov, n.d.; Dueñas and Lee, n.d.) provides powerful visualization tools and new perspectives for the regulation of neurogenesis, promoting our understanding of complex adult neurogenesis. The advancement of these technologies greatly aids our understanding of the relationship between abnormal AHN and cognitive function, as well as the research of future intervention treatments.

4.2.3 The major trends and advantages of studies related to AHN

Cluster analysis and burst detection analysis are valuable tools for determining the general research trends in the field of AHN. In

keyword cluster analysis, we found that common keywords mainly focus on the role of AHN in various central nervous system diseases. In burst detection, we found that literature and keywords in a continuous burst state focus on the relationship between AHN and aging, AD, health, and other diseases. Therefore, we inferred that one of the current research focuses in the field of AHN is exploring the mechanistic role of AHN in the development of cognitive diseases, such as depression and AD. AD is the most common type of dementia, and patients with AD show functional impairments in memory and cognitive functions. Some studies reported that adult hippocampal neurogenesis and neuronal maturation are inhibited in patients with AD, while gliogenesis increases in these patients (Hollands et al., 2017). Several mouse models indicated that adult neurogenesis is impaired in the hippocampal region in AD, and newly proliferated granule neurons fail to integrate into the existing network, leading to spatial memory deficits (Richetin et al., 2017). In addition, in human brain specimens and rodent experiments in various neurodegenerative diseases, such as Parkinson's disease, frontotemporal degeneration, vascular dementia, and aging, there are reports of reduced numbers and functional impairments of newly generated neurons. These abnormalities are closely related to declined cognitive ability (Hattiangady and Shetty, 2008; Nuber et al., 2008; Cho et al., 2015; Kim et al., 2017).

"Anxiety" is the keyword with the highest intensity in keyword burst analysis, making it a hotspot in the field of AHN research. AHN is widely described as a key function of the hippocampus, highly sensitive to the effects of stress. Environmental challenges, such as unpredictable chronic mild stress, prenatal stress, chronic social defeat, early life stress, and glucocorticoid application, all impair hippocampal neurogenesis (Kessler et al., 1985; McEwen, 2004; Czéh et al., 2007; Dagytė et al., 2009). Adult cells in the ventral DG appear to be particularly susceptible to these stressors (Schoenfeld and Cameron, 2015). Prolonged stressors may create a vicious cycle, where stress damages neurogenesis, low neurogenesis fails to alleviate stress, and further loses neurons born in adulthood. Similar effects have also been observed in non-human primates, where social isolation or subordinate status reduces neurogenesis and leads to anhedonia (Perera et al., n.d.). In dealing with stress, reducing or enhancing neurogenesis can regulate anxiety-like and depression-like behaviors (Anacker and Hen, 2017). Therefore, from a clinical perspective, neurogenesis has significant implications for the development of emotional and anxiety disorders, and increasing neurogenesis may be a potential therapeutic strategy to promote the reversal of emotional disorders and cognitive flexibility, for the treatment of patients with depression and anxiety, which may be one of the reasons why "anxiety" has become a hotspot in the field of AHN research.

Given the close relationship between AHN and cognitive impairment diseases, we believe that therapies targeting AHN will become the research prospect in this field. In basic research, researchers have demonstrated the beneficial effects of drug intervention, growth factor stimulation of neural stem cell proliferation, exercise, and other methods on improving AHN and cognitive disorders (Cui et al., 2015; Norevik et al., 2023). However, these therapeutic methods from basic research are still in the preclinical research stage, and the translation of experimental results mainly obtained from mice to the human brain still faces challenges due to species differences, genetic background, gender, and age. Therefore, safe and efficient treatment strategies targeting AHN will become a hot topic in future AHN research. In addition, how does AHN lead to cognitive decline? Are the abnormalities of AHN the same in different diseases? What is the detailed mechanism of abnormal AHN, and are there any intervention targets for abnormal neurogenesis? For the prospect of medical career and the development of human health, these questions are also worth more rigorous and systematic clinical and basic research work to explore deeply.

5 Limitations

This study does have some limitations. First, this study solely focused on publications from the Web of Science core literature database, which means that many pertinent publications from other databases, like Medline, Scopus, and the Cochrane Library, were not included. Second, our study only included English publications, excluding publications from other languages. This might result in an underrepresentation of the contributions from non-English publications. Third, the CiteSpace analysis, which is based on the number and structural changes of citations and the theory of information fitness, is influenced by the quantity and structural changes of citations. It was a 'citation-based' tools to uncover the potential trends and hotspots, thus may not fully represent the true quality of articles.

6 Conclusion

This comprehensive bibliometric analysis reports the current state of research on AHN, providing insights into current trends and hotspots. This study indicated that the relationship between AHN and cognitive diseases, such as AD, depression, etc., has become a prominent research hotspot. Further studies on the mechanisms of abnormal AHN and treatments targeting AHN can contribute to the prevention and treatment of cognitive diseases.

Data availability statement

The original contributions presented in the study are included in the article/supplementary material, further inquiries can be directed to the corresponding authors.

Author contributions

YL: Writing – original draft, Writing – review & editing, Conceptualization, Data curation, Formal analysis, Investigation, Methodology, Project administration, Software, Supervision. JZ: Data curation, Formal analysis, Methodology, Project administration, Supervision, Validation, Writing – original draft, Writing – review & editing, Software. XG: Conceptualization, Data curation, Formal

analysis, Funding acquisition, Investigation, Methodology, Project administration, Resources, Software, Supervision, Validation, Visualization, Writing – review & editing, Writing – original draft. SJ: Data curation, Funding acquisition, Methodology, Project administration, Resources, Software, Supervision, Writing – review & editing, Writing – original draft.

Funding

The author(s) declare financial support was received for the research, authorship, and/or publication of this article. This work was supported by Technological Innovation 2030-Major Projects of "Brain Science and Brain-like Research" (2022ZD0206200) to XG, Shanghai Rising-Star Program (21QC1400300) to XG, National Natural Science Foundation of China (no. 82371245, 81701092) to XG and SJ, Natural Science Foundation of Shandong Province (ZR2020MH129) to SJ, Shanghai Municipal Key Clinical Specialty (shslczdzk03601) and Shanghai Engineering Research Center of Peri-operative Organ Support and Function Preservation (20DZ2254200).

Conflict of interest

The authors declare that the research was conducted in the absence of any commercial or financial relationships that could be construed as a potential conflict of interest.

Publisher's note

References

Alexandrov, T. Spatial metabolomics and imaging mass spectrometry in the age of artificial intelligence. *Annu. Rev. Biomed. Data Sci.* 3, 61–87. doi: 10.1146/annurev-biodatasci-011420-031537

Altman, J. (1963). Autoradiographic investigation of cell proliferation in the brains of rats and cats. *Anat. Rec.* 145, 573–591. doi: 10.1002/ar.1091450409

Amaral, D. G., Scharfman, H. E., and Lavenex, P. (2007). The dentate gyrus: fundamental neuroanatomical organization (dentate gyrus for dummies). *Prog. Brain Res.* 163, 3–22. doi: 10.1016/S0079-6123(07)63001-5

Anacker, C., and Hen, R. (2017). Adult hippocampal neurogenesis and cognitive flexibility—linking memory and mood. *Nat. Rev. Neurosci.* 18, 335–346. doi: 10.1038/nrn.2017.45

Anacker, C., Luna, V. M., Stevens, G. S., Millette, A., Shores, R., Jimenez, J. C., et al. (2018). Hippocampal neurogenesis confers stress resilience by inhibiting the ventral dentate gyrus. *Nature* 559, 98–102. doi: 10.1038/s41586-018-0262-4

Babcock, K. R., Page, J. S., Fallon, J. R., and Webb, A. E. (2021). Adult hippocampal neurogenesis in aging and Alzheimer's disease. *Stem Cell Rep.* 16, 681–693. doi: 10.1016/j.stemcr.2021.01.019

Barkho, B. Z., Song, H., Aimone, J. B., Smrt, R. D., Kuwabara, T., Nakashima, K., et al. (2006). Identification of astrocyte-expressed factors that modulate neural stem/progenitor cell differentiation. *Stem Cells Dev.* 15, 407–421. doi: 10.1089/scd.2006.15.407

Berger, T., Lee, H., Young, A. H., Aarsland, D., and Thuret, S. (2020). Adult hippocampal neurogenesis in major depressive disorder and Alzheimer's disease. *Trends Mol. Med.* 26, 803–818. doi: 10.1016/j.molmed.2020.03.010

Boldrini, M., Fulmore, C. A., Tartt, A. N., Simeon, L. R., Pavlova, I., Poposka, V., et al. (2018). Human hippocampal neurogenesis persists throughout aging. *Cell Stem Cell* 22, 589–599.e5. doi: 10.1016/j.stem.2018.03.015

Boldrini, M., Hen, R., Underwood, M. D., Rosoklija, G. B., Dwork, A. J., Mann, J. J., et al. (2012). Hippocampal angiogenesis and progenitor cell proliferation are increased with antidepressant use in major depression. *Biol. Psychiatry* 72, 562–571. doi: 10.1016/j.biopsych.2012.04.024

Cameron, H. A., and Glover, L. R. (2015). Adult neurogenesis: beyond learning and memory. *Annu. Rev. Psychol.* 66, 53–81. doi: 10.1146/annurev-psych-010814-015006

Clelland, C. D., Choi, M., Romberg, C., et al. (2009). A functional role for adult hippocampal neurogenesis in spatial pattern separation. *Sci.* 325:210–213. doi: 10.1126/science.1173215

Chancey, J. H., Adlaf, E. W., Sapp, M. C., Pugh, P. C., Wadiche, J. I., and Overstreet-Wadiche, L. S. (2013). GABA depolarization is required for experience-dependent synapse unsilencing in adult-born neurons. *J. Neurosci.* 33, 6614–6622. doi: 10.1523/JNEUROSCI.0781-13.2013

Chen, C., and Song, M. (2019). Visualizing a field of research: a methodology of systematic scientometric reviews. *PLoS One* 14:e0223994. doi: 10.1371/journal.pone.0223994

Cho, K. O., Lybrand, Z. R., Ito, N., Brulet, R., Tafacory, F., Zhang, L., et al. (2015). Aberrant hippocampal neurogenesis contributes to epilepsy and associated cognitive decline. *Nat. Commun.* 6:6606. doi: 10.1038/ncomms7606

Cope, E. C., and Gould, E. (2019). Adult neurogenesis, glia, and the extracellular matrix. *Cell Stem Cell* 24, 690–705. doi: 10.1016/j.stem.2019.03.023

Corenblum, M. J., Ray, S., Remley, Q. W., Long, M., Harder, B., Zhang, D. D., et al. (2016). Reduced Nrf2 expression mediates the decline in neural stem cell function during a critical middle-age period. *Aging Cell* 15, 725–736. doi: 10.1111/acel.12482

Cui, L., Duchamp, N. S., Boston, D. J., Ren, X., Zhang, X., Hu, H., et al. (2015). NF-kappaB is involved in brain repair by stem cell factor and granulocyte-colony stimulating factor in chronic stroke. *Exp. Neurol.* 263, 17–27. doi: 10.1016/j.expneurol.2014.08.026

Czéh, B., Müller-Keuker, J. I. H., Rygula, R., Abumaria, N., Hiemke, C., Domenici, E., et al. (2007). Chronic social stress inhibits cell proliferation in the adult medial prefrontal cortex: hemispheric asymmetry and reversal by fluoxetine treatment. *Neuropsychopharmacology* 32, 1490–1503. doi: 10.1038/sj.npp.1301275

Dagytė, G., van der Zee, E. A., Postema, F., Luiten, P. G. M., den Boer, J. A., Trentani, A., et al. (2009). Chronic but not acute foot-shock stress leads to temporary suppression of cell proliferation in rat hippocampus. *Neuroscience* 162, 904–913. doi: 10.1016/j.neuroscience.2009.05.053

Danielson, N. B., Kaifosh, P., Zaremba, J. D., Lovett-Barron, M., Tsai, J., Denny, C. A., et al. Distinct contribution of adult-born hippocampal granule cells to context encoding. *Neuron* 90, 1097–4199. doi: 10.1016/j.neuron.2016.02.019

David, D. J., Samuels, B. A., Rainer, Q., et al. (2009). Neurogenesis-dependent and -independent effects of fluoxetine in an animal model of anxiety/depression. *Neuron.* 62:479–493. doi: 10.1016/j.neuron.2009.04.017

Deng, W., Aimone, J. B., and Gage, F. H. (2010). New neurons and new memories: how does adult hippocampal neurogenesis affect learning and memory? *Nat. Rev. Neurosci.* 11, 339–350. doi: 10.1038/nrn2822

Denoth-Lippuner, A., and Jessberger, S. (2021). Formation and integration of new neurons in the adult hippocampus. *Nat. Rev. Neurosci.* 22, 223–236. doi: 10.1038/s41583-021-00433-z

Drew, L. J., Kheirbek, M. A., Luna, V. M., et al. (2016). Activation of local inhibitory circuits in the dentate gyrus by adult-born neurons. *Hippocampus.* 26:763–778. doi: 10.1002/hipo.22557

Dueñas, M. E., and Lee, Y. J. Single-cell metabolomics by mass spectrometry imaging. *Adv. Exp. Med. Biol.* 1280, 69–82. doi: 10.1007/978-3-030-51652-9_5

Dupret, D., Revest, J. M., Koehl, M., et al. (2008). Spatial relational memory requires hippocampal adult neurogenesis. *PLoS One.* 3:e1959. doi: 10.1371/journal.pone.0001959

Fanselow, M. S., and Dong, H. W. (2010). Are the dorsal and ventral hippocampus functionally distinct structures? *Neuron* 65, 7–19. doi: 10.1016/j.neuron.2009.11.031

Ge, S., Yang, C. H., Hsu, K. S., Ming, G. L., and Song, H. (2007). A critical period for enhanced synaptic plasticity in newly generated neurons of the adult brain. *Neuron* 54, 559–566. doi: 10.1016/j.neuron.2007.05.002

Goncalves, J. T., Schafer, S. T., and Gage, F. H. (2016). Adult neurogenesis in the Hippocampus: from stem cells to behavior. *Cell* 167, 897–914. doi: 10.1016/j.cell.2016.10.021

Hattiangady, B., and Shetty, A. K. (2008). Implications of decreased hippocampal neurogenesis in chronic temporal lobe epilepsy. *Epilepsia* 49, 26–41. doi: 10.1111/j.1528-1167.2008.01635.x

Hollands, C., Tobin, M. K., Hsu, M., Musaraca, K., Yu, T. S., Mishra, R., et al. (2017). Depletion of adult neurogenesis exacerbates cognitive deficits in Alzheimer's disease by compromising hippocampal inhibition. *Mol. Neurodegener.* 12:64. doi: 10.1186/s13024-017-0207-7

Jimenez, J. C., Su, K., Goldberg, A. R., Luna, V. M., Biane, J. S., Ordek, G., et al. (2018). Anxiety cells in a hippocampal-hypothalamic circuit. *Neuron* 97, 670–683.e6. doi: 10.1016/j.neuron.2018.01.016

Kawaguchi, D., Furutachi, S., Kawai, H., Hozumi, K., and Gotoh, Y. (2013). Dll1 maintains quiescence of adult neural stem cells and segregates asymmetrically during mitosis. *Nat. Commun.* 4:1880. doi: 10.1038/ncomms2895

Kempermann, G. (2015). Adult neurogenesis: an evolutionary perspective. *Cold Spring Harb. Perspect. Biol.* 8:a018986. doi: 10.1101/cshperspect.a018986

Kempermann, G., Gage, F. H., Aigner, L., Song, H., Curtis, M. A., Thuret, S., et al. (2018). Human adult neurogenesis: evidence and remaining questions. *Cell Stem Cell* 23, 25–30. doi: 10.1016/j.stem.2018.04.004

Kempermann, G., Song, H., and Gage, F. H. (2015). Neurogenesis in the adult Hippocampus. *Cold Spring Harb. Perspect. Biol.* 7:a018812. doi: 10.1101/cshperspect.a018812

Kempermann, G., Wiskott, L., and Gage, F. H. (2004). Functional significance of adult neurogenesis. *Curr. Opin. Neurobiol.* 14, 186–191. doi: 10.1016/j.conb.2004.03.001

Kessler, R. C., Price, R. H., and Wortman, C. B. (1985). Social factors in psychopathology: stress, social support, and coping processes. *Annu. Rev. Psychol.* 36, 531–572. doi: 10.1146/annurev.ps.36.020185.002531

Kim, J. H., Ko, P. W., Lee, H. W., Jeong, J. Y., Lee, M. G., Kim, J. H., et al. (2017). Astrocyte-derived lipocalin-2 mediates hippocampal damage and cognitive deficits in experimental models of vascular dementia. *Glia* 65, 1471–1490. doi: 10.1002/glia.23174

Lagace, D. C., Donovan, M. H., DeCarolis, N. A., Farnbauch, L. A., Malhotra, S., Berton, O., et al. (2010). Adult hippocampal neurogenesis is functionally important for stress-induced social avoidance. *Proc. Natl. Acad. Sci. USA* 107, 4436–4441. doi: 10.1073/pnas.0910072107

Lazarov, O., and Hollands, C. (2016). Hippocampal neurogenesis: learning to remember. *Prog. Neurobiol.* 138-140, 1–18. doi: 10.1016/j.pneurobio.2015.12.006

Leiter, O., Zhuo, Z., Rust, R., Wasielewska, J. M., Grönnert, L., Kowal, S., et al. (2022). Selenium mediates exercise-induced adult neurogenesis and reverses learning deficits induced by hippocampal injury and aging. *Cell Metab.* 34, 408–423.e8. doi: 10.1016/j.cmet.2022.01.005

Li, Y.-D., Luo, Y. J., Chen, Z. K., Quintanilla, L., Cherasse, Y., Zhang, L., et al. (2022). Hypothalamic modulation of adult hippocampal neurogenesis in mice confers activity-dependent regulation of memory and anxiety-like behavior. *Nat. Neurosci.* 25, 630–645. doi: 10.1038/s41593-022-01065-x

Li, W. P., Su, X. H., Hu, N. Y., Hu, J., Li, X. W., Yang, J. M., et al. (2022). Astrocytes mediate cholinergic regulation of adult hippocampal neurogenesis and memory through M(1) muscarinic receptor. *Biol. Psychiatry* 92, 984–998. doi: 10.1016/j.biopsych.2022.04.019

Marx, W., Lane, M., Hockey, M., Aslam, H., Berk, M., Walder, K., et al. (2021). Diet and depression: exploring the biological mechanisms of action. *Mol. Psychiatry* 26, 134–150. doi: 10.1038/s41380-020-00925-x

McEwen, B. S. (2004). Protection and damage from acute and chronic stress: allostasis and allostatic overload and relevance to the pathophysiology of psychiatric disorders. *Ann. N. Y. Acad. Sci.* 1032, 1–7. doi: 10.1196/annals.1314.001

Moreno-Jiménez, E. P., Flor-García, M., Terreros-Roncal, J., Rábano, A., Cafini, F., Pallas-Bazarra, N., et al. (2019). Adult hippocampal neurogenesis is abundant in neurologically healthy subjects and drops sharply in patients with Alzheimer's disease. *Nat. Med.* 25, 554–560. doi: 10.1038/s41591-019-0375-9

Nakashiba, T., Cushman, J. D., Pelkey, K. A., et al. (2012). Young dentate granule cells mediate pattern separation, whereas old granule cells facilitate pattern completion. *Cell.* 149:188–201. doi: 10.1016/j.cell.2012.01.046

Norevik, C. S., Huuha, A. M., Røsbjørgen, R. N., Hildegard Bergersen, L., Jacobsen, K., Miguel-Dos-Santos, R., et al. (2023). Exercised blood plasma promotes hippocampal neurogenesis in the Alzheimer's disease rat brain. *J. Sport Health Sci.* 13, 245–255. doi: 10.1016/j.jshs.2023.07.003

Nuber, S., Petrasch-Parwez, E., Winner, B., Winkler, J., von Hörsten, S., Schmidt, T., et al. (2008). Neurodegeneration and motor dysfunction in a conditional model of Parkinson's disease. *J. Neurosci.* 28, 2471–2484. doi: 10.1523/JNEUROSCI.3040-07.2008

Pelkey, K. A., Chittajallu, R., Craig, M. T., Tricoire, L., Wester, J. C., and McBain, C. J. (2017). Hippocampal GABAergic inhibitory interneurons. *Physiol. Rev.* 97, 1619–1747. doi: 10.1152/physrev.00007.2017

Perera, T. D., Dwork, A. J., Keegan, K. A., Thirumangalakudi, L., Lipira, C. M., Joyce, N., et al. Necessity of hippocampal neurogenesis for the therapeutic action of antidepressants in adult nonhuman primates. *PLoS One* 6:e17600. doi: 10.1371/journal.pone.0017600

Richetin, K., Moulis, M., Millet, A., Arràzola, M. S., Andraini, T., Hua, J., et al. (2017). Amplifying mitochondrial function rescues adult neurogenesis in a mouse model of Alzheimer's disease. *Neurobiol. Dis.* 102, 113–124. doi: 10.1016/j.nbd.2017.03.002

Sahay, A., Scobie, K. N., Hill, A. S., et al. (2011). Increasing adult hippocampal neurogenesis is sufficient to improve pattern separation. *Nature.* 472:466–470. doi: 10.1038/nature09817

Samuels, B. A., and Hen, R. (2011). Neurogenesis and affective disorders. *Eur. J. Neurosci.* 33, 1152–1159. doi: 10.1111/j.1460-9568.2011.07614.x

Santarelli, L., Saxe, M., Gross, C., Surget, A., Battaglia, F., Dulawa, S., et al. (2003). Requirement of hippocampal neurogenesis for the behavioral effects of antidepressants. *Science* 301, 805–809. doi: 10.1126/science.1083328

Schmidt-Hieber, C., Jonas, P., and Bischofberger, J. (2004). Enhanced synaptic plasticity in newly generated granule cells of the adult hippocampus. *Nature.* 429:184–187. doi: 10.1038/nature02553

Schoenfeld, T. J., and Cameron, H. A. (2015). Adult neurogenesis and mental illness. *Neuropsychopharmacology* 40, 113–128. doi: 10.1038/npp.2014.230

Sierra, A., Encinas, J. M., Deudero, J. J. P., Chancey, J. H., Enikolopov, G., Overstreet-Wadiche, L. S., et al. (2010). Microglia shape adult hippocampal neurogenesis through apoptosis-coupled phagocytosis. *Cell Stem Cell* 7, 483–495. doi: 10.1016/j.stem.2010.08.014

Sorrells, S. F., Paredes, M. F., Cebrian-Silla, A., Sandoval, K., Qi, D., Kelley, K. W., et al. (2018). Human hippocampal neurogenesis drops sharply in children to undetectable levels in adults. *Nature* 555, 377–381. doi: 10.1038/nature25975

Spalding, K. L., Bergmann, O., Alkass, K., Bernard, S., Salehpour, M., Huttner, H. B., et al. (2013). Dynamics of hippocampal neurogenesis in adult humans. *Cell* 153, 1219–1227. doi: 10.1016/j.cell.2013.05.002

Tartt, A. N., Mariani, M. B., Hen, R., Mann, J. J., and Boldrini, M. (2022). Dysregulation of adult hippocampal neuroplasticity in major depression: pathogenesis and therapeutic implications. *Mol. Psychiatry* 27, 2689–2699. doi: 10.1038/s41380-022-01520-y

Terreros-Roncal, J., Moreno-Jiménez, E. P., Flor-García, M., Rodríguez-Moreno, C. B., Trinchero, M. F., Cafini, F., et al. (2021). Impact of neurodegenerative diseases on human adult hippocampal neurogenesis. *Science* 374, 1106–1113. doi: 10.1126/science.abl5163

Tobin, M. K., Musaraca, K., Disouky, A., Shetti, A., Bheri, A., Honer, W. G., et al. (2019). Human hippocampal neurogenesis persists in aged adults and Alzheimer's disease patients. *Cell Stem Cell* 24, 974–982.e3. doi: 10.1016/j.stem.2019.05.003

Toda, T., Parylak, S. L., Linker, S. B., and Gage, F. H. (2019). The role of adult hippocampal neurogenesis in brain health and disease. *Mol. Psychiatry* 24, 67–87. doi: 10.1038/s41380-018-0036-2

Torres-López, C., Cuartero, M. I., García-Culebras, A., de la Parra, J., Fernández-Valle, M. E., Benito, M., et al. (2023). Ipsilesional hippocampal GABA is elevated and correlates with cognitive impairment and maladaptive neurogenesis after cortical stroke in mice. *Stroke* 54, 2652–2665. doi: 10.1161/STROKEAHA.123.043516

Vauzour, D., Camprubi-Robles, M., Miquel-Kergoat, S., Andres-Lacueva, C., Bánáti, D., Barberger-Gateau, P., et al. (2017). Nutrition for the ageing brain: towards evidence for an optimal diet. *Ageing Res. Rev.* 35, 222–240. doi: 10.1016/j.arr.2016.09.010

Wu, H., Li, Y., Tong, L., Wang, Y., and Sun, Z. (2021). Worldwide research tendency and hotspots on hip fracture: a 20-year bibliometric analysis. *Arch. Osteoporos.* 16:73. doi: 10.1007/s11657-021-00929-2

Yeung, A. W. K., Tzvetkov, N. T., Balacheva, A. A., Georgieva, M. G., Gan, R. Y., Jozwik, A., et al. (2020). Lignans: quantitative analysis of the research literature. *Front. Pharmacol.* 11:37. doi: 10.3389/fphar.2020.00037

Zainuddin, M. S., and Thuret, S. (2012). Nutrition, adult hippocampal neurogenesis and mental health. *Br. Med. Bull.* 103, 89–114. doi: 10.1093/bmb/lds021

Zhang, R., Quan, H., Wang, Y., and Luo, F. (2023). Neurogenesis in primates versus rodents and the value of non-human primate models. *Natl. Sci. Rev.* 10:nwad248. doi: 10.1093/nsr/nwad248

Zhao, C., Deng, W., and Gage, F. H. (2008). Mechanisms and functional implications of adult neurogenesis. *Cell.* 132:645–660. doi: 10.1016/j.cell.2008.01.033

frontiers | Frontiers in Pharmacology

TYPE Original Research
PUBLISHED 27 August 2024
DOI 10.3389/fphar.2024.1458046

OPEN ACCESS

EDITED BY
Weijie Xie,
Tongji University, China

REVIEWED BY
Honghao Wang,
Guangzhou First People's Hospital, China
Jinzhou Feng,
First Affiliated Hospital of Chongqing Medical University, China

*CORRESPONDENCE
Sheng Chen,
mztcs@163.com
Xiang Zhang,
zhangxiang1213@hotmail.com
Meiyu Geng,
mygeng@simm.ac.cn
Yong Hao,
yhao23@126.com

†These authors have contributed equally to this work

RECEIVED 01 July 2024
ACCEPTED 12 August 2024
PUBLISHED 27 August 2024

CITATION
Zhou Q, Xie Z, He L, Sun G, Meng H, Luo Z, Feng Y, Chu X, Li L, Zhang J, Hao Y, Geng M, Zhang X and Chen S (2024) Multi-omics profiling reveals peripheral blood biomarkers of multiple sclerosis: implications for diagnosis and stratification.
Front. Pharmacol. 15:1458046.
doi: 10.3389/fphar.2024.1458046

Multi-omics profiling reveals peripheral blood biomarkers of multiple sclerosis: implications for diagnosis and stratification

Qinming Zhou [1,2,3†], Zuoquan Xie [4†], Lu He [1,3†], Guangqiang Sun[5], Huanyu Meng[1,3], Zhiyu Luo[5], Yuan Feng[5], Xingkun Chu[5], Liang Li[5], Jing Zhang[5], Yong Hao [6*], Meiyu Geng [4,7*], Xiang Zhang[8,9*] and Sheng Chen [1,2,3*]

[1]Department of Neurology and Institute of Neurology, Ruijin Hospital, Shanghai Jiao Tong University School of Medicine, Shanghai, China, [2]Co-innovation Center of Neuroregeneration, Nantong University, Nantong, China, [3]Clinical Center for Rare Diseases, Ruijin Hospital, Shanghai Jiao Tong University School of Medicine, Shanghai, China, [4]State Key Laboratory of Drug Research, Shanghai Institute of Materia Medica, Chinese Academy of Sciences, Shanghai, China, [5]Shanghai Green Valley Pharmaceutical Co., Ltd, Shanghai, China, [6]Departement of Neurology, Renji Hospital, Shanghai Jiao Tong University School of Medicine, Shanghai, China, [7]Shandong Laboratory of Yantai Drug Discovery, Bohai Rim Advanced Research Institute for Drug Discovery, Yantai, Shandong, China, [8]Department of Neurology, Huashan Hospital Fudan University and Institute of Neurology, Fudan University, Shanghai, China, [9]National Center for Neurological Disorders, Shanghai, China

Background: Multiple sclerosis (MS), a chronic autoimmune disorder marked by demyelination in the central nervous system, is exceptionally uncommon in China, and remains poorly understood in terms of its peripheral blood manifestations.

Methods: We conducted a cohort study comprising 39 MS patients and 40 normal controls (NC). High-dimensional mass cytometry, protein arrays, and targeted metabolomics were utilized to profile immune subsets, proteins, and metabolites in blood. Differences in multi-omics signatures were scrutinized across varying MS subtypes.

Results: Immune profiling demonstrated an elevation in various B cell subsets and monocytes, alongside a reduction in dendritic cells among MS patients. Proteomic data revealed a downregulation in neurotrophic and tissue repair proteins. Metabolomic assessment showed a noted decrease in anti-inflammatory molecules and sphingolipids. Integrated analysis identified distinct molecular patterns distinguishing MS from controls. Additionally, multi-omics differences among different MS subtypes were uncovered. Notably, hippuric acid levels was consistently lower in MS subgroups with greater disease severity.

Conclusion: This study represents the pioneering exploration of multi-omics in Chinese MS patients, presenting a comprehensive view of the peripheral blood changes in MS. Our study underscores the robust capability of multi-omics

10.3389/fphar.2024.1458046

assessments in identifying peripheral blood biomarkers that delineate the varied clinical presentation, and facilitates future development of biomarkers and targeted therapeutic interventions in MS.

KEYWORDS

multiple sclerosis, multi-omics, blood immune phenotyping, proteomic, metabolomic, clinically isolated syndrome, secondary progressive MS

1 Introduction

Multiple sclerosis (MS) stands as a persistent autoimmune affliction of the central nervous system, persisting without an established etiology. Within China, MS is considered a relatively uncommon condition, with the age- and sex-adjusted incidence of 0.235 per 100,000 person-years (Tian et al., 2020; Zhou et al., 2022). MS is characterized by a wide range of clinical presentations and an erratic progression, complicating the establishment of therapeutic strategies and prognostic assessments. Although significant strides have been made in molecular research, the exact processes that drive the advancement of MS are still not fully understood. Although there

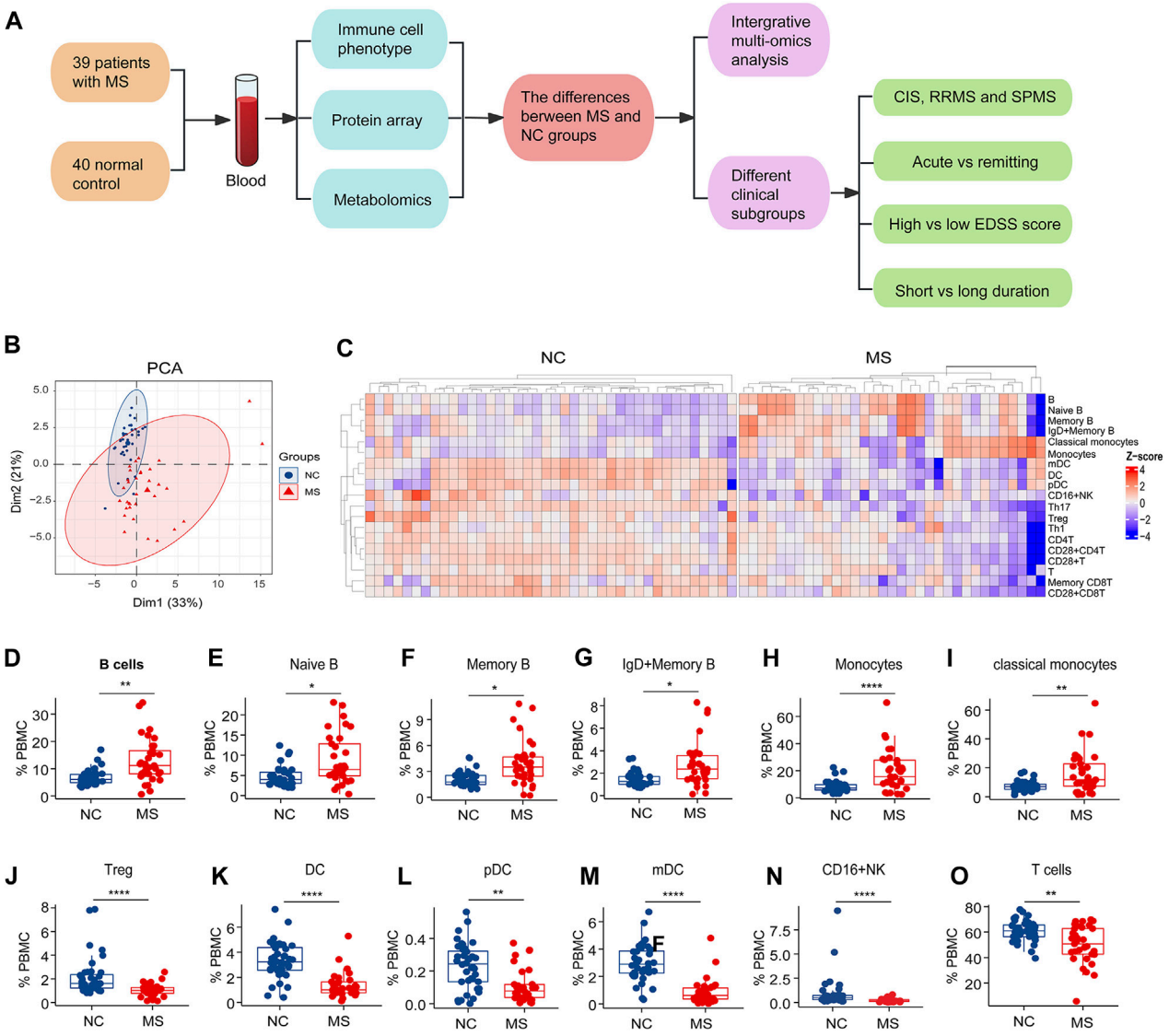

FIGURE 1
The study design and changes of blood immune subsets in MS. **(A)** The study flowchart. **(B)** PCA analysis of immune cells subsets between NC and MS. **(C)** Heatmap of differential expressed immune cell subsets ($p < 0.05$) in two groups (NC and MS). **(D–O)** Box plot of significantly differential immune cell subsets in MS compared to NC. *$P < 0.05$, **$P < 0.01$, ***$P < 0.001$, ****$P < 0.0001$, using Wilcox test.

have been some indicators to monitor disease progression, a definitive clinical indicator is yet to be developed (Zhang et al., 2021; Zhou et al., 2022). This heterogeneity in clinical manifestations hinders both the prediction of disease outcomes and the formulation of treatment plans.

In the realm of medical practice, most MS cases initially manifest as clinically isolated syndrome (CIS), where symptoms suggestive of MS arise but a conclusive diagnosis often remains elusive (Koubiyr et al., 2020). While relapsing-remitting MS (RRMS) represents the most frequent clinical subtype of MS, the lack of effective control over relapses can result in patients advancing to secondary progressive MS (SPMS), for which treatments are notably scarce (Du et al., 2023). Nevertheless, clear-cut distinctions among CIS, RRMS, and SPMS have yet to be definitively delineated.

Over the past 10 years, "omics" methodologies have emerged as a powerful means for quantifying differentially expressed molecular entities. Their integration into MS research is anticipated to deepen our comprehension of the disease. To date, most omics investigations into MS have concentrated on cerebrospinal fluid (CSF) studies (Bhargava and Calabresi, 2016; Lorefice et al., 2023). While CSF may offer greater tissue specificity, obtaining a sample requires a lumbar puncture, which is uncomfortable and invasive. Moreover, prior researches into MS omics have primarily leveraged single omics methods, lacking an integrated understanding of the complex attributes of the disease (Singh et al., 2019c; Reinke et al., 2014). Plasma presents a compelling alternative due to its more accessible sampling and considerable promise in the identification of biomarkers that encapsulate the global expression profile from multiple tissues and cell types.

In this study, we presented the pioneering exploration of multi-omics in Chinese patients with MS (Figure 1A). We employed a multi-omics framework, analyzing immune cell phenotypes, and levels of proteins and metabolites in peripheral blood samples from MS patients and normal controls (NC). And integrative analysis was used to identify peripheral signatures discriminate MS from NC. Comparative analyses were used differing MS clinical subtypes to identify markers reflective of disease activity and progression. The identified biomarkers bear potential for improving diagnostic accuracy, framing prognosis, and informing therapeutic approaches for individuals afflicted with MS.

2 Materials and methods

2.1 Participants

A cohort of 39 MS patients and 40 NC were recruited from Ruijin Hospital and Huashan Hospital, Shanghai, China. The study was approved by the Ethics Committee of Ruijin Hospital and Huashan Hospital and conducted in accordance with the principles of the Helsinki Declaration. All participants provided written informed consent.

All the MS patient fulfilled the international consensus diagnostic criteria for MS (Thompson et al., 2018). CIS is defined as a monophasic clinical episode characterized by patient-reported symptoms and objective findings that reflect a focal or multifocal inflammatory demyelinating event in CNS. This event develops acutely or subacutely, lasting for a minimum of 24 h, with or without recovery, and occurs in the absence of fever or infection. It is comparable to a typical multiple sclerosis relapse but occurs in a patient not known to have multiple sclerosis. In addition, all enrolled patients with CIS tested negative for oligoclonal bands. SPMS has a progressive course following an initial relapsing-remitting course (Oh et al., 2019). The progressive course is characterized by steadily increasing objectively documented neurological disability independent of relapses. The exclusion criteria were: 1) cardiovascular and/or metabolic diseases; 2) psychiatric disorders and/or neurologic disease other than MS; 3) body mass index (weight/height^2) higher than 30; or 4) pregnancy.

2.2 Mass cytometry analysis of blood immune cells

Blood samples were collected from both MS patients and NC individuals in K2 EDTA tubes provided by BD (Part #366643). Post-centrifugation at 350 *g* for a duration of 10 min, the plasma obtained from the upper fraction was stored at −80°C for later analysis. The cell fraction at the bottom underwent lysis of red blood cells for 10 min at ambient temperature. These cells were subsequently rinsed twice with phosphate-buffered saline (PBS) and labeled using the Human Immune Monitoring Panel Kit from Fluidigm (Catalogue #201324). Initial staining with Cisplatin from Fluidigm (Catalogue #201064) was conducted at a concentration of 0.1 μM, followed by surface marker staining for 4 min. Fc receptors were blocked by a 10-min incubation with Cell Staining Buffer at room temperature. A blend of surface antibodies was introduced to the cells for half an hour while kept on ice. The cells were then washed using the staining buffer and fixed using paraformaldehyde (1.6% solution, Thermo Fisher, Catalogue #28908) for 10 min at ambient temperature. Cells were resuspended in Ir-Interchelator solution from Fluidigm (Catalogue #201192B) within Fix/Perm buffer (Fluidigm, Catalogue #201067) and incubated overnight within a temperature range of 2°C–8°C. Subsequently, cells were resuspended in the Fluidigm Cell Acquisition Solution (Catalogue #201237) amended with EQ Four Element Calibration beads at a 1:10 ratio (Fluidigm, Catalogue #201078) and passed through a 35 μm nylon mesh filtration cap (Corning, No. #352235). Acquisition of the cells was performed on a Helios Mass Cytometer (Fluidigm) at a collection rate of 200–300 events per second. Data from the mass cytometry were then transferred and processed using the Cytobank analysis platform, employing CD45highCD66-gating to remove granulocytes from the analysis.

2.3 Human Cytokine Antibody Array analysis

Protein detection in the plasma samples was performed by RayBiotech (Guangzhou, China), utilizing the Quantibody® Human Cytokine Antibody Array 440 kit (RayBiotech, Inc., Catalog # QAH-CAA-440). The protocol was conducted in accordance with the guidelines provided by the manufacturer. Concisely, slide wells were prepped by adding 100 μL of sample diluent to each and allowing a 30-min incubation at ambient temperature to block non-specific binding sites. Subsequently, 100 μL of either the plasma samples or standard proteins were dispensed into the wells and permitted to incubate for 2 h at room temperature. The wells were then subjected to a series of

washes—five times with Wash Buffer I and twice with Wash Buffer II, using 150 μL of each buffer for 5 min per wash, all at room temperature. Following the washes, each well received 80 μL of a detection antibody cocktail for a 2-h incubation at room temperature. Post-washing, wells were incubated with 80 μL of Cy3-equivalent dye labeled streptavidin for 1 h at room temperature. Following a final wash, the signal was captured via a laser scanning device.

2.4 MxP® Quant 500 kit metabolite measurements

Targeted metabolomic profiling was conducted utilizing the MxP® Quant 500 kit by BIOCRATES Life Sciences AG, Innsbruck, Austria, in conjunction with an advanced ultra-performance liquid chromatography/tandem mass spectrometry (UPLC-MS/MS) system comprising an ExionLC UPLC (Sciex) coupled with a QTRAP 6500+ triple quadrupole/linear ion trap MS/MS (Sciex) (Xie et al., 2024). This integrated system enables the quantitative and/or semiquantitative assessment of up to 630 endogenous and microbiota-related metabolites. Aligned with regulatory benchmarks set forth by the United States Food and Drug Administration (FDA) and the European Medicines Agency (EMA) for bioanalytical method validation, the MxP® Quant 500 kit is specifically tailored and verified for use in human plasma analysis, incorporating internal and calibration standards to guarantee accurate quantification and consistent reproducibility within the analytical results.

2.5 Statistical analysis

To prepare the data for subsequent analysis, we excluded blood-borne immune cells, plasma cytokines, and metabolites with ≥30% missing values, followed by K-nearest neighbor (KNN) imputation of missing values.

The samples were from two cohorts: NC and MS. PCA (principal component analysis) is an unconstrained ordination method for dimension reduction. PCA could determinate PCs (principal component) which explain the most variance for data. Therefore, PCA projects high dimensional data on 2-dimensional scatterplot which enable the assessment of sample grouping. We used Wilcox to assess the associations of blood-borne immune cells, plasma, and cytokines with MS. We selected differential features based on Benjamini Hochberg adjusted *p*-values, with *p*-values <0.05 considered statistically significant. Heatmap was used to visualize the differential features profiles with ComplexHeatmap R package. Bar plots were made to visualize the change of differential features between MS and NC, CIS, RRMS and SPMS, acute phase and remitting phase, EDSS-H and EDSS-L, T2 and T1 by ggpubr R package.

2.6 Integrative multi-omics analysis

To identify important signatures that highly correlated among multi-omics and potentially discriminative for MS and NC, we performed Data Integration Analysis for Biomarker discovery using Latent Component (DIABLO) on omics data of the immune cells, the plasma proteins and metabolites (LC-MS). DIABLO is based on PLS-DA and aims to integrate multi-omics data by maximizing covariance between all pairs of datasets (Singh et al., 2019a). Prior to DIABLO, multi-omics data was log transformed. As discrimination is prioritized, the design matrix was set to 0.1. DIABLO performed 10 times repeat of 10-fold cross validation by block.splsda and tune.block.splsda functions in mixomics, to tune successively model hyperparameters for a final model which minimize classification error rate.

The first 2 components from the final model are considered and demonstrated in scatterplot using plotIndiv function for samples and plotVar function for features. Clustering of samples by group (NC/MS) and features by omics dataset was assessed. The mixomics package also provides loadingplot function and cim function to reveal important features (selected by DIABLO) for each omics dataset and combined in a heatmap, respectively. Heatmap that computed by cim function added a dendrogram with hierarchical clustering (Euclidean distance and complete linkage). The model performance was visualized by ROC curve calculated by auroc function also in mixomics. Only the importance features selected in component 1 of each omics dataset were assessed. DIABLO circles plot displayed the relationships between multiple sets of variables (correlation cut-off: r = 0.5) from component 1 and 2 that measured across the samples, which is useful in understanding how different types of biological data interact or correlate with each other.

3 Results

3.1 Characteristics of participants

The study enrolled 40 normal controls (NC group, 13 males and 27 females) and 39 MS patients (MS group, 11 males and 28 females). The average age for NC and MS groups was 35.3 ± 14.2 and 35.0 ± 14.5 years, respectively. Based on disease progression, the MS patients were further categorized into CIS (n = 14), RRMS (n =17), and SPMS (n = 8) groups. Within the MS group, a total of 33 patients were subjected to a blood immune cell subset analysis, 28 patients had their plasma protein levels assessed, and 30 patients underwent a plasma metabolomics profile analysis. The MS group had an average EDSS score of 2.0 ± 1.2, with an average disease duration of 22.8 ± 24.4 months (Supplementary Table S1).

3.2 Alterations of blood immune cell subsets in MS

To meticulously detail the variations in blood immune cell subclasses associated with MS, our study employed mass spectrometry to quantify 27 distinct immune cell subtypes (Supplementary Figure S1A). PCA revealed distinctive patterns of blood immune subsets in MS compared to the NC group (Figure 1B). We subsequently performed a comparative analysis of immune cell subtypes between the MS and NC cohorts.

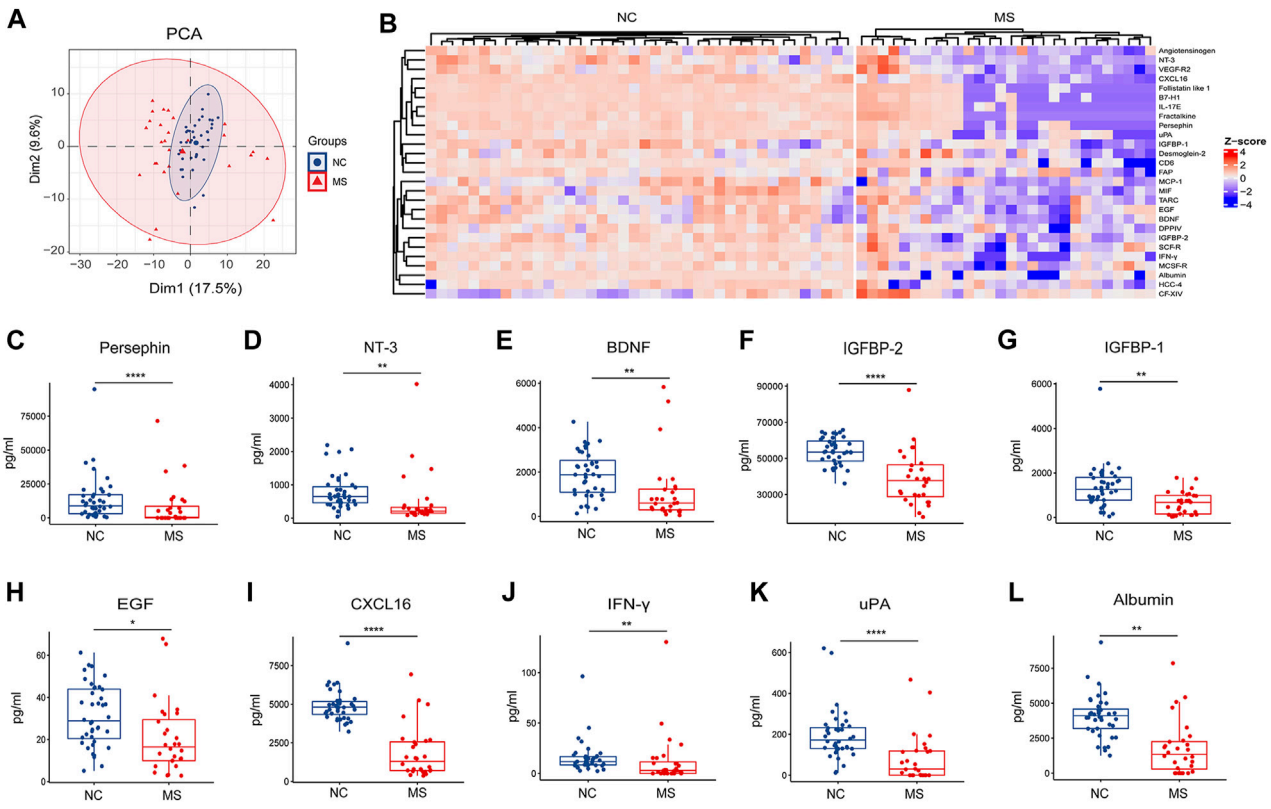

FIGURE 2
Changes of plasma proteins in MS. **(A)** PCA analysis of proteins between NC and MS. **(B)** Heatmap of differential proteins ($p < 0.05$) in two groups (NC and MS). **(C–L)** Box plot of significantly differential expressed plasma proteins in MS compared to NC. *$P < 0.05$, **$P < 0.01$, ***$P < 0.001$, ****$P < 0.0001$, using Wilcox test.

Notably, both the general B cell population and specific subsets—naïve B cells, memory B cells, as well as IgD + memory B cells—alongside monocytes and classical monocytes, were found in increased numbers in the MS group relative to the NC group (Figures 1C–I).

Conversely, our analysis revealed a significant decrease in the levels of regulatory T cells (Tregs), dendritic cells (DCs), specifically both plasmacytoid DCs (pDCs) and myeloid DCs (mDCs), as well as $CD16^+$ natural killer (NK) cells, T cells, and various T cell subsets, including $CD4^+$ T cells, Th1, Th17, memory $CD8^+$ T cells, $CD28^+$ T cells, $CD28^+$ $CD4^+$ T cells, and $CD28^+$ $CD8^+$ T cells, within the MS group when compared to NC (Figures 1J–O; Supplementary Figures S1B–H).

3.3 Alterations of plasma proteins in MS

We initiated a protein array analysis targeting the expression levels of 440 plasma proteins. PCA analysis showed that the plasma protein expression patterns in MS were similar to those observed in the NC group (Figure 2A). Subsequent differential analysis revealed a broad spectrum of plasma proteins that were changed in MS (Figure 2B).

Notably, our findings demonstrate a significant reduction in the expression of neurotrophic factors within the MS group, specifically persephin, neurotrophin-3 (NT-3), and brain-derived neurotrophic factor (BDNF) (Figures 2C–E). In addition, there was a discernible decrease in the levels of insulin-like growth factor-binding protein 2 (IGFBP-2), insulin-like growth factor-binding protein 1 (IGFBP-1), and epidermal growth factor (EGF) in the MS group (Figures 2F–H). Some molecules linked with immune surveillance [C-X-C motif chemokine 16 (CXCL16) and interferon-gamma (IFN-γ)], urokinase-type plasminogen activator (uPA) and albumin were also found to be reduced in MS (Figures 2I–L).

3.4 Alterations of plasma metabolites in MS

Targeted metabolomics assessed the presence of 630 plasma metabolites to delineate differences between the MS and NC groups. We employed liquid chromatography-mass spectrometry (LC-MS) for the detection of small molecular metabolites and flow injection analysis (FIA) for large molecular lipids. The distinct profiles between MS and NC were observed in the PCA plots generated from LC-MS data (Figure 3A).

Comparative analysis of the small molecular metabolites uncovered numerous metabolites that were significantly altered in MS, (Figure 3B; Supplementary Figure S2A). Notably, the most dramatic declines for the MS group were observed for dehydroepiandrosterone sulfate (DHEAS), 3-methylhistidine (3-Met-His), trans-4-hydroxyproline (t4-OH-Pro), arginine (Arg), tryptophan (Trp), and cortisol (Figure 3C). In contrast, the most pronounced increases were found in lactate (Lac), ornithine (Orn), hypoxanthine, choline, aspartic acid (Asp), and glutamic acid (Glu) within the MS cohort (Figure 3D).

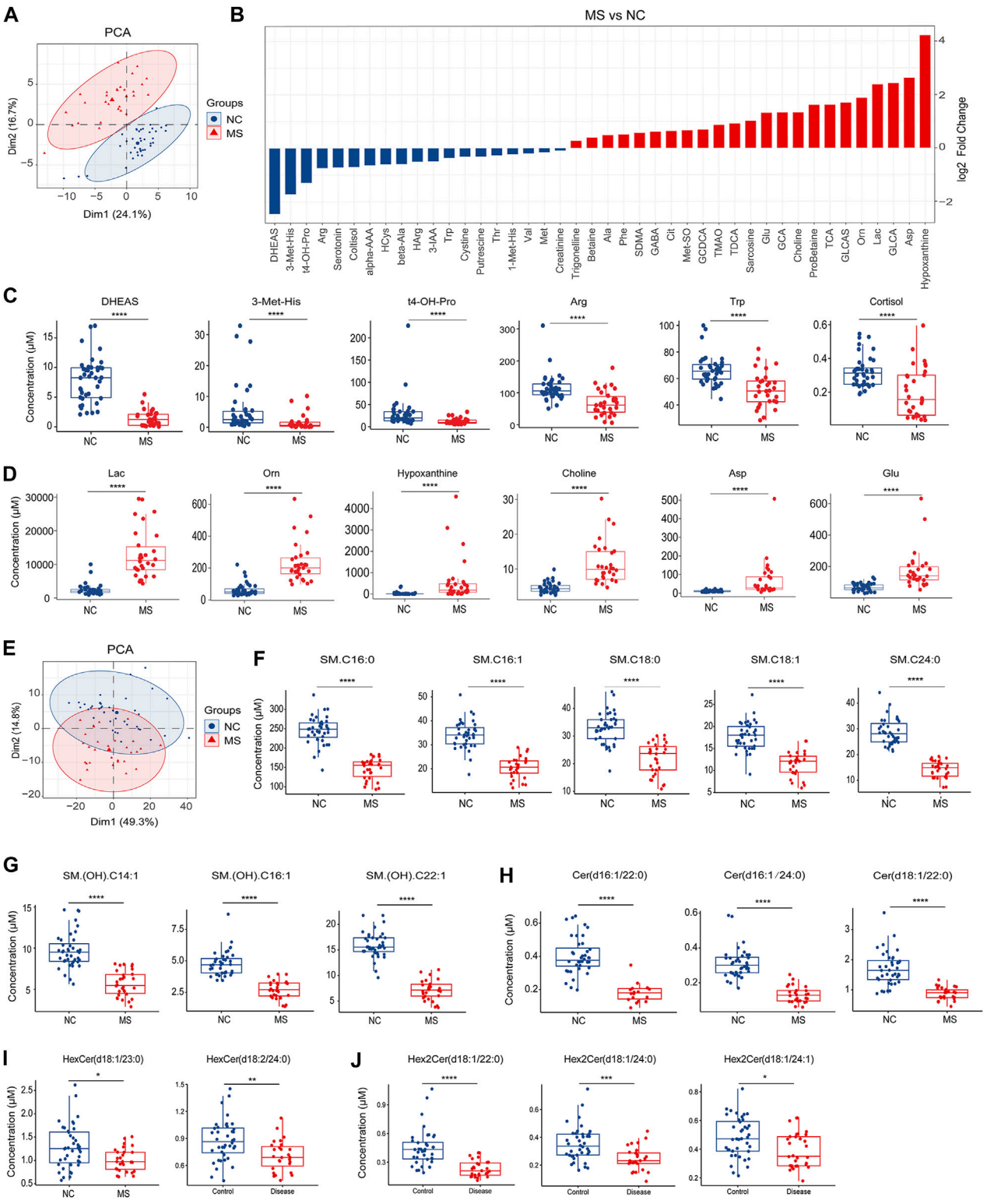

FIGURE 3
Changes of plasma metabolites in MS. **(A)** PCA analysis of plasma small molecular metabolites (LC-MS) in MS compared to NC. **(B)** Bar plot of significantly differential metabolites between NC and MS, $P < 0.05$. **(C)** Box plot of significantly decreased plasma metabolites in MS compared to NC. **(D)** Box plot of significantly increased plasma metabolites in MS compared to NC. **(E)** PCA analysis of plasma lipids (FIA) in MS compared to NC. **(F–J)** Box plot of significantly decreased plasma sphingolipids in MS compared to NC. *$P < 0.05$, **$P < 0.01$, ***$P < 0.001$, ****$P < 0.0001$, using Wilcox test.

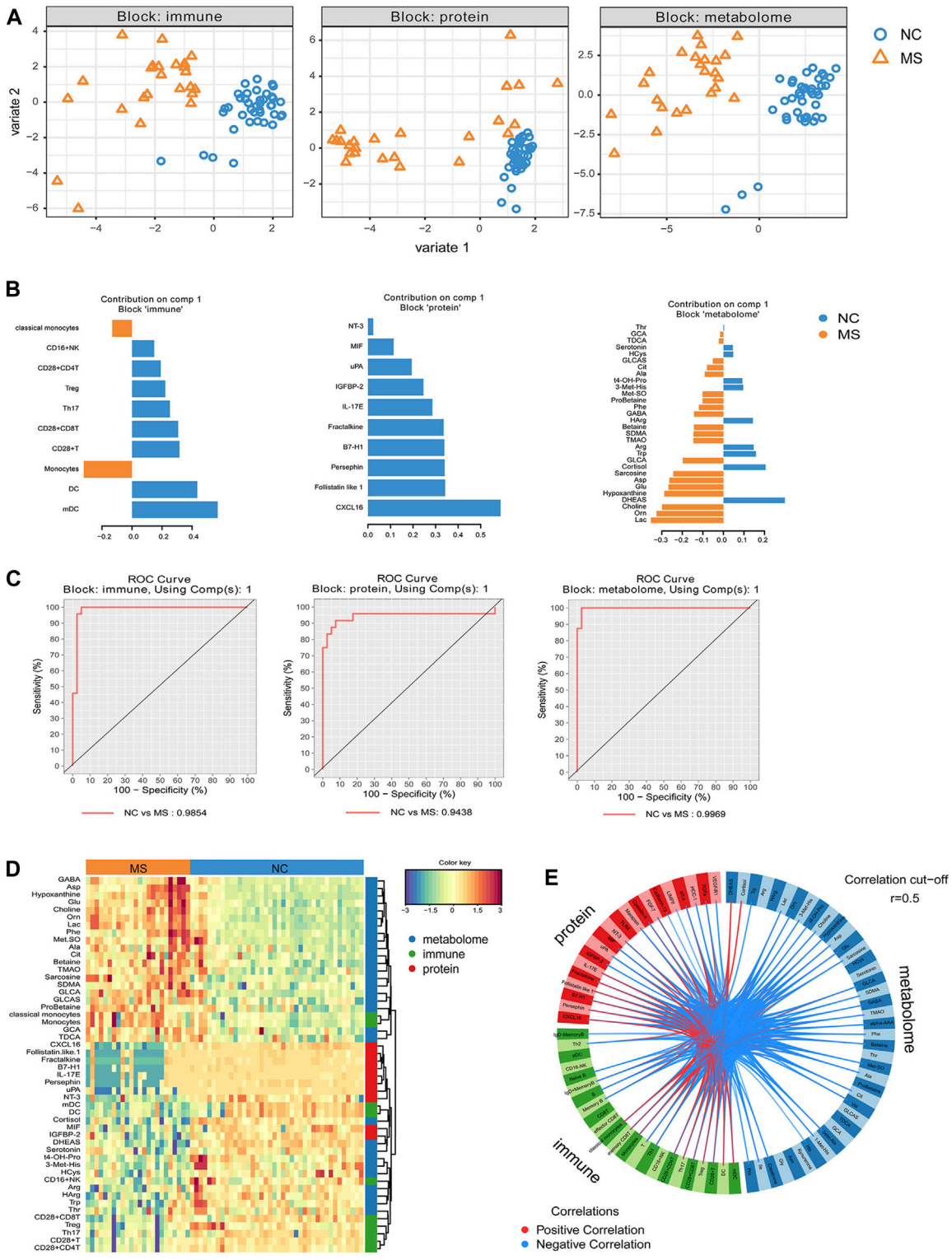

FIGURE 4
Integrative analysis revealed discriminative features between MS and NC. The highly correlated multi-omics signatures that discriminate NC and MS were identified from supervised model using DIABLO. **(A)** The scatterplot of samples using PlotIndiv on first 2 component for each block (immune cell subsets, proteins, small molecular metabolites). **(B)** Loading plot of component 1 from supervised model for each block, important signatures obtained from DIABLO were ordered by absolute importance (x-axis), colors indicated the class for which the median expression value is the highest for each feature. **(C)** ROC curve based on component 1 of each block (omics). ROC prediction models based on 70% of the samples and using 30% of the samples for prediction. **(D)** Heatmap of features selected by DIABLO. Dendrograms of features show the hierarchical relationship of the selected features based on Euclidean distance and complete linkage clustering. Samples on the x-axis are grouped by diagnosis (NC and MS). **(E)** DIABLO circle plot. Correlations between each feature from components 1 and 2 are plotted as a circle plot, and features with correlations above 0.5 (absolute value) were selected.

Regarding lipid metabolites, MS and NC groups were distinguishable as evidenced by the PCA plots (Figure 3E). Subsequent differential analysis between the MS and NC cohorts unmasked a multitude of lipid alterations (Supplementary Figure S2B). Crucially, our analysis underscored a pronounced reduction in sphingolipids within the MS group, including sphingomyelins (Figures 3F, G; Supplementary Figures S3A, B), ceramides (Figure 3H; Supplementary Figures S3C), hexosylceramides (Figure 3I), and dihexosylceramides (Figure 3J). Besides, we also identified a significant array of alterations in other lipid classes such as phosphatidylcholines (PCs), triglycerides (TGs), and cholesterol esters (CEs) (Supplementary Table S2).

3.5 Integrative features for discriminating MS from NC

We conducted a DIABLO approach to identify a highly interrelated multi-omics signature that effectively differentiates MS from NC. Each aspect—immune subsets, proteins, and metabolites—displayed distinct profiles between MS and NC (Figure 4A). The immunity-related discrepancies consisted of augmented proportions of monocytes and classical monocytes in MS, in contrast to the higher proportions of DCs, myeloid dendritic cells (mDCs), and $CD28^+$ T cells in NC. Within the proteomic landscape, NC demonstrated higher levels of CXCL16, follistatin-like 1, and persephin amongst other proteins; whilst metabolically, MS was characterized by higher levels of Lac, Orn, and choline, alongside diminished levels of DHEAS, cortisol, and Trp (Figure 4B). Employing these distinguishing features, we developed receiver operating characteristic (ROC) prediction models by training on 70% of the sample population and validating on the remaining 30%. This analysis demonstrated robust differentiation between MS and NC, with computed area under the curve (AUC) values of 0.98 for immune cell subtypes, 0.94 for proteins, and 0.99 for metabolites (Figure 4C).

Furthermore, DIABLO analysis revealed a pronounced correlation among monocytes, classical monocytes, and multiple metabolites (e.g., glycocholic acid [GCA], taurodeoxycholic acid [TDCA], glycolithocholic acid [GLCA], glycolithocholic acid sulfate [GLCAS], probetaine, symmetric dimethylarginine [SDMA], etc.), which were predominantly present in the MS group. There was also a tight correlation and lower representation of CXCL16, follistatin-like 1, fractalkine, programmed cell death 1 ligand 1 (B7-H1), interleukin-17E (IL-17E), Persephin, and uPA in MS. Additionally, another community featuring mDC, DC, cortisol, macrophage migration inhibitory factor (MIF), IGFBP-2, DHEAS, and others was closely correlated and underrepresented in MS (Figure 4D). Circus plot analysis further visualized the highly correlated variables ($r > 0.5$), showcasing the interconnectedness of these variables (Figure 4E).

3.6 Differences in peripheral signatures between different clinical subgroups

We categorized MS patients into distinct clinical subgroups based on various clinical parameters, such as disease stage, severity, phase, and disease duration. Our subsequent analysis aimed to elucidate differences in peripheral biomarkers among these diverse clinical subgroups.

Firstly, we assessed variances among the clinical stages of CIS, RRMS, and SPMS. Our investigation into immune cell population differences among these subgroups yielded no significant variances. However, notable differences emerged in protein and metabolites levels (Figures 5A–J; Supplementary Figures S4A–T). Notably, pentraxin-3 displayed a considerable reduction in RRMS compared to CIS, while tumor necrosis factor-related apoptosis-inducing ligand 3 (TRAIL-R3), dickkopf-3 (DKK-3), follistatin-like 1, hippuric acid (HipAcid), Hex3Cer(d18:1/20:0), and PC.ae.C36:2 exhibited decreased levels in both RRMS and SPMS relative to CIS (Figures 5A–G). Tissue inhibitors of metalloproteinases 2 (TIMP-2) and (SM) (OH).C22:1 were lower in SPMS compared to CIS or RRMS (Figures 5H, I). The level of Hex2Cer(d18:1/14:0) was higher in SPMS relative to CIS and RRMS (Figure 5J).

Secondly, patients in the acute phase had a greater proportion of B cells and naïve B cells alongside lower levels of monocytes, classical and non-classical monocytes, and mDCs (Figure 6A). Concomitantly, the acute phase was associated with elevated concentrations of various proteins such as interleukin-17F (IL-17F), macrophage inflammatory protein-3 alpha (MIP3a), and follistatin-like 1 (Figure 6B). Additionally, analysis of the acute phase showed diminished levels of several bile acids [taurocholic acid (TCA), GCA, TDCA] relative to the remitting phase (Figure 6C).

Thirdly, we stratified patients according to the Expanded Disability Status Scale (EDSS). As compared to the EDSS-L group (EDSS<3), the EDSS-H group (EDSS ≥3) had an increased presence of IgD + memory B cells (Figure 6D), increased level of albumin and reduced levels of several proteins [lectin-like oxidized low-density lipoprotein receptor 1 (LOX-1), urokinase plasminogen activator receptor (uPAR), nerve growth factor receptor (NGF-R), etc.] (Figure 6E), the increased level of serotonin, and lower levels of several plasma metabolites (Asp, HipAcid, etc.) (Figure 6F).

Finally, MS patients were categorized based on disease duration into T1 (≤12 months) and T2 groups (>12 months). In comparison to T1 group, T2 group exhibited a higher ratio of $CD8^+$ T cells (Figure 6G), lower concentrations of several proteins (leptin, AFP, B7-H3, etc.), higher level of delta-like ligand 1 (DLL1) (Figure 6H), and reduced levels of HipAcid (Figure 6I).

In addition, our study discerned substantial differential expression profiles of various lipid classes, including phospholipids, triglycerides, diglycerides, and sphingolipids, across distinct clinical subgroups of MS patients (Supplementary Figures S5A–C).

4 Discussion

In our current research, we conducted a comparative analysis of peripheral blood immune subsets, proteomic profiles, and metabolomic data between MS patients and healthy controls. This comparison identified distinct peripheral biomarkers that differentiate MS patients from NC and to examine the interrelationships among these biomarkers, as well as the peripheral difference in different subgroups of MS based on clinical classification.

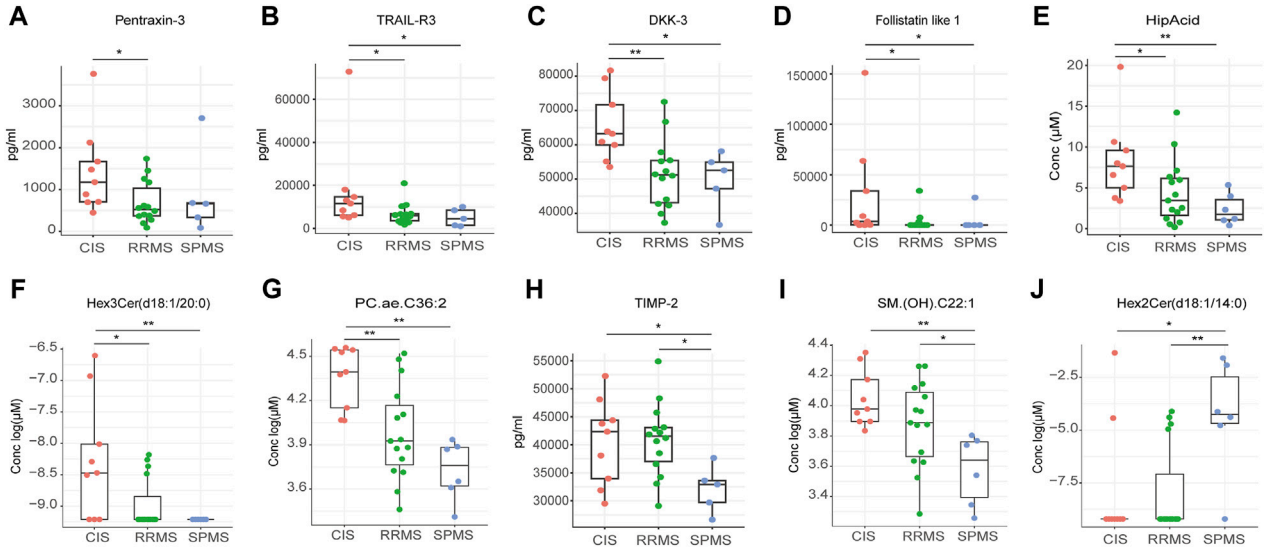

FIGURE 5
Differential peripheral features among CIS, RRMS, and SPMS. **(A–J)** Box plot showing the expression levels of proteins and metabolites among three groups. *$P < 0.05$, **$P < 0.01$, ***$P < 0.001$, ****$P < 0.0001$, using Kruskal-Wallis test.

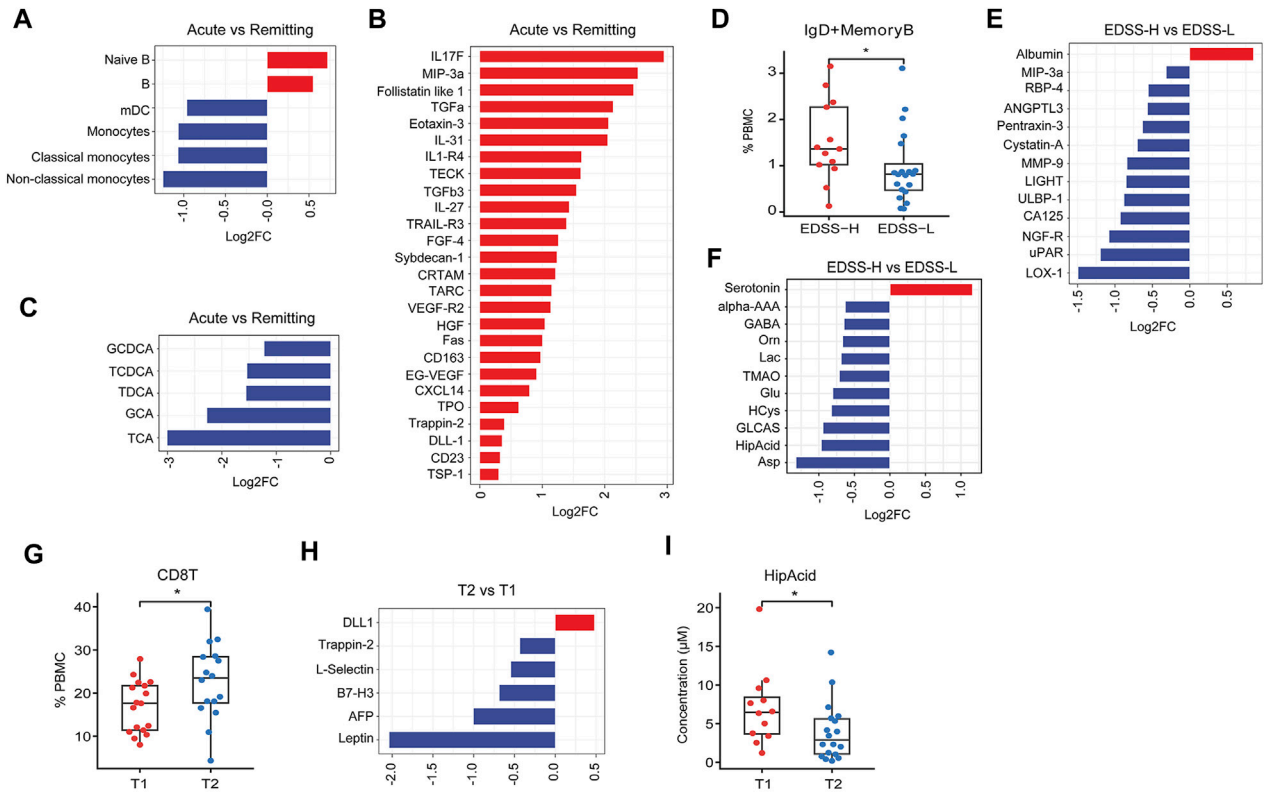

FIGURE 6
Difference in peripheral features between different clinical subgroups. **(A–C)** Bar plot of significantly differential expressed immune subset, proteins, metabolites ($P < 0.05$) between acute phase and remitting phase subgroups. **(D)** Box plot of IgD$^+$ memory B cells in EDSS-H and EDSS-L subgroups. **(E, F)** Bar plot of significantly differential expressed proteins and metabolites ($P < 0.05$) between EDSS-H and EDSS-L subgroups. **(G)** Box plot of CD8T cells in T1 and T2 subgroups. **(H)** Bar plot of significantly differential expressed proteins ($P < 0.05$) between T2 and T1 subgroups. **(I)** Box plot of HipAcid in T1 and T2 subgroups. *$P < 0.05$, **$P < 0.01$, using Wilcox test.

4.1 Multi-omics offered a comprehensive depiction of the alterations in peripheral blood

In this study, substantial variations were detected in peripheral blood immune cell populations. Particularly noteworthy were the elevated levels of B cell and monocyte subsets, crucial for antibody synthesis and the mediation of inflammatory responses. Concurrently, Tregs, known for their immunosuppressive functions, were found to be depleted in MS, underscoring the central role of immune dysregulation in the disease's pathogenesis. Additionally, a coordinated decline in DC and T cell subpopulations was identified in MS patients. These cell types are vital in immune surveillance, and their reduced numbers could increase the vulnerability to pathogens like viruses, which are potential etiological factors in MS(Tarlinton et al., 2020).

Proteomic analysis revealed the downregulation of several proteins associated with neural repair, including persephin, NT-3, BDNF, IGFBP-2, IGFBP-1, and EGF in MS patients. In the metabolomic profile, heightened levels of metabolites associated with inflammation or vascular injury, such as Lac, TMAO, choline, hypoxanthine, and cytotoxic bile acids, were noted. Concurrently, lower levels of anti-inflammatory metabolites such as DHEAS and cortisol (Rutkowski et al., 2014; Whitehouse, 2011) were observed. These findings collectively imply a role for peripheral inflammation and damage in the evolution of MS.

Interestingly, a significant decrease was observed in a few plasma sphingolipids in MS patients, including sphingomyelins, ceramides, and hexosylceramides. Since sphingolipids are key constituents of the myelin sheath and critical to CNS integrity and function, including cell growth, differentiation, and myelination (Hannun and Obeid, 2018; Leal et al., 2022; Dasgupta and Hogan, 2001), their decrement may influence remyelination processes. This result aligns with a prior study showing the decline of sphingolipids in the blood of MS patients (Momchilova et al., 2022). The underlying reasons for the decrease in these sphingolipids remain unclear; one possibility is increased clearance mediated by anti-sphingolipid antibodies. This hypothesis is in part supported by literature demonstrating elevated levels of antibodies against phosphatidylcholine in the serum of MS patients (Sádaba et al., 2020; Sánchez-Vera et al., 2023).

4.2 The distinctive features of peripheral blood changes across different clinical subtypes

To explore the difference in the pathogenesis among different clinical subtypes, we conducted comparisons of the immune subtypes, proteins, and metabolites. In the analysis comparing CIS, RRMS and SPMS, we found higher levels of TRAIL-R3, DKK-3, follistatin-like 1 in CIS than both RRMS and SPMS groups. TRAIL-R3 acts as a decoy receptor, mitigating apoptosis by sequestering the TRAIL ligand away from pro-apoptotic receptors (Jong et al., 2022), potentially aiding in cellular survival by hindering TRAIL-induced apoptotic pathways. DKK-3, a member of the Dickkopf protein family, regulates the Wnt signaling pathway, which influences cell fate determination, proliferation, and migration (Mourtada et al., 2023). Follistatin-like 1, known for its multifaceted role as a cytokine, exhibits a spectrum of functions from pro-inflammatory to anti-inflammatory actions (Mattiotti et al., 2018; Chaly et al., 2014). The observed decline in TRAIL-R3, DKK-3, and follistatin-like 1, HipAcid, Hex3Cer(d18:1/20:0) and PC.ae.C36:2 levels as MS progresses from CIS to RRMS or SPMS may hold implications for disease advancement.

In clinical practice, predicting the transition from RRMS to SPMS poses a significant challenge due to the absence of definitive biomarkers. Identifying early risk factors for SPMS development is crucial, as it allows for the timely initiation of effective treatment strategies aimed at mitigating disease progression. Our study revealed the significant reduction of TIMP-2 in SPMS patients compared to those with RRMS. TIMP-2, a member of the TIMP family, functions as an inhibitor of Matrix Metalloproteinase-2 (MMP-2). Previous studies showed that the presence of MMP-2 has been hypothesized to be linked to the chronic progressive phase of MS(Avolio et al., 2005; Fainardi et al., 2009). The interplay between TIMP-2 and MMP-2 is marked by TIMP-2's irreversible inactivation of MMP-2 through its binding to the enzyme's catalytic zinc cofactor. Moreover, Avolio et al. discovered that the serum MMP-2/TIMP-2 ratio was significantly higher in individuals with SPMS compared to those with RRMS(Avolio et al., 2003). This finding positions TIMP-2 as a promising candidate for a biomarker capable of distinguishing between SPMS and RRMS. Furthermore, the alterations observed in the levels of specific sphingolipids, such as Hex2Cer(d18:1/14:0) and SM. (OH).C22:1, in SPMS underscore the critical role these lipids may play in disease progression. The biological significance and repercussions of these specific variations are yet to be fully understood and thus represent a focal point for future research to clarify their impact on disease etiology and progression.

Furthermore, we investigated distinct characteristics across different levels of disability (EDSS-H vs EDSS-L), disease activity (acute vs remitting phase), and disease duration (T2 vs T1). Differential analysis between EDSS-H and EDSS-L groups revealed a higher abundance of IgD^+ memory B cells in the EDSS-H group, suggesting an association with disease severity. Notably, albumin levels were significantly higher in the EDSS-H group. In the context of MS, the upsurge of albumin in circulation could stimulate the expression of pro-inflammatory cytokines and impair astrocytic function (LeVine, 2016). Consistent with previous literatures (Niino et al., 2009; Duddy et al., 2007; DiSano et al., 2021), our findings highlighted the elevated presence of B cells and naïve B cells in MS patients during the acute phase compared to the remission phase, reinforcing the pivotal role of B cells in MS pathogenesis. In contrast, both mDCs and monocyte levels were lower during the acute phase relative to the remission phase, possibly reflecting a depletion of innate immune cells during the acute phase, coinciding with a consistent elevation of plasma cytokines, indicative of an acute inflammatory response. Additionally, a higher representation of $CD8^+$T cells was observed in patients with a more extended disease course, implying their involvement in long-term disease pathogenesis.

Our analysis revealed a noteworthy trend showing HipAcid levels to be consistently diminished in MS subgroups. The gradient observed when comparing CIS, RRMS, and SPMS, as well as among various subgroups (EDSS-H vs EDSS-L; acute vs. remitting; T2 vs T1), positions HipAcid as a compelling candidate biomarker for MS. HipAcid is a derivative of carboxylic acid produced in the liver through the enzymatic bonding of benzoic acid with glycine, and

subjects with physical frailty generally exhibit reduced plasma and urine levels of HipAcid (Ticinesi et al., 2023). The noted reduction in HipAcid concentrations could be attributed to the frailty of greater severity subgroups.

Taken together, the discovery of substances potentially associated with the progression of MS may offer valuable clues for future research into the mechanisms of disease progression. This could aid in better identifying MS patients prone to progression, enabling early intervention, and slowing the progression of disability.

4.3 The integration analysis revealed a strong correlation among various categories of biological molecules

DIABLO is a multivariate analytical technique that integrate diverse categories of "omics" data to identify biomarkers with consistent significance across various layers (Singh et al., 2019b). In the context of our study, the DIABLO method facilitated the discernment of a clear distinction between MS patients and NC, enabling us to identify key peripheral signatures. A range of critical biomarkers emerged as top signatures for discriminating MS from NC, including mDC, DC, monocytes, CXCL16, follistatin-like 1, persephin, Lac, Orn, and choline, among others. Importantly, the study unveiled variables that were highly intercorrelated across three distinct "omics" analyses. The comprehensiveness of the DIABLO approach allowed for the construction of an in-depth profile that not only distinguishes MS from NC but also elucidates the complex interrelationships inherent within each group, affording novel insights into their respective biological processes.

5 Limitation

Firstly, given the relatively low prevalence of MS, the sample size included in our study was limited, specifically for patients with CIS or SPMS. Secondly, the research methodology employed was of a retrospective and cross-sectional nature, which inherently presents certain limitations in capturing the full longitudinal trajectory of the disease. Thirdly, the exclusivity of our analysis to MS without juxtaposition against other neurological disorders may limit the specificity of our findings to this disease. Lastly, the selected patients had been subjected to a variety of treatments, including no treatment, corticosteroids, and various disease-modifying therapies, making it difficult to rule out the potential interference on the results of the study.

6 Conclusion

This was the first study of multi-omics in Chinese MS patients, to elucidate the multi-faceted molecular alterations in the peripheral blood of MS patients. The study further distinguished multi-omics signatures among different MS clinical subtypes. The findings provided a nuanced view of the disease's systemic impact, and underscored their relevance for pathogenetic studies, disease monitoring, and the early detection of progressive MS subtypes. Future work will focus on validating these findings in a larger cohort, and elucidating the mechanistic basis of these biomarkers with the goal of improving patient outcomes.

Data availability statement

The data analyzed in this study is subject to the following licenses/restrictions: The data that support the findings of this study are available from the corresponding author upon reasonable request. Requests to access these datasets should be directed to Sheng Chen, mztcs@163.com.

Ethics statement

The studies involving humans were approved by Ethics Committee of Ruijin Hospital and Ethics Committee of Huashan Hospital. The studies were conducted in accordance with the local legislation and institutional requirements. The participants provided their written informed consent to participate in this study.

Author contributions

QZ: Data curation, Formal Analysis, Investigation, Writing–original draft, Writing–review and editing. ZX: Data curation, Formal Analysis, Investigation, Writing–review and editing. LH: Data curation, Investigation, Writing–review and editing. GS: Data curation, Investigation, Methodology, Writing–review and editing. HM: Data curation, Investigation, Writing–review and editing. ZL: Data curation, Investigation, Methodology, Writing–review and editing. YF: Data curation, Investigation, Methodology, Writing–review and editing. XC: Data curation, Investigation, Methodology, Writing–review and editing. LL: Data curation, Investigation, Writing–review and editing, Methodology. JZ: Writing–review and editing, Data curation, Investigation. YH: Conceptualization, Project administration, Writing–review and editing. MG: Conceptualization, Project administration, Writing–review and editing, Funding acquisition. XZ: Conceptualization, Project administration, Writing–review and editing, Resources. SC: Conceptualization, Project administration, Supervision, Writing–review and editing.

Funding

The author(s) declare that financial support was received for the research, authorship, and/or publication of this article. This research was supported by the Natural Science Foundation of China for Innovation Research Group (No. 81821005), the Shanghai Municipal Science and Technology Major Project, the Lingang Laboratory (LG202101-01-01), the Medical-engineering cross fund of Shanghai Jiaotong University (YG2022QN009), the Shandong Laboratory Program (SYS202205), and the National Natural Science Foundation of China (82201558).

Acknowledgments

We thank all the study participants for their dedicated collaboration in this work, and the patients and their families who participated in this study.

Conflict of interest

Authors GS, ZL, YF, XC, LL, and JZ were employed by Shanghai Green Valley Pharmaceutical Co., Ltd.

The remaining authors declare that the research was conducted in the absence of any commercial or financial relationships that could be construed as a potential conflict of interest.

Publisher's note

Supplementary material

The Supplementary Material for this article can be found online at: https://www.frontiersin.org/articles/10.3389/fphar.2024.1458046/full#supplementary-material

References

Avolio, C., Filippi, M., Tortorella, C., Rocca, M. A., Ruggieri, M., Agosta, F., et al. (2005). Serum MMP-9/TIMP-1 and MMP-2/TIMP-2 ratios in multiple sclerosis: relationships with different magnetic resonance imaging measures of disease activity during IFN-beta-1a treatment. *Mult. Scler.* 11, 441–446. doi:10.1191/1352458505ms1193oa

Avolio, C., Ruggieri, M., Giuliani, F., Liuzzi, G. M., Leante, R., Riccio, P., et al. (2003). Serum MMP-2 and MMP-9 are elevated in different multiple sclerosis subtypes. *J. Neuroimmunol.* 136, 46–53. doi:10.1016/s0165-5728(03)00006-7

Bhargava, P., and Calabresi, P. A. (2016). Metabolomics in multiple sclerosis. *Mult. Scler.* 22, 451–460. doi:10.1177/1352458515622827

Chaly, Y., Hostager, B., Smith, S., and Hirsch, R. (2014). Follistatin-like protein 1 and its role in inflammation and inflammatory diseases. *Immunol. Res.* 59, 266–272. doi:10.1007/s12026-014-8526-z

Dasgupta, S., and Hogan, E. L. (2001). Chromatographic resolution and quantitative assay of CNS tissue sphingoids and sphingolipids. *J. Lipid Res.* 42, 301–308. doi:10.1016/s0022-2275(20)31692-8

Disano, K. D., Gilli, F., and Pachner, A. R. (2021). Memory B cells in multiple sclerosis: emerging players in disease pathogenesis. *Front. Immunol.* 12, 676686. doi:10.3389/fimmu.2021.676686

Duddy, M., Niino, M., Adatia, F., Hebert, S., Freedman, M., Atkins, H., et al. (2007). Distinct effector cytokine profiles of memory and naive human B cell subsets and implication in multiple sclerosis. *J. Immunol.* 178, 6092–6099. doi:10.4049/jimmunol.178.10.6092

DU, S., Yuan, C., Zhou, Q., Huang, X., Meng, H., Chen, M., et al. (2023). Deep learning-based PET/MR radiomics for the classification of annualized relapse rate in multiple sclerosis. *Mult. Scler. Relat. Disord.* 75, 104750. doi:10.1016/j.msard.2023.104750

Fainardi, E., Castellazzi, M., Tamborino, C., Trentini, A., Manfrinato, M. C., Baldi, E., et al. (2009). Potential relevance of cerebrospinal fluid and serum levels and intrathecal synthesis of active matrix metalloproteinase-2 (MMP-2) as markers of disease remission in patients with multiple sclerosis. *Mult. Scler.* 15, 547–554. doi:10.1177/1352458509102372

Hannun, Y. A., and Obeid, L. M. (2018). Sphingolipids and their metabolism in physiology and disease. *Nat. Rev. Mol. Cell Biol.* 19, 175–191. doi:10.1038/nrm.2017.107

Jong, K. X. J., Mohamed, E. H. M., and Ibrahim, Z. A. (2022). Escaping cell death via TRAIL decoy receptors: a systematic review of their roles and expressions in colorectal cancer. *Apoptosis* 27, 787–799. doi:10.1007/s10495-022-01774-5

Koubiyr, I., Deloire, M., Besson, P., Coup, P., Dulau, C., Pelletier, J., et al. (2020). Longitudinal study of functional brain network reorganization in clinically isolated syndrome. *Mult. Scler.* 26, 188–200. doi:10.1177/1352458518813108

Leal, A. F., Suarez, D. A., Echeverri-Pe A, O. Y., Albarrac N, S. L., Alm Ciga-D Az, C. J., and Espejo-Mojica Á, J. (2022). Sphingolipids and their role in health and disease in the central nervous system. *Adv. Biol. Regul.* 85, 100900. doi:10.1016/j.jbior.2022.100900

Levine, S. M. (2016). Albumin and multiple sclerosis. *BMC Neurol.* 16, 47. doi:10.1186/s12883-016-0564-9

Lorefice, L., Pitzalis, M., Murgia, F., Fenu, G., Atzori, L., and Cocco, E. (2023). Omics approaches to understanding the efficacy and safety of disease-modifying treatments in multiple sclerosis. *Front. Genet.* 14, 1076421. doi:10.3389/fgene.2023.1076421

Mattiotti, A., Prakash, S., Barnett, P., and van den Hoff, M. J. P. (2018). Follistatin-like 1 in development and human diseases. *Cell Mol. Life Sci.* 75 (13), 2339–2354. doi:10.1007/s00018-018-2805-0

Momchilova, A., Pankov, R., Alexandrov, A., Markovska, T., Pankov, S., Krastev, P., et al. (2022). Sphingolipid catabolism and glycerophospholipid levels are altered in erythrocytes and plasma from multiple sclerosis patients. *Int. J. Mol. Sci.* 23, 7592. doi:10.3390/ijms23147592

Mourtada, J., Thibaudeau, C., Wasylyk, B., and Jung, A. C. (2023). The multifaceted role of human dickkopf-3 (DKK-3) in development, immune modulation and cancer. *Cells* 13, 75. doi:10.3390/cells13010075

Niino, M., Hirotani, M., Miyazaki, Y., and Sasaki, H. (2009). Memory and naïve B-cell subsets in patients with multiple sclerosis. *Neurosci. Lett.* 464, 74–78. doi:10.1016/j.neulet.2009.08.010

Oh, J., Alikhani, K., Bruno, T., Devonshire, V., Giacomini, P. S., Giuliani, F., et al. (2019). Diagnosis and management of secondary-progressive multiple sclerosis: time for change. *Neurodegener. Dis. Manag.* 9, 301–317. doi:10.2217/nmt-2019-0024

Reinke, S. N., Broadhurst, D. L., Sykes, B. D., Baker, G. B., Catz, I., Warren, K. G., et al. (2014). Metabolomic profiling in multiple sclerosis: insights into biomarkers and pathogenesis. *Mult. Scler.* 20, 1396–1400. doi:10.1177/1352458513516528

Rutkowski, K., Sowa, P., Rutkowska-Talipska, J., Kuryliszyn-Moskal, A., and Rutkowski, R. (2014). Dehydroepiandrosterone (DHEA): hypes and hopes. *Drugs* 74, 1195–1207. doi:10.1007/s40265-014-0259-8

Sádaba, M. C., Rothhammer, V., Mu Oz, Ú., Sebal, C., Escudero, E., Kivis Kk, P., et al. (2020). Serum antibodies to phosphatidylcholine in MS. *Neurol. Neuroimmunol. Neuroinflamm* 7, e765. doi:10.1212/NXI.0000000000000765

Singh, A., Shannon, C. P., Gautier, B., Rohart, F., Vacher, M., Tebbutt, S. J., et al. (2019a). DIABLO: an integrative approach for identifying key molecular drivers from multi-omics assays. *Bioinformatics* 35, 3055–3062. doi:10.1093/bioinformatics/bty1054

Singh, A., Shannon, C. P., Gautier, B., Rohart, F., Vacher, M., Tebbutt, S. J., et al. (2019b). DIABLO: an integrative approach for identifying key molecular drivers from multi-omics assays. *Bioinformatics* 35, 3055–3062. doi:10.1093/bioinformatics/bty1054

Singh, V., Tripathi, A., and Dutta, R. (2019c). Proteomic approaches to decipher mechanisms underlying pathogenesis in multiple sclerosis patients. *Proteomics* 19, e1800335. doi:10.1002/pmic.201800335

Sánchez-Vera, I., Escudero, E., Mu Oz, Ú., and S Daba, M. C. (2023). IgM to phosphatidylcholine in multiple sclerosis patients: from the diagnosis to the treatment. *Ther. Adv. Neurol. Disord.* 16, 17562864231189919. doi:10.1177/17562864231189919

Tarlinton, R. E., Martynova, E., Rizvanov, A. A., Khaiboullina, S., and Verma, S. (2020). Role of viruses in the pathogenesis of multiple sclerosis. *Viruses* 12, 643. doi:10.3390/v12060643

Thompson, A. J., Banwell, B. L., Barkhof, F., Carroll, W. M., Coetzee, T., Comi, G., et al. (2018). Diagnosis of multiple sclerosis: 2017 revisions of the McDonald criteria. *Lancet Neurol.* 17, 162–173. doi:10.1016/S1474-4422(17)30470-2

Tian, D. C., Zhang, C., Yuan, M., Yang, X., Gu, H., Li, Z., et al. (2020). Incidence of multiple sclerosis in China: a nationwide hospital-based study. *Lancet Reg. Health West Pac* 1, 100010. doi:10.1016/j.lanwpc.2020.100010

Ticinesi, A., Guerra, A., Nouvenne, A., Meschi, T., and Maggi, S. (2023). Disentangling the complexity of nutrition, frailty and gut microbial pathways during aging: a focus on hippuric acid. *Nutrients* 15, 1138. doi:10.3390/nu15051138

Whitehouse, M. W. (2011). Anti-inflammatory glucocorticoid drugs: reflections after 60 years. *Inflammopharmacology* 19, 1–19. doi:10.1007/s10787-010-0056-2

Xie, Z., Huang, J., Sun, G., He, S., Luo, Z., Zhang, L., et al. (2024). Integrated multi-omics analysis reveals gut microbiota dysbiosis and systemic disturbance in major depressive disorder. *Psychiatry Res.* 334, 115804. doi:10.1016/j.psychres.2024.115804

Zhang, M., Ni, Y., Zhou, Q., He, L., Meng, H., Gao, Y., et al. (2021). (18)F-florbetapir PET/MRI for quantitatively monitoring myelin loss and recovery in patients with multiple sclerosis: a longitudinal study. *EClinicalMedicine* 37, 100982. doi:10.1016/j.eclinm.2021.100982

Zhou, Q., Zhang, T., Meng, H., Shen, D., Li, Y., He, L., et al. (2022). Characteristics of cerebral blood flow in an Eastern sample of multiple sclerosis patients: a potential quantitative imaging marker associated with disease severity. *Front. Immunol.* 13, 1025908. doi:10.3389/fimmu.2022.1025908

frontiers | Frontiers in Pharmacology

TYPE Original Research
PUBLISHED 28 August 2024
DOI 10.3389/fphar.2024.1450211

OPEN ACCESS

EDITED BY
Weijie Xie,
Tongji University, China

REVIEWED BY
Ning Jiang,
Chinese Academy of Medical Sciences and Peking Union Medical College, China
Ruijuan Guan,
First Affiliated Hospital of Guangzhou Medical University, China

*CORRESPONDENCE
Gao Xiuli,
gaoxl@gmc.edu.cn

RECEIVED 17 June 2024
ACCEPTED 12 August 2024
PUBLISHED 28 August 2024

CITATION
Chencen L, Shuo Z, Zhiyu C, Xiaoyu F, Min Z, Pengjiao W and Xiuli G (2024) (+)-catechin protects PC12 cells against CORT-induced oxidative stress and pyroptosis through the pathways of PI3K/AKT and Nrf2/HO-1/NF-κB. *Front. Pharmacol.* 15:1450211. doi: 10.3389/fphar.2024.1450211

(+)-catechin protects PC12 cells against CORT-induced oxidative stress and pyroptosis through the pathways of PI3K/AKT and Nrf2/HO-1/NF-κB

Lai Chencen[1,2,3], Zhang Shuo[1,4], Chen Zhiyu[1,2], Fu Xiaoyu[1,2], Zhang Min[1,2], Wang Pengjiao[1,2,5] and Gao Xiuli[1,2]*

[1]State Key Laboratory of Functions and Applications of Medicinal Plants and School of Pharmacy, Guizhou Medical University, Guiyang, China, [2]Center of Microbiology and Biochemical Pharmaceutical Engineering, Guizhou Medical University, Guiyang, China, [3]Department of Nosocomial Infection, The First Affiliated Hospital of Guizhou University of Traditional Chinese Medicine, Guiyang, China, [4]Experimental Animal Center of Guizhou Medical University, Guiyang, China, [5]Guizhou Provincial Engineering Research Center of Food Nutrition and Health, Guizhou Medical University, Guiyang, China

Pyroptosis induced by oxidative stress is a significant contributor to mental health disorders, including depression (+)-Catechin (CA), a polyphenolic compound prevalent in various food sources, has been substantiated by prior research to exhibit potent antioxidant properties and potential antidepressant effects. Nonetheless, the precise antidepressive mechanisms and effects of CA remain incompletely elucidated. In this study, we employed corticosterone (CORT) and PC12 cells to develop a cellular model of depression, aiming to investigate the protective effects of CA against CORT-induced cellular damage. Our objective was to elucidate the underlying mechanisms of protective action. We utilized transcriptomic analysis to identify differentially expressed genes and employed bioinformatics approaches to predict the potential mechanisms of CA's protective effects in PC12 cells. These transcriptomic predictions were subsequently validated through western blot analysis. The findings indicated that CA possesses the capacity to mitigate oxidative stress and suppress pyroptosis in PC12 cells via the activation of the PI3K/AKT signaling pathway. This activation subsequently modulates the Nrf2/HO1/NF-κB pathways, thereby providing protection to PC12 cells against damage induced by CORT. Furthermore, we investigated the interaction between CA and the Keap1 protein employing molecular docking and protein thermal shift assays. We propose that CA can activate Nrf2 through two mechanisms to decrease reactive oxygen species (ROS) levels and inhibit pyroptosis: one mechanism involves the activation of the PI3K/AKT signaling pathway, and the other involves direct binding to Keap1, leading to an increase in p-Nrf2.

KEYWORDS

(+)-catechin, oxidative stress, pyroptosis, PI3K/Akt signal pathway, Nrf2/HO-1/NF-κB signal pathway

Introduction

Depression, a prevalent mental illness with serious consequences, has become one of the most significant mental health disorders worldwide in the 21st century (Rehm and Shield, 2019). Current estimates indicate that approximately 10% of the global population is affected by depression (Rao et al., 2021). With the accelerating pace of modern life and the rise in stress levels, the number of individuals suffering from depression is projected to increase. Particularly following the outbreak of Coronavirus Disease 2019 (COVID-19), stressors such as economic pressure and restricted activities have further exacerbated the incidence of various mental illnesses, including depression (Zhu et al., 2024). Depression has now become the second leading cause of death after cancer and has been recognized by the WHO as one of the main causes of disability worldwide. Currently, the commonly used antidepressants are mainly tricyclic antidepressants and monoamine oxidase inhibitors, but in clinical practice, about one-third of patients do not benefit from these two types of drug treatments (Nikolin et al., 2022). Furthermore, the limitations of those antidepressants, such as extended treatment durations and severe side effects (Hao et al., 2021), highlight the need of discovering more effective and less harmful alternatives for treatment.

The etiology of depression is multifaceted, encompassing strong associations with stress, inflammation, immune function, neurotransmitter imbalances, and genetic predispositions (Wang et al., 2022; Wang et al., 2021; McGuffin and Rivera, 2015; Uzbekov and Maximova, 2015). Oxidative stress, arising from an imbalance between pro-oxidant and antioxidant processes within the body, is pivotal in the development of depression (Bhatt et al., 2020). Prolonged exposure to oxidative stress may result in an overabundance of reactive oxygen species (ROS) in cells, leading to neurotoxic effects (Liao et al., 2023). During the development of depression, excessive accumulation of ROS in the brain can impair the antioxidant defense system of nerve cells, alter and damage the permeability of the cell and organelle membranes, leading to intracellular lipid peroxidation and organelle damage (Qin et al., 2007; He et al., 2024). Moreover, evidence indicates that ROS act as a key activator of the NLRP3 inflammasome (Liu et al., 2023), and a connection between depression and pyroptosis mediated by the NLRP3 inflammasome was reported recently (Xia et al., 2023). Pyroptosis is a form of programmed cell death. Unlike apoptosis, pyroptosis results in a pro-inflammatory outcome. Pyroptosis is initiated by activation of the inflammasome, particularly NLRP3, which plays a key role in neuroinflammation. Upon activation, NLRP3 triggers Caspase-1, leading to the maturation of the inflammatory cytokine IL-1β and the executioner of pyroptosis, GSDMD (Xie et al., 2019). This process culminates in cell death and the production of various pro-inflammatory mediators. Notably, elevated oxidative stress and pro-inflammatory mediators are prominently observed in the brains of patients with depression. Therefore, reducing oxidative stress and pro-inflammatory mediators to protect neurons from damage may be crucial for the treatment of depression (Xia et al., 2023). Modulating the NLRP3 inflammasome to diminish pyroptosis is essential for effective depression management.

Nuclear factor-like 2 (Nrf2) functions as a transcription factor that mitigates oxidative damage by initiating a suite of antioxidant response pathways. The interaction between Keap1 and Nrf2, wherein Keap1 typically inhibits the Nrf2 activity, is a classical regulatory mechanism (Baird and Yamamoto, 2020). After dissociation from Keap1, Nrf2 translocates to the nucleus and enhances the expression of antioxidant genes containing antioxidant response elements (ARE), such as heme oxygenase-1 (HO-1) and superoxide dismutase (SOD), which aid in the elimination of ROS and play a key role in maintaining cellular redox balance (Satoh et al., 2006). Beyond the classical regulatory mechanisms, Nrf2 activity is also modulated through Keap1-independent regulation. Kinases such as c-Jun N-terminal Kinase (JNK), Protein Kinase C (PKC) and Extracellular Signal-regulated Kinases (ERK) can promote the phosphorylation and nuclear translocation of Nrf2 (Zuo et al., 2022). Numerous studies have demonstrated that enhancing the phosphorylation and nuclear translocation of Nrf2 can ameliorate the depressive models both *in vivo* and *in vitro* (Chou et al., 2023; Sun et al., 2022; Si et al., 2023). Thus, augmenting the phosphorylation and nuclear translocation of Nrf2 to activate the cell's intrinsic antioxidant system may represent a novel direction in the development of antidepressant drugs.

Catechins is a class of flavanol compounds characterized by multiple phenolic hydroxyl groups. These compounds are widely distributed in plants and are particularly abundant in certain fruits and edible plants such as cocoa, tea leaves, and raspberries. Catechins include a range of compounds such as (+)-catechin (CA), (−)-epicatechin (EC), (−)-epigallocatechin (EGC), (−)-epicatechingallate (ECG), and (−)-epigallocatechingallate (EGCG) (Bernatoniene and Kopustinskiene, 2018). Due to their potent antioxidant activity, catechins are recognized as important dietary supplements in countries including the United States, France, and Finland. (Wu et al., 2021). As one of the catechins, CA also exhibits significant antioxidant properties. The mechanism is likely similar to that of other catechins, involving the binding of free radicals through the phenolic hydroxyl groups present in its structure. This binding inhibits the chain reactions of free radicals and decreases lipid peroxidation within cells (Bernatoniene and Kopustinskiene, 2018). Known for its potent antioxidant properties, CA offers protective effects against various conditions, including liver and cardiac damage, DNA damage, and diabetes (Baranwal et al., 2022; Abd El-Aziz et al., 2012; Haza and Morales, 2011; Kobayashi et al., 2010). In terms of neuroprotection, CA has shown efficacy. A study by Margarita et al. demonstrated that CA, when combined with exercise, synergistically enhances neuroprotection in aging rats (Ramis et al., 2021). Heo et al. found that CA could mitigate Aβ-induced apoptosis (Heo and Lee, 2005). Additionally, studies have indicated that prolonged intake of CA can alleviate depressive behaviors induced by CORT in a rat model (Lee et al., 2013). However, this study primarily examines the mitigate effect of CA on the hypothalamic-pituitary-adrenal (HPA) axis and depressive-like behavior in rats, without elucidating the specific molecular mechanisms underlying CA's antidepressant action. Given the high lipid content in the brain and the low antioxidant capacity of neurons, it is hypothesized that the antioxidant properties of CA is closely related to its antidepressant effect. However, the precise molecular mechanisms that connect the antioxidative and antidepressive effects of CA have yet to be comprehensively elucidated. In this study, PC12 cells with neuronal characteristics will be employed, and a concentration of

400 μM CORT will be used to establish a cellular model of depression, based on existing literature, to investigate the potential antidepressant mechanisms of CA.

Materials and methods

Antibodies and reagents

(+)-Catechin (purity > 97%) was sourced from Macklin in China. Aladdin, also from China, supplied corticosterone. Affbiotech supplied primary antibodies for NF-κB p65, NF-κB p-p65 (Ser536) and synaptophysin, with GSDMD (Full length + N terminal), ASC and NLRP3 antibodies being provided by abclonal. Proteintech delivered antibodies specific to PSD95, keap1, IL-1β, and β-tubulin. Abmart supplied Anti-HO-1 and Nrf2. Huabiotech supplied cleaved-caspase1, p-Nrf2, AKT, p-AKT (S473), PI3K, p-PI3K and Lamin B1 antibodies. Zenbio supplied NQO1 antibody. To evaluate cell viability, the cell counting kit-8 was obtained from NCMbiotech in China. Beyotime provided the ROS detection kit, utilizing DCFH-DA for intracellular H_2O_2 and oxidative stress analysis. The FAM-FLICA Caspase Assay kit was bought from Immunochemistry Technologies.

Cell culture and treatment

The differentiated PC12 cell cultures were cultivated in DMEM supplemented with 10% FBS, and incubated in a 5% CO2 atmosphere at 37°C. Once the cells achieved approximately 80% confluence, they were transferred to 6-well plates for further culturing. After a serum-free overnight incubation, the cells underwent treatment with CA and 400 μM corticosterone for a period of 24 h.

Cell viability assay

PC12 cell viability was evaluated using the MTT as per the manufacturer's instructions. The cells were seeded at a concentration of 5,000 cells per well in 96-well dishes and grown in Dulbecco's Modified Eagle Medium (DMEM), with three wells per experimental group. After the treatment, 10 μL of the MTT solution were added to every well, followed by an incubation at 37°C for four more hours. Discard the supernatant and add 150 μL of DMSO to each well. Afterward, the level of light absorption was measured at a wavelength of 490 nm.

RNA sequencing

Set up three groups: the control group (con group), the corticosterone group (CORT group), and the CA group. The con group was incubated with serum-free DMEM medium, the CORT group with 400 μM corticosterone, and the CA group with both 200 μM CA and 400 μM CORT. After 24 h, PC12 cells were collected from each group (n = 3 for each group), and libraries were constructed and sequenced by Wuhan Maiwei Metabolic Biotechnology Co., Ltd. DESeq2 software was used to analyze differential gene expression, with criteria of p-value ≤ 0.05 and | Log2 Fold Change| ≥ 1. To conduct KEGG pathway analysis and Gene Ontology (GO) functional enrichment, visit the Metascape website at https://metascape.org.

ROS measurements

The levels of intracellular hydrogen peroxide and oxidative stress were evaluated using the DCFH-DA assay. PC12 cells were seeded at a density of 5 × 10^4 cells per well in 24-well plates and treated with either regular medium or 400 μM corticosterone for 24 h, with or without CA at 100 μM or 200 μM concentrations. Following this, the DCFH-DA assay was applied to measure changes in ROS levels, adhering to the guidelines provided by the supplier. Cells were exposed to DCFH-DA at 37°C for half an hour, then the dye was eliminated and the cells were washed two times with PBS at a pH of 7.4. Analysis was performed using a Leica fluorescence microscope from Germany and ImageJ software version 1.49 from the NIH in the United States.

Determination of SOD, LDH and MDA

MDA levels, SOD activity, and LDH content were assessed with assay kits from Nanjing Jiancheng Bioengineering Institute, in accordance with the manufacturer's instructions.

Molecular docking

Keap1's crystal structure was obtained from the RCSB Protein Data Bank website. Modifications, including the elimination and hydrogenation of ethanol and water molecules, as well as the refinement of amino acids, were performed using AutoDock 1.5.7. The 3D chemical structure of CA was obtained from PubChem, its energy was minimized, and the outcome was stored in MOL2 format. This structure was then imported into AutoDock 1.5.7, where all flexible bonds were set to rotate by default and the docking ligands were prepared in PDBQT format. Docking was executed with AutoDock Vina 1.1.2, and the results were visualized using PyMOL.

Cellular thermal shift assay

The Cell Thermal Shift Assay (CETSA) was utilized to evaluate the stability of the Keap1 protein following the previous protocol (Qin et al., 2022). PC12 cells were cultured in a dish with a density of 1 × 10^7 cells per dish. Cells were cultured in DMEM medium containing or lacking 200 μM CA for a period of 2 h. After the incubation period, the cells were collected, rinsed with PBS, and then suspended in 500 μL of PBS. The cells were then divided into seven aliquots. These samples were heated at temperatures ranging from 42°C to 54°C in increments of 2°C for 3 min each. Then, the samples experienced alternating rounds of being frozen in liquid nitrogen and then thawed in a water bath at 25°C, this process was done three times. After centrifuging each sample at 12,000 revolutions per

minute for 20 min, the liquid above the sediment was moved to a small tube made by Eppendorf. Subsequently, Western blot analysis was performed using a Keap1-specific antibody.

Extraction of proteins followed by analysis using Western blotting

Cellular proteins were extracted from each sample using a pre-heated buffer containing sodium dodecyl sulfate (SDS) (100 μL). The nuclear protein extraction kit (Solarbio, China) was employed to extract nuclear proteins from cells. 10 μL samples of cell lysates or nuclear were separated on 8%–10% SDS-polyacrylamide gels and then transferred to PVDF membranes from Millipore. The membranes were blocked using 5% nonfat milk in TBST buffer for 60 min at room temperature, then incubated with primary antibodies overnight at 4°C. After triple washing with TBST, the membranes were further incubated with suitable secondary antibodies (Bioprimacy, China) for 60 min at room temperature (The dilutions of antibodies used in the western blotting assay are listed in Table 1). Protein bands were identified utilizing an ECL system and recorded with an imaging device from Bio-Rad in the United States. The intensity of the bands was measured using ImageJ software, and the visualization of the data was done using GraphPad Prism 8. The presented data are pooled from a minimum of three separate experiments.

TABLE 1 Antibodies used in this study. Abbreviations used are as follows: r-rabbit, m-mouse, p-phosphorylated, WB-western blot.

Antibody	Host	WB Dilution	Secondary antibody dilution
PSD95	r	1:1500	1:8000
Synaptophysin	r	1:1000	1:8000
NLRP3	r	1:1000	1:8000
Caspase1 p10	r	1:500	1:8000
ASC	r	1:1000	1:8000
IL-1β	m	1:500	1:8000
GSDMD	r	1:1000	1:8000
Nrf2	r	1:2000	1:8000
p-Nrf2	r	1:1000	1:8000
HO-1	r	1:1000	1:8000
NQO1	r	1:1500	1:8000
NF-κB p65	r	1:2000	1:8000
NF-κB p-p65	r	1:1000	1:8000
Keap1	m	1:1500	1:8000
β-tubulin	m	1:8000	1:8000
Lamin B	r	1:4000	1:8000
β-actin	r	1:5000	1:8000

Flow cytometry assay

After treating with pancreatic enzymes, PC12 cells were collected and then centrifuged at 1000 g for 5 min. Post-centrifugation, the cells underwent a PBS rinse for two times before being resuspended. For the staining process, the FAM-FLICA Caspase Assay kit was employed. Initially, the cells were treated with a diluted Caspase-1 probe for approximately 30 min, which was then followed by a brief incubation with a diluted PI stain for 5 min. The cellular analysis was subsequently carried out on a flow cytometer to assess the staining outcomes. The total rate of pyroptosis is calculated as the percentage of activated Caspase1-positive cells.

Statistical analysis

For comparing two groups in the CCK-8 assay, a Welch's *t*-test was applied. Group comparisons were examined through one-way ANOVA, with subsequent analysis using the Least Significant Difference (LSD) test. Results are expressed as the mean ± SEM and are derived from three separate experimental trials. A significance level of $p < 0.05$ was taken into account for statistical analysis.

Results

CA protects PC12 cells against neurotoxicity induced by CORT

As shown in Figures 1A, B, the viability of PC12 cells significantly decreased at CA concentrations exceeding 600 μM. Additionally, CA at concentrations of 100 μM, 200 μM, and 300 μM enhance the viability of PC12 cells when exposed to 400 μM CORT. However, no significant differences were observed in the impact of 200 μM and 300 μM CA on cells exposed to CORT. Therefore, concentrations of 100 μM and 200 μM CA were chosen for further experiments.

CA mitigates CORT-induced synaptic impairment in PC12 cells

Figure 2A–C illustrate that CORT reduces the expression of PSD95 and synaptophysin proteins in PC12 cells after a 24-hour incubation. Conversely, co-treatment with 200 μM CA alongside CORT significantly mitigates this effect.

Mechanism prediction and experimental verification of CA protection against CORT-induced damage in PC12 cells

PC12 cells were subjected to three conditions: untreated, exposed to 400 μM CORT alone, and co-treated with 400 μM CORT and 200 μM CA for 24 h RNA-seq transcriptome analysis was then conducted. As shown in Figure 3A, CA reversed some of the differential gene expression induced by CORT. The CA group exhibited differential expression in 519 genes, with 237 genes upregulated and 282 genes downregulated, compared to the

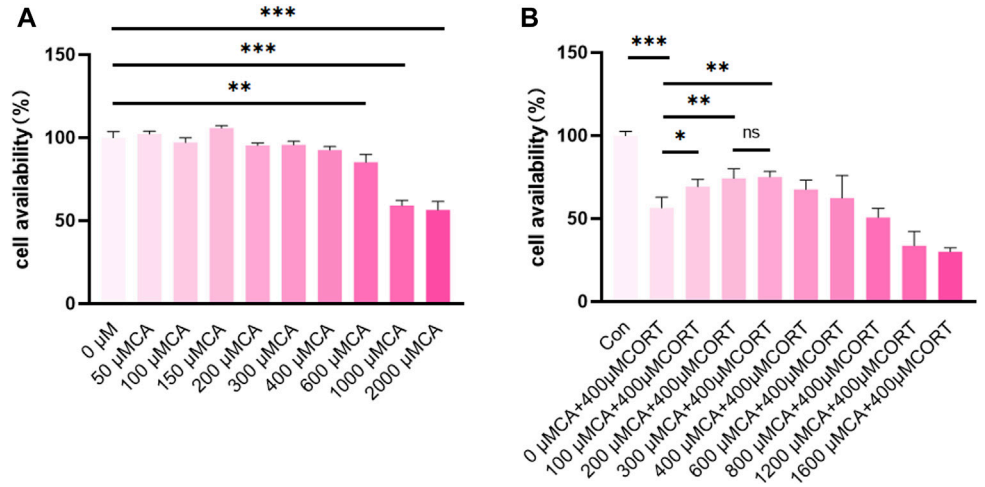

FIGURE 1
CA protects PC12 cells from CORT-induced neurotoxicity. **(A, B)** cell availability; Significant difference *$p < 0.05$, **$p < 0.01$,***$p < 0.001$. Data are mean ± SEM (n = 3).

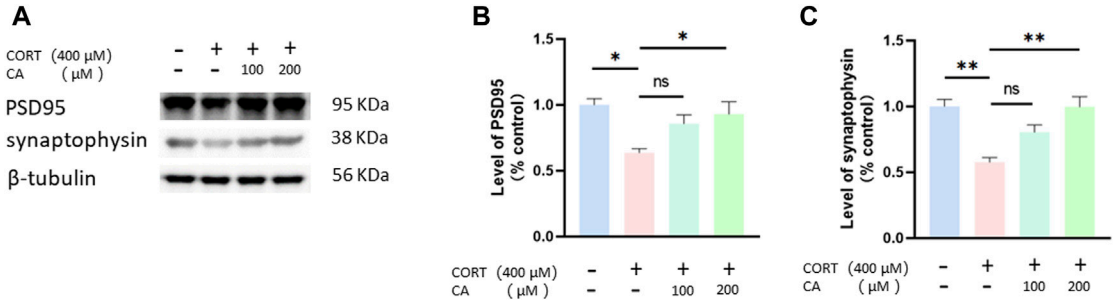

FIGURE 2
CA increases PSD95 and synaptophysin protein in PC12 cells. **(A)** Representative blot. **(B, C)** semiquantitative analysis of PSD95 and synaptophysin. Significant difference *$p < 0.05$, **$p < 0.01$, *ns = not significant*. Data are mean ± SEM (n = 3).

CORT group (Figure 3B). Analysis of enriched GO terms and KEGG pathways in genes differentially expressed between the 200 μM CA group and the CORT group indicates that CA plays a potential role in protecting cells from ROS-induced damage in neurological disorders. This protection occurs mainly through the modulation of energy metabolism-related biological processes and cellular components, and the PI3K/AKT signaling pathway. (Figures 3C, D). The results suggest that CA may protect cells from CORT-induced damage by activating the PI3K/AKT pathway and reducing oxidative stress.

CA alleviates CORT-induced damage in PC12 cells by reducing the generation of ROS and MDA, while also enhancing SOD activity

Figure 4A, B illustrate that the presence of 100 μM and 200 μM CA significantly decreases ROS production in PC12 cells. Intracellular levels of MDA and SOD activity exhibited distinct responses to treatment (Figures 4C, D). Specifically, MDA levels increased and SOD activity decreased after incubation with 400 μM CORT. In contrast, treatment with 200 μM CA ameliorated these effects. Consequently, CA reduces CORT-induced damage in PC12 cells, resulting in decreased LDH release, as depicted in Figure 4E.

CA reduced CORT-induced pyroptosis in PC12 cells

Previous research indicates that CORT can increase ROS generation, thus inducing pyroptosis in nerve cells. To investigate whether CA could protect PC12 cells from CORT-induced pyroptosis, we employed a flow cytometry assay. As illustrated in Figure 5, incubation with CORT alone resulted in a total pyroptosis rate exceeding 12% in PC12 cells. Co-incubation with 100 μM and 200 μM CA significantly alleviated this effect. We consequently examined the changes in pyroptosis-associated proteins in PC12 cells using western blotting assay. Figure 6 illustrates a

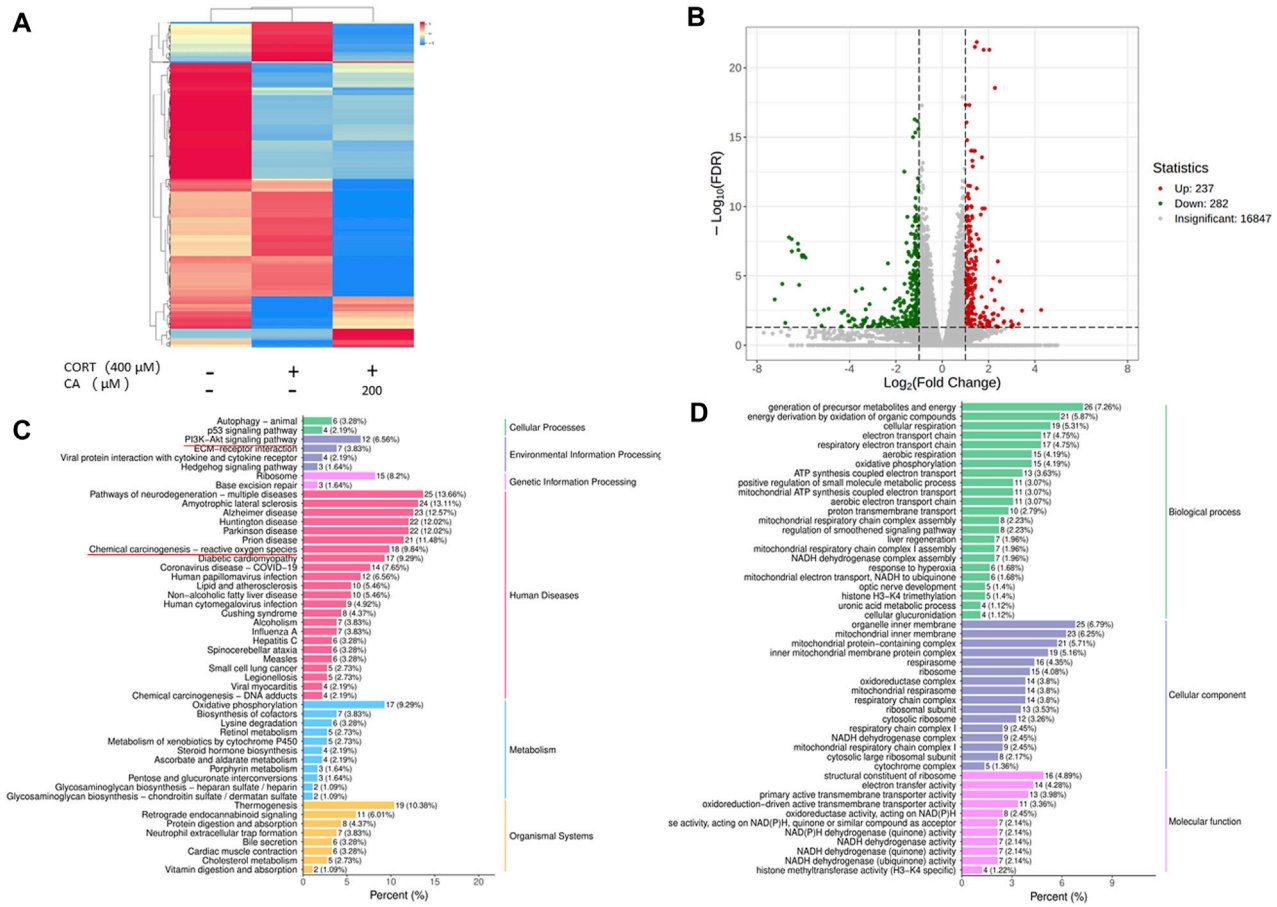

FIGURE 3
Mechanism prediction of CA protection against CORT-induced damage in PC12 cells by transcriptomics. **(A)** Hitmap of differential gene expression. **(B)** Volcano plot analysis (CORT vs.200 μM CA). **(C)** KEGG enrichment analyses of differential genes (CORT vs.200 μM CA). **(D)** GO enrichment analyses of differential genes (CORT vs.200 μM CA).

notable increase in the levels of NLRP3, ASC, cleaved-caspase1, IL-1β, and cleaved-GSDMD following CORT treatment, while CA mitigates this impact.

CA activates CORT-induced inhibition of the PI3K/AKT signal pathway

To empirically confirm the transcriptomic findings, we conducted Western blot assays to assess the PI3K/AKT pathway in PC12 cells. Figure 7 illustrates that treatment with 200 μM CA markedly elevated p-PI3K and p-AKT levels, which were diminished in the CORT-exposed group. Based on these results, we suggest that 200 μM CA may reactivate the PI3K/AKT signal pathway, previously inhibited by CORT, potentially offering a protective benefit.

CA stimulates the Nrf2/ho-1/NF-κB pathway in PC12 cells

To further elucidate how CA protects PC12 cells from CORT-induced effects, we employed Western blotting assay. As depicted in Figures 8, 9, CORT significantly decreases the levels of HO-1, NQO1 and p-Nrf2 and Nrf2 in the nucleus (Nrf2 (N)), while simultaneously increasing the level of phosphorylated NF-κB p-p65. Conversely, the levels of overall Nrf2 and NF-κB remains unchanged. The test showed that 200 μM CA significantly boosted the levels of p-Nrf2, Ho-1 and NQO1, while reducing the levels of NF-κB p-p65 compared to the control groups.

CA can bind to Keap1 protein, as revealed by molecular docking and CETSA

As shown in Figure 10A, CA binds to the Keap1 protein with a binding energy of −9.8 kJ/mol, indicates a strong binding affinity. In the PC12-based CETSA, we assessed the thermal stability of Keap1 using a specific Keap1 antibody. The results indicated that the thermal denaturation profile of Keap1 became significantly more stable upon incubation with CA (Figures 10B, C).

Discussion

It is widely acknowledged that prolonged exposure to stress can lead to depression. When a stressor is detected, the HPA axis

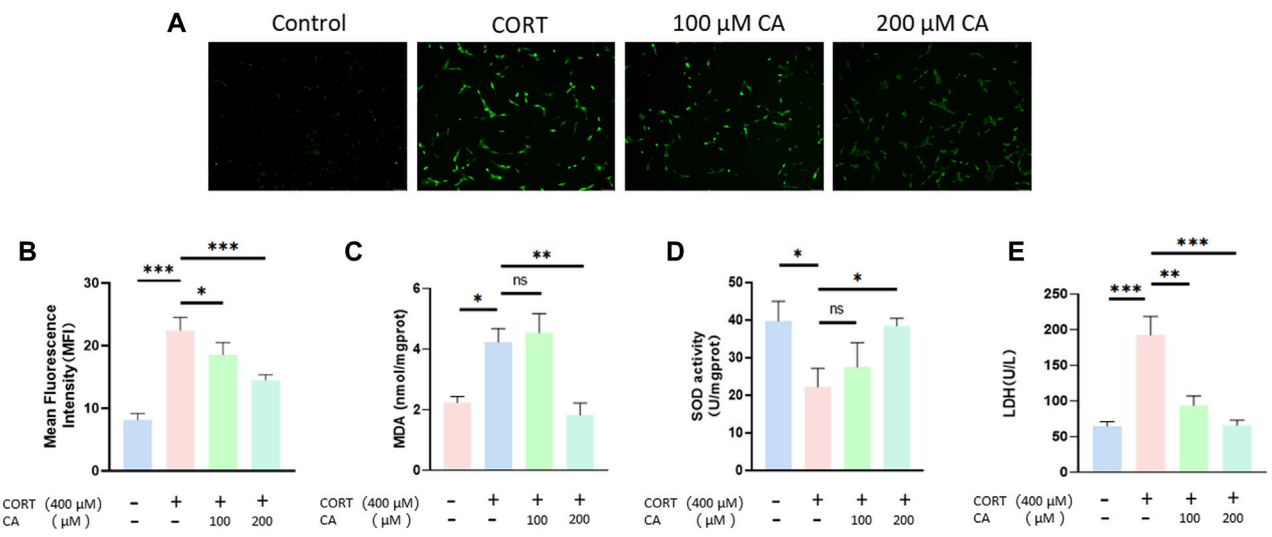

FIGURE 4
Effect of CA on oxygen species (ROS) production, extracellular LDH, intracellular MDA levels and SOD activity in PC12 cells. **(A)** Representative fluorescence images of ROS production in PC12 cells. **(B)** Intracellular ROS level of PC12 cells. **(C)** Intracellular MDA levels of PC12 cells **(D)** Intracellular SOD activity in PC12 cells. **(E)** Extracellular LDH levels of PC12 cells. Significant difference *$p < 0.05$, **$p < 0.01$,***$p < 0.001$. Data are mean ± SEM (n = 3).

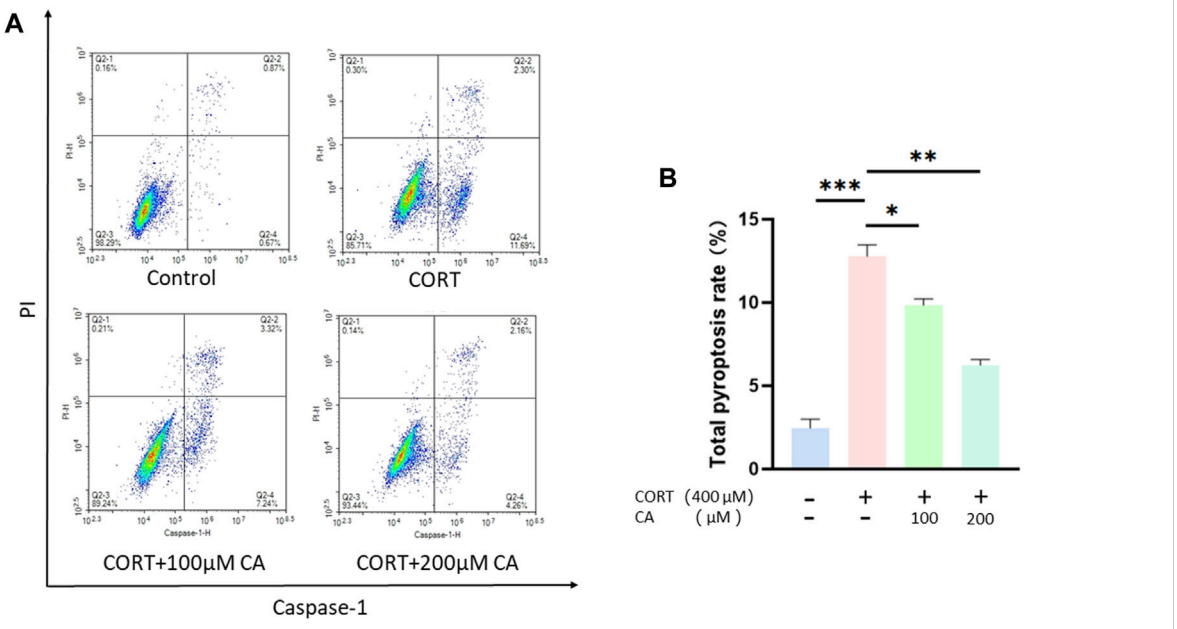

FIGURE 5
CA reduce pyroptosis rate in PC12 cells. **(A)** Representative images of flow cytometry. **(B)** Pyroptosis rate in PC12 cells. Significant difference *$p < 0.05$, **$p < 0.01$,***$p < 0.001$. Data are mean ± SEM (n = 3).

becomes more excitable, leading to the release of glucocorticoids from the adrenal glands (Muscari et al., 2022). Among these, cortisol,a glucocorticoid, is found at abnormally high levels in both the plasma and brain tissue of individuals suffering from depression (Blanco and Conant, 2021). Previous *in vitro* studies have demonstrated that cortisol can inflict harm on PC12 cells, establishing the cortisol-induced PC12 cell model as a widely accepted *in vitro* representation of depressive conditions (He et al., 2023). In this research, we uses PC12 cells and 400 μM CORT to simulate a cellular model of depression following previous study (Zhou et al., 2017). Our cell viability assays revealed that CA at concentrations below 400 μM do not adversely impact the survival of PC12 cells. Furthermore, when PC12 cells are co-treated with varying concentrations of CA alongside a fixed 400 μM concentration of CORT, compared to 0 μM of CA, we observed enhanced cell viability at the 100 μM, 200 μM, and 300 μM levels of CA. Interestingly, the

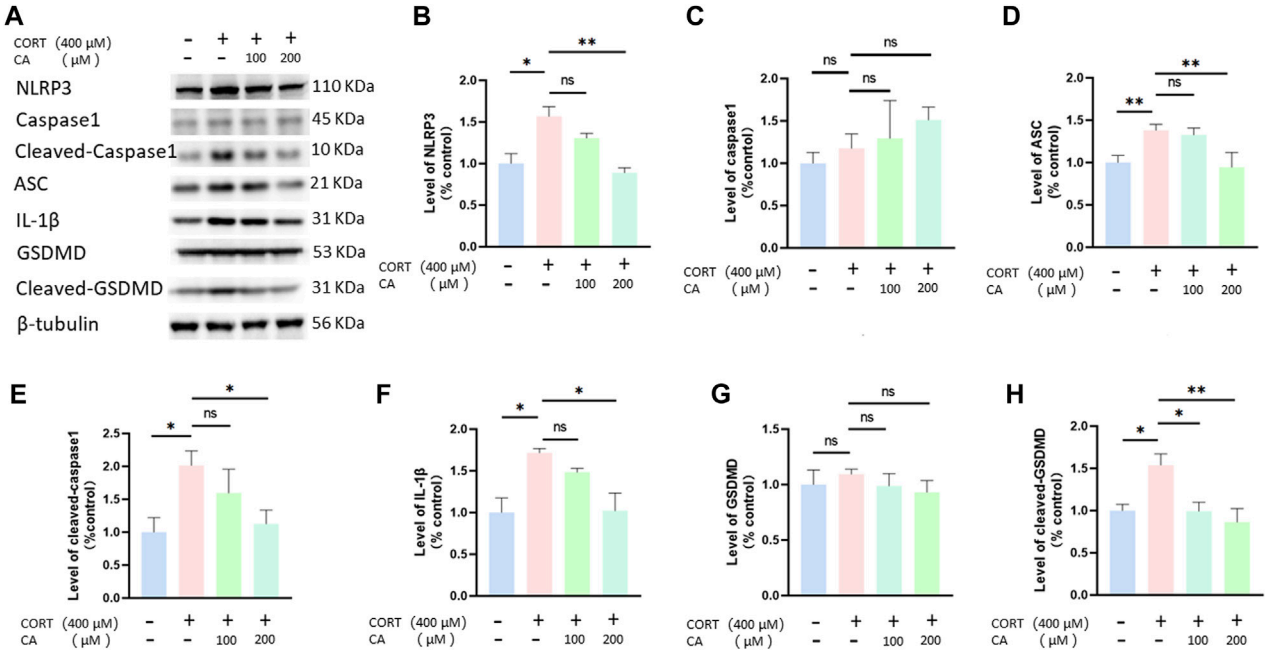

FIGURE 6
CA effects pyroptosis-associated proteins in PC12 cells. **(A)** Representative blot. **(B–H)** semiquantitative analysis of NLRP3, caspase1, ASC, cleaved-caspase1, IL-1β, GSDMD and Cleaved-GSDMD. Significant difference *$p < 0.05$, **$p < 0.01$, *ns = not significant*. Data are mean ± SEM (n = 3).

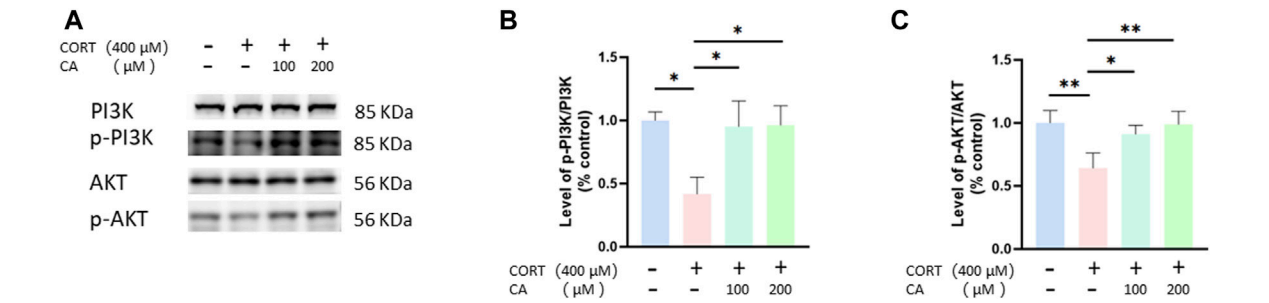

FIGURE 7
CA influence PI3K/AKT signal pathway in PC12 cells. **(A)** Representative blot. **(B, C)** semiquantitative analysis of p-PI3K/PI3K and p-AKT/AKT. Significant difference *$p < 0.05$, **$p < 0.01$, *ns = not significant*. Data are mean ± SEM (n = 3).

viability of PC12 cells showed no notable variation when exposed to 200 μM and 300 μM doses of CA in combination with CORT. Consequently, we selected the concentrations of 100 μM and 200 μM for CA to conduct our subsequent experiments.

Neuroplasticity refers to the brain's ability to undergo temporary changes in its organization and function in response to different stimuli, such as stress. This adaptability enables the brain to adjust and reorganize itself to accommodate environmental changes. Recent research has established a strong connection between depressive disorders and hippocampal synaptic plasticity (Parekh et al., 2022). Synaptophysin and PSD95 are proteins associated with the presynaptic and postsynaptic elements (Lai et al., 2022). Studies have shown that increasing the levels of synaptophysin and PSD95 in the hippocampus of mice can help alleviate depression-like behaviors (Kong et al., 2023). Our experimental findings indicate that exposure to CORT diminished the expression of synaptophysin and PSD95 in PC12 cells. In contrast, concurrent treatment with 200 μM CA and CORT enhances the expression of these proteins. This suggests that CA may protect PC12 cells from CORT-induced synaptic dysfunction.

To investigate the potential mechanisms of underlying CA's protective effect on cell damage induced by CORT, we collected PC12 cells from three groups (control group, CORT group, and 200 μM CA group) and conducted RNA-seq transcriptome analysis. The protective effect of CA on CORT-induced damage in PC12 cells is hypothesized to stem from its capacity to regulate intracellular functions, modulate the PI3K/AKT signaling, and reduce ROS production.

Oxidative stress occurs when the body's oxidation and antioxidant systems are imbalanced due to external factors,

10.3389/fphar.2024.1450211

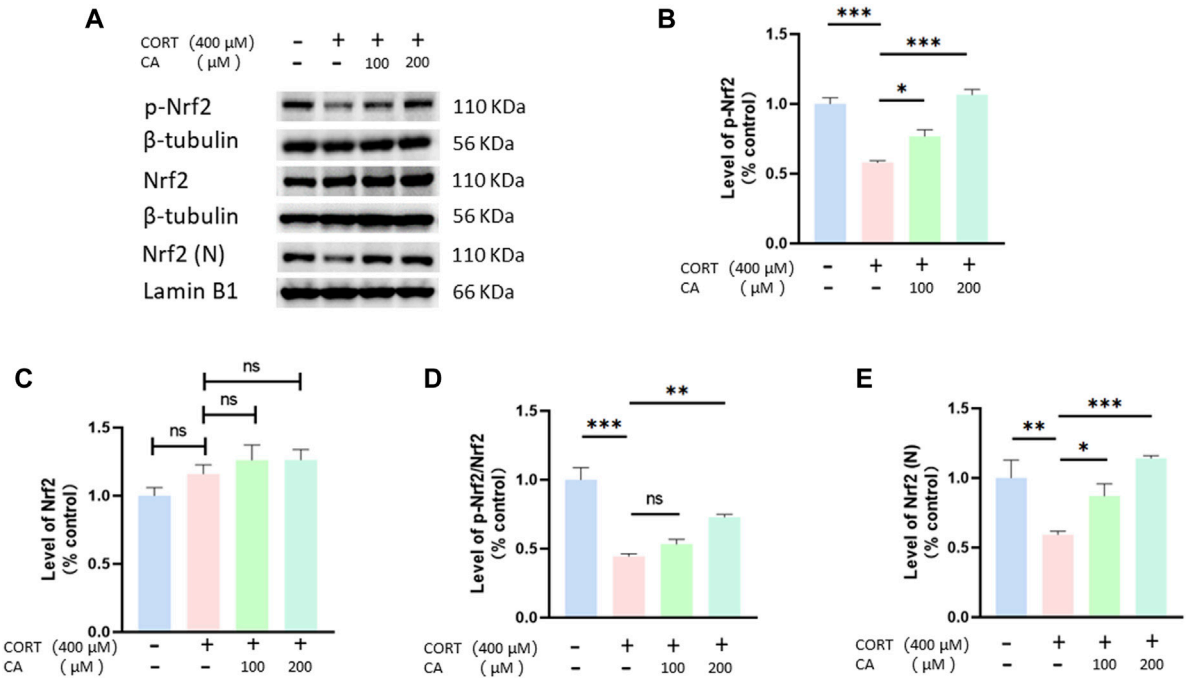

FIGURE 8
CA influence Nrf2, p-Nrf2 and Nrf2 (N) in PC12 cells. **(A)** Representative blot. **(B–E)** semiquantitave analysis of p-Nrf2, Nrf2 p-Nrf2/Nrf2 and Nrf2 (N). Significant difference *p < 0.05, **p < 0.01, ***p < 0.001, ns = not significant. Data are mean ± SEM (n = 3)

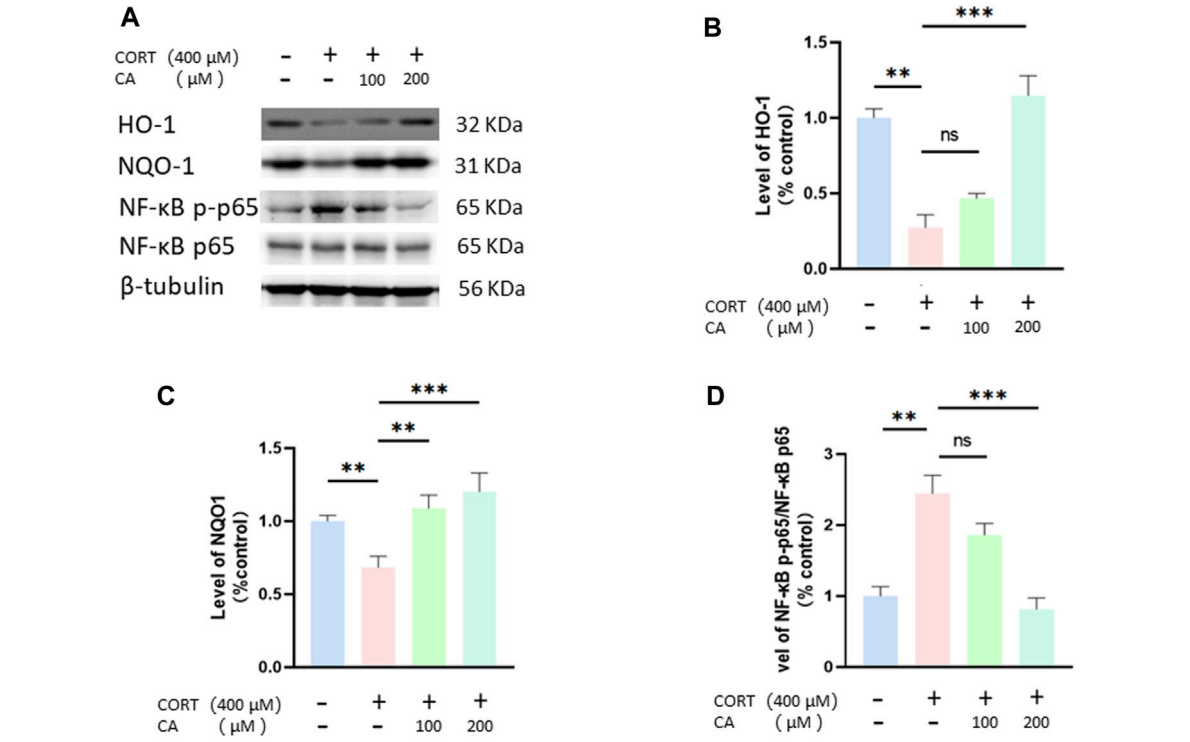

FIGURE 9
CA influences HO-1, NQO1 and NF-κB in PC12 cells. **(A)** Representative blot. **(B–D)** semiquantitative analysis of p-Nrf2, HO-1, NQO1 and NF-κB p-p65. Significant difference **p < 0.05, **p < 0.01,***p < 0.001, ns = not significant*. Data are mean ± SEM (n = 3).

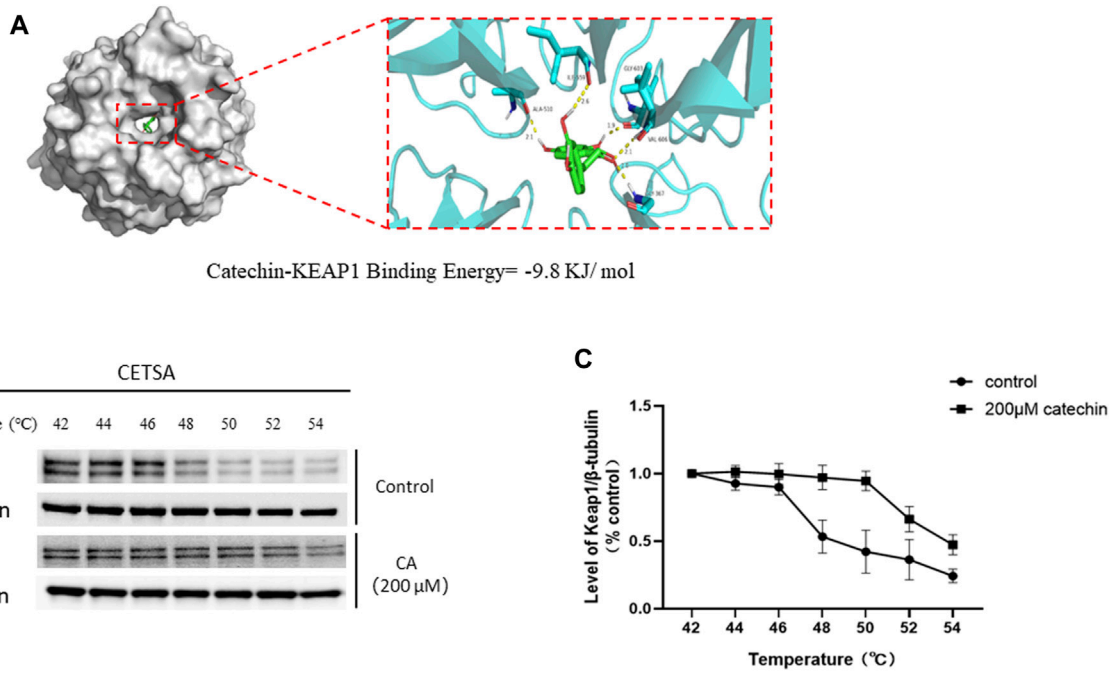

FIGURE 10
Molecular docking and thermal stability test of CA and Keap1 protein based on PC12 cells. **(A)** Molecular models of Catechin binding to Keap1 proteins. **(B)** Representative blot in Cellular thermal shift assay (CETSA). **(C)** Quantification of Keap1 abundance from CETSA.

resulting in the excessive production of ROS (Zhang B. et al., 2022; Zorov et al., 2014). ROS, MDA and SOD are key indicators for assessing oxidative stress (Zhou et al., 2017; Chao et al., 2021). Excessive ROS levels can cause lipid peroxidation, resulting in the creation of MDA and the linking of large molecules like proteins and nucleic acids, which can harm cell wellbeing. The concentration of MDA is a significant marker that indicates the body's antioxidant potential, offering insight into the rate and severity of lipid peroxidation, and thereby indicating the extent of oxidative tissue damage (Veljovic et al., 2022). SOD, an antioxidant enzyme present in living organisms, facilitates the conversion of superoxide anion radicals into oxygen and hydrogen peroxide. This enzyme plays a crucial role in balancing oxidative and antioxidant processes in the body, and is closely associated with the development and progression of depressive disorders (Jiménez-Fernández et al., 2022). Moreover, LDH is widely present in animals, plants, microorganisms, and isolated cells, acting as the final rate-limiting enzyme in glycolysis and catalyzing the reversible reaction between pyruvate and lactate. When cells are damaged and rupture, LDH leaks into the extracellular space, making it an important indicator for assessing cell damage. Our study demonstrates that CA at concentrations of 100 μM and 200 μM can reduce the elevated extracellular LDH levels in the PC12 cell model of depression. This suggests that CA provides protection to PC12 cells in the depressive model, aligning with the findings of the cell viability assays. Furthermore, compared to the CORT group, the 200 μM group shows a significant decrease in ROS and MDA levels and a marked increase in SOD levels. This suggests that CA exerts its protective effect on PC12 cells damaged by CORT by mitigating oxidative stress and consistent with the predictions of transcriptomics.

Pyroptosis, a caspase1-dependent form of cell death, is regulated by GSDM family proteins, such as GSDMD. This process is characterized by inflammasome activation, cell membrane pore formation, and the release of IL-1β (Shi et al., 2015; Kuang et al., 2017). The NLRP3 inflammasome is central to mediating pyroptosis, exerting a critical influence within the pathway. Studies indicate that excessive ROS production, causing oxidative stress, plays a key role in triggering the NLRP3 inflammasome, which is associated with various neurological disorders, such as depression (Zhong et al., 2018; Han et al., 2021; Tao et al., 2021; Gu et al., 2022). Consequently, interventions aimed at mitigating oxidative stress, ROS generation, NLRP3 inflammasome activity and pyroptosis are emerging as crucial targets for depression therapy. Previous research has found that CORT incubation can induce pyroptosis in PC12 cells (Chai et al., 2022). Therefore, we examined the pyroptosis in PC12 cells using flow cytometry and detected the expression of pyroptosis-related proteins through Western blot analysis. The findings suggest that CA can reverse CORT-induced pyroptosis in PC12 cells. The effect may be attributed to the anti-oxidative stress properties of CA.

We investigated whether CA's ability to reduce CORT-induced oxidative stress aligns with transcriptomics predictions. Western blot analysis confirmed that CA activates the PI3K/AKT signaling pathway, findings consistent with our transcriptomic results. Moreover, the PI3K/AKT signaling pathway has been documented to influence neural plasticity and cell viability, a basically conclusion that aligns with our observations regarding synaptic plasticity and cell viability (Na et al., 2022). Nrf2 is recognized as a crucial regulatory factor that maintains the body's redox balance by functioning as a transcription factor in

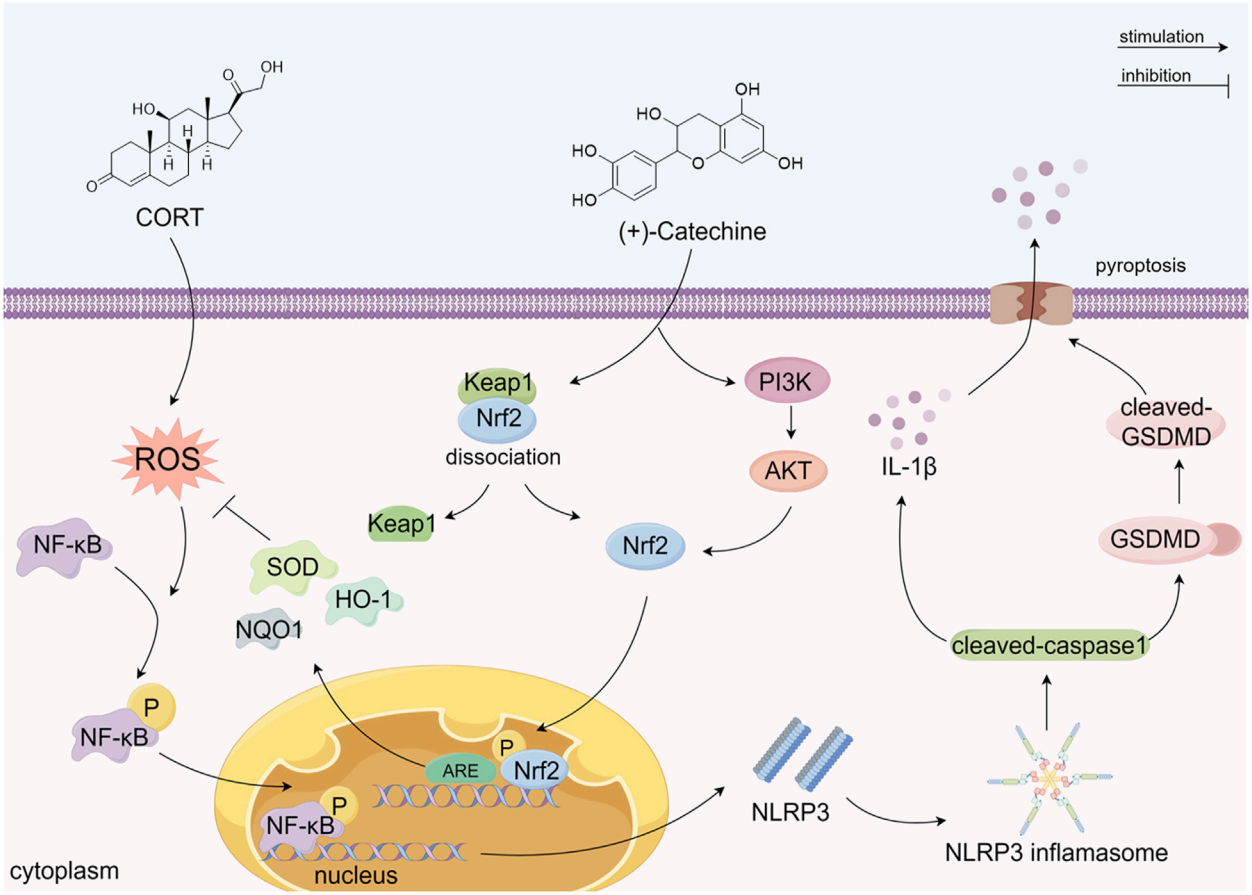

FIGURE 11
The possible mechanism of CA alleviating CORT-induced damage in PC12 cells. (By Figdraw).

response to oxidative stress (Ma, 2013). Keap1 acts as a suppressor of Nrf2, when bound, Nrf2 is rendered inactive. However, the dissociation of Keap1 from Nrf2 leads to Nrf2 phosphorylation and subsequent nuclear translocation. Within the nucleus, Nrf2 bines to antioxidant response elements, triggering the transcription of genes pivotal for antioxidant defense, including Ho-1, NQO1, and SOD (Liao et al., 2023). Additionally, research has found that the activation of Nrf2 and HO-1 can suppress NF-kB activation, thereby inhibiting NLRP3 and reducing cell pyroptosis (Zhang Y. et al., 2022). The PI3K/AKT pathway acts as an upstream signal to Nrf2, and studies have demonstrated that activation of the PI3K signaling pathway can enhance the Nrf2 phosphorylation and nuclear translocation (Chou et al., 2023; Hannan et al., 2020). This perspective supports our research findings on the PI3K/AKT signaling pathway and Nrf2, p-Nrf2, as well as Nrf2 (N). Moreover, previous studies have shown that CA can induce the dissociation of Keap1 and Nrf2 by forming a stable bond with the Nrf2 protein on Keap1, leading to the activation of Nrf2 (Islam et al., 2023; Jing et al., 2018). Therefore, molecular docking studies were performed revealing that CA forms a stable complex with the Keap1 protein. This was further substantiated by cellular thermal shift assays, which demonstrated that CA enhances Keap1 stability at elevated temperature. Hence, we propose two mechanisms by which CA activates Nrf2 to reduce ROS generation and prevent cell pyroptosis: one involves activating the PI3K/AKT signaling pathway, and the other entails binding with Keap1.

However, this study exclusively examined the potential protective effects of CA and its underlying molecular mechanisms using a cellular model of depression, rather than an animal model, which introduces certain limitations to the research. To determine whether CA possesses potential for development as an antidepressant drug, *in vivo* experiments are imperative. Despite these limitations, our research provides valuable reference points for future studies.

Conclusion

In summary, our study explored the protective effects of CA on cell depression models induced by CORT and its underlying mechanisms. The results confirmed that CA plays a significant protective role against CORT-induced cell damage. As shown in Figure 11, this protective effect is believed to stem from CA's activation of the PI3K/AKT signaling pathway and its interaction with Keap1, which leads to Nrf2 phosphorylation and subsequent activation of the Nrf2/HO1 pathway. This activation reduces ROS production and inhibits NF-κB phosphorylation. It is believed that

these processes collectively suppress NLRP3 formation and the expression of pyroptosis-related proteins. The study highlights the potential of CA in alleviating oxidative stress and pyroptosis in the CORT-induced cell depression model, suggesting a promising avenue for the development of innovative antidepressant treatments.

Declaration of Generative AI and AI-assisted technologies in the writing process

In the preparation of this manuscript, the authors have utilized ChatGPT 4.0 for polishing the language, but have not employed AI for the acquisition of scientific perspectives. All language, after being polished, has been reviewed by the authors. The authors assume full responsibility for the content of the publication.

Data availability statement

The data presented in the study are deposited in the NCBI repository, accession number PRJNA1148779. Available at: https://www.ncbi.nlm.nih.gov/bioproject/PRJNA1148779.

Ethics statement

Ethical approval was not required for the studies on animals in accordance with the local legislation and institutional requirements because only commercially available established cell lines were used.

Author contributions

LC: Data curation, Methodology, Software, Writing–original draft, Writing–review and editing, Formal Analysis, Validation, Visualization. ZS: Conceptualization, Methodology, Project administration, Validation, Writing–original draft. CZ: Formal Analysis, Investigation, Methodology, Software, Visualization, Writing–original draft. FX: Data curation, Formal Analysis, Validation, Visualization, Writing–original draft. ZM: Conceptualization, Data curation, Methodology, Project administration, Supervision, Writing–review and editing. WP: Conceptualization, Methodology, Project administration, Supervision, Writing–review and editing. GX: Conceptualization, Project administration, Resources, Supervision, Writing–original draft, Writing–review and editing.

Funding

The author(s) declare that financial support was received for the research, authorship, and/or publication of this article. This research work was funded by the Qiannan Rrefecture Science and Technology Bureau ([2023]05).

Conflict of interest

The authors declare that the research was conducted in the absence of any commercial or financial relationships that could be construed as a potential conflict of interest.

Publisher's note

All claims expressed in this article are solely those of the authors and do not necessarily represent those of their affiliated organizations, or those of the publisher, the editors and the reviewers. Any product that may be evaluated in this article, or claim that may be made by its manufacturer, is not guaranteed or endorsed by the publisher.

References

Abd El-Aziz, T. A., Mohamed, R. H., Pasha, H. F., and Abdel-Aziz, H. R. (2012). Catechin protects against oxidative stress and inflammatory-mediated cardiotoxicity in adriamycin-treated rats. *Clin. Exp. Med.* 12, 233–240. doi:10.1007/s10238-011-0165-2

Baird, L., and Yamamoto, M. (2020). The molecular mechanisms regulating the KEAP1-NRF2 pathway. *Mol. Cell Biol.* 40, e00099–20. doi:10.1128/MCB.00099-20

Baranwal, A., Aggarwal, P., Rai, A., and Kumar, N. (2022). Pharmacological actions and underlying mechanisms of catechin: a review. *Mini Rev. Med. Chem.* 22, 821–833. doi:10.2174/1389557521666210902162120

Bernatoniene, J., and Kopustinskiene, D. M. (2018). The role of catechins in cellular responses to oxidative stress. *Molecules* 23, 965. doi:10.3390/molecules23040965

Bhatt, S., Nagappa, A. N., and Patil, C. R. (2020). Role of oxidative stress in depression. *Drug Discov. Today* 25, 1270–1276. doi:10.1016/j.drudis.2020.05.001

Blanco, I., and Conant, K. (2021). Extracellular matrix remodeling with stress and depression: studies in human, rodent and zebrafish models. *Eur. J. Neurosci.* 53, 3879–3888. doi:10.1111/ejn.14910

Chai, Y., Cai, Y., Fu, Y., Wang, Y., Zhang, Y., Zhang, X., et al. (2022). Salidroside ameliorates depression by suppressing NLRP3-mediated pyroptosis via P2X7/NF-κB/NLRP3 signaling pathway. *Front. Pharmacol.* 13, 812362. doi:10.3389/fphar.2022.812362

Chao, B., Zhang, L., Pan, J., Zhang, Y., Chen, Y., Xu, M., et al. (2021). Stanniocalcin-1 overexpression prevents depression-like behaviors through inhibition of the ROS/NF-κB signaling pathway. *Front. Psychiatry* 12, 644383. doi:10.3389/fpsyt.2021.644383

Chou, T.-W., Huang, H.-S., Panyod, S., Huang, Y.-J., and Sheen, L.-Y. (2023). Korean red ginseng water extract produces antidepressant-like effects through involving monoamines and brain-derived neurotrophic factor in rats. *J. Ginseng Res.* 47, 552–560. doi:10.1016/j.jgr.2023.01.003

Gu, S., Li, Y., Jiang, Y., Huang, J. H., and Wang, F. (2022). Glymphatic dysfunction induced oxidative stress and neuro-inflammation in major depression disorders. *Antioxidants (Basel)* 11, 2296. doi:10.3390/antiox11112296

Han, X., Xu, T., Fang, Q., Zhang, H., Yue, L., Hu, G., et al. (2021). Quercetin hinders microglial activation to alleviate neurotoxicity via the interplay between NLRP3 inflammasome and mitophagy. *Redox Biol.* 44, 102010. doi:10.1016/j.redox.2021.102010

Hannan, M. A., Dash, R., Sohag, A. A. M., Haque, M. N., and Moon, I. S. (2020). Neuroprotection against oxidative stress: phytochemicals targeting TrkB signaling and the nrf2-ARE antioxidant system. *Front. Mol. Neurosci.* 13, 116. doi:10.3389/fnmol.2020.00116

Hao, W., Wu, J., Yuan, N., Gong, L., Huang, J., Ma, Q., et al. (2021). Xiaoyaosan improves antibiotic-induced depressive-like and anxiety-like behavior in mice through modulating the gut microbiota and regulating the NLRP3 inflammasome in the colon. *Front. Pharmacol.* 12, 619103. doi:10.3389/fphar.2021.619103

Haza, A. I., and Morales, P. (2011). Effects of (+)-Catechin and (-)-Epicatechin on heterocyclic amines-induced oxidative DNA damage. *J. Appl. Toxicol.* 31, 53–62. doi:10.1002/jat.1559

He, J., Han, D., Jia, C., Xie, J., Zhu, F., Wei, J., et al. (2023). Integrating network pharmacology, molecular docking and pharmacological evaluation for exploring the

polyrhachis vicina rogers in ameliorating depression. *Drug Des. Devel Ther.* 17, 717–735. doi:10.2147/DDDT.S399183

He, X., Liang, D., Zhou, J., Li, K., Xie, B., Liang, C., et al. (2024). Nucleus-targeting DNase I self-assembly delivery system guided by pirarubicin for programmed multi-drugs release and combined anticancer therapy. *Int. J. Biol. Macromol.* 267, 131514. doi:10.1016/j.ijbiomac.2024.131514

Heo, H. J., and Lee, C. Y. (2005). Epicatechin and catechin in cocoa inhibit amyloid beta protein induced apoptosis. *J. Agric. Food Chem.* 53, 1445–1448. doi:10.1021/jf048989m

Islam, M. A., Medha, M. M., Nahar, A. U., Al Fahad, M. A., Siraj, M. A., and Seidel, V. (2023). Cancer protective role of selected dietary polyphenols via modulating keap1/nrf2/ARE and interconnected signaling pathways. *Nutr. Cancer* 75, 1065–1102. doi:10.1080/01635581.2023.2183546

Jiménez-Fernández, S., Gurpegui, M., Garrote-Rojas, D., Gutiérrez-Rojas, L., Carretero, M. D., and Correll, C. U. (2022). Oxidative stress parameters and antioxidants in adults with unipolar or bipolar depression versus healthy controls: systematic review and meta-analysis. *J. Affect Disord.* 314, 211–221. doi:10.1016/j.jad.2022.07.015

Jing, X., Zhang, J., Huang, Z., Sheng, Y., and Ji, L. (2018). The involvement of Nrf2 antioxidant signalling pathway in the protection of monocrotaline-induced hepatic sinusoidal obstruction syndrome in rats by (+)-Catechin hydrate. *Free Radic. Res.* 52, 402–414. doi:10.1080/10715762.2018.1437914

Kobayashi, H., Tanaka, Y., Asagiri, K., Asakawa, T., Tanikawa, K., Kage, M., et al. (2010). The antioxidant effect of green tea catechin ameliorates experimental liver injury. *Phytomedicine* 17, 197–202. doi:10.1016/j.phymed.2009.12.006

Kong, C. H., Park, K., Kim, D. Y., Kim, J. Y., Kang, W. C., Jeon, M., et al. (2023). Effects of oleanolic acid and ursolic acid on depression-like behaviors induced by maternal separation in mice. *Eur. J. Pharmacol.* 956, 175954. doi:10.1016/j.ejphar.2023.175954

Kuang, S., Zheng, J., Yang, H., Li, S., Duan, S., Shen, Y., et al. (2017). Structure insight of GSDMD reveals the basis of GSDMD autoinhibition in cell pyroptosis. *Proc. Natl. Acad. Sci. U.S.A.* 114, 10642–10647. doi:10.1073/pnas.1708194114

Lai, C., Chen, Z., Ding, Y., Chen, Q., Su, S., Liu, H., et al. (2022). Rapamycin attenuated zinc-induced tau phosphorylation and oxidative stress in rats: involvement of dual mTOR/p70S6K and Nrf2/HO-1 pathways. *Front. Immunol.* 13, 782434. doi:10.3389/fimmu.2022.782434

Lee, B., Sur, B., Kwon, S., Yeom, M., Shim, I., Lee, H., et al. (2013). Chronic administration of catechin decreases depression and anxiety-like behaviors in a rat model using chronic corticosterone injections. *Biomol. Ther.* 21, 313–322. doi:10.4062/biomolther.2013.004

Liao, D., Shangguan, D., Wu, Y., Chen, Y., Liu, N., Tang, J., et al. (2023). Curcumin protects against doxorubicin induced oxidative stress by regulating the keap1-nrf2-ARE and autophagy signaling pathways. *Psychopharmacol. (berl.)* 240, 1179–1190. doi:10.1007/s00213-023-06357-z

Liu, X., Zhang, R., Fan, J., Chen, Y., Wang, H., Ge, Y., et al. (2023). The role of ROS/P38 MAPK/NLRP3 inflammasome cascade in arsenic-induced depression-/anxiety-like behaviors of mice. *Ecotoxicol. Environ. Saf.* 261, 115111. doi:10.1016/j.ecoenv.2023.115111

Ma, Q. (2013). Role of Nrf2 in oxidative stress and toxicity. *Annu. Rev. Pharmacol. Toxicol.* 53, 401–426. doi:10.1146/annurev-pharmtox-011112-140320

McGuffin, P., and Rivera, M. (2015). The interaction between stress and genetic factors in the etiopathogenesis of depression. *World Psychiatry* 14, 161–163. doi:10.1002/wps.20230

Muscari, I., Fierabracci, A., Adorisio, S., Moretti, M., Cannarile, L., Thi Minh Hong, V., et al. (2022). Glucocorticoids and natural killer cells: a suppressive relationship. *Biochem. Pharmacol.* 198, 114930. doi:10.1016/j.bcp.2022.114930

Na, L., Yanhong, Z., Jingwei, L., Dazhong, S., Lin, J., Pang, Q., et al. (2022). Protective effects of ginsenoside CK against oxidative stress-induced neuronal damage, assessed with 1H-NMR-Based metabolomics. *Acta Mater. Medica* 1, 392–399. doi:10.15212/AMM-2022-0009

Nikolin, S., Owens, K., Francis-Taylor, R., Chaimani, A., Martin, D. M., Bull, M., et al. (2022). Comparative efficacy, cognitive effects and acceptability of electroconvulsive therapies for the treatment of depression: protocol for a systematic review and network meta-analysis. *BMJ Open* 12, e068313. doi:10.1136/bmjopen-2022-068313

Parekh, P. K., Johnson, S. B., and Liston, C. (2022). Synaptic mechanisms regulating mood state transitions in depression. *Annu. Rev. Neurosci.* 45, 581–601. doi:10.1146/annurev-neuro-110920-040422

Qin, L., Wu, X., Block, M. L., Liu, Y., Breese, G. R., Hong, J.-S., et al. (2007). Systemic LPS causes chronic neuroinflammation and progressive neurodegeneration. *Glia* 55, 453–462. doi:10.1002/glia.20467

Qin, X., Wang, R., Xu, H., Tu, L., Chen, H., Li, H., et al. (2022). Identification of an autoinhibitory, mitophagy-inducing peptide derived from the transmembrane domain of USP30. *Autophagy* 18, 2178–2197. doi:10.1080/15548627.2021.2022360

Ramis, M. R., Sarubbo, F., Moranta, D., Tejada, S., Lladó, J., Miralles, A., et al. (2021). Neurochemical and cognitive beneficial effects of moderate physical activity and catechin in aged rats. *Antioxidants Basel, Switz.* 10, 621. doi:10.3390/antiox10040621

Rao, J., Qiao, Y., Xie, R., Lin, L., Jiang, J., Wang, C., et al. (2021). Fecal microbiota transplantation ameliorates stress-induced depression-like behaviors associated with the inhibition of glial and NLRP3 inflammasome in rat brain. *J. Psychiatric Res.* 137, 147–157. doi:10.1016/j.jpsychires.2021.02.057

Rehm, J., and Shield, K. D. (2019). Global burden of Disease and the impact of mental and addictive disorders. *Curr. Psychiatry Rep.* 21, 10. doi:10.1007/s11920-019-0997-0

Satoh, T., Okamoto, S.-i., Cui, J., Watanabe, Y., Furuta, K., Suzuki, M., et al. (2006). Activation of the Keap1/Nrf2 pathway for neuroprotection by electrophilic [correction of electrophillic] phase II inducers. *Proc. Natl. Acad. Sci.* 103, 768–773. doi:10.1073/pnas.0505723102

Shi, J., Zhao, Y., Wang, K., Shi, X., Wang, Y., Huang, H., et al. (2015). Cleavage of GSDMD by inflammatory caspases determines pyroptotic cell death. *Nature* 526, 660–665. doi:10.1038/nature15514

Si, L., Xiao, L., Xie, Y., Xu, H., Yuan, G., Xu, W., et al. (2023). Social isolation after chronic unpredictable mild stress perpetuates depressive-like behaviors, memory deficits and social withdrawal via inhibiting ERK/KEAP1/NRF2 signaling. *J. Affect. Disord.* 324, 576–588. doi:10.1016/j.jad.2022.12.092

Sun, J.-Y., Liu, Y.-T., Jiang, S.-N., Guo, P.-M., Wu, X.-Y., and Yu, J. (2022). Essential oil from the roots of paeonia lactiflora pall. Has protective effect against corticosterone-induced depression in mice via modulation of PI3K/akt signaling pathway. *Front. Pharmacol.* 13, 999712. doi:10.3389/fphar.2022.999712

Tao, W., Hu, Y., Chen, Z., Dai, Y., Hu, Y., and Qi, M. (2021). Magnolol attenuates depressive-like behaviors by polarizing microglia towards the M2 phenotype through the regulation of Nrf2/HO-1/NLRP3 signaling pathway. *Phytomedicine* 91, 153692. doi:10.1016/j.phymed.2021.153692

Uzbekov, M. G., and Maximova, N. M. (2015). Monoamine-hormonal interactions in the pathogenesis of anxious depression. *Zhurnal Nevrol. i psikhiatrii Im. S.S. Korsakova* 115, 52–55. doi:10.17116/jnevro20151151252-55

Veljovic, T., Djuric, M., Mirnic, J., Gusic, I., Maletin, A., Ramic, B., et al. (2022). Lipid peroxidation levels in saliva and plasma of patients suffering from periodontitis. *J. Clin. Med.* 11, 3617. doi:10.3390/jcm11133617

Wang, H., He, Y., Sun, Z., Ren, S., Liu, M., Wang, G., et al. (2022). Microglia in depression: an overview of microglia in the pathogenesis and treatment of depression. *J. Neuroinflamm.* 19, 132. doi:10.1186/s12974-022-02492-0

Wang, H.-Q., Wang, Z.-Z., and Chen, N.-H. (2021). The receptor hypothesis and the pathogenesis of depression: genetic bases and biological correlates. *Pharmacol. Res.* 167, 105542. doi:10.1016/j.phrs.2021.105542

Wu, Q., Chen, Y., Ouyang, Y., He, Y., Xiao, J., Zhang, L., et al. (2021). Effect of catechin on dietary AGEs absorption and cytotoxicity in caco-2 cells. *Food Chem.* 355, 129574. doi:10.1016/j.foodchem.2021.129574

Xia, C.-Y., Guo, Y.-X., Lian, W.-W., Yan, Y., Ma, B.-Z., Cheng, Y.-C., et al. (2023). The NLRP3 inflammasome in depression: potential mechanisms and therapies. *Pharmacol. Res.* 187, 106625. doi:10.1016/j.phrs.2022.106625

Xie, C., Wu, W., Tang, A., Luo, N., and Tan, Y. (2019). lncRNA GAS5/miR-452-5p reduces oxidative stress and pyroptosis of high-glucose-stimulated renal tubular cells. *Diabetes, Metabolic Syndrome Obes. Targets Ther.* 12, 2609–2617. doi:10.2147/DMSO.S228654

Zhang, B., Pan, C., Feng, C., Yan, C., Yu, Y., Chen, Z., et al. (2022a). Role of mitochondrial reactive oxygen species in homeostasis regulation. *Redox Rep.* 27, 45–52. doi:10.1080/13510002.2022.2046423

Zhang, Y., Zhao, Z., Zhao, X., Xie, H., Zhang, C., Sun, X., et al. (2022b). HMGB2 causes photoreceptor death via down-regulating Nrf2/HO-1 and up-regulating NF-κB/NLRP3 signaling pathways in light-induced retinal degeneration model. *Free Radic. Biol. Med.* 181, 14–28. doi:10.1016/j.freeradbiomed.2022.01.018

Zhong, Z., Liang, S., Sanchez-Lopez, E., He, F., Shalapour, S., Lin, X.-J., et al. (2018). New mitochondrial DNA synthesis enables NLRP3 inflammasome activation. *Nature* 560, 198–203. doi:10.1038/s41586-018-0372-z

Zhou, Y.-Z., Li, X., Gong, W.-X., Tian, J.-S., Gao, X.-X., Gao, L., et al. (2017). Protective effect of isoliquiritin against corticosterone-induced neurotoxicity in PC12 cells. *Food Funct.* 8, 1235–1244. doi:10.1039/c6fo01503d

Zhu, T., Liu, H., Gao, S., Jiang, N., Chen, S., and Xie, W. (2024). Effect of salidroside on neuroprotection and psychiatric sequelae during the COVID-19 pandemic: a review. *Biomed. Pharmacother.* 170, 115999. doi:10.1016/j.biopha.2023.115999

Zorov, D. B., Juhaszova, M., and Sollott, S. J. (2014). Mitochondrial reactive oxygen species (ROS) and ROS-induced ROS release. *Physiol. Rev.* 94, 909–950. doi:10.1152/physrev.00026.2013

Zuo, C., Cao, H., Song, Y., Gu, Z., Huang, Y., Yang, Y., et al. (2022). Nrf2: an all-rounder in depression. *Redox Biol.* 58, 102522. doi:10.1016/j.redox.2022.102522

frontiers | Frontiers in Pharmacology

TYPE Original Research
PUBLISHED 03 September 2024
DOI 10.3389/fphar.2024.1463339

OPEN ACCESS

EDITED BY
Song Zhang,
Shanghai Jiao Tong University, China

REVIEWED BY
Ming-Gang Liu,
Oujiang Laboratory (Zhejiang Lab for Regenerative Medicine, Vision and Brain Health), China
He Liu,
Zhejiang University School of Medicine and Huzhou Central Hospital, China

*CORRESPONDENCE
Jiaping Ruan,
495316355@qq.com
Zhengliang Ma,
mazhengliang1964@nju.edu.cn

†These authors have contributed equally to this work and share first authorship

‡These authors have contributed equally to this work and share last authorship

RECEIVED 11 July 2024
ACCEPTED 20 August 2024
PUBLISHED 03 September 2024

CITATION
Guo S, Wang Y, Duan Q, Gu W, Fu Q, Ma Z and Ruan J (2024) Activation of EphrinB2/EphB2 signaling in the spine cord alters glia-neuron interactions in mice with visceral hyperalgesia following maternal separation. *Front. Pharmacol.* 15:1463339. doi: 10.3389/fphar.2024.1463339

Activation of EphrinB2/EphB2 signaling in the spine cord alters glia-neuron interactions in mice with visceral hyperalgesia following maternal separation

Shufen Guo[1†], Yu Wang[1,2†], Qingling Duan[1], Wei Gu[2], Qun Fu[2], Zhengliang Ma[1,2*‡] and Jiaping Ruan[2*‡]

[1]Department of Anesthesiology, Nanjing Drum Tower Hospital Clinical College of Nanjing University of Chinese Medicine, Nanjing, Jiangsu, China, [2]Department of Anesthesiology, Nanjing Drum Tower Hospital, Affiliated Hospital of Medical School, Nanjing University, Nanjing, Jiangsu, China

Background: Sress early in life has been linked to visceral hyperalgesia and associated functional gastrointestinal disorders. In a mouse model of visceral hyperalgesia, we investigated whether the EphB2 receptor and its EphrinB2 ligand in spinal cord contribute to dysregulation of glia-neuron interactions.

Methods: An established mouse model of stress due to maternal separation (MS). Pups were separated from their mothers for 14 days during early development, then analyzed several weeks later in terms of visceral sensitivity based on the abdominal withdrawal reflex score and in terms of expression of c-fos, EphrinB2, EphB2, and phosphorylated MAP kinases (ERK, p38, JNK).

Results: Visceral hyperalgesia due to MS upregulated EphB2, EphrinB2 and c-fos in the spinal cord, and c-fos levels positively correlated with those of EphB2 and EphrinB2. Spinal astrocytes, microglia, and neurons showed upregulation of EphB2, EphrinB2 and phosphorylated MAP kinases. Blocking EphrinB2/EphB2 signaling in MS mice reduced visceral sensitivity, activation of neurons and glia, and phosphorylation of NMDA receptor. Activating EphrinB2/EphB2 signaling in unstressed mice induced visceral hyperalgesia, upregulation of c-fos, and activation of NMDA receptor similar to maternal separation.

Conclusion: The stress of MS during early development may lead to visceral hyperalgesia by upregulating EphrinB2/EphB2 in the spinal cord and thereby altering neuron-glia interactions.

KEYWORDS

visceral hyperalgesia, maternal separation, ephrinB2/ephB2, glia-neuron, NMDA receptor

Introduction

Irritable bowel syndrome and other functional gastrointestinal disorders usually involve visceral hyperalgesia, in which nerves in the gut are hypersensitive to stimuli (Chey, Kurlander, and Eswaran, 2015). A strong risk factor for visceral hyperalgesia is stress early in life (Hu et al., 2020), but what molecules and pathways mediate the relationship between the two are poorly understood. What is known is that the dorsal root ganglion sends visceral

pain signals to the dorsal horn in the spine (Louwies et al., 2019), which transmits the signals further to neural networks involved in nociception (Moloney et al., 2015). Also known is that two types of glia, microglia and astrocytes, can be activated by stress (Ji, Berta, and Nedergaard, 2013) to release pro-inflammatory cytokines that regulate neuronal activity (Milligan and Watkins, 2009) in a way that triggers and maintains visceral hyperalgesia (Dodds et al., 2016; Song et al., 2014). Unknown is how stress alters glia-neuron interactions to give rise to chronic hypersensitivity in the gut.

The EphB2 receptors and EphrinB2 ligands are found in peripheral tissues and mature brain, where they play a pivotal role in regulating diverse physiological and pathophysiological processes (Wu et al., 2021; Duan et al., 2024). Peripheral EphrinB2/EphB2 receptor was involved in visceral hypersensitivity in postinfectious irritable bowel syndrome (IBS) rats (Zhang et al., 2019). EphrinB2/EphB2 receptor tyrosine kinases also plays a key role in the structural and functional plasticity of synapses during early neurodevelopment as well as in the mature brain and spinal cord (Lim, Matsuda, and Poo, 2008; Klein and Kania, 2014). EphB2 demonstrates the capacity to orchestrate functional presynaptic specializations while also governing postsynaptic maturation through the promotion of spine morphogenesis and recruitment of neurotransmitter receptors (Kayser et al., 2006; Planagumà et al., 2016). Moreover, EphrinB2/EphB2 mediates heightened neural activation and excitatory synaptic transmission in cases of neuropathic pain (Song et al., 2008). Both EphB2 and EphrinB2 proteins are expressed in neurons and glia, where they help regulate the correct formation of neuronal circuits (Lauterbach and Klein, 2006). Activation of EphrinB2/EphB2 signaling in the spine can lead to hyperalgesia by altering neural development and synaptic plasticity (Bundesen et al., 2003; Chen et al., 2022), apparently through multiple mechanisms dependent on, and independent of, the *N*-methyl-D-aspartate (NMDA) receptor (Ma et al., 2020). Conversely, inhibition of EphB2/EphrinB2 signaling dampens chronic pain in animal models of inflammatory, neuropathic, and cancer pain (Zhou et al., 2015b; Liu et al., 2013). Therefore, we hypothesized that altered signaling involving the EphB2 receptor and its EphrinB2 ligand may lead to altered interactions between glia and neurons in visceral hyperalgesia.

We investigated here the effects of EphrinB2/EphB2 on glia-neuron interactions in the spine in mice that were separated for a defined period from their mothers during early development. In this animal model, the stress arising from maternal separation is known to induce visceral hyperalgesia (Du et al., 2019), which can be measured as abdominal withdrawal reflex after colorectal distension (Li et al., 2023). Among the potential molecules affected by EphrinB2/EphB2 signaling, we focused on c-fos because its upregulation correlates with activation of neurons during nociception (Coggeshall, 2005) and on MAP kinases, because activation of these kinases correlates with activation of EphB2 (Poliakov et al., 2008a) and because we showed previously that MAP kinases mediate at least some of the effects of EphrinB/EphB signaling on synaptic plasticity (Ruan et al., 2010) and nociception (Cao et al., 2008).

Methods

Mouse model of visceral hyperalgesia

All animal procedures were approved by the Animal Ethics Committee at Nanjing Medical University. Adult male and female C57BL/6 mice (Laboratory Animal Center of Nanjing Medical University, Nanjing, China) were housed with *ad libitum* access to food and water. Newborn male pups were separated from their dams in the same cage by an opaque isolation board for 3 h daily from 9:00 to 12:00 h from postnatal days 2–15, then the board was removed and pups were returned to their dams (Du et al., 2019). Control pups were raised under the same conditions except that no isolation board was introduced into the cage. All pups were weaned and separated from their dams on postnatal day 21, and analyzed as described below starting at 8 weeks of age.

The numbers of animals and replicate measurements in different experiments were based on our previous experience (Ruan et al., 2010; Cao et al., 2008).

Effects of inhibiting or activating EphrinB2/EphB2 signaling in the mouse model

Mice that experienced maternal separation or not were anesthetized intraperitoneally using sodium pentobarbital (40 mg/kg), then injected intrathecally with one of the following: a chimera of EphB2 with Fc (catalog no. 467-B2, R&D Systems, Minnesota, United States), which binds to EphrinB2 and prevents it from stimulating endogenous EphB2; a chimera of EphrinB2 and Fc (catalog no. 496-EB, R&D Systems, Minnesota, United States), which binds and activates endogenous EphB2; or, as a negative control, recombinant Fc from human IgG1 (catalog no. 110-HG, R&D Systems, Minnesota, United States). Injections EphB2-Fc or EphrinB2-Fc(0.1-μg or 0.5-μg/5 μL, i. t., daily for three consecutive days) were made between vertebrae L5 and L6 using a 25-μL Hamilton microinjector (Ruan et al., 2010), and tail flicking was interpreted as successful puncture. Injections were delivered within 30 s, the needle was left in place for 15 s, then the needle was gently removed. All doses of the drug are based on the results of the pre-experimental studies in reference to Zhou et al. (2015a). The detailed dose and treatment time point for each drug are given in the illustration section.

Assessment of visceral sensitivity

Visceral sensitivity was quantified by scoring the abdominal withdrawal reflex following colorectal distention (Li et al., 2023). Mice were lightly anesthetized with 1%–1.5% isoflurane, then a rubber balloon was carefully inserted into the colorectum 3 cm from the anus and secured to the base of the tail using hypoallergenic silk tape. Animals were placed individually into a clear box (20 × 10 × 18 cm), allowed to habituate for 10–15 min, then the balloon was inflated sequentially for 20 s at pressures of 20, 40 and 60 mmHg. The balloon was deflated for 2–3 min between inflations. The abdominal withdrawal reflex was scored from 0 to 4 as described (Chen et al., 2022) by investigators blinded to mouse grouping. Scores were averaged from triplicate measurements on each animal.

In immunohistochemistry, immunofluorescence staining and Western blotting experiments to compare activation or expression of key proteins between mice that experienced maternal separation or not (see below), colorectal distension stimulation was performed at 60 mmHg every 3 min during 15 min. We chose these conditions

to avoid damaging the colorectal tissue, given that the balloon had to be inflated at 60 mmHg in order to induce nociceptive behaviors.

Immunohistochemistry against key proteins in the spine

Mice were anesthetized under isoflurane before transcardial perfusion and injected with saline and 4% paraformaldehyde, then the spinal cord was removed and sliced into sections 20 μm thick using a cryostat (CM1800, Leica, Germany). Sections were washed in phosphate-buffered saline (PBS), blocked in goat serum for 30 min, then incubated with primary antibodies against the following proteins: EphB2 (1:200; catalog no. MABN726, Merck & Millipore, United States), EphrinB2 (1:100; catalog no. HPA008999, Merck & Millipore, United States), phospho-ERK (1:200; catalog no. sc-136521, Santa Cruz, Dallas, United States), phospho-p38 (1:200; catalog no. sc-166182, Santa Cruz, Dallas, United States), phospho-JNK (1:200; catalog no. sc-6254, Santa Cruz, Dallas, United States), c-fos (1:500; catalog no. sc-166940, Santa Cruz, Dallas, United States), GFAP (1:200; catalog no. sc-33673, Santa Cruz, Dallas, United States), NeuN (1:1500; catalog no. ABN90, Merck & Millipore, United States), and Iba1 (1:200; catalog no. sc-32725, Santa Cruz, Dallas, United States). Subsequently, the sections were rinsed three times with PBS and incubated for 2 h with anti-rabbit Alexa Fluor 488 (1:500, Invitrogen, California, United States) or anti-mouse Alexa Fluor 555 (1:500, Invitrogen, California, United States) antibodies. After washing with PBS for 3 times, incubate with DAPI.

Immunostained sections were examined under Olympus microscope (1–71, Olympus, Japan) and images were analyzed using ImageJ software (National Institutes of Health, United States).

Western blotting against key proteins in the spine

Under isoflurane anesthesia, mice were sacrificed, the spinal cord was removed, flash-frozen in liquid nitrogen, then thawed and lysed in RIPA lysis buffer. Equal amounts of total protein (30 μg) were fractionated by SDS-PAGE and transferred onto polyvinylidene difluoride membranes, which were immersed in blocking buffer (Beyotime, Shanghai, China), then incubated with primary antibodies against the following proteins: EphB2 (1:500; catalog no. MABN726, Merck & Millipore, United States), EphrinB2 (1:500; catalog no. HPA008999, Merck & Millipore, United States), phospho-ERK (1:500; catalog no. sc-136521, Santa Cruz, Dallas, United States), ERK (1:500; catalog no. sc-514302, Santa Cruz, Dallas, United States), phospho-p38 (1:500; catalog no. sc-166182, Santa Cruz, Dallas, United States), p38 (1:500; catalog no. sc-7972, Santa Cruz, Dallas, United States), phospho-JNK (1:500; catalog no. sc-6254, Santa Cruz, Dallas, United States), JNK (1:500; catalog no. sc-137019, Santa Cruz, Dallas, United States), GFAP (1:200; catalog no. sc-33673, Santa Cruz, Dallas, United States), NeuN (1:2000; catalog no. ABN90, Merck & Millipore, United States), Iba1 (1:500; catalog no. sc-32725, Santa Cruz, Dallas, United States), NR2B (1:1000; catalog no. 42125, Cell Signaling Technology, Massachusetts, United States), phospho-NR2B (TYR1472) (1:1000; catalog no.4208, Cell Signaling Technology, Massachusetts, United States), c-fos (1:1000; catalog no. sc-166940, Santa Cruz, Dallas, United States), and Actin (1:2000; catalog no. sc-8432, Santa Cruz, Dallas, United States). Membranes were washed three times with Tris-buffered saline containing 0.1% Tween-20 (TBST), then incubated for 2 h at room temperature with horseradish peroxidase-conjugated goat secondary antibodies against mouse IgG (1:5000; catalog no. AP124P, Merck & Millipore, United States) or rabbit IgG (1:5000; catalog no. AP132P, Merck & Millipore, United States). Membranes were again washed three times with TBST, images were scanned with Micro Chemi (DNR Bio-imaging systems, Jerusalem, Israel) and the optical densities of detected bands were quantified using Image software J (US National Institutes of Health, Bethesda, MD, United States).

Statistical analysis

Data were analyzed and figures prepared using Graph Pad Prism 9.0.0 (Inc., San Diego, CA). Data were reported as mean ± SEM unless stated otherwise. Pairwise differences were assessed for significance using the two-tailed unpaired Student's t-test, while differences among three or more groups were assessed using one- or two-way analysis of variance. Differences associated with $p < 0.05$ were considered significant.

Results

Visceral hyperalgesia due to maternal separation involves upregulation of EphB2, EphrinB2 and c-fos in the spine

Mice were subjected to colorectal distension (CRD) following maternal separation (MS). The schematic diagram and time course of CRD combined with abdominal withdrawal reflex (AWR) score under pressures of 20, 40, and 60 mmHg are shown in Figure 1A . The records confirmed that separating mouse pups from their mothers for a 14-day period soon after birth led to visceral hyperalgesia several weeks later, which we detected as an increase in abdominal withdrawal reflex in response to colorectal distension, the AWR score of MS mice did not change at 20 mmHg but increased significantly at 40 and 60 mmHg (Figure 1B). The stronger reflex was associated with upregulation of c-fos (Figure 1C), which signals neuronal activation during nociception (Coggeshall, 2005), as well as with upregulation of EphB2 and EphrinB2 (Figure 1D). The time points for the detection of EphrinB2/EphB2, and Fos protein expression are set at 60 min and 90 min after CRD, respectively. In fact, levels of c-fos correlated positively with those of EphB2 and EphrinB2 (Figure 1E). These results suggest that stress due to maternal separation induces visceral hyperalgesia by activating EphrinB2/EphB2 signaling.

Visceral hyperalgesia involves activation of MAP kinases in spine cells in which EphB2 is upregulated

Visceral hyperalgesia due to maternal separation was associated with activation of three MAP kinases known to act downstream of

10.3389/fphar.2024.1463339

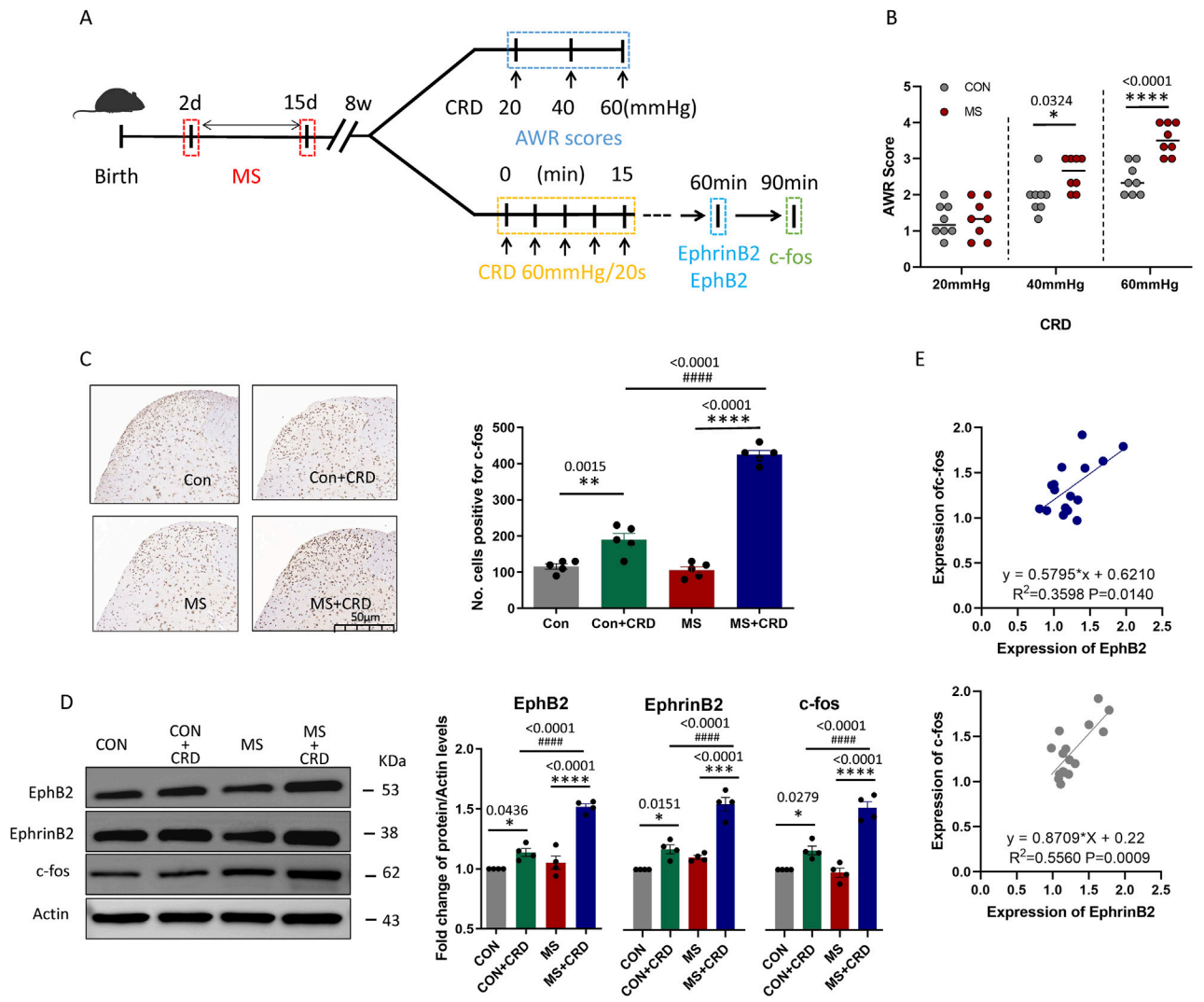

FIGURE 1
Maternal separation early in development causes visceral hyperalgesia in response to colorectal distension. **(A)** Schematic illustration of the experimental protocol. CRD, colorectal distension; MS, maternal separation **(B)** Score on abdominal withdrawal reflex after colorectal distension. Quantification is shown for eight animals per condition. CON, control. *$P < 0.05$, ****$P < 0.0001$ vs. CON, based on two-way repeated-measures ANOVA, followed by the Bonferroni multiple-comparisons test. **(C)** Representative thin sections of spinal cord after immunostaining against c-fos and quantification of cells expressing c-fos. CRD induced Fos protein expression in superficial lamine of spinal cord, we count the c-fos$^+$ neurons in lamine I-V of spinal cord of view at magnification ×10 and average the results. Results are shown for five animals per condition. Scale bar, 50 μm. Based on one-way ANOVA and the Bonferroni multiple-comparisons test: **$P < 0.01$, ****$P < 0.0001$ between CON and CON + CRD or between MS and MS + CRD; $^{\#\#\#\#}P < 0.0001$ between CON + CRD and MS + CRD. **(D)** Representative Western blotting of total lysate of spine tissue and quantification of EphB2 and EphrinB2. Protein levels were normalized to those of Actin in the same sample, and the relative protein level in the control group without CRD was defined as 1. Quantification is shown for four animals per treatment. Based on one-way ANOVA and the Bonferroni multiple-comparisons test: *$P < 0.05$, ****$P < 0.0001$ between CON and CON + CRD or between MS and MS + CRD; $^{\#\#\#\#}P < 0.0001$ between CON + CRD and MS + CRD. **(E)** Correlation between levels of c-fos and levels of EphB2 or EphrinB2 based on Western blotting of total lysates of spine tissue.

EphB2: ERK, p38 and JNK (Figure 2A). Immunofluorescence staining of thin sections from the spine showed that EphB2-positive cells in the spinal cord mainly co-expressed with these kinases 60min after CRD (Figures 2B–D). In the control group, we observed a small amount of EphB2 or MAPKs activation, but the co-expression of these receptors were significant less than those in MS group (Figure 2E). The ratio of EphB2 + p-ERK, EphB2 + p-p38 and EphB2 + p-JNK to EphB2 was 70.02%, 61.46% and 76.05%, respectively (Figure 2F, left). While the ratio of EphB2 + p-ERK to p-ERK, EphB2 + p-p38 to p-p38 and EphB2 + p-JNK to p-JNK was 72.16%,74.36% and 71.93%, respectively (Figure 2F, right). These results suggest that the stress caused by maternal separation stimulates EphrinB2/EphB2 signaling, which in turn activates MAP kinases.

Visceral hyperalgesia involves activation of neurons, astrocytes and microglia in the dorsal horn of the spine

Visceral hyperalgesia due to maternal separation was associated with upregulation of EphB2 and EphrinB2 in three

10.3389/fphar.2024.1463339

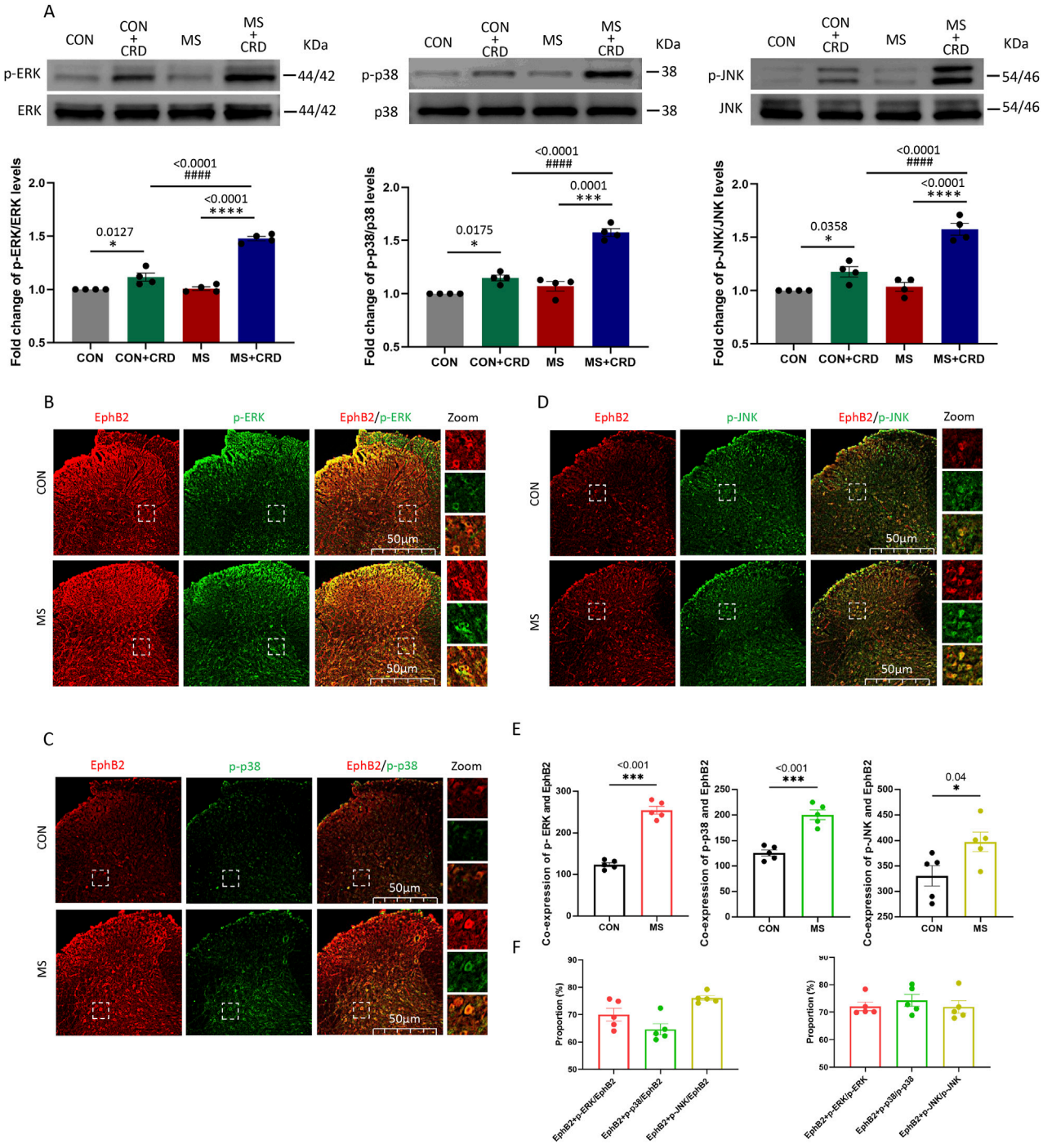

FIGURE 2
Visceral hyperalgesia in response to colorectal distension activates EphrinB2/EphB2 signaling and downstream MAP kinases. Mice were subjected to maternal separation (MS) early in development or not (CON), then later subjected to colorectal distension (CRD) or not. **(A)** Representative western blots of total lysate from spinal cord and quantification of the active, phosphorylated forms of the MAP kinases ERK, p38 and JNK. Levels of phosphorylated protein were normalized to those of the corresponding total protein, and the relative level of phosphorylated protein in the control group without CRD was defined as 1. Quantification is shown for four animals per condition. Based on one-way ANOVA and the Bonferroni multiple-comparisons test: $^{*}P < 0.05$, $^{****}P < 0.0001$ between CON and CON + CRD or between MS and MS + CRD; $^{\#\#\#\#}P < 0.0001$ between CON + CRD and MS + CRD. **(B–D)** Immunostaining of thin sections of spinal cord against EphB2 (red) and the phosphorylated forms of p38, ERK, or JNK (green). Scale bar, 50 μm. The boxed regions in the large images are shown at higher magnification on the *far right* ("Zoom"). **(E)** Co-expression of spinal EphB2 and MAPKs. Based on one-way ANOVA and the Bonferroni multiple-comparisons test: $^{*}P < 0.05$, $^{***}P < 0.001$ between CON and MS. **(F)** Proportion of spinal cord cells expressing each activated MAP kinase that also expressed EphB2 (*left plot*) or proportion of spinal cord cells expressing EphB2 that also expressed each of the phosphorylated MAP kinases (*right plot*).

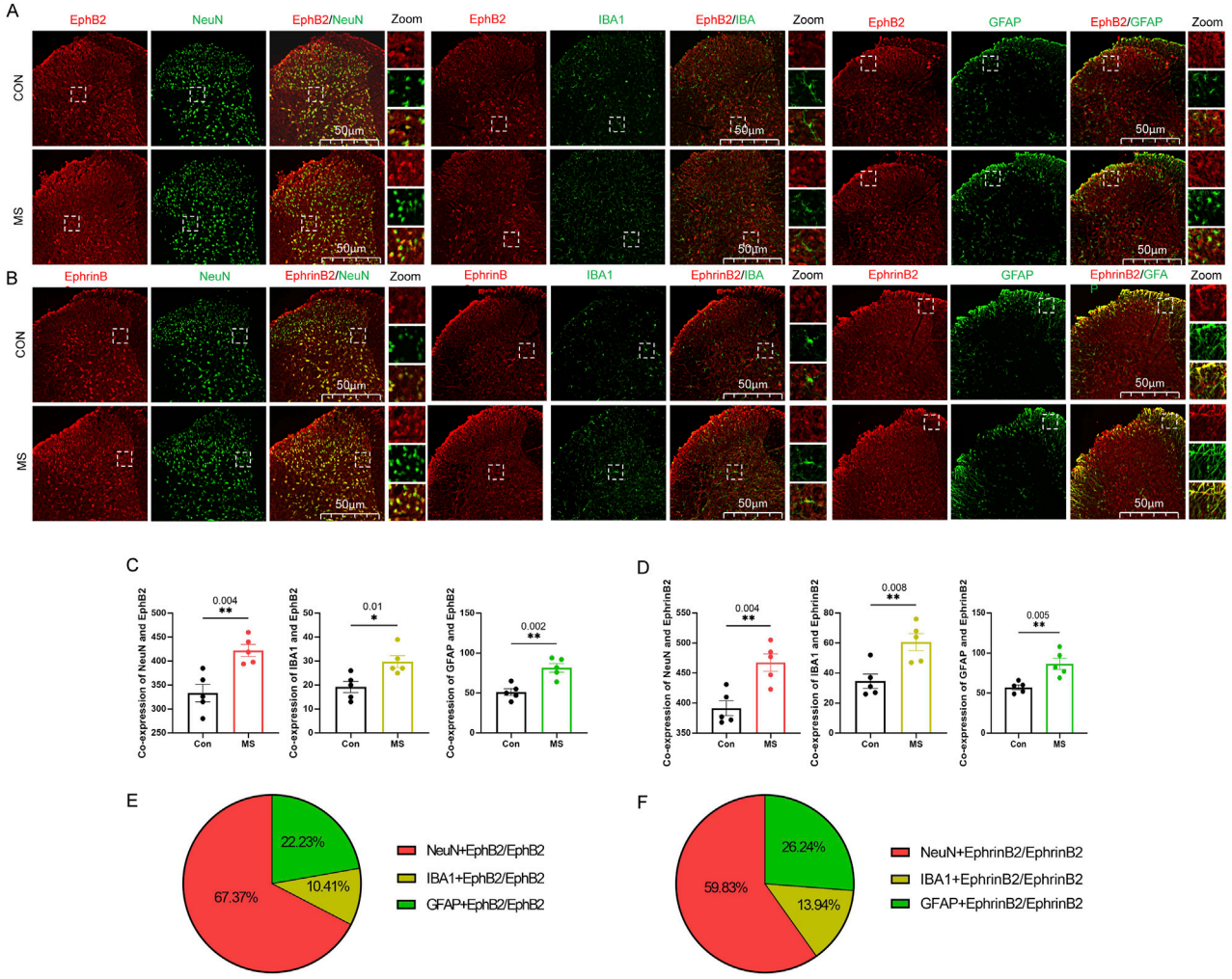

FIGURE 3
Expression of EphrinB2 and EphB2 in neurons, astrocytes and microglia in spinal cord. **(A, B)** Mice that with (MS) or without (Con) experienced maternal separation were subjected to colorectal distension, then the spinal cord was thin-sectioned and immunostained against EphB2 **(A)** or EphrinB2 **(B)** and a marker for neurons (NeuN), activated microglia (Iba1), or astrocytes (GFAP). Scale bar, 50 μm. The boxed regions in the large images are shown at higher magnification on the *far right* ("Zoom"). **(C, D)** Co-expression of spinal EphB2 or EphrinB2 and NeuN, Iba1or GFAP. Based on one-way ANOVA and the Bonferroni multiple-comparisons test: *P < 0.05, **P < 0.01 between CON and MS. **(E, F)** The proportion of EphB2 **(E)** or EphrinB2**(F)** activation in neurons (NeuN), microglia (Iba1), or astrocytes (GFAP).

key cell types in the dorsal horn of the spine: neurons, which we identified based on immunostaining against NeuN; astrocytes, based on immunostaining against GFAP; and activated microglia, based on immunostaining against Iba1 in the dorsal horn at 60min (Figures 3A, B). We also observed that a small amount of EphB2 or EphrinB2 was activated in neurons, microglia or astrocytes in the control group, but the amount of co-expression was significantly lower than those in the MS group (Figures 3C, D). The proportion of EphB2 activation in neurons, microglia and astrocytes was 67.37%, 10.14% and 22.23%, respectively. While the proportion of EphrinB2 activation in neurons, microglia and astrocytes was 59.83%, 13.94% and 26.24%, respectively (Figures 3E, F). These results suggest that visceral hyperalgesia induced by MS activates the EphrinB2/EphB2 signaling pathway in neurons and is accompanied by activation of this signaling pathway in microglia and astrocytes.

Inhibition of EphrinB2/EphB2 signaling mitigates the effects of maternal separation

All our experiments so far pointed to EphrinB2/EphB2 signaling as a driver of visceral hyperalgesia due to maternal separation. Consistent with this idea, pretreatment with repeated administration of EphB2-Fc (0.5-μg, i. t., daily for three consecutive days, see experimental protocol in Figure 4A) before CRD inhibited such signaling in mice that had experienced maternal separation mitigated their abdominal withdrawal reflex in response to colorectal distension (Figure 4B), while also downregulating c-fos (Figure 4C). In support of the reliability of our results, inhibiting EphrinB2/EphB2 signaling did not significantly alter the abdominal withdrawal reflex in mice that had not experienced maternal separation, nor did it alter c-fos expression in the absence of colorectal distension.

10.3389/fphar.2024.1463339

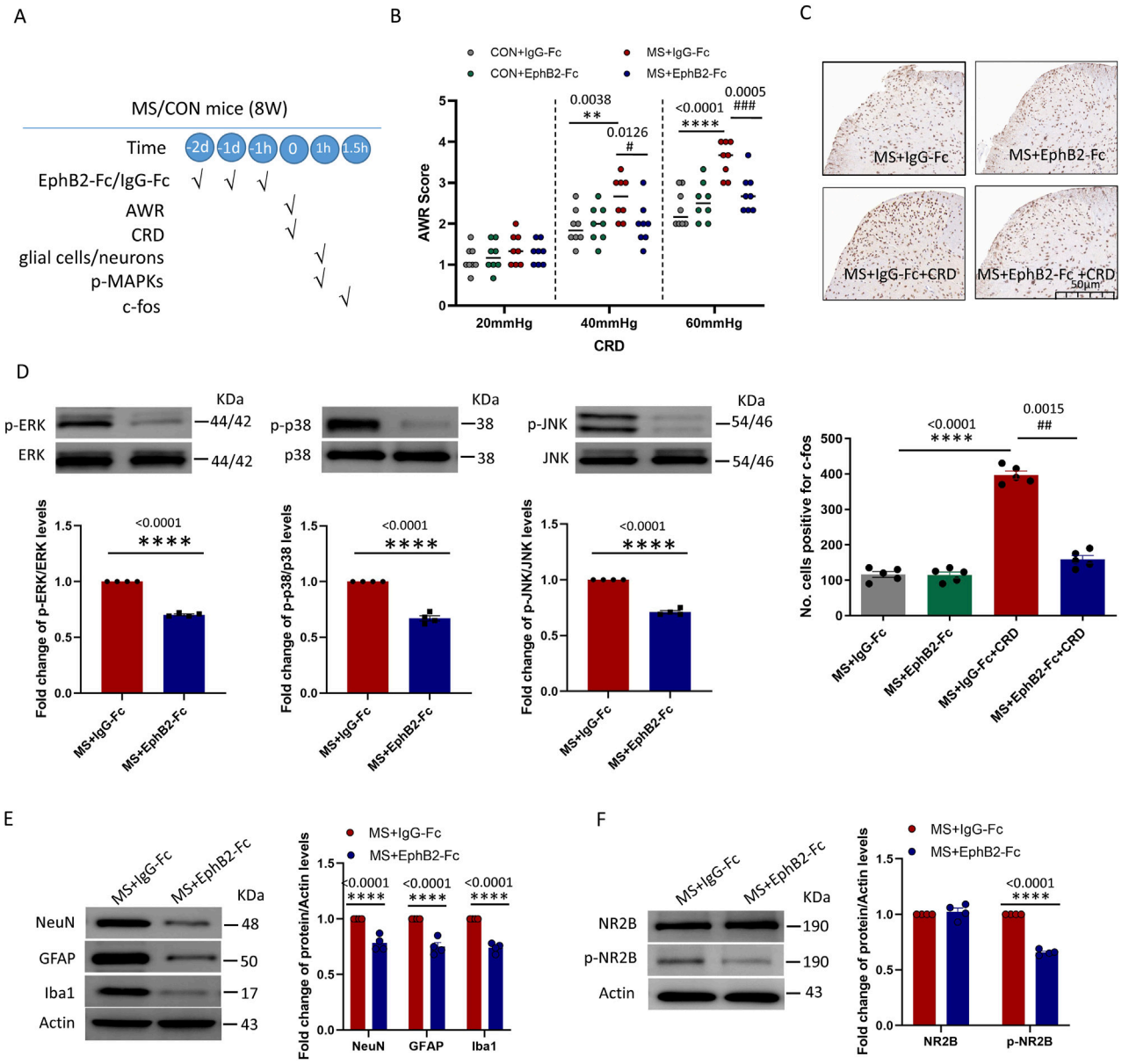

FIGURE 4
Inhibition of EphrinB2/EphB2 signaling mitigates the effects of maternal separation. **(A)** Schematic illustration of the experimental protocol. Mice were subjected to maternal separation (MS) early in development or not (CON), intrathecally injected with a chimera of EphB2 and Fc (EphB2-Fc) that inhibits EphB2 signaling or a negative-control chimera (IgG-Fc), then subjected to colorectal distension (CRD), during which the abdominal withdrawal reflex (AWR) was measured. Subsequently, the spinal cord was analyzed by Western blotting and immunohistochemistry to observe expression of key proteins. **(B)** AWR score during CRD. Quantification is shown for eight animals per condition. Based on two-way repeated-measure ANOVA and the Bonferroni multiple-comparisons test: $^{**}P < 0.01$, $^{****}P < 0.0001$ between CON + IgG-Fc and MS + IgG-Fc; $^{\#}P < 0.05$, $^{\#\#\#}P < 0.001$ between MS + IgG-Fc and MS + EphB2-Fc. **(C)** Representative micrographs of spinal cord tissue after immunostaining against c-fos and quantification of the number of cells expressing c-fos. We count the c-fos + neurons in lamine I-V of spinal cord of view at magnification x10 and average the results. Results are shown for five animals per condition. Scale bar, 50 μm. Based on one-way ANOVA and the Bonferroni multiple-comparisons test: $^{****}P < 0.0001$ between MS + IgG-Fc and MS + IgG-Fc + CRD; $^{\#\#}P < 0.01$ between MS + IgG-Fc + CRD and MS + EphB2-Fc + CRD. **(D–F)** Representative western blots of total lysate from spinal cord and quantification of **(D)** the active, phosphorylated forms of the MAP kinases ERK, p38 and JNK; **(E)** the cell type markers NeuN, GFAP and Iba1; or **(F)** NR2B and NR2B phosphorylated on Tyr1472. Levels of phosphorylated protein were normalized to those of the corresponding total protein, while levels of markers, NR2B or phospho-NR2B were normalized to those of Actin; the resulting relative protein levels in the MS+IgG-Fc group were defined as 1. Quantification is shown for four animals per condition. Based on unpaired t-test, $^{****}P < 0.0001$ compared with MS + IgG-Fc group.

These therapeutic effects of inhibiting EphrinB2/EphB2 signaling were associated with reduced activation of the three MAP kinases ERK, p38 and JNK in the spine (Figure 4D), as well as lower overall numbers of neurons, astrocytes, and activated microglia (Figure 4E). Given that the NMDA receptor appears to mediate at least some nociceptive signaling by EphrinB/EphB (Liu et al., 2013), we analyzed phosphorylation of the NMDA receptor subunit NR2B in the presence or absence of EphrinB2/

10.3389/fphar.2024.1463339

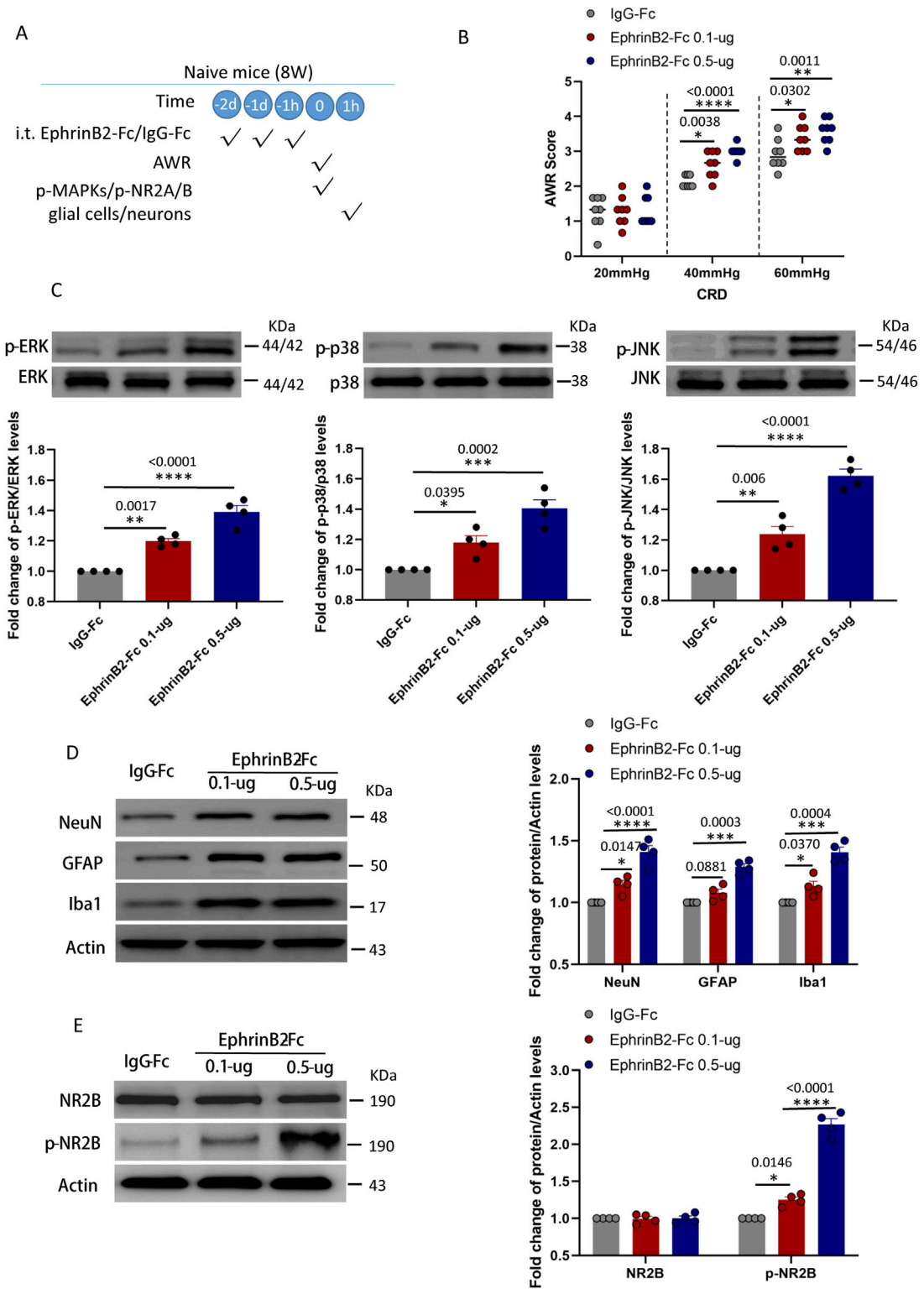

FIGURE 5
Activation of EphrinB2/EphB2 signaling reproduces the effects of maternal separation in naïve mice. **(A)** Schematic illustration of the experimental protocol. Mice that had not experienced maternal separation early in development were intrathecally injected with a chimera of EphrinB2 and Fc (EphB2-Fc) that activates EphB2 signaling or a negative-control chimera (IgG-Fc), then subjected to colorectal distension (CRD), during which the abdominal withdrawal reflex (AWR) was measured. Subsequently, the spinal cord was analyzed by Western blotting and immunohistochemistry to observe expression of key proteins. **(B)** AWR score during CRD. Quantification is shown for eight animals per condition. Based on two-way repeated-measure ANOVA and the Bonferroni multiple-comparisons test: $^{*}P < 0.05$, $^{**}P < 0.01$, $^{****}P < 0.0001$ vs IgG-Fc group. **(C)** Representative western blots of total lysate from spinal cord and quantification of the active, phosphorylated forms of the MAP kinases ERK, p38 and JNK. Levels of phosphorylated protein were normalized to those of the corresponding total protein, and the relative level of phosphorylated protein in the IgG-Fc group was defined as 1. Quantification is shown for four animals per condition. Based on one-way ANOVA and Bonferroni multiple comparisons test, $^{*}P < 0.05$, $^{**}P < 0.01$, $^{***}P <$ (*Continued*)

FIGURE 5 (Continued)
0.001, ****P < 0.0001 vs. IgG-Fc group, n = 4 mice in each group. **(D, E)** Representative western blots of total lysate from spinal cord and quantification of **(D)** the cell type markers NeuN, GFAP and Iba1; or **(E)** NR2B and NR2B phosphorylated on Tyr1472. Protein levels were normalized to those of Actin, and the relative protein level in the IgG-Fc group was defined as 1. Quantification is shown for four animals per condition. Based on one-way ANOVA and Bonferroni multiple comparisons test, *P < 0.05, ***P < 0.001, ****P < 0.0001 vs. IgG-Fc group.

EphB2 inhibition. Such inhibition partially reversed the phosphorylation of NR2B induced by colorectal distension, without affecting total levels of NR2B (Figure 4F).

These results support the idea that EphrinB2/EphB2 signaling helps mediate visceral hyperalgesia due to maternal separation, at least in part by stimulating the NMDA receptor.

Activation of EphrinB2/EphB2 signaling reproduces the effects of maternal separation in naïve mice

The above results suggested that the activation of endogenous EphB2 receptor promotes activation of glial cells and neurons, and produced viscera hyperalgesia after CRD in MS mice. NMDA receptor may contributed to the activation of glial cells and neurons in this process. A corollary of this idea is that activation of EphrinB2/EphB2 signaling should induce changes in naïve mice similar to those observed in animals that experienced maternal separation. We tested this idea by giving naïve mice exogenous EphrinB2 (0.1-μg or 0.5-μg, i. t., daily for three consecutive days, see experimental protocol in Figure 5A). As predicted, the resulting activation of EphrinB2/EphB2 signaling led to visceral hyperalgesia as measured following colorectal distension (Figure 5B), and in the spine it activated the three MAP kinases (Figure 5C); increased numbers of neurons, astrocytes and activated microglia (Figure 5D); and increased levels of phosphorylated NR2B and c-fos (Figure 5E), especially in the higher dose (EphrinB2-Fc 0.5-μg) group. These effects were stronger in animals given the higher dose of exogenous EphrinB2, indicating dose dependence.

These results strongly support a model of visceral hyperalgesia in which EphrinB2/EphB2 signaling in the spine acts *via* MAP kinases to alter interactions among neurons, microglia and astrocytes.

Discussion

Our work using an established mouse model of early life stress provides evidence of a pathway through which such stress can lead to visceral hyperalgesia later in life. Our experiments suggest a model in which hyperalgesia occurs when activation of EphrinB2/EphB2 signaling alters interactions between glia and neurons in the dorsal horn of the spine through mechanisms at least partly dependent on the NMDA receptor and downstream MAP kinases. Our findings highlight EphrinB2/EphB2 signaling and, more generally, glia-neuron interactions in the dorsal horn as potential therapeutic targets against visceral hyperalgesia arising from stress early in life.

EphrinB2/EphB2 signaling plays important roles in early development of the nervous system (Vasileiou et al., 2013), synaptic plasticity among neurons in the dorsal hone (Liu et al., 2013) and responses to injury (Steinle et al., 2002). At the same time, the signaling pathway contributes to various types of chronic pain (Zhou et al., 2015b; Liu et al., 2013) and, as we show here, to visceral hyperalgesia similar to that in functional gastrointestinal disorders.

We found that the activation of EphrinB2/EphB2 signaling associated with visceral hyperalgesia occurred in astrocytes, microglia cells and neurons in the spine, consistent with the fact that glia and neurons contribute to "central sensitization" in hyperalgesia (Ji et al., 2003; Sengupta, 2009). Indeed, spinal astrocytes and microglia interact with neurons *via* synapses (Song et al., 2014), so their interactions are likely key determinants of central sensitization. For example, activated glia release inflammatory mediators that induce excessive excitatory neuronal activity involving the NMDA receptor (Milligan and Watkins, 2009; Ernst et al., 2019). Activated neurons, for their part, release neurotransmitters that can stimulate glia (Tsuda et al., 2005). Our work justifies deeper analysis of these interactions and how they malfunction in functional gastrointestinal disorders.

We focused on the MAP kinases p38, JNK and ERK because all three are important second messengers in spinal cord during nociception (Zhuang et al., 2006; Poliakov et al., 2008a). *In vitro* studies revealed a dependent positive feedback loop between EphB2 receptors and the Ras-MAPK pathway, that is, EphB2 receptors activate the Ras-MAPK pathway, and the latter increases the amount of EphB2 activation through the dependent positive feedback loop (Liu et al., 2013). The activation of EphB2 is accompanied by the activation of ERK in DRG neurons after nerve injury, and intrathecal administration of EphB2 receptor blocker can inhibit nerve injury-induced pain and ERK activation (Ma et al., 2020; Poliakov et al., 2008b). In this study, we found that EphB2 receptor was highly co-expressed with the three MAPKs. It suggest that the stress caused by maternal separation stimulates EphrinB2/EphB2 signaling, which in turn activates MAP kinases. Moreover, EphrinBs binding to EphBs also induces direct extracellular interaction between EphB and NMDARs (Dalva et al., 2000), resulting in NMDAR aggregation and enhancement of NMDAR dependent Ca^{2+} flux (Takasu et al., 2002). EphB2 controls the function of NMDA receptors (Ma et al., 2020; Shao et al., 2023). Our results add visceral hyperalgesia to the contexts in which EphrinB2/EphB2 signaling has been shown to stimulate NMDA receptor activity.

Combined with our and others findings, we propose that in mice exposed to maternal separation, colorectal distension upregulates EphrinB2 in pre-synaptic neurons of the spine, which activates EphB2 in post-synaptic neurons (Figure 6). This activation turns on downstream MAP kinases in the neurons, altering gene expression, perhaps *via* the transcription factors CREB and c-fos. The altered gene expression may affect synapse formation and plasticity (Zhang et al., 2019). In parallel, activated EphB2 on post-synaptic neurons, perhaps acting *via* Src, may induce the NMDA receptor to import

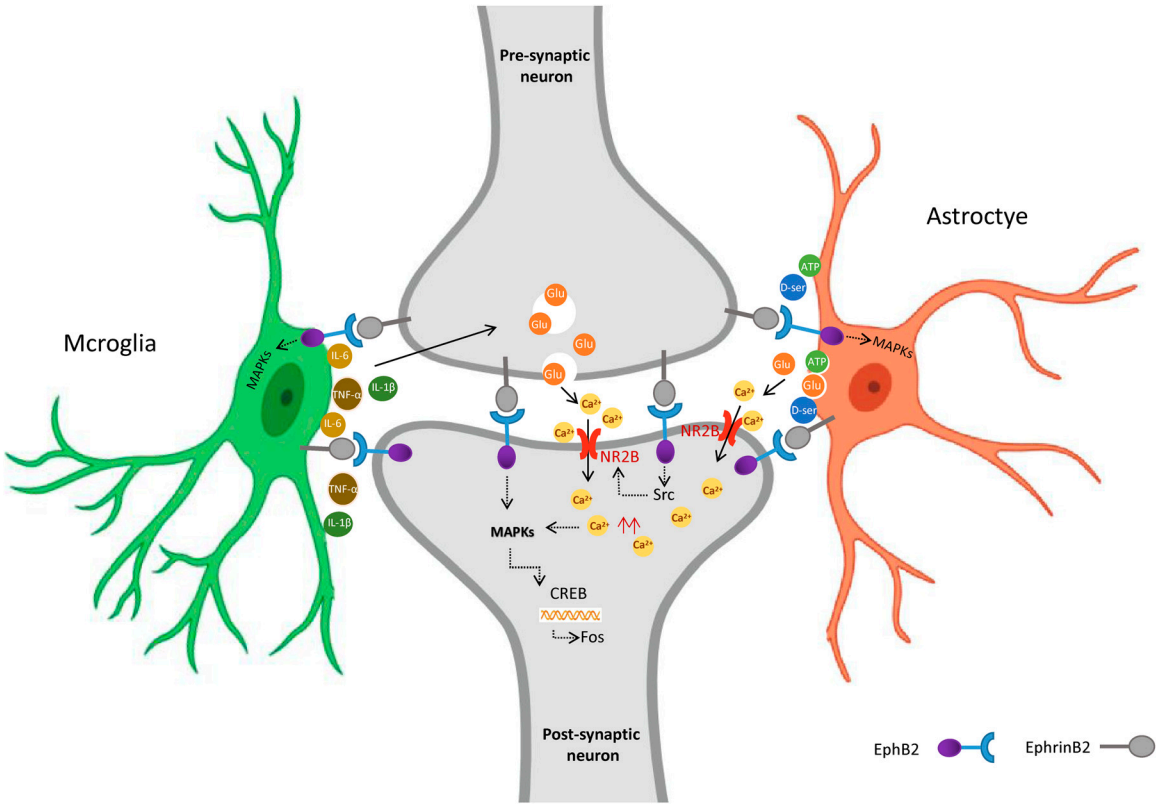

FIGURE 6
Proposed model for the role of EphrinB2/EphB2 signaling in visceral hyperalgesia due to stress in early life. Activation of spinal EphrinB2/EphB2 signaling alters glia-neuron interactions, which contributes to visceral hyperalgesia arising from the stress of earlier maternal separation. Upon activation of EphrinB2/EphB2 signaling, spinal astrocytes and microglia interact with neurons via synapses, activated glia release inflammatory mediators that induce excessive excitatory neuronal activity involving the NMDA receptor. Figure Created with BioRender.com.

Ca^{2+}, which stimulates MAP kinases. Given that astrocytes and microglia also express EphrinB2 and EphB2, they may form a "quadruple synapse" in which all 3 cell types interact. Upon activation of EphrinB2/EphB2 signaling, microglia may secrete inflammatory mediators that induce pre-synaptic neurons to release glutamate, which activates NMDA receptors in post-synaptic neurons. Astrocytes, for their part, may secrete gliotransmitters such as glutamate, ATP, and D-serine, which stimulate postsynaptic neuron excitation. Whether MAP kinases mediate some of these effects in microglia and astrocytes remains to be seen, but it seems possible in light of our finding that most MAP kinase activation occurred in spine cells in which EphB2 was upregulated.

The present study has several limitations. Firstly, only the model of visceral hyperalgesia in male mice established by mother separation was investigated, and the potential impact of gender differences on visceral pain within this model was not explored. Secondly, only the effects of blocking or activating EphrinB2/EphB2 on CRD-induced visceral hyperalgesia were assessed, and the potential effects of activating this signaling pathway on the intestinal nervous system and intestinal morphology were not examined. Thirdly, the effect of blocking microglia or astrocytes on neurons has not been explored and should be considered in future studies. Finally,the bidirectional signals of EphrinBs/EphBs were found to be involved in the pro-inflammatory reaction of endothelial cells and leukocytes (Liu et al., 2014). While the activation of EphrinB2 in spinal cord astrocytes played an important role in the pathological changes of amyotrophic lateral sclerosis (ALS) (Urban et al., 2024). Our study only investigated the role of the forward signal activated by the EphB2 receptor, not the role of the reverse signal caused by the activation of EphrinB2. Future studies should further investigate whether the activation of EphrinB2 reverse signaling is involved in visceral hyperalgesia and its mechanism.

Conclusion

Activation of EphrinB2/EphB2 signaling alters glia-neuron interactions in the spine, which contributes to visceral hyperalgesia arising from the stress of earlier maternal separation. Targeting EphrinB2/EphB2 signaling may be a promising approach for treating stress-induced visceral hyperalgesia in functional gastrointestinal disorders.

Data availability statement

The raw data supporting the conclusions of this article will be made available by the authors, without undue reservation.

Ethics statement

The animal study was approved by The Animal Ethics Committee at Nanjing Medical University. The study was conducted in accordance with the local legislation and institutional requirements.

Author contributions

SG: Data curation, Formal Analysis, Methodology, Software, Writing–original draft. YW: Data curation, Formal Analysis, Methodology, Software, Writing–original draft. QD: Formal Analysis, Methodology, Writing–original draft. WG: Investigation, Methodology, Writing–review and editing. QF: Investigation, Methodology, Writing–review and editing. ZM: Formal Analysis, Funding acquisition, Methodology, Supervision, Writing–review and editing. JR: Data curation, Formal Analysis, Funding acquisition, Methodology, Supervision, Validation, Writing–review and editing.

Funding

The author(s) declare that financial support was received for the research, authorship, and/or publication of this article. This research was supported by the National Natural Science Foundation of China (81971044) and Fundings for Special Project from the Affiliated Drum Tower Hospital, Medical School of Nanjing University (RC2021-006).

Conflict of interest

The authors declare that the research was conducted in the absence of any commercial or financial relationships that could be construed as a potential conflict of interest.

Publisher's note

All claims expressed in this article are solely those of the authors and do not necessarily represent those of their affiliated organizations, or those of the publisher, the editors and the reviewers. Any product that may be evaluated in this article, or claim that may be made by its manufacturer, is not guaranteed or endorsed by the publisher.

Supplementary material

The Supplementary Material for this article can be found online at: https://www.frontiersin.org/articles/10.3389/fphar.2024.1463339/full#supplementary-material

References

Bundesen, L. Q., Scheel, T. A., Bregman, B. S., and Kromer, L. F. (2003). Ephrin-B2 and EphB2 regulation of astrocyte-meningeal fibroblast interactions in response to spinal cord lesions in adult rats. *J. Neurosci.* 23 (21), 7789–7800. doi:10.1523/JNEUROSCI.23-21-07789.2003

Cao, J. L., Ruan, J. P., Ling, D. Y., Guan, X. H., Bao, Q., Yuan, Y., et al. (2008). Activation of peripheral ephrinBs/EphBs signaling induces hyperalgesia through a MAPKs-mediated mechanism in mice. *Pain* 139 (3), 617–631. doi:10.1016/j.pain.2008.06.023

Chen, T., Chen, S., Zheng, X., Zhu, Y., Huang, Z., Jia, L., et al. (2022). The pathological involvement of spinal cord EphB2 in visceral sensitization in male rats. *Stress* 25 (1), 166–178. doi:10.1080/10253890.2022.2054698

Chey, W. D., Kurlander, J., and Eswaran, S. (2015). Irritable bowel syndrome: a clinical review. *Jama* 313 (9), 949–958. doi:10.1001/jama.2015.0954

Coggeshall, R. E. (2005). Fos, nociception and the dorsal horn. *Prog. Neurobiol.* 77 (5), 299–352. doi:10.1016/j.pneurobio.2005.11.002

Dalva, M. B., Takasu, M. A., Lin, M. Z., Shamah, S. M., Hu, L., Gale, N. W., et al. (2000). EphB receptors interact with NMDA receptors and regulate excitatory synapse formation. *Cell* 103 (6), 945–956. doi:10.1016/s0092-8674(00)00197-5

Dodds, K. N., Beckett, E. A., Evans, S. F., Grace, P. M., Watkins, L. R., and Hutchinson, M. R. (2016). Glial contributions to visceral pain: implications for disease etiology and the female predominance of persistent pain. *Transl. Psychiatry* 6 (9), e888. doi:10.1038/tp.2016.168

Du, W. J., Hu, S., Li, X., Zhang, P. A., Jiang, X., Yu, S. P., et al. (2019). Neonatal maternal deprivation followed by adult stress enhances adrenergic signaling to advance visceral hypersensitivity. *Neurosci. Bull.* 35 (1), 4–14. doi:10.1007/s12264-018-0318-3

Duan, G. B., Wang, J. W., Sun, H. H., Dong, Z. Y., Zhang, Y., Wang, Z. X., et al. (2024). Overexpression of EphB2 in the basolateral amygdala is crucial for inducing visceral pain sensitization in rats subjected to water avoidance stress. *CNS Neurosci. Ther.* 30 (2), e14611. doi:10.1111/cns.14611

Ernst, A. S., Böhler, L. I., Hagenston, A. M., Hoffmann, A., Heiland, S., Sticht, C., et al. (2019). EphB2-dependent signaling promotes neuronal excitotoxicity and inflammation in the acute phase of ischemic stroke. *Acta Neuropathol. Commun.* 7 (1), 15. doi:10.1186/s40478-019-0669-7

Hu, S., Sun, Q., Du, W. J., Song, J., Li, X., Zhang, P. A., et al. (2020). Adult stress promotes purinergic signaling to induce visceral pain in rats with neonatal maternal deprivation. *Neurosci. Bull.* 36 (11), 1271–1280. doi:10.1007/s12264-020-00575-7

Ji, R. R., Berta, T., and Nedergaard, M. (2013). Glia and pain: is chronic pain a gliopathy? *Pain* 154 (1), S10–s28. doi:10.1016/j.pain.2013.06.022

Ji, R. R., Kohno, T., Moore, K. A., and Woolf, C. J. (2003). Central sensitization and LTP: do pain and memory share similar mechanisms? *Trends Neurosci.* 26 (12), 696–705. doi:10.1016/j.tins.2003.09.017

Kayser, M. S., McClelland, A. C., Hughes, E. G., and Dalva, M. B. (2006). Intracellular and trans-synaptic regulation of glutamatergic synaptogenesis by EphB receptors. *J. Neurosci.* 26 (47), 12152–12164. doi:10.1523/jneurosci.3072-06.2006

Klein, R., and Kania, A. (2014). Ephrin signalling in the developing nervous system. *Curr. Opin. Neurobiol.* 27, 16–24. doi:10.1016/j.conb.2014.02.006

Lauterbach, J., and Klein, R. (2006). Release of full-length EphB2 receptors from hippocampal neurons to cocultured glial cells. *J. Neurosci.* 26 (45), 11575–11581. doi:10.1523/jneurosci.2697-06.2006

Li, Y. C., Wang, Q., Li, M. G., Hu, S. F., and Xu, G. Y. (2023). A paraventricular hypothalamic nucleus input to ventral of lateral septal nucleus controls chronic visceral pain. *Pain* 164 (3), 625–637. doi:10.1097/j.pain.0000000000002750

Lim, B. K., Matsuda, N., and Poo, M. M. (2008). Ephrin-B reverse signaling promotes structural and functional synaptic maturation *in vivo*. *Nat. Neurosci.* 11 (2), 160–169. doi:10.1038/nn2033

Liu, H., Devraj, K., Möller, K., Liebner, S., Hecker, M., and Korff, T. (2014). EphrinB-mediated reverse signalling controls junctional integrity and pro-inflammatory differentiation of endothelial cells. *Thromb. Haemost.* 112 (1), 151–163. doi:10.1160/th13-12-1034

Liu, S., Liu, Y. P., Song, W. B., and Song, X. J. (2013). EphrinB-EphB receptor signaling contributes to bone cancer pain via Toll-like receptor and proinflammatory cytokines in rat spinal cord. *Pain* 154 (12), 2823–2835. doi:10.1016/j.pain.2013.08.017

Louwies, T., Ligon, C. O., Johnson, A. C., and Greenwood-Van Meerveld, B. (2019). Targeting epigenetic mechanisms for chronic visceral pain: a valid approach for the development of novel therapeutics. *Neurogastroenterol. Motil.* 31 (3), e13500. doi:10.1111/nmo.13500

Ma, P., Chen, P., Zhou, Z. L., Mo, R. F., Wu, M., and Song, X. J. (2020). Activation of EphB receptors contributes to primary sensory neuron excitability by facilitating Ca2+ influx directly or through Src kinase-mediated N-methyl-D-aspartate receptor phosphorylation. *Pain* 161 (7), 1584–1596. doi:10.1097/j.pain.0000000000001855

Milligan, E. D., and Watkins, L. R. (2009). Pathological and protective roles of glia in chronic pain. *Nat. Rev. Neurosci.* 10 (1), 23–36. doi:10.1038/nrn2533

Moloney, R. D., O'Mahony, S. M., Dinan, T. G., and Cryan, J. F. (2015). Stress-induced visceral pain: toward animal models of irritable-bowel syndrome and associated comorbidities. *Front. Psychiatry* 6, 15. doi:10.3389/fpsyt.2015.00015

Planagumà, J., Haselmann, H., Mannara, F., Petit-Pedrol, M., Grünewald, B., Aguilar, E., et al. (2016). Ephrin-B2 prevents N-methyl-D-aspartate receptor antibody effects on memory and neuroplasticity. *Ann. Neurol.* 80 (3), 388–400. doi:10.1002/ana.24721

Poliakov, A., Cotrina, M. L., Pasini, A., and DG %J The Journal of cell biology Wilkinson (2008a). Regulation of EphB2 activation and cell repulsion by feedback control of the MAPK pathway. *J. Cell Biol.* 183 (5), 933–947. doi:10.1083/jcb.200807151

Poliakov, A., Cotrina, M. L., Pasini, A., and Wilkinson, D. G. (2008b). Regulation of EphB2 activation and cell repulsion by feedback control of the MAPK pathway. *J. Cell Biol.* 183 (5), 933–947. doi:10.1083/jcb.200807151

Ruan, J. P., Zhang, H. X., Lu, X. F., and Liu, Y. P. (2010). EphrinBs/EphBs signaling is involved in modulation of spinal nociceptive processing through a mitogen-activated protein kinases-dependent mechanism. 112 (5):1234–1249. doi:10.1097/ALN.0b013e3181d3e0df

Sengupta, J. N. (2009). Visceral pain: the neurophysiological mechanism. *Handb. Exp. Pharmacol.* 194, 31–74. doi:10.1007/978-3-540-79090-7_2

Shao, Y., Cai, Y., Chen, T., Hao, K., Luo, B., Wang, X., et al. (2023). Impaired erythropoietin-producing hepatocellular B receptors signaling in the prefrontal cortex and hippocampus following maternal immune activation in male rats. *Genes Brain Behav.* 22, e12863. doi:10.1111/gbb.12863

Song, D. D., Li, Y., Tang, D., Huang, L. Y., and Yuan, Y. Z. (2014). Neuron-glial communication mediated by TNF-α and glial activation in dorsal root ganglia in visceral inflammatory hypersensitivity. *Am. J. Physiol. Gastrointest. Liver Physiol.* 306 (9), G788–G795. doi:10.1152/ajpgi.00318.2013

Song, X. J., Zheng, J. H., Cao, J. L., Liu, W. T., Song, X. S., and Huang, Z. J. (2008). EphrinB-EphB receptor signaling contributes to neuropathic pain by regulating neural excitability and spinal synaptic plasticity in rats. *Pain* 139 (1), 168–180. doi:10.1016/j.pain.2008.03.019

Steinle, J. J., Meininger, C. J., Forough, R., Wu, G., Wu, M. H., and Granger, H. J. (2002). Eph B4 receptor signaling mediates endothelial cell migration and proliferation via the phosphatidylinositol 3-kinase pathway. *J. Biol. Chem.* 277 (46), 43830–43835. doi:10.1074/jbc.M207221200

Takasu, M. A., Dalva, M. B., Zigmond, R. E., and Greenberg, M. E. (2002). Modulation of NMDA receptor-dependent calcium influx and gene expression through EphB receptors. *Science* 295 (5554), 491–495. doi:10.1126/science.1065983

Tsuda, M., Inoue, K., and Salter, M. W. (2005). Neuropathic pain and spinal microglia: a big problem from molecules in small glia. *Trends Neurosci.* 28 (2), 101–107. doi:10.1016/j.tins.2004.12.002

Urban, M. W., Charsar, B. A., Heinsinger, N. M., Markandaiah, S. S., Sprimont, L., Zhou, W., et al. (2024). EphrinB2 knockdown in cervical spinal cord preserves diaphragm innervation in a mutant SOD1 mouse model of ALS. *Elife* 12. doi:10.7554/eLife.89298

Vasileiou, I., Adamakis, I., Patsouris, E., and Theocharis, S. (2013). Ephrins and pain. *Expert Opin. Ther. Targets* 17 (8), 879–887. doi:10.1517/14728222.2013.801456

Wu, J., Lu, B., Yang, R., Chen, Y., Chen, X., and Li, Y. (2021). EphB2 knockdown decreases the formation of astroglial-fibrotic scars to promote nerve regeneration after spinal cord injury in rats. *CNS Neurosci. Ther.* 27 (6), 714–724. doi:10.1111/cns.13641

Zhang, L., Wang, R., Bai, T., Xiang, X., Qian, W., Song, J., et al. (2019). EphrinB2/ephB2-mediated myenteric synaptic plasticity: mechanisms underlying the persistent muscle hypercontractility and pain in postinfectious IBS. *Faseb J.* 33 (12), 13644–13659. doi:10.1096/fj.201901192R

Zhou, X. L., Wang, Y., Zhang, C. J., Yu, L. N., Cao, J. L., and Yan, M. J. N. (2015a). PKA is required for the modulation of spinal nociceptive information related to ephrinB-EphB signaling in mice. 284:546–554. doi:10.1016/j.neuroscience.2014.10.025

Zhou, X. L., Zhang, C. J., Wang, Y., Wang, M., Sun, L. H., Yu, L. N., et al. (2015b). EphrinB-EphB signaling regulates spinal pain processing via PKCγ. *Neuroscience* 307, 64–72. doi:10.1016/j.neuroscience.2015.08.048

Zhuang, Z. Y., Wen, Y. R., Zhang, D. R., Borsello, T., Bonny, C., Strichartz, G. R., et al. (2006). A peptide c-Jun N-terminal kinase (JNK) inhibitor blocks mechanical allodynia after spinal nerve ligation: respective roles of JNK activation in primary sensory neurons and spinal astrocytes for neuropathic pain development and maintenance. *J. Neurosci.* 26 (13), 3551–3560. doi:10.1523/jneurosci.5290-05.2006

frontiers | Frontiers in Pharmacology

TYPE Correction
PUBLISHED 27 September 2024
DOI 10.3389/fphar.2024.1491784

OPEN ACCESS

EDITED AND REVIEWED BY
Song Zhang,
Shanghai Jiao Tong University, China

*CORRESPONDENCE
Jiaping Ruan,
495316355@qq.com
Zhengliang Ma,
mazhengliang1964@nju.edu.cn

†These authors have contributed equally to this work and share first authorship

‡These authors have contributed equally to this work and share last authorship

RECEIVED 05 September 2024
ACCEPTED 19 September 2024
PUBLISHED 27 September 2024

CITATION
Guo S, Wang Y, Duan Q, Gu W, Fu Q, Ma Z and Ruan J (2024) Corrigendum: Activation of EphrinB2/EphB2 signaling in the spine cord alters glia-neuron interactions in mice with visceral hyperalgesia following maternal separation.
Front. Pharmacol. 15:1491784.
doi: 10.3389/fphar.2024.1491784

Corrigendum: Activation of EphrinB2/EphB2 signaling in the spine cord alters glia-neuron interactions in mice with visceral hyperalgesia following maternal separation

Shufen Guo[1†], Yu Wang[1,2†], Qingling Duan[1], Wei Gu[2], Qun Fu[2], Zhengliang Ma[1,2*‡] and Jiaping Ruan[2*‡]

[1]Department of Anesthesiology, Nanjing Drum Tower Hospital Clinical College of Nanjing University of Chinese Medicine, Nanjing, Jiangsu, China, [2]Department of Anesthesiology, Nanjing Drum Tower Hospital, Affiliated Hospital of Medical School, Nanjing University, Nanjing, Jiangsu, China

KEYWORDS

visceral hyperalgesia, maternal separation, ephrinB2/ephB2, glia-neuron, NMDA receptor

A Corrigendum on
Activation of EphrinB2/EphB2 signaling in the spine cord alters glia-neuron interactions in mice with visceral hyperalgesia following maternal separation

by Guo S, Wang Y, Duan Q, Gu W, Fu Q, Ma Z and Ruan J (2024). Front. Pharmacol. 15:1463339. doi: 10.3389/fphar.2024.1463339

In the published article, there was an error in Figure 1D as published. In Figure 1D "Actin" was incorrectly written as "GAPDH". The corrected Figure 1 and its caption appear below.

In the published article, there was an error in Figure 2E as published. The ordinate "Co-expression of p-JNK and EphB2" in Figure 2E is missing. The corrected Figure 2 and its caption appear below.

In the published article, there was an error in Figures 4E, F as published. In Figures 4E, F "Actin" was incorrectly written as "GAPDH". The corrected Figure 4 and its caption appear below.

In the published article, there was an error in Figures 5D, E as published. In Figures 5D, E "Actin" was incorrectly written as "GAPDH". The corrected Figure 5 and its caption appear below.

The authors apologize for this error and state that this does not change the scientific conclusions of the article in any way. The original article has been updated.

10.3389/fphar.2024.1491784

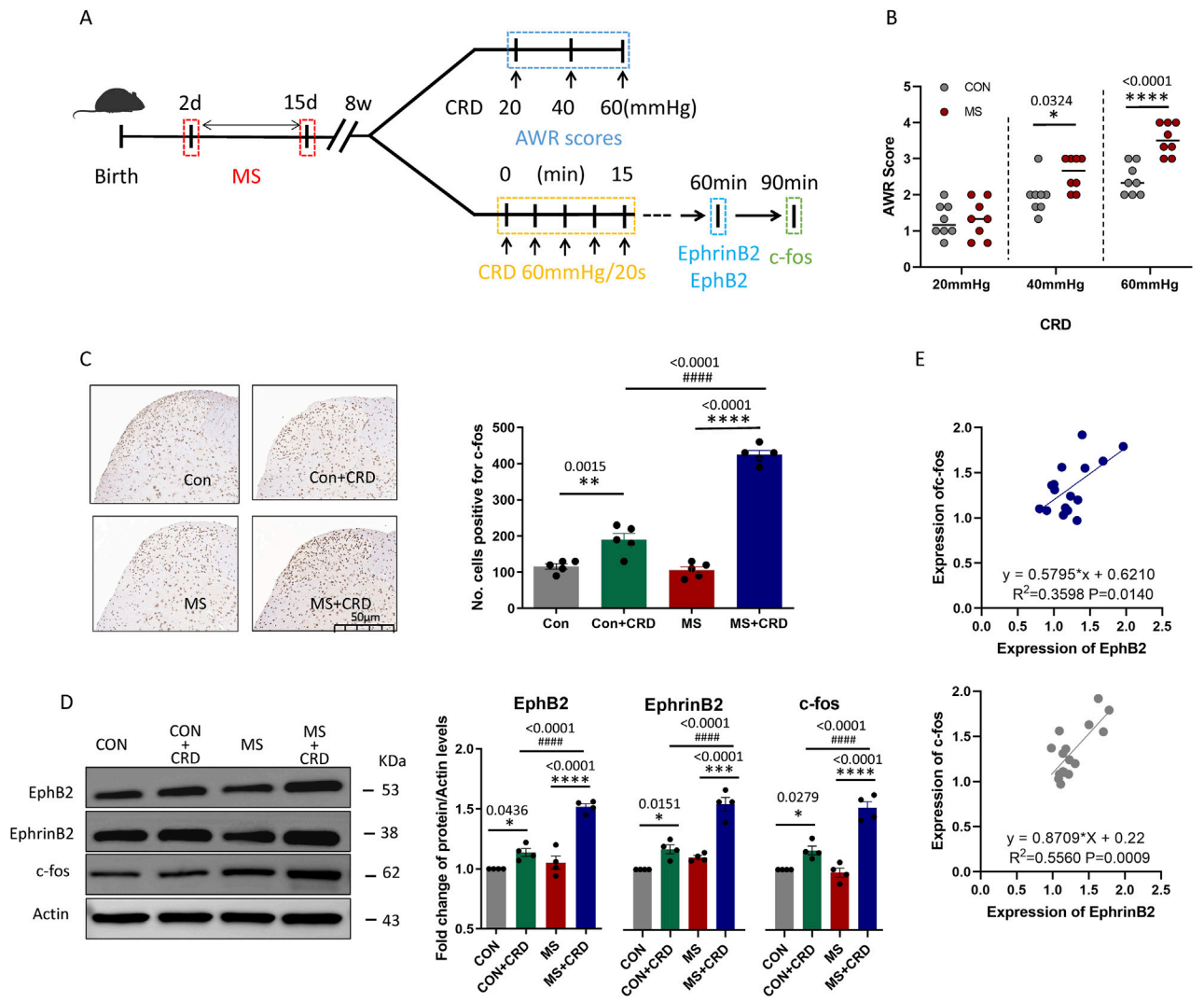

FIGURE 1
Maternal separation early in development causes visceral hyperalgesia in response to colorectal distension. **(A)** Schematic illustration of the experimental protocol. CRD, colorectal distension; MS, maternal separation **(B)** Score on abdominal withdrawal reflex after colorectal distension. Quantification is shown for eight animals per condition. CON, control. *$P < 0.05$, ****$P < 0.0001$ vs. CON, based on two-way repeated-measures ANOVA, followed by the Bonferroni multiple-comparisons test. **(C)** Representative thin sections of spinal cord after immunostaining against c-fos and quantification of cells expressing c-fos. CRD induced Fos protein expression in superficial lamine of spinal cord, we count the c-fos$^+$ neurons in lamine I-V of spinal cord of view at magnification ×10 and average the results. Results are shown for five animals per condition. Scale bar, 50 μm. Based on one-way ANOVA and the Bonferroni multiple-comparisons test: **$P < 0.01$, ****$P < 0.0001$ between CON and CON + CRD or between MS and MS + CRD; $^{\#\#\#\#}P < 0.0001$ between CON + CRD and MS + CRD. **(D)** Representative Western blotting of total lysate of spine tissue and quantification of EphB2 and EphrinB2. Protein levels were normalized to those of Actin in the same sample, and the relative protein level in the control group without CRD was defined as 1. Quantification is shown for four animals per treatment. Based on one-way ANOVA and the Bonferroni multiple-comparisons test: *$P < 0.05$, ****$P < 0.0001$ between CON and CON + CRD or between MS and MS + CRD; $^{\#\#\#\#}P < 0.0001$ between CON + CRD and MS + CRD. **(E)** Correlation between levels of c-fos and levels of EphB2 or EphrinB2 based on Western blotting of total lysates of spine tissue.

Publisher's note

10.3389/fphar.2024.1491784

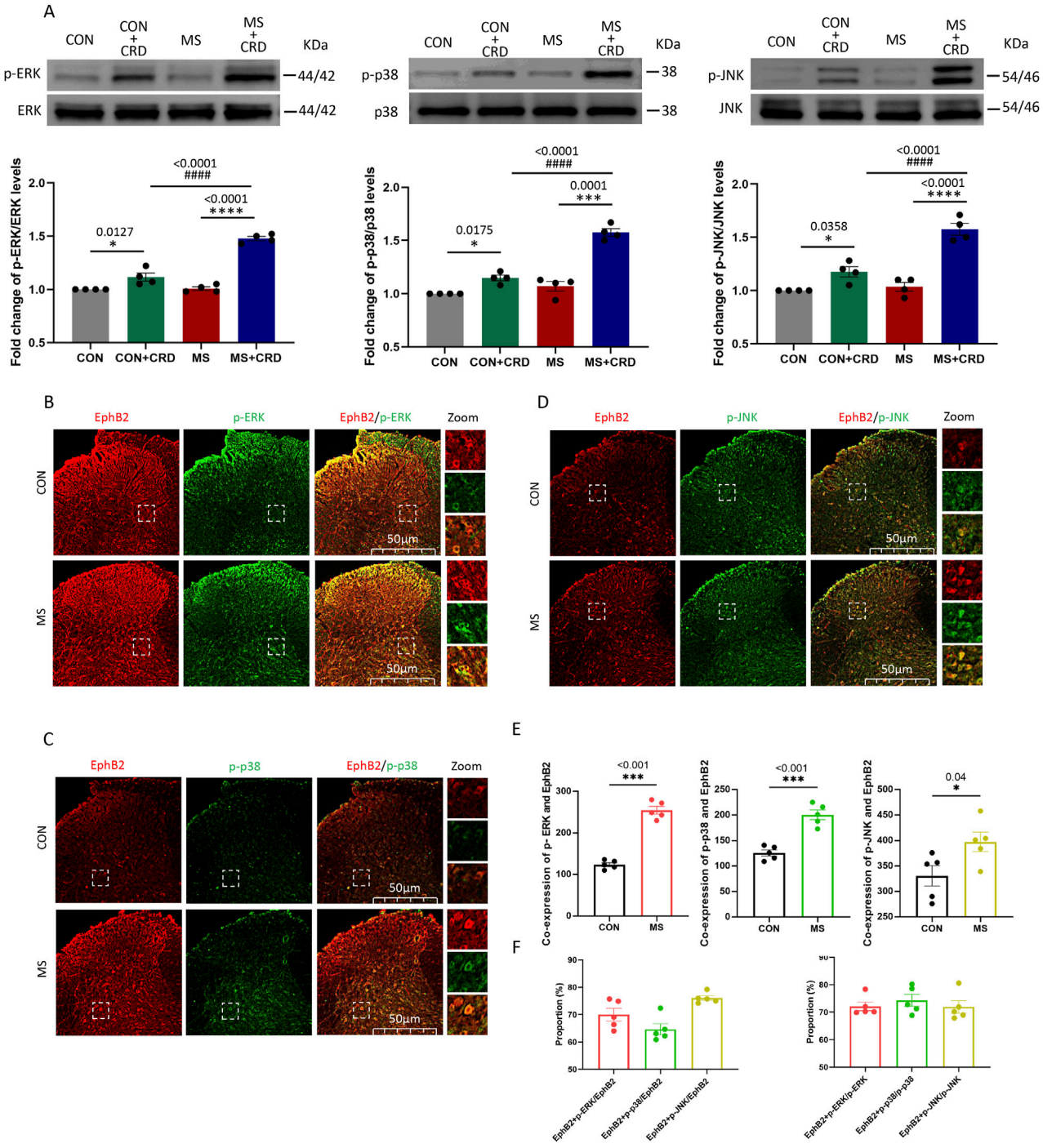

FIGURE 2
Visceral hyperalgesia in response to colorectal distension activates EphrinB2/EphB2 signaling and downstream MAP kinases. Mice were subjected to maternal separation (MS) early in development or not (CON), then later subjected to colorectal distension (CRD) or not. **(A)** Representative western blots of total lysate from spinal cord and quantification of the active, phosphorylated forms of the MAP kinases ERK, p38 and JNK. Levels of phosphorylated protein were normalized to those of the corresponding total protein, and the relative level of phosphorylated protein in the control group without CRD was defined as 1. Quantification is shown for four animals per condition. Based on one-way ANOVA and the Bonferroni multiple-comparisons test: $^{*}P < 0.05$, $^{****}p < 0.0001$ between CON and CON + CRD or between MS and MS + CRD; $^{\#\#\#\#}P < 0.0001$ between CON + CRD and MS + CRD. **(B–D)** Immunostaining of thin sections of spinal cord against EphB2 (red) and the phosphorylated forms of p38, ERK, or JNK (green). Scale bar, 50 μm. The boxed regions in the large images are shown at higher magnification on the *far right* ("Zoom"). **(E)** Co-expression of spinal EphB2 and MAPKs. Based on one-way ANOVA and the Bonferroni multiple-comparisons test: $^{*}P < 0.05$, $^{***}P < 0.001$ between CON and MS. **(F)** Proportion of spinal cord cells expressing each activated MAP kinase that also expressed EphB2 (*left plot*) or proportion of spinal cord cells expressing EphB2 that also expressed each of the phosphorylated MAP kinases (*right plot*).

10.3389/fphar.2024.1491784

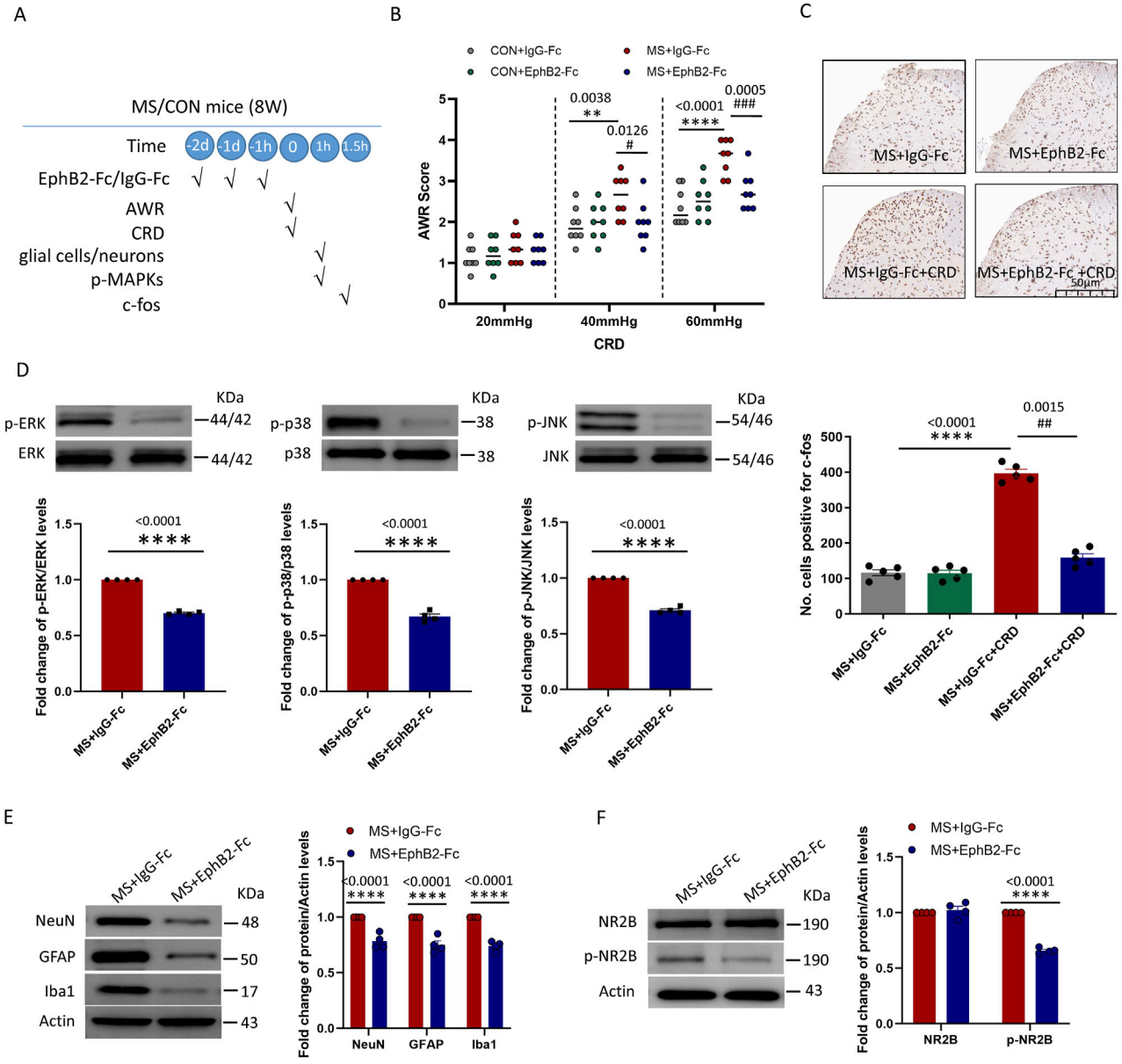

FIGURE 4
Inhibition of EphrinB2/EphB2 signaling mitigates the effects of maternal separation. **(A)** Schematic illustration of the experimental protocol. Mice were subjected to maternal separation (MS) early in development or not (CON), intrathecally injected with a chimera of EphB2 and Fc (EphB2-Fc) that inhibits EphB2 signaling or a negative-control chimera (IgG-Fc), then subjected to colorectal distension (CRD), during which the abdominal withdrawal reflex (AWR) was measured. Subsequently, the spinal cord was analyzed by Western blotting and immunohistochemistry to observe expression of key proteins. **(B)** AWR score during CRD. Quantification is shown for eight animals per condition. Based on two-way repeated-measure ANOVA and the Bonferroni multiple-comparisons test: $^{**}P < 0.01$, $^{****}P < 0.0001$ between CON + IgG-Fc and MS + IgG-Fc; $^{\#}P < 0.05$, $^{\#\#\#}P < 0.001$ between MS + IgG-Fc and MS + EphB2-Fc. **(C)** Representative micrographs of spinal cord tissue after immunostaining against c-fos and quantification of the number of cells expressing c-fos. We count the c-fos + neurons in lamine I-V of spinal cord of view at magnification x10 and average the results. Results are shown for five animals per condition. Scale bar, 50 μm. Based on one-way ANOVA and the Bonferroni multiple-comparisons test: $^{****}P < 0.0001$ between MS + IgG-Fc and MS + IgG-Fc + CRD; $^{\#\#}P < 0.01$ between MS + IgG-Fc + CRD and MS + EphB2-Fc + CRD. **(D–F)** Representative western blots of total lysate from spinal cord and quantification of **(D)** the active, phosphorylated forms of the MAP kinases ERK, p38 and JNK; **(E)** the cell type markers NeuN, GFAP and Iba1; or **(F)** NR2B and NR2B phosphorylated on Tyr1472. Levels of phosphorylated protein were normalized to those of the corresponding total protein, while levels of markers, NR2B or phospho-NR2B were normalized to those of Actin; the resulting relative protein levels in the MS+IgG-Fc group were defined as 1. Quantification is shown for four animals per condition. Based on unpaired t-test, $^{****}P < 0.0001$ compared with MS + IgG-Fc group.

10.3389/fphar.2024.1491784

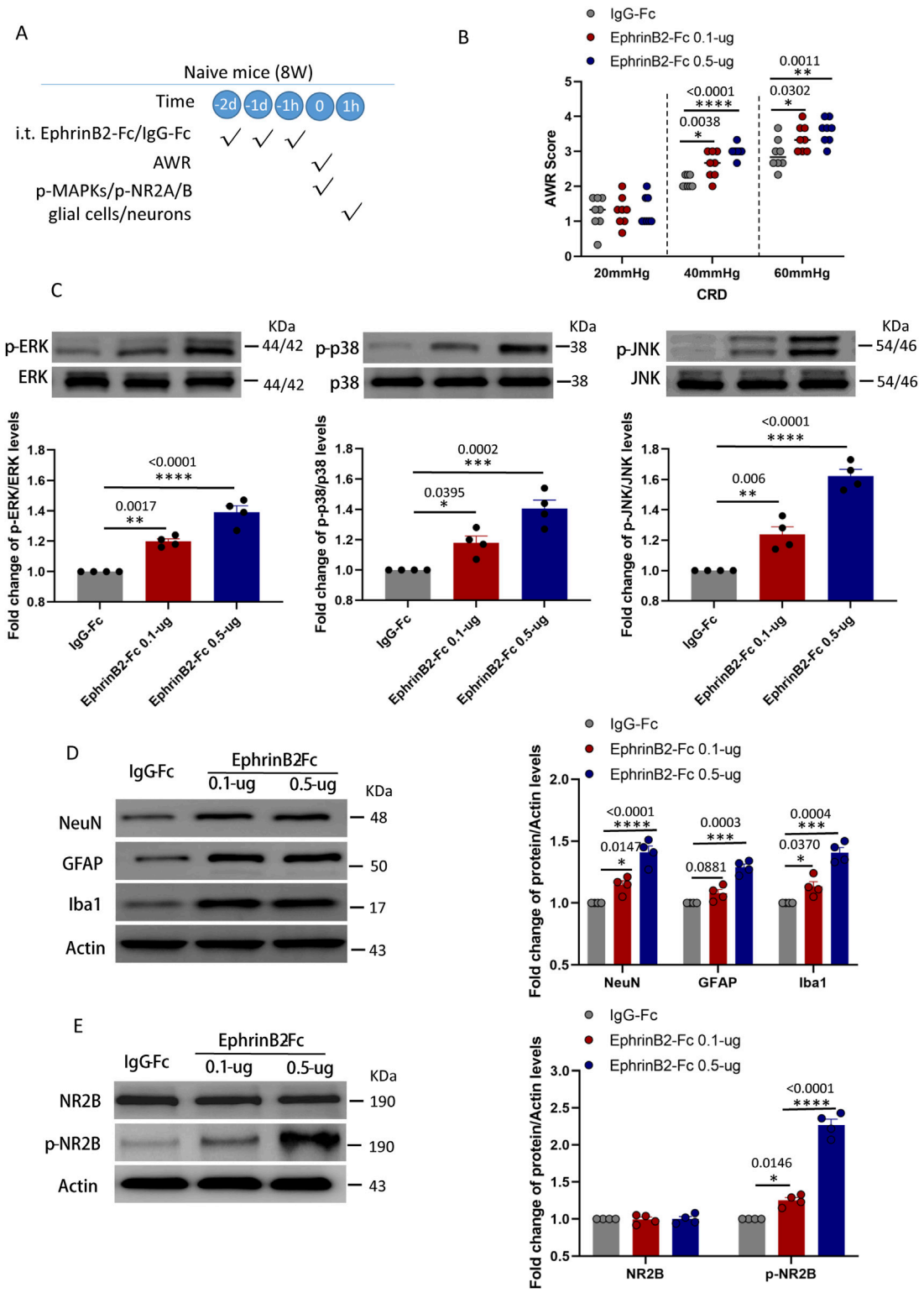

FIGURE 5
Activation of EphrinB2/EphB2 signaling reproduces the effects of maternal separation in naïve mice. **(A)** Schematic illustration of the experimental protocol. Mice that had not experienced maternal separation early in development were intrathecally injected with a chimera of EphrinB2 and Fc (EphB2-Fc) that activates EphB2 signaling or a negative-control chimera (IgG-Fc), then subjected to colorectal distension (CRD), during which the abdominal withdrawal reflex (AWR) was measured. Subsequently, the spinal cord was analyzed by Western blotting and immunohistochemistry to observe expression of key proteins. **(B)** AWR score during CRD. Quantification is shown for eight animals per condition. Based on two-way repeated-measure ANOVA and the Bonferroni multiple-comparisons test: $^{*}P < 0.05$, $^{**}P < 0.01$, $^{****}P < 0.0001$ vs IgG-Fc group. **(C)** Representative western blots of total lysate from spinal cord and quantification of the active, phosphorylated forms of the MAP kinases ERK, p38 and JNK. Levels of phosphorylated protein
(*Continued*)

FIGURE 5 (Continued)
were normalized to those of the corresponding total protein, and the relative level of phosphorylated protein in the IgG-Fc group was defined as 1. Quantification is shown for four animals per condition. Based on one-way ANOVA and Bonferroni multiple comparisons test, *$P < 0.05$, **$P < 0.01$, ***$P < 0.001$, ****$P < 0.0001$ vs. IgG-Fc group, n = 4 mice in each group. **(D, E)** Representative western blots of total lysate from spinal cord and quantification of **(D)** the cell type markers NeuN, GFAP and Iba1; or **(E)** NR2B and NR2B phosphorylated on Tyr1472. Protein levels were normalized to those of Actin, and the relative protein level in the IgG-Fc group was defined as 1. Quantification is shown for four animals per condition. Based on one-way ANOVA and Bonferroni multiple comparisons test, *$P < 0.05$, ***$P < 0.001$, ****$P < 0.0001$ vs. IgG-Fc group.

frontiers | Frontiers in Pharmacology

TYPE Original Research
PUBLISHED 27 September 2024
DOI 10.3389/fphar.2024.1429177

OPEN ACCESS

EDITED BY
Weijie Xie,
Tongji University, China

REVIEWED BY
Peijun Ju,
Shanghai Mental Health Center, China
Shuang Wang,
Zhejiang University, China
Jing Ding,
Fudan University, China

*CORRESPONDENCE
Yong Hao,
yhao23@126.com
Yangtai Guan,
yangtaiguan@sina.com

†These authors have contributed equally to this work and share first authorship

RECEIVED 07 May 2024
ACCEPTED 13 September 2024
PUBLISHED 27 September 2024

CITATION
Xue C, Wang Y, Peng J, Feng S, Guan Y and Hao Y (2024) Unraveling the pathogenic mechanism of a novel filamin a frameshift variant in periventricular nodular heterotopia. *Front. Pharmacol.* 15:1429177. doi: 10.3389/fphar.2024.1429177

Unraveling the pathogenic mechanism of a novel filamin a frameshift variant in periventricular nodular heterotopia

Chunran Xue[1†], Yishu Wang[1†], Jing Peng[1†], Sisi Feng[2], Yangtai Guan[3*] and Yong Hao[1*]

[1]Department of Neurology, Renji Hospital, Shanghai Jiaotong University School of Medicine, Shanghai, China, [2]State Key Laboratory of Cell Biology, CAS Center for Excellence in Molecular Cell Science, Institute of Biochemistry and Cell Biology, University of Chinese Academy of Sciences, Chinese Academy of Sciences, Shanghai, China, [3]Department of Neurology, Punan Branch, Renji Hospital, Shanghai Jiaotong University School of Medicine, Shanghai, China

Background: Periventricular nodular heterotopia (PVNH) is a neuronal migration disorder caused by the inability of neurons to move to the cortex. Patients with PVNH often experience epilepsy due to ectopic neuronal discharges. Most cases of PVNH are associated with variations in filamin A (*FLNA*), which encodes an actin-binding protein. However, the underlying pathological mechanisms remain unclear.

Methods: Next-generation sequencing was performed to detect variants in the patient with PVNH, and the findings were confirmed using Sanger sequencing. Iterative threading assembly refinement was used to predict the structures of the variant proteins, and the search tool for the retrieval of interacting genes/proteins database was used to determine the interactions between FLNA and motility-related proteins. An induced pluripotent stem cell (iPSC) line was generated as a disease model by reprogramming human peripheral blood mononuclear cells. The FLNA expression in iPSCs was assessed using western blot and quantitative real-time polymerase chain reaction (qRT-PCR). Immunofluorescence analysis was performed to determine the arrangement of F-actin.

Results: A novel *FLNA* frameshift variant (NM_001456.3: c.1466delG, p. G489Afs*9) was identified in a patient with PVNH and epilepsy. Bioinformatic analysis indicated that this variation was likely to impair FLNA function. Western blot and qRT-PCR analysis of iPSCs derived from the patient's peripheral blood mononuclear cells revealed the absence of FLNA protein and mRNA. Immunofluorescence analysis suggested an irregular arrangement and disorganization of F-actin compared to that observed in healthy donors.

Conclusion: Our findings indicate that the frameshift variant of *FLNA* (NM_001456.3: c.1466delG, p. G489Afs*9) impairs the arrangement and organization of F-actin, potentially influencing cell migration and causing PVNH.

KEYWORDS

filamin A, periventricular nodular heterotopia, epilepsy, induced pluripotent stem cell, f-actin

1 Introduction

Periventricular nodular heterotopia (PVNH) is a neuronal migration disorder characterized by the inability of neurons to move from the periventricular region to the cortex during cortical formation (Sarkisian, et al., 2008; Sheen, et al., 2001), resulting in the abnormal distribution of neuronal nodules along the ventricles. Multiple genetic mutations are associated with PVNH, with filamin A (*FLNA*)-associated PVNH being the most common type (Sarkisian et al., 2008). Knockdown of *FLNA* in rats impairs neuronal migration, leading to increased susceptibility to seizures, highlighting the key role of *FLNA* in the pathogenesis of PVNH (Carabalona, et al., 2012).

The *FLNA* is located on the X chromosome and encodes an actin-binding protein. The relationship between *FLNA* and F-actin was demonstrated in 2001 using *FLNA*-deficient human melanoma cells (Flanagan, et al., 2001). These *FLNA*-deficient human melanoma cells exhibited different actin organization and were unable to maintain surface stabilization and support movement (Flanagan et al., 2001). Thus, it was hypothesized that cells without *FLNA* lose the ability to migrate from the lateral ventricle to the cerebral cortex because of the effect of the orthogonal actin network, and several studies have supported this deduction (Welter, et al., 2020; Hu, et al., 2017). Additionally, *FLNA*-deficient human seminoma cells exhibited irregular organization of F-actin and impaired cell motility (Welter et al., 2020). Another study demonstrated that the loss of *FLNA* in chondrocytes reduced F-actin fiber formation (Hu et al., 2017). However, the exact pathogenic mechanism underlying *FLNA*-associated PVNH and the relationship between *FLNA* and F-actin in PVNH remain unclear.

In addition to its role as an actin-binding protein, FLNA functions as a signaling protein by binding to numerous cellular components, including enzymes and channels, and modulating their activity (Nakamura, et al., 2011; van der Flier and Sonnenberg, 2001). For example, FLNA phosphorylation promotes golgi-to-lipid stripe rearrangement of Big two to activate Big 2-dependent adenosine diphosphate-ribosylation factor 1 at the cell membrane (Zhang, et al., 2013), which is required for cell migration and adhesion (Heuvingh, et al., 2007). Thus, the *FLNA* variant may also affect interactive proteins related to cell motility and further impair cell migration.

Over the past 2 decades, various *FLNA* variants have been identified in PVNH, including single-nucleotide variants, indels, and submicroscopic genomic copy number variations, with both familial and sporadic cases reported (Liu, et al., 2017; Parrini, et al., 2006). Patients with *FLNA*-associated PVNH often experience seizures (Sarkisian et al., 2008), though their intelligence and cognition are often normal (Lange, et al., 2015). Some individuals may present with extracerebral manifestations, including cardiovascular abnormalities, connective tissue disorders, and pulmonary hypoplasia (Gómez-Garre, et al., 2006; Lange et al., 2015; Masurel-Paulet, et al., 2011). Except for heterotopic nodules with periventricular distribution, magnetic resonance imaging (MRI) may reveal an enlarged cerebrospinal fluid space around the cerebellum, with normal cerebellar and fourth ventricle anatomy (Lange et al., 2015; Liu et al., 2017). Other brain malformations, such as corpus callosum hypoplasia and lateral deformation of the anterior horns, are also observed in some patients (Lange et al., 2015).

Herein, we report a novel frameshift variant in a patient with sporadic PVNH and epilepsy. Bioinformatics analysis revealed that this variant may be pathogenic. Peripheral blood mononuclear cells (PBMCs) were obtained from the patient and reprogrammed to generate an induced pluripotent stem cell (iPSC) line. Western blot (WB) and quantitative real-time polymerase chain reaction (qRT-PCR) results revealed the absent expression of FLNA in iPSCs derived from the patient. Furthermore, immunofluorescence analysis of iPSCs showed an irregular arrangement of F-actin in patient-derived iPSCs compared to that of healthy donor-derived iPSCs, providing an insight into the possible pathological mechanisms of *FLNA*-associated PVNH.

2 Materials and methods

2.1 Subjects

The patient was treated in the Department of Neurology, Ningbo Branch, Renji Hospital, Shanghai Jiao Tong University School of Medicine. The patient and her parents signed a consent form prior to participating in the study. The study was conducted in accordance with the Declaration of Helsinki and approved by the Medical Ethics Committee of Renji Hospital, Shanghai Jiao Tong University School of Medicine (KY 2022-074-B).

2.2 Genetic analysis

Next-generation sequencing (NGS) was performed to identify genetic variants. Briefly, DNA was isolated using Blood DNA Kit V2 (CW2553) following the manufacturer's instructions and sheared. The KAPA Library Preparation Kit (Kapa Biosystems, KR0453) was used to prepare the DNA library. NGS analyses were conducted using the SeqCap Mixed Partitioning System. Sanger sequencing was performed to validate this variant. These outcomes match those of previous NGS analyses.

2.3 Protein structure modeling and constructing protein-protein interaction (PPI) network

The tertiary structure of the variant was predicted using the iterative threading assembly refinement (I-TASSER) software. PyMOL Molecular Graphics software was used to display the three-dimensional structure of the protein. The search tool for the retrieval of interacting genes/proteins (STRING) database was used to construct the PPIs for FLNA and visualized using Cytoscape software (version 3.8.2).

2.4 Generation and validation of the patient-derived iPSC line

Peripheral blood mononuclear cells were isolated using density centrifugation. The isolated and cultivated PMBCs were transduced with non-integrating episomal vectors according to the manufacturer's protocol for the CytoTune-iPS 2.0 Sendai Reprogramming Kit (Thermo Fisher Scientific, Waltham, MA, United States). On Day 20, emergent stem cell colonies were manually selected, plated on Matrigel-coated plates, and multiplied in mTeSR1. When the cells reached 80% confluence, they were collected and seeded to evaluate their spontaneous differentiation. ADICON Clinical Laboratories Inc., Shanghai, China performed the karyotyping analysis.

2.5 Immunofluorescence staining

Cells were fixed in 4% paraformaldehyde for 15 min and incubated in phosphate-buffered saline (PBS) containing 5% bovine serum albumin (BSA) and 0.1% Triton X-100 for 30 min at room temperature. The cells were then treated with primary antibodies diluted in PBS containing 1% BSA overnight at 4°C, followed by an hour at room temperature with secondary antibodies. Cell nuclei were stained with 4′,6-diamidino-2-phenylindole (DAPI), and the cells were observed and photographed using a fluorescence microscope. The following antibodies were used: Pax6 (BD Biosciences), Brachyury (BD Biosciences, Franklin Lakes, NJ, United States), alpha-fetoprotein (AFP) (BD Biosciences), Phalloidin (APExBIO), and FLNA (Santa Cruz) were used for staining.

2.6 Flow cytometry

Single-cell suspensions were prepared, fixed, and permeabilized. Cells were stained for 30 min at 4°C with fluorochrome-conjugated antibodies, including phycoerythrin (PE) anti-stage-specific embryonic antigen-4 (SSEA-4), PE anti-octamer-binding transcription factor ¾ (OCT3/4), and PE anti-Nanog (BD Biosciences). Stained cells were analyzed using a FACSFortessa flow cytometer (BD Biosciences).

2.7 Western blot

The iPSCs were homogenized in lysis buffer containing protease inhibitors, placed on ice for 15 min, and centrifuged at 20,000 g for 15 min to isolate the protein supernatant. The supernatant was mixed with a 5-fold loading buffer, boiled for 10 min, resolved using sodium dodecyl sulfate-polyacrylamide gel electrophoresis on 10% gels (glyceraldehyde-3-phosphate dehydrogenase [GAPDH]) or 6% gels (FLNA) and blotted onto polyvinylidene fluoride membranes using a Mini-Trans-Blot system. The membranes were blocked with 5% BSA in tris-buffered saline Tween-20 for 1 h at room temperature and incubated with primary antibodies overnight at 4°C. The following day, the membranes were washed thrice, incubated with horseradish peroxidase (HRP)-conjugated secondary antibodies for 1 h at room temperature, and washed thrice. An enhanced chemiluminescence kit (Pierce, Apalachicola, KL, United States) was used to detect protein signals. The FLNA antibody (Santa Cruz, Dallas, TX, United States), GAPDH antibody (Proteintech, Rosemont, IL, United States), and HRP-conjugated mouse IgG antibody (Beyotime, Jiangsu, China) were used.

2.8 RNA extraction and qRT-PCR

RNA was extracted using an RNA kit from TIANGEN (Hebei, China) in accordance with the manufacturer's instructions and reverse-transcribed using GoScript Reverse Transcriptase (Promega, Madison, WI, United States). The ABI Q6 (Life Technologies) system and SYBR Green Master Mix (Roche, Basel, Switzerland) were used to conduct qRT-PCR according to the manufacturer's instructions. The primer sequences are listed in Table 1.

3 Results

3.1 Clinical history

The patient was a 26-year-old Chinese female with a history of epilepsy. She experienced two seizures at intervals of a year. Before the seizures, the patient felt dazed and lost consciousness with blue lips and a pale complexion, but no limb twitching. The seizures continued for approximately 5–6 min resolving spontaneously. The patient didn't exhibit developmental delay, cognitive impairment as well as psychiatric or behavioral abnormalities based on her statement and presentation. No perinatal injuries such as preterm labor or hypoxic-ischemic encephalopathy happened when she was born, but she experienced a febrile seizure at the age of one. No similar symptoms were observed in the patient's relatives. The patient was diagnosed with epilepsy based on epileptiform discharges detected during an ambulatory electroencephalogram (Figure 1A). To further identify the etiology, cranial MRI was conducted and revealed multiple abnormal signals along the lateral ventricle bilaterally, which indicated PVNH (Figures 1B, C). No obvious abnormalities were observed on Holter monitoring or cardiac ultrasonography.

3.2 Identification of a novel frameshift variant of *FLNA*

A heterozygous frameshift variant, c.1466delG, in *FLNA* was identified in the patient's PBMCs using NGS, leading to changes in the protein sequence p. G489Afs*9. Sanger sequencing confirmed the presence of this variant (Figure 2A), while it was absent in *FLNA* of her biological parents (Figures 2B, C). Thus, it was clearly a sporadic variant that has not been reported previously in the existing databases (PubMed, HGMDpro, gnomAD, and ClinVar). Additionally, the variation was rated as "pathogenic" according to the American College of Medical Genetics and Genomics guidelines.

TABLE 1 Primer sequences used in qRT-PCR.

Gene	Primer	Sequence (5′to 3′)	Targeting exons
FLNA	Primer 1-F	GGAAGAAGATCCAGCAGAACA	Exon 3
	Primer 1-R	CCTCCAACAGCGCGATAA	Exon 3
FLNA	Primer 2-F	GGAACCTGAAGCTGATCCTG	Exon 3
	Primer 2-R	TCTTGGCCTCCTCATCCT	Exon 3
FLNA	Primer 3-F	GTGATCAGCCAGTCGGAAAT	Exon 38
	Primer 3-R	TAAACTCTGCAGGCTCAAAGG	Exon 38
FLNA	Primer 4-F	GCGCTGCTTGTCTTCTTTG	Exon 48
	Primer 4-R	CTTTATTCCTCTTGGCTGGAGA	Exon 48

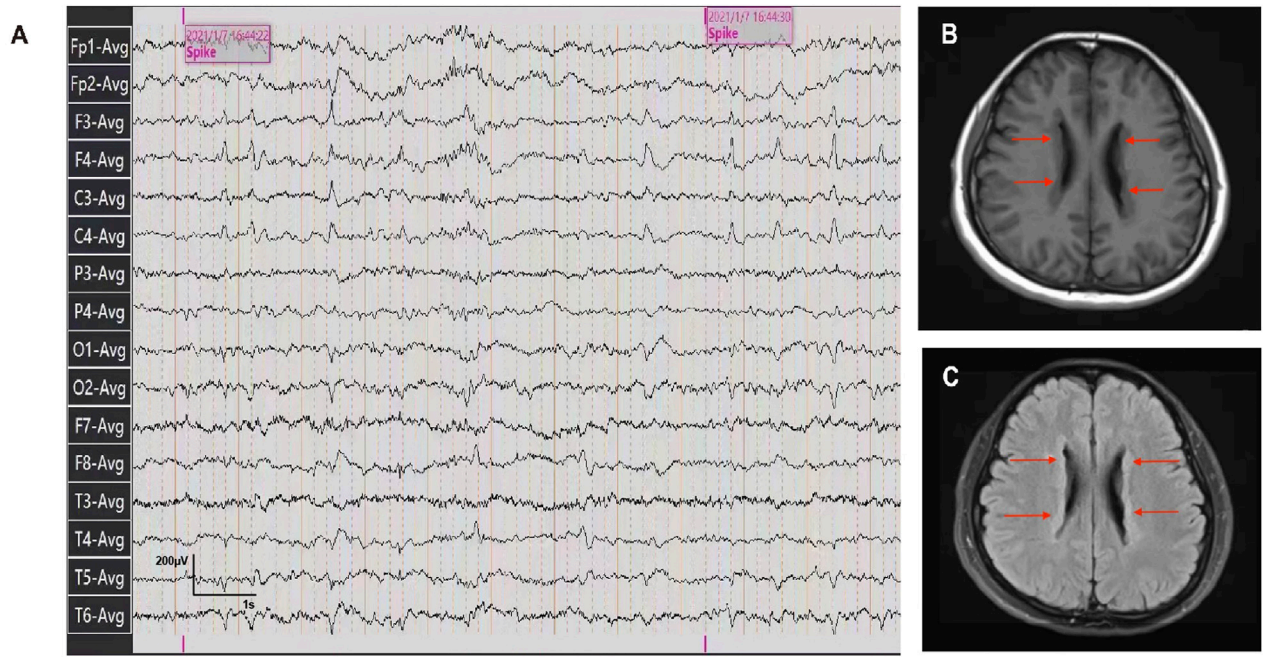

FIGURE 1
Ambulatory electroencephalogram and cranial MRI images of the patient. **(A)** Ambulatory electroencephalogram detected epileptiform discharges. **(B, C)** T1-weighted and T2 FLAIR images of the patient detected the bilateral periventricular nodular.

3.3 Structure analysis suggests loss of function in the variant FLNA

FLNA consists of one conserved actin-binding domain (ABD) and 24 repeat immunoglobulin-like domains (Zhou, et al., 2021) (Figure 3A). Two calpain-sensitive hinges segment the 24 domains into Rod1 (Reps. 1–15), Rod2 (Reps. 16–23), and Rep.24 (Zhou et al., 2021). The ABD domain, which contains two calponin homology sequences, facilitates actin binding (van der Flier and Sonnenberg, 2001). Rod1 is an extended chain, while Rod2 is more flexible and highly variable with a folded structure (Zhou et al., 2021). Rep.24 mediates the dimerization of FLNA (Nakamura, et al., 2007).

The deletion of this nucleotide results in a frameshift variant of *FLNA*, altering the 489th amino acid from glycine to alanine and introducing a premature stop codon. This results in the early termination of protein synthesis, leading to truncated protein length, from 2647 to 496 amino acids, significantly affecting structure and function. Based on the UniProt database, both the variant and termination sites of the protein were located in Rep. 3 (Figure 3B). The predicted overall structure of the wild-type FLNA in the AlphaFold Protein Structure Database is presented in Figure 3C, and the structure of the variant protein was predicted using I-TASSER (Figure 3D). Parts of Rod 1, Rod 2, and Rep. 24 are absent in the putative variant protein structure. The FLNA exists mainly as a homodimer that binds to F-actin, which is mediated by Rep. 24, as depicted in Figure 3A. Its function in binding to actin and affecting orthogonal branching relies on the formation of a homodimer, while the monomer does not function (Zhou et al., 2021). Therefore, the variant protein is likely to lose its original function due to structural changes.

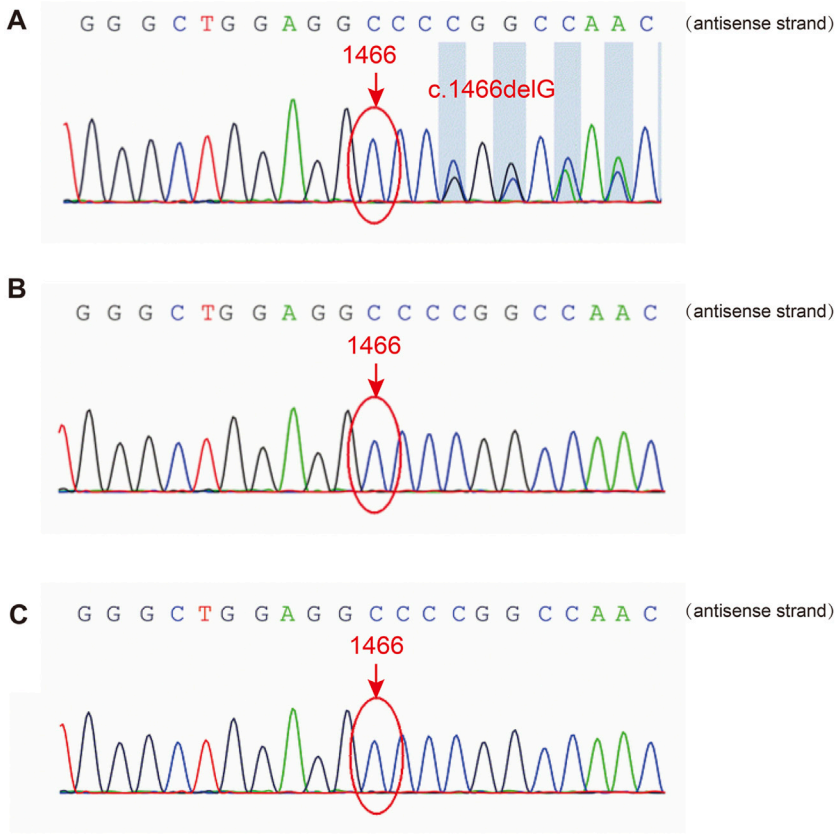

FIGURE 2
Sanger sequencing of *FLNA* in the patient and her parents. **(A)** The *FLNA* variant (c.1466del, p. G489Afs*9) was detected in the patient. **(B, C)** The variant was not detected in her father or mother.

3.4 FLNA is related to proteins involved in cell migration

Additionally, FLNA serves as a scaffold for signaling proteins, many of which are involved in cell movement and migration. The STRING database was used to construct the PPI network of FLNA (Figure 4). Proteins that interacted directly with FLNA were retained in the network. Based on the functions recorded in the UniProt database, proteins related to cell migration are marked in orange, such as CDC42 and the integrin ITGB2. Therefore, the PPI network indicated that FLNA plays an important role in cell migration as a signaling protein. The loss of FLNA function is likely to affect cell migration by affecting cell signaling.

3.5 Successful generation of patient-derived iPSC line

To further investigate the pathogenesis of the *FLNA* variant that causes PVNH and epilepsy, an iPSC line was generated from the PBMCs of patients. The PBMCs were transduced with the non-integrating reprogramming factors OCT3/4, KLF, c-Myc, and Sox 2, and iPSCs were selected after 20 days of transduction (Figure 5A). Karyotyping analysis did not detect any abnormalities and revealed a diploid 46 and XX karyotype (Figure 5B). Expression of the pluripotency markers Nanog, SSEA4, and OCT4 was confirmed using flow cytometry (Figure 5C). The ability of iPSCs to differentiate into the three germ layers was characterized by the expression of Pax 6 (ectoderm), Brachury (mesoderm), and AFP (endoderm) (Figure 5D). Therefore, these results indicated that the iPSC line was successfully generated.

3.6 *FLNA* variant impairs F-actin arrangement

To further investigate the expression of *FLNA* in the patient, WB and qRT-PCR were performed using patient-derived iPSCs. Notably, WB revealed a complete absence of wild-type protein expression in patient-derived iPSCs compared to iPSCs generated from two healthy donors (Figure 6A). Four primers targeting different loci of the wild-type *FLNA* gene were designed to detect mRNA levels of wild-type *FLNA*. The FLNA variant site of *FLNA* is located in exon 10. Primers 1 and 2 were designed to be complementary to the sequences in exon 3, whereas primers 3 and 4 were designed to be complementary to the sequences in exons 38 and 48, respectively. Thus, the mRNA of the wild-type and variant *FLNA* can be detected by primers 1 and 2, whereas only the mRNA of wild-type *FLNA* can be detected by primers 3 and 4. The results suggested that none of the four primers detected mRNA of

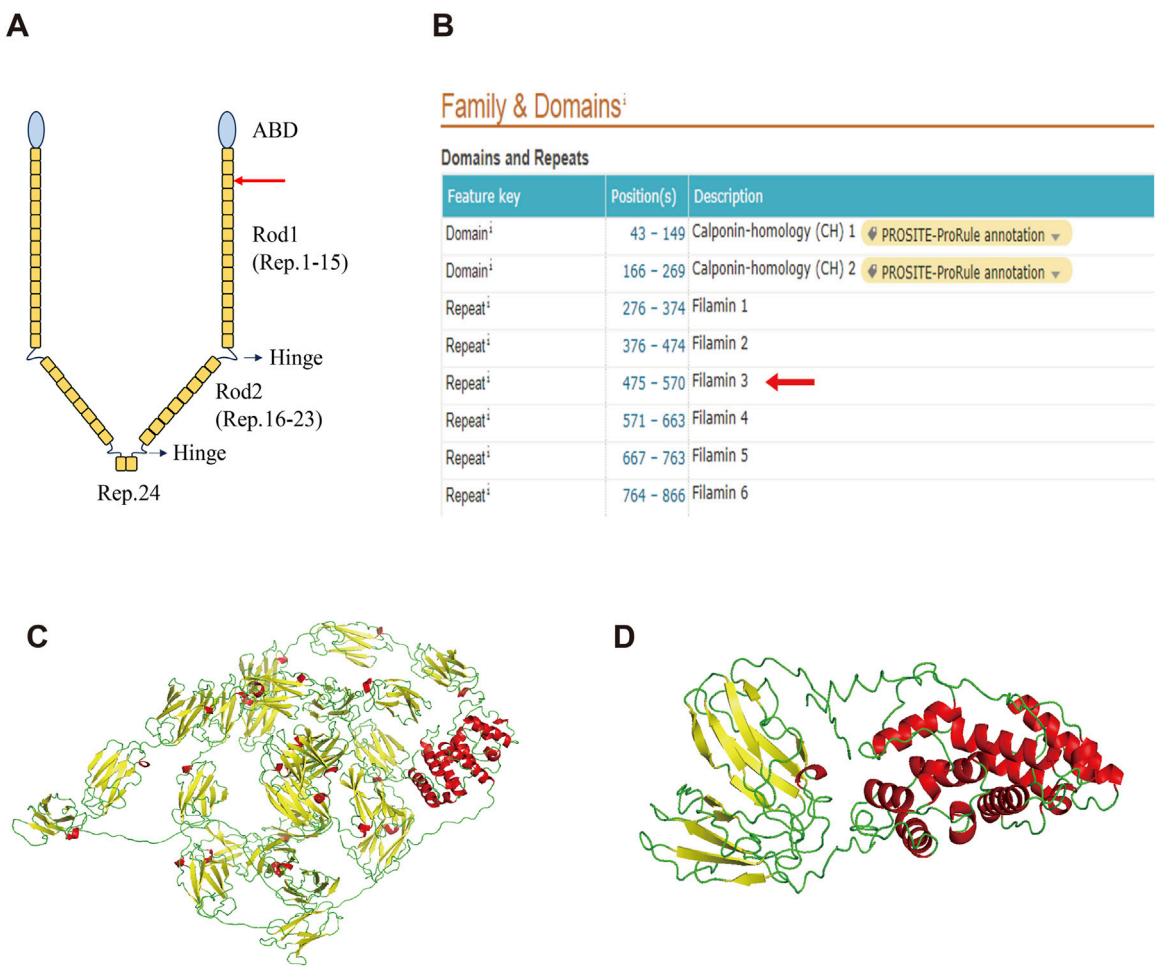

FIGURE 3
Structure of the wild-type FLNA and variant FLNA. **(A)** Schematic diagram illustrates the structure of FLNA. The red arrow indicates the variant and termination sites. **(B)** Domain positions of FLNA as shown in the UniProt database. Both the variant and termination sites are located in Rep. 3 (red arrow). **(C)** Predicted overall structure of wild-type FLNA from the AlphaFold Protein Structure database. **(D)** Predicted structure of the variant FLNA using I-TASSER. α-helix is shown in red, β-sheet in yellow, and random coil in green.

variant *FLNA* (Figure 6B), indicating that the variant *FLNA* may not be transcribed or degraded immediately after transcription.

As an actin-binding protein, FLNA has been implicated in the promotion of the orthogonal branching of the actin network, thereby impacting cell migration. Consistent with the WB results, immunofluorescence staining of wild-type FLNA revealed the absence of FLNA in patient-derived iPSCs (Figure 6C). Additionally, immunofluorescence staining revealed that F-actin was more neatly arranged in healthy donor-derived iPSCs, with higher expression in the pericellular area near the cell membrane. However, F-actin was more irregularly arranged and disorganized in patient-derived iPSCs (Figure 6C). Moreover, the F-actin arranged along the cell periphery appeared to be broken. Disorders of the F-actin network may be responsible for impaired cell migration.

4 Discussion

PVNH is a malformation of the cerebral cortex characterized by heterotopic neurons lining the lateral ventricles owing to the failed migration of neurons during cortical formation (Sarkisian et al., 2008). Affected patients may present with epilepsy due to ectopic discharge. The *FLNA* is one of the identified genes associated with PVNH(Sarkisian et al., 2008). Multiple *FLNA* variants have been reported in patients with PVNH. In our study, we identified a novel *FLNA* frameshift variant (NM_001456.3: c.1466delG, p. G489Afs*9) in a patient with PVNH with epilepsy as a sporadic case, which has not been reported in the available databases (PubMed, HGMDpro, gnomAD, and ClinVar).

FLNA is located on the X-chromosome and encodes a 280 kDa protein comprising an ABD domain and 24 repeat β-sheets resembling the immunoglobulin domain (Zhou et al., 2021). The ABD of *FLNA* allows the protein to bind to F-actin and is involved in cytoskeletal organization (Yamazaki, et al., 2002). The newly discovered *FLNA* variant (NM_001456.3: c.1466delG, p. G489Afs*9) leads to the premature introduction of a stop codon, resulting in the shortening of the protein length from 2647 to 496 amino acids, so the variant protein is composed of only the ABD domain, Rep 1-2, and incomplete Rep3. Massive loss of bases may cause nonsense-mediated mRNA decay, an important

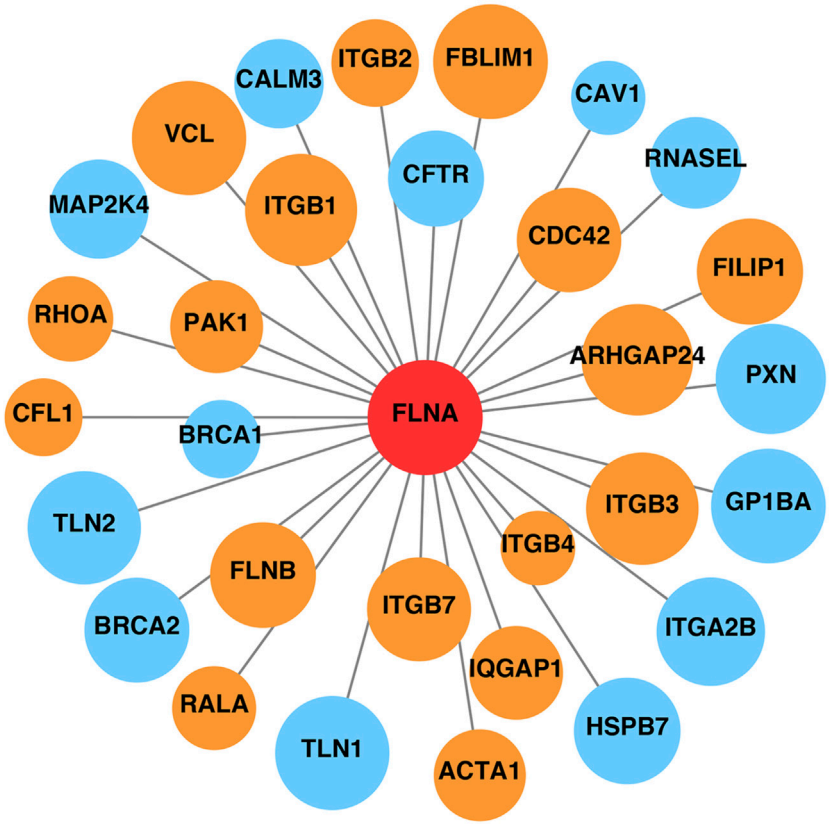

FIGURE 4
Protein-protein interaction network of FLNA. Proteins related to cell migration are marked in orange, and other proteins unrelated to cell migration are marked in blue. The area of the circles is proportional to the combined score between FLNA and related proteins.

mechanism that detects premature termination codons and triggers mRNA degradation to avoid the accumulation of truncated and potentially harmful proteins. Additionally, if the mRNA remains and is transcribed into a protein, the large number of lost fragments significantly alters the structure of FLNA based on the prediction, and furthermore, it is highly likely to affect the function of the protein.

In addition to the ABD domain, the Rep1-24 domain plays an essential role and serves as a scaffold for various binding partners, including receptors, channels, and intracellular signaling molecules (Zhou et al., 2021). Many FLNA-partner complexes are involved in the regulation of cell adhesion and motility. The PPI network of FLNA showed its interactions with a wide range of proteins, many of which are associated with cell adhesion, spreading, and migration. For example, CDC42 is a small GTPase belonging to the Rho family, which serves as a key regulator of actin dynamics. CDC42 plays an important role in inducing actin reorganization and filopodium formation, thus regulating cell migration (Nobes and Hall, 1995; Ohta, et al., 1999).

We successfully generated iPSCs from the patients' PBMCs, which were used to further explore pathogenic mechanisms. Results of WB and qRT-PCR revealed the absence of both wild-type and variant *FLNA* in iPSCs derived from the patient, which was unexpected. The variant in our study was heterozygous on the X chromosome. According to the X chromosome stochastic inactivation theory, random X chromosome inactivation shuts down gene transcription on one of the two X chromosomes in females (Harper, 2011). Thus, some of the cells in the patient were expected to express wild-type *FLNA*. Many factors affect cellular transcription, including epigenetic and transcription factor regulation. The skewing of X chromosome inactivation may be responsible for this result. An unusual degree of skewing of X-chromosome inactivation was identified in females with X-linked gene mutations even in a female without any X-chromosomal abnormality; however, the reason for this remains unknown (Tukiainen, et al., 2017; Viggiano, et al., 2016). Whether skewed inactivation occurred in this patient requires further investigation.

Although an association between *FLNA* mutations and PVNH has been demonstrated, the mechanism by which *FLNA* defects cause PVNH remains controversial. Several studies have demonstrated that loss of FLNA disrupts the arrangement of the F-actin cytoskeleton and impairs cell motility in tumor cells (Flanagan et al., 2001; Welter et al., 2020). However, whether the *FLNA* variants affect the F-actin cytoskeleton in PVNH remains unknown. In this study, we investigated the F-actin network in iPSCs derived from patients with PVNH and two healthy donors. F-actin staining showed an irregular arrangement and organization of the F-actin network in patient-derived iPSCs compared to that of healthy donor-derived iPSCs. F-actin in iPSCs from the two healthy

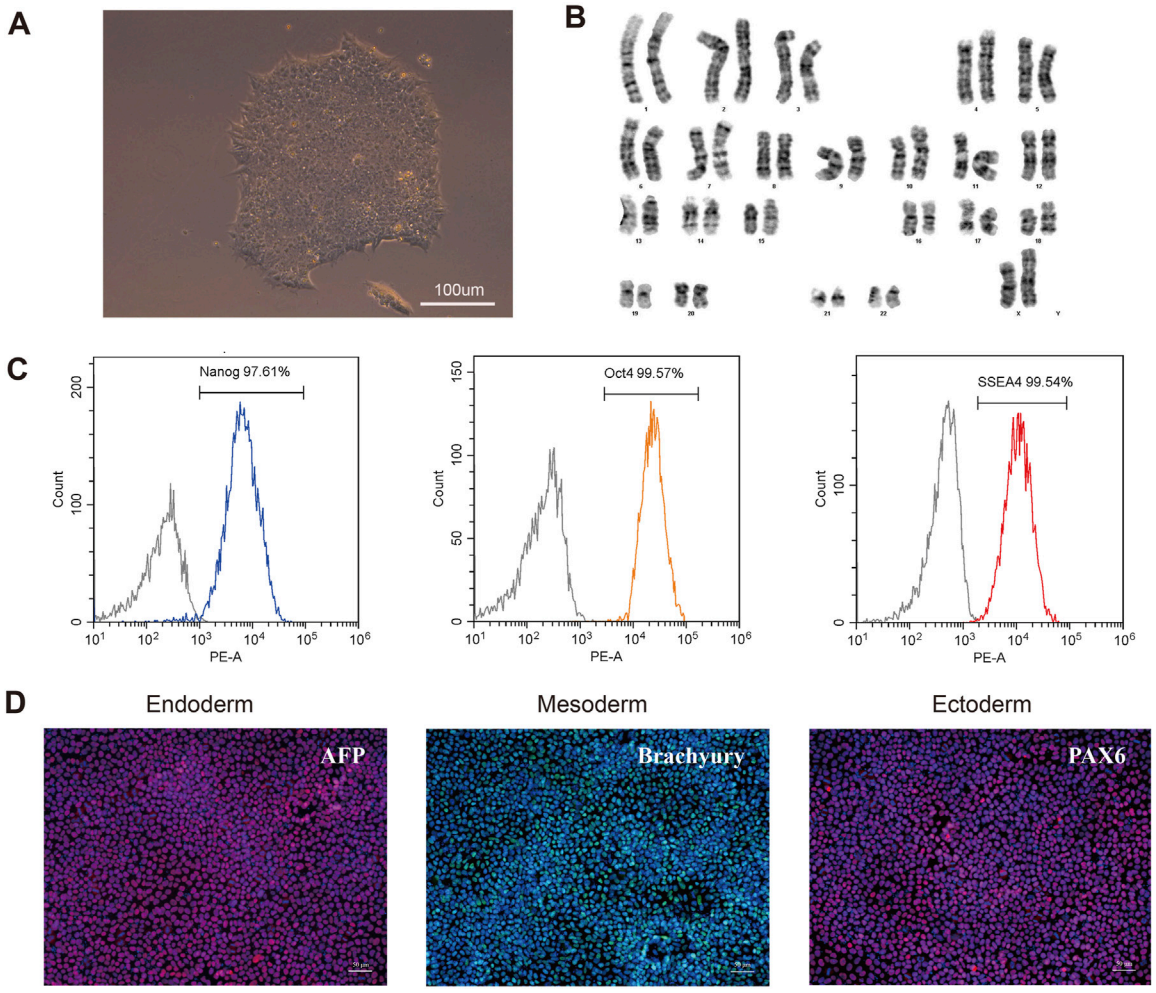

FIGURE 5
Characterization of the patient-derived iPSC. **(A)** Morphology of selected iPSC colonies. Scale bar: 100 μm. **(B)** Karyotype analysis of the iPSC line indicated no detectable abnormality. **(C)** Expression of pluripotent markers was confirmed by flow cytometry analysis (Nanog, OCT4, SSEA4). **(D)** Differentiation capacity of iPSCs into the three germ layers: ectoderm (Pax6), mesoderm (Brachyury) and endoderm (AFP) markers, demonstrated by immunofluorescent staining. Scale bar: 50 μm.

donors was neatly organized in the cytoplasm, whereas in iPSCs from patients, it appeared to be broken and irregularly arranged. These results suggested that FLNA is essential for regulating the orthogonal structure of F-actin. Therefore, the loss of FLNA function may impair cell migration by influencing the arrangement of F-actin, resulting in the migration failure of newborn neurons and PVNH. To our knowledge, this is the first study exploring the pathogenesis of *FLNA*-associated PVNH in patient-derived iPSCs. Our results are similar to previous findings that FLNA deficiency impaired cell motility by affecting the arrangement of F-actin in human seminoma cells and melanoma cells (Flanagan et al., 2001; Welter et al., 2020). Several studies have explored the mechanisms underlying PVNH in animal models. Carabalona et al. found that *FLNA*-knockdown rats exhibited PVNH. They did not focus on the arrangement of F-actin but suggested that disorganization of radial glia may be the cause of *FLNA*-associated PVNH(Carabalona et al., 2012). Whether the same phenomenon occurs in animal models warrants further exploration. However, it is reported that *FLNA*-deficient mice showed no differences in F-actin levels and didn't exhibit PVNH (Feng, et al., 2006; Hart, et al., 2006). There are several possible explanations for the findings. Both teams studied fibroblasts, which are inherently less motile, and therefore may not cause significant differences in F-actin and cell motility. In addition, it is possible that in the neonatal neuronal cells of mice, FLNB, another actin-binding protein, strongly compensates for the function of FLNA; therefore, no significant ectopic neuronal nodules appear.

Here, we report a novel variant of *FLNA* in a patient with epilepsy and PVNH. Although variants of *FLNA* have been found to cause PVNH, the underlying pathogenic mechanism remains unclear. We successfully generated an iPSC line from the patient's PBMCs and discovered that the variant caused the absence of FLNA, which impaired the arrangement of F-actin. Our findings suggest that this variant of *FLNA* plays a role in cell migration and the pathogenesis of *FLNA*-associated PVNH. To date, no study has used cells from patients

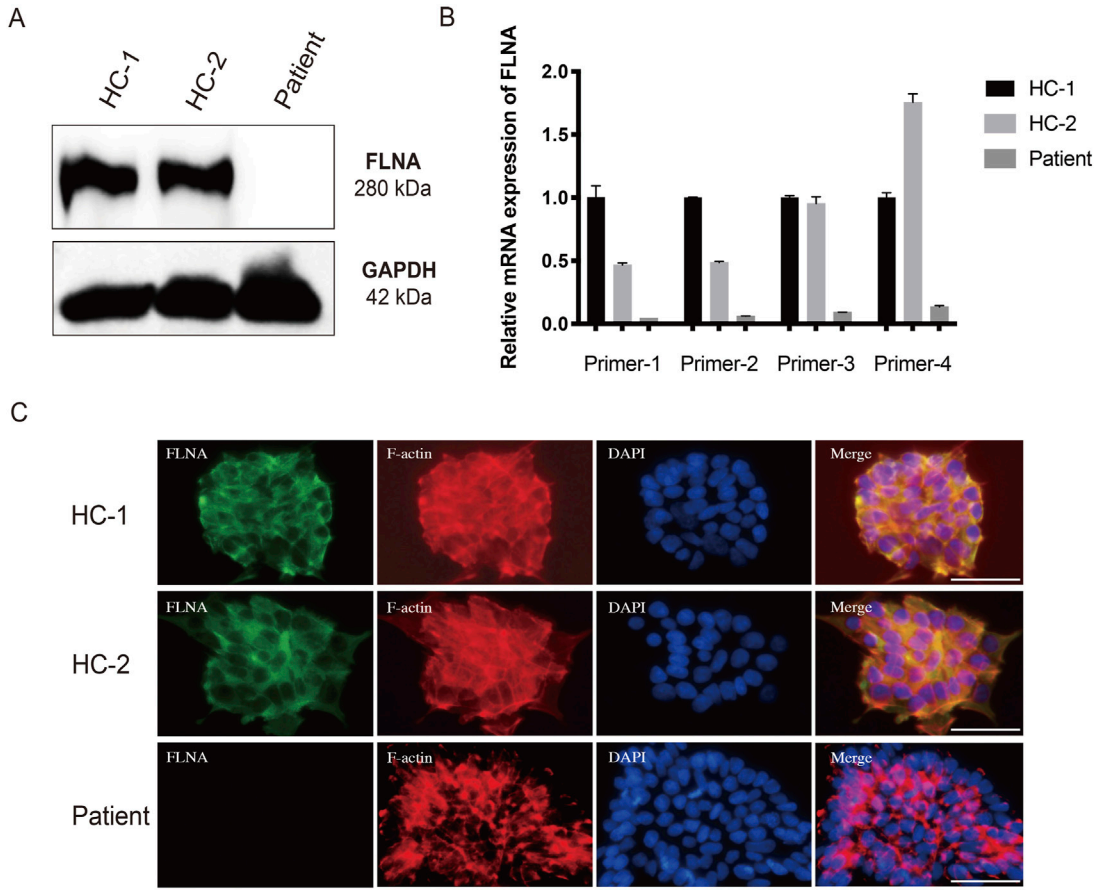

FIGURE 6
Loss of FLNA impairs the arrangement of F-actin in patient-derived iPSCs. **(A)** Protein levels of FLNA was tested using western blot. GAPDH served as internal reference. **(B)** The mRNA expression of wild-type and variant FLNA was assessed using quantitative polymerase chain reaction analysis. **(C)** Arrangement of F-actin illustrated using immunofluorescence. iPSCs stained with immunolabeled antibodies for FLNA (green) and phalloidin for F-actin (red). Nuclei (blue) were visualized using DAPI. Merged images are shown on the right. Scale bar: 25 μm.

to investigate this mechanism, making our findings important. However, this study has some limitations. As the results were based on a single patient, a larger population of patients is needed to further identify the mechanism. Additionally, the migration ability was not evaluated, and it was necessary to differentiate iPSCs into neurons *in vitro* to further study their migration and discharge functions. Moreover, the mechanism of epilepsy in the *FLNA*-associated PVNH is still unclear. Several clinical studies have found that heterotopic lesions produce aberrant connectivity with normal brain regions and both of them are involved in the development of epileptogenic networks (Jacobs, et al., 2009; Pizzo, et al., 2017), but the exact mechanism needs to be explored further in an animal model of *FLNA*-associated PVNH.

Data availability statement

The original contributions presented in the study are publicly available. This data can be found here: https://www.ncbi.nlm.nih.gov/sra/PRJNA1163365.

Ethics statement

The studies involving humans were approved by the Medical Ethics Committee of Renji Hospital, Shanghai Jiao Tong University School of Medicine. The studies were conducted in accordance with the local legislation and institutional requirements. The participants provided their written informed consent to participate in this study. Written informed consent was obtained from the individual(s) for the publication of any potentially identifiable images or data included in this article.

Author contributions

CX: Investigation, Methodology, Writing–original draft. YW: Investigation, Methodology, Writing–review and editing. JP: Methodology, Writing–original draft. SF: Investigation, Writing–review and editing. YG: Conceptualization, Funding acquisition, Project administration, Supervision,

Writing–review and editing. YH: Conceptualization, Funding acquisition, Project administration, Supervision, Writing–review and editing.

Funding

The author(s) declare that financial support was received for the research, authorship, and/or publication of this article. This work was supported by the National Natural Science Foundation of China (82071445, 82371454), Shanghai Municipal Science and Technology Commission Biomedical Science and Technology Support Project (21S11902200), National Major Translational Medicine Science and Technology Infrastructure (Shanghai) open subject project (TMSK-2021-111), Key project of Medical and Engineering Crossing of University of Shanghai for Science and Technology (1020308405), Shanghai Collaborative Innovation Center for Translational Medicine and Healthy China, Buchang Zhiyuan Heart and Brain Health Public Welfare Project Fund (HIGHER061).

Conflict of interest

The authors declare that the research was conducted in the absence of any commercial or financial relationships that could be construed as a potential conflict of interest.

Publisher's note

Supplementary material

The Supplementary Material for this article can be found online at: https://www.frontiersin.org/articles/10.3389/fphar.2024.1429177/full#supplementary-material

References

Carabalona, A., Beguin, S., Pallesi-Pocachard, E., Buhler, E., Pellegrino, C., Arnaud, K., et al. (2012). A glial origin for periventricular nodular heterotopia caused by impaired expression of Filamin-A. *Hum. Mol. Genet.* 21 (5), 1004–1017. doi:10.1093/hmg/ddr531

Feng, Y., Chen, M. H., Moskowitz, I. P., Mendonza, A. M., Vidali, L., Nakamura, F., et al. (2006). Filamin A (FLNA) is required for cell-cell contact in vascular development and cardiac morphogenesis. *Proc. Natl. Acad. Sci. U. S. A.* 103 (52), 19836–19841. doi:10.1073/pnas.0609628104

Flanagan, L. A., Chou, J., Falet, H., Neujahr, R., Hartwig, J. H., and Stossel, T. P. (2001). Filamin A, the Arp2/3 complex, and the morphology and function of cortical actin filaments in human melanoma cells. *J. Cell Biol.* 155 (4), 511–517. doi:10.1083/jcb.200105148

Gómez-Garre, P., Seijo, M., Gutiérrez-Delicado, E., Castro del Río, M., de la Torre, C., Gómez-Abad, C., et al. (2006). Ehlers-Danlos syndrome and periventricular nodular heterotopia in a Spanish family with a single FLNA mutation. *J. Med. Genet.* 43 (3), 232–237. doi:10.1136/jmg.2004.029173

Harper, P. S. (2011). Mary Lyon and the hypothesis of random X chromosome inactivation. *Hum. Genet.* 130 (2), 169–174. doi:10.1007/s00439-011-1013-x

Hart, A. W., Morgan, J. E., Schneider, J., West, K., McKie, L., Bhattacharya, S., et al. (2006). Cardiac malformations and midline skeletal defects in mice lacking filamin A. *Hum. Mol. Genet.* 15 (16), 2457–2467. doi:10.1093/hmg/ddl168

Heuvingh, J., Franco, M., Chavrier, P., and Sykes, C. (2007). ARF1-mediated actin polymerization produces movement of artificial vesicles. *Proc. Natl. Acad. Sci. U. S. A.* 104 (43), 16928–16933. doi:10.1073/pnas.0704749104

Hu, J., Lu, J., Goyal, A., Wong, T., Lian, G., Zhang, J., et al. (2017). Opposing FlnA and FlnB interactions regulate RhoA activation in guiding dynamic actin stress fiber formation and cell spreading. *Hum. Mol. Genet.* 26 (7), 1294–1304. doi:10.1093/hmg/ddx047

Jacobs, J., Levan, P., Châtillon, C. E., Olivier, A., Dubeau, F., and Gotman, J. (2009). High frequency oscillations in intracranial EEGs mark epileptogenicity rather than lesion type. *Brain* 132 (Pt 4), 1022–1037. doi:10.1093/brain/awn351

Lange, M., Kasper, B., Bohring, A., Rutsch, F., Kluger, G., Hoffjan, S., et al. (2015). 47 patients with FLNA associated periventricular nodular heterotopia. *Orphanet J. Rare Dis.* 10, 134. doi:10.1186/s13023-015-0331-9

Liu, W., Yan, B., An, D., Xiao, J., Hu, F., and Zhou, D. (2017). Sporadic periventricular nodular heterotopia: classification, phenotype and correlation with Filamin A mutations. *Epilepsy Res.* 133, 33–40. doi:10.1016/j.eplepsyres.2017.03.005

Masurel-Paulet, A., Haan, E., Thompson, E. M., Goizet, C., Thauvin-Robinet, C., Tai, A., et al. (2011). Lung disease associated with periventricular nodular heterotopia and an FLNA mutation. *Eur. J. Med. Genet.* 54 (1), 25–28. doi:10.1016/j.ejmg.2010.09.010

Nakamura, F., Osborn, T. M., Hartemink, C. A., Hartwig, J. H., and Stossel, T. P. (2007). Structural basis of filamin A functions. *J. Cell Biol.* 179 (5), 1011–1025. doi:10.1083/jcb.200707073

Nakamura, F., Stossel, T. P., and Hartwig, J. H. (2011). The filamins: organizers of cell structure and function. *Cell Adh Migr.* 5 (2), 160–169. doi:10.4161/cam.5.2.14401

Nobes, C. D., and Hall, A. (1995). Rho, rac, and cdc42 GTPases regulate the assembly of multimolecular focal complexes associated with actin stress fibers, lamellipodia, and filopodia. *Cell.* 81 (1), 53–62. doi:10.1016/0092-8674(95)90370-4

Ohta, Y., Suzuki, N., Nakamura, S., Hartwig, J. H., and Stossel, T. P. (1999). The small GTPase RalA targets filamin to induce filopodia. *Proc. Natl. Acad. Sci. U. S. A.* 96 (5), 2122–2128. doi:10.1073/pnas.96.5.2122

Parrini, E., Ramazzotti, A., Dobyns, W. B., Mei, D., Moro, F., Veggiotti, P., et al. (2006). Periventricular heterotopia: phenotypic heterogeneity and correlation with Filamin A mutations. *Brain* 129 (Pt 7), 1892–1906. doi:10.1093/brain/awl125

Pizzo, F., Roehri, N., Catenoix, H., Medina, S., McGonigal, A., Giusiano, B., et al. (2017). Epileptogenic networks in nodular heterotopia: a stereoelectroencephalography study. *Epilepsia* 58 (12), 2112–2123. doi:10.1111/epi.13919

Sarkisian, M. R., Bartley, C. M., and Rakic, P. (2008). Trouble making the first move: interpreting arrested neuronal migration in the cerebral cortex. *Trends Neurosci.* 31 (2), 54–61. doi:10.1016/j.tins.2007.11.009

Sheen, V. L., Dixon, P. H., Fox, J. W., Hong, S. E., Kinton, L., Sisodiya, S. M., et al. (2001). Mutations in the X-linked filamin 1 gene cause periventricular nodular heterotopia in males as well as in females. *Hum. Mol. Genet.* 10 (17), 1775–1783. doi:10.1093/hmg/10.17.1775

Tukiainen, T., Villani, A. C., Yen, A., Rivas, M. A., Marshall, J. L., Satija, R., et al. (2017). Landscape of X chromosome inactivation across human tissues. *Nature* 550 (7675), 244–248. doi:10.1038/nature24265

van der Flier, A., and Sonnenberg, A. (2001). Structural and functional aspects of filamins. *Biochim. Biophys. Acta* 1538 (2-3), 99–117. doi:10.1016/s0167-4889(01)00072-6

Viggiano, E., Ergoli, M., Picillo, E., and Politano, L. (2016). Determining the role of skewed X-chromosome inactivation in developing muscle symptoms in carriers of Duchenne muscular dystrophy. *Hum. Genet.* 135 (7), 685–698. doi:10.1007/s00439-016-1666-6

Welter, H., Herrmann, C., Fröhlich, T., Flenkenthaler, F., Eubler, K., Schorle, H., et al. (2020). Filamin A orchestrates cytoskeletal structure, cell migration and stem cell characteristics in human seminoma TCam-2 cells. *Cells* 9 (12), 2563. doi:10.3390/cells9122563

Yamazaki, M., Furuike, S., and Ito, T. (2002). Mechanical response of single filamin A (ABP-280) molecules and its role in the actin cytoskeleton. *J. Muscle Res. Cell Motil.* 23 (5-6), 525–534. doi:10.1023/a:1023418725001

Zhang, J., Neal, J., Lian, G., Hu, J., Lu, J., and Sheen, V. (2013). Filamin A regulates neuronal migration through brefeldin A-inhibited guanine exchange factor 2-dependent Arf1 activation. *J. Neurosci.* 33 (40), 15735–15746. doi:10.1523/jneurosci.1939-13.2013

Zhou, J., Kang, X., An, H., Lv, Y., and Liu, X. (2021). The function and pathogenic mechanism of filamin A. *Gene* 784, 145575. doi:10.1016/j.gene.2021.145575

frontiers | Frontiers in Neuroscience

TYPE Original Research
PUBLISHED 30 October 2024
DOI 10.3389/fnins.2024.1485179

OPEN ACCESS

EDITED BY
Zezhi Li,
Guangzhou Medical University, China

REVIEWED BY
Anna Bielecka Wajdman,
Medical University of Silesia, Poland
Bangshan Liu,
Central South University, China
Tianhong Zhang,
Shanghai Jiao Tong University, China

*CORRESPONDENCE
Ze Yu
✉ alibaba0026@163.com
Wei Feng
✉ ffww06@163.com

†These authors have contributed equally to this work

RECEIVED 23 August 2024
ACCEPTED 14 October 2024
PUBLISHED 30 October 2024

CITATION
Zhao K, Wang Y, Liu Q, Yu Z and Feng W (2024) Efficacy comparison of five antidepressants in treating anxiety and depression in cancer and non-cancer patients.
Front. Neurosci. 18:1485179.
doi: 10.3389/fnins.2024.1485179

Efficacy comparison of five antidepressants in treating anxiety and depression in cancer and non-cancer patients

Kuan Zhao[1,2†], Youyang Wang[1,2†], Qun Liu[1,2], Ze Yu[1,2*] and Wei Feng[1,2*]

[1]Department of Psychological Medicine, Fudan University Shanghai Cancer Center, Shanghai, China, [2]Department of Oncology, Shanghai Medical College, Fudan University, Shanghai, China

Introduction: Cancer patients have a heightened susceptibility to anxiety and depressive disorders, which significantly impact the effectiveness of cancer treatments and long-term quality of life. This study aimed to compare the efficacy of different antidepressants in cancer and non-cancer patients.

Methods: A total of 610 patients diagnosed with depressive episodes and/or anxiety disorders were retrospectively included and divided into a cancer group and a non-cancer control group. Antidepressants used included escitalopram, duloxetine, sertraline, venlafaxine, and vortioxetine, combined with trazodone or not. The Patient Health Questionnaire-9 (PHQ-9) and the Generalized Anxiety Disorder Questionnaire-7 (GAD-7) scores were used to evaluate the efficacy after 4 weeks and 8 weeks of systematic antidepressants treatment.

Results: Compared to the non-cancer group, the cancer group had higher proportions of females, older individuals, and patients with poor sleep quality, while reporting fewer somatic symptoms at baseline (all $p < 0.05$). PHQ-9 and GAD-7 scores in cancer patients treated with antidepressants were significantly lower than baseline at week 4 and week 8 (all $p < 0.05$). The sertraline group demonstrated significantly less improvement in GAD-7 scores at week 4 and in both GAD-7 and PHQ-9 scores at week 8 compared to the escitalopram group, while duloxetine, venlafaxine, and vortioxetine showed comparable efficacy to escitalopram. Antidepressants combined with trazodone showed significant improvement in PHQ-9 scores at week 4 compared to those without trazodone. The gynecological cancer group showed significantly more improvement in GAD-7 and PHQ-9 scores at week 4 and 8 compared to breast cancer patients.

Conclusion: Antidepressant treatment in cancer patients with anxiety and depression is as effective as in non-cancer patients. The efficacy of escitalopram is comparable to duloxetine, venlafaxine, and vortioxetine, all of which outperformed sertraline in cancer patients.

KEYWORDS

cancer, anxiety, depression, antidepressants, efficacy

1 Introduction

An estimated 19.3 million new cancer cases and nearly 10 million cancer-related deaths were recorded globally in 2020, highlighting urgent concerns in global cancer management (Sung et al., 2021; Qiu et al., 2021). Cancer patients were more susceptible to major depressive disorder (MDD) and anxiety symptoms than non-cancer patients (Vehling et al., 2022; Mitchell et al., 2011). However, whether the efficacy of common antidepressants used in cancer patients has seldom been investigated.

Cancer patients usually suffer from physical and phycological pathologies leading to anxiety and depression, such as immune dysregulation, increased inflammation, anhedonia due to altered cortisol levels, mental trauma from a sudden positive cancer diagnosis, and physical symptoms caused by the side effects of chemotherapeutic treatments. Emotional disorders are also attributed to patients' fear of death, unpleasant changes in the local environment, reduced social interactions, psychological stress, and persistent depression (Chan et al., 2023; Fetcho et al., 2023). The risk of self-injury in cancer patients with untreated emotional disorders has been increased significantly, affecting their quality of life (QoL) (Heinrich et al., 2023; Grassi, 2020). Therefore, the management of anxiety and depression is important in improving patients' adaptation and well-being.

Although antidepressants are commonly prescribed and established as effective treatments for anxiety and depression in non-cancer patients, their efficacy in cancer patients is not well-defined. Furthermore, cancer patients usually have aberrant inflammatory alternation, leading to decreased psychomotor speed, which has been associated with poor antidepressant treatment response (Goldsmith et al., 2016). To address these questions, here we aim to compare the efficacy of antidepressants in cancer and non-cancer patients, and also to evaluate the efficacy of escitalopram, duloxetine, sertraline, venlafaxine, and vortioxetine, combined with trazodone or not among cancer patients.

2 Materials and methods

2.1 Subjects

The data for this study were collected from the database of patients visiting the Department of Psychology at Fudan University Shanghai Cancer Center between July 2021 and September 2023. Ethics approval was obtained from Medical Ethics Committee, Fudan University Shanghai Cancer Center. The eligibility criteria for patients were as follows: (1) age $\geq$ 18 years; (2) diagnosed with "depressive episode" and/or "anxiety disorder" according to ICD-10; (3) completed psychological assessments at the initial visit; and (4) received antidepressant treatment. The exclusion criteria included: (1) inability to understand or execute relevant assessments; (2) comorbid schizophrenia, bipolar disorder, epilepsy, cognitive impairment, or other psychiatric conditions; and (3) continuing medications for pre-existing antidepressants for more than one week or were concurrently using antipsychotics, mood stabilizers, or other psychotropic medications. Following the screening procedure, a total of 610 patients were enrolled in this study.

2.2 Behavioral assessments

For the behavioral evaluations, we collected patients' demographics such as gender and age, and clinical characteristics, including the cancer type, staging, past/ongoing anti-cancer treatments, history of psychiatric diagnosis (if any), type of antidepressant used, and scores on 9-item Patient Health Questionnaire (PHQ-9), PHQ-15, GAD-7, Pittsburgh Sleep Quality Index (PSQI), and Visual Analog Scale (VAS) for pain. Follow-up assessments were conducted at 4-week and 8-week post-enrollment time points, with evaluations of PHQ-9 and GAD-7 scores (see Figure 1 for details). PHQ-9 is a self-reporting scale used to assess the severity of depression in patients. It consists of 9 items, with each item scoring on a Likert scale ranging from 0 to 3, resulting in a total score of 0 to 27. A score of $\geq$ 8 in cancer patients is considered clinically significant for depression (Manea et al., 2012). GAD-7 is another self-reporting scale designed to evaluate the severity of anxiety in patients. It comprises 7 items, each scoring on a Likert scale from 0 to 3, yielding a total score of 0 to 21. A score of $\geq$ 10 in cancer patients indicates clinically significant anxiety (Esser et al., 2018). The PHQ-15 is used to assess the severity of somatic symptoms in patients. It includes 15 somatic symptom clusters, including some of the common symptoms such as fatigue, pain, and various gastrointestinal disorders, as observed in cancer patients (Kroenke et al., 2002). PSQI is used to evaluate the patient's sleep quality over one month. A score of $>$ 5 suggests poor sleep quality, which has been validated in cancer patients (Momayyezi et al., 2021). The VAS is measured on a 0–10 scale and assesses the current level of pain experienced by the patient. Its reliability and reproducibility have been validated in cancer patients (Li et al., 2021).

2.3 Antidepressants

Patients were divided into antidepressants groups according to their prescription. Commonly used antidepressants were compared in this study, including selective serotonin reuptake inhibitors (SSRIs) like escitalopram and sertraline, serotonin-norepinephrine reuptake inhibitors (SNRIs) such as venlafaxine and duloxetine, and vortioxetine, which has multiple effects on serotonin receptors. Escitalopram, in particular, was used as the control drug due to its relatively high efficacy and lower incidence of side effects compared to other antidepressants in general population (Yin et al., 2023).

2.4 Cancer type categories and current cancer stage

In the cancer group, patients were categorized as follows: breast cancer (132), digestive system cancer (45), endocrine organ cancer (27), gynecological cancer (34), head and neck cancer (13), hematologic malignancy (4), lung cancer (19), soft tissue cancer (4), and male reproductive/urinary system cancer (10). Treatment modalities included surgery (222), radiotherapy (81), chemotherapy (142), immunotherapy (9), targeted therapy (34), and endocrine therapy (49). Patients were further grouped based

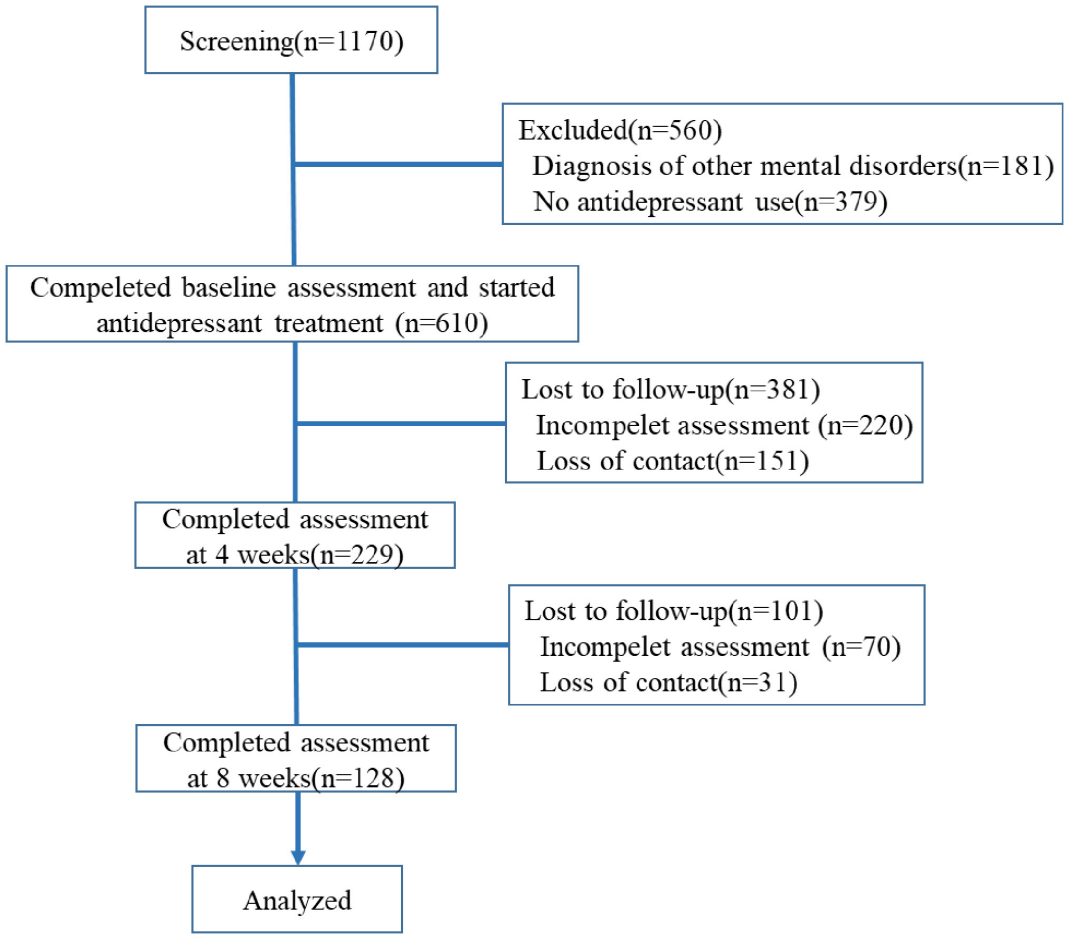

FIGURE 1
Study flow chart.

on their current cancer stage: undergoing treatment (202), in remission (60), and cancer reoccurring (20).

2.5 Statistical analysis

All statistical analyses were performed using R (version 4.3.0). Quantitative data were expressed as mean ± standard deviation (SD) or median. Patients were divided into two groups – non-cancer and cancer. The t-test was used to compare differences in quantitative data between the two groups. A non-parametric test was conducted for non-normally distributed data. The chi-square (χ^2) test was used to compare differences in qualitative data between the groups. The population of patients with intention-to-treat was analyzed in this study, and missing values were adjusted. A mixed linear model (LMM) was used to analyze repeatedly measured data, using maximum likelihood estimation to estimate model parameters. This approach allows LMM to utilize available observed data for estimation, even in the presence of missing values. Subgroup analysis was conducted for patients in the cancer group. The Akaike Information Criterion (AIC) was used to measure the goodness of fit of a statistical model; a smaller AIC value indicates a better model fit. For linear mixed models, different models may have different fixed effects and random effects structures, and AIC provides a unified standard to evaluate and compare these models (Liu et al., 2024). A p-value of < 0.05 indicated the statistical significance of the result.

3 Results

3.1 Baseline characteristics

A total of 610 patients were included in this study, with 288 patients in the cancer group and 322 patients in the non-cancer group (Table 1). The age and gender were significantly different in cancer and non-cancer groups.

Psychiatric diagnoses and antidepressant use differed significantly between the cancer and non-cancer groups ($p < 0.05$). In the cancer group, 45.83% had depressive episodes, 51.14% had anxiety disorders, and 49.72% had comorbid depression and anxiety, compared to 54.17%, 48.86%, and 50.28% in the non-cancer group. The proportion of first-episode patients was similar in the cancer group (48.70%) and the non-cancer group (51.30%), with no significant difference ($p = 0.14$). Cancer patients used escitalopram and duloxetine more frequently, while

TABLE 1 Comparison of clinical characteristics between cancer group and non-cancer group at baseline.

		Cancer group (288)	Non-cancer group (322)	t/χ^2	p
Gender*	Male	46 (33.86%)	90 (66.14%)	12.60	<0.01
	Female	242 (51.15%)	232 (48.85%)		
Age*		50 ± 12	38 ± 16	94.43	<0.01
Psychiatric diagnosis *	Depressive episode	22 (45.83%)	58 (54.17%)	14.44	<0.01
	Anxiety disorders	94 (51.14%)	90 (48.86%)		
	Comorbid depression and anxiety	172 (49.72%)	174 (50.28%)		
Episode Type	First	244 (48.70%)	257 (51.30%)	2.17	0.14
	Relapse	44 (40.37%)	65 (59.63%)		
Antidepressants* (categories and dose)				36.50	<0.01
	Duloxetine	15 (65.20%)	8 (34.80%)		
	Dose(mg)	52.50 ± 14.88	61.33 ± 22.00	−1.14	0.27
	Escitalopram	246 (54.10%)	209 (45.90%)		
	Dose(mg)	14.59 ± 3.61	14.50 ± 3.87	0.27	0.79
	Sertraline	12 (21.14%)	45 (78.86%)		
	Dose(mg)	75.00 ± 33.71	88.89 ± 41.48	−1.20	0.24
	Venlafaxine	20(32.25%)	42(67.75%)		
	Dose(mg)	116.25 ± 61.92	142.86 ± 61.56	−1.58	0.12
	Vortioxetine	2 (15.40%)	11 (84.60%)		
	Dose(mg)	15 ± 7.07	15 ± 4.47	0.00	1.00
Combined trazodone*	Yes	195 (54.56%)	166 (46.43%)	16.43	<0.01
	No	93 (37.36%)	156 (62.64%)		
Scale assessment*	PHQ-9*	13.50 ± 5.85	14.70 ± 6.52	6.37	0.01
	GAD-7	12.97 ± 5.13	13.20 ± 5.33	0.40	0.52
	VAS	2.77 ± 3.64	2.87 ± 2.63	1.24	0.26
	PHQ-15*	11.16 ± 4.58	12.13 ± 5.37	4.54	0.03
	PSQI*	13.68 ± 4.51	12.16 ± 4.43	18.25	<0.01

p: p-values (2-tailed); *$p < 0.05$; PHQ-9, Patient Health Questionnaire-9; GAD-7, Generalized Anxiety Disorder Questionnaire-7; VAS, Visual Analog Scale; PHQ-15, 15-item Patient Health Questionnaire; PSQI, Pittsburgh Sleep Quality Index.

trazodone was mainly used in combination therapy in the cancer group ($p < 0.01$). The doses of antidepressants between the two groups were equivalent, with no statistically significant differences detected ($p > 0.05$). PHQ-9, PSQI and PHQ-15 scores score at baseline was significantly different in the cancer group within the non-cancer group (all $p < 0.05$). However, there was no significant difference in GAD-7 and VAS scores between the two groups ($p > 0.05$).

3.2 Correlation analysis of behavioral assessment results

A correlation analysis was conducted to investigate relationships among the patient's age and baseline behavioral assessment results (Figure 2). It demonstrated that elder patients tend to have significantly lower GAD-7, PHQ-9, and PHQ-15, but higher PSQI scores. Positive correlations were observed among all behavioral assessment scores with each other ($p < 0.01$).

3.3 Comparative efficacy of antidepressants in cancer and non-cancer patients

3.3.1 Efficacy without adjusting confound factors

The PHQ-9 and GAD-7 scores significantly reduced after 4- and 8-weeks treatment of antidepressants, while no significant differences were found in the improvement of scores between the cancer and non-cancer groups (Figures 3A, B, $p > 0.05$). We then compared the efficacy of five antidepressants in cancer patients (Figures 3C, D). After 4 weeks of treatment, PHQ-9 scores decreased in all antidepressant groups except the vortioxetine group, while GAD-7 scores decreased in all five groups. After 8 weeks, both PHQ-9 and GAD-7 scores significantly decreased in the escitalopram, sertraline, venlafaxine, and vortioxetine groups. The duloxetine group lacked sufficient data after 8 weeks due to patient loss to follow-up.

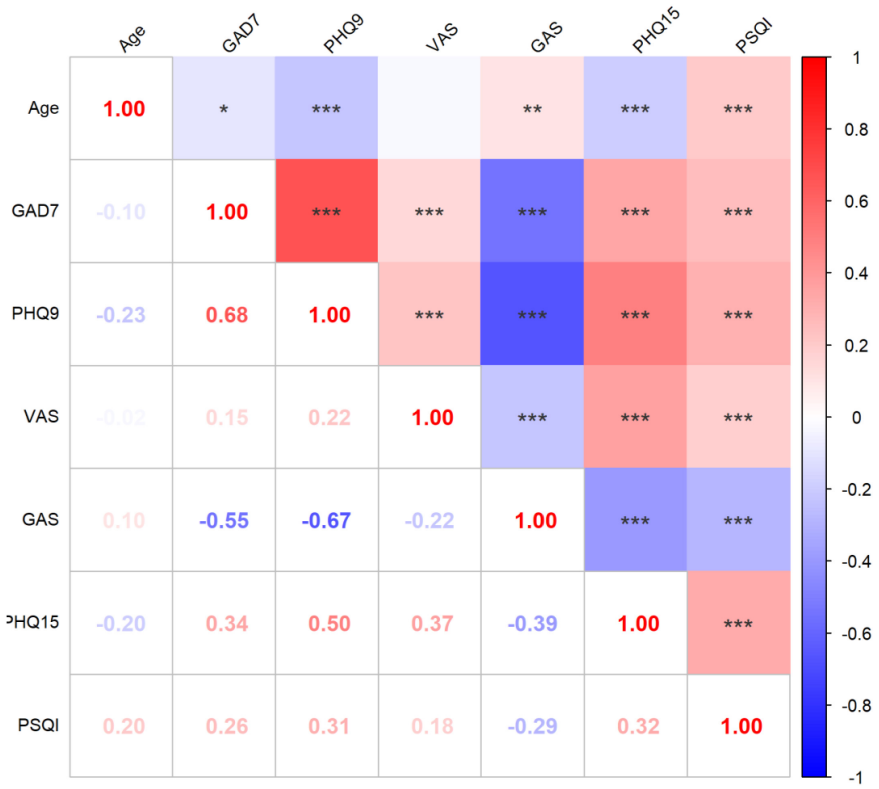

FIGURE 2
Correlation analysis of behavioral assessment results. *$p < 0.05$, **$p < 0.01$, ***$p < 0.001$; PHQ-9, Patient Health Questionnaire-9; GAD-7, Generalized Anxiety Disorder Questionnaire-7; VAS, Visual Analog Scale; PHQ-15, 15-item Patient Health Questionnaire; PSQI, Pittsburgh Sleep Quality Index. The gradient color error bar represents the Pearson's *r*-value.

3.3.2 Efficacy after adjusting confound factors

(1) Impact of treatment duration

To adjust various confounding factors and the interaction effects of repeated measurement, we employed linear mixed model to evaluate the efficacy of antidepressants (Oberg and Mahoney, 2007). It demonstrated that the duration of antidepressants treatment (4 or 8 weeks) had a significant effect on the outcome ($p < 0.05$). Among the various models tested, those with smallest AIC value was considered the best fit and demonstrated in Table 2 ($p < 0.01$). After adjusting baseline age, gender, anxiety or depression diagnoses, and episode type, the GAD-7 and PHQ-9 scores at the 4th and 8th weeks decreased significantly compared to baseline values (4th week change of GAD-7: $\beta = -7.46$, SE = 0.0.52, $p < 0.001$; 4th week change of PHQ-9: $\beta = -7.45$, SE = 0.58, $p < 0.001$; 8th week change of GAD-7: $\beta = -8.93$, SE = 0.68, $p < 0.001$; 8th week change of PHQ-9: $\beta = -9.58$, SE = 0.76, $p < 0.001$).

(2) Efficacy in cancer and non-cancer groups

The PHQ-9 and GAD-7 scores were not different between cancer and non-cancer patients in the fix model (both $p > 0.05$). The cancer status group × time interaction effects remained insignificant after controlling for confounding factors (all $p > 0.05$).

(3) Efficacy in antidepressants groups

When comparing the four antidepressants with escitalopram, only the PHQ-9 scores in the venlafaxine group was lower ($\beta = 1.63$, SE = 0.74, $p < 0.05$). No significant differences were observed with other antidepressants compared to escitalopram. The antidepressants group × time interaction effects in the sertraline group became significantly less pronounced at week 4 for GAD-7 ($\beta = 2.69$, SE = 1.07, $p < 0.05$) score changes compared to escitalopram, and at week 8 for both GAD-7 ($\beta = 3.77$, SE = 1.81, $p < 0.05$) and PHQ-9 ($\beta = 3.75$, SE = 2.02, $p < 0.05$) score changes compared to escitalopram. When comparing antidepressants with and without trazodone, the group without trazodone showed significantly less pronounced PHQ-9 score changes at week 4 compared to the group with trazodone (4th-week PHQ-9 change: $\beta = 2.06$, SE = 0.74, $p < 0.01$). No significant differences were found in the trazodone group at the 8th-week time point.

3.3.3 Cancer type-specific antidepressant response

A linear mixed model analysis was performed in the subgroup of patients with different cancer types, adjusting for the type of antidepressants and current cancer stage as confounding factors. The analysis also considered various treatment modalities, including surgery, radiotherapy, chemotherapy, immunotherapy, and endocrine therapy, to assess their impact on psychological outcomes (Supplementary Table 1). At baseline, patients in remission showed significantly lower PHQ-9 scores ($\beta = -1.76$, SE = 0.74, $p < 0.05$) compared to those undergoing treatment. And compared to breast cancer patients, patients with endocrine organ cancer had significantly higher GAD-7 ($\beta = 2.49$, SE = 1.09, $p < 0.05$) and PHQ-9 scores ($\beta = 2.73$, SE = 1.22, $p < 0.05$). Gynecological cancer patients had higher PHQ-9 scores ($\beta = 2.61$,

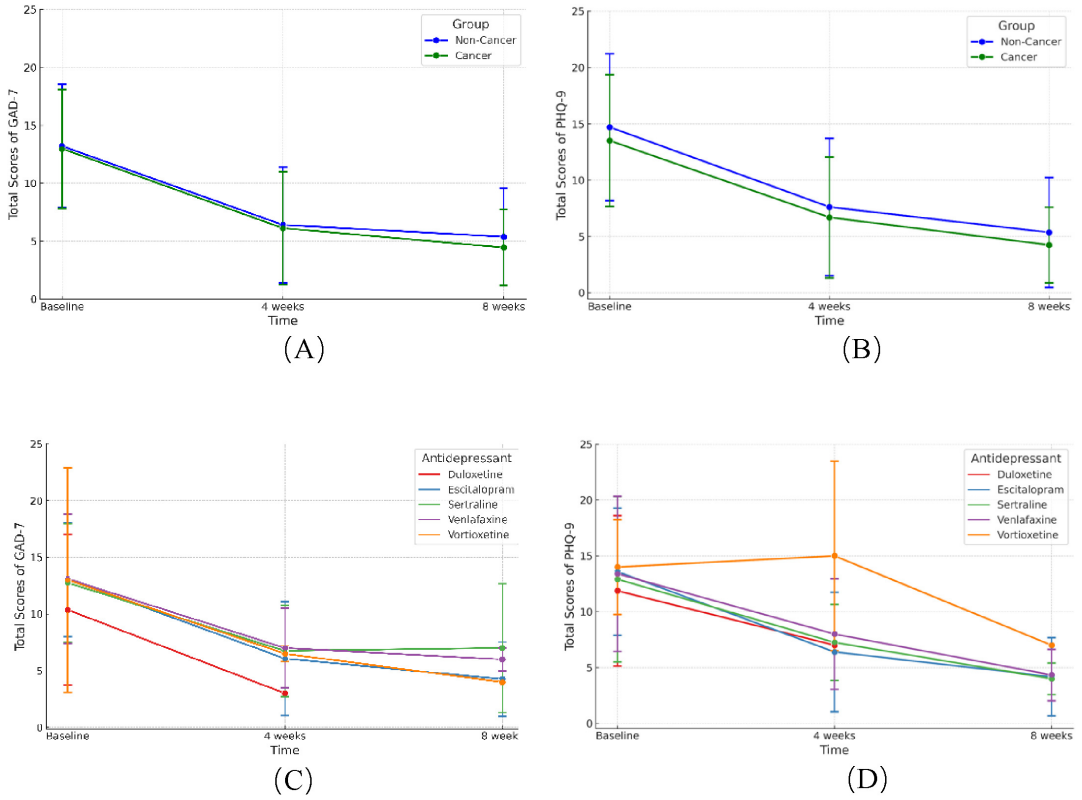

FIGURE 3
Change of GAD-7 and PHQ-9 scores after 4 and 8 weeks of antidepressants treatment. **(A,B)** Change of GAD-7 **(A)** and PHQ-9 **(B)** scores between cancer and non-cancer groups after 4 and 8 weeks of antidepressants. **(C,D)** Improvement of GAD-7 **(C)** and PHQ-9 **(D)** scores with five different antidepressants in cancer patients. GAD-7, Generalized Anxiety Disorder Questionnaire-7; PHQ-9, Patient Health Questionnaire-9.

SE = 1.06, $p < 0.05$). Hematologic malignancy patients showed significantly elevated PHQ-9 scores (β = 6.58, SE = 2.74, $p < 0.05$). Lung cancer patients had significantly higher PHQ-9 scores (β = 3.59, SE = 1.39, $p < 0.05$), while male reproductive/urinary system cancer patients had significantly elevated GAD-7 (β = 6.26, SE = 1.60, $p < 0.001$) and PHQ-9 scores (β = 5.93, SE = 1.79, $p < 0.01$). Interaction effects between cancer type and time indicated that gynecological cancer patients exhibited a significant reduction in PHQ-9 scores at week 4 (β = −5.84, SE = 2.42, $p < 0.05$) and in both PHQ-9 (β = −7.58, SE = 3.28, $p < 0.05$) and GAD-7 scores (β = −5.62, SE = 2.90, $p < 0.05$) at week 8, as compared to breast cancer patients. Radiotherapy had a significant effect, with patients not receiving it showing lower GAD-7 scores (β = −1.85, SE = 0.69, $p < 0.01$) at baseline. No significant effects were found for the other treatments on PHQ-9 or GAD-7 scores.

4 Discussion

Cancer patients are more susceptible to anxiety and depressive disorders, yet the management are often under-addressed, resulting in compromised quality of life. Given the significant heterogeneity in biological, environmental, and psychological factors underlying these conditions, the efficacy of a given antidepressant may differ in cancer patients compared to the general non-cancer population (Lynall and McIntosh, 2023). Therefore, in this study we found that the efficacy of antidepressants is comparable in cancer and non-cancer patients in treating anxiety and depressive disorders. Notably, the efficacy of escitalopram matches that of duloxetine, venlafaxine, and vortioxetine, each of which surpassed sertraline in cancer patients.

The retrospective cohort study included cancer and non-cancer patients receiving antidepressant treatments. The cancer group had approximately five times as many females as males, likely due to the prevalence of breast cancer or the higher susceptibility of females to depression and anxiety disorders, aligning with previous research (Parker and Brotchie, 2010). Cancer patients also experienced poorer sleep quality and a higher incidence of insomnia compared to non-cancer subjects, often treated with low doses of trazodone (≤ 50mg/kg) as an alternative to conventional sedatives to enhance sleep quality (Wichniak et al., 2017),. Currently, no standard antidepressant regimen is recommended for cancer patients with chronic anxiety and depression. In this study, escitalopram was the most frequently prescribed and used as the control, primarily due to its efficacy, tolerability, drug interactions, cost-effectiveness, and availability.

According to the monoamine hypothesis, second-generation antidepressants effectively alleviate depression and anxiety disorders by modulating the levels of serotonin, norepinephrine, dopamine, and other neurotransmitters

TABLE 2 Results of the mixed linear model of factors influencing PHQ-9 and GAD-7.

Variables	Categories	GAD-7 scores	PHQ-9 scores
Follow-up time	Baseline	0	0
	Week 4	−7.46 (0.52)***	−7.45 (0.58)***
	Week 8	−8.93 (0.68)***	−9.58 (0.76)***
Cancer status	Cancer	0	0
	Non-cancer	−0.04 (0.44)	0.22 (0.48)
Episode Type	First	0	0
	Relapse	0.27 (0.53)	0.45 (0.59)
Antidepressants	Escitalopram	0	0
	Duloxetine	−0.48 (1.05)	−1.05 (1.15)
	Sertraline	−1.04 (0.72)	0.28 (0.80)
	Venlafaxine	0.57 (0.67)	1.63 (0.74)*
	Vortioxetine	−1.36 (1.41)	1.02 (1.56)
Combined trazodone	Yes	0	0
	No	0.76 (0.67)*	−1.27 (0.46)**
Interaction effects (influencing factors × time)			
Week 4−baseline			
Cancer status group (non-cancer) × time		−0.31 (0.64)	−0.88 (0.72)
Episode Type(relapse) × time		0.36 (0.77)	0.77 (0.86)
Antidepressants group × time			
Escitalopram		0	0
Duloxetine		2.63 (2.28)	3.34 (2.54)
Sertraline		2.69 (1.07)*	1.68 (1.20)
Venlafaxine		1.44 (1.04)	0.99 (1.16)
Vortioxetine		3.40 (2.17)	3.27 (2.43)
Combined trazodone(no) × time		0.76 (0.67)	2.06 (0.74)**
Week 8 – baseline			
Cancer status group (non-cancer) × time		0.70 (0.81)	0.47(0.91)
Episode Type(relapse) × time		0.16 (1.11)	0.19(1.24)
Antidepressants group × time			
Escitalopram		0	0
Duloxetine		−0.64 (3.1)	1.62 (3.47)
Sertraline		3.77 (1.81)*	3.75 (2.02)*
Venlafaxine		0.02 (1.30)	−0.74(1.45)
Vortioxetine		1.82 (2.52)	−1.57(2.81)
Combined trazodone (no) × time		0.88 (0.88)	1.55 (0.98)

Values represent estimated effect sizes (β) and corresponding standard errors (SE); *$p < 0.05$, **$p < 0.01$, ***$p < 0.001$; PHQ-9, Patient Health Questionnaire-9; GAD-7, Generalized Anxiety Disorder Questionnaire-7.

(Krishnan and Nestler, 2008). However, previous reports on the effectiveness of antidepressants in cancer patients have been inconsistent. On the one hand, the ASCO guidelines did not include antidepressant treatments as the first-line approach for managing anxiety and depression in adult cancer patients (Andersen et al., 2023). Previous studies also suggested paroxetine and desipramine's effects in breast cancer patients might be similar to a placebo (Musselman et al., 2006; Rutherford and Roose, 2013). On the other hand, another meta-analysis suggested that antidepressants can reduce the acute depressive symptoms of cancer patients, but only with limited quality of evidence (Vita et al., 2023). In this study, cancer patients showed significant improvements in anxiety and depression symptoms at the 4th and 8th weeks of follow-up, similar to non-cancer patients. Our findings support the standardized prescription of antidepressants for managing anxiety and depression in cancer patients.

Furthermore, escitalopram has been shown to be more effective than sertraline in the treatment of anxiety and depression. Another network meta-analysis including 21 antidepressants suggests that escitalopram might have the highest efficacy and tolerability in the general population (Cipriani et al., 2018). Another study on breast cancer survivors suggest that escitalopram can effectively alleviate hot flashes and depressive symptoms (Biglia et al., 2018). Our study was consistent with prior findings and confirmed the role of escitalopram in its efficacy in cancer patients.

Different cancer types exhibited varied responses to antidepressant treatments. In this study, breast cancer patients were selected as the control group due to their larger numbers. These individuals experience a broad spectrum of psychological and emotional trauma from various factors such as post-surgical body shape changes, lymphedema, fertility issues, and hormonal imbalances (Pilevarzadeh et al., 2019). Compared with the breast cancer patients, gynecological cancer patients showed higher initial depression scores but responded better to antidepressants, likely influenced by peri-menopausal changes post-oophorectomy. Despite a favorable prognosis, thyroid cancer survivors often face psychological distress and reduced quality of life, driven by factors like fear of recurrence, ongoing surveillance, and feelings of isolation (Dionisi-Vici et al., 2021). Similarly, hematologic malignancy patients have higher rates of depression, potentially linked to symptom burden, including fatigue, sleep disruption, and pain, as well as the fear of recurrence (Kuczmarski et al., 2024). Lung cancer, male reproductive/urinary system cancer patients also showed higher initial anxiety and depression scores, potentially linked to significant somatic symptoms: inflammatory cytokine disorders in lung cancer, and psychological issues related to sexual function, urinary complications, pain, and anhedonia in male reproductive/urinary system cancer (Watts et al., 2014; Sharpley et al., 2023; Mcfarland et al., 2020). Therefore, when assessing anxiety and depression in cancer patients, it is crucial to consider the unique characteristics of different cancer types to more accurately understand the underlying symptoms.

This study was conducted at a single hospital in China with a predominantly Chinese patient population, which may limit the generalizability of the findings to other healthcare settings and populations. Moreover, while the effectiveness assessment was based on self-reported survey data, incorporating objective medical parameters, such as brain imaging or hippocampal volume, could provide a deeper understanding of the neuropsychological impact on patients. Future multi-center studies that include diverse demographics and combine both subjective and medical assessments would help validate and expand upon these results.

5 Conclusion

In conclusion, our study suggest that antidepressants are equally effective in treating anxiety and depression in cancer patients as they are in the non-cancer population. Among five antidepressants, escitalopram equals duloxetine, venlafaxine, and vortioxetine, and may have a superior effect compared to sertraline. Patients with different types of cancer experience varying degrees of psychological symptoms. Of note, gynecological cancer patients may respond quickly to antidepressant treatments compared to breast cancer patients. Our study highlights the necessity of personalized psychiatric care in oncology management, advocating for antidepressant treatments tailored to specific cancer types and patient psychological profiles. Integrating comprehensive mental health strategies into cancer care can greatly enhance patient quality of life, potentially improving therapeutic outcomes and treatment adherence.

Data availability statement

The raw data supporting the conclusions of this article will be made available by the authors, without undue reservation.

Ethics statement

The studies involving humans were approved by the Medical Ethics Committee, Fudan University Shanghai Cancer Center. The studies were conducted in accordance with the local legislation and institutional requirements. The participants provided their written informed consent to participate in this study. Written informed consent was obtained from the individual(s) for the publication of any potentially identifiable images or data included in this article.

Author Contributions

KZ: Conceptualization, Data curation, Formal analysis, Methodology, Validation, Visualization, Writing – original draft. YW: Data curation, Formal analysis, Investigation, Methodology, Writing – original draft. QL: Data curation, Investigation, Resources, Writing – original draft. ZY: Conceptualization, Project administration, Software, Visualization, Writing – review and editing. WF: Conceptualization, Funding acquisition, Methodology, Project administration, Resources, Software, Supervision, Writing – review and editing.

Funding

The author(s) declare financial support was received for the research, authorship, and/or publication of this article. This work was supported by the Talent Introduction Fund of Fudan University Shanghai Cancer Center [YJRC202105], Shanghai Anticancer Association EYAS PROJECT [HYXH2022072], Beijing Xisike Clinical Oncology Research Foundation [HYXH2023005], and three-year action plan for strengthening the construction of the public health system in Shanghai [GWVI-11.2-XD23].

Acknowledgments

We want to thank all participants who shared their experiences with this study.

Conflict of interest

The authors declare that the research was conducted in the absence of any commercial or financial relationships that could be construed as a potential conflict of interest.

Publisher's note

Supplementary material

The Supplementary Material for this article can be found online at: https://www.frontiersin.org/articles/10.3389/fnins.2024.1485179/full#supplementary-material

References

Andersen, B., Lacchetti, C., Ashing, K., Berek, J., Berman, B., Bolte, S., et al. (2023). Management of anxiety and depression in adult survivors of cancer: ASCO guideline update. *J. Clin. Oncol.* 41, 3426–3453. doi: 10.1200/JCO.23.00293

Biglia, N., Bounous, V., Susini, T., Pecchio, S., Sgro, L., Tuninetti, V., et al. (2018). Duloxetine and escitalopram for hot flushes: Efficacy and compliance in breast cancer survivors. *Eur. J. Cancer Care* 27:84. doi: 10.1111/ecc.12484

Chan, K., Poller, W., Swirski, F., and Russo, S. (2023). Central regulation of stress-evoked peripheral immune responses. *Nat. Rev. Neurosci.* 24, 591–604. doi: 10.1038/s41583-023-00729-2

Cipriani, A., Furukawa, T., and Salanti, G. (2018). Comparative efficacy and acceptability of 21 antidepressant drugs for the acute treatment of adults with major depressive disorder: A systematic review and network meta-analysis. *Lancet* 391, 1357–1366. doi: 10.1016/S0140-6736(17)32802-7

Dionisi-Vici, M., Fantoni, M., Botto, R., Felicetti, F., Rossetto, R., Gallo, M., et al. (2021). Distress, anxiety, depression and unmet needs in thyroid cancer survivors: A longitudinal study. *Endocrine* 74, 603–610. doi: 10.1007/s12020-021-02786-y

Esser, P., Hartung, T., Friedrich, M., Johansen, C., Wittchen, H., Faller, H., et al. (2018). The generalized anxiety disorder screener (GAD-7) and the anxiety module of

the hospital and depression scale (HADS-A) as screening tools for generalized anxiety disorder among cancer patients. *Psychooncology* 27, 1509–1516. doi: 10.1002/pon.4681

Fetcho, R., Parekh, P., Chou, J., Kenwood, M., Chalençon, L., Estrin, D., et al. (2023). A stress-sensitive frontostriatal circuit supporting effortful reward-seeking behavior. *Neuron* 112:473–487.e4. doi: 10.1016/j.neuron.2023.10.020

Goldsmith, D., Haroon, E., Woolwine, B., Jung, M., Wommack, E., Harvey, P., et al. (2016). Inflammatory markers are associated with decreased psychomotor speed in patients with major depressive disorder. *Brain Behav. Immun.* 56, 281–288. doi: 10.1016/j.bbi.2016.03.025

Grassi, L. (2020). Psychiatric and psychosocial implications in cancer care: The agenda of psycho-oncology. *Epidemiol. Psychiatr. Sci.* 29, e89. doi: 10.1017/S2045796019000829

Heinrich, M., Hofmann, L., Baurecht, H., Kreuzer, P., Knüttel, H., Leitzmann, M., et al. (2023). Author Correction: Suicide risk and mortality among patients with cancer. *Nat. Med.* 29:3268. doi: 10.1038/s41591-023-02307-6

Krishnan, V., and Nestler, E. (2008). The molecular neurobiology of depression. *Nature* 455, 894–902. doi: 10.1038/nature07455

Kroenke, K., Spitzer, R., and Williams, J. (2002). The PHQ-15: Validity of a new measure for evaluating the severity of somatic symptoms. *Psychosom. Med.* 64, 258–266. doi: 10.1097/00006842-200203000-00008

Kuczmarski, T., Roemer, L., and Odejide, O. (2024). Depression in patients with hematologic malignancies: The current landscape and future directions. *Blood Rev.* 65:101182. doi: 10.1016/j.blre.2024.101182

Li, Y., Ma, J., and Lu, G. (2021). Hydromorphone for cancer pain. *Cochrane Database Syst. Rev.* 8:CD011108. doi: 10.1002/14651858.CD011108.pub3

Liu, Y., Hau, K., and Liu, H. (2024). Linear mixed-effects models for dependent data: Power and accuracy in parameter estimation. *Multivar. Behav. Res.* 59, 978–994.

Lynall, M., and McIntosh, A. (2023). The heterogeneity of depression. *Am. J. Psychiatry* 180, 703–704. doi: 10.1002/j.2051-5545.2011.tb00061.x

Manea, L., Gilbody, S., and McMillan, D. (2012). Optimal cut-off score for diagnosing depression with the patient health questionnaire (PHQ-9): A meta-analysis. *CMAJ* 184, E191–E196.

Mcfarland, D. C., Jutagir, D. R., and Miller, A. H. (2020). Tumor mutation burden and depression in lung cancer: Association with inflammation. *J. Natl. Compr. Cancer Netw.* 18, 434–442.

Mitchell, A., Chan, M., Bhatti, H., Halton, M., Grassi, L., Johansen, C., et al. (2011). Prevalence of depression, anxiety, and adjustment disorder in oncological, haematological, and palliative-care settings: A meta-analysis of 94 interview-based studies. *Lancet Oncol.* 12, 160–174.

Momayyezi, M., Fallahzadeh, H., Farzaneh, F., and Momayyezi, M. (2021). Sleep quality and cancer-related fatigue in patients with cancer. *J. Car. Sci.* 10, 145–152.

Musselman, D., Somerset, W., Guo, Y., Manatunga, A., Porter, M., Penna, S., et al. (2006). A double-blind, multicenter, parallel-group study of paroxetine, desipramine, or placebo in breast cancer patients (stages I, II, III, and IV) with major depression. *J. Clin. Psychiatry* 67, 288–296.

Oberg, A. L., and Mahoney, D. W. (2007). Linear mixed effects models. *Methods Mol. Biol.* 404, 213–234.

Parker, G., and Brotchie, H. (2010). Gender differences in depression. *Int. Rev. Psychiatry* 22, 429–436. doi: 10.3109/09540261.2010.492391

Pilevarzadeh, M., Amirshahi, M., Afsargharehbagh, R., Rafiemanesh, H., Hashemi, S. M., and Balouchi, A. (2019). Global prevalence of depression among breast cancer patients: A systematic review and meta-analysis. *Breast Cancer Res. Treat.* 176, 519–533.

Qiu, H., Cao, S., and Xu, R. (2021). Cancer incidence, mortality, and burden in China: A time-trend analysis and comparison with the United States and United Kingdom based on the global epidemiological data released in 2020. *Cancer Commun.* 41, 1037–1048.

Rutherford, B., and Roose, S. P. A. (2013). model of placebo response in antidepressant clinical trials. *Am. J. Psychiatry* 170, 723–733. doi: 10.1176/appi.ajp.2012.12040474

Sharpley, C., Christie, D., Arnold, W., and Bitsika, V. (2023). Network analysis of depression in prostate cancer patients: Implications for assessment and treatment. *Psychooncology* 32, 368–374.

Sung, H., Ferlay, J., Siegel, R., Laversanne, M., Soerjomataram, I., and Jemal, A. (2021). Global cancer statistics 2020: GLOBOCAN estimates of incidence and mortality worldwide for 36 cancers in 185 countries. *CA Cancer J. Clin.* 71, 209–249. doi: 10.3322/caac.21660

Vehling, S., Mehnert-Theuerkauf, A., Philipp, R., Härter, M., Kraywinkel, K., Kuhnert, R., et al. (2022). Prevalence of mental disorders in patients with cancer compared to matched controls - secondary analysis of two nationally representative surveys. *Acta Oncol.* 61, 7–13. doi: 10.1080/0284186X.2021.1992008

Vita, G., Compri, B., Matcham, F., Barbui, C., and Ostuzzi, G. (2023). Antidepressants for the treatment of depression in people with cancer. *Cochrane Database Syst. Rev.* 3:Cd011006. doi: 10.1002/14651858.CD011006.pub3

Watts, S., Leydon, G., Birch, B., Prescott, P., Lai, L., Eardley, S., et al. (2014). Depression and anxiety in prostate cancer: A systematic review and meta-analysis of prevalence rates. *BMJ Open* 4:e003901.

Wichniak, A., Wierzbicka, A., and Walęcka, M. (2017). Effects of antidepressants on sleep. *Curr. Psychiatry Rep.* 19:63.

Yin, J., Song, X., Wang, C., Lin, X., and Miao, M. (2023). Escitalopram versus other antidepressive agents for major depressive disorder: A systematic review and meta-analysis. *BMC Psychiatry* 23:876. doi: 10.1186/s12888-023-05382-8

frontiers | Frontiers in Pharmacology

TYPE Original Research
PUBLISHED 06 January 2025
DOI 10.3389/fphar.2024.1460513

OPEN ACCESS

EDITED BY
Song Zhang,
Shanghai Jiao Tong University, China

REVIEWED BY
Wenhan Yang,
Central South University, China
Yikang Liu,
United Imaging Intelligence, United States

*CORRESPONDENCE
Xi Jiang,
xijiang@uestc.edu.cn
Keith M. Kendrick,
kkendrick@uestc.edu.cn

RECEIVED 06 July 2024
ACCEPTED 09 December 2024
PUBLISHED 06 January 2025

CITATION
Hagan AT, Xu L, Klugah-Brown B, Li J, Jiang X and Kendrick KM (2025) The pharmacodynamic modulation effect of oxytocin on resting state functional connectivity network topology. *Front. Pharmacol.* 15:1460513. doi: 10.3389/fphar.2024.1460513

The pharmacodynamic modulation effect of oxytocin on resting state functional connectivity network topology

Abraham Tonny Hagan, Lei Xu, Benjamin Klugah-Brown, Jialin Li, Xi Jiang* and Keith M. Kendrick*

MOE Key Laboratory for Neuroinformation, The Clinical Hospital of Chengdu Brain Science Institute, University of Electronic Science and Technology of China, Chengdu, China

Introduction: Neuroimaging studies have demonstrated that intranasal oxytocin has extensive effects on the resting state functional connectivity of social and emotional processing networks and may have therapeutic potential. However, the extent to which intranasal oxytocin modulates functional connectivity network topology remains less explored, with inconsistent findings in the existing literature. To address this gap, we conducted an exploratory data-driven study.

Methods: We recruited 142 healthy males and administered 24 IU of intranasal oxytocin or placebo in a randomized controlled double-blind design. Resting-state functional MRI data were acquired for each subject. Network-based statistical analysis and graph theoretical approaches were employed to evaluate oxytocin's effects on whole-brain functional connectivity and graph topological measures.

Results: Our results revealed that oxytocin altered connectivity patterns within brain networks involved in sensory and motor processing, attention, memory, emotion and reward functions as well as social cognition, including the default mode, limbic, frontoparietal, cerebellar, and visual networks. Furthermore, oxytocin increased local efficiency, clustering coefficients, and small-world propensity in specific brain regions including the cerebellum, left thalamus, posterior cingulate cortex, right orbitofrontal cortex, right superior frontal gyrus, left inferior frontal gyrus, and right middle orbitofrontal cortex, while decreasing nodal path topological measures in the left and right caudate.

Discussion: These findings suggest that intranasal oxytocin may produce its functional effects through influencing the integration and segregation of information flow within small-world brain networks, particularly in regions closely associated with social cognition and motivation.

KEYWORDS

oxytocin, resting state fMRI, small-worldness, graph theory, pharmacodynamics

Introduction

The human brain has an intricate network of interconnected regions which form the functional connectome that is fundamental to how it processes all aspects of information influencing complex sensory, motor, cognitive and emotional behaviors (Sporns, 2011a; Van den Heuvel et al., 2012; Cromwell et al., 2020; Wasserman and Wasserman, 2023). Dysfunctions in these neural connections have been associated with neurological, mental and psychiatric disorders, including anxiety, autism, depression, schizophrenia, epilepsy and Alzheimer's disease (Marín, 2012; Jiang et al., 2023) and it is important to identify potential therapeutic interventions.

Oxytocin (OT), a hypothalamic neuropeptide hormone, has garnered significant interest as a neuromodulator in cognitive processes due to its involvement in social cognition and motivation (Kendrick et al., 2018; Quintana et al., 2021) and recent clinical trials reporting improved social functioning in individuals with autism spectrum disorder (Audunsdottir et al., 2024; Le et al., 2022). OT receptors are predominantly found in key regions of the social brain, including the hippocampus, cingulate cortex, insula, amygdala, basal ganglia and medial prefrontal cortex (Gimpl and Fahrenholz, 2001; Quintana et al., 2019) and there is considerable interest in establishing the effects of OXT administration on these regions and their functional connections. Resting-state fMRI (rsfMRI) is a valuable technique for investigating intrinsic brain connectivity independently of specific tasks (Canario et al., 2021). By analyzing spontaneous fluctuations in blood oxygenation level dependent (BOLD) signals, rsfMRI allows us to map functional interactions between brain regions and explore how these interactions are influenced by interventions or pharmacological manipulations (Snyder, 2022; Smitha et al., 2017).

A number of studies have examined the effects of intranasal administration of OT on resting state functional connectivity, although findings have been variable (Seeley et al., 2018). One fairly consistent finding has been for increased functional connectivity between the medial frontal cortex and the amygdala (Eckstein et al., 2017; Kou et al., 2022; Kovács and Kéri, 2015; Sripada et al., 2013). This pathway is important for emotional control and several clinical studies have also reported that OT can either increase resting state functional connectivity between frontal regions and the amygdala in autism (Procyshyn et al., 2022) and social anxiety (Dodhia et al., 2014) or in post-traumatic stress disorder (Frijling et al., 2016; Koch et al., 2016). Other studies have reported effects of intranasal oxytocin on amygdalo-hippocampal functional connectivity in either healthy (Coenjaerts et al., 2023) or autistic (Alaerts et al., 2019) individuals. However, these studies were mostly region of interest based and studies at the whole brain level have reported more extensive resting state changes in involving frontal and striatal reward processing regions and the cerebellum (Zhao et al., 2019a), with weakened functional connectivity between frontal and striatal and motor regions also being found to be improved in schizophrenia patients (Korann et al., 2022). Additionally, a large-scale effective connectivity study using resting state data has found increased connectivity following intranasal OT between frontal, salience, social cognition, reward and amygdala networks (Jiang et al., 2021), although a very small scale one only found effects on the effective connectivity between the dorsolateral prefrontal cortex and the precuneus in the central executive network (Kumar et al., 2020). The effects of OT on resting state networks may also be influenced by OT receptor genotype (Kou et al., 2022; Seeley et al., 2018) Overall, therefore findings investigating resting state-based changes based on conventional analysis of time-series in region pairs has produced varied results.

Several studies have attempted to establish more network based effects of intranasal OT using independent component analysis of resting state data, although again with somewhat different findings. Two studies have reported that OT particularly increased functional connectivity between attention and salience and default mode networks, implying modulation of attentional processing (Brodmann et al., 2017; Xin et al., 2021) while another found evidence for increased functional connectivity involving the mentalizing network (temperoparietal junction) and the default mode network, but decreased between it and the medial prefrontal network (Wu H. et al., 2020).

Graph-theoretical techniques may offer an alternative robust framework for quantifying the effects of OT on both global and local properties of brain networks (Wig et al., 2011; Lang et al., 2012; Fornito et al., 2016). By modeling the brain as a graph, with nodes representing brain regions and edges representing functional connections, this technique can examine how OT influences efficiency, resilience, and integration within the brain using measures, including small-world propensity, clustering coefficient, characteristic path length, global efficiency, and local efficiency (Bassett and Bullmore, 2017). However, one particular aspect of brain connectivity that has gained significant attention in recent years is the concept of "small-world networks." The human brain exhibits as a small-world network topology, characterized by a delicate balance between local clustering and short path length. This organization enables effective information processing while minimizing wiring costs (Sporns, 2011b). Disruptions in small-world network topology are associated with various neuropsychiatric disorders, including autism spectrum disorder, schizophrenia, and depression (Cao et al., 2015). Notably, modularity and clustering coefficients are also frequently used to quantify topological segregation properties in brain networks (Boccaletti et al., 2006; Rubinov and Sporns, 2010). The clustering coefficient, a frequently employed metric in brain research, serves as a representation of brain topology (Bullmore and Sporns, 2009) and several studies have established a correlation between mental illness, cognitive function, and this coefficient (Sæther et al., 2023; Ohi et al., 2017). Additionally, the average shortest path within neural networks, a prevalent indicator of the brain's small-world characteristics, mirrors its capacity for efficient information integration.

Several small scale graph theoretical studies have suggested that OT may modulate regional but not global processing to influence integration of networks associated with cognitive, attention, theory of mind and sensory processing (Martins et al., 2021; Zheng et al., 2021; Davies et al., 2024). However, findings from these small studies have been variable and it is important to implement this powerful approach in a larger cohort of subjects in order to establish more robustly what influence OT has on modulating both regional and global network processing and the precise nature of this in terms of integration within different systems.

In the current study we have therefore carried out a whole-brain resting state study on a large cohort of healthy subjects (n = 142) employing a graph-theoretical methodology to establish the pharmacodynamic effects of intranasal OT on brain functional connectivity network topology. Our hypothesis based on previous findings was that intranasal OT would influence the integration and segregation of information within the graph measures and functional connectivity patterns of the brain.

Materials and methodology

Participants

139 non-smoking healthy adult male subjects were recruited via advertisement at the University of Electronic Science and Technology of China. Only males were recruited for the current study in line with most other OT resting state studies and to avoid potential complications in controlling for menstrual cycle effects in females. In terms of inclusion and exclusion criteria, all subjects were right-handed and self-reported having no current or previous mental health problems, neurological disorders or other medical conditions. They were instructed not to consume alcohol or caffeine in the last 24 h prior to the start of the study. To control for group differences in psychological traits, anxiety and mood, all participants completed the Becks Depression Inventory (BDI-2) (Beck et al., 1996), State-Trait Anxiety Inventory (STAI) (Spielberger, 1983), Positive and Negative Affect Schedule, (PANAS) (Watson et al., 1988), autism spectrum quotient (ASQ) (Baron-Cohen et al., 2001) and Empathy quotient (EQ) (Allison et al., 2011). All subjects gave written informed consent and the study was approved by the University of Electronic Science and Technology of China ethical committee. The study protocol was in accordance with the latest revision of the declaration of Helsinki.

Study design

The study employed a randomized OT–placebo (PLC) controlled double blind between group design where each participant was randomly assigned to administer either OT or PLC intranasally.

Procedure

Test sessions were conducted by trained study staff. Participants were instructed to stay well hydrated before their visits but to abstain from caffeine, alcohol, and use of recreational drugs in the 24 h, leading up to their appointment. Participants were randomly assigned using a computer-based algorithm to self-administer either 24 IUs (three puffs per nostril given 30 s apart) of OT (OT plus glycerine, sodium chloride and sterile water; Sichuan Defeng Pharmaceutical Co. Ltd., Sichuan, China) or PLC (identical ingredients as the OT spray except for OT, also provided by Sichuan Defeng Pharmaceutical Co. Ltd., Sichuan, China) at the start of the full study visit as this dosage is well established, maintaining safety, efficacy, comparability and consistency across studies while ensuring reproducibility of our findings in the broader oxytocin research community which aligns with a number of previous OT-administration studies (Frijling et al., 2016; Koch et al., 2016; Parker et al., 2017; Yao et al., 2017) nasal spray administration followed standard recommendations (Guastella et al., 2013) and the rsfMRI scan started 45 min after the nasal sprays. Participants completed the questionnaires immediately prior to administering the nasal spray. In the scanner, participants were instructed to relax with open eyes but without falling asleep and without thinking of anything in particular (Patriat et al., 2013; Raimondo et al., 2021).

fMRI acquisition

MRI data were collected on a 3T GE MR750 Discovery MRI system (General Electric Medical System, Milwaukee, WI, USA). Functional gradient-echo-planar imaging (EPI) data were acquired during the resting-state paradigm (38 interleaved slices, TR 2s, TE 30 ms, FOV 252 × 252 × 133 mm, 80 × 80 × 38 mm matrix, flip angle 90°, in plane resolution of 3.15 × 3.15 mm, slice thickness 3.5 mm, 0 mm skip). The resting state scan lasted about 8 min, and 240 time points were acquired. Whole-brain high-resolution three-dimensional T1-weighted anatomical reference images were also acquired using an MP-RAGE sequence (sagittal plane, FOV = 240 mm × 240 -mm × 170; 1 × 1 × 1 mm isotropic voxels). Processing and analysis of brain images were performed using Statistical Parametric Mapping (SPM8) software (www.fifil.ion.ucl.ac.uk/spm).

fMRI data preprocessing

Standard preprocessing procedures were employed including slice time correction, motion correction with artifact rejection (scan-to-scan motion threshold 2 mm), spatial normalization, and smoothing with an 8 mm Gaussian kernel as implemented in the Functional Connectivity Toolbox (CONN; http://www.nitrc.org/projects/conn/; Whitfield-Gabrieli and Nieto-Castanon, 2012). Prior to analysis, data were denoised using "aCompCor," an anatomically informed component-based noise correction, to correct for physiological and other sources of noise from white matter and cerebrospinal fluid (Behzadi et al., 2007).

Data analysis

The study comprised two treatment groups (OT (N = 67, aged 22.09 ± 2.44 years) and PLC (N = 72 aged 21.69 ± 2.57 years) in a between-group design. The data from the 139 participants were analyzed and the brain signals extracted from the 116 brain regions according to the Automated Anatomical Labelling (AAL) brain atlas. To determine the effects of OT on the intrinsic connectivity among brain regions, Pearson correlation of mean fMRI time series between any pair of the 116 regions was calculated, and subsequently transformed to z-maps using Fisher r-to-z transformation. The Z-matrix values conformed to a Gaussian distribution, and the data was subsequently examined for outliers

before proceeding with statistical tests. A network-based statistics (NBS) approach was then used to identify the whole-brain functional connectivity difference between subjects administered with OT compared to PLC with head motion effects measured as the mean framewise displacement (FD) and age included as a covariate (ANOVA, FWE < 0.05).

Graph estimation and network characterization

The z-transformed connectivity matrices were utilized to construct brain graphs, which represented the functional connectome for each subject. Subsequently, the functional network properties for each subject were calculated based on the corresponding functional connectivity matrix. The functional connectivity metrics were binarized to generate undirected adjacency matrices, wherein the correlation above the proportional threshold was set to 1, and 0 otherwise. This binarization was performed to include only the strongest functional network connections. Subsequently, a variety of sparsity thresholds were implemented on the correlation matrices, ranging from 10% to 50% in increments of 1%. This was done to facilitate accurate estimation of small-world propensity parameters and to reduce the occurrence of false edges, as suggested by Feng et al. (2012). For each individual participating in this study, we defined sparsity as the proportion of present edges within a network. Initially, the mean connectivity matrix representing the two treatment groups was computed. Subsequently, both global and nodal network metrics were computed for each level of sparsity.

The global network metrics examined in this study included clustering coefficients, characteristic path lengths, and network efficiency parameters, specifically global efficiency and local efficiency. In addition to these traditional metrics, we computed small-world propensity to assess how each node within the network balances local clustering with short path lengths. Small-world propensity quantifies small-world-like properties by comparing each node's local clustering coefficient and local path length to those of a random network (Telesford et al., 2011). This measure provides insight into the local efficiency and integration of each node, revealing how individual regions contribute to the broader network organization. A node with high small-world propensity demonstrates strong local clustering and short path lengths to other nodes, reflecting its ability to efficiently communicate with distant regions of the network.

Similarly, the nodal network metrics, such as nodal efficiency, nodal degree, and nodal betweenness centrality, were also computed. However, the graph measures of interest to investigate our hypothesis were the small-world propensity measures, clustering coefficients, characteristic path lengths, nodal path, efficiency (local and global), and nodal degree. While these selected measures prevent redundancy since some of these metrics exhibit relationships with one another, either proportionally or inversely, they also provide comprehensive view of brain network organization, each capturing a distinct aspect of brain function. Mathematically, these key metrics are presented as follows:

Global efficiency (E_{glob})

Global efficiency measures the efficiency of information exchange across the entire network. It is the average of the inverse shortest path lengths between all pairs of nodes (Wang et al., 2009).

$$E_{glob} = \frac{1}{N(N-1)} \sum_{i \neq j \in G} \frac{1}{d_{ij}}$$

where by N is the number of nodes in the network and d_{ij} is the shortest path length between nodes i and j.

Local efficiency (E_{loc})

Local efficiency quantifies the efficiency of communication within the local neighborhood of a node (Hayasaka and Laurienti, 2010).

$$E_{loc} = \frac{1}{N} \sum_{i \in G} E_{glob}(G_i)$$

where by $E_{glob}(G_i)$ is the global efficiency computed for the subgraph G_i containing only the neighbors of node i.

Clustering coefficient (C)

The clustering coefficient measures the tendency of a node's neighbors to be connected to each other. A high clustering coefficient indicates that neighboring nodes form tightly knit clusters or triangles (Sporns et al., 2007)

$$C = \frac{1}{N} \sum_{i \in G} \frac{2T_i}{k_i(k_i - 1)}$$

where by T_i is the number of triangles involving node i and k_i is the degree of node i (number of edges connected to i).

Small-world propensity (γ_i)

The Small-World Propensity (γ_i) quantifies the degree to which a given brain region (node i) exhibits small-world properties, which are characterized by high local clustering and short path lengths relative to a random network (Bassett and Bullmore, 2006). This measure was computed for each node using the following formula:

$$\gamma_i = \frac{C_{local,observed(i)}}{C_{local,random(i)}} \times \frac{L_{local,observed(i)}}{L_{local,random(i)}}$$

where by $C_{local,observed(i)}$ is the local clustering coefficient of node (i) in the observed network and $C_{local,random(i)}$ is the local clustering coefficient of node (i) in a random network with the same number of nodes and edges.

Again, $L_{local,observed(i)}$ is the local path length of node (i) in the observed network and $L_{local,random(i)}$ is the local path length of node (i) in the random network.

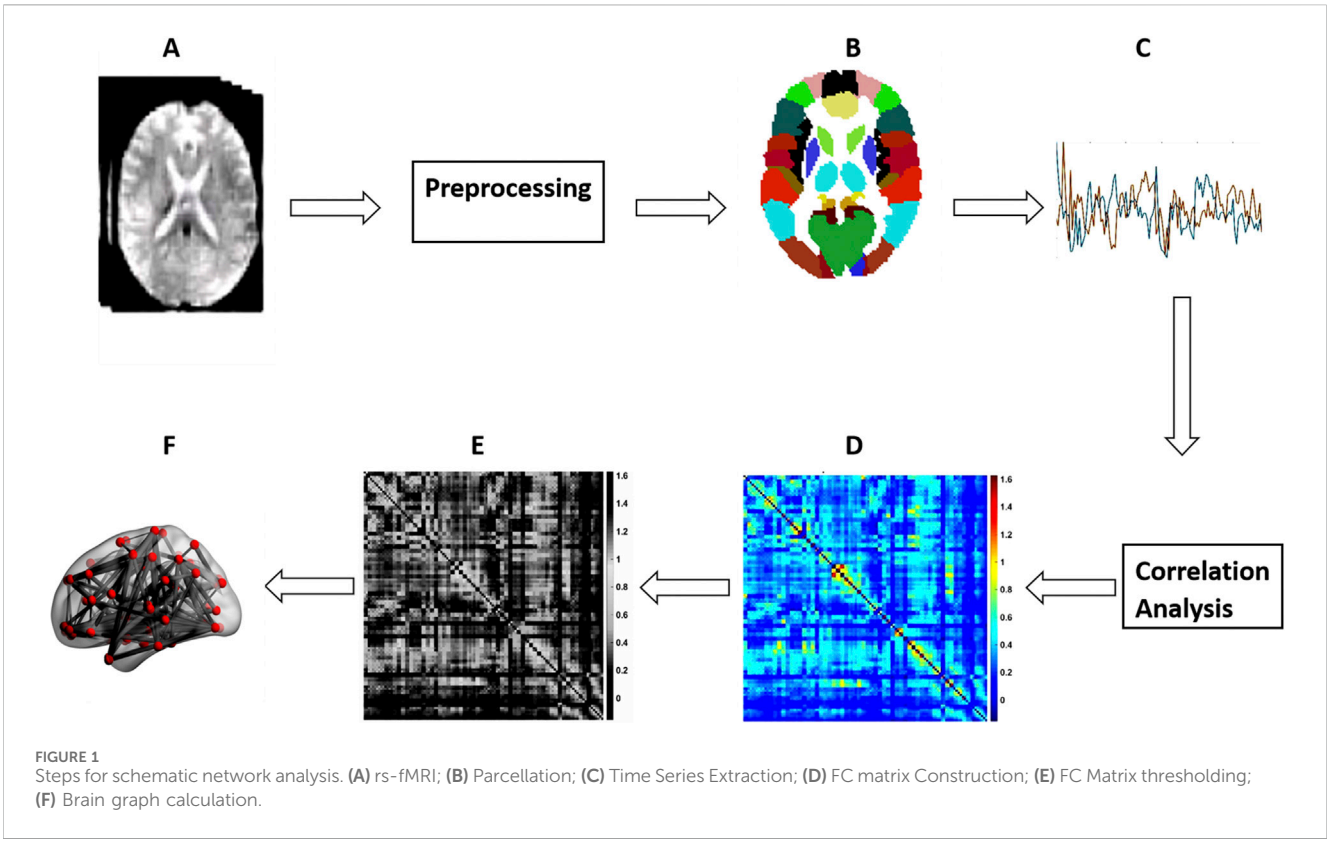

FIGURE 1
Steps for schematic network analysis. **(A)** rs-fMRI; **(B)** Parcellation; **(C)** Time Series Extraction; **(D)** FC matrix Construction; **(E)** FC Matrix thresholding; **(F)** Brain graph calculation.

Nodal degree (k_i)

The degree of a node is the number of direct connections (edges) it has to other nodes (Zalesky et al., 2010).

$$k_i = \sum_{j \in G} A_{ij}$$

where by A_{ij} is the adjacency matrix element, indicating whether nodes i and j are connected ($A_{ij} = 1$) or not ($A_{ij} = 0$).

Characteristic path length (L)

The characteristic path length is the average shortest path length between all pairs of nodes in the network (Van Wijk et al., 2010).

$$L = \frac{1}{N(N-1)} \sum_{i \neq j \in G} d_{ij}$$

where by d_{ij} is the shortest path length between nodes i and j. For more details, a recent review by Rubinov and Sporns (2010) offers comprehensive definitions and descriptions of these metrics.

The GraphVar toolbox was employed for the various graph measures computations (Kruschwitz et al., 2015; Waller et al., 2018). Additionally, the area under the curve (AUC) was used to summarize each possible value for each of the metrics analyzed on the graph (Pickering and Endre, 2012). This allowed us to generate short estimates for each graph metric that are sensitive to topological variations in brain networks and independent of the selection of a single threshold. Therefore, we used AUC parameters instead of raw values for the entirety of our statistical analyzes with graph measures. This process is illustrated diagrammatically in Figure 1.

Statistical analysis

We tested for significant differences in FC between the OT and PLC groups at the level of individual brain connections. This was achieved through univariate testing, which assessed the connectivity of each individual link within the brain's functional network. To control for multiple comparisons, we applied Network-Based Statistics (NBS). This method identified clusters of brain regions with significantly altered connectivity between the two groups, allowing us to detect subnetworks showing FC differences while minimizing false positives.

To further strengthen the reliability of our results, we conducted permutation testing, where the group assignments (OT vs. PLC) were randomly shuffled across 1,000 iterations. This approach compared the observed FC differences to the distribution of differences obtained from the randomizations, ensuring that the observed results were not due to chance and bolstering confidence in their robustness. Then, we examined differences in network topology between the OT and PLC groups by applying sparsity thresholding ranging from 10% to 50%. This approach allowed us to

TABLE 1 Demographics and clinical characteristics data.

Variables (mean ± SD)	OT	PLC	t-value	*p*-value
No. of subjects	67 (Male)	72 (male)		
Age	22.09 ± 2.44	21.69 ± 2.57	0.931	0.353
EQ score	37.87 ± 13.37	40.12 ± 13.68	−0.984	0.326
ASQ score	21.54 ± 8.87	20.21 ± 7.42	0.954	0.338
BDI score	6.15 ± 5.55	5.18 ± 5.59	1.025	0.307
STAI score	39.91 ± 9.85	39.37 ± 9.77	0.364	0.716
PANAS (POS)	27.07 ± 7.92	27.20 ± 7.93	−0.107	0.914
PANAS (NEG)	14.43 ± 5.82	15.05 ± 5.87	−0.653	0.514

Abbreviations: Becks Depression Inventory (BDI), State-trait Anxiety Inventory (STAI); EQ, empathy quotient; ASQ, autism spectrum quotient; Positive and Negative Affect Schedule (PANAS); SD, Standard Deviation; POS, positive; NEG, negative.

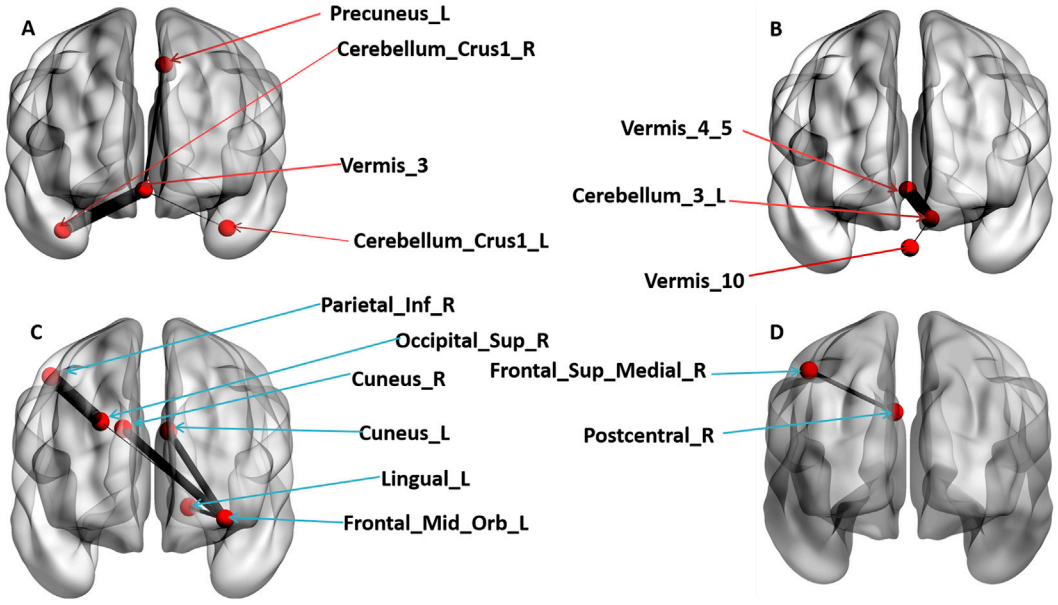

FIGURE 2
The coronal view of significant Functional connectivity patterns of brain regions that survived multiple FDR corrections ($p < 0.05$). **(A)** denotes increased FC patterns of OT group compared to PLC group. **(B)** denotes increased FC patterns in OT group compared to PLC group. **(C)** denotes decreased FC patterns in OT group compared to PLC group. **(D)** denotes decreased FC patterns in OT group compared to PLC group. The red arrows points to brain regions that revealed increased FC patterns while the blue arrows point to brain regions that revealed a decreased FC pattern.

test how the treatment effects on brain connectivity varied across different network densities, ensuring that our results were not influenced by a specific threshold. Finally, to account for multiple comparisons and reduce the risk of Type I errors, we employed FDR corrections, with results considered significant only if the corrected *p*-value was $p < 0.05$.

Additionally, two sample two tailed t-tests were employed to estimate the between group differences in nodal metrics. 1,000 permutations were performed on the AUC of the network metrics through a permutation based non-parametric test. FDR correction for multiple comparisons was then used to identify findings that achieved a significance of $p < 0.05$.

Results

Subject demographics and behavioral measures

The analysis of the questionnaire data revealed that there were no significant differences in age, psychological traits or mood indices between the treatment groups. Independent sample t-tests revealed no significant disparity in the mean FD in head motion between the treatment groups. Three participants needed to be excluded due to their failure to attend all of the experimental session resulting in a final sample consisting of 139 healthy male participants (See Table 1).

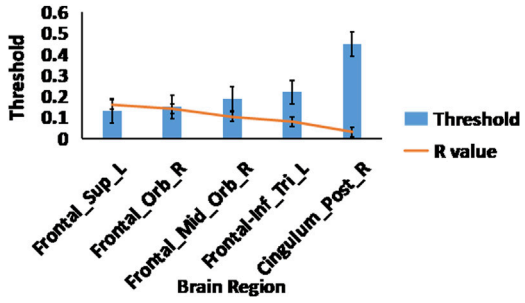

FIGURE 3
Small world propensity measures. The effects of OT compared to PLC on the small world propensity network metric using 2-sample t-test, After FDR multiple corrections ($p < 0.05$); the displayed brain regions were significant. The blue bars represent sparsity threshold while the orange line represents the R-values.

Effects of OT on functional connectivity patterns/network edges

The influence of OT on FC patterns was examined. Following multiple FDR corrections, significant differences between the OT and PLC groups were observed. The OT group showed increased FC patterns between the cerebellar vermis_3 and the left precuneus (r = 0.098, p = 0.001), the cerebellar vermis 3 and left crus1 (r = 0.096, p = 0.001) and between the cerebellar vermis 3 and right crus1 (r = 0.105, p = 0.001) respectively (see Figure 2A). The OT group also showed increased FC between the left cerebellum 3 and the vermis 4 and 5 (r = 0.120, p = 0.001), as well as between the left cerebellum 3 and the vermis 10 (r = 0.118, p = 0.001) (see Figure 2B).

Furthermore, the OT group showed reduced FC patterns across interconnected brain regions, including the left middle orbitofrontal cortex and the left cuneus (r = −0.097, p = 0.001), left middle orbitofrontal cortex and right cuneus (r = −0.1005, p = 0.001), left middle orbitofrontal cortex and the left lingual gyrus (r = −0.090, p = 0.001), left middle orbitofrontal cortex and the right superior occipital gyrus (r = −0.084, p = 0.001), the right superior occipital gyrus and the right inferior parietal cortex (r = −0.110, p = 0.001) and finally between the right posterior central sulcus and the right medial superior frontal cortex (r = −0.095, p = 0.001) regions of the brain. Figures 2C, D) presents detailed significant regions. Again, the results were visualized using BrainNet Viewer (Xia et al., 2013).

Effects of OT on the global and nodal metrics

After multiple FDR correction, we observed the following treatment effects on global and nodal metric measures:

Global efficiency

There were no significant treatment effects on the global efficiency measure for the OT relative to PLC group after multiple FDR corrections.

Small-world propensity

Analysis of the small world propensity network topology measure revealed significant differences between OT relative to PLC after multiple FDR correction. OT increased the small world propensity topological measures of the right posterior cingulate cortex (r = 0.032, p = 0.001), right orbitofrontal cortex (r = 0.142, p = 0.001), right superior frontal gyrus (r = 0.161, p = 0.001), left inferior frontal gyrus (r = 0.081, p = 0.001) and right middle orbitofrontal cortex (r = 0.103, p = 0.001) (see Figure 3).

Clustering coefficient

Significant differences after FDR multiple correction occurred for clustering coefficients of several nodes of the brain in the OT compared to PLC group. OT increased the clustering coefficient of the cerebellar vermis 3 brain region across different network sparsity thresholds and that of the left Thalamus region (see Table 2).

Nodal path

OT relative to PLC significantly decreases nodal path lengths in the right and left caudate regions of the brain across different network sparsity thresholds after multiple FDR correction (see Table 2).

Local efficiency

OT relative to PLC significantly increased local efficiency of the cerebella vermis 3 and 10 brain regions after multiple FDR correction (see Table 2).

Discussion

The objective of the current study was to investigate the pharmacodynamic impact of OT on whole-brain FC network topology in a large cohort of adult male healthy subjects. Utilizing an exploratory and data-driven approach, we aimed to examine differences in pairwise FC patterns at the whole brain level and the effects of OT on small world propensity network topology. By employing graph theory, the study sought to provide insights into the functional brain networks modulated by OT at rest and to clarify the nature of these changes to provide a deeper insight into how OT influences human social behavior and cognition.

Differences in functional connectivity between OT and PLC

Our key findings revealed that, compared to PLC, intranasal OT modulates inter-regional FC patterns, small-worldness, and regional organization of topographical networks in the resting human brain. We identified that OT's modulatory effects were associated with widespread brain regions, in frontal, parietal and occipital cortices as well as sub-cortical and cerebellar regions. These regions form networks that enhance information robustness in the human brain during cognitive control and executive functions and are involved in planning, decision-making, working memory, motor control, learning, and emotional regulation. However, our findings showed no significant differences after multiple false discovery rate FDR corrections in the global efficiency topological measure and the

TABLE 2 The effects of OT on the global and nodal topological measures (nodal path, clustering coefficient and local efficiency).

Threshold	Node path	Direction	R-Value	*p*-value (FDR- corr)
0.26	left Caudate	OT < PLC	−0.295	0.001
0.26	Right Caudate	OT < PLC	−0.277	0.001
0.27	left Caudate	OT < PLC	−0.272	0.001
0.27	Right Caudate	OT < PLC	−0.311	0.001
0.30	Right Caudate	OT < PLC	−0.195	0.001
0.32	left Caudate	OT < PLC	−0.178	0.001
0.33	left Caudate	OT < PLC	−0.207	0.001
0.37	left Caudate	OT < PLC	−0.188	0.001
0.38	left Caudate	OT < PLC	−0.225	0.001
0.39	left Caudate	OT < PLC	−0.216	0.001
0.40	left Caudate	OT < PLC	−0.235	0.001
0.41	left Caudate	OT < PLC	−0.201	0.001
Threshold	Local Efficiency	Direction	R-Value	*p*-value (FDR-corr)
0.10	Vermis_3	OT > PLC	0.202	0.001
0.11	Vermis_3	OT > PLC	0.212	0.001
0.12	Vermis_3	OT > PLC	0.214	0.001
0.15	Vermis_3	OT > PLC	0.215	0.001
0.46	Vermis_10	OT > PLC	0.119	0.001
Threshold	Clustering Coefficient	Direction	R-Value	*p*-value (FDR-corr)
0.11	Vermis_3	OT > PLC	0.184	0.001
0.12	Vermis_3	OT > PLC	0.194	0.001
0.23	Left Thalamus	OT > PLC	0.089	0.001

FDR-corr indicates FDR-corrected *p* values, all <0.001. *For healthy males, the topological effect of treatment compared the difference values (OT, minus PLC) between groups.

mean functional connectivity of OT compared to PLC, regarding global information transfer across brain regions of the human connectome. This is consistent with several previous studies (Poppy, 2014; Santander, 2017; Martins et al., 2021; Zheng et al., 2021).

In terms of altered patterns of resting state functional connectivity intranasal OT administration promoted both increased and decreased connectivity in a number of brain regions in line with some previous findings (Eckstein et al., 2017; Sripada et al., 2013; Zhao et al., 2019b). The most notable increased in functional connectivity particularly involved the cerebellum and included that between the posterior cerebellar vermis and other regions of the cerebellum as well as the precuneus in the default mode network. The vermis, situated within the cerebellum, has recently been shown in animal studies to play an important role in the social brain network (Chao et al., 2021; 2023). The vermis may orchestrate the neural framework essential for Social Recognition Memory (SRM), a process that entails the identification of familiar individuals to establish and sustain social connections (Saito, 2023; Van Overwalle et al., 2020b). Similarly, the cerebellum, while traditionally known for its role in motor control, has been shown in recent research to participate in cognitive functions and emotional responses (Lee, 2023). The increased functional connectivity between vermis 3 and the precuneus may reflect an effect of OT on facilitating judgment of mental states in others (Schmidt et al., 2020; Van Overwalle et al., 2020a). Interestingly, several previous resting state studies have reported effects of OT on cerebellum functional connectivity with one study reporting decreased connectivity with reward areas (putamen) (Zhao et al., 2019b), and another with increased connectivity with the amygdala (Eckstein et al., 2017) which might suggest differential effects on reward and emotional control.

On the other hand, we found evidence for reduced functional connectivity between the medial orbitofrontal cortex and visual processing regions (cuneus, lingual gyrus, superior occipital gyrus) as well as the inferior parietal cortex. This circuitry may represent risk taking circuitry (Rolls et al., 2022) and intranasal OT has been reported to reduce risk taking (Patel et al., 2015).

The effects of OT on global and nodal metrics

The human brain's topological characteristics, such as hubs, small-worldness, and network efficiency, are of great functional importance (Bullmore and Sporns, 2009; Bassett and Bullmore, 2009). The small-world network, as proposed by Bullmore and Sporns (2009), is an optimized and highly efficient network model that supports cognitive fitness, functional segregation, and information processing integration. It balances short path lengths and high local clustering to cater to both global and local processing needs (Kaiser and Hilgetag, 2006). While the small world propensity metric quantifies how closely a network resembles this small-world structure, characterized by high clustering and short path lengths, we found in the current study that OT, compared to PLC, enhanced the small-world propensity of the network, particularly in frontal cortical regions including the right orbitofrontal cortex, right middle orbitofrontal cortex, left inferior frontal gyrus and the superior frontal gyrus. This finding is opposite to that reported by Zheng et al. (2021) but may reflect their small sample size. Oxytocin also enhanced small-world propensity network topology in the posterior cingulate cortex, a highly evolved brain region responsible for higher cognitive functions such as thinking, planning, and decision-making. These frontal and parietal regions play a vital role in complex cognitive control and executive functions, including planning, decision-making, working memory, and cognitive control. This aligns with previous studies indicating that abnormalities in these brain regions typically result in functional cognitive decline (Dickerson and Sperling, 2008; Christopher and Strafella, 2013). Dysfunctions in these areas are also often associated with developmental disorders such as attention deficit hyperactivity disorder and autism spectrum disorder, where executive function deficits are prevalent. As a result, the modulatory effects of intranasal OT administration on these critical brain regions further support its potential as a therapeutic agent for neurodevelopmental disorders.

The graph metric known as the "clustering coefficient topology" is utilized in network analysis to quantify the interconnectedness among a node's neighbors in the context of brain networks. OT increased clustering coefficient topology in the study suggesting that it may enhance the local interconnectedness of neurons in the brain, potentially leading to more efficient information processing within local networks. However, it is important to note that the specific effects can vary depending on the context and the individual's overall health and mental state. Evidence suggests that brain networks possess a high clustering coefficient, indicating that neighboring regions of the brain are likely to be interconnected (Yin et al., 2017). Specifically, OT increased clustering coefficient in the vermis and thalamus, which are part of complex networks and contribute to various cognitive and motor functions. The thalamus, which is globally connected with distributed cortical regions, serves as an integrative hub of the functional network. Similarly, the vermis, which is associated with bodily posture and locomotion, is part of the spinocerebellum system and receives somatic sensory input from the head and proximal body parts via ascending spinal pathways (Hordacre and McCambridge, 2018; Kaut et al., 2020; Loutit et al., 2021). Recent studies indicate that the cerebellar vermis plays a role in managing a specific aspect of social memory in mice, highlighting its function in the brain's social network (Chao et al., 2021; 2023). Consequently, an increase in the clustering coefficient suggests that OT may enhance the local interconnectedness of neurons in the brain, potentially leading to more efficient information processing within local networks.

Local efficiency, a key metric in network analysis, measures the efficiency of information transfer in each node's neighborhood. Evidence suggests that an increase in local efficiency signifies high fault tolerance, as it indicates that the network remains well connected when any node is removed. In the current study, we found that OT increased the local efficiency network topology in vermis 3 and 10 brain regions at different sparsity thresholds, compared to PLC. This aligns with a recent study from Martins et al. (2021), which reported an increase in the local efficiency measure of the brain regions related to the cerebellum, right cuneal cortex and the right posterior superior temporal gyrus. For a healthy brain to exhibit small-world properties, an increase in local efficiency and the clustering coefficient would reveal a more optimal balance between local specialization and global integration, facilitating efficient information processing and robustness against damage.

Furthermore, we observed that OT, compared to PLC, decreased the nodal path length basal ganglia brain reward regions (left caudate and right caudate) at different sparsity thresholds. The nodal path length in a network is a measure of the average shortest path between a node and all other nodes in the network. A decrease in this measure could indicate more efficient information transfer within specific brain regions. The caudate nucleus is involved in various cognitive and emotional functions, but is primarily known for its role in reward, and plays a pivotal role in various higher neurological functions including planning the execution of movement, learning, memory, reward, motivation, emotion, and romantic interaction (Schultz, 2016; Takakusaki et al., 2004). Overall therefore, OT may be promoting more efficient information transfer with the caudate to facilitate its functions, and has been shown to modulate responses to socially rewarding stimuli in this region (Kou et al., 2021; Scheele et al., 2013).

Limitations

Several limitations should be acknowledged in the context of the current findings. Firstly, only male participants were included in the current study in line with most other resting state studies and therefore it is possible that OT may have different effects in females and this will need to be confirmed in future studies. Secondly, we did not include resting state fMRI scans within subjects before and after OT administration, as suggested by Wu J. T. et al. (2020), which might have produced different results. Lastly, we focused on static network alterations rather than constructing a temporal dynamic network model after OT administration. This limitation prevented us from gaining further insight into the modulatory effects of OT on causal relations. Therefore, we suggest that future research should employ a more dynamic approach to better understand the effects of OT on brain networks.

In conclusion, findings in the current study revealed that intranasal OT administration induces alterations in functional

connectivity patterns and enhances small-world topological networks within the social brain of healthy adult males. These results suggest that intranasal OT possesses pharmacodynamic properties capable of modulating connectivity and organization in the social brain to improve its processing efficiency. These findings provide further support for the development of OT administration as potential therapeutic strategy in disorders with social dysfunction. However, further research is necessary to fully elucidate the underlying mechanisms and clinical implications of these brain network effects.

Data availability statement

The raw data supporting the conclusions of this article will be made available by the authors, without undue reservation.

Ethics statement

The studies involving humans were approved by the University of Electronic Science and Technology of China Ethical Committee. The studies were conducted in accordance with the local legislation and institutional requirements. The participants provided their written informed consent to participate in this study.

Author contributions

AH: Formal Analysis, Investigation, Methodology, Project administration, Visualization, Writing–original draft, Writing–review and editing. LX: Investigation, Methodology, Writing–original draft, Writing–review and editing. BK-B: Writing–original draft, Writing–review and editing. JL: Investigation, Writing–original draft, Writing–review and editing. XJ: Conceptualization, Formal Analysis, Investigation, Methodology, Project administration, Resources, Supervision, Visualization, Writing–original draft, Writing–review and editing. KK: Conceptualization, Data curation, Formal Analysis, Funding acquisition, Investigation, Methodology, Project administration, Resources, Software, Supervision, Validation, Visualization, Writing–original draft, Writing–review and editing.

Funding

The author(s) declare that financial support was received for the research, authorship, and/or publication of this article. This work was supported by National Natural Science Foundation of China (62276050), Sichuan Science and Technology Program (2024NSFSC0655).

Conflict of interest

The authors declare that the research was conducted in the absence of any commercial or financial relationships that could be construed as a potential conflict of interest.

The author(s) declared that they were an editorial board member of Frontiers, at the time of submission. This had no impact on the peer review process and the final decision.

Publisher's note

References

Alaerts, K., Bernaerts, S., Vanaudenaerde, B., Daniels, N., and Wenderoth, N. (2019). Amygdala–hippocampal connectivity is associated with endogenous levels of oxytocin and can be altered by exogenously administered oxytocin in adults with autism. *Biol. Psychiatry Cognitive Neurosci. Neuroimaging* 4 (7), 655–663. doi:10.1016/j.bpsc.2019.01.008

Allison, C., Baron-Cohen, S., Wheelwright, S. J., Stone, M. H., and Muncer, S. J. (2011). Psychometric analysis of the Empathy quotient (EQ). *Personality Individ. Differ.* 51 (7), 829–835. doi:10.1016/j.paid.2011.07.005

Audunsdottir, K., Sartorius, A. M., Kang, H., Glaser, B., Boen, R., Nærland, T., et al. (2024). The effects of oxytocin administration on social and routinized behaviors in autism: a preregistered systematic review and meta-analysis. *Psychoneuroendocrinology* 167, 107067. doi:10.1016/j.psyneuen.2024.107067

Baron-Cohen, S., Wheelwright, S., Skinner, R., Martin, J., and Clubley, E. (2001). The autism-spectrum quotient (AQ): evidence from asperger syndrome/high-functioning autism, males and females, scientists and mathematicians. *J. Autism Dev. Disord.* 31, 5–17. doi:10.1023/A:1005653411471

Bassett, D. S., and Bullmore, E. (2006). Small-world brain networks. *Neurosci. a Rev. J. bringing Neurobiol. neurology psychiatry* 12 (6), 512–523. doi:10.1177/1073858406293182

Bassett, D. S., and Bullmore, E. T. (2009). Human brain networks in health and disease. *Curr. Opin. neurology* 22 (4), 340–347. doi:10.1097/WCO.0b013e32832d93dd

Bassett, D. S., and Bullmore, E. T. (2017). Small-world brain networks revisited. *Neurosci.* 23 (5), 499–516. doi:10.1177/1073858416667720

Beck, A. T., Steer, R. A., and Brown, G. (1996). *Beck depression inventory–II (BDI-II) [database record]*. APA PsycTests. doi:10.1037/t00742-000

Behzadi, Y., Restom, K., Liau, J., and Liu, T. T. (2007). A component based noise correction method (CompCor) for BOLD and perfusion based fMRI. *Neuroimage* 37 (1), 90–101. doi:10.1016/j.neuroimage.2007.04.042

Boccaletti, S., Latora, V., Moreno, Y., Chavez, M., and Hwang, D. U. (2006). Complex networks: structure and dynamics. *Phys. Rep.* 424 (4-5), 175–308. doi:10.1016/j.physrep.2005.10.009

Brodmann, K., Gruber, O., and Goya-Maldonado, R. (2017). Intranasal oxytocin selectively modulates large-scale brain networks in humans. *Brain Connect.* 7 (7), 454–463. doi:10.1089/brain.2017.0528

Bullmore, E., and Sporns, O. (2009). Complex brain networks: graph theoretical analysis of structural and functional systems. *Nat. Rev. Neurosci.* 10 (3), 186–198. doi:10.1038/nrn2575

Canario, E., Chen, D., and Biswal, B. (2021). A review of resting-state fMRI and its use to examine psychiatric disorders. *Psychoradiology* 1 (1), 42–53. doi:10.1093/psyrad/kkab003

Cao, M., Wang, Z., and He, Y. (2015). Connectomics in psychiatric research: advances and applications. *Neuropsychiatric Dis. Treat.* 11, 2801–2810. doi:10.2147/NDT.S63470

Chao, O. Y., Pathak, S. S., Zhang, H., Augustine, G. J., Christie, J. M., Kikuchi, C., et al. (2023). Social memory deficit caused by dysregulation of the cerebellar vermis. *Nat. Commun.* 14 (1), 6007. doi:10.1038/s41467-023-41744-2

Chao, O. Y., Zhang, H., Pathak, S. S., Huston, J. P., and Yang, Y. M. (2021). Functional convergence of motor and social processes in lobule IV/V of the mouse cerebellum. *Cerebellum* 20, 836–852. doi:10.1007/s12311-021-01246-7

Christopher, L., and Strafella, A. P. (2013). Neuroimaging of brain changes associated with cognitive impairment in Parkinson's disease. *J. Neuropsychology* 7 (2), 225–240. doi:10.1111/jnp.12015

Coenjaerts, M., Adrovic, B., Trimborn, I., Philipsen, A., Hurlemann, R., and Scheele, D. (2023). Effects of exogenous oxytocin and estradiol on resting-state functional connectivity in women and men. *Sci. Rep*. 13 (1), 3113. doi:10.1038/s41598-023-29754-y

Cromwell, H. C., Abe, N., Barrett, K. C., Caldwell-Harris, C., Gendolla, G. H., Koncz, R., et al. (2020). Mapping the interconnected neural systems underlying motivation and emotion: a key step toward understanding the human affectome. *Neurosci. and Biobehav. Rev.* 113, 204–226. doi:10.1016/j.neubiorev.2020.02.032

Davies, C., Martins, D., Dipasquale, O., McCutcheon, R. A., De Micheli, A., Ramella-Cravaro, V., et al. (2024). Connectome dysfunction in patients at clinical high risk for psychosis and modulation by oxytocin. *Mol. psychiatry* 29 (5), 1241–1252. doi:10.1038/s41380-024-02406-x

Dickerson, B. C., and Sperling, R. A. (2008). Functional abnormalities of the medial temporal lobe memory system in mild cognitive impairment and Alzheimer's disease: insights from functional MRI studies. *Neuropsychologia* 46 (6), 1624–1635. doi:10.1016/j.neuropsychologia.2007.11.030

Dodhia, S., Hosanagar, A., Fitzgerald, D. A., Labuschagne, I., Wood, A. G., Nathan, P. J., et al. (2014). Modulation of resting-state amygdala-frontal functional connectivity by oxytocin in generalized social anxiety disorder. *Neuropsychopharmacology* 39 (9), 2061–2069. doi:10.1038/npp.2014.53

Eckstein, M., Markett, S., Kendrick, K. M., Ditzen, B., Liu, F., Hurlemann, R., et al. (2017). Oxytocin differentially alters resting state functional connectivity between amygdala subregions and emotional control networks: inverse correlation with depressive traits. *Neuroimage* 149, 458–467. doi:10.1016/j.neuroimage.2017.01.078

Feng, Y., Bai, L., Ren, Y., Chen, S., Wang, H., Zhang, W., et al. (2012). FMRI connectivity analysis of acupuncture effects on the whole brain network in mild cognitive impairment patients. *Magn. Reson. Imaging* 30 (5), 672–682. doi:10.1016/j.mri.2012.01.003

Fornito, A., Zalesky, A., and Bullmore, E. (2016). *Fundamentals of brain network analysis*. Cambridge: Academic Press.

Frijling, J. L., van Zuiden, M., Koch, S. B., Nawijn, L., Veltman, D. J., and Olff, M. (2016). Intranasal oxytocin affects amygdala functional connectivity after trauma script-driven imagery in distressed recently trauma-exposed individuals. *Neuropsychopharmacology* 41 (5), 1286–1296. doi:10.1038/npp.2015.278

Gimpl, G., and Fahrenholz, F. (2001). The oxytocin receptor system: structure, function, and regulation. *Physiol. Rev.* 81 (2), 629–683. doi:10.1152/physrev.2001.81.2.629

Guastella, A. J., Hickie, I. B., McGuinness, M. M., Otis, M., Woods, E. A., Disinger, H. M., et al. (2013). Recommendations for the standardisation of oxytocin nasal administration and guidelines for its reporting in human research. *Psychoneuroendocrinology* 38 (5), 612–625. doi:10.1016/j.psyneuen.2012.11.019

Hayasaka, S., and Laurienti, P. J. (2010). Comparison of characteristics between region-and voxel-based network analyses in resting-state fMRI data. *NeuroImage* 50 (2), 499–508. doi:10.1016/j.neuroimage.2009.12.051

Hordacre, B., and McCambridge, A. (2018). Motor control: structure and function of the nervous system. *Neurol. Physiother. Pocketb.*, 29–32.

Jiang, X., Ma, X., Geng, Y., Zhao, Z., Zhou, F., Zhao, W., et al. (2021). Intrinsic, dynamic and effective connectivity among large-scale brain networks modulated by oxytocin. *Neuroimage* 227, 117668. doi:10.1016/j.neuroimage.2020.117668

Jiang, X., Shou, X. J., Zhao, Z., Chen, Y., Meng, F., Le, J., et al. (2023). A brain structural connectivity biomarker for autism spectrum disorder diagnosis in early childhood. *Psychoradiology* 3, kkad005. doi:10.1093/psyrad/kkad005

Kaiser, M., and Hilgetag, C. C. (2006). Nonoptimal component placement, but short processing paths, due to long-distance projections in neural systems. *PLoS Comput. Biol.* 2 (7), e95. doi:10.1371/journal.pcbi.0020095

Kaut, O., Mielacher, C., Hurlemann, R., and Wüllner, U. (2020). Resting-state fMRI reveals increased functional connectivity in the cerebellum but decreased functional connectivity of the caudate nucleus in Parkinson's disease. *Neurological Res.* 42 (1), 62–67. doi:10.1080/01616412.2019.1709141

Kendrick, K. M., Guastella, A. J., and Becker, B. (2018). Overview of human oxytocin research. *Behav. Pharmacol. Neuropeptides Oxytocin* 35, 321–348. doi:10.1007/7854_2017_19

Koch, C., Massimini, M., Boly, M., and Tononi, G. (2016). Neural correlates of consciousness: progress and problems. *Nat. Rev. Neurosci.* 17 (5), 307–321. doi:10.1038/nrn.2016.22

Korann, V., Jacob, A., Lu, B., Devi, P., Thonse, U., Nagendra, B., et al. (2022). Effect of intranasal oxytocin on resting-state effective connectivity in schizophrenia. *Schizophr. Bull.* 48 (5), 1115–1124. doi:10.1093/schbul/sbac066

Kou, J., Lan, C., Zhang, Y., Wang, Q., Zhou, F., Zhao, Z., et al. (2021). In the nose or on the tongue? Contrasting motivational effects of oral and intranasal oxytocin on arousal and reward during social processing. *Transl. psychiatry* 11 (1), 94. doi:10.1038/s41398-021-01241-w

Kou, J., Zhang, Y., Zhou, F., Sindermann, C., Montag, C., Becker, B., et al. (2022). A randomized trial shows dose-frequency and genotype may determine the therapeutic efficacy of intranasal oxytocin. *Psychol. Med.* 52(10), 1959–1968. doi:10.1017/S0033291720003803

Kovács, B., and Kéri, S. (2015). Off-label intranasal oxytocin use in adults is associated with increased amygdala-cingulate resting-state connectivity. *Eur. Psychiatry* 30 (4), 542–547. doi:10.1016/j.eurpsy.2015.02.010

Kruschwitz, J. D., List, D., Waller, L., Rubinov, M., and Walter, H. (2015). GraphVar: a user-friendly toolbox for comprehensive graph analyses of functional brain connectivity. *J. Neurosci. methods* 245, 107–115. doi:10.1016/j.jneumeth.2015.02.021

Kumar, J., Iwabuchi, S. J., Völlm, B. A., and Palaniyappan, L. (2020). Oxytocin modulates the effective connectivity between the precuneus and the dorsolateral prefrontal cortex. *Eur. archives psychiatry Clin. Neurosci.* 270 (5), 567–576. doi:10.1007/s00406-019-00989-z

Lang, E. W., Tomé, A. M., Keck, I. R., Górriz-Sáez, J. M., and Puntonet, C. G. (2012). Brain connectivity analysis: a short survey. *Comput. Intell. Neurosci.* 2012 (1), 412512. doi:10.1155/2012/412512

Le, J., Zhang, L., Zhao, W., Zhu, S., Lan, C., Kou, J., et al. (2022). Infrequent intranasal oxytocin followed by positive social interaction improves symptoms in autistic children: a pilot randomized clinical trial. *Psychotherapy Psychosomatics* 91 (5), 335–347. doi:10.1159/000524543

Lee, S. (2023). *The study of rhesus monkey's behavior and neural connectivity in social-hierarchy: experimental modeling and implementation of computational analysis schemes*. Doctoral dissertation. Arizona, United States: The University of Arizona.

Loutit, A. J., Vickery, R. M., and Potas, J. R. (2021). Functional organization and connectivity of the dorsal column nuclei complex reveals a sensorimotor integration and distribution hub. *J. Comp. Neurology* 529 (1), 187–220. doi:10.1002/cne.24942

Marín, O. (2012). Interneuron dysfunction in psychiatric disorders. *Nat. Rev. Neurosci.* 13 (2), 107–120. doi:10.1038/nrn3155

Martins, D., Dipasquale, O., and Paloyelis, Y. (2021). Oxytocin modulates local topography of human functional connectome in healthy men at rest. *Commun. Biol.* 4 (1), 68. doi:10.1038/s42003-020-01610-z

Ohi, K., Shimada, T., Nemoto, K., Kataoka, Y., Yasuyama, T., Kimura, K., et al. (2017). Cognitive clustering in schizophrenia patients, their first-degree relatives and healthy subjects is associated with anterior cingulate cortex volume. *NeuroImage Clin.* 16, 248–256. doi:10.1016/j.nicl.2017.08.008

Parker, K. J., Oztan, O., Libove, R. A., Sumiyoshi, R. D., Jackson, L. P., Karhson, D. S., et al. (2017). Intranasal oxytocin treatment for social deficits and biomarkers of response in children with autism. *Proc. Natl. Acad. Sci.* 114 (30), 8119–8124. doi:10.1073/pnas.1705521114

Patel, N., Grillon, C., Pavletic, N., Rosen, D., Pine, D. S., and Ernst, M. (2015). Oxytocin and vasopressin modulate risk-taking. *Physiology and Behav.* 139, 254–260. doi:10.1016/j.physbeh.2014.11.018

Patriat, R., Molloy, E. K., Meier, T. B., Kirk, G. R., Nair, V. A., Meyerand, M. E., et al. (2013). The effect of resting condition on resting-state fMRI reliability and consistency: a comparison between resting with eyes open, closed, and fixated. *NeuroImage* 78, 463–473. doi:10.1016/j.neuroimage.2013.04.013

Pickering, J. W., and Endre, Z. H. (2012). New metrics for assessing diagnostic potential of candidate biomarkers. *Clin. J. Am. Soc. Nephrol.* 7 (8), 1355–1364. doi:10.2215/CJN.09590911

Poppy, C. L. (2014). Functional Activation and Connectivity under the Influence of oxytocin: an explorative Study using functional magnetic resonance imaging *(Master's thesis)*. Oslo, Norway: University of Oslo.

Procyshyn, T. L., Lombardo, M. V., Lai, M. C., Jassim, N., Auyeung, B., Crockford, S. K., et al. (2022). Oxytocin enhances basolateral amygdala activation and functional connectivity while processing emotional faces: preliminary findings in autistic vs non-autistic women. *Soc. cognitive Affect. Neurosci.* 17 (10), 929–938. doi:10.1093/scan/nsac016

Quintana, D. S., Lischke, A., Grace, S., Scheele, D., Ma, Y., and Becker, B. (2021). Advances in the field of intranasal oxytocin research: lessons learned and future directions for clinical research. *Mol. Psychiatry* 26 (1), 80–91. doi:10.1038/s41380-020-00864-7

Quintana, D. S., Rokicki, J., van der Meer, D., Alnæs, D., Kaufmann, T., Córdova-Palomera, A., et al. (2019). Oxytocin pathway gene networks in the human brain. *Nat. Commun.* 10 (1), 668. doi:10.1038/s41467-019-08503-8

Raimondo, L., Oliveira, Í. A. F., Heij, J., Priovoulos, N., Kundu, P., Leoni, R. F., et al. (2021). Advances in resting state fMRI acquisitions for functional connectomics. *NeuroImage* 243, 118503. doi:10.1016/j.neuroimage.2021.118503

Rolls, E. T., Wan, Z., Cheng, W., and Feng, J. (2022). Risk-taking in humans and the medial orbitofrontal cortex reward system. *NeuroImage* 249, 118893. doi:10.1016/j.neuroimage.2022.118893

Rubinov, M., and Sporns, O. (2010). Complex network measures of brain connectivity: uses and interpretations. *Neuroimage* 52 (3), 1059–1069. doi:10.1016/j.neuroimage.2009.10.003

Saito, V. M. (2023). Cerebellar vermis joins the brain's social network. *Commun. Biol.* 6 (1), 1291. doi:10.1038/s42003-023-05673-6

Santander, T. (2017). *The social (neural) network: Towards a unifying endophenotype between genes and behavior Doctoral dissertation*. Virginia, United States: University of Virginia.

Sæther, L. S., Ueland, T., Haatveit, B., Maglanoc, L. A., Szabo, A., Djurovic, S., et al. (2023). Inflammation and cognition in severe mental illness: patterns of covariation and subgroups. *Mol. Psychiatry* 28 (3), 1284–1292. doi:10.1038/s41380-022-01924-w

Scheele, D., Wille, A., Kendrick, K. M., Stoffel-Wagner, B., Becker, B., Güntürkün, O., et al. (2013). Oxytocin enhances brain reward system responses in men viewing the face of their female partner. *Proc. Natl. Acad. Sci.* 110 (50), 20308–20313. doi:10.1073/pnas.1314190110

Schmidt, A., Davies, C., Paloyelis, Y., Meyer, N., De Micheli, A., Ramella-Cravaro, V., et al. (2020). Acute oxytocin effects in inferring others' beliefs and social emotions in people at clinical high risk for psychosis. *Transl. psychiatry* 10 (1), 203. doi:10.1038/s41398-020-00885-4

Schultz, W. (2016). Reward functions of the basal ganglia. *J. neural Transm.* 123, 679–693. doi:10.1007/s00702-016-1510-0

Seeley, S. H., Chou, Y.-h., and O'Connor, M.-F. (2018). Intranasal oxytocin and OXTR genotype effects on resting state functional connectivity: a systematic review. *Neurosci. Biobehav. Rev.* 95, 17–32. doi:10.1016/j.neubiorev.2018.09.011

Smitha, K. A., Akhil Raja, K., Arun, K. M., Rajesh, P. G., Thomas, B., Kapilamoorthy, T. R., et al. (2017). Resting state fMRI: a review on methods in resting state connectivity analysis and resting state networks. *Neuroradiol. J.* 30 (4), 305–317. doi:10.1177/1971400917697342

Snyder, A. Z. (2022). Intrinsic brain activity and resting state networks. *Neurosci. 21st century basic Clin.*, 1939–1990. doi:10.1007/978-3-030-88832-9_133

Spielberger, C. D. (1983). *State-Trait Anxiety Inventory for Adults (STAI-AD) [Database record]*. APA PsycTests. doi:10.1037/t06496-000

Sporns, O. (2011a). The human connectome: a complex network. *Ann. N. Y. Acad. Sci.* 1224 (1), 109–125. doi:10.1111/j.1749-6632.2010.05888.x

Sporns, O. (2011b). The non-random brain: efficiency, economy, and complex dynamics. *Front. Comput. Neurosci.* 5, 5. doi:10.3389/fncom.2011.00005

Sporns, O., Honey, C. J., and Kötter, R. (2007). Identification and classification of hubs in brain networks. *PloS one* 2 (10), e1049. doi:10.1371/journal.pone.0001049

Sripada, C. S., Phan, K. L., Labuschagne, I., Welsh, R., Nathan, P. J., and Wood, A. G. (2013). Oxytocin enhances resting-state connectivity between amygdala and medial frontal cortex. *Int. J. Neuropsychopharmacol.* 16 (2), 255–260. doi:10.1017/S1461145712000533

Takakusaki, K., Saitoh, K., Harada, H., and Kashiwayanagi, M. (2004). Role of basal ganglia–brainstem pathways in the control of motor behaviors. *Neurosci. Res.* 50 (2), 137–151. doi:10.1016/j.neures.2004.06.015

Telesford, Q. K., Joyce, K. E., Hayasaka, S., Burdette, J. H., and Laurienti, P. J. (2011). The ubiquity of small-world networks. *Brain connect.* 1 (5), 367–375. doi:10.1089/brain.2011.0038

Van den Heuvel, M. P., Kahn, R. S., Goñi, J., and Sporns, O. (2012). High-cost, high-capacity backbone for global brain communication. *Proc. Natl. Acad. Sci. U. S. A.* 109 (28), 11372–11377. doi:10.1073/pnas.1203593109

Van Overwalle, F., Manto, M., Cattaneo, Z., Clausi, S., Ferrari, C., Gabrieli, J. D., et al. (2020a). Consensus paper: cerebellum and social cognition. *Cerebellum* 19, 833–868. doi:10.1007/s12311-020-01155-1

Van Overwalle, F., Van de Steen, F., van Dun, K., and Heleven, E. (2020b). Connectivity between the cerebrum and cerebellum during social and non-social sequencing using dynamic causal modelling. *NeuroImage* 206, 116326. doi:10.1016/j.neuroimage.2019.116326

Van Wijk, B. C., Stam, C. J., and Daffertshofer, A. (2010). Comparing brain networks of different size and connectivity density using graph theory. *PloS one* 5 (10), e13701. doi:10.1371/journal.pone.0013701

Waller, L., Brovkin, A., Dorfschmidt, L., Bzdok, D., Walter, H., and Kruschwitz, J. D. (2018). GraphVar 2.0: a user-friendly toolbox for machine learning on functional connectivity measures. *J. Neurosci. methods* 308, 21–33. doi:10.1016/j.jneumeth.2018.07.001

Wang, J., Wang, L., Zang, Y., Yang, H., Tang, H., Gong, Q., et al. (2009). Parcellation-dependent small-world brain functional networks: a resting-state fMRI study. *Hum. brain Mapp.* 30 (5), 1511–1523. doi:10.1002/hbm.20623

Wasserman, T., and Wasserman, L. D. (2023). The human connectome: an overview. *Aprax. Neural Netw. Model*, 35–48. doi:10.1007/978-3-031-24105-5_3

Watson, D., Clark, L. A., and Tellegen, A. (1988). Development and validation of brief measures of positive and negative affect: the PANAS scales. *J. Personality Soc. Psychol.* 54 (6), 1063–1070. doi:10.1037/0022-3514.54.6.1063

Whitfield-Gabrieli, S., and Nieto-Castanon, A. (2012). Conn: a functional connectivity toolbox for correlated and anticorrelated brain networks. *Brain Connect.* 2 (3), 125–141. doi:10.1089/brain.2012.0073

Wig, G. S., Schlaggar, B. L., and Petersen, S. E. (2011). Concepts and principles in the analysis of brain networks. *Ann. N. Y. Acad. Sci.* 1224 (1), 126–146. doi:10.1111/j.1749-6632.2010.05947.x

Wu, H., Feng, C., Lu, X., Liu, X., and Liu, Q. (2020a). Oxytocin effects on the resting-state mentalizing brain network. *Brain imaging Behav.* 14 (6), 2530–2541. doi:10.1007/s11682-019-00205-5

Wu, J. T., Leung, K., and Leung, G. M. (2020b). Nowcasting and forecasting the potential domestic and international spread of the 2019-nCoV outbreak originating in Wuhan, China: a modelling study. *Lancet* 395 (10225), 689–697. doi:10.1016/S0140-6736(20)30260-9

Xia, M., Wang, J., and He, Y. (2013). BrainNet Viewer: a network visualization tool for human brain connectomics. *PloS one* 8 (7), e68910. doi:10.1371/journal.pone.0068910

Xin, F., Zhou, F., Zhou, X., Ma, X., Geng, Y., Zhao, W., et al. (2021). Oxytocin modulates the intrinsic dynamics between attention-related large-scale networks. *Cereb. Cortex* 31 (3), 1848–1860. doi:10.1093/cercor/bhy295

Yao, S., Bergan, J., Lanjuin, A., and Dulac, C. (2017). Oxytocin signaling in the medial amygdala is required for sex discrimination of social cues. *eLife* 6, e31373. doi:10.7554/eLife.31373

Yin, Z., Li, J., Zhang, Y., Ren, A., Von Meneen, K. M., and Huang, L. (2017). Functional brain network analysis of schizophrenic patients with positive and negative syndrome based on mutual information of EEG time series. *Biomed. Signal Process. Control* 31, 331–338. doi:10.1016/j.bspc.2016.08.013

Zalesky, A., Fornito, A., Harding, I. H., Cocchi, L., Yücel, M., Pantelis, C., et al. (2010). Whole-brain anatomical networks: does the choice of nodes matter? *NeuroImage* 50 (3), 970–983. doi:10.1016/j.neuroimage.2009.12.027

Zhao, Z., Ma, X., Geng, Y., Zhao, W., Zhou, F., Wang, J., et al. (2019a). Oxytocin differentially modulates specific dorsal and ventral striatal functional connections with frontal and cerebellar regions. *Neuroimage* 184, 781–789. doi:10.1016/j.neuroimage.2018.09.067

Zhao, Z., Ma, X., Geng, Y., Zhao, W., Zhou, F., Wang, J., et al. (2019b). Oxytocin differentially modulates specific dorsal and ventral striatal functional connections with frontal and cerebellar regions. *Neuroimage* 184, 781–789. doi:10.1016/j.neuroimage.2018.09.067

Zheng, S., Punia, D., Wu, H., and Liu, Q. (2021). Graph theoretic analysis reveals intranasal oxytocin induced network changes over frontal regions. *Neuroscience* 459, 153–165. doi:10.1016/j.neuroscience.2021.01.018

frontiers | Frontiers in Pharmacology

TYPE Original Research
PUBLISHED 20 January 2025
DOI 10.3389/fphar.2024.1509520

OPEN ACCESS

EDITED BY
Weijie Xie,
Tongji University, China

REVIEWED BY
Laiba Arshad,
Forman Christian College, Pakistan
Agnieszka Gunia-Krzyżak,
Jagiellonian University Medical College, Poland

*CORRESPONDENCE
Longfei Mao,
9906405@haust.edu.cn
Jianji Wang,
jwang@htu.edu.cn

RECEIVED 11 October 2024
ACCEPTED 18 December 2024
PUBLISHED 20 January 2025

CITATION
Hou X, Mao L, Zhang H, Wang L, He B, Guo J and Wang J (2025) Design, synthesis, and anti-inflammatory activity of 2H-1,4-benzoxazin-3(4H)-one derivatives modified with 1,2,3-triazole in LPS-induced BV-2 cells.
Front. Pharmacol. 15:1509520.
doi: 10.3389/fphar.2024.1509520

Design, synthesis, and anti-inflammatory activity of 2H-1,4-benzoxazin-3(4H)-one derivatives modified with 1,2,3-triazole in LPS-induced BV-2 cells

Xixi Hou[1,2], Longfei Mao[3]*, Huibin Zhang[3], Lan Wang[3], Baoyu He[4], Jingjing Guo[4] and Jianji Wang[1]*

[1]Key Laboratory of Green Chemical Media and Reactions, Ministry of Education, Collaborative Innovation Center of Henan Province for Green Manufacturing of Fine Chemicals, School of Chemistry and Chemical Engineering, Henan Normal University, Xinxiang, Henan, China, [2]The First Affiliated Hospital, College of Clinical Medicine of Henan University of Science and Technology, Luoyang, Henan, China, [3]College of Basic Medicine and Forensic Medicine, Henan University of Science and Technology, Luoyang, Henan, China, [4]Centre for Artificial Intelligence Driven Drug Discovery, Faculty of Applied Sciences, Macao Polytechnic University, Macao, China

Given the potent anti-inflammatory properties of the 1,2,3-triazole structure and the wide use of 2H-1,4-benzoxazin-3(4H)-one in developing treatments for neurodegenerative diseases, a series of 2H-1,4-benzoxazin-3(4H)-one derivatives were synthesized by introducing a 1,2,3-triazole moiety. Screening for anti-inflammatory activity in microglial cells revealed that compounds e2, e16, and e20 exhibited the most promising effects without significant cytotoxicity. These compounds effectively reduced LPS-induced NO production and significantly decreased the transcription levels of pro-inflammatory cytokines IL-1β, IL-6, and TNF-α. Furthermore, they downregulated the transcription and protein levels of the inflammation-related enzymes iNOS and COX-2 in response to LPS stimulation. To further investigate the anti-inflammatory mechanisms of these derivatives in microglia, the intracellular ROS levels and the activation of the Nrf2-HO-1 signaling pathway were analyzed. The results indicated that the 2H-1,4-benzoxazin-3(4H)-one derivatives significantly activated the Nrf2-HO-1 pathway, reduced LPS-induced ROS production, and alleviated microglial inflammation. Molecular docking studies suggested that compounds e2, e16, and e20 could interact with Nrf2-related binding sites, preventing its degradation by Keap1. Additionally, acute toxicity tests in mice demonstrated that compound e16 exhibited favorable safety.

KEYWORDS

1,2,3-triazoles, 2H-1,4-benzoxazin-3(4H)-one, microglial cells, LPS-induced, antiinflammatory

1 Introduction

Microglial inflammation is a hallmark of brain injury and plays a significant role in the pathogenesis of neurodegenerative diseases such as depression, Alzheimer's disease, Parkinson's disease, and multiple sclerosis (Yoon et al., 2023). As the key immune cells in the central nervous system (CNS), the primary physiological function of microglia is to regulate the brain's immune defense mechanisms (Sasimol et al., 2018). When activated by

lipopolysaccharide (LPS), microglia increase intracellular reactive oxygen species (ROS), leading to oxidative stress responses. This induces the production of intracellular inducible nitric oxide synthase (iNOS) and cyclooxygenase-2 (COX-2), promoting the release of large amounts of inflammatory factors such as nitric oxide (NO), interleukin-1β (IL-1β), interleukin-6 (IL-6), and tumor necrosis factor-α (TNF-α), subsequently causing neuronal damage (Zhu et al., 2021). Numerous studies have shown that depression is accompanied by the activation of the inflammatory response system, with changes in pro-inflammatory cytokine levels in the brains of depressed patients, such as increased secretion of interleukins (IL) and tumor necrosis factor (TNF), particularly elevated levels of IL-1β, IL-6, and TNF-α (Jung et al., 2023; Li et al., 2024). Therefore, inhibiting microglial inflammation may be a potential method for treating neuroinflammatory diseases like depression.

1,2,3-Triazole is a very important class of nitrogen-containing five-membered aromatic heterocyclic compounds, which can serve as functional heterocyclic compounds, be embedded in polycyclic structures, or be used to connect multiple active molecules (Guan et al., 2024). Its planar rigid structure has a π-π conjugated system and a large dipole moment (μ), making it prone to non-covalent interactions (Cidade et al., 2021), such as hydrophobic effects, electrostatic interactions, van der Waals forces, and hydrogen bonding. These interactions endow it with good biological functions, enabling it to bind with various enzymes and receptors in the body (Mao et al., 2020), exhibiting a wide range of pharmacological activities including anti-cancer, antiviral, anti-inflammatory, antibacterial, and antimalarial properties (Hou et al., 2024; Xu et al., 2019; Begam et al., 2022; Liu et al., 2024). 1,2,3-Triazole can act as an electronic isostere for structures like amides (Chen et al., 2022; He et al., 2020), esters, carboxylic acids, and alkenes, making it an important drug molecule building block for the development of innovative drugs (Kim et al., 2015; Xie et al., 2023).

Some compounds with a 1,2,3-triazole structure can inhibit the activity or secretion function of inflammatory factors, thereby exerting anti-inflammatory effects and potentially serving as drugs for treating inflammation-related diseases (Shafi et al., 2012). For example, Madasu's research group used guggulsterone B as the core structure and introduced a 1,2,3-triazole group via a Cu-catalyzed Huisgen 1,3-dipolar cycloaddition reaction. These compounds not only exhibit excellent antitumor activity but also possess good anti-inflammatory activity. Among them, compound **27** (Figure 1) significantly inhibited the inflammatory cytokines TNF-α (IC_{50}: 7.83 ± 0.95 μM) and IL-1β (IC_{50}: 15.84 ± 0.82 μM), outperforming guggulsterone B (Madasu et al., 2020). Rao's research group designed and synthesized a series of novel 1,2,3-triazole-substituted N-phenyl isoxazolone derivatives (6a-6p) and screened them for anti-inflammatory activity. Among these, compound **6m** (Figure 1) showed significant inhibition of IL-1β secretion (IC_{50}: 7.9 ± 1.36 μM) (Sambasiva Rao et al., 2014). Felipe's research group designed and synthesized a series of compounds containing 1,2,3-triazole based on the structures of neolignans and celecoxib. Among these, compound **L12** (Figure 1) exhibited excellent anti-inflammatory activity. Molecular docking studies revealed that the binding mode of compound **L12** at the COX-2 active site was similar to that of celecoxib (docking score: −70.387 KJ/mol), indicating its potential as a COX-2 inhibitor (Felipe et al., 2022). Mengheres' group used a copper-catalyzed azide-alkyne cycloaddition reaction to obtain eight novel 1,2,3-triazole-linked isoflavone-benzodiazepine compounds. The evaluation of their anti-inflammatory activity by inhibiting cell viability and NO production in LPS-induced BV-2 cells showed that some compounds exhibited superior NO inhibitory activity compared to natural isoflavones, with compound **40** (Figure 1) reducing NO release by 64.28% without affecting BV-2 cell viability (Menghere et al., 2020).

2H-1,4-Benzoxazin-3(4H)-one is an important nitrogen and oxygen-containing heterocyclic compound with broad biological activity and relatively low biological toxicity (Hasui et al., 2011; Zhou et al., 2014; Yan et al., 2019; Sagam et al., 2024). A large number of derivatives based on this core structure have been synthesized, especially for use in research related to psychiatric diseases. Jiang's research group constructed an artificial intelligence drug generation system capable of targeting multiple G protein-coupled receptors (GPCRs) using deep recurrent neural networks (RNN) and multi-task deep neural networks (MTDNN). They discovered that compound **3** (Figure 2), which has a 2H-1,4-Benzoxazin-3(4H)-one scaffold, exhibited strong activity against dopamine D2 receptors, serotonin 5-HT1A, and 5-HT2A receptors, making it a potential lead compound for the treatment of complex neuropsychiatric disorders [28]. Claudio's research group designed and synthesized compound **7d** (Figure 2), which has a 2H-1,4-Benzoxazin-3(4H)-one scaffold and can non-competitively inhibit human acetylcholinesterase (hAChE) activity with a Ki value of 20.2 ± 0.9 μM, indicating its potential as a treatment for Alzheimer's disease (Méndez-Rojas et al., 2018). Smid's research group designed compound **45c** (Figure 2), which also has a 2H-1,4-Benzoxazin-3(4H)-one scaffold. It can act as a potent dopamine D2 receptor antagonist and exhibits high activity in inhibiting serotonin reuptake, suggesting its potential for the treatment of depression.

Given the excellent anti-inflammatory properties of the 1,2,3-triazole structure and the widespread application of 2H-1,4-Benzoxazin-3(4H)-one in the development of drugs for neurodegenerative diseases, we propose to structurally modify 2H-1,4-Benzoxazin-3(4H)-one with a 1,2,3-triazole moiety. This modification aims to investigate whether it can impart or enhance anti-inflammatory activity in BV2 neural cells. By doing so, we hope to discover lead compounds with outstanding anti-inflammatory properties that can be further developed into drugs for treating neurodegenerative diseases.

2 Chemistry

In this route, 6-amino-2H-benzo[b][1,4]oxazin-3(4H)-one (**a**) was used as raw material and it reacted with 3-ethynylbenzoic acid under the action of HATU and DIPEA to obtain 3-ethynyl-N-(3-oxo-3,4-dihydro-2H-benzo[b][1,4]oxazin-6-yl)benzamide (**b**). Compound **b** was reacted with azide compounds of different substituents to obtain 24 novel structure target compounds (**e1-e24**) as shown in Figure 3 and Table 1. Compounds (**f1-f24**) were prepared using the same method as shown in Figure 3 and Table 2. The structures of the target compound were confirmed through ^{1}H and ^{13}C nuclear magnetic resonance (^{1}H NMR and ^{13}C NMR) spectroscopy.

10.3389/fphar.2024.1509520

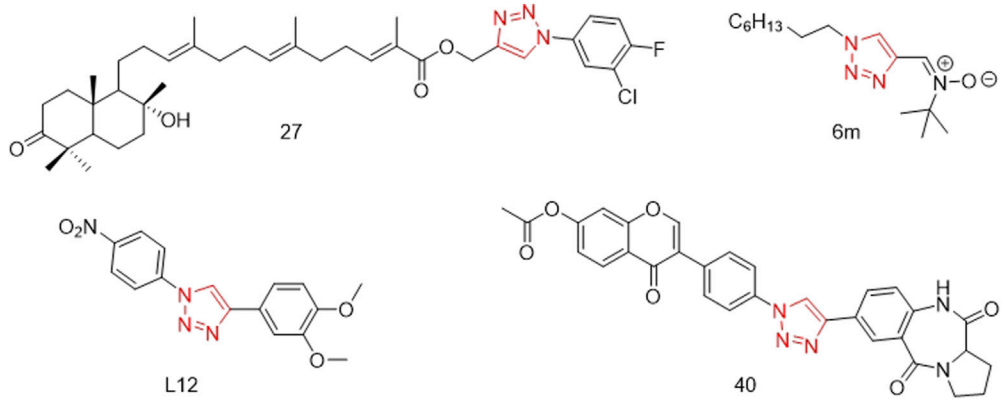

FIGURE 1
Structures of compound 27, compound 6m, compound L12 and compound 40 (the red is 1,2,3-triazole structure).

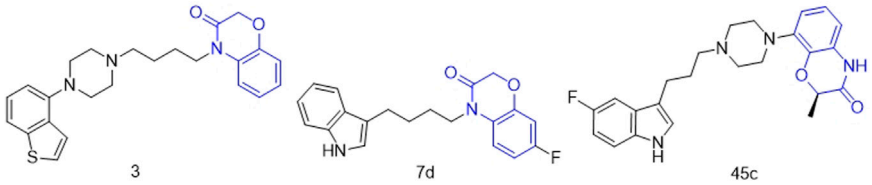

FIGURE 2
Structures of compound 3, compound 7d and compound 45c (the green is 2H-1,4-Benzoxazin-3(4H)-one structure).

3 Results

3.1 2H-1,4-benzoxazin-3(4H)-one derivatives inhibited LPS-induced NO production in BV-2 cells

To assess the anti-inflammatory activities of 2H-1,4-Benzoxazin-3(4H)-one derivatives, the NO levels in the supernatant of BV-2 microglial cells were measured using the Griess method. Resveratrol was used as a positive control, and 20 μM of resveratrol reduced the NO levels in the cell supernatant to 42.02% ± 2.50% of the LPS group. As shown in Table 3, the LPS-induced NO production in BV-2 cells aftertreated by 2H-1,4-Benzoxazin-3(4H)-one derivatives at a concentration of 10 μM are summarized. Additionally, the effects of these compounds on the viability of BV-2 microglial cells were assessed using the MTT assay. Based on the above data, a structure-activity relationship analysis of the compounds was conducted. By comparing the activity data of compounds with the same substituents in the e and j series, such as **e1** and **f5**, **e2** and **f6**, **e6** and **f9**, **e7** and **f2**, **e12** and **f13**, **e13** and **f8**, **e16** and **f16**, **e19** and **f4**, and the terminal alkyne intermediates **b** and **d**, we can clearly observe that the e series compounds are more effective at reducing NO levels in BV-2 cells and exhibit no significant cytotoxicity in BV-2 cells, especially compounds **e2**, **e16**, and **e20**, which show no obvious cytotoxicity and have the best anti-inflammatory effects.

3.2 2H-1,4-benzoxazin-3(4H)-one derivatives downregulated LPS-induced pro-inflammatory cytokine mRNA levels in BV2 microglial cells

Under LPS induction, the transcription levels of pro-inflammatory factors such as IL-1β, IL-6, and TNF-α in BV-2 microglial cells were significantly increased. To further determine the inhibitory activity of **e2**, **e16**, and **e20** on LPS-induced inflammation in microglial cells, the transcription levels of these pro-inflammatory factors in BV-2 microglial cells were measured using Real-time PCR. The results showed that **e2**, **e16**, and **e20** at a concentration of 10 μM significantly downregulated the mRNA levels of the pro-inflammatory factors IL-1β, IL-6, and TNF-α in LPS-induced microglial cells, as shown in Figure 4. This indicates that the aforementioned 2H-1,4-Benzoxazin-3(4H)-one derivatives inhibited the transcription of several key cellular inflammatory factors in LPS-induced BV-2 cells.

3.3 2H-1,4-benzoxazin-3(4H)-one derivatives downregulated LPS-induced iNOS and COX-2 expression levels in BV2 microglial cells

The expression of inflammation-related enzymes, such as iNOS and COX-2, is also an important indicator of inflammatory effects.

10.3389/fphar.2024.1509520

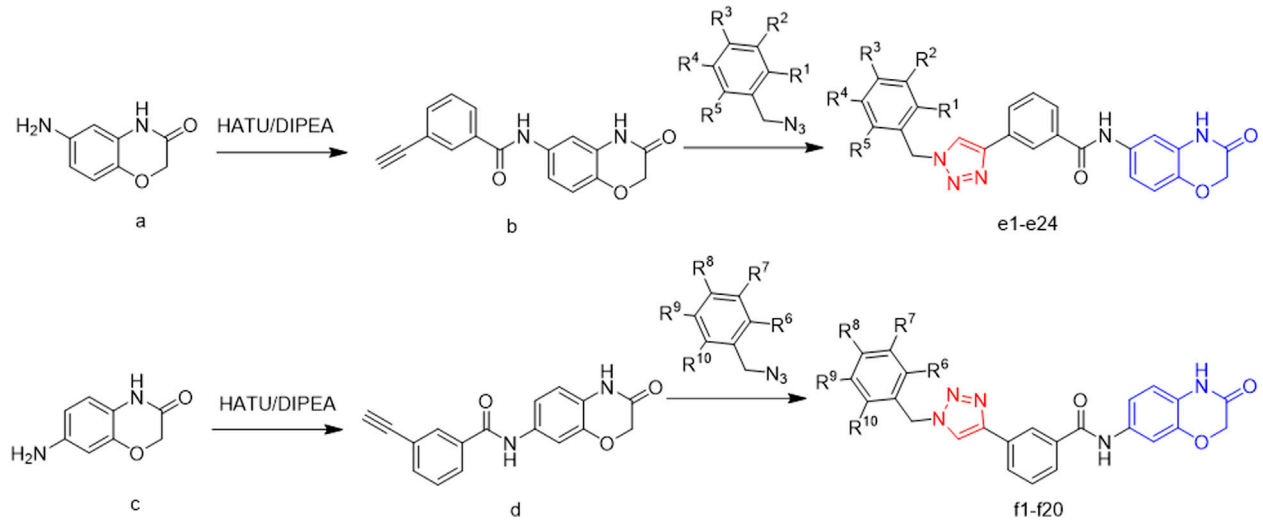

FIGURE 3
The reaction routes to compounds e1-e24 and j1-j20.

Therefore, the impacts of 2H-1,4-Benzoxazin-3(4H)-one derivatives on the transcription and protein levels of iNOS and COX-2 were further investigated. Under LPS treatment, the transcription levels of iNOS and COX-2 in BV-2 microglial cells significantly increased, along with corresponding increases in protein levels. However, after treatment with 10 μM e2, e16, and e20 respectively, both the transcription and protein levels of iNOS and COX-2 were significantly downregulated, as shown in Figure 5. This indicates that 2H-1,4-Benzoxazin-3(4H)-one derivatives can significantly reduce the levels of iNOS and COX-2 in BV-2 cells induced by LPS.

3.4 2H-1,4-benzoxazin-3(4H)-one derivatives reduced lps-induced ROS accumulation in BV-2 microglial cells

Oxidative stress can promote inflammation in microglial cells. Therefore, the regulatory effects of 2H-1,4-Benzoxazin-3(4H)-one derivatives on intracellular reactive oxygen were further investigated. The intracellular ROS levels were measured using flow cytometry, with DCFH-DA probes reflecting the ROS content within cells. After LPS treatment, ROS levels in BV-2 microglial cells significantly increased, whereas treatment with 10 μM e2, e16, and e20 significantly reduced intracellular ROS levels to 64.25% ± 6.96%, 57.90% ± 12.04%, and 42.56% ± 5.19% of the LPS group, respectively, as shown in Figure 6. This indicates that 2H-1,4-Benzoxazin-3(4H)-one derivatives can alleviate LPS-induced oxidative stress in BV-2 cells.

3.5 2H-1,4-benzoxazin-3(4H)-one derivatives promoted activation of the Nrf2-HO-1 pathway

To further clarify the mechanism by which 2H-1,4-Benzoxazin-3(4H)-one derivatives regulated microglial cell inflammation, the Nrf2-HO-1 signaling pathway involved in oxidative stress regulation was examined. In the LPS group, Nrf2 protein levels showed no significant change. However, after treatment with 10 μM 2H-1,4-Benzoxazin-3(4H)-one derivatives, Nrf2 protein levels significantly increased. Additionally, the downstream HO-1 protein levels were also assessed (Figure 7). The results were consistent with those of Nrf2, showing that 10 μM e2, e16, and e20 significantly increased HO-1 protein levels. These results indicated that 2H-1,4-Benzoxazin-3(4H)-one derivatives could significantly activate the antioxidant Nrf2-HO-1 signaling pathway to reduce intracellular ROS levelsand thereby exert antioxidant effects to mitigate LPS-induced inflammatory effects in microglial cells.

3.6 Predicted binding modes of e2, e16, and e20 with Keap1

Molecular docking is a prevalent method for predicting reliable binding modes between ligands and target proteins. Based on the aforementioned results, e2, e16, and e20 may target Keap1 to prevent Nrf2 binding. To understand the binding modes, molecular docking was employed to predict the binding interactions between these three small molecules and the Keap1 protein. As shown in Figure 8, the three molecules engage in key electrostatic interactions with important arginine residues of Keap1. In Figures 8A, B, the aldehydes of e2 form a hydrogen bond with Arg 415, while the benzene ring is involved in pi-pi stacking interactions with Tyr 572. The aldehydes of e16 form two hydrogen bonds with Arg 380 and Asn 382, and the benzene ring engages in pi-pi stacking with Tyr 525 (Figures 8C, D). The nitrobenzene of e20 forms a pi-cation interaction, a hydrogen bond, and a salt bridge with Tyr 334, Asn 382, and Arg 380, respectively. Additionally, the 1,2,3-triazoles share pi-cation and pi-pi stacking interactions with Arg 415 and Tyr 572, while the benzene ring participates in pi-pi stacking with Tyr 525 (Figures 8E, F). It has been demonstrated that the presence of an acidic moiety is essential for achieving potent

10.3389/fphar.2024.1509520

TABLE 1 R-group of compounds e1-e24.

Compounds	R^1	R^2	R^3	R^4	R^5
e1	H	H	Br	H	H
e2	H	CH_3	H	CH_3	H
e3	H	F	F	F	H
e4	NC	H	H	F	H
e5	F	H	H	H	Cl
e6	H	Cl	F	H	H
e7	H	Cl	H	H	H
e8	F	H	H	Cl	H
e9	H	H	F	H	H
e10	F	H	H	H	H
e11	H	Br	H	Br	H
e12	F	H	Br	H	H
e13	H	CF_3	H	H	H
e14	Cl	H	H	H	Cl
e15	NC	H	H	H	H
e16	H	H	CF_3	H	H
e17	Br	H	H	H	H
e18	H	F	H	H	H
e19	H	H	I	H	H
e20	NO_2	H	H	H	H
e21	H	H	Cl	H	H
e22	CF_3	H	H	H	H
e23	H	H	H	H	H
e24	Cl	H	H	F	H

TABLE 2 R-group of compounds f1–f20.

Compounds	R^6	R^7	R^8	R^9	R^{10}
f1	Cl	H	H	H	Cl
f2	H	Cl	H	H	H
f3	F	H	H	H	H
f4	H	H	I	H	H
f5	H	H	Br	H	H
f6	H	CH_3	H	CH_3	H
f7	CN	H	H	H	H
f8	H	CF_3	H	H	H
f9	H	Cl	F	H	H
f10	F	H	H	H	F
f11	CN	H	H	F	H
f12	Br	H	H	H	H
f13	F	H	Br	H	H
f14	H	F	H	H	H
f15	Cl	H	H	H	F
f16	H	H	CF_3	H	H
f17	H	Br	H	H	H
f18	H	H	Cl	H	H
f19	H	I	H	H	H
f20	CH_3	H	H	H	H

activity in a lead compound (Davies et al., 2016). Therefore, e2, e16, and e20 may be potential molecules to prevent the binding of Keap1 and Nrf2 by occupying the binding site of Nrf2.

3.7 The acute toxicity test of compound e16 in mice

We further evaluated the safety of compound **e16** through an acute toxicity study in KM mice. Male and female mice were divided into two groups: a control group and an **e16**-treated group. The treatment group received 800 mg/kg of compound **e16** via oral gavage, while the control group was given an equivalent volume of solvent. Body weight was monitored over a 15-day period. At the end of the study, blood samples were collected from the retro-orbital sinus to assess the biochemical markers GPT and GOT, and the major organs—heart, liver, spleen, lungs, and kidneys—were weighed and subjected to HE staining.

As shown in Figure 9A, there were no significant differences in body weight between the **e16**-treated and control groups. Similarly, Figure 9B shows no significant changes in the organ indices of the major organs between the groups. Biochemical analysis revealed a slight, but not statistically significant, increase in GPT levels in the **e16**-treated group (Figure 9C). Furthermore, HE staining of the major organs (heart, liver, spleen, lungs, and kidneys) showed no significant histopathological differences between the **e16**-treated and control groups (Figure 9D). These results suggest that compound **e16** has a favorable safety profile, providing experimental support for its potential clinical use.

4 Discussion

In this study, a series of 2H-1,4-benzoxazin-3(4H)-one derivatives were synthesized. Screening for anti-inflammatory activity revealed that compounds **e2**, **e16**, and **e20** demonstrated the best anti-inflammatory effects without significant cytotoxicity. It was found that these compounds act on Nrf2-related sites, preventing Nrf2 degradation by KEAP1. By activating the Nrf2-HO-1 signaling pathway, they reduced LPS-induced ROS levels, inhibited the expression of inflammation-related enzymes iNOS and COX-2, and decreased the production of pro-inflammatory factors such as NO, IL-1β, IL-6, and TNF-α.

Microglia-mediated neuroinflammation contributes to the development of neurodegenerative diseases. Microglia produce large amounts of inflammatory factors that disrupt neuronal

TABLE 3 The inhibitory effects of the 2H-1,4-Benzoxazin-3(4H)-one derivatives on LPS-induced NO production in BV-2 cells.

Compounds	NO production[a]	Cell viability[b]	Compounds	NO production[a]	Cell viability[b]
e1	60.91 ± 11.84*	90.68 ± 3.68	f1	70.51 ± 4.29**	50.48 ± 2.52$^{\#\#\#}$
e2	54.66 ± 8.93**	101.60 ± 1.48	f2	103.1 ± 2.59	47.01 ± 3.02$^{\#\#\#}$
e3	62.37 ± 4.89**	72.95 ± 11.47	f3	79.55 ± 11.36	51.24 ± 1.96$^{\#\#\#}$
e4	88.31 ± 8.26	86.55 ± 3.09$^{\#}$	f4	100.4 ± 8.81	47.66 ± 2.84$^{\#\#\#}$
e5	92.08 ± 10.49	44.11 ± 8.32$^{\#\#}$	f5	101.1 ± 1.64	45.87 ± 5.42$^{\#\#\#}$
e6	57.05 ± 9.11**	74.52 ± 3.10$^{\#\#}$	f6	94.63 ± 9.73	56.96 ± 3.34$^{\#\#\#}$
e7	64.67 ± 6.27**	74.4 ± 8.64$^{\#}$	f7	95.49 ± 2.00	89.51 ± 1.50$^{\#\#}$
e8	90.73 ± 13.31	83.56 ± 15.64	f8	105.8 ± 6.01	61.27 ± 4.61$^{\#\#\#}$
e9	80.16 ± 4.71*	75.57 ± 2.27$^{\#\#\#}$	f9	103.6 ± 5.07	62.99 ± 2.67$^{\#\#\#}$
e10	81.90 ± 6.33*	73.86 ± 2.26$^{\#\#\#}$	f10	79.67 ± 7.00*	68.51 ± 1.10$^{\#\#\#}$
e11	44.44 ± 3.66***	44.05 ± 2.31$^{\#\#\#}$	f11	100.9 ± 8.62	68.16 ± 3.81$^{\#\#\#}$
e12	71.74 ± 4.39**	101.1 ± 1.95	f12	58.55 ± 6.08**	55.99 ± 8.19$^{\#\#}$
e13	69.36 ± 9.52*	80.31 ± 11.92	f13	98.17 ± 12.10	44.94 ± 2.49$^{\#\#\#}$
e14	26.17 ± 3.53***	52.21 ± 3.79$^{\#\#\#}$	f14	79.52 ± 5.91*	47.69 ± 5.03$^{\#\#\#}$
e15	75.72 ± 1.30***	83.77 ± 6.27	f15	89.12 ± 3.81*	68.88 ± 10.66$^{\#}$
e16	59.23 ± 4.36***	88.23 ± 10.66	f16	87.54 ± 5.32	52.45 ± 6.93$^{\#\#}$
e17	36.45 ± 6.21***	45.97 ± 7.44$^{\#\#}$	f17	88.45 ± 7.00	49.12 ± 5.16$^{\#\#\#}$
e18	72.85 ± 2.67***	62.49 ± 2.08$^{\#\#\#}$	f18	101.50 ± 3.56	45.38 ± 4.67$^{\#\#\#}$
e19	66.38 ± 14.44	103.2 ± 1.72	f19	91.53 ± 6.46	54.73 ± 0.856$^{\#\#\#}$
e20	59.19 ± 3.28***	104.1 ± 2.70	f20	105.9 ± 5.87	55.97 ± 3.84$^{\#\#\#}$
e21	87.61 ± 2.49	97.90 ± 6.42	b	65.61 ± 3.59***	75.99 ± 6.59#
e22	67.2 ± 7.12	45.48 ± 2.91	d	92.26 ± 8.95	87.95 ± 8.82
e23	91.99 ± 5.43	89.02 ± 8.41			
e24	77.65 ± 3.47	74.02 ± 5.01			
Positive control- Resveratrol (20 μM)	42.02 ± 2.50***				

*$P < 0.05$, **$P < 0.01$, ***$P < 0.001$ vs. the LPS, group, $^{\#}P < 0.05$, $^{\#\#}P < 0.01$, $^{\#\#\#}P < 0.001$ vs. the control group; n = 3.
[a]NO data were normalized by mean value of LPS, group, which was set to 100%.
[b]Cell viability data were normalized by mean value of control group, which was set to 100%.

TABLE 4 List of primers used in Real-Time PCR.

Gene	Forward primer (5′-3′)	Reverse primer (5′-3′)
IL-1β	GCAACTGTTCCTGAACTCAACT	ATCTTTTGGGGTCCGTCAACT
IL-6	GGAGGCTTAATTACACATGTT	TGATTTCAAGATGAATTGGAT
TNF-α	CCCTCACACTCAGATCATCTTCT	GCTACGACGTGGGCTACAG
iNOS	GTTCTCAGCCCAACAATACAAA	GTGGACGGGTCGATGTCAC
COX-2	TTGAAGACCAGGAGTACAGC	GGTACAGTTCCATGACATCG
GAPDH	GGTGAAGGTCGGTGTGAACG	GGTAGGAACACGGAAGGCCA

function and promote neuronal death (Gao et al., 2023; Zhang et al., 2023; Cintia et al., 2024) Numerous studies have shown that intervening in microglial inflammation effectively alleviates neurodegenerative diseases (Dong et al., 2019; Sun et al., 2021). For example, rutin reduces glial proliferation and neuroinflammation in the brains of Alzheimer's disease (AD)

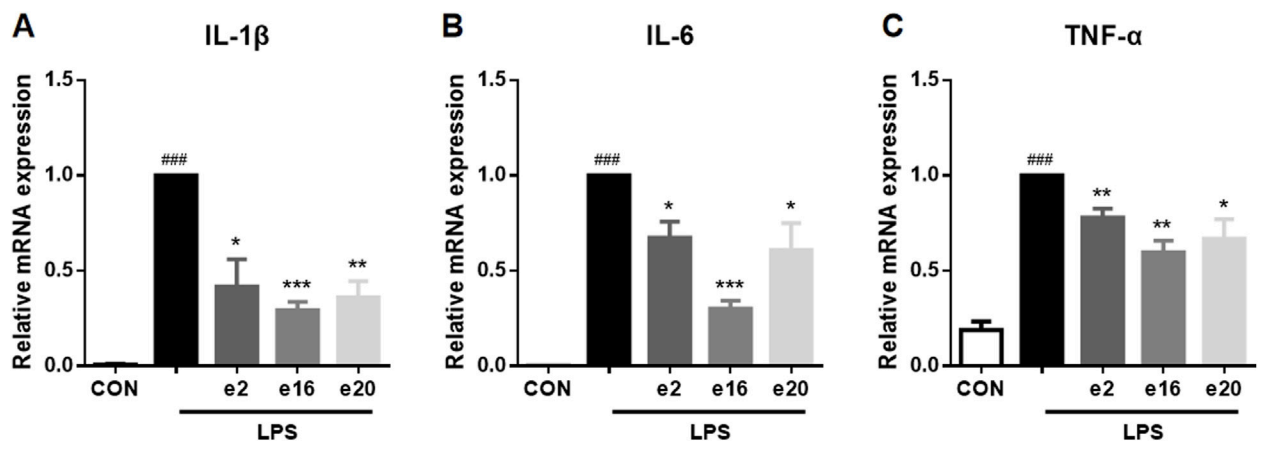

FIGURE 4
The 2H-1,4-Benzoxazin-3(4H)-one derivatives downregulated the mRNA levels of pro-inflammatory cytokines in LPS-induced BV-2 microglial cells. **(A–C)** The mRNA levels of IL-1β **(A)**, IL-6 **(B)**, and TNF-α **(C)** were measured by real-time PCR (n = 3). Data are presented as mean ± SEM. $^{###}P < 0.001$ compared to the CON group; $^{*}P < 0.05$, $^{**}P < 0.01$, $^{***}P < 0.001$ compared to the LPS group.

mice by downregulating the NF-κB pathway, inhibiting microglial phagocytosis of synapses, reducing synaptic loss, and improving cognitive performance. Dimethyl fumarate suppresses the expression of STAT3/C3 and C3 receptor in astrocytes and isolated microglia of App-KI mice, thereby inhibiting astrocyte-microglial interactions, alleviating neuroinflammation, and improving cognitive decline and behavior in AD.

Our study found that 2H-1,4-benzoxazin-3(4H)-one derivatives **e2**, **e16**, and **e20** significantly improve microglial inflammation and thus hold promise for developing therapeutics for neurodegenerative diseases.

The role of microglia in neurodegenerative diseases, toxicology, and immunology represents a rapidly expanding area of biomedical research, requiring a large number of animal experiments. Using microglia-like cell lines can accelerate research while reducing the need for continuous cell preparation and animal studies, provided the cell lines faithfully replicate *in vivo* conditions or primary microglial cells (PM). The immortalized mouse microglial cell line BV-2 is often used as a substitute for PM. Studies have reassessed the advantages and limitations of BV-2 cells and compared their response to lipopolysaccharide (LPS) with that of microglia *in vitro* and *in vivo*. Transcriptomic (480 genes) and proteomic analyses following LPS stimulation revealed that the response patterns of BV-2 cells are similar to those of PM. BV-2 cells exhibit normal regulatory and functional responses to IFN-gamma and can stimulate other glial cells. Therefore, BV-2 cells appear to be an effective substitute for PM in many experimental setups, replicating *in vivo* microglial inflammatory responses, including characteristic gene expression, secretion of inflammatory factors, cell migration, and studies of complex intercellular interactions (Kristensen et al., 2009). Due to their accessibility, ease of manipulation, and short experimental cycles, BV-2 cells are widely used as a cell model for studying microglial inflammation (Wang et al., 2021; Wang et al., 2024).

In this study, we used BV-2 microglial cells to establish an *in vitro* neuroinflammation screening model. We identified the regulatory effects of compounds **e2**, **e16**, and **e20** on microglial inflammation. These compounds significantly inhibited the expression of inflammation-related enzymes iNOS and COX-2, reduced the production of pro-inflammatory factors such as NO, IL-1β, IL-6, and TNF-α induced by LPS, and laid the foundation for further *in vivo* experiments on anti-neuroinflammation.

The Nrf2-HO-1 signaling pathway plays a crucial role in cellular oxidative stress responses and is essential in neuroinflammation. Nrf2 (nuclear factor erythroid 2-related factor 2) is a transcription factor that typically binds to Keap1 (Kelch-like ECH-associated protein 1) in the cytoplasm, maintaining Nrf2 in a low-activity state. Upon activation of the signaling pathway, Nrf2 dissociates from Keap1, translocates into the nucleus, and activates the expression of downstream genes such as HO-1, exerting antioxidant, anti-apoptotic, and anti-inflammatory effects (Li et al., 2021). Therefore, activating the Nrf2 signaling pathway can help alleviate neuroinflammation.

For instance, peppermint leaf extract induces CREB/Nrf2/HO-1-related antioxidant signaling in microglial cells, suppressing the production of pro-inflammatory enzymes and mediators such as NO, iNOS, COX-2, TNF-α, and IL-6 following LPS stimulation (Park et al., 2022). Similarly, S. alopecuroides extract alleviates the release of NO, PGE2, TNF-α, IL-6, and IL-1β induced by LPS by promoting Nrf2 nuclear translocation and HO-1 expression (Yang et al., 2016).

In this study, molecular docking analysis revealed potential binding sites of compounds **e2**, **e16**, and **e20** with Nrf2. The compounds were shown to interfere with the interaction between Keap1 and Nrf2, increasing Nrf2 protein levels, activating the downstream HO-1 antioxidant protein expression, reducing LPS-induced intracellular ROS accumulation, and alleviating neuroinflammation.

5 Conclusion

In this study, a series of 2H-1,4-Benzoxazin-3(4H)-one derivatives were synthesized by introducing a 1,2,3-triazole group. Screening for anti-inflammatory activity in microglial cells

10.3389/fphar.2024.1509520

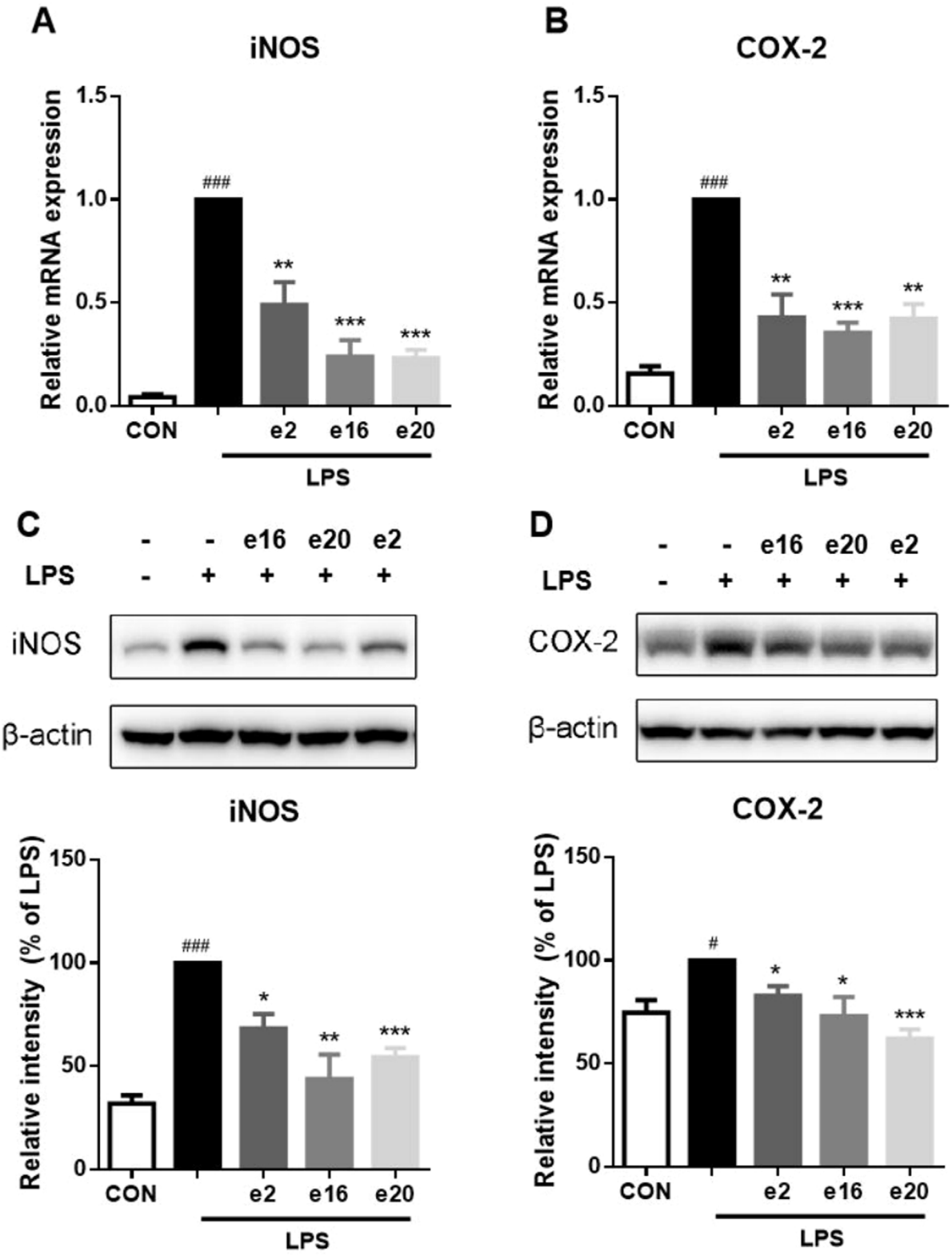

FIGURE 5
2H-1,4-Benzoxazin-3(4H)-one derivatives downregulated LPS-induced iNOS and COX-2 transcription and protein levels in BV2 microglial cells. **(A,B)** The mRNA levels of iNOS **(A)** and COX-2 **(B)** were measured by real-time PCR (n = 3). **(C,D)** The protein levels of iNOS **(C)** and COX-2 **(D)** were measured by western blot (n = 3). Data in the figure are presented as mean ± SEM. $^{\#}P < 0.05$, $^{\#\#\#}P < 0.001$ compared to the CON group; $^{*}P < 0.05$, $^{**}P < 0.01$, $^{***}P < 0.001$ compared to the LPS group.

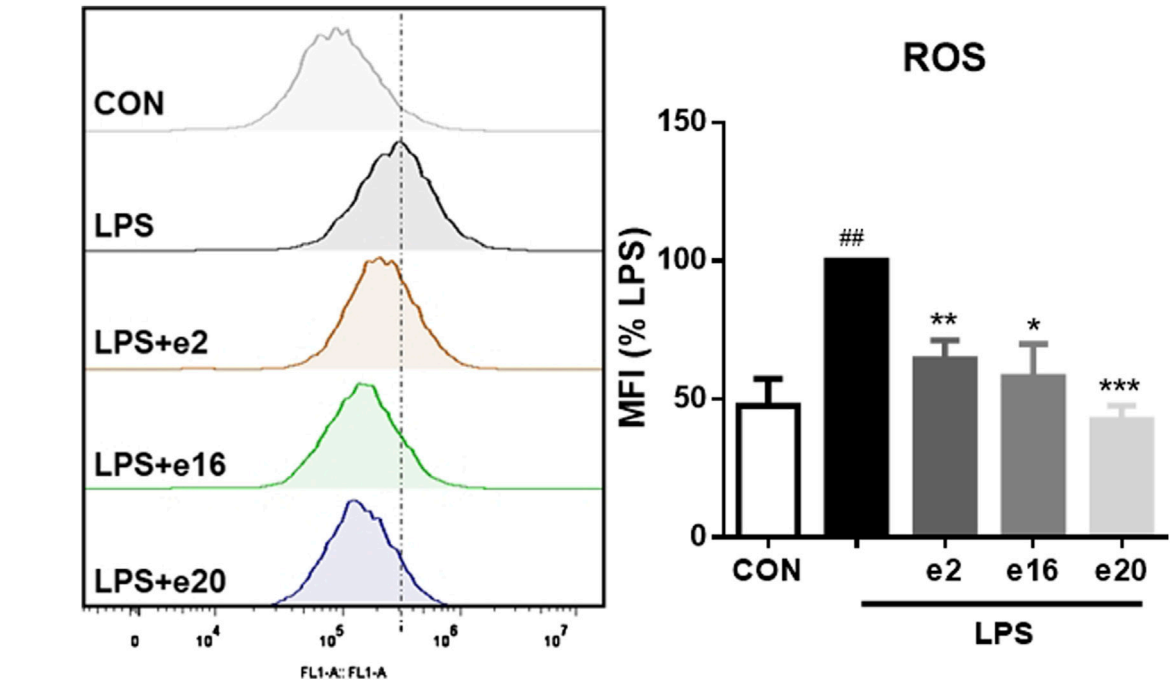

FIGURE 6
2H-1,4-Benzoxazin-3(4H)-one Derivatives downregulated LPS-induced ROS levels in BV-2 microglial cells (n = 3). Data are presented as mean ± S.E.M. $^{\#\#}P < 0.01$ compared to the CON group; $^{*}P < 0.05$, $^{**}P < 0.01$, $^{***}P < 0.001$ compared to the LPS group.

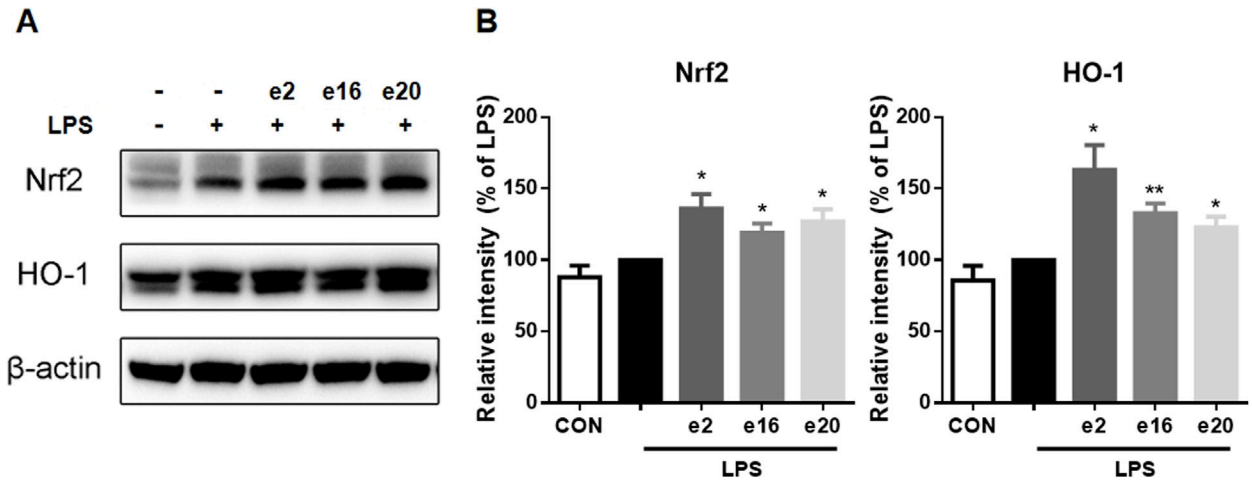

FIGURE 7
2H-1,4-Benzoxazin-3(4H)-one derivatives increased Nrf2-HO-1 protein levels in LPS-induced BV-2 Microglial Cells (n = 3). Data are presented as mean ± S.E.M. $^{*}P < 0.05$, $^{**}P < 0.01$ compared to the LPS group.

revealed that compounds e2, e16, and e20 exhibited the best anti-inflammatory effects without significant cytotoxicity. Consequently, these compounds were selected for further investigation of their anti-inflammatory effects and mechanisms in BV-2 microglial cells. It was found that e2, e16, and e20 not only reduced LPS-induced NO production but also significantly decreased the transcription levels of the pro-inflammatory factors IL-1β, IL-6, and TNF-α. Additionally, the transcription and protein levels of upstream inflammation-related enzymes iNOS and COX-2 were examined, revealing that these compounds significantly lowered transcription and protein levels of iNOS and COX-2 in LPS-induced BV-2 cells. To further explore the mechanisms underlying the anti-inflammatory effects of 2H-1,4-Benzoxazin-3(4H)-one derivatives in microglial cells, intracellular ROS levels and the Nrf2-HO-1 signaling pathway were investigated. The results showed that the 2H-1,4-Benzoxazin-3(4H)-one derivatives significantly activated the intracellular Nrf2-HO-1 signaling pathway, reduced LPS-induced ROS levels, and alleviated the inflammatory state of microglial cells.

10.3389/fphar.2024.1509520

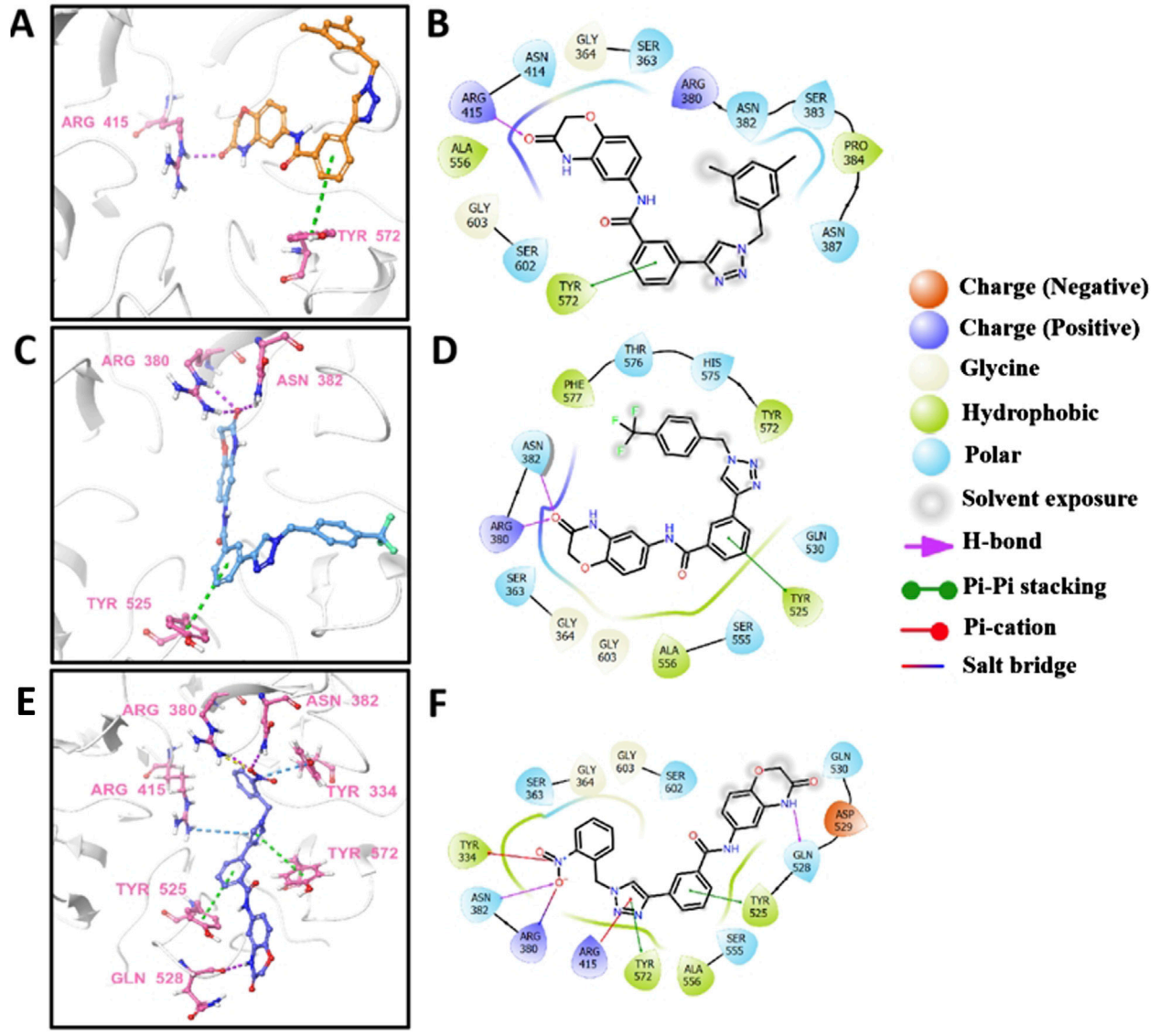

FIGURE 8
The predicted 3D models and schematic 2D diagrams illustrate the interactions between ligands and Keap1. The protein is represented as a white cartoon, while the ligands are depicted as sticks. Magenta dashed lines indicate hydrogen bonds, green dashed lines indicate pi-pi stacking, blue dashed lines indicate salt bridge, and yellow dashed lines indicate salt bridge. **(A,C, E)** the 3D diagrams of the Keap1-e2 complex, Keap1-e16 complex, and Keap1-e20 complex, respectively. **(B,D, F)** the 2D diagrams representing the interactions of ligand molecules with the amino acid residues at the binding site: **(B)** Keap1-e2 complex, **(D)** Keap1-e16 complex, and **(F)** Keap1-e20 complex.

By molecular docking, it can be intuitively observed that compounds e2, e16, and e20 can act on Nrf2-related sites, preventing the degradation of Nrf2 by KEAP1. Additionally, acute toxicity tests in mice revealed that compound e16 exhibited good safety.

6 Experimental

6.1 Materials and chemistry

2H-1,4-Benzoxazin-3(4H)-one linked 1,2,3-triazole derivatives were synthesized in-house. Dulbecco's modified Eagle medium (DMEM) was obtained from LifeTech (Grand Island, NY, United States). Fetal bovine serum (FBS) was purchased from Gibco (Grand Island, NY, United States). Griess reagent, β-actin antibody and Protease Inhibitor Cocktail were obtained from Sigma-Aldrich (St. Louis, Missouri, United States). Reactive Oxygen Species (ROS) Assay Kit was obtained from Beyotime Biotechnology (Shanghai, China). COX-2 antibody was purchased from Cell Signaling Technology (Beverly, MA, United States). iNOS antibody was purchased from BD Biosciences (San Jose, CA, United States). Nrf2 antibody and HO-1 antibody were purchased from Proteintech (Wuhan, China).

10.3389/fphar.2024.1509520

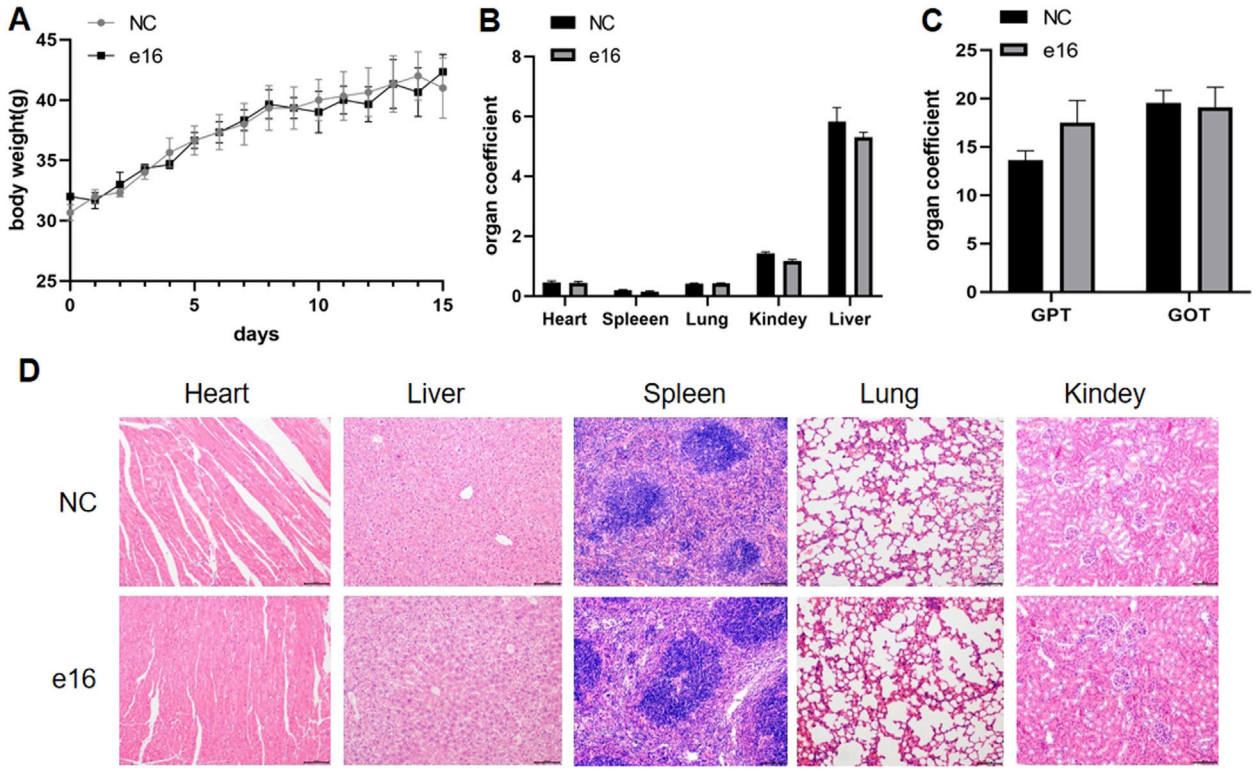

FIGURE 9
Acute toxicity experiments of compound **e16** were conducted in mice. **(A)** The body wight of mice were recorded for 15 days after treatment. **(B)** The acute toxicity experiments examined the effects of **e16** on mouse organs. **(C)** Effect of acute toxicity experimental studies on blood biochemical indices GPT and GOT in mice. **(D)** H&E staining were performed on various organs of mice treated with compound **e16**.

6.1.1 General synthetic procedure for compound b (the method is applicable to the preparation of compound d)

Compound a (0.02 mol), 3-aminophenylacetylene (0.03 mol), HATU (0.03 mol), DIPEA (0.06 mol), and 250 mL of DMF were added to a 500 mL reaction flask at room temperature. The mixture was stirred under a nitrogen atmosphere for 24 h. The progress of the reaction was monitored by TLC. After 24 h, the reaction was complete, and the solution turned light brown. DMF was removed under vacuum, and the reaction mixture was extracted with dichloromethane (150 mL × 3). The combined organic layers were washed with saturated sodium chloride solution (150 mL × 2) until the pH reached 7. The organic phase was concentrated under vacuum, yielding a viscous brownish-yellow liquid. Methanol was then slowly added dropwise under ultrasonic agitation, resulting in the precipitation of a solid. The solid was filtered, washed, and dried to obtain compound b (4.6 g). ^{1}H NMR(400MHz, DMSO-d_6): 10.76 (s, 1H), 10.26 (s, 1H), 8.04 (s, 1H), 7.96 (d, J = 8.0Hz, 1H), 7.68 (d, J = 8.0Hz, 1H), 7.54–7.52 (m, 2H), 7.25–7.22 (m, 1H), 6.93 (d, J = 8.0Hz, 1H), 4.54 (s, 2H), 4.30 (s, 1H). ^{13}C NMR(400MHz, DMSO-d_6): 165.5, 164.6, 143.6, 140.0, 135.7, 134.9, 134.1, 131.0, 129.4, 128.7, 122.3, 116.4, 115.6, 108.9, 83.3, 82.0, 67.3.

6.1.2 General synthetic procedure for compounds e1-e24 (the method is applicable to the preparation of compound f1-f20)

To a reaction flask, compound b (3 mmol), the substituted azide (3.6 mmol), tert-butanol (70 mL), water (70 mL), and tetrahydrofuran (70 mL) were added, followed by anhydrous copper sulfate (0.6 mmol) and sodium ascorbate (1 mmol). The mixture was stirred and refluxed at 70°C for 6 h. The progress of the reaction was monitored by TLC. Upon completion, the reaction mixture was extracted with dichloromethane (100 mL × 3), and the organic layers were combined and washed with saturated sodium chloride solution (100 mL × 2). The combined organic phase was then washed with brine (100 mL × 2), dried over sodium sulfate, and concentrated under vacuum to yield the crude product. The product was purified by recrystallization from ethyl acetate, resulting in the desired compound, which was pure enough for further characterization and anti-inflammatory studies.

The spectroscopic characterization of compounds **e1-e24** and **f1-f20** is provided as follow.

3-(1-(4-bromobenzyl)-1H-1,2,3-triazol-4-yl)-N-(3-oxo-3,4-dihydro-2H-benzo[b][1,4]oxazin-6-yl)benzamide (compound **e1**): Pure 98.9%. white solid, HR-MS(ESI): Calcd. C24H19BrN5O3 $[M+H]^+$ *m/z*: 504.0671, found: 504.0657. ^{1}H NMR(400MHz, DMSO-d_6): 10.78 (s, 1H), 10.29 (s, 1H), 8.72 (s, 1H), 8.38 (s, 1H), 8.04 (d, J = 8.0Hz, 1H), 7.88 (d, J = 8.0Hz, 1H), 7.62–7.53 (m, 4H), 7.34 (d, J = 8.0Hz, 2H), 7.26 (d, J = 12.0Hz, 1H), 6.93 (d, J = 12.0Hz, 1H), 5.67 (s, 2H), 4.55 (s, 2H). ^{13}C NMR(100MHz, DMSO-d_6): 165.5, 146.6, 139.9, 136.1, 135.7, 134.3, 132.2, 131.2, 130.7, 129.4, 128.5, 127.6, 127.5, 124.8, 122.5, 121.9, 116.4, 115.6, 109.0, 67.3, 52.8.

3-(1-(3,5-dimethylbenzyl)-1H-1,2,3-triazol-4-yl)-N-(3-oxo-3,4-dihydro-2H-benzo[b][1,4]oxazin-6-yl)benzamide (compound **e2**):

Pure 99.3%. white solid, HR-MS(ESI): Calcd. C26H24N5O3 $[M+H]^+$ *m/z*: 454.1879, found: 454.1964. ^1H NMR(400MHz, DMSO-d_6): 10.78 (s, 1H), 10.29 (s, 1H), 8.69 (s, 1H), 8.39 (s, 1H), 8.05 (d, J = 8.0Hz, 1H), 7.88 (d, J = 8.0Hz, 1H), 7.59–7.54 (m, 2H), 7.26 (d, J = 12.0Hz, 1H), 6.98–6.92 (m, 4H), 5.58 (s, 2H), 4.55 (s, 2H), 2.26 (s, 6H). ^{13}C NMR(100MHz, DMSO-d_6): 165.5, 146.5, 139.9, 138.4, 136.1, 134.3, 131.3, 130.0, 129.4, 128.4, 127.6, 127.5, 126.1, 124.8, 122.4, 116.4, 115.6, 109.0, 67.3, 53.6, 21.3.

N-(3-oxo-3,4-dihydro-2H-benzo[b][1,4]oxazin-6-yl)-3-(1-(3,4,5-trifluorobenzyl)-1H-1,2,3-triazol-4-yl)benzamide (compound **e3**): Pure 97.6%. white solid, HR-MS(ESI): Calcd. C24H17F3N5O3 $[M+H]^+$ *m/z*: 480.1283, found: 480.1282. ^1H NMR(400MHz, DMSO-d_6): 10.78 (s, 1H), 10.30 (s, 1H), 8.74 (s, 1H), 8.38 (s, 1H), 8.04 (d, J = 8.0Hz, 1H), 7.89 (d, J = 12.0Hz, 1H), 7.62–7.58 (m, 1H), 7.54 (s, 1H), 7.43–7.39 (m, 2H), 7.27–7.24 (m, 1H), 6.94 (d, J = 8.0Hz, 1H), 5.58 (s, 2H), 4.55 (s, 2H). ^{13}C NMR(100MHz, DMSO-d_6): 165.5, 146.6, 139.9, 136.2, 134.2, 131.1, 129.4, 128.5, 127.6, 124.9, 122.6, 113.8, 113.7, 113.6, 113.6, 108.9, 67.3, 60.2, 52.1, 21.2, 14.5.

3-(1-(2-cyano-5-fluorobenzyl)-1H-1,2,3-triazol-4-yl)-N-(3-oxo-3,4-dihydro-2H-benzo[b][1,4]oxazin-6-yl)benzamide (compound **e4**): Pure 97.1%. white solid, HR-MS(ESI): Calcd. C25H18FN6O3 $[M+H]^+$ *m/z*: 469.1424, found: 469.1412. ^1H NMR(400MHz, DMSO-d_6): 10.78 (s, 1H), 10.31 (s, 1H), 8.77 (s, 1H), 8.39 (s, 1H), 8.07–8.05 (m, 2H), 7.90 (d, J = 12.0Hz, 1H), 7.63–7.59 (m, 1H), 7.5–7.41 (m, 3H), 7.27–7.24 (m, 1H), 6.94 (d, J = 8.0Hz, 1H), 5.91 (s, 2H), 4.55 (s, 2H). ^{13}C NMR(100MHz, DMSO-d_6): 165.5, 146.5, 142.4, 139.9, 137.0, 136.9, 136.2, 134.3, 131.1, 129.5, 128.5, 127.6, 124.9, 123.0, 118.0, 117.7, 117.4, 117.2, 116.7, 116.4, 115.6, 109.0, 108.4, 67.3, 51.5.

3-(1-(2-chloro-6-fluorobenzyl)-1H-1,2,3-triazol-4-yl)-N-(3-oxo-3,4-dihydro-2H-benzo[b][1,4]oxazin-6-yl)benzamide (compound **e5**): Pure 98.3%. white solid, HR-MS(ESI): Calcd. C24H18ClFN5O3 $[M+H]^+$ *m/z*: 478.1082, found: 478.1063. ^1H NMR(400MHz, DMSO-d_6): 10.78 (s, 1H), 10.28 (s, 1H), 8.69 (s, 1H), 8.38 (s, 1H), 8.06 (d, J = 8.0Hz, 1H), 7.87 (d, J = 8.0Hz, 1H), 7.60–7.52 (m, 3H), 7.46–7.35 (m, 2H), 7.27–7.24 (m, 1H), 6.94 (d, J = 12.0Hz, 1H), 5.79 (s, 2H), 4.55 (s, 2H). ^{13}C NMR(100MHz, DMSO-d_6): 165.5, 146.2, 139.9, 136.2, 135.5, 134.3, 132.4, 132.3, 131.1, 129.4, 128.5, 127.5, 126.3, 124.9, 122.6, 116.4, 115.6, 115.3, 109.0, 67.3, 45.2.

3-(1-(3-chloro-4-fluorobenzyl)-1H-1,2,3-triazol-4-yl)-N-(3-oxo-3,4-dihydro-2H-benzo[b][1,4]oxazin-6-yl)benzamide (compound **e6**): Pure 97.7%. white solid, HR-MS(ESI): Calcd. C24H18ClFN5O3 $[M+H]^+$ *m/z*: 478.1082, found: 478.1062. ^1H NMR(400MHz, DMSO-d_6): 10.78 (s, 1H), 10.30 (s, 1H), 8.75 (s, 1H), 8.38 (s, 1H), 8.04 (d, J = 12.0Hz, 1H), 7.89 (d, J = 8.0Hz, 1H), 7.69–7.67 (m, 1H), 7.60 (t, J_1 = 8.0Hz, J_2 = 8.0Hz, 1H), 7.54 (s, 1H), 7.46–7.42 (m, 2H), 7.25 (dd, J_1 = 4.0Hz, J_2 = 4.0Hz, 1H), 6.94 (d, J = 8.0Hz, 1H), 5.69 (s, 2H), 4.55 (s, 2H). ^{13}C NMR(100MHz, DMSO-d_6): 165.5, 146.6, 139.9, 136.1, 134.3, 130.9, 129.6, 129.5, 129.4, 128.5, 127.5, 124.9, 122.5, 120.2, 120.1, 117.9, 117.7, 116.4, 115.6, 109.0, 67.3, 52.2.

3-(1-(3-chlorobenzyl)-1H-1,2,3-triazol-4-yl)-N-(3-oxo-3,4-dihydro-2H-benzo[b][1,4]oxazin-6-yl)benzamide (compound e7): Pure 96.5%. white solid, HR-MS(ESI): Calcd. C24H19ClN5O3 $[M+H]^+$ *m/z*: 460.1176, found: 460.1163. ^1H NMR(400MHz, DMSO-d_6): 10.78 (s, 1H), 10.30 (s, 1H), 8.76 (s, 1H), 8.39 (s, 1H), 8.05 (d, J = 12.0Hz, 1H), 7.89 (d, J = 8.0Hz, 1H), 7.60 (t, J = 8.0Hz, 1H), 7.54 (s, 1H), 7.48–7.43 (m, 3H), 7.35–7.32 (m, 1H), 7.26 (dd, J_1 = 4.0Hz, J_2 = 4.0Hz, 1H), 6.94 (d, J = 8.0Hz, 1H), 5.71 (s, 2H), 4.55 (s, 2H). ^{13}C NMR(100MHz, DMSO-d_6): 165.5, 146.6, 139.9, 138.7, 136.1, 134.3, 133.8, 131.2, 129.4, 128.7, 128.5, 128.3, 127.6, 127.1, 124.9, 122.6, 116.4, 115.6, 109.0, 67.3, 52.8.

3-(1-(5-chloro-2-fluorobenzyl)-1H-1,2,3-triazol-4-yl)-N-(3-oxo-3,4-dihydro-2H-benzo[b][1,4]oxazin-6-yl)benzamide (compound **e8**): Pure 97.9%. white solid, HR-MS(ESI): Calcd. C24H18ClFN5O3 $[M+H]^+$ *m/z*: 478.1082, found: 478.1063. ^1H NMR(400MHz, DMSO-d_6): 10.78 (s, 1H), 10.30 (s, 1H), 8.74 (s, 1H), 8.39 (s, 1H), 8.07 (s, 1H), 7.88 (s, 1H), 7.61–7.25 (m, 6H), 6.94 (d, J = 8.0Hz, 1H), 5.74 (s, 2H), 4.55 (s, 2H). ^{13}C NMR(100MHz, DMSO-d_6): 165.5, 160.7, 158.2, 146.5, 139.9, 138.5, 136.2, 134.3, 131.1, 131.0, 129.4, 128.5, 127.6, 125.2, 125.1, 124.9, 122.6, 118.3, 118.1, 116.4, 115.6, 109.0, 67.3, 47.3.

3-(1-(4-fluorobenzyl)-1H-1,2,3-triazol-4-yl)-N-(3-oxo-3,4-dihydro-2H-benzo[b][1,4]oxazin-6-yl)benzamide (compound **e9**): Pure 95.2%. white solid, HR-MS(ESI): Calcd. C24H19FN5O3 $[M+H]^+$ *m/z*: 444.1472, found: 444.1479. ^1H NMR(400MHz, DMSO-d_6): 10.80 (s, 1H), 10.31 (s, 1H), 8.73 (s, 1H), 8.38 (s, 1H), 8.06–8.04 (m, 1H), 7.88 (d, J = 8.0Hz, 1H), 7.62–7.44 (m, 4H), 7.27–7.24 (m, 2H), 6.94 (d, J = 8.0Hz, 1H), 5.68 (s, 2H), 4.56 (s, 2H). ^{13}C NMR(100MHz, DMSO-d_6): 165.5, 163.6, 161.2, 146.6, 139.8, 136.1, 135.8, 134.2, 132.6, 131.2, 129.5, 128.4, 127.5, 124.8, 122.4, 116.4, 116.2, 116.0, 115.6, 108.9, 67.3, 52.8.

3-(1-(2-fluorobenzyl)-1H-1,2,3-triazol-4-yl)-N-(3-oxo-3,4-dihydro-2H-benzo[b][1,4]oxazin-6-yl)benzamide (compound **e10**): Pure 96.7%. white solid, HR-MS(ESI): Calcd. C24H19FN5O3 $[M+H]^+$ *m/z*: 444.1472, found: 444.1465. ^1H NMR(400MHz, DMSO-d_6): 10.78 (s, 1H), 10.29 (s, 1H), 8.71 (s, 1H), 8.39 (s, 1H), 8.04 (d, J = 8.0Hz, 1H), 7.88 (d, J = 8.0Hz, 1H), 7.61–7.26 (m, 7H), 6.94 (d, J = 8.0Hz, 1H), 5.74 (s, 2H), 4.55 (s, 1H). ^{13}C NMR(100MHz, DMSO-d_6): 165.5, 146.5, 139.9, 136.1, 134.3, 131.2, 129.4, 128.5, 127.6, 125.4, 124.8, 123.2, 123.0, 122.5, 116.4, 116.2, 116.0, 115.6, 109.0, 67.3, 47.6.

3-(1-(3,5-dibromobenzyl)-1H-1,2,3-triazol-4-yl)-N-(3-oxo-3,4-dihydro-2H-benzo[b][1,4]oxazin-6-yl)benzamide (compound **e11**): Pure 98.4%. white solid, HR-MS(ESI): Calcd. C24H18Br2N5O3 $[M+H]^+$ *m/z*: 581.9776, found: 581.9769. ^1H NMR(400MHz, DMSO-d_6): 10.78 (s, 1H), 10.30 (s, 1H), 8.78 (s, 1H), 8.39 (s, 1H), 8.06 (d, J = 8.0Hz, 1H), 7.91–7.82 (m, 2H), 7.64–7.59 (m, 3H), 7.55 (d, J = 4.0Hz, 1H), 7.27–7.25 (m, 1H), 6.94 (d, J = 8.0Hz, 1H), 5.71 (s, 2H), 4.55 (s, 1H). ^{13}C NMR(100MHz, DMSO-d_6): 165.5, 146.7, 140.7, 139.9, 136.2, 134.3, 133.7, 130.6, 129.5, 128.5, 127.6, 124.9, 123.2, 122.8, 116.4, 115.6, 109.0, 67.3, 52.4, 52.0, 49.0.

3-(1-(4-bromo-2-fluorobenzyl)-1H-1,2,3-triazol-4-yl)-N-(3-oxo-3,4-dihydro-2H-benzo[b][1,4]oxazin-6-yl)benzamide (compound **e12**): Pure 95.7%. white solid, HR-MS(ESI): Calcd. C24H18BrFN5O3 $[M+H]^+$ *m/z*: 522.0577, found: 522.0571. ^1H NMR(400MHz, DMSO-d_6): 10.77 (s, 1H), 10.29 (s, 1H), 8.70 (s, 1H), 8.38 (s, 1H), 8.05 (d, J = 8.0Hz, 1H), 7.88 (d, J = 8.0Hz, 1H), 7.66–7.37 (m, 5H), 7.25 (d, J = 8.0Hz, 1H), 6.93 (d, J = 8.0Hz, 1H), 5.72 (s, 2H), 4.55 (s, 1H). ^{13}C NMR(100MHz, DMSO-d_6): 165.5, 146.5, 139.9, 136.1, 134.2, 132.9, 132.8, 131.1, 129.4, 128.6, 128.5, 128.5, 127.5, 124.8, 122.8, 122.6, 119.7, 119.5, 116.4, 115.6, 109.0, 67.3, 47.2.

N-(3-oxo-3,4-dihydro-2H-benzo[b][1,4]oxazin-6-yl)-3-(1-(3-(trifluoromethyl)benzyl)-1H-1,2,3-triazol-4-yl)benzamide (compound

e13): Pure 94.8%. white solid, HR-MS(ESI): Calcd. C25H19F3N5O3 $[M+H]^+$ *m/z*: 494.1440, found: 494.1429. ^1H NMR(400MHz, DMSO-d_6): 10.78 (s, 1H), 10.30 (s, 1H), 8.79 (s, 1H), 8.39 (s, 1H), 8.06–7.55 (m, 8H), 7.26 (d, J = 8.0Hz, 1H), 6.94 (d, J = 8.0Hz, 1H), 5.82 (s, 2H), 4.55 (s, 2H). ^{13}C NMR(100MHz, DMSO-d_6): 165.5, 139.9, 137.7, 136.1, 134.3, 132.6, 131.2, 130.5, 129.5, 128.5, 127.6, 125.5, 125.4, 125.1, 124.9, 122.7, 116.4, 115.6, 109.0, 67.3, 52.8.

3-(1-(2,6-dichlorobenzyl)-1H-1,2,3-triazol-4-yl)-N-(3-oxo-3,4-dihydro-2H-benzo[b][1,4]oxazin-6-yl)benzamide (compound e14): Pure 97.7%. white solid, HR-MS(ESI): Calcd. C24H18Cl2N5O3 $[M+H]^+$ *m/z*: 494.0787, found: 494.0780. ^1H NMR(400MHz, DMSO-d_6): 10.78 (s, 1H), 10.28 (s, 1H), 8.65 (s, 1H), 8.38 (s, 1H), 8.06 (d, J = 8.0Hz, 1H), 7.86 (d, J = 12.0Hz, 1H), 7.62–7.48 (m, 5H), 7.25 (d, J = 8.0Hz, 1H), 6.93 (d, J = 8.0Hz, 1H), 5.88 (s, 2H), 4.55 (s, 2H). ^{13}C NMR(100MHz, DMSO-d_6): 165.6, 165.5, 146.1, 139.9, 136.5, 136.2, 134.3, 132.1, 131.1, 130.6, 129.5, 129.4, 128.5, 127.5, 127.5, 124.9, 122.5, 116.3, 115.6, 108.9, 67.3, 49.3.

3-(1-(2-cyanobenzyl)-1H-1,2,3-triazol-4-yl)-N-(3-oxo-3,4-dihydro-2H-benzo[b][1,4]oxazin-6-yl)benzamide (compound **e15)**: Pure 96.8%. white solid, HR-MS(ESI): Calcd. C25H19N6O3 $[M+H]^+$ *m/z*: 451.1519, found: 451.1507. ^1H NMR(400MHz, DMSO-d_6): 10.79 (s, 1H), 10.31 (s, 1H), 8.77 (s, 1H), 8.40 (s, 1H), 8.07 (d, J = 8.0Hz, 1H), 7.92 (dd, J_1 = 8.0Hz, J_2 = 8.0Hz, 2H), 7.77 (t, J = 8.0Hz, 1H), 7.63–7.47 (m, 4H), 7.28–7.25 (m, 1H), 6.94 (d, J = 8.0Hz, 1H), 5.91 (s, 2H), 4.56 (s, 2H). ^{13}C NMR(100MHz, DMSO-d_6): 165.5, 146.5, 139.9, 139.0, 136.2, 134.3, 134.3, 133.9, 131.1, 130.0, 129.7, 129.5, 128.5, 127.6, 124.9, 122.9, 117.4, 116.4, 115.6, 111.7, 109.0, 67.3, 51.8.

N-(3-oxo-3,4-dihydro-2H-benzo[b][1,4]oxazin-6-yl)-3-(1-(4-(trifluoromethyl)benzyl)-1H-1,2,3-triazol-4-yl)benzamide (compound **e16)**: Pure 94.2%. white solid, HR-MS(ESI): Calcd. C25H19F3N5O3 $[M+H]^+$ *m/z*: 494.1440, found: 494.1435. ^1H NMR(400MHz, DMSO-d_6): 10.78 (s, 1H), 10.30 (s, 1H), 8.78 (s, 1H), 8.39 (s, 1H), 8.06 (d, J = 12.0Hz, 1H), 7.91–7.88 (m, 1H), 7.78 (d, J = 8.0Hz, 2H), 7.60–7.54 (m, 4H), 7.25 (dd, J_1 = 4.0Hz, J_2 = 4.0Hz, 1H), 6.94 (d, J = 8.0Hz, 1H), 5.82 (s, 2H), 4.55 (s, 2H). ^{13}C NMR(100MHz, DMSO-d_6): 165.5, 146.7, 141.0, 139.9, 136.1, 134.3, 131.2, 129.5, 129.3, 129.1, 129.0, 128.5, 127.6, 126.2, 126.2, 124.9, 122.8, 116.4, 115.6, 109.0, 67.3, 52.9.

3-(1-(2-bromobenzyl)-1H-1,2,3-triazol-4-yl)-N-(3-oxo-3,4-dihydro-2H-benzo[b][1,4]oxazin-6-yl)benzamide (compound **e17)**: Pure 99.0%. white solid, HR-MS(ESI): Calcd. C24H19BrN5O3 $[M+H]^+$ *m/z*: 504.0671, found: 504.0666. ^1H NMR(400MHz, DMSO-d_6): 10.80 (s, 1H), 10.31 (s, 1H), 8.70 (s, 1H), 8.40 (s, 1H), 8.07 (d, J = 8.0Hz, 1H), 7.89 (d, J = 8.0Hz, 1H), 7.72 (d, J = 8.0Hz, 2H), 7.62–7.24 (m, 6H), 6.94 (d, J = 8.0Hz, 1H), 5.77 (s, 2H), 4.55 (s, 2H). ^{13}C NMR(100MHz, DMSO-d_6): 165.5, 146.4, 139.9, 136.1, 135.1, 134.3, 133.4, 131.2, 131.1, 131.0, 129.5, 128.8, 128.5, 127.5, 124.8, 123.4, 122.8, 122.5, 116.4, 115.6, 108.9, 67.3, 53.7.

3-(1-(3-fluorobenzyl)-1H-1,2,3-triazol-4-yl)-N-(3-oxo-3,4-dihydro-2H-benzo[b][1,4]oxazin-6-yl)benzamide (compound **e18)**: Pure 98.7%. white solid, HR-MS(ESI): Calcd. C24H19FN5O3 $[M+H]^+$ *m/z*: 444.1472, found: 444.1473. ^1H NMR(400MHz, DMSO-d_6): 10.77 (s, 1H), 10.29 (s, 1H), 8.75 (s, 1H), 8.38 (s, 1H), 8.05 (d, J = 12.0Hz, 1H), 7.88 (d, J = 8.0Hz, 1H), 7.59 (t, J = 8.0Hz, 1H), 7.54 (d, J = 4.0Hz, 1H), 7.48–7.43 (m, 1H), 7.26–7.17 (m, 4H), 6.93 (d, J = 8.0Hz, 1H), 5.71 (s, 2H), 4.54 (s, 2H). ^{13}C NMR(100MHz, DMSO-d_6): 165.5, 146.6, 139.9, 139.0, 136.1, 134.3, 131.4, 131.3, 131.2, 129.4, 128.5, 127.6, 127.5, 124.8, 124.5, 124.5, 122.6, 116.4, 115.6, 115.4, 115.2, 109.0, 67.3, 52.9.

3-(1-(4-iodobenzyl)-1H-1,2,3-triazol-4-yl)-N-(3-oxo-3,4-dihydro-2H-benzo[b][1,4]oxazin-6-yl)benzamide (compound **e19)**: Pure 97.6%. white solid, HR-MS(ESI): Calcd. C24H19IN5O3 $[M+H]^+$ *m/z*: 552.0533, found: 552.0547. ^1H NMR(400MHz, DMSO-d_6): 10.77 (s, 1H), 10.28 (s, 1H), 8.71 (s, 1H), 8.37 (s, 1H), 8.04 (d, J = 12.0Hz, 1H), 7.88 (d, J = 8.0Hz, 1H), 7.11 (d, J = 8.0Hz, 2H), 7.61–7.53 (m, 2H), 7.26–7.17 (m, 3H), 6.93 (d, J = 8.0Hz, 1H), 5.65 (s, 2H), 4.54 (s, 2H). ^{13}C NMR(100MHz, DMSO-d_6): 165.5, 165.5, 146.6, 139.9, 138.0, 136.1, 134.3, 131.2, 130.7, 129.5, 128.4, 127.5, 127.5, 124.8, 122.5, 116.4, 115.6, 108.9, 95.0, 67.3, 53.0.

3-(1-(2-nitrobenzyl)-1H-1,2,3-triazol-4-yl)-N-(3-oxo-3,4-dihydro-2H-benzo[b][1,4]oxazin-6-yl)benzamide (compound **e20)**: Pure 95.5%. white solid, HR-MS(ESI): Calcd. C24H19N6O5 $[M+H]^+$ *m/z*: 471.1417, found: 471.1409. ^1H NMR(400MHz, DMSO-d_6): 10.80 (s, 1H), 10.32 (s, 1H), 8.81 (s, 1H), 8.39 (s, 1H), 8.30–8.22 (m, 2H), 8.05 (d, J = 8.0Hz, 1H), 7.87 (dd, J_1= 8.0Hz, J2= 8.0Hz, 2H), 7.72 (t, J = 8.0Hz, 1H), 7.61 (t, J = 4.0Hz, 1H), 7.55 (d, J = 4.0Hz, 1H), 7.27–7.24 (m, 1H), 6.94 (d, J = 8.0Hz, 1H), 5.88 (s, 2H), 4.55 (s, 2H). ^{13}C NMR(100MHz, DMSO-d_6): 165.5, 165.5, 148.4, 146.7, 139.9, 138.4, 136.1, 135.2, 134.2, 131.1, 130.9, 129.5, 128.5, 127.5, 124.8, 123.7, 123.3, 122.8, 116.4, 115.6, 108.9, 67.3, 52.5.

3-(1-(4-chlorobenzyl)-1H-1,2,3-triazol-4-yl)-N-(3-oxo-3,4-dihydro-2H-benzo[b][1,4]oxazin-6-yl)benzamide (compound **e21)**: Pure 97.1%. white solid, HR-MS(ESI): Calcd. C24H19ClN5O3 $[M+H]^+$ *m/z*: 460.1176, found: 460.1191. ^1H NMR(400MHz, DMSO-d_6): 10.80 (s, 1H), 10.31 (s, 1H), 9.42 (s, 1H), 8.74 (s, 1H), 8.38 (s, 1H), 8.04 (d, J = 8.0Hz, 1H), 7.88 (d, J = 8.0Hz, 1H), 7.59 (t, J = 8.0Hz, 1H), 7.54 (d, J = 4.0Hz, 1H), 7.40 (d, J = 8.0Hz, 2H), 7.26–7.24 (m, 1H), 6.94 (d, J = 8.0Hz, 1H), 5.69 (s, 2H),4.55 (s, 2H). ^{13}C NMR(100MHz, DMSO-d_6): 165.5, 146.6, 144.3, 139.9, 135.3, 134.2, 132.2, 131.2, 130.4, 129.5, 129.3, 128.4, 127.5, 127.5, 122.4, 116.4, 115.6, 108.9, 67.3, 52.7.

N-(3-oxo-3,4-dihydro-2H-benzo[b][1,4]oxazin-6-yl)-3-(1-(2-(trifluoromethyl)benzyl)-1H-1,2,3-triazol-4-yl)benzamide (compound **e22)**: Pure 96.7%. white solid, HR-MS(ESI): Calcd. C25H19F3N5O3 $[M+H]^+$ *m/z*: 494.1440, found: 494.1447. ^1H NMR(400MHz, DMSO-d_6): 10.80 (s, 1H), 10.32 (s, 1H), 8.73 (s, 1H), 8.41 (s, 1H), 8.07 (d, J = 8.0Hz, 1H), 7.90–7.83 (m, 2H), 7.72 (t, J = 8.0Hz, 1H), 7.63–7.54 (m, 3H), 7.30–7.24 (m, 2H), 6.94 (d, J = 8.0Hz, 1H), 5.88 (s, 2H), 4.55 (s, 2H). ^{13}C NMR(100MHz, DMSO-d_6):165.5, 146.5, 139.9, 136.1, 134.2, 133.9, 133.7, 131.1, 130.8, 129.4, 128.5, 127.5, 126.7, 124.9, 123.0, 116.4, 115.6, 108.9, 67.3, 50.3.

3-(1-benzyl-1H-1,2,3-triazol-4-yl)-N-(3-oxo-3,4-dihydro-2H-benzo[b][1,4]oxazin-6-yl)benzamide (compound **e23)**: Pure 97.6%. white solid, HR-MS(ESI): Calcd. C24H20N5O3 $[M+H]^+$ *m/z*: 426.1566, found: 426.1567. ^1H NMR(400MHz, DMSO-d_6): 10.79 (s, 1H), 10.30 (s, 1H), 8.74 (s, 1H), 8.38 (s, 1H), 8.05 (d, J = 8.0Hz, 1H), 7.88 (d, J = 8.0Hz, 1H), 7.61–7.53 (m, 2H), 7.43–7.34 (m, 5H), 7.26–7.23 (m, 1H), 6.93 (d, J = 12.0Hz, 1H), 5.68 (s, 2H), 4.55 (s, 2H). ^{13}C NMR(100MHz, DMSO-d_6): 165.5, 146.6, 136.4, 136.1, 134.2, 133.0, 131.2, 129.3, 128.7, 128.4, 128.4, 127.5, 127.5, 122.5, 116.4, 115.6, 112.1, 108.9, 108.7, 67.3, 53.5.

3-(1-(2-chloro-5-fluorobenzyl)-1H-1,2,3-triazol-4-yl)-N-(3-oxo-3,4-dihydro-2H-benzo[b][1,4]oxazin-6-yl)benzamide (compound

e24): Pure 97.6%. white solid, HR-MS(ESI): Calcd. C24H18ClFN5O3 $[M+H]^+$ *m/z*: 478.1082, found: 478.1075. ^{1}H NMR(400MHz, DMSO-d_6): 10.81 (s, 1H), 10.33 (s, 1H), 8.74 (s, 1H), 8.41 (s, 1H), 8.08 (d, J = 8.0Hz, 1H), 7.90 (d, J = 8.0Hz, 2H), 7.63–7.55 (m, 3H), 7.36–7.26 (m, 3H), 6.95 (d, J = 8.0Hz, 1H), 5.79 (s, 2H), 4.56 (s, 2H).^{13}C NMR(100MHz, DMSO-d_6): 165.5, 162.5, 160.0, 146.4, 139.9, 136.2, 135.6, 135.5, 134.3, 132.0, 131.9, 131.1, 129.4, 128.7, 128.5, 127.6, 124.9, 122.8, 118.4, 118.1, 117.9, 117.7, 116.4, 115.6, 108.9, 67.3, 51.1.

3-(1-(2,6-dichlorobenzyl)-1H-1,2,3-triazol-4-yl)-N-(3-oxo-3,4-dihydro-2H-benzo[b][1,4]oxazin-7-yl)benzamide (compound **f1**): Pure 97.1%. white solid, HR-MS(ESI): Calcd. C24H18Cl2N5O3 $[M+H]^+$ *m/z*: 494.0787, found: 494.0775. ^{1}H NMR(400MHz, DMSO-d_6): 10.67 (s, 1H), 10.27 (s, 1H), 8.66 (s, 1H), 8.38 (s, 1H), 8.07 (d, J = 8.0Hz, 1H), 7.87 (d, J = 8.0Hz, 1H), 7.62–7.56 (m, 3H), 7.52–7.45 (m, 2H), 7.38–7.35 (m, 1H), 6.88 (d, J = 8.0Hz, 1H), 5.88 (s, 2H), 4.57 (s, 2H). ^{13}C NMR(100MHz, DMSO-d_6): 165.6, 164.9, 146.0, 143.5, 136.5, 136.1, 135.0, 132.1, 131.2, 130.6, 129.5, 129.4, 129.3, 128.6, 127.5, 124.9, 123.6, 122.5, 116.0, 114.8, 109.1, 67.3, 49.3.

3-(1-(3-chlorobenzyl)-1H-1,2,3-triazol-4-yl)-N-(3-oxo-3,4-dihydro-2H-benzo[b][1,4]oxazin-7-yl)benzamide (compound **f2**): Pure 98.4%. white solid, HR-MS(ESI): Calcd. C24H19ClN5O3 $[M+H]^+$ *m/z*: 460.1176, found: 460.1162. ^{1}H NMR(400MHz, DMSO-d_6): 10.66 (s, 1H), 10.28 (s, 1H), 8.77 (s, 1H), 8.39 (s, 1H), 8.06 (d, J = 4.0Hz, 1H), 7.88 (d, J = 8.0Hz, 1H), 7.60 (t, J = 8.0Hz, 1H), 7.50–7.48 (m, 2H), 7.44–7.33 (m, 4H), 6.88 (d, J = 8.0Hz, 1H), 5.71 (s, 2H), 4.58 (s, 2H).^{13}C NMR(100MHz, DMSO-d_6): 165.6, 164.9, 146.6, 143.5, 138.7, 136.1, 135.0, 133.8, 131.2, 129.5, 128.7, 128.5, 128.3, 127.5, 127.1, 124.8, 123.6, 122.6, 116.0, 114.8, 109.1, 67.3, 52.8, 49.0.

3-(1-(2-fluorobenzyl)-1H-1,2,3-triazol-4-yl)-N-(3-oxo-3,4-dihydro-2H-benzo[b][1,4]oxazin-7-yl)benzamide (compound **f3**): Pure 95.9%. white solid, HR-MS(ESI): Calcd. C24H19FN5O3 $[M+H]^+$ *m/z*: 444.1472, found: 444.1463. ^{1}H NMR(400MHz, DMSO-d_6): 10.67 (s, 1H), 10.27 (s, 1H), 8.72 (s, 1H), 8.39 (s, 1H), 8.06 (d, J = 4.0Hz, 1H), 7.88 (d, J = 8.0Hz, 1H), 7.59 (t, J = 8.0Hz, 1H), 7.50–7.26 (m, 6H), 6.88 (d, J = 8.0Hz, 1H), 5.74 (s, 2H), 4.58 (s, 2H).^{13}C NMR(100MHz, DMSO-d_6): 165.6, 164.9, 161.8, 159.4, 146.5, 143.5, 136.1, 135.0, 131.3, 129.5, 128.5, 127.5, 125.4, 124.8, 123.6, 123.2, 123.0, 122.6, 116.2, 116.0, 114.9, 109.1, 67.3, 47.6.

3-(1-(4-iodobenzyl)-1H-1,2,3-triazol-4-yl)-N-(3-oxo-3,4-dihydro-2H-benzo[b][1,4]oxazin-7-yl)benzamide (compound **f4**): Pure 97.8%. white solid, HR-MS(ESI): Calcd. C24H19IN5O3 $[M+H]^+$ *m/z*: 552.0533, found: 552.0515. ^{1}H NMR(400MHz, DMSO-d_6): 10.70 (s, 1H), 10.30 (s, 1H), 8.73 (s, 1H), 8.37 (s, 1H), 8.05 (d, J = 4.0Hz, 1H), 7.88 (d, J = 8.0Hz, 1H), 7.78 (d, J = 8.0Hz, 2H), 7.60 (t, J = 8.0Hz, 1H), 7.49 (s, 1H), 7.26 (dd, J_1 = 4.0Hz, J_2 = 4.0Hz, 1H), 7.18 (d, J = 4.0Hz, 2H), 6.87 (d, J = 8.0Hz, 1H), 5.65 (s, 2H), 4.58 (s, 2H).^{13}C NMR(100MHz, DMSO-d_6): 165.5, 165.0, 146.6, 143.5, 138.0, 136.1, 136.1, 135.0, 131.2, 130.7, 129.5, 128.5, 127.5, 124.8, 123.6, 122.5, 114.8, 109.1, 95.0, 67.2, 52.9.

3-(1-(4-bromobenzyl)-1H-1,2,3-triazol-4-yl)-N-(3-oxo-3,4-dihydro-2H-benzo[b][1,4]oxazin-7-yl)benzamide (compound **f5**): Pure 94.8%. white solid, HR-MS(ESI): Calcd. C24H19BrN5O3 $[M+H]^+$ *m/z*: 504.0671, found: 504.0665. ^{1}H NMR(400MHz, DMSO-d_6): 10.67 (s, 1H), 10.28 (s, 1H), 8.71 (s, 1H), 8.36 (s, 1H), 8.04 (d, J = 8.0Hz, 1H), 7.88 (d, J = 8.0Hz, 1H), 7.60 (d, J = 8.0Hz, 2H), 7.48 (s, 1H), 7.37–7.33 (m, 3H), 6.88 (d, J = 8.0Hz, 1H), 5.66 (s, 2H), 4.57 (s, 2H).^{13}C NMR(100MHz, DMSO-d_6): 165.6, 165.0, 146.6, 143.5, 136.0, 135.7, 134.9, 132.2, 131.2, 130.7, 129.5, 128.5, 127.5, 124.8, 123.6, 122.5, 121.9, 116.0, 114.9, 109.2, 67.2, 52.8.

3-(1-(3,5-dimethylbenzyl)-1H-1,2,3-triazol-4-yl)-N-(3-oxo-3,4-dihydro-2H-benzo[b][1,4]oxazin-7-yl)benzamide (compound **f6**): Pure 96.2%. white solid, HR-MS(ESI): Calcd. C26H24N5O3 $[M+H]^+$ *m/z*: 454.1879, found: 454.1867. ^{1}H NMR(400MHz, DMSO-d_6): 10.67 (s, 1H), 10.28 (s, 1H), 8.71 (s, 1H), 8.39 (s, 1H), 8.06 (d, J = 8.0Hz, 1H), 7.88 (d, J = 8.0Hz, 1H), 7.60 (t, J = 4.0Hz, 2H), 7.50 (s, 1H), 7.38 (dd, J_1 = 4.0Hz, J_2 = 4.0Hz, 1H), 6.99 (s, 3H), 6.88 (d, J = 8.0Hz, 1H), 5.58 (s, 2H), 4.58 (s, 2H), 2.26 (s, 6H).^{13}C NMR(100MHz, DMSO-d_6): 165.6, 164.9, 146.5, 143.5, 138.4, 136.1, 136.1, 135.0, 131.3, 130.0, 129.5, 128.5, 127.4, 124.8, 123.6, 122.4, 116.0, 114.9, 109.1, 67.3, 53.6, 21.3.

3-(1-(2-cyanobenzyl)-1H-1,2,3-triazol-4-yl)-N-(3-oxo-3,4-dihydro-2H-benzo[b][1,4]oxazin-7-yl)benzamide (compound **f7**): Pure 95.8%. white solid, HR-MS(ESI): Calcd. C25H19N6O3 $[M+H]^+$ *m/z*: 451.1519, found: 451.1504. ^{1}H NMR(400MHz, DMSO-d_6): 10.67 (s, 1H), 10.29 (s, 1H), 8.75 (s, 1H), 8.38 (s, 1H), 8.06 (d, J = 8.0Hz, 1H), 7.94 (d, J = 8.0Hz, 1H), 7.89 (d, J = 8.0Hz, 1H), 7.76 (t, J = 8.0Hz, 1H), 7.63–7.59 (m, 2H), 7.50–7.48 (m, 2H), 7.36 (dd, J_1 = 4.0Hz, J_2 = 4.0Hz, 1H), 6.88 (d, J = 8.0Hz, 1H), 5.90 (s, 2H), 4.58 (s, 2H). ^{13}C NMR(100MHz, DMSO-d_6): 165.6, 165.0, 146.5, 143.5, 138.9, 136.1, 135.0, 134.3, 133.9, 131.1, 130.1, 129.8, 129.5, 128.6, 127.5, 124.9, 123.6, 122.9, 117.4, 116.0, 114.9, 111.7, 109.2, 67.2, 51.8.

N-(3-oxo-3,4-dihydro-2H-benzo[b][1,4]oxazin-7-yl)-3-(1-(3-(trifluoromethyl)benzyl)-1H-1,2,3-triazol-4-yl)benzamide (compound **f8**): Pure 97.2%. white solid, HR-MS(ESI): Calcd. C25H19F5N5O3 $[M+H]^+$ *m/z*: 494.1440, found: 494.1433. ^{1}H NMR(400MHz, DMSO-d_6): 10.62 (s, 1H), 10.24 (s, 1H), 8.70 (s, 1H), 8.31 (s, 1H), 7.99 (d, J = 8.0Hz, 1H), 7.82 (d, J = 8.0Hz, 1H), 7.71–7.66 (m, 2H), 7.60–7.53 (m, 3H), 7.42 (s, 1H), 7.29 (d, J = 8.0Hz, 1H), 6.84 (d, J = 8.0Hz, 1H), 5.74 (s, 2H), 4.58 (s, 2H). ^{13}C NMR(100MHz, DMSO-d_6): 165.7, 165.1, 146.6, 143.5, 137.6, 136.0, 134.9, 132.6, 131.1, 130.5, 130.1, 129.8, 129.6, 128.6, 127.5, 125.8, 125.5, 125.5, 125.0, 125.0, 124.8, 123.6, 123.0, 122.6, 116.0, 115.0, 109.2, 67.2, 52.8.

3-(1-(3-chloro-4-fluorobenzyl)-1H-1,2,3-triazol-4-yl)-N-(3-oxo-3,4-dihydro-2H-benzo[b][1,4]oxazin-7-yl)benzamide (compound **f9**): Pure 98.0%. white solid, HR-MS(ESI): Calcd. C24H18ClFN5O3 $[M+H]^+$ *m/z*: 478.1082, found: 478.1073. ^{1}H NMR(400MHz, DMSO-d_6): 10.68 (s, 1H), 10.29 (s, 1H), 8.75 (s, 1H), 8.38 (s, 1H), 8.06 (d, J = 4.0Hz, 1H), 7.89 (d, J = 8.0Hz, 1H), 7.69–7.59 (m, 2H), 7.50–7.36 (m, 4H), 6.89 (d, J = 8.0Hz, 1H), 5.70 (s, 2H), 4.58 (s, 2H). ^{13}C NMR(100MHz, DMSO-d_6): 165.6, 165.0, 158.7, 146.6, 143.5, 136.1, 135.0, 134.1, 134.1, 131.2, 131.0, 130.9, 129.7, 129.6, 129.5, 129.5, 129.5, 128.5, 127.5, 124.8, 123.6, 122.5, 117.9, 117.7, 116.0, 114.9, 109.2, 67.2, 52.6, 52.2.

3-(1-(2,6-difluorobenzyl)-1H-1,2,3-triazol-4-yl)-N-(3-oxo-3,4-dihydro-2H-benzo[b][1,4]oxazin-7-yl)benzamide (compound **f10**): Pure 96.9%. white solid, HR-MS(ESI): Calcd. C24H18F2N5O3 $[M+H]^+$ *m/z*: 462.1378, found: 462.1370. ^{1}H NMR(400MHz, DMSO-d_6): 10.66 (s, 1H), 10.26 (s, 1H), 8.71 (s, 1H), 8.38 (s, 1H), 8.06 (d, J = 4.0Hz, 1H), 7.87 (d, J = 8.0Hz, 1H), 7.61–7.49 (m, 3H), 7.38 (d, J = 4.0Hz, 1H), 7.21 (t, J = 8.0Hz, 2H), 6.88 (d, J = 8.0Hz, 1H), 5.74 (s, 2H), 4.58 (s, 2H). ^{13}C NMR(100MHz, DMSO-d_6): 165.6, 164.9, 146.4, 143.5, 136.1, 132.2, 131.1, 129.4,

128.5, 127.5, 124.9, 123.6, 122.5, 116.0, 114.9, 112.5, 112.3, 109.1, 67.3.

3-(1-(2-cyano-5-fluorobenzyl)-1H-1,2,3-triazol-4-yl)-N-(3-oxo-3,4-dihydro-2H-benzo[b][1,4]oxazin-7-yl)benzamide (compound **f11**): Pure 96.5%. white solid, HR-MS(ESI): Calcd. $C_{25}H_{18}FN_6O_3$ $[M+H]^+$ *m/z*: 469.1424, found: 469.1410. ^1H NMR(400MHz, DMSO-d_6): 10.66 (s, 1H), 10.29 (s, 1H), 8.77 (s, 1H), 8.38 (s, 1H), 8.07–8.04 (m, 1H), 7.89 (d, J = 8.0Hz, 1H), 7.61 (t, J = 8.0Hz, 1H), 7.49–7.35 (m, 4H), 6.88 (d, J = 8.0Hz, 1H), 5.90 (s, 2H), 4.58 (s, 2H). ^{13}C NMR(100MHz, DMSO-d_6): 166.2, 165.6, 164.9, 163.7, 146.5, 143.5, 142.4, 142.3, 137.0, 136.9, 136.1, 135.0, 131.1, 129.5, 128.6, 127.6, 124.9, 123.6, 123.0, 118.0, 117.7, 117.5, 117.2, 116.7, 116.0, 114.9, 109.1, 108.5, 108.4, 67.3, 51.5.

3-(1-(2-bromobenzyl)-1H-1,2,3-triazol-4-yl)-N-(3-oxo-3,4-dihydro-2H-benzo[b][1,4]oxazin-7-yl)benzamide (compound **f12**): Pure 98.2%. white solid, HR-MS(ESI): Calcd. $C_{24}H_{19}BrN_5O_3$ $[M+H]^+$ *m/z*: 504.0671, found: 504.0666. ^1H NMR(400MHz, DMSO-d_6): 10.67 (s, 1H), 10.28 (s, 1H), 8.69 (s, 1H), 8.39 (s, 1H), 8.06 (d, J = 4.0Hz, 1H), 7.88 (d, J = 4.0Hz, 1H), 7.72 (d, J = 8.0Hz, 1H), 7.60 (t, J = 8.0Hz, 1H), 7.49–7.43 (m, 2H), 7.38–7.27 (m, 3H), 6.88 (d, J = 8.0Hz, 1H), 5.77 (s, 2H), 4.58 (s, 2H). ^{13}C NMR(100MHz, DMSO-d_6): 165.6, 164.9, 146.4, 143.5, 136.1, 135.1, 135.0, 133.4, 131.2, 131.1, 130.9, 129.5, 128.8, 128.5, 127.5, 123.6, 123.4, 122.8, 116.0, 114.9, 109.1, 67.3, 53.7.

3-(1-(4-bromo-2-fluorobenzyl)-1H-1,2,3-triazol-4-yl)-N-(3-oxo-3,4-dihydro-2H-benzo[b][1,4]oxazin-7-yl)benzamide (compound **f13**): Pure 96.6%. white solid, HR-MS(ESI): Calcd. $C_{24}H_{18}BrFN_5O_3$ $[M+H]^+$ *m/z*: 522.0577, found: 522.0572. ^1H NMR(400MHz, DMSO-d_6): 10.67 (s, 1H), 10.27 (s, 1H), 8.71 (s, 1H), 8.38 (s, 1H), 8.06 (d, J = 4.0Hz, 1H), 7.88 (d, J = 8.0Hz, 1H), 7.63–7.36 (m, 8H), 6.88 (d, J = 8.0Hz, 1H), 5.72 (s, 2H), 4.58 (s, 2H). ^{13}C NMR(100MHz, DMSO-d_6): 165.6, 164.9, 146.5, 143.5, 136.1, 135.0, 133.0, 132.9, 132.8, 131.2, 129.5, 128.6, 128.5, 128.3, 127.5, 124.8, 123.6, 122.8, 122.6, 119.7, 119.5, 116.0, 114.9, 109.1, 67.3, 47.7, 47.2.

3-(1-(3-fluorobenzyl)-1H-1,2,3-triazol-4-yl)-N-(3-oxo-3,4-dihydro-2H-benzo[b][1,4]oxazin-7-yl)benzamide (compound **f14**): Pure 95.1%. white solid, HR-MS(ESI): Calcd. $C_{24}H_{19}FN_5O_3$ $[M+H]^+$ *m/z*: 444.1472, found: 444.1463. ^1H NMR(400MHz, DMSO-d_6): 10.67 (s, 1H), 10.28 (s, 1H), 8.76 (s, 1H), 8.39 (s, 1H), 8.06 (d, J = 8.0Hz, 1H), 7.88 (d, J = 8.0Hz, 1H), 7.60 (d, J = 8.0Hz, 1H), 7.50–7.45 (m, 2H), 7.38 (dd, J1 = 4.0Hz, J2 = 4.0Hz, 1H), 7.25–7.17 (m, 3H), 6.88 (d, J = 8.0Hz, 1H), 5.72 (s, 2H), 4.58 (s, 2H). ^{13}C NMR(100MHz, DMSO-d_6): 165.6, 164.9, 163.8, 161.4, 146.6, 143.5, 139.0, 138.9, 135.0, 131.4, 131.3, 131.2, 129.5, 128.5, 127.5, 124.8, 124.5, 124.5, 123.6, 122.6, 116.0, 115.4, 115.2, 114.9, 109.1, 67.3, 52.9.

3-(1-(2-chloro-6-fluorobenzyl)-1H-1,2,3-triazol-4-yl)-N-(3-oxo-3,4-dihydro-2H-benzo[b][1,4]oxazin-7-yl)benzamide (compound **f15**): Pure 94.7%. white solid, HR-MS(ESI): Calcd. $C_{24}H_{18}ClFN_5O_3$ $[M+H]^+$ *m/z*: 478.1082, found: 478.1069. ^1H NMR(400MHz, DMSO-d_6): 10.66 (s, 1H), 10.26 (s, 1H), 8.69 (s, 1H), 8.37 (s, 1H), 8.06 (d, J = 8.0Hz, 1H), 7.87 (d, J = 8.0Hz, 1H), 7.61–7.35 (m, 5H), 6.88 (d, J = 8.0Hz, 1H), 5.79 (s, 2H), 4.57 (s, 2H). ^{13}C NMR(100MHz, DMSO-d_6): 165.6, 164.9, 146.2, 143.5, 136.1, 135.0, 132.4, 132.3, 131.1, 129.4, 128.6, 127.5, 126.4, 124.9, 123.6, 122.6, 116.0, 115.6, 115.3, 114.9, 109.1, 67.2, 45.1.

N-(3-oxo-3,4-dihydro-2H-benzo[b][1,4]oxazin-7-yl)-3-(1-(4-(trifluoromethyl)benzyl)-1H-1,2,3-triazol-4-yl)benzamide (compound **f16**): Pure 97.6%. white solid, HR-MS(ESI): Calcd. $C_{25}H_{19}F_3N_5O_3$ $[M+H]^+$ *m/z*: 494.1440, found: 494.1418. ^1H NMR(400MHz, DMSO-d_6): 10.67 (s, 1H), 10.28 (s, 1H), 8.78 (s, 1H), 8.39 (s, 1H), 8.06 (d, J = 8.0Hz, 1H), 7.89 (d, J = 8.0Hz, 1H), 7.79–7.76 (m, 3H), 7.61–7.59 (m, 4H), 7.50 (s, 1H), 7.37 (d, J = 8.0Hz, 1H), 5.82 (s, 2H), 4.58 (s, 2H). ^{13}C NMR(100MHz, DMSO-d_6): 165.5, 164.9, 146.7, 143.5, 141.0, 136.1, 135.0, 131.2, 129.5, 129.4, 129.4, 129.1, 128.5, 127.5, 126.2, 126.2, 126.0, 126.0, 124.8, 123.6, 122.8, 116.0, 114.9, 109.1, 67.3, 53.2, 52.9.

3-(1-(3-bromobenzyl)-1H-1,2,3-triazol-4-yl)-N-(3-oxo-3,4-dihydro-2H-benzo[b][1,4]oxazin-7-yl)benzamide (compound **f17**): Pure 96.7%. white solid, HR-MS(ESI): Calcd. $C_{24}H_{19}BrN_5O_3$ $[M+H]^+$ *m/z*: 504.0671, found: 504.0657. ^1H NMR(400MHz, DMSO-d_6): 10.67 (s, 1H), 10.28 (s, 1H), 8.76 (s, 1H), 8.39 (s, 1H), 8.07–8.04 (m, 1H), 7.90–7.87 (m, 1H), 7.62–7.56 (m, 3H), 7.50 (s, 4H), 7.38–7.37 (m, 3H), 6.88 (d, J = 8.0Hz, 1H), 5.70 (s, 2H), 4.58 (s, 2H). ^{13}C NMR(100MHz, DMSO-d_6): 165.6, 164.9, 146.6, 143.5, 138.9, 136.1, 135.0, 131.6, 131.5, 131.2, 129.5, 128.5, 127.5, 127.5, 124.8, 123.6, 122.67, 122.3, 116.0, 114.8, 109.1, 67.3, 52.7, 49.0.

3-(1-(4-chlorobenzyl)-1H-1,2,3-triazol-4-yl)-N-(3-oxo-3,4-dihydro-2H-benzo[b][1,4]oxazin-7-yl)benzamide (compound **f18**): Pure 95.8%. white solid, HR-MS(ESI): Calcd. $C_{24}H_{19}ClN_5O_3$ $[M+H]^+$ *m/z*: 460.1176, found: 460.1152. ^1H NMR(400MHz, DMSO-d_6): 10.67 (s, 1H), 10.27 (s, 1H), 8.73 (s, 1H), 8.38 (s, 1H), 8.05 (d, J = 8.0Hz, 1H), 7.88 (d, J = 8.0Hz, 1H), 7.60 (t, J = 8.0Hz, 1H), 7.49–7.46 (m, 3H), 7.42–7.35 (m, 3H), 6.88 (d, J = 8.0Hz, 1H), 5.69 (s, 2H), 4.58 (s, 2H). ^{13}C NMR(100MHz, DMSO-d_6): 165.6, 164.9, 146.6, 143.5, 136.1, 135.3, 135.0, 133.4, 131.2, 130.4, 129.5, 129.3, 128.5, 127.5, 124.8, 123.6, 122.5, 116.0, 114.9, 109.1, 67.3, 52.8.

3-(1-(3-iodobenzyl)-1H-1,2,3-triazol-4-yl)-N-(3-oxo-3,4-dihydro-2H-benzo[b][1,4]oxazin-7-yl)benzamide (compound **f19**): Pure 97.1%. white solid, HR-MS(ESI): Calcd. $C_{24}H_{19}IN_5O_3$ $[M+H]^+$ *m/z*: 552.0533, found: 552.0517. ^1H NMR(400MHz, DMSO-d_6): 10.67 (s, 1H), 10.28 (s, 1H), 8.76 (s, 1H), 8.38 (s, 1H), 8.05 (d, J = 8.0Hz, 1H), 7.88 (d, J = 8.0Hz, 1H), 7.79 (s, 1H), 7.41 (d, J = 8.0Hz, 1H), 7.60 (t, J = 8.0Hz, 1H), 7.50 (s, 1H), 7.38 (t, J = 4.0Hz, 2H), 7.21 (t, J = 4.0Hz, 2H), 6.88 (d, J = 8.0Hz, 1H), 5.66 (s, 2H), 4.58 (s, 2H). ^{13}C NMR(100MHz, DMSO-d_6): 165.6, 164.9, 146.6, 143.5, 138.8, 137.4, 137.0, 136.1, 135.0, 131.4, 131.2, 129.5, 128.5, 127.9, 127.5, 124.8, 123.6, 122.6, 116.0, 114.8, 109.1, 95.5, 67.3, 52.6.

3-(1-(2-methylbenzyl)-1H-1,2,3-triazol-4-yl)-N-(3-oxo-3,4-dihydro-2H-benzo[b][1,4]oxazin-7-yl)benzamide (compound **f20**): Pure 96.4%. white solid, HR-MS(ESI): Calcd. $C_{25}H_{22}N_5O_3$ $[M+H]^+$ *m/z*: 440.1723, found: 440.1714. ^1H NMR(400MHz, DMSO-d_6): 10.66 (s, 1H), 10.26 (s, 1H), 8.63 (s, 1H), 8.37 (s, 1H), 8.06 (d, J = 4.0Hz, 1H), 7.86 (d, J = 8.0Hz, 1H), 7.58 (t, J = 8.0Hz, 1H), 7.48 (s, 1H), 7.35 (d, J = 8.0Hz, 1H), 7.27–7.16 (m, 4H), 6.87 (d, J = 8.0Hz, 1H), 5.68 (s, 2H), 4.57 (s, 2H). ^{13}C NMR(100MHz, DMSO-d_6): 165.6, 164.9, 146.4, 143.5, 136.8, 136.1, 135.0, 134.4, 131.3, 130.9, 130.9, 129.4, 129.2, 128.8, 128.5, 127.4, 126.8, 124.8, 123.6, 122.4, 116.0, 114.8, 109.1, 67.3, 51.7, 19.1.

6.2 Biological study

6.2.1 Drug preparation and administration

Test compounds were dissolved in dimethyl sulfoxide (DMSO) at 10 mM as stock solution and diluted before *in vitro* drug

administration. For the *in vivo* experiments, test compound were dissolved by 5% DMSO, 40% PEG300, 1% Tween 80 and saline for gavage administration.

6.2.2 Cell culture

BV-2 cells (National Collection of Authenticated Cell Cultures, China). Cells were cultured in Dulbecco's modified Eagle's medium (LifeTech, Grand Island, NY, United States) supplemented with 10% heat-inactivated fetal bovine serum (Gibco, Grand Island, NY, United States) at 37°C in a humidified atmosphere containing 5% CO_2.

6.2.3 Griess assay

BV-2 cells were seeded at a density of 2×10^4 cells per well in a 96-well culture plate and incubated in a humidified incubator with 5% CO_2 at 37°C. After 24 h of incubation, 10 μM of the test compounds were added to the treatment group and incubated for 2 h. Subsequently, LPS was added to both the treatment group and the LPS model group to achieve a final concentration of 100 ng/mL. The cells were then incubated for another 24 h. After incubation, 50 μL of the supernatant from each well was mixed with 50 μL of Griess reagent and incubated at room temperature for 15 min. The optical density (OD) at 540 nm was measured using a microplate reader (Biotek).

6.2.4 MTT assay

BV-2 cells were seeded at a density of 2×10^4 cells per well in a 96-well culture plate and incubated in a humidified incubator with 5% CO2 at 37°C. After 24 h of incubation, 10 μM of the test compounds were added to the treatment group and incubated for 2 h. Subsequently, LPS was added to both the treatment group and the LPS model group to achieve a final concentration of 100 ng/mL. The cells were then incubated for another 24 h. Following this, 0.5 mg/mL MTT was added to each well for viable cell staining. After 1 h of incubation, the culture medium was discarded, and 100 μL of DMSO was added to each well. The plate was then shaken to fully dissolve the formazan crystals. The optical density (OD) at 490 nm was measured using a microplate reader (Biotek).

6.2.5 Real-time PCR and transcriptome analysis

Total RNA was extracted using TRNzol (Tiangen Biotech Co., LTD., Beijing, China) following the manufacturer's instructions. Complementary DNA (cDNA) was synthesized using the HiScript III RT SuperMix for qPCR (Vazyme Biotech Co., Ltd., Nanjing, China) with 500 ng of total RNA. Quantitative real-time PCR was performed using the ChamQ Pro Universal SYBR qPCR Master Mix (Vazyme Biotech Co., Ltd., Nanjing, China) on an ABI 7500 real-time PCR system (Applied Biosystems, Foster City, CA), according to the manufacturer's instructions. The primers used are listed in Table 4. Relative gene expression was calculated using the ΔΔCT method.

6.2.6 Western blot analysis

Whole cell extracts were prepared by lysing cells on ice for 30 min using RIPA lysis buffer containing 1 mM NaF, 1 mM Na3VO4, 1 mM PMSF, and 1% Protease Inhibitor Cocktail (Sigma, St. Louis, MO, United States). The lysates were centrifuged at 12,000 g for 15 min at 4°C, and the supernatants were collected. Protein concentrations were measured using the BCA protein assay (Thermo Scientific, Rockford, IL, United States) according to the manufacturer's instructions.

Western blotting was performed based on previously described methods. Equal amounts of protein were separated by sodium dodecyl sulfate polyacrylamide gel electrophoresis (SDS-PAGE) and transferred onto 0.2 μm nitrocellulose membranes (Whatman, Maidstone, Kent, United Kingdom). The membranes were blocked in 5% skimmed milk in Tris-buffered saline with Tween 20 (TBST; 50 mM Tris base, 150 mM NaCl, 0.05% v/v Tween 20, pH 7.4) for at least 1 h and then incubated with primary antibodies overnight at 4°C. Following incubation, the blots were washed three times with TBST buffer and then incubated with horseradish peroxidase-conjugated secondary antibodies (1:5,000, Kangchen Biotechnology, Shanghai, China) for 1 h at room temperature. The blots were developed using an enhanced chemiluminescence reagent (Millipore Corporation, Bedford, MA, United States) after three additional washes with TBST buffer. Protein band intensities were analyzed using ImageJ software.

The primary antibodies used were as follows: anti-COX-2 (1:1,000, Cell Signaling Technology, Beverly, MA, United States), anti-iNOS (1:500, BD Biosciences, San Jose, CA, United States), anti-Nrf2 (1:1,000, Proteintech, Wuhan, China), anti-HO-1 (1:5,000, Proteintech, Wuhan, China), and anti-β-actin (1:10,000, Sigma-Aldrich, St. Louis, MO, United States).

6.2.7 Cellular ROS level measurement

BV-2 microglia cells were seeded at a density of 1×10^5 cells per well in a 12-well culture plate. After treatment with LPS for 18 h, the cells were collected by trypsin digestion. 1 mL of DCFH-DA staining solution was added and incubated at 37°C for 30 min. The cells were washed twice with 1 × PBS and mean fluorescence intensity (MFI) was detected using a flow cytometer (BD Accuri™ C6, United States).

6.2.8 Acute toxicity test

Kunming mice (half male and half female, 8 weeks old) were randomly allocate into 4 groups: e16-treated group (male), e16-treated group (female), Vehicle group (male) and Vehicle group (female). The Vehicle groups were given corresponding solvents, while the e16 groups were given the e16 solution (250 mg/kg, respectively). Body weight and appearance were monitored for a total period of 15 days (from the first day after treating with e16). The mice were killed on the 15th day, and blood samples were collected for the biochemistry test. Then, we measured liver and kidney function indicators such as alanine aminotransferase (ALT) and aspartate aminotransferase (AST) (Nanjing Jiancheng Bioengineering Institute, China). The organs (heart, liver, spleen, lungs, kidneys) were harvested, weighed and fixed in 10% formaldehyde and paraffin-embedded for histological examination. Finally, these sections were stained with haematoxylin and eosin for light microscopic examination.

6.2.9 Statistical analyses

Data were presented as means ± SEM and performed using Graph Prim 7.0. A two-tailed Student's *t*-test or one-way analysis of variance followed by a Student-Newman-Keuls (SNK) test were used to assess significant differences. $P < 0.05$ was considered statistically significant.

6.2.10 Molecular docking methods

The X-ray crystal structure of mouse Keap1 [PDB ID: 1X2R (Padmanabhan et al., 2006)] which possesses an Nrf2 binding site was retrieved from the Protein Data Bank (https://www.rcsb.org) with a resolution value of 1.70 Å. The initial structure was processed using Protein Preparation Wizard in Schrödinger (Sastry et al., 2013). The chemical structures of e2, e16, and e20 were prepared using the LigPrep module (Schrödinger, 2021). The Nrf2 binding site was defined as the docking area by using the Receptor Grid Generation tool, and the Grid file was used to dock ligands into receptor protein to identify the potential binding modes (Friesner et al., 2004).

Data availability statement

The datasets presented in this study can be found in online repositories. The names of the repository/repositories and accession number(s) can be found in the article/Supplementary Material.

Ethics statement

The animal study was approved by The Laboratory Animal Welfare and Ethical review of Henan Institute of Science and Technology. The study was conducted in accordance with the local legislation and institutional requirements.

Author contributions

XH: Data curation, Investigation, Writing–original draft. LM: Conceptualization, Data curation, Funding acquisition, Project administration, Writing–review and editing. HZ: Data curation, Investigation, Methodology, Writing–original draft. LW: Data curation, Formal Analysis, Writing–original draft. BH: Data curation, Software, Writing–original draft. JG: Software, Supervision, Writing–original draft. JW: Conceptualization, Investigation, Methodology, Project administration, Writing–review and editing.

Funding

The author(s) declare that financial support was received for the research, authorship, and/or publication of this article. This work was supported by the Key Scientific Research Projects of Universities in Henan Province (24A350006) and The Henan Province Medical Science and Technology Research Project (LHGJ20230450) and the International Science and Technology Cooperation Project of Henan Province of China (242102520016).

Conflict of interest

The authors declare that the research was conducted in the absence of any commercial or financial relationships that could be construed as a potential conflict of interest.

Generative AI statement

The author(s) declare that no Generative AI was used in the creation of this manuscript.

Publisher's note

References

Begam, R., Shajahan, A., Shefin, B., and Murugan, V. (2022). Synthesis of novel naphthalimide tethered 1,2,3-triazoles: *in vitro* biological evaluation and docking study of anti-inflammatory inhibitors. *J. Mol. Struct.* 1254, 132364. doi:10.1016/j.molstruc.2022.132364

Chen, H., Guan, X., Liu, Q., Yang, L., Guo, J., Gao, F., et al. (2022). Co-assembled nanocarriers of *de novo* thiol-activated hydrogen sulfide donors with an RGDFF pentapeptide for targeted therapy of non-small cell lung cancer. *ACS Appl. Mater. and Interfaces* 14, 53475–53490. doi:10.1021/acsami.2c14570

Cidade, H., Pinto, M., and Correia-da-Silva, M. (2021). Recent advances in bioactive flavonoid hybrids linked by 1,2,3-triazole ring obtained by click Chemistry. *Molecules* 27, 230. doi:10.3390/molecules27010230

Cintia, R., Liliana, B., Ozgur, O. C., Milorad, D., Fladmark, K. E., Sibel, E., et al. (2024). The immune system in Parkinson's disease: what we know so far. *Brain* 10. doi:10.1093/brain/awae177

Davies, T. G., Wixted, W. E., Coyle, J. E., Griffiths-Jones, C., Hearn, K., Mcmenamin, R. L., et al. (2016). Mono-acidic inhibitors of the kelch-like ech-associated protein 1: nuclear factor erythroid 2-related factor 2 (Keap1:Nrf2) protein-protein interaction with high cell potency identified by fragment-based Discovery. *J. Med. Chem.* 3991, 3991–4006. doi:10.1021/acs.jmedchem.6b00228

Dong, Y., Li, X., Cheng, J., and Hou, L. (2019). Drug development for Alzheimer's disease: microglia induced neuroinflammation as a target? *Int. J. Mol. Sci.* 20, 558. doi:10.3390/ijms20030558

Felipe, J. L., Cassamale, T. B., Loureno, L. D., Carvalho, D. B., Neves, A. R. D., Duarte, R. C. F., et al. (2022). Anti-inflammatory, ulcerogenic and platelet activation evaluation of novel 1,4-diaryl-1,2,3-triazole neolignan-celecoxib hybrids. *Bioorg. Chem.* 119, 105485. doi:10.1016/j.bioorg.2021.105485

Friesner, R. A., Banks, J. L., Murphy, R. B., Halgren, T. A., Klicic, J. J., Mainz, D. T., et al. (2004). Glide: a new approach for rapid, accurate docking and scoring. 1. Method and assessment of docking accuracy. *J. Med. Chem.* 47, 1739–1749. doi:10.1021/jm0306430

Gao, C., Jiang, J., Tan, Y., and Chen, S. (2023). Microglia in neurodegenerative diseases:mechanism and potential therapeutic targets. *Signal Transduct. Target. Ther.* 8, 359–4782. doi:10.1038/s41392-023-01588-0

Guan, Q., Xing, S., Wang, L., Zhu, J., Guo, C., Xu, C., et al. (2024). Triazoles in medicinal Chemistry: physicochemical properties, bioisosterism, and application. *J. Med. Chem.* 67, 7788–7824. doi:10.1021/acs.jmedchem.4c00652

Hasui, T., Matsunaga, N., Ora, T., Ohyabu, N., Nishigaki, N., Imura, Y., et al. (2011). Identification of benzoxazin-3-one derivatives as novel, potent, and selective nonsteroidal mineralocorticoid receptor antagonists. *J. Med. Chem.* 54, 8616–8631. doi:10.1021/jm2011645

He, X., Chen, H., Xu, C., Fan, J., Xu, W., Li, Y., et al. (2020). Ratiometric and colorimetric fluorescent probe for hypochlorite monitor and application for bioimaging in living cells, bacteria and zebrafish. *J. Hazard. Mater.* 388, 122029. doi:10.1016/j.jhazmat.2020.122029

Hou, X., Mao, L., Guo, Y., Wang, L., Peng, L., Wang, H., et al. (2024). Synthesis and antitumor activity of dolutegravir derivatives bearing 1,2,3-triazole moieties. *BMC Chem.* 18, 97. doi:10.1186/s13065-024-01205-3

Jung, H. J., Cho, D. Y., Han, J. H., Park, K. D., Choi, D. K., Kim, E., et al. (2023). Synthesis of 1-(4-(dimethylamino)phenyl)-3,4-diphenyl-1H-pyrrole-2,5-dione analogues and their anti-inflammatory activities in lipopolysaccharide-induced BV2 cells. *Bioorg Med. Chem. Lett.* 92, 129408. doi:10.1016/j.bmcl.2023.129408

Kim, T. W., Yong, Y., Shin, S. Y., Jung, H., Park, K. H., Lee, Y. H., et al. (2015). Synthesis and biological evaluation of phenyl-1H-1,2,3-triazole derivatives as anti-inflammatory agents. *Bioorg. Chem.* 59, 1–11. doi:10.1016/j.bioorg.2015.01.003

Kristensen, S. L., Hedtjärn, M., Schrattenholz, A., Henn, A., Pörzgen, P. P., and Leist, M. (2009). The suitability of BV2 cells as alternative model system for primary microglia cultures or for animal experiments examining brain inflammation. *Altex* 26, 83–94. doi:10.14573/altex.2009.2.83

Li, N., Guo, Y., Gong, Y., Zhang, Y., Fan, W., Yao, K., et al. (2021). The anti-inflammatory actions and mechanisms of acupuncture from acupoint to target organs via neuro-immune regulation. *J. Inflamm. Res.* 14, 7191–7224. doi:10.2147/JIR.S341581

Li, T., Li, Y., Chen, J., Nan, M., Zhou, X., Yang, L., et al. (2024). Hyperibone J exerts antidepressant effects by targeting ADK to inhibit microglial P2X7R/TLR4-mediated neuroinflammation. *J. Adv. Res.* doi:10.1016/j.jare.2024.07.015

Liu, Z., Liu, J., Gao, E., Mao, L., Hu, S., and Li, S. (2024). Synthesis and *in vitro* antitumor activity evaluation of gefitinib-1,2,3-triazole derivatives. *Molecules* 29, 837. doi:10.3390/molecules29040837

Madasu, C., Karri, S., Sangaraju, R., Sistla, R., and Uppuluri, M. V. (2020). Synthesis and biological evaluation of some novel 1,2,3-triazole hybrids of myrrhanone B isolated from Commiphora mukul gum resin: identification of potent antiproliferative leads active against prostate cancer cells (PC-3). *Eur. J. Med. Chem.* 188, 111974. doi:10.1016/j.ejmech.2019.111974

Mao, L. F., Wang, Y. W., Zhao, J., Xu, G. Q., and Li, Y. M. (2020). Discovery of icotinib-1,2,3-triazole derivatives as Ido1 inhibitors. *Front. Pharmacol.* 11, 579024. doi:10.3389/fphar.2020.579024

Méndez-Rojas, C., Quiroz, G., Faúndez, M., Gallardo-Garrido, C., Pessoa-Mahana, C. D., Chung, H., et al. (2018). Synthesis and biological evaluation of potential acetylcholinesterase inhibitors based on a benzoxazine core. *Arch. Der Pharm.* 351, e1800024. doi:10.1002/ardp.201800024

Menghere, G., Olajide, O., and Hemming, K. (2020). The synthesis and anti-inflammatory evaluation of 1,2,3-triazole linked isoflavone benzodiazepine hybrids. *ARKIVOC* 2020, 306–321. doi:10.24820/ark.5550190.p011.396

Padmanabhan, B., Tong, K. I., Ohta, T., Nakamura, Y., Scharlock, M., Ohtsuji, M., et al. (2006). Structural basis for defects of Keap1 activity provoked by its point mutations in lung cancer. *Mol. Cell* 21, 689–700. doi:10.1016/j.molcel.2006.01.013

Park, Y. J., Yang, H. J., Li, W., Oh, Y. C., and Go, Y. (2022). Menthae herba attenuates neuroinflammation by regulating CREB/Nrf2/HO-1 pathway in BV2 microglial cells. *Antioxidants (Basel, Switz.)* 11, 649. doi:10.3390/antiox11040649

Sagam, R. R., Azam, M., Al-Resayes, S. I., Banothu, D., Nukala, S. K., and Thirukovela, N. S. (2024). IMesCuCl/TBHP system for aqueous oxidative amidation: synthesis of new amide derivatives as EGFR targeting anti-breast cancer agents and computational studies. *J. Mol. Struct.* 1308, 137922. doi:10.1016/j.molstruc.2024.137922

Sambasiva Rao, P., Kurumurthy, C., Veeraswamy, B., Santhosh Kumar, G., Poornachandra, Y., Ganesh Kumar, C., et al. (2014). Synthesis of novel 1,2,3-triazole substituted-N-alkyl/aryl nitrone derivatives, their anti-inflammatory and anticancer activity. *Eur. J. Med. Chem.* 80, 184–191. doi:10.1016/j.ejmech.2014.04.052

Sasimol, U., Chayanut, K., Peraphan, P., Thanyaluck, P., and Prachya, K. (2018). Sesamin suppresses LPS-induced microglial activation via regulation of TLR4 expression. *J. Funct. Foods* 49, 32–43. doi:10.1016/j.jff.2018.08.020

Sastry, G. M., Adzhigirey, M., Day, T., Annabhimoju, R., and Sherman, W. (2013). Protein and ligand preparation: parameters, protocols, and influence on virtual screening enrichments. *J. Comput. Aided Mol. Des.* 27, 221–234. doi:10.1007/s10822-013-9644-8

Schrödinger, L. J. S. I. N. Y. (2021). *Schrödinger release 2022-3: LigPrep*. Ny, USA.

Shafi, S., Mahboob Alam, M., Mulakayala, N., Mulakayala, C., Vanaja, G., Kalle, A. M., et al. (2012). Synthesis of novel 2-mercapto benzothiazole and 1,2,3-triazole based bis-heterocycles: their anti-inflammatory and anti-nociceptive activities. *Eur. J. Med. Chem.* 49, 324–333. doi:10.1016/j.ejmech.2012.01.032

Sun, X. Y., Li, L. J., Dong, Q. X., Zhu, J., Liu, R. T., Hou, S. J., et al. (2021). Rutin prevents tau pathology and neuroinflammation in a mouse model of Alzheimer's disease. *J. Neuroinflammation* 18, 131. doi:10.1186/s12974-021-02182-3

Wang, L., Zhao, D., Wang, H., Wang, L., Liu, X., and Zhang, H. (2021). FPS-ZM1 inhibits LPS-induced microglial inflammation by suppressing JAK/STAT signaling pathway. *Int. Immunopharmacol.* 100, 108117. doi:10.1016/j.intimp.2021.108117

Wang, L. L., Wang, H., Lin, S. J., Xu, X. Y., Hu, W. J., Liu, J., et al. (2024). ABBV-744 alleviates LPS-induced neuroinflammation via regulation of BATF2-IRF4-STAT1/3/5 axis. *Acta Pharmacol. Sin.* 45, 2077–2091. doi:10.1038/s41401-024-01318-4

Xie, H., Mao, L., Fan, G., Wu, Z., Wang, Y., Hou, X., et al. (2023). Design and synthesis of cabotegravir derivatives bearing 1,2,3-triazole and evaluation of anti-liver cancer activity. *Front. Pharmacol.* 14, 1265289. doi:10.3389/fphar.2023.1265289

Xu, Z., Zhao, S. J., and Liu, Y. (2019). 1,2,3-Triazole-containing hybrids as potential anticancer agents: current developments, action mechanisms and structure-activity relationships. *Eur. J. Med. Chem.* 183, 111700. doi:10.1016/j.ejmech.2019.111700

Yan, G., Pu, C., Lan, S., Zhong, X., Li, R., Hou, X., et al. (2019). Discovery of 4-phenyl-2H-benzo[b] [1,4]oxazin-3(4H)-one derivatives as potent and orally active PI3K/mTOR dual inhibitors. *Eur. J. Med. Chem.* 178, 667–686. doi:10.1016/j.ejmech.2019.06.021

Yang, L., Wang, Z.-D., Li, Z.-R., Chen, M.-H., Li, X.-M., Guo, C., et al. (2016). Anti-neuroinflammatory effect of Sophoraflavanone G from Sophora alopecuroides in LPS-activated BV2 microglia by MAPK, JAK/STAT and Nrf2/HO-1 signaling pathways. *Phytomedicine Int. J. Phytotherapy and Phytopharm.* 23, 1629–1637. doi:10.1016/j.phymed.2016.10.007

Yoon, S. H., Cho, D. Y., Han, J. H., Choi, D. K., Kim, E., and Park, J. Y. (2023). Synthesis of 1-(5-(4-chlorophenyl)-1-(2,4-dichlorophenyl)-4-methyl-1H-pyrazol-3-yl)-2-morpholinoethane-1,2-dione analogues and their inhibitory activities with reduced cytotoxicity in lipopolysaccharide-induced BV2 cells. *Bioorg Med. Chem. Lett.* 79, 129061. doi:10.1016/j.bmcl.2022.129061

Zhang, W., Xiao, D., Mao, Q., and Xia, H. (2023). Role of neuroinflammation in neurodegeneration development. *Signal Transduct. Target. Ther.* 8, 267–3680. doi:10.1038/s41392-023-01486-5

Zhou, X. W., Ma, H. L., Zhang, X., Jing, S. Y., Miao, J. Y., and Zhao, B. X. (2014). Synthesis of 6-cinnamoyl-2H-benzo[b] [1,4]oxazin-3(4H)-ones and their effects on A549 lung cancer cell growth. *Eur. J. Med. Chem.* 79, 95–101. doi:10.1016/j.ejmech.2014.03.087

Zhu, L. Q., Fan, X. H., Li, J. F., Chen, J. H., Wang, Z., Hu, X. L., et al. (2021). Discovery of a novel inhibitor of nitric oxide production with potential therapeutic effect on acute inflammation. *Bioorg. and Med. Chem. Lett.* 44, 128106. doi:10.1016/j.bmcl.2021.128106

Frontiers in Pharmacology

Explores the interactions between chemicals and living beings

The most cited journal in its field, which advances access to pharmacological discoveries to prevent and treat human disease.

Discover the latest Research Topics

See more →

Frontiers

Avenue du Tribunal-Fédéral 34
1005 Lausanne, Switzerland
frontiersin.org

Contact us

+41 (0)21 510 17 00
frontiersin.org/about/contact